LASER WELDING OF HIGH CARBON STEELS

by

Eric Ng Eng Seng BEng.(Hons)

Thesis presented for the Degree of Doctor of Philosophy under general regulations

Department of Mechanical Engineering
Faculty of Engineering
University of Glasgow
June, 1999.

SYNOPSIS

Laser welding, unlike conventional arc or gas welding, can be effectively utilised to produce high quality, clean and tough welds in high carbon steels. Results of welding high carbon steel are presented. The weld characteristics related to the fast cooling rate were critically evaluated and methods to reduce the rate of cooling were developed. The grain size produced in the fusion and narrow heat affected zones significantly affected the mechanical properties of the welded joint. Three lasers were used: Nd:YAG, CO_2 and a high power laser diode (HPDL).

The investigations were carried out using a pulsed, 400 W, Nd:YAG laser, a CW, 1.2 kW, CO_2 laser and a CW, 1.4 kW high power diode laser. For the Nd:YAG laser, the dual beam delivery system was achieved with a step index fibre to produce in-line process heat-treatment during welding. The spatial and temporal temperature distribution was controlled in the weld region to generate the desired mechanical properties, without losing the benefits of this low distortion joining process. For the CO_2 laser system, a dual beam system was successfully designed, fabricated and the performance of the multiple beam system was evaluated. The welding quality was characterised by quantifying the effect of different laser parameters and welding geometry, including flat, angular, clamped and unclamped.

The welding performance of the Nd:YAG laser was dependent on the welding speed, pulse width and pulse repetition frequency (PRF). The effect of varying the laser parameters was quantified by measuring the hardness profiles, tensile strength, weld width, weld penetration and the rate of weld volume formation. Furthermore, microscopic examination was conducted at the welded joint. The quality of the welds was improved by increasing the pulse width and pulse repetition frequency (PRF), achieving a deeper penetration, wider weld width and greater weld volume formation rate and a tougher weld. At a slower welding speed, and for higher pulse width and PRF, the hardness profiles were greatly reduced due to the greater spatial overlap of laser beam on the workpiece.

To provide heat treatment to enhance the weld quality, a dual beam delivery system was developed to implement the pre-heating or post-heating technique, simultaneously during the welding process. The weld quality for the dual beam geometry was compared to that achieved with a normal weld (single beam system). The dual beam system was effective in controlling the cooling rate to achieve the desired weld characteristics. For instance: reducing the hardness profile, improving the microstructure, achieving a wider weld bead, deeper weld penetration, a higher tensile strength and, furthermore, cracking was eliminated.

To greatly reduce the time spent experimenting and therefore the cost, a multifactorial designed experiment was done. This enabled the effect of numerous laser parameters and different weld geometries to be investigated simultaneously. The multifactorial designed experiments can also show the effect of interactions between parameters; this cannot be done using the one-at-a-time experimental method. The parameters investigated included: pulse width, PRF, translation speed, and normal, pre-heating and post-heating beam delivery geometries. The disadvantages of doing multifactorial investigations are that the results generally only show a trend, although a trend can highlight important laser parameters that need further investigation and optimisation. A general linear model was used to find the laser parameters which had a significant effect on the weld quality. This resulted in a faster, more efficient way to optimise the welding process. The weld quality was quantified by measuring the aspect ratio, weld volume formation rate and tensile strength, for the normal, pre-heated and post-heated welds.

The results from two different angles of incidence (0°,30°) for Nd:YAG laser welding were compared, as were effects of the pulse width and pulse repetition frequency (PRF) on the mechanical and microscopic properties of the weld. It was concluded that for the 30° welding configuration, a slower cooling rate was achieved, leading to a less brittle weld. The grain structure was typically fine and granular, and the structure was completely modified at the fusion zone. Additionally, a lower aspect ratio, higher

tensile strength and greater weld volume formation rate was obtained; this was due to the wider weld width produced with this geometry. Ultimately, a higher welding speed was achieved with the 30° clamping geometry.

Welds done with clamped and unclamped geometries and a CO_2 laser were compared. The clamped geometry gave improved hardness characteristics and produced a refine grain structure. Whereas, for the same operating conditions, the unclamped geometry gave a deeper weld penetration and wider weld width.

For CO_2 laser welding, preliminary experiments were devised to investigate a scanning beam technique for pre-heating or post-heating. This enabled control of the sample's phase transitions to deliver the specific desired weld characteristics, and showed significant improvement in the mechanical properties of the weld. Further, the results from this scanning technique were employed to develop a dual beam CO_2 laser system to achieve in-line process tempering to ameliorate the poor weld characteristics associated with single beam delivery systems.

A high power diode laser was used to weld the high carbon steel and the weld quality was compared to the conventional CO_2 laser. Hardly any thermal effects were generated, indicating that heat dissipation was too fast for the present level of power density delivered by the diode laser. It is shown that lower hardness profiles, wider weld bead, higher tensile strength and greater weld volume formation rate were achieved with the CO_2 laser.

For the CO_2 laser, a 30° clamped geometry was designed and fabricated to perform welding. The flat and 30° welding quality were assessed. The 30° weld configuration offered a substantial improvement in hardness, and less brittle welds were produced compared to the flat welding geometry.

An image processing system comprising a CCD camera acquisition and processing board were fabricated and tested. This system offered real time capability to measure

the fusion zone and surface irregularities. The image of the welded specimens were captured and the trace was correlated to the weld seam to analyse a bad or good quality weld surface. This system was successfully used to monitor the weld quality.

In conclusion, future work and systems are proposed which offer higher efficiencies and improvements in the design of dual beam delivery systems.

ACKNOWLEDGEMENT

I would like to express my gratitude to Dr Ian. A Watson for the helpful discussion, guidance, and patience on this research project throughout my Ph.D. work. In particular, his commitments to the research and his sharing of his knowledge and time that made this research a success.

Special thanks and appreciation are due to Jimmy Wilson, Brian Robb, George Falconer, Vic Mclauglin, Ian Peden and Alex Torry, who were there to help me to fabricate components and aiding with the experiments.

Finally, I would like to thank Isabelle Lawson for preparing the drawings throughout this thesis.

CONTENTS

LIST OF FIGURES

Figures From Chapter Two:

Figures From Chapter Three:

Figures From Chapter Four:

Figures From Chapter Five:

Figures From Chapter Six:

Figures From Chapter Seven:

LIST OF TABLES

Tables

NOMENCLATURE

		UNITS
A	focus beam area	m^2
C	specific heat capacity	$Jkg^{-1}k^{-1}$
D	pulse duration	ms
E	pulse energy	J
ε	emissivity	
Io	power intensity	Wm^{-2}
K	thermal conductivity	$Wm^{-1}k^{-1}$
κ	thermal diffusivity	$m^{-2}s$
L	thickness of material	mm
L_v	latent heat vaporisation	Jkg^{-1}
Po	mean output power	W
ρ	material density	kgm^{-3}
R	pulse repetition frequency	Hz
T_b	temperature boiling point	K
T_m	temperature melting point	K
z	distance penetrating into the sample	mm

CHAPTER ONE
INTRODUCTION TO LASER WELDING

1.1 Laser Systems Review

Since the introduction of laser technology to manufacturing, which began in earnest in the mid 1960s, CO_2 and Nd:YAG lasers have been recognized for their separate inherent processing capabilities. In the early 1970's the push for greater cavity efficiencies led to the development of the fast-axial-flow CO_2 laser. This cavity design offered the advantage of a ten fold increase in the average output power per meter of discharge over the slow-flow CO_2 laser and a reduction in package size of the unit. The down side of the development was the requirement of high speed roots blowers to recirculate the lasing gases. These blowers tended to ingest foreign material into the laser resonator, which in some cases caused catastrophic blower seizure, and they were an additional cost. Refinements were made to meet the stringent environmental requirements for installation of CO_2 lasers on automotive assembly lines.

Despite the physical limitations inherent in the design of the CO_2 laser a devoted following has been gained since the introduction of the first machines. The early slow-flow CO_2 lasers were large, complex machines. This was necessary to extract a useful amount of power from the resonator. The requirements for even higher power CO_2 lasers, necessary to increase cut speed and weld penetration for industrial applications drove further development on the CO_2 laser.

CO_2 lasers with average powers from several hundred watts to multi-kilowatts such as 50 kW, are utilized for on-line high speed cutting, welding and heat-treatment applications in many industries. Nd:YAG lasers on the other hand, previously limited from several watts to no more than four hundred watts, are utilized in automotive industry for marking, electronics welding and drilling in off-line applications. They are capable of delivering high peak irradiance per pulse and such as ideal for material removal of highly reflective and refractive materials, for instance: cutting and welding

of aluminum and titanium, where little thermal structural disturbance to the adjacent areas can be tolerated.

In recent years, several parallel development projects in the United States, Europe and Japan have been undertaken to bring the average power of the Nd:YAG laser above the four hundred watt level. With the improvements of optical coatings, glasses, cavities and power supplies the Nd:YAG laser technology has moved into the multi-kilowatt output range, and now 4 kW Nd:YAG lasers are commercially available. The Nd:YAG laser is a solid state device which requires no moving parts to generate the beam and occupies considerably less space of an equivalent power CO_2 laser. One advantage of the high power Nd:YAG over CO_2 laser is the ability to deliver the beam via fibre-optic. This affords greater flexibility in the placement of the laser, and this allows the laser head to be carried by most motion mechanisms closer to the workpiece, reducing the beam path length and complexity of the beam delivery system for many industrial applications. The fibre-optic delivery system also allows the user to multi-plex the beam to multiple stations thereby increasing the "beam on" time at the workpiece. Thus, this beam delivery approach compliments the installation of lasers on existing automotive robot lines. The minimum focused beam spot size that can be achieved is smaller for the Nd:YAG laser than for the CO_2 device because of its shorter operating wavelength.

Nd:YAG laser applications has included: transformation hardening, surface remelting and cladding on a range of industrially important materials. Operational benefits of using the Nd:YAG laser are its ability to access remote areas, to process small pipes, offers low distortion, high precision and the ability to improve mechanical properties of surfaces. There is a strong demand to develop increasingly higher power Nd:YAG lasers. This is especially true with optical fibre delivery system to process heavier and thicker materials in automobile, aerospace and material industries. The output power can be increased by scaling up the Nd:YAG rod size and optimising the resonator to obtain a high power with a low divergence and high beam quality is still problematic. Many efforts have been made overcome this disadvantage, for instance: the further

development of the slab laser, tube laser and LD excited Nd:YAG laser. Another method to increase the Nd:YAG laser output power is to combine the laser beams from laser oscillators. Three 1 kW Nd:YAG laser beams were combined to increase the laser output power for material processing. The beams were transmitted through optical fibres and collimated by three collimator lenses and combined at the focal point by a condensing lens to achieve a total power of 3 kW at the processing point. Due to the fact that the Nd:YAG laser beam is easily transmitted an optical fibre, it is rather simple to combine the beams at the workpiece to increase the processing power.

1.2 LASER BEAM INTERACTION MECHANISMS

In recent documented studies by the British Welding Institute, improved coupling efficiencies were exhibited when using Nd:YAG laser in welding galvanized steel, yielding far less porosity in the weld joint interface. Crafer [1.1] made a detailed study with a 2 kW CW laser, this was seen to be an efficient device for producing high speed butt welding, thus, the welding appears complementary to electron beam welding where greater thickness can be handled at the expense of welding in a vacuum environment. For typical welding conditions, it is essential to understand the physical aspects of keyhole formation. A comprehensive model for the formation and evolution of the laser welding keyhole was proposed by Sernak [1.2]. The dynamic behaviour of the keyhole is decisive in laser beam welding, it can stimulate weld pool oscillations, causing weld seam defects such as ripple formation, reported by Postacioglu [1.3]. Fabbro *et al.* [1.4] discussed a deep penetration welding process based on a model that estimated the relative importance of Fresnel and Inverse Bremsstrahlung absorption mechanisms as a function of welding conditions and the energy deposition along the keyhole. This was analyzed with different experimental conditions. For higher laser irradiance, a keyhole formation region is reached, this correlation disappears and the absorption reaches 95 % during the welding process. Fabbro *et al.*[1.4] made a detailed investigation to understand the precise role of laser induced plasmas; he concluded that this was not the main mechanism of coupling the laser light inside the keyhole. The effect of plasma is less important for the Nd:YAG laser because this wavelength is more penetrative.

Studies indicate that the high peak power. short pulse width produced by a high pulse repetition frequency CO_2 laser would eliminate the plasma formation generated above the workpiece surface of the weld, reported by Watson *et al.*[1.5]. Willmott *et al.* [1.6] has developed a system to detect the formation and failure of the plasma which influences the keyhole formation for the CO_2 welding process. The formation of a plasma close to the workpiece surface exerts a considerable influence on the interaction process, it is important to observe the condition of the plasma formation inorder to determine the optimal regimes for the welding process.

1.3 STATE-OF-ART IN LASER WELDING

In the past five years a considerable amount of development work has gone on regarding laser welding for automotive, shipbuilding and aircraft industries. There have been many reasons for the drive to laser weld automobiles, including the reduction of material in the weld flanges, improvement in the integrity of the weld, and flexibility in design of the vehicles allowing a greater product range to satisfy increasing consumer demand. Until recently, the introduction of the laser to the automotive welding line has been inhibited by the limitations of the laser itself.

Grevey [1.7] generated a model to investigate the heat transfer characteristic of the weld area, by using a one dimensional numerical calculation. Hayashi *et at.* [1.8] made a detailed study on the effect of induction pre-heating just before welding, and he concluded that in the case of pipe welding, the welding speed increased with the pre-heat temperature. Brenner *et al.* [1.9], demonstrated the technique of induction heating used to support laser beam welding and showed enhanced quality of laser welding of high carbon steel. Brenner used laser induction welding to weld car drive shafts and gear plants, no cracks were observed. The rapid cooling rates associated with single beam laser welding greatly influence the mechanical properties of the weld, these can be reduced by introducing a minor pre-heat or post-heat treatments. Frewin *et al.* [1.10] developed a three dimensional finite element model of heat flow during pulsed laser welding to provide better understanding of the heat flow during pulsed laser welding.

An experimental set-up was developed by Irving [1.11] to monitor the temporal temperature distribution with an detector. Anon *et al.* [1.12] described that the welded joint of high carbon steel can be improved using laser welding with a filler rod. With conventional and single beam welding processes. it is often difficult to avoid crack of fusion defect and brittle welds, particularly when welding high carbon steels. Using a pre-heating or post-heating beam, the temperature profile of the material can be controlled so that the grain structure can be completely modified. Whilst there have been some attempts in the literature to establish the benefits of dual beam delivery or mutli-scanning systems, there has been little detailed work done in this area. A multi-pass laser welding technique was introduced by Arata [1.13] based on the optimized parameters. The effect of two beams, in tandem on the welding process, is briefly discussed by Scott *et al* [1.14]. It is important to know the heating and cooling rate, which is essential for predicting the microstructure behavior, the grain size of the heat affected and fusion zones, distortion and mechanical properties. Toru *et al.* [1.15] examined the preventive methods for the spatter loss, and in particular, with dual Nd:YAG laser beams for welding.

In the present study, the results of a detailed investigation of dual beam delivery systems are presented, this shows the influence of: translation velocity, pulse width, pulse repetition frequency (PRF) and different clamping geometries on the weld quality for Nd:YAG and CO_2 laser welding of high carbon steels; this is discussed in Chapters 3 and 6, respectively. A slower cooling rate was achieved with a 30° incident beam, resulting in a less brittle weld, and the benefits of welding at 30° is presented in Chapter 5. Thus, Glumann [1.16] concluded that the combination of beams set at angles of 30° resulted in a higher process stability according to the theoretical considerations. Problems of implementing the measurement system on-line into a laser welding process environment are discussed by Mettke *et al.* [1.17].

An advantage of Nd:YAG laser processing is its shorter wavelength; consequently, because of the dependency of the material's emissivity on the wavelength, energy is

absorbed by the material more readily than for the CO_2 laser and a lower energy can be used for welding, allowing greater control of the heat input. This is particularly useful when working with thin materials.

1.4 SCOPE OF CURRENT WORK

Compared with arc and gas welding the energy input to a laser weld is extremely small, such that the laser welding characteristics are dominated by rapid quenching of the fusion region via conduction to the surrounding environment. This leads to significant problems for laser welded joints, that may be subjected to cyclic loading due to high hardness induced in the fusion and heat-affected zones. This results in poor component fatigue life. Such hardness discontinuities in the fusion and heat affected zones are dependent on the spatio-temporal temperature distribution during the welding process.

The scope of the present work can be defined as investigating the most appropriate laser parameters and techniques to achieve favorable mechanical properties and good weld quality in high carbon steels, for the CO_2 and Nd:YAG laser welding. Both CO_2 and Nd:YAG laser systems are specifically designed to offer enhanced laser welding capabilities, as discussed in Chapter 2. The laser welding of high carbon steel parts is used in numerous industrial applications; for instance: welding of drive shafts, nose type rail members for crossing, bottom blade of grass cutting machine, gear plants and components. However, the high carbon steel material is difficult to weld and often cracks are produced in the weld region. This is particularly true for high carbon steel . To overcome the cracking problem, other work has been investigated, for instance: the development of using induction heating and furnace preheating prior to welding. Therefore, the high carbon steel selected in this study was chosen as an extremely difficult case with the industrial applications and problems as discussed.

It was noted that hardness depends on the hardenability of the steel, on the cooling rate and to the prior austenite grain size. The hardenability of a steel may generally correlated well with the carbon equivalent (CE). In the carbon equivalent formula, the hardening effect of each alloying element is compared with that of carbon. The relevant

alloy content (in mass %) is divided by a factor that gives the carbon equivalent of that element. According to Lancaster [1.18], a formula that was adopted and in slightly modified form, is

$$CE = C + \frac{Mn}{6} + \frac{Cu + Ni}{15} + \frac{Cr + Mo + V}{5} \qquad (1)$$

However, this formula is applicable to plain carbon and carbon-manganese steels, but not to low-alloy steels or low-alloy Cr-Mo types. The carbon equivalent formula can be used to calculate the hardness of the heat affected zones using a hardness equivalent, which takes account of the cooling rate, and also weldability, which determines the maximum permissible cooling rate for avoiding hydrogen-induced weld cracking. A steel consisting of a carbon content greater than 0.25 % resulted in a brittle structure, and is particularly susceptible to hydrogen induced cold cracking, moreover, when it is subjected to cyclic loading, there tends to be fatigue failure.

A CO_2 laser system with a dual-beam assembly was fabricated to achieve in-line heat-treatment and welding. The experiments investigated the weld quality of high carbon steel to quantify the effects of laser parameters, for instance: welding velocity, pulse width and pulse repetition frequency. The effect of these parameters were quantified by examining the mechanical properties of the welds, for the CO_2 and Nd:YAG laser welding.

A dual-beam delivery system was employed to investigate the effect of laser heat treatment by pre-heating or post-heating the welded samples, for both CO_2 and Nd:YAG lasers. Thus, the heat-treatment process consisted of heating the workpiece and extending the cooling time. With a lower rate of cooling, the temperature gradient decreases and improves the mechanical properties of the laser welded joints, as discussed in Chapter 3.

In Chapter 4, a multi-factorial experiment was designed to assess the effect and interactions of a number of different laser parameters and different weld geometries.

This included: pulse width, pulse repetition frequency (PRF), translation speed, and normal, pre-heating and post-heating beam delivery geometries.

The weld quality and hardness characteristics were quantified after implementing an angular welding technique; this ameliorated the poor characteristics associated with rapid cooling. Two different angles of incidence (0°,30°) for welding were chosen and the pulse width and pulse repetition frequency (PRF) on the mechanical and microscopic properties of the material were examined in detail, the results are discussed in Chapter 5.

The performance of a multiple scanning beam CO_2 laser system was investigated, where the normal, post-heating and pre-heating welding results were compared. It was found that pre-heating or post-heating of the welded samples gave a significant improvement in mechanical properties of the welded joints over single beam delivery system, as discussed in Chapter 6.

An image processing system was developed that offered real time capability to determine the weld quality via measurement of the weld width, surface roughness and heat affected zone; this is discussed fully in Chapter 7. The system comprised an inexpensive CCD camera (625 x 380), acquisition and processing boards. The weld was imaged onto the CCD with a 135 mm focal length lens mounted in bellows. Recent development in laser welding can be improved by developing reliable sensors that accurately record the weld characteristics and provide a feedback signal to control the laser process parameters appropriately.

CHAPTER ONE REFERENCES

[1.1] Crafer, R. "A 2 kW CO_2 Laser System For Welding Sheet Material". The 3rd International Conference on advance in welding process. vol 1, May 1974. 178 - 179.

[1.2] Sernak, V. Hopkins, J. McCay, M. McCay, T. "A Concept For A Hydrodynamic of Keyhole Formation", The 13th International Congress On Applications Of Lasers And Electro-optics, Nov 1994. 641-643.

[1.3] Postacioglu, N. Kapadia, P. Dowden, J. "Theory of The Oscillation of An Ellipsoidal Weld Pool In Laser Welding". Journal of Physic D: Appl Phys.**24**. 1288-90.

[1.4] Fabbro, R. Poueyo-Verwaerde, A. "Modelling of Deep penetration Laser welding Process: Application to The Analysis of The Energy Coupling Inside The Keyhole", The 14th International Congress On Applications Of Lasers And Electro-optics, San Deigo, Nov 1995, 979-981.

[1.5] Watson, I. Chatwin, C. "Segmented Ballasted Electrodes For A Large-Volume, Sub-atmospheric, Transversely Excited Pulsed Laser". Journal of Phys. D:Appl Phys, **28**, 258-260, 1995.

[1.6] Willmott, N. Hibberd, R. Steen, W. "Keyhole/Plasma Sensing System for Laser-Welding Control System", [1.4]. Santa Clara, Nov 1988, 109-111.

[1.7] Grevey, D. Desplats, H. Andrzejewski, H. "Laser Welding Diagrams Showing The Weld Penetration Using YAG Laser", Laser in Engineering, Vol 2, **2**, 1993, 157 - 159.

[1.8] Hayashi, T. Inaba, Y. Matuhiro, Y. Yamada, T. Kudo, T. "Development of High Power Laser Welding For Pipe", The International Congress On Applications Of Lasers And Electro-optics, ICALEO'97. San Deigo, Nov 1997, 132-135.

[1.9] Brenner, B. Gnann, R. Duschek, C. Lynen, T. Beyer, E. "Laser Induction Welding of Hardenable Steels", The International Congress On Applications Of Lasers And Electro-optics, ICALEO'97, San Deigo, Nov 1997, Section A, 61-70.

[1.10] Frewin, M. Scott, A. "Numerical and Experimental Investigation of Pulsed Nd:YAG Laser Welding", The International Congress On Applications Of Lasers And Electro-optics, ICALEO'95, San Deigo, Nov 1995, 904-908.

[1.11] Irving, R. "High power Laser Welds Carbon Steel Plate". Iron Age, Vol 225, **23**, 48 - 49.

[1.12] Anon, "Laser Welder for Sheet Steel Production Processes". Transactions of The Iron and Steel Institute of Japan.1986 , Vol 26, **2**, 120.

[1.13] Arata, Y. Maruo, H. Miyamoto, I. Nishio, R. "Transactions of The Iron and Steel Institute of Japan, Dec1986, Vol 15, **2**. 199 - 206.

[1.14] Scott, A. Frewin, M. "Tandem Nd:YAG Laser Welding". The International Congress On Applications Of Lasers And Electro-optics. ICALEO'97, San Deigo, Nov 1997, Section G, 44-50.

[1.15] Toru, N. Hiroshi, M. Shigeki, F. Akira, O. Katsuori, T. Kudo, T. "Welding Characteristic With Two YAG Laser Beams", The International Congress On Applications Of Lasers And Electro-optics, ICALEO'97, San Deigo, Nov 1997, 181-184.

[1.16] Glumann, C. Ph.D Thesis. University of Stuttgart. Germany. 1995, to be published.

[1.17] Mettke, C. Ng, E. Watson, I. "Monitoring Nd:YAG and CO_2 laser weld quality". The European Conference on Laser and Electro-Optic/European Quantum Electronics Conference, Sept 1998.

[1.18] Lancaster, J. " Metallurgy of Welding". Abington Publisher, 6th Edition, **1**, 1999.

CHAPTER TWO
CO_2 AND Nd:YAG LASER WELDING SYSTEMS

2.1 Introduction

The use of high power lasers in material processing applications has been a subject of interest for many researchers during the last two decades, as discussed in Chapter 1. Lasers have been applied for a range of processes such as cutting, welding, surface hardening, alloying and cladding of many materials. Moreover, laser welding is advantageous over conventional techniques; for instance, it is a fast process, produces low distortion and a high quality finish. Abdullah *et al* [2.1] and Steen *et al* [2.2] observed that compared to arc or gas welding, the energy input to a laser weld is extremely small; this results in an untempered martensitic structure in the samples due to the rapid quenching rate of the surrounding material. A high carbon steel was used in these particular studies. Further, a low heat input into the workpiece results in a small fusion zone and heat affected zone. Zerroukat *et al.* [2.3] theoretically modelled the laser material interaction and studied the heat transfer mechanism by conduction to the surrounding environment, this results in a melt zone that can be precisely controlled. This can be a used to determine the grain structure of the fusion and heat-affected zones. Greater understanding of the basic phenomena of laser welding and better control of the process is leading to improved weld quality. Glumann *et al* [2.4] reported that the cavities and blowholes could be suppressed when two lasers were used one after the other in a practical welding process. Dausinger *et al* [2.5] observed an increase in welding process stability when a dual beam technique or Nd:YAG laser (shorter wavelength) was applied. In this work, the two lasers used to weld the high carbon steels were: Ferranti's MFKP continuous wave 1 kW CO_2 device and Lumonic's pulsed, 400W Nd:YAG laser. The effect of the laser parameters and weld geometry on the sample's mechanical properties in the welded region was investigated, for the CO_2 and Nd:YAG lasers. The laser systems are described below.

2.2 Nd:YAG Laser Welding System

A Lumonic's MS830 Nd:YAG laser (1.06 μm) with a maximum capacity of 400 watts mean power was used to weld gauge plates. In the present study, the Nd:YAG laser system was used in-conjunction with the multi-flex beam delivery system which was designed to be used in the Lumonic's range of industrial Nd:YAG pulsed laser. This system provided a means of sharing the energy of the beam simultaneously between four different fibre optics to achieve in-line process tempering. In the present case, two focusing heads were fitted onto an IBM Scara Robot. Schematics of the single and dual beam delivery systems are shown in **Figures 2.1 and 2.2**, respectively. In the case of pre-heating or post-heating the sample, the laser power was divided so that 70% was coupled to the weld beam and 30% was directed to the heat-treatment process. The weld beam diameter was 2 mm, and the beam diameter was 20 mm for the post-heating or pre-heating process. This processing method was designed to slow down the rate of cooling of the sample before or after welding with the main beam. The normal welding process was achieved with 200 W of laser power. In all cases, an output power of 154 W was detected at the exit of optical fiber used for welding. The power loss was due to the optical fiber delivery system and lenses. An argon or helium shielding gas was used at a source pressure of 1 Bar as indicated on the pressure gauge. Two different angles of incidence (0°,30°) of the weld beam were used for welding and compared as were effects of the pulse width and pulse repetition frequency (PRF) on the mechanical and microscopic properties of the materials. **Figures 2.3 and 2.4** show two different type of experimental set-ups that were used for this study, the flat and 30° welding geometries, respectively. Focusing was done by adjusting the height of the gauge plate. The effects of two different types of clamping geometries were compared as this is important in reducing the rate of cooling, and in particular, this results in different weld mechanical properties, this is discussed in Chapter 5.

2.3 CO_2 Laser Welding Systems

The present investigation used a 1 kW, CW, CO_2 laser (Ferranti MFKP), operating at 10.6 μm, to weld gauge plates. The translation velocity was changed from 7 to 11

mm/s, using different welding geometries to study the influence on the cooling process. discussed in Chapter 6. **Figures 2.5 and 2.6**, respectively, show a schematic of the clamped and unclamped geometries that were used for welding. A He shielding gas pressure of 0.25 bar was used with a nozzle diameter of 5 mm. Furthermore, a multi-pass scanning technique was implemented to eliminate the rapid quenching rate and ameliorate the poor weld characteristics. This initial investigation used a single beam system for pre-heating and/or post-heating the workpiece to control the sample's phase transitions and to deliver specific weld characteristics. For the single beam system, in the case of pre-heating, a number of initial passes of the beam were made to heat up the sample; this was followed by an additional pass to weld the material. The post-weld heat treatment was achieved by performing a number of passes after welding. The amount of heating can be easily controlled by changing the number of passes; 10 passes were selected in the present cases. Whilst not precluding it, this obviated the need to fabricate the dual-beam delivery system and is an ideal approach for indrustrial users to achieve heat-treatment simultaneously during welding to improve the weld quality. **Figure 2.7** shows the final dual beam delivery system that was fabricated to achieve heat-treatment simultaneously during laser welding, this is further discussed in Chapter 6.

2.4 System To Measure and Monitor Laser Weld Quality

An image processing system was developed that offered real time capability to determine the weld quality via measurement of the weld width and surface roughness, this is discussed in Chapter 7. **Figure 2.8** shows the configuration of the monitoring device used in this study, it comprised a CCD camera and a PC to drive an oscilloscope to capture images within a particular time. Two sources of white light were inclined at 2° from the horizontal base, these illuminated the welded specimens placed onto the translation stage. A digital LeCroy 9310 oscilloscope was used in this experiments. The weld was imaged onto the CCD with a 135 mm focal length lens mounted in bellows. After placing the specimens onto the translation stage, the oscilloscope was set and both light sources illuminated the welded region. Every fifth line was recorded and

saved onto the hard-disk of the PC as a binary file. This limited the volume of data. In all cases, the line scan traces and 3-D plots were generated by commercial software package such as Microsoft Excel. The trace between the peak-peak indicated the weld width, and a 3D scan provided the information on the surface irregularities and the weld appearance. This device was capable of providing useful information on the quality of the weld seam.

2.5 Sample Preparation For Analysis of Weld Quality

In all cases, the high carbon steel gauge plates that were welded had a nominal composition of 0.5 and 0.85 % C, 0.4% Si, 1.1% Mn, 0.4% Cr, 0.25% V and 0.4% W. The mechanical properties of the sample are given in Table 2.1. All of the samples welded with Lumonic's MS830 Nd:YAG laser were machined prior to welding to dimensions of 75 x 50 x 0.88 mm. Gauge plate of 2 mm thickness was welded with the 1 kW CO_2 laser (Ferranti, MFKP). The tolerance of the length and width of the samples was ± 0.1 mm. After machining, the samples were ground (Type J, B.A.60.P.V, medium grain) to ensure smooth, flat surfaces. After welding, the sample's were sectioned, moulded, etched in nital (3% nitric acid and 97% methanol), photographed and the microstructure was examined to quantify the weld quality. Furthermore, the Vicker's hardness profile of the weld was measured, transverse to the weld direction and as a function of depth, using a Reichiert 1541555 Vicker's hardness testing machine with a diamond indenter of 70 gm load. An Instron tensile tester machine with a cross-head speed 0.5 mm/s was used to measure the tensile strength along the weld joints. The weld depth and bead width were measured using a Mitutoyo PJ-300 profile projector. The welds were inspected using an optical microscope to study any weld defects or cracks and the microstructure in the weld region.

2.6 System Used To Measure The Temperature Profiles

To monitor the relative temperature of the welded material, temporal temperature measurements were taken throughout the experiments with four thermocouple wires attached to the specimen's surface, 2 mm away from the weld region. Two

thermocouple wires (T1 and T2) were arranged adjacent to each other at the beginning of the weld, see Chapter 3, and the other two thermocouple wires (T3 and T4) were arranged adjacent to each other at the end of the weld. The signals from the thermocouples were amplified and fed into an ADC card, located in a PC. Software was written in Turbo C language to collect the data.

CHAPTER TWO REFERNCES

[2.1] Abdullah, H. Ng, E. Chatwin, C. Watson, I. "In Line Process Annealing Of Laser Welded High Carbon Steel", The 14th International Congress On Applications Of Lasers And Electro-optics. San Diego. Nov 1995. 964-973.

[2.2] Steen, W. Chen, C. West, D. "Laser Suface Melting of Cast Irons And Alloy Cast Irons", The Industrial Laser Annual Handbook, 1985. 84-86.

[2.3] Zerroukat, Chatwin, C. "Heat Flow Computations For CW-Laser-Material Interaction ", Journal of Lasers in Engineering, Gordon & Breach Science. Switzerland, 3(2) (1994), 113-123.

[2.4] Glumann, C. Rapp, J. Dausinger, F. Hugel, H. "Welding with a combination of CO_2 lasers - advantages in processing and quality". The 12th International Congress On Applications Of Lasers And Electro-optics, Orlando, 1993, 672.

[2.5] Dausinger, F. Faisst, F. Hack, R. Rapp, J. Hugel, H. "Welding of aluminum: Challenge and chance for laser technology". The 14th International Congress On Applications Of Lasers And Electro-optics, San Diego, Nov 1995, 1059-1067.

Table 2.1 Measurement mechanical properties of substrate material

Type of Steel	Yield Strength (MN/mm^2)	Ultimate Strength (MN/mm^2)	Vickers Hardness (Kg/mm^2)
High Carbon Steel	340.9	568.2	260

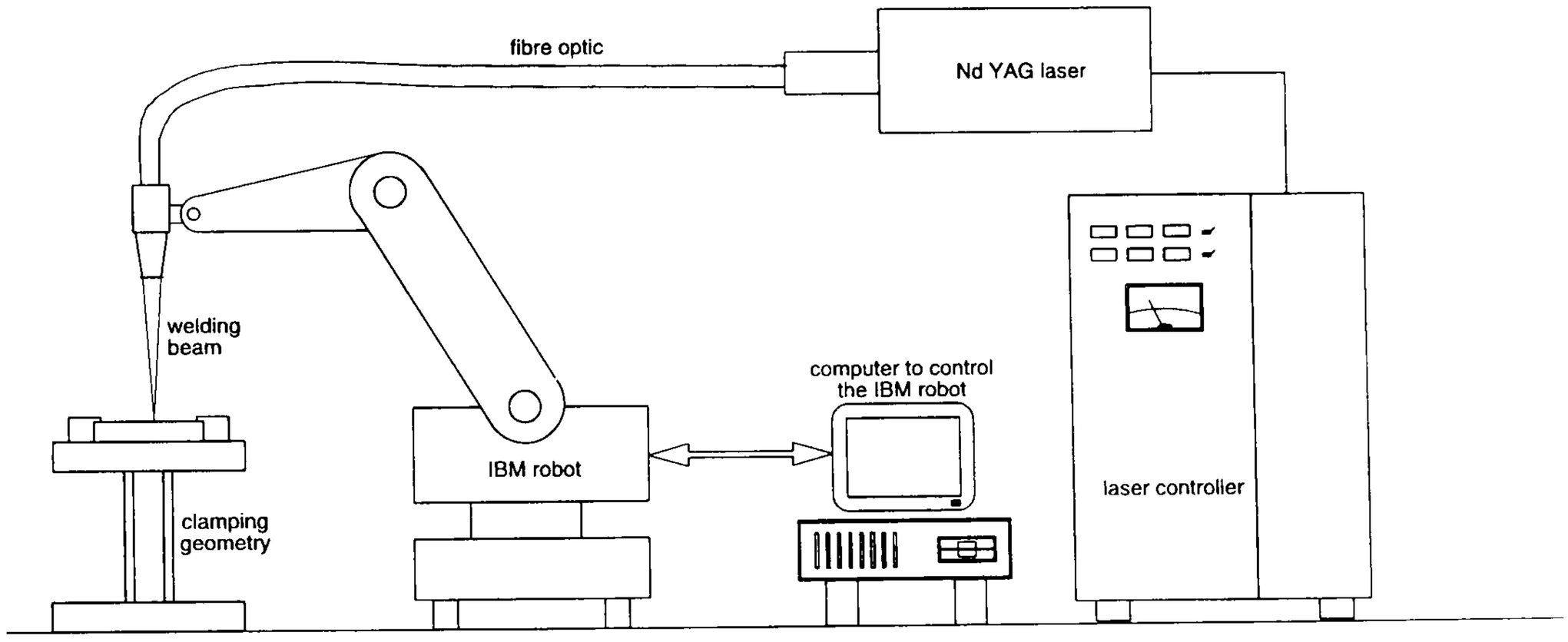

Figure 2.1 Nd:YAG single beam delivery system

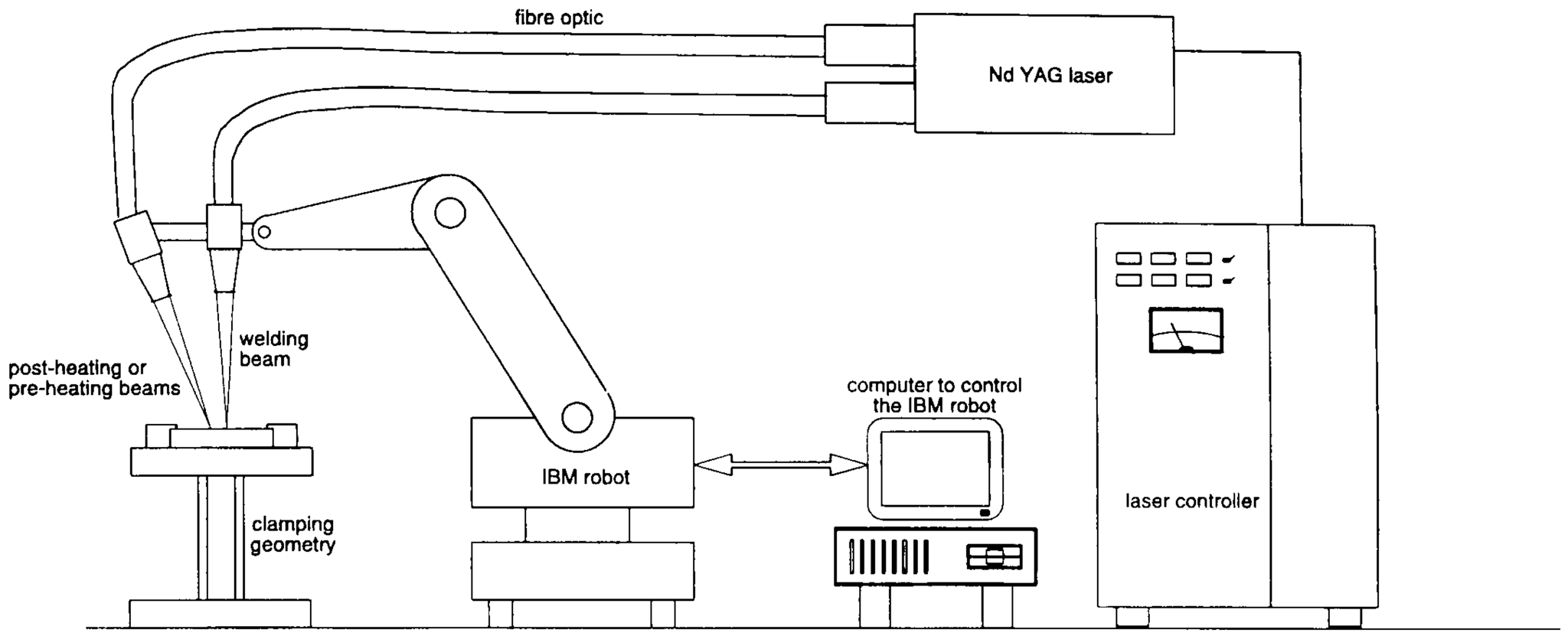

Figure 2.2 Nd:YAG dual-beam delivery system

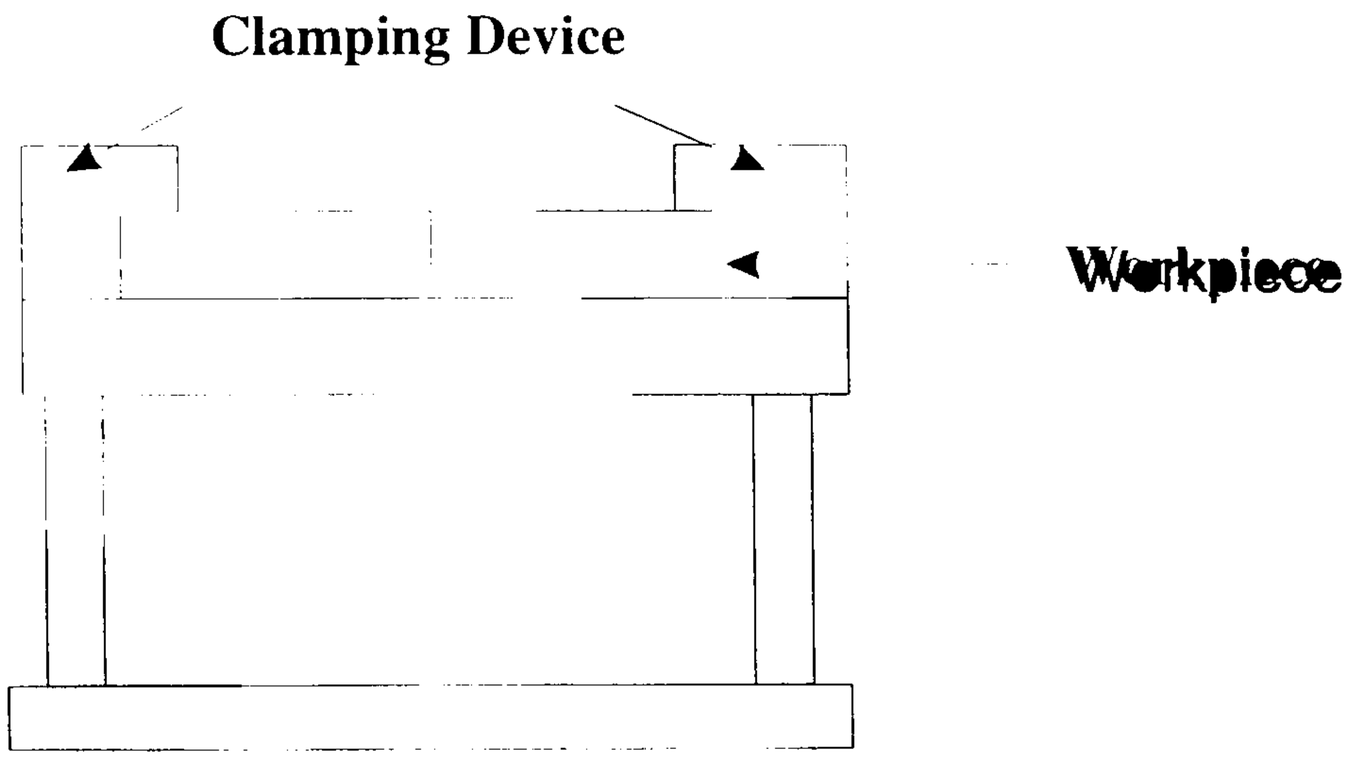

Figure 2.3. Flat welding geometry

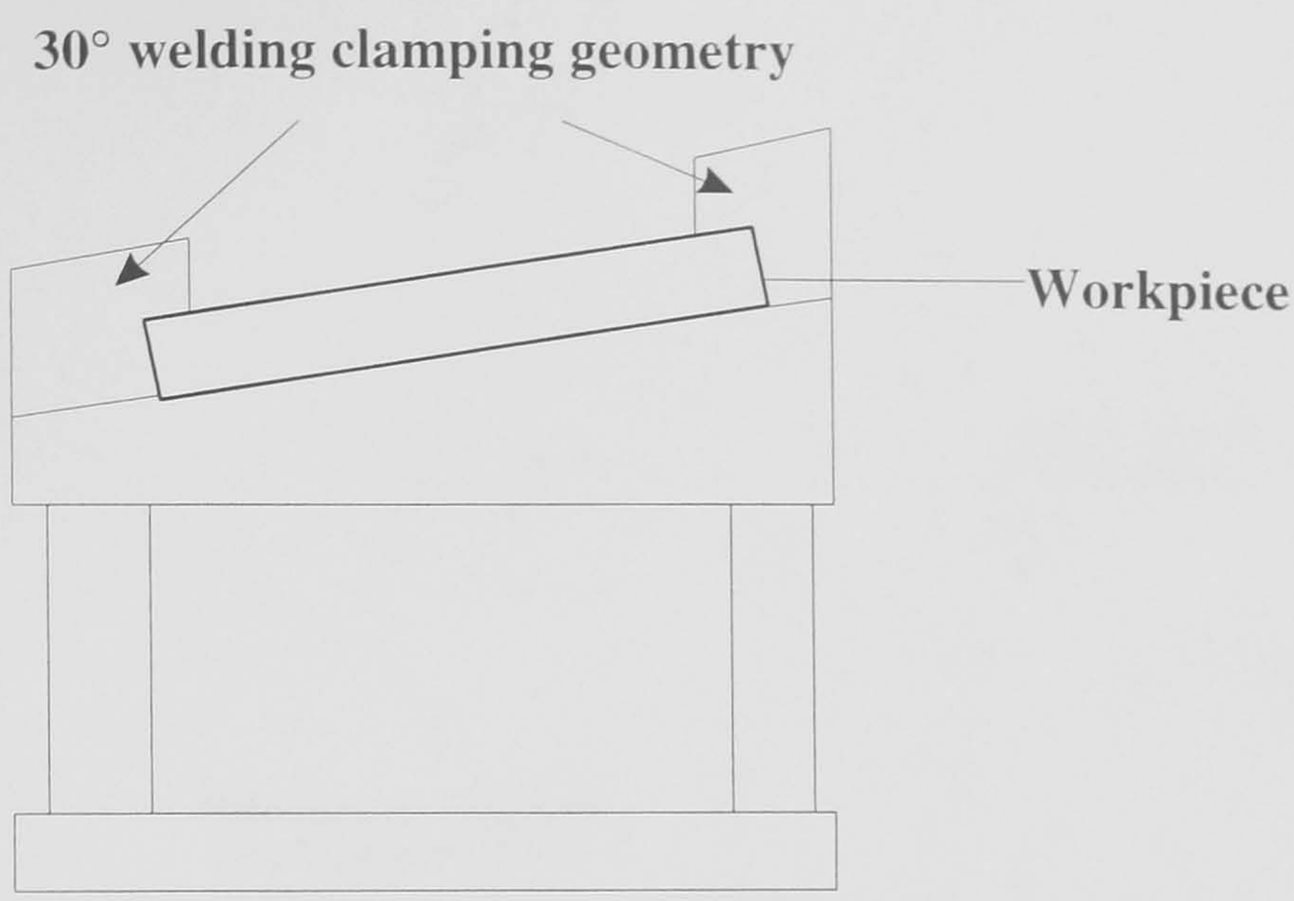

Figure 2.4. 30° welding geometry

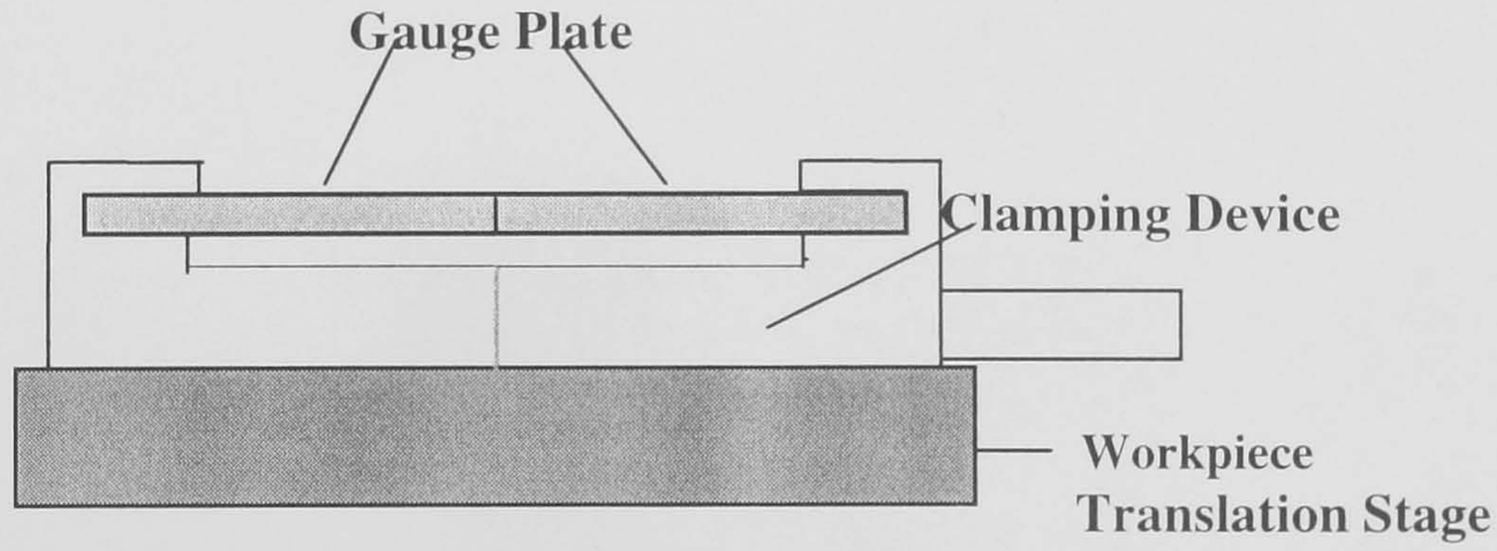

Figure 2.5 Clamped Geometry For Laser Welding

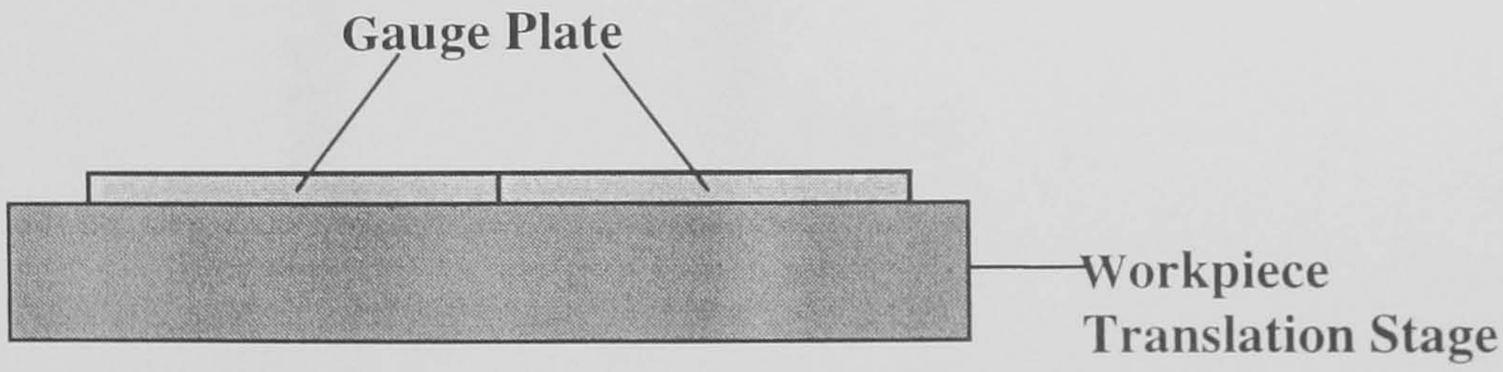

Figure 2.6 Unclamped Geometry For Laser Welding

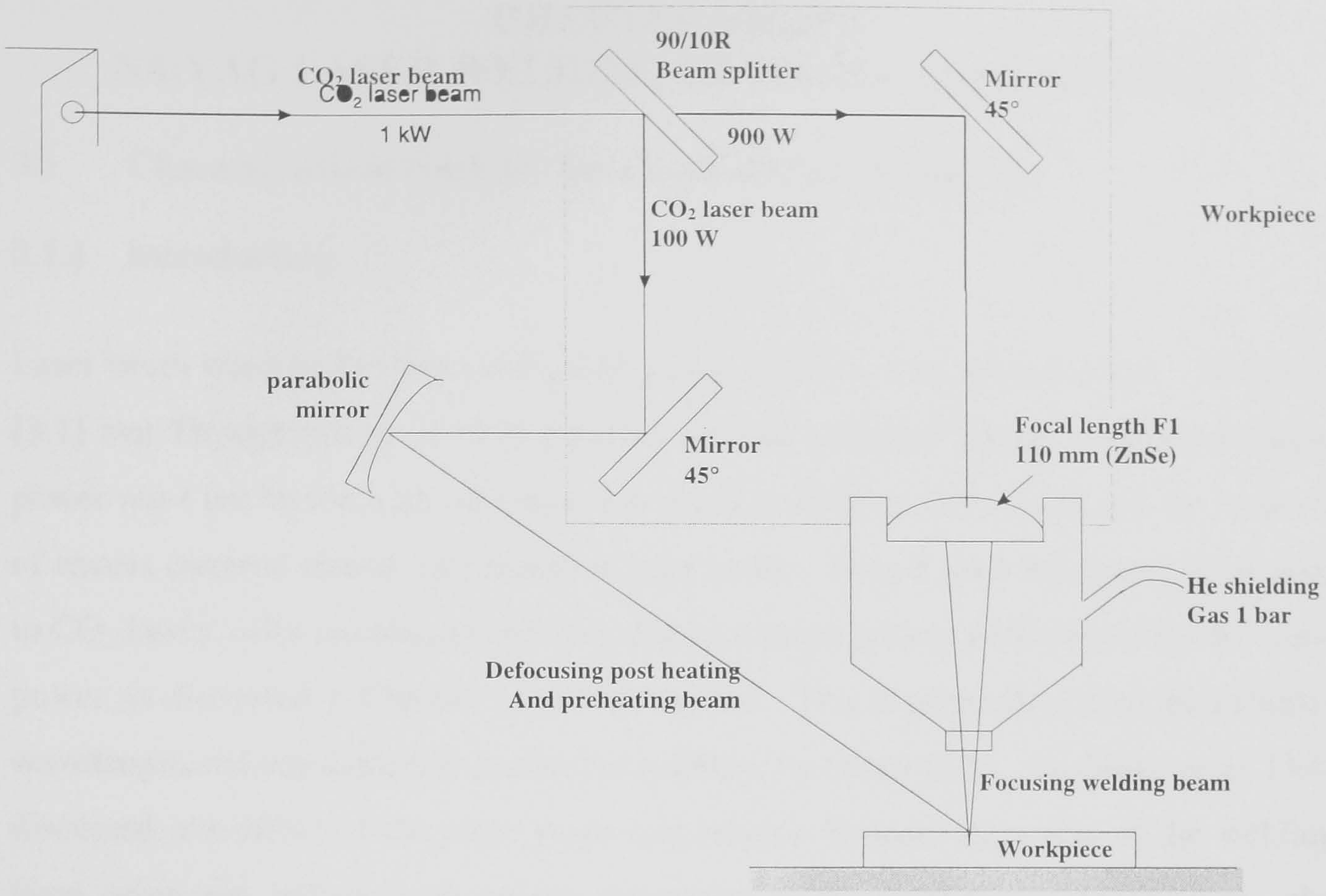

Figure 2.7 CO_2 laser : dual beam delivery system for pre-heating and post- heating

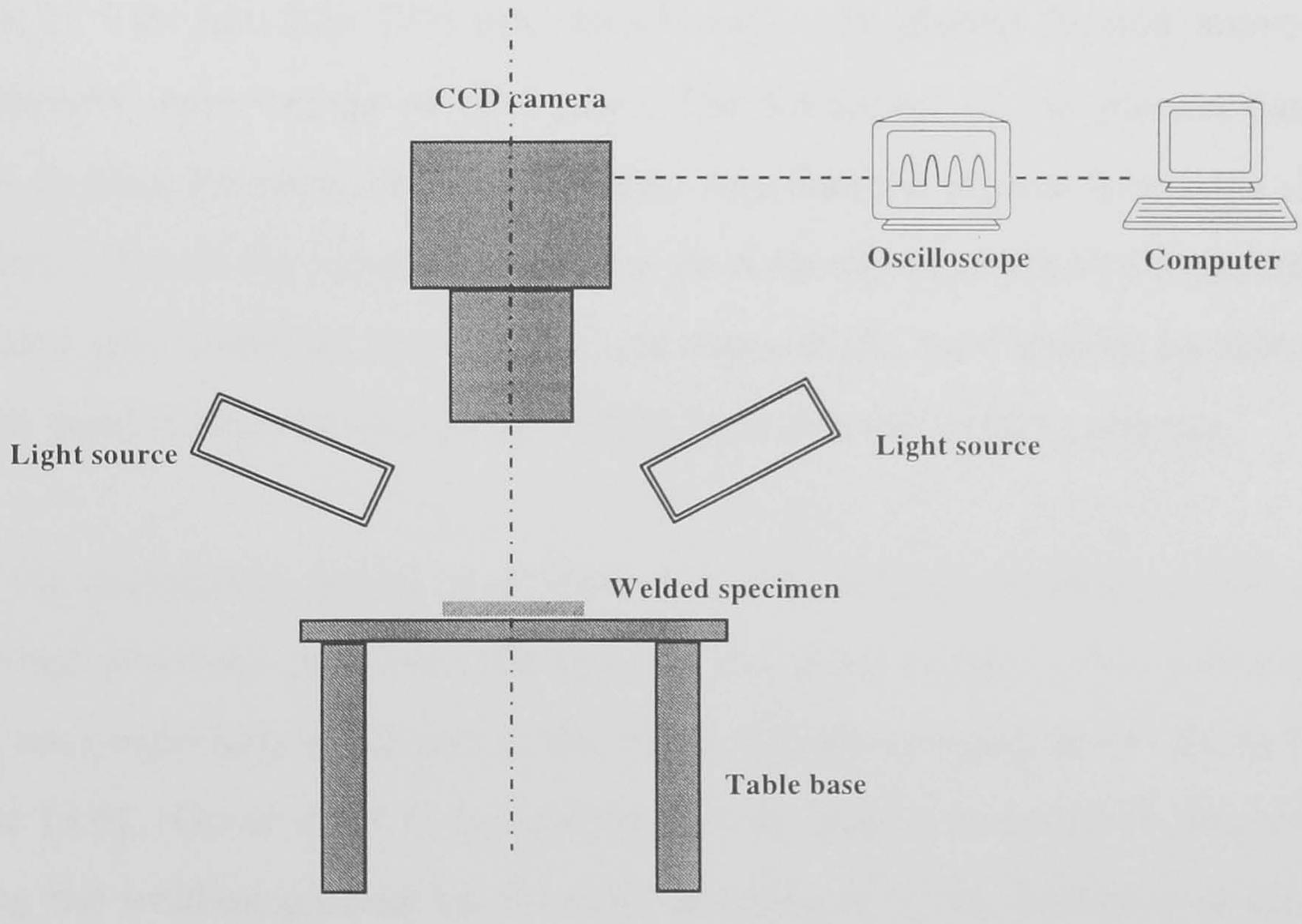

Figure 2.8 Weld quality monitoring system

CHAPTER THREE
Nd:YAG LASER WELDING OF HIGH CARBON STEELS

3.1 Characteristic of Nd:YAG laser welded high carbon steel

3.1.1 Introduction

Laser beam welding has been utilised to join a variety of metals and alloys. Weisman [3.1] and Thyagarajan *et al* [3.2] reported that for diffusion limited welding the laser power must not be too high otherwise too much material is evaporated and the removal of excess material results, in general, in poor welds. Pulsed Nd:YAG lasers, compared to CO_2 lasers, offer advantages in being able to achieve greater weld depths for the same power, as discussed in Chapter 2 - see Section 2.1. This is primarily due to their shorter wavelength and consequently greater focusability, by Olsen [3.3]. Yoshioka *et al.* [3.4] discussed, the effect of the pulse shape and relation between deviation of the welding focal point and influence on energy absorption by the workpiece. Furthermore, the absorption of optical energy of most metallic materials usually processed by lasers is much greater at 1.06 μm than 10.6 μm; additionally, any plasma formed above the workpiece absorbs more energy at 10.6 μm. The formation of the plasma can be controlled by pulsing the laser with pulse widths less than the plasma formation time. The detrimental effect of the induced plasma can be reduced and controlled by using the proper shielding gas, moreover, assist gases can improve the weld quality by reducing porosity in the weld region and increasing energy input into the welding process.

When lasers are operated in pulsed mode there are some distinct advantages. For non-diffusion limited processes, however, the keyhole can close rapidly. This can lead to high cooling rates especially in the root of the weld; this was investigated by Steen [3.5] and Schwartz [3.6]. Gu *et al* [3.7] discovered that the maintenance of the keyhole is critical during the welding process because any disturbance to the keyhole can lead to poor penetration and reduction in the weld strength. Honeycombe *et al.* [3.8] found that poor mechanical welds often occur due to rapid quenching in the fusion zone via conduction to the surrounding material. This work investigates the mechanical

properties of Nd:YAG laser welded joints of high carbon steel gauge plate, moreover, the performance of a single laser beam, was assessed and compared to a dual beam delivery system in Sections 3.3 and 3.4. In this present case, the process regime is conduction welding. The weld quality was quantified by measuring: the depth of weld penetration, weld width, hardness characteristics and tensile strength for different translation velocities, pulse repetition frequencies (PRF) and pulse widths. The mechanical properties of CO_2 laser welded high carbon steels has been previously reported by Ng *et al.* [3.9], these are discussed in Chapter 6.

3.1.2 Welding and Analysis

The experimental set-up used for this study is shown in **Figure 2.1** see Chapter 2. A Lumonic's MS830 Nd:YAG laser was used, operating at 1.06 μm with a maximum mean power capacity of 400 watts. A fibre optic beam delivery system was used which was robotically manipulated to produce a butt weld of the gauge plates, at constant power of 154 W, and a He shielding gas at the source pressure of 5 x 10^4 Pa indicated on the pressure gauge. The effects of varying the welding velocity, pulse repetition frequency and pulse width on the weld quality were investigated. The gauge plates (0.88 mm) that were welded had a nominal composition of 0.85 wt % C, 0.4 wt % Si, 1.1 wt % Mn, 0.4 wt % Cr, 0.25 wt % V and 0.4 wt % W. The mechanical properties of the gauge plate are given in Chapter 2, see Table 2.1. After welding the sample's were sectioned, moulded, etched in nital (3% nitric acid and 97% methanol), photographed and examined. The materials microhardness, depth of weld penetration and bead width were measured to quantify the effect of varying the laser parameters. For all the measurements, the graphs show an average value of three experiments. The errors observed for all the experiments was less than ± 1.2 %, each of the data points plotted in the graph in this thesis is the average of 3 values. The error is not significant and is hardly seen. Thus, the error bars are omitted in most of the cases for clarify. Figures 3.1 to 3.3 and 3.10 to 3.12, show example of the typical error that were observed in the experiments. The Vicker's hardness profile of the weld was measured, transverse to the weld direction and as a function of depth, using a Reichiert 1541555 Vicker's hardness

testing machine with a diamond indenter of 70 g load. The weld depth and bead width were measured using a Mitutoyo PJ-300 profile projector. The tensile tester was an Instron tensile machine, comprising a highly sensitive and accurate load weighing system, with a 10 kN load applied to the welded specimens and cross-head speed of 5 mm/s.

3.1.3 Weld Characteristics

3.1.3.1 Tensile Test

Tensile tests aimed at determining the mechanical properties of the laser welded plates were significantly inferior to those of the parent plates. When tensile failure occurred in the welded region, no deformation of the weld was evident, indicating that brittle fracture, due to the sample's high hardness, had been the likely cause of failure. **Figures 3.1, 3.2** and **3.3** show the maximum and minimum tensile strengths, that resulted in failure at the welded region, as a function of the pulse width, translation velocity and PRF respectively. From **Figures 3.1** and **3.2**, it can be seen that the tensile strength increased with increasing pulse width ranging from 6 to 12 ms and translation velocity from 3.5 to 5 mm/s. For a partial weld, the tensile strength increased from 49.09 to 95.16 MN/m^2, for a corresponding pulse width from 6 to 12 ms. No full penetration weld was achieved in this case. When the translation velocity was increased from 4 mm/s to 5 mm/s, the tensile strength increased from 79.72 to 97.34 MN/m^2. A full penetration weld was achieved with a translation velocity of 3.5 mm/s and in this case the tensile strength was 75.2 MN/m^2.

The effect of PRF on tensile strength can be seen in **Figure 3.3**. Interestingly, for a partial weld, the tensile strength decreased from 68.23 to 52.82 MN/m^2, for a corresponding increase in the PRF from 6 to 8 Hz. This represents a decrease in the strength of 22.5 %. A full penetration weld was achieved with a PRF of 9 Hz and in this case the tensile strength was 34.14 MN/m^2. From **Table 3.1**, the ultimate tensile strength of the base material was 586.2 MN/m^2. The strength of the welded samples was considerably lower than this value, indicating the difficulty of welding high carbon

steel. This work evaluated the performance of the normal laser beam delivery system to provide a comparison of different beam delivery systems. Ng *et al.* [3.10].

3.1.3.2 Hardness Characteristics

The gauge plate was welded, sectioned transverse to the weld direction, moulded, and etched in nital, photographed and examined. A diamond pyramid indenter with a load of 70 g was used to measure the microhardness transverse across the weld, and as a function of depth. **Figures 3.4, 3.5** and **3.6** show, respectively, the measured microhardness transverse across the weld for: translation velocities between 3.5 - 5 mm/s, pulse widths between 6 - 12 ms, and frequencies between 6 - 9 Hz. From **Figure 3.4**, it is seen that the hardness transverse across the weld increased with the welding speed, and in all cases the peak hardness occurred at the centre of the weld. The peak hardness reduced significantly for lower translation velocities. For example, for a translation velocity of 5 mm/s, the peak hardness was 1619 kg/mm^2; this reduced by 38.1 % to 1002 kg/mm^2 for a translation velocity of 3.5 mm/s. **Figures 3.5** and **3.6** show that the hardness at the HAZ region reduced with increasing pulse width and pulse repetition frequency. By increasing the pulse width from 6 ms to 12 ms, the hardness at the centre of the weld reduced by 30.5 % from 1839 kg/mm^2 to 1277 kg/mm^2. The hardness across the weld was greatest for the lowest PRF. For a PRF of 6 Hz, the peak hardness was 1855 kg/mm^2, however, this was reduced by 10.8 % to 1655 kg/mm^2 for a PRF of 9 Hz. The lowest peak hardness at the centre of the HAZ was observed for a translation velocity of 3.5 mm/s, pulse width of 12 ms and PRF of 9 Hz. Whereas, the maximum peak hardness at the centre of HAZ was observed for a translation velocity of 5 mm/s, pulse width of 6 ms and PRF of 6 Hz. In all cases, the large hardness gradients across the weld would lead to fracturing, especially if the gauge plate was subjected to cyclic loading.

Figures 3.7, 3.8 and **3.9** show, the hardness profiles, at the centre of the weld and as a function of depth for: different translation velocities, pulse widths and pulse repetition frequencies, respectively. From **Figure 3.7**, it can be seen that the rate of change of

hardness as a function of depth reduced with translation velocity. Moreover, the largest variation was observed near the surface, where the hardness decreased from 1619 to 1022 kg/mm^2, for a decrease in the translation velocity from 5 mm/s to 3.5 mm/s. At a depth of 0.5 mm, there was little variation in the hardness for the range of translation velocities investigated. As the pulse width was increased, a reduction in the rate of change of hardness as a function of depth was observed, see **Figure 3.8**. The largest spatial hardness variation was observed near the surface. Here, the hardness decreased from 1839 kg/mm^2 to 1367 kg/mm^2 for an increase in the pulse width from 6 ms to 12 ms. At a depth of 0.5 mm, there was less variation in the hardness over the range of pulse lengths examined. Interestingly, as the PRF was increased (**Figure 3.9**) from 7 - 9 Hz, then at a depth of 0.4 mm there was practically no difference in the hardness. These values, however, were considerably lower than those measured at 6 Hz. For example, the largest variation occurred at the depth of 0.2 mm, here the hardness decreased from 1577 kg/mm^2 to 962 kg/mm^2 for an increase in the PRF of 6 Hz to 9 Hz, and this difference was much less above depths of 0.3 mm. In all cases, the hardness was attributed to the high cooling rate depressing the transformation temperature which resulted in brittle welds.

3.1.3.3 Penetration

Figures 3.10, 3.11 and **3.12** show the weld depth as a function of translation velocity, pulse width and PRF respectively. In each case the mean power was 200 W. The weld depth increased with decreasing translation velocity (**Figure 3.10**), increasing pulse width (**Figure 3.11**), and increasing PRF (**Figure 3.12**). The maximum penetration was 0.88 mm; this was achieved with a translation velocity of 3.5 mm/s. The penetration was reduced by 28 % with a translation velocity of 5 mm/s to a value of 0.63 mm. From **Figure 3.12**, it can be seen that the weld penetration increased from 0.59 mm to 0.86 mm for a corresponding increase in the pulse widths from 6 ms to 12 ms respectively. This represents an increase in the weld penetration of 45.7 %. As the PRF was increased to 9 Hz, the weld penetration increased to 0.88 mm and a full penetration weld

was achieved. The minimum weld penetration (0.55 mm) was achieved with a PRF of 6 Hz. The weld penetration increased by 60 % over the range of PRFs investigated.

3.1.3.4 Bead Width

The weld width was measured as a function of translation velocity, pulse width and PRF, and the results can be seen in **Figure 3.13, 3.14 and 3.15**, respectively. From **Figure 3.13**, for a translation velocity of 3.5 mm/s, a maximum weld width of 1.25 mm was achieved. Interestingly, the weld width reduced by only 8 % to 1.15 mm, for an increase in the welding velocity from 3.5 to 5 mm/s. Increasing the pulse width (**Figure 3.14**) from 6 to 12 ms resulted in an increase in the weld width of 21.7 %, from 1.06 to 1.29 mm. With an increase in the PRF (**Figure 3.15**) from 6 to 9 Hz the weld width increased from 1.22 to 1.39 mm, this represents an increase in the weld width of 13.9 %.

3.1.3.5 Rate Of Formation Of The Weld Volume

The rate of formation of the weld volume was found by multiplying the weld width, weld depth and the translation velocity. The weld volumes were calculated as a function of translation velocity, pulse width and PRF, and these results are shown in **Figures 3.16, 3.17** and **3.18**, respectively. From **Figure 3.16**, it is clearly observed that the rate of formation of the weld volume reduced with increasing translation velocity. For example, with a translation velocity of 3.5 mm/s, the largest rate of formation was 4.07 mm^3/s. For an increase of 43 % in the translation velocity (5 mm/s), the weld volume formation rate reduced by 11.3 % to 3.61 mm^3/s. The calculation of the weld volume formation rate however, does not take account of the shape of the weld, other than weld depth and weld width.

Figures 3.17 and **3.18** show clearly that the weld formation rate increased with increasing pulse width and pulse repetition frequency. For instance, for a pulse width of 6 ms the weld formation rate was about 3.13 mm^3/s and this was increased by 77 % to 5.55 mm^3/s for a pulse width of 12 ms. Moreover, for a PRF of 6 Hz, the weld formation rate was approximately 3.36 mm^3/s and this was increased by 86 % to 6.26

mm^3/s, for a PRF of 9 Hz. The overall power delivered to the workpiece remained constant, consequently, for the higher PRF the pulse energy would be less.

3.1.3.6 Microstructure Study Of The Weld

The microstructure of the welded specimens was examined in the HAZ, the fusion zone and the base metal. **Figures 3.19** and **3.20** show, respectively, the top view of the fusion zone for pulse width of 6 ms and 12 ms. From **Figure 3.19**, crack formation is evident at the top of the fusion zone. The fact that the cracks usually occur through the centreline of the weld is due to the solidification pattern of the weld metal. Since the parent material is much cooler the weld solidifies inwards which means that the centre of the weld is last to solidify and is thus much weaker at the temperature at which cracking occurs. No cracking was observed when the pulse width was doubled to 12 ms, **Figure 3.20**. Wang *et al.* [3.11] reported that a general feature of laser welded high carbon steel is the formation of a martensite structure in the fusion zone, due to the rapid quenching rate, and finely dispersed carbides. As can be seen in **Figures 3.21** and **3.22**, martensitic structures appear in the fusion zone and this also consists essentially of ferrite, which is heavily super-saturated with carbon. Moreover, this also gives rise to cementite and pearlite formation, and the grain size at the fusion zone will be more coarser, and will suffer from brittleness. When a hyper-eutectoid steel that is those containing more than 0.83 wt % C-, its structure should consist of cementite in a matrix of hard martensite. **Figures 3.23** and **3.24** show, respectively, typical pictures of the fusion zone for a higher PRF and lower translation velocity. With this combination of laser parameters there is a reduced cooling rate, so that the grain size becomes finer and spherical in form. Here, the grain structure in the fusion zone was transformed to a more granular and refined grain. **Figures 3.25a** and **3.25b** show, the distribution in the grain size that was observed at the parent metal, heat affected zone and fusion zone; this was due to the different rates of cooling between these regions was first discovered by Goswami *et al.* [3.12]. Additionally, the welded specimen exhibited a complex transformation structure in sharply defined narrow bands comprising a heat affected zone at the junction between the weld and base metal. By varying the translation

velocity, pulse length and PRF, the grain structure was completely modified in the fusion zone. By appropriate selection of the laser parameters, the desired characteristics of the welded material can be achieved.

3.1.4 Conclusions of normal Nd:YAG laser welding

A number of welds were fabricated for a range of translation velocities, pulse widths and PRF. The weld quality was quantified by measuring the sample's tensile strength, hardness profile, weld width, depth of penetration and from examination of its microstructure. The results have shown that the tensile strength greatly increased with an increase in the pulse length and a reduction in the pulse repetition frequency. For partial welds, the tensile strength increased by 48.4 % for an increase of pulse width from 6 to 12 ms, and the tensile strength was reduced by 22.5 % with an increase in the PRF from 6 Hz to 8 Hz.

The hardness profiles transverse across the weld region decreased with translation velocity, and increased with pulse width and PRF. For instance, the peak hardness at the weld centre was reduced from 1839 kg/mm^2 to 1277 kg/mm^2 for an increase in the pulse width from 6 to 12 ms. By increasing the PRF from 6 Hz to 9 Hz, the peak hardness at the weld centre was reduced from 1855 kg/mm^2 to 1655 kg/mm^2. Furthermore, the hardness transverse to the weld direction decreased from 1619 kg/mm^2 to 1002 kg/mm^2 with a decrease of translation velocity from 5 to 3.5 mm/s.

It is evident that the hardness profile will be dependent on the thermal distribution around the fusion zone. Moreover, in the present case, the hardness profiles were greatly reduced due to greater spatial overlap of the beam on the workpiece at the slower welding velocities, for higher pulse widths and higher pulse repetition rates. This resulted in effectively reducing the rate of cooling of the fusion zone. The hardness as a function of weld depth was greatly reduced with increasing pulse length and PRF. Interestingly, the rate of change of hardness as a function of depth reduced with decreasing translation velocity.

Because of the rapidly cooled high carbon steel, the main weld region consisted of a martensitics structure, moreover, crack formation was observed at the top of the fusion zone. A slower cooling rate was achieved with a higher pulse width, and no cracking was observed. A general feature of all the specimens was that the main weld region consisted of a cementite and carbides structures. The grain size was coarser and less dense near the fusion zone with a higher welding velocity and a lower PRF. For an increase in the PRF and a reduction in welding velocity, the structure was completely modified at the fusion zone. The rate of cooling was slower, resulting in a less brittle weld. The grain structure that appeared in the fusion zone was typically more refine and granular.

The quality of the welds was improved by increasing the PRF and pulse width. This was quantified by measuring the penetration depth and bead width, both of which decreased with increasing translation velocity. The deepest and widest weld was achieved for a translation velocity of 3.5 mm/s, PRF of 9 Hz and pulse width of 12 ms. Therefore, from the results obtained in the present study, it is apparent that a higher strength weld can be achieved by increasing the pulse width and the translation velocity.

The rate of formation of the weld volume increased with pulse width and PRF. Interestingly, for a change of translation velocity from 3.5 to 5 mm/s, the weld formation rate reduced by only 11.3 %. Moreover, for an increase in the pulse width (from 6 ms to 12 ms) and PRF (from 6 Hz to 9 Hz), the average weld volume formation rate increased by about 82 %.

When optimising the weld quality, there is a trade off between the lower hardness characteristics achieved with a lower translation velocity, the increased HAZ and reduced process speed. In many practical application, the width of the HAZ may not be a critical factor in determining the weld quality, so it is likely that the process speed will need to be maximised for the desired hardness properties.

3.2 Characterization of tempering process of laser welded high carbon steel produced by dual beam delivery system

3.2.1. Introduction

To extend even further the wide spread use of laser material processing applications in industry, there is a need to understand in greater detail the interaction between the laser beam and the workpiece, the possible disadvantages of the process and how they can be overcome. Kajanpa *et al.* [3.13] observed that laser welding does not produce any electromagnetic forces in the melt to facilitate mixing, and Mimatsu *et al.* [3.14] suggested that with better knowledge of the energy absorption processes, it is possible to optimise the energy penetrating through the plasma layer that is generated above the workpiece, when the laser beam interacts with metallic surfaces as reported by Pueyo-verwaerde *et al.* [3.15]. The Nd:YAG pulsed laser can be used to process a wide range of materials and offers a high degree of flexibility and control over the welding process, moreover, Milewski *et al.* [3.16] discovered that the pulsed laser beam welding reduces the heat input and allows control of the grain orientation. For example, tempering or post-heating of the workpiece can be achieved easily with fibre optic beam delivery systems and allows control over the microstructure of the sample.

Abdullah *et al* [3.17] reported a major problem of processing high carbon steels or similar material is that any hardness discontinuities transverse across a weld that is subject to cyclic loading will lead to a poor component fatigue life. More significantly, the carbon content makes it essential to apply a post-weld heat cycle to avoid cracking at the fusion zone during cooling was observed by Pan *et al.* [3.18]. Such hardness profiles are often induced with a single-beam delivery system as discussed in Section 3.1, and Ng *et al.* [3.19]. The spatial hardness discontinuities in the fusion and heat affected zones are dependent on the spatial-temporal temperature distribution during the welding process. Scott *et al* [3.20] developed a model to predict the size and shape of the weld zone, he concluded that when dual beams are focused onto the material and completely overlapped, the depth of penetration increases. Consequently, a dual-beam technique was employed to investigate the effect of laser heat treatment on high carbon

steel gauge plate. Previous studies by Burdekin *et al.*[3.21] have included use of welding high carbon steel gauge plate without any heat treatment. Tempering is usually used to reduce hardness of the welded joints, and this leads to an improvement in the tensile strength was reported by Ng *et al.* [3.22]. Thus the heat treatment process consisted of heating the material and extending the cooling time. Wang *et al.* [3.23] suggested that with lower rates of cooling, the temperature gradient decreases and the formation of martensite may decrease. This results in a more refined and granular microstructure found in the heat affected zone and fusion zone than that obtained by using a single-beam delivery system. Byer *et al.* [3.24] described the combination of an induction laser weld technique, this resulted in crack free laser weld, tempering steels would therefore considerably improve the industrial range of applications for laser welding. It is most convenient to use dual or multiple beams where the advantages of laser processing and beam delivery system dominate over combination technologies where it is difficult to control the heat input as with, for example, induction heating. Okorokov *et al.* [3.25] realized that optimizing the annealing process is essential to produce better quality welds.

Liu *et al.* [3.26] used a laser to preheat high-melting metals to increase the speed of machining. Improvements were observed in the surface finish, the cutting forces were reduced and the tool life was increased. Theoretical investigations into the effects of pre-heating and post-heating of laser welds have been done by Liu *et al.* [3.27]. The dual-beam delivery system reduced the rate of cooling. The post-heating weld treatment was more effective in reducing the rate of cooling, and the pre-heat treatment was more effective in reducing the temperature gradient in the transverse direction, see Section 3.3. In this work, the results of a detailed experimental investigation comparing the weld quality for normal laser welding as discussed in Section 3.1 (single-beam delivery system) are given, and those welded with a post-heated treatment (dual-beam delivery system). The results were quantified by measuring the aspect ratio, weld widths, hardness characteristics and tensile strengths, in the same manner as previously described in Section 3.1.3.

3.2.2 Welding and Analysis

The welding was done with a Lumonic's MS830 Nd:YAG laser, operating at 1.06 μm and with a maximum output power capacity of 400 watts. A dual-beam fibre optic beam delivery system was used to achieve in-line process tempering with a constant total power of 285 watts. Here the laser power was divided so that 70% was coupled to the weld beam and 30 % was directed into post-heating. The amount of losses taken into account for all the optical lens and fiber optic beam delivery system resulted in a constant power of 154 W and 72 W used to produce the butt weld and post-heating of gauge plates, respectively. A schematic of the dual-beam delivery system is shown in **Figure 2.2** - see Chapter 2. For a dual beam delivery system, a weld was produced by the weld beam focused to about 2 mm diameter, and this was followed by the post-heating beam diameter of about 20 mm. This processing method was designed to slow down the rate of cooling of the sample after welding with the weld beam. For the normal weld geometry, 145 W of laser power was used to produce a weld with a single beam delivery system. The focused beam spot size was about 2 mm and normal to the welding direction. In all cases, the focus of the laser beam was brought down to the surface of the workpiece, the laser beam tranverse speed was 5 mm/sec, and a He shielding gas was used at a source pressure of 5×10^4 Pa indicated on the pressure gauge.

High carbon steel gauge plate, with a nominal composition as described in Section 2.5. The mechanical properties of the sample are given in **Table 2.1**. The errors observed for all the experiments was less than ± 1 %, each of the data points plotted in the graph in this thesis is the average of 3 values. The error is not significant and is hardly seen. Thus, the error bars are omitted in most of the cases for clarify. All of the samples were machined to the dimension of 75 X 50 X 0.88 mm. The tolerance of the length and width of the samples was ± 0.1 mm. After machining, the samples were ground (Type J, B.A.60.P.V. medium grain) to ensure smooth, flat surfaces. After welding, the workpieces were sectioned, moulded, polished, etched (2 % nital) and photographed. To quantify the weld quality, the hardness profiles were measured, with a Reichiert

154155 Vicker's hardness testing machine. transverse along the weld direction and as a function of depth. A Instron tensile tester machine with a cross-head speed 0.5 mm/s was used to measure the tensile strength along the weld joints. The weld depth and bead width were measured using a Mitutoyo PJ-300 profile projector. The welds were inspected using an optical microscope to study any weld defects or cracks and the microstructure in the weld region. The parameters that were used in this experiment for the normal welding and the two beam weld geometry are listed in **Table 3.1**. To monitor the relative temperature of the welded material. temperature measurements were taken throughout the experiments with four thermocouple wires attached to the specimen's surface, 2 mm away from the weld region. Two thermocouple wires (T1 and T2) were arranged adjacent to each other at the beginning of the weld, see **Figure 3.26**, and the other two thermocouple wires (T3 and T4) were arranged adjacent to each other at the end of the weld. The signals from the thermocouples were amplified and fed into an ADC card, located in a PC. Software was written in Turbo C language to collect the data.

3.2.3 Weld Characteristics

3.2.3.1 Hardness Characteristics

All Vicker's hardness tests were performed across the heat affected zone, fusion zone and base metal to determine the strength across the weld joints. The hardness measurements for both the normal and post-heated welds were made across the weld and as a function of depth at the weld centre. The extent of the material affected by the different welding processes was determined by their hardness profiles, examination of the microstructure, tensile tests, and measurement of the weld width, weld depth and weld volume formation rate. **Figures 3.27** and **3.28** show the percentage reduction in the peak hardness for the post-heated samples relative to the normal weld at different PRFs and pulse widths transverse across the weld region. The laser power was 200 W (pulse energy from 33 J to 22.2 J, and pulse repetition frequency (PRF) from 6 Hz to 9 Hz respectively) for the normal welding. For the post-heating geometry, the laser power (285 W) was split in the ratio of 7:3 (weld: post-heating).

For the normal weld configuration, the hardness profile was attributed to the rapid cooling rate which produced poor mechanical joints due to the hardness discontinuities. The effect of PRF on the peak hardness reduction can be seen in **Figure 3.27**. Interestingly, increasing the PRF showed a lower percentage reduction in peak hardness relative to normal weld. There was a slight decrease in peak hardness from 6 Hz to 7 Hz, and the percentage of hardness reduction decreased further above 7 Hz. For a PRF of 6 Hz, there was nearly 50.5 % reduction in peak hardness transverse across the weld, and the percentage of hardness reduction was greatly reduced to 18.8 %, for a PRF of 9 Hz. From **Figure 3.28** shows the dependence of the percentage reduction in the peak hardness of the weld at different pulse widths, it is seen that the percentage reduction in the peak hardness was independent of the pulse width over the range of values investigated. The average percentage reduction in the peak hardness of the weld was 55.8 %. Post-heating of the workpiece was more effective in improving the weld hardness characteristics than the normal weld; this is illustrated clearly by **Figures 3.27** and **3.28**. Post-heating produced lower hardness profiles relative to the normal weld; and hence, with reduced non-uniformities in the hardness profiles, the likelihood of cracking, when subjected to cyclic loading, was reduced.

The hardness profiles as a function of depth can be seen in **Figures 3.29** and **3.30**. **Figure 3.29** shows the variation in the depth-hardness for different pulse widths, and **Figure 3.30** shows this variation for different PRFs. With the normal weld geometry, the hardness decreased with depth into the sample. In general, for a given depth, the hardness reduced with increasing PRF and pulse width. Interestingly, the post-heating technique produced a uniform hardness transverse across the weld and along the weld depth.

3.2.3.2 Tensile Test

Tensile tests were performed, at a crosshead velocity of 0.5 mm/sec, to determine the mechanical properties of the welds done with both geometries. **Figure 3.31** shows the tensile strength, which resulted in failure of the butt welded joints, as a function of pulse

width. For a post-heating weld, the tensile strength increased from 105.11 MN/mm^2 to 128.63 MN/mm^2 for a corresponding pulse width from 6 ms to 12 ms. No full penetration was achieved in this case. It can be seen that the tensile strength was greater for the welds done with the post-heating geometry. For post-heating, the tensile strength increased with pulse width. Whereas for the normal welds no full penetration was achieved over the range of pulse widths investigated, the tensile strength was greatly increased from 16.53 to 53.33 MN/mm^2, for an increase in the pulse width from 6 ms to 8 ms. However above 8 ms, the tensile strength increased with pulse width. For a pulse width of 12 ms, the tensile strength was 128.83 MN/mm^2 for the post-heated weld and 81.86 MN/mm^2 for the normal weld. This represents an increase in the tensile strength of 57.3 % for the partial welds. In all cases, no penetration welds were achieved with both normal and post-heating geometries. From **Table 2.1** the ultimate tensile strength of the base material was 586.2 MN/mm^2. The strength of welded samples was considerably lower than this value for both normal and post-heated weld geometries.

It is apparent from **Figure 3.32** that the percentage difference in tensile strength for the post-heating and normal weld geometries, is clearly observed that the difference in tensile strength falls with increasing pulse width, for both single and dual beam systems. The greatest difference in tensile strength was observed at 6 ms. This drop in the percentage difference is due to the rise in the tensile strength for pulse widths above 6 ms, as shown in **Figure 3.31**.

The effect of PRF on the tensile strength can be seen in **Figure 3.33**. Interestingly, increasing the PRF reduced the tensile strength for the post-heated welds, but slightly increased the tensile strength for the normal welds. For the post-heated welds, the reduction of strength is due to the slight spatter loss on the top of the fusion zone, when the two beams overlapped each other. Toru *et al* [3.1] reported that a drastic increase in the power density would be harmful to the keyhole balance after the keyhole formation by a pulsed laser beam under this condition. In all cases, both normal and post-heated welds, no full penetration was achieved with an increasing PRF from 6 to 8 Hz. When

the PRF was increased from 6 to 8 Hz, the tensile strength decreased from 138.4 MN/mm^2 to 109.2 MN/mm^2 and no full penetration was achieved, for the post heated weld. Whereas, for the normal weld, no full penetration was achieved for a corresponding increase in the PRF from 6 to 8 Hz but a full penetration weld was achieved with a PRF of 9 Hz, and in this case the tensile strengths were 56.4 MN/mm^2 and 100.3 MN/mm^2, for the normal and post-heated welds, respectively. This difference in tensile strength was at a minimum for a PRF of 9 Hz and here the difference was 43.8 %, relative to the normal weld. The maximum difference in tensile strength was about 65 %, this was observed at a PRF of 7 Hz. The strength of the welded samples was considerably lower compared to the ultimate tensile strength of the base material shown in **Table 2.1**, indicating the difficulty of welding high carbon steels. However, in all cases, the tensile strength was greatest for the post-heated welds, and the strength of the welded samples was significantly improved.

Figure 3.34 shows that the percentage difference in tensile strength for the different beam geometries as a function of pulse repetition frequency was largest at a PRF of 7 Hz. From **Figure 3.33**, it is clearly seen that above 7 Hz, the tensile strength for the post-heated weld fell rapidly, and slightly increased in strength for the normal weld. This leads to a reduction in the percentage difference in tensile strength for the different beam geometries with PRF above 7 Hz (**Figure 3.34**). From **Figures 3.31** and **3.33**, it can be seen that for the post-heating geometry, the weld strength was superior to the normal weld geometry for the range of parameters investigated.

3.2.3.3 Aspect Ratio

The aspect ratio for both the normal and post-heated laser welds was found by dividing the weld penetration by the weld width. The dependency of the aspect ratio on the PRF and pulse width is shown in **Figures 3.35** and **3.36**. **Figure 3.35** shows that for the normal and post-heated weld, the aspect ratio increased with the PRF. Compared to the normal weld process, the aspect ratios for the post-heated welds were higher because of the deeper penetration.

It can be seen in **Figure 3.36** that the aspect ratio generally increased with the pulse width for the normal welding process. This is due to the higher penetration that was achieved with the normal welding over the entire range investigated. Whereas, for the post-heated welds, the aspect ratio decreased with increasing pulse width. For an increase in pulse width above 8 ms, the aspect ratio remained constant for the post-heating geometry compared to the normal weld because of the wider bead width.

3.2.3.4 Weld Beads

In **Figure 3.37**, where the weld width is plotted as a function of the pulse width for both weld geometries, it is seen that the weld width increased with pulse width for both the normal and post-heated welds. In all cases, however, the weld width was greatest for the post-heated welds. From **Figure 3.38**, which shows the dependency of the weld width on the PRF, it is seen that the weld width slightly reduced with increasing frequency for the post-heated welds and increased for the normal weld geometry.

3.2.3.5 Rate of Formation of The Weld Volume

The rate of formation of the weld volume was taken as the product of the weld width, weld depth, and the translation velocity (5 mm/s) for the normal and post-heated welds. The dependency of the weld volume formation rate on the pulse width for the normal and post-heated geometries can be seen in **Figure 3.39**.

For the normal weld geometry, the weld volume increased with pulse width, whereas for the post-heated welds, the weld volume was independent of the pulse width over the range of values investigated. For pulse widths below 10 ms, the weld volume formation rate was greatest for the dual-beam geometry. For the pulse widths above 10 ms, the weld volume was greatest for the normal weld geometry. For the normal weld geometry and pulse width of 6 ms the weld formation rate was 3.13 mm^3/s, this increased by 77 % to 5.55 mm^3/s for a pulse width of 12 ms. The average volume formation rate for the post-heated welds was 4.34 mm^3/s.

The calculated volume formation rates at different PRFs for the normal and post-heating welds are shown in **Figure 3.40**. The volume formation rate increased with PRF for the normal weld geometry, and stayed practically constant for the dual beam delivery system. For a PRF of 6 Hz, the weld formation rate was 3.36 mm^3/s for the normal weld geometry and this increased by 86 % to 6.26 mm^3/s for a PRF of 9 Hz. For the post-heated geometry, the average weld formation rate was 5.46 mm^3/sec.

3.2.3.6 Microstructure Study of The Welds

The microstructure of the welded specimens was examined in the HAZ, the fusion zone and the base material. **Figure 3.41** shows a typical normal laser weld that had not received any in-line post-heating. The crack formation is evident at the top of the fusion zone. The centre-line cracking in the weld region is dependent on the cooling pattern of the weld metal. Since the parent metal is much cooler, thus, the weld solidifies inward which means that the centre of the weld is last to solidify and is thus much weaker at the temperature at which cracking occurs. The cooling speed is much faster at the fusion zone rather than at the heat-affected zones of the welded samples. The austenite transforms to fine martensite rapidly and some retain to room temperature, thus, the microstructure of the weld region is mainly fine martensite, retained austenite and finely dispersed carbides. Indeed, the shift of the Ms temperature towards lower values with the increase of carbon content may induce the proportion of martensite form in the weld region. **Figure 3.42** shows the effect of post-heating the samples with the same laser parameters as the normal weld. Quite clearly, no cracking was observed, agrees with the experimental results reported by Byer *et al.* [3.24], see Section 3.2.1. **Figures 3.41** and **3.42** show a typical picture of the fusion zone for a normal and post-heated welds, for a pulse width of 6 ms and PRF of 10 Hz. Additionally, the post-heated weld specimen exhibited a complex transformation structure in different layers of banding comprising a heat-affected zone at the junction between the weld and parent metal, **Figure 3.43**. Also a normal weld interface between the weld and parent metal was shown in **Figure 3.44**. The fusion zone consisted of a martensitic structure because of the rapid cooling rate; thus, the grain structure was smaller in the fusion zone and

coarser near the heat affected zone, as shown in **Figure 3.45**. Goswami *et al.* [3.28] observed the effect due to the different rates of cooling between both of these regions. **Figure 3.45** shows a typical picture of a fusion zone, for the normal weld, that had not received any post-heating, and the coarse grain consisted of finely dispersed carbides and martensites were observed. Due to the weld thermal cycle, the structure was completely modified at the fusion zone. **Figure 3.46** shows the fusion zone for a typical post-heated weld. Here, the grain structure in the fusion zone was transformed to a fine and granular grain. With the dual beam system, the cooling rate was rather slow and the temperature gradient decreases. Furthermore, the austenite may transform to fine pearlite when the cooling speed is slow, and the quantity of martensite may decrease. In general, the post-heated weld geometry reduced the rate of cooling and also promoted the formation of fine grain boundary, this resulted in forming a favorable mechanical structure as similarly reported by Diehl *et al.* [3.29].

3.2.3.7 Temperature Profile

A simple model was generated, discussed in Appendix A, to investigate the mechanism of heating and cooling rate of the welded sample. The relative temperature of the gauge plate during the weld process was monitored. **Figures 3.47** and **3.48** show the temperature profiles that were measured for the normal weld configuration for pulse widths of 6 ms and 12 ms, respectively, with a total laser power of 200 W. Measurements were taken near the beginning (T1 and T2) and end (T3 and T4) of the weld with four thermocouples attached to the surface of the specimen. These temperature values were normalised. As the beam made its closest approach to the thermocouples, the temperature quickly rose at the positions of T1 and T2, the temperature peaked and then decayed as the beam passed. As the beam approached the positions of T3 and T4, the temperature rose to a greater value for T3 and T4 because the integrated input energy was greater near the end of the weld. The weld was completed after 13 seconds. With a pulse width of 12 ms a wider weld width and higher temperature profile was observed. **Figure 3.49** shows the measured temperature variation for the post-heated weld with a pulse width of 12 ms. Here the profiles were

more complex, and a secondary rise in temperature was observed; this can be attributed to the post-heating beam. From these temperature profiles, it is apparent that with the post-heating technique the temperature dropped at a slower rate than with the normal weld geometry. The post-heating technique produced a non-uniform and wider temperature profile than the normal weld geometry, and this led to a slower rate of cooling. The spatial hardness discontinuities are dependent on the temperature distribution during the welding process. Moreover, different beam delivery systems and laser process parameters will lead to different rates of heat transfer characteristics, grain size and ultimately to different weld characteristics.

3.2.4 Conclusions of Nd:YAG laser welding with in-line post-heated process

The laser weld quality of high carbon steels was investigated for two different beam geometries and a range of laser parameters. The beam geometries comprised a single-beam and dual-beam delivery system. The weld quality was quantified by: measuring the sample's hardness profile transverse to the weld direction and as a function of depth, examination of the microstructure, measurement of the tensile strength, weld width, aspect ratio and weld volume formation rate.

The hardness profiles were measured transverse to the weld direction, the hardness decreased with increasing PRF and pulse width for both weld geometries, however, the hardness gradients were less for the post-heated welds. The greatest peak hardness was reduced by nearly 50.5 % for a PRF of 6 Hz for a post-heated weld, and a lower reduction in the peak hardness was achieved by increasing the PRF to 9 Hz. It is evident that the hardness profile will be dependent on the thermal distribution around the fusion zone. Moreover, in the present case, the peak hardness reduction was achieved with a dual-beam system, this is due to greater spatial overlap of the beam on the workpiece with the post-heating beam. This resulted in effectively reducing the rate of cooling of the fusion zone, resulting in a less brittle weld, and it is clearly illustrated that the secondary rise in temperature attributed to the post-heating beam. However, post-heating the sample was effective in improving the weld hardness profiles across the

weld region, and this greatly reduced the likelihood of cracking when subjected to cyclic loading. The hardness as a function of weld depth was greatly reduced with increasing pulse width and PRF, for both normal and post-heated weld geometries. The hardness did not differ significantly as a function of depth for the post-heated geometry for a given pulse width or PRF. For a given depth, however, the hardness reduced with PRF and pulse width. For the normal weld geometry, the hardness reduced with depth into the sample, and for a given depth the hardness reduced with increasing PRF and pulse width.

The tensile strength was greatest for the annealing geometry and increased with pulse width. For a pulse width of 12 ms, a partial weld was achieved for both systems but the tensile strength was over 57 % greater for the dual-beam delivery system. The maximum difference in strength was 84 %, for a pulse width of 6 ms, and the difference in tensile strength decreased with an increase in pulse width to 12 ms. The tensile strength reduced with increasing PRF for the dual-beam delivery system, but slightly increased for the normal weld. Thus, the strength of welded samples showed considerable improvement for post-heated weld treatment. In general, the welded joints are weakened more by the weld discontinuities. It could therefore be expected that the rapid cooling rate affects the mechanical properties of the resultant joint either by causing a loss of tensile strength, and an increase in hardness between both fusion and heat affected zones. The strength of the welded samples was considerably lower than the parent metal for both normal and post-heated weld geometries, most of the plastic strain occurs in the weld. Thus, the strength of the welded samples show considerable improvement for the post-heated weld treatment.

For post-heated welds, the aspect ratio decreased with increasing pulse width from 6 to 12 ms because of the increase in the bead width. This is due to the weld width increase with pulse width, and wider weld bead produced for the post-heated welds.

The rate of formation of the weld volume was independent on the pulse width for the post-heated welds but increased with pulse width for the normal weld geometry. Interestingly, for pulse widths above about 10 ms, the weld volume formation rate was greatest for the normal weld geometry. The formation rate increased by about 77 % from 3.13 to 5.55 mm^3/s for the normal beam geometry when the pulse width was doubled from 6 to 12 ms. Whereas the average weld volume formation rate for the post-heated welds was 4.34 mm^3/s. The formation rate was approximately constant for the dual-beam delivery system for different PRF, but for the normal weld geometry the formation rate increased.

For the post-heated welds, martensitic structures were observed in the fusion zone and a complex grain transformation was observed in the heat affected zone. For an increased pulse width, the structure was completely modified at the fusion zone. These effects were consistent with the observed physical parameters of the weld quality. For the post-heated welds, the microhardness decreased gradually due to the reduction of martensite, and the cooling rate was greatly reduced which lead the grain structure in the fusion zone to transform to a fine and granular grain. The change of microstructure is responsible for the variation of microhardness transverse to the weld region and along the weld depth.

The temperature profiles measured for the different beam geometries can be used to explain the observed characteristics of the laser welded specimens. The rate of cooling, for example, was slower for the dual-beam delivery system. This leads to reduced hardness profiles and an increased tensile strength. Moreover, increasing the pulse width reduced the rate of cooling and increased the tensile strength.

The effects of the laser parameters and two different beam geometries on the laser weld quality have been investigated. The weld characteristics were consistent with the temperature history of the samples.

3.3 Nd:YAG laser welded high carbon steel with in-line pre-heated process

3.3.1 Introduction

Heat treatment of materials with lasers, especially during welding process has gained importance in recent years. Advantages of laser welding over conventional welding such as tungsten inert gas and arc welding, include: faster process speed, lower distortion and precise welding was reported by Zheng *et al.* [3.30]. To increase the depth of a melt zone it is necessary to understand the interaction between the laser beam and the workpiece. During laser welding, a cavity or keyhole is created that enhances the energy transfer from the laser beam to the material. The keyhole is surrounded by molten metal and as the laser beam moves relative to the workpiece the molten pool solidifies and the weld is formed. The speed of formation and maintenance of the keyhole is essential to maintain the weld quality. A model was developed by Kroos *et al.* [3.31] to control the penetration depth in a welding process; this depends on the laser beam intensity and the material's properties. For a high laser intensity, a plasma may be generated that shields the workpiece, therefore reducing the energy coupled into the material. Poueyo *et al* [3.32] and Behler *et al* [3.33] studied the dependency of the quality of the weld on the laser beam parameters, and they concluded that the plasma which is strongly influenced by the use of assist gases.

Abdullah *et al.* [3.34] made an experimental study to investigate the high cooling rate occurs in the fusion region via conduction to the surrounding material during laser welding; this allows untempered martensitic structures to form in the fusion zone was reported by Metzbower *et al.* [3.35]. Major et al. [3.36] suggested that we must quantify the weld quality dependence on the laser variable process parameters, material properties and environmental conditions. Thus, to eliminate poor weld characteristics, a pre-heating technique can be used to control the sample's phase transition properties and the high rate of cooling. Moon [3.37] concluded that, to lower the hardness of the welds, preheat or post-heat treatment can be done by a simple additional pass over the weld following the first pass.

Thus, this is a very simple and economical way of heat treating a welded sample compared to conventional process. Brenner *et al.* [3.38] gave a brief explanation of a novel technique on the first industrial application of laser induction welding; for instance: laser induction welding of a car drive shaft, the production of tailor blank for light weight structures and gear components as well as motor accessories. Most of the beneficial effects of heat-treatment can be attributed to specific solidification structures. The analysis contained herein compare the weld quality for normal laser welding and those welded with a pre-heat treatment. The results are quantified by measuring the weld depth, weld width, hardness characteristics and tensile strength.

3.3.2 Welding and Analysis

A Lumonic's MS830 Nd:YAG laser (1.06 μm), with a maximum output power capacity of 400 watts was used to weld 0.88 mm thick high carbon steel gauge plate. In the present case, the dual beam fibre optic delivery system was used to achieve in-line process heat treatment with a constant power of 285 watts as discussed in previous Section 2.2 -see **Figure 2.2**. In the case of pre-heating, the laser power was divided so that 70% was coupled to the weld beam and 30% was directed into pre-heating. The weld beam diameter was 2 mm and the pre-heating beam diameter was 20 mm. The amount of losses taken into account for all the optical lens and fiber optic beam delivery system resulted in a constant power of 154 W and 72 W used to produce the butt weld and re-heating of gauge plates, respectively. This processing method was designed to heat the material before welding with the main beam. High carbon steel gauge plate, with the same nominal composition as discussed in Section 3.2.2 was used. After welding, the workpieces were sectioned, moulded, polished, etched (2% nital) and photographed. In all cases, the errors observed for all the experiments was less than ± 1.3 %, each of the data points plotted in the graph in this thesis is the average of 3 values. The error is not significant and is hardly seen. Thus, the error bars are omitted in most of the cases for clarify. To quantify the weld quality, the hardness profiles were measured, with a Reichiert 154155 Vicker's hardness testing machine, transverse along the weld direction and as a function of depth. Furthermore, an Instron tensile tester

machine was used to measure the tensile strength along the weld joints with a cross-head speed 0.5 mm/sec. The weld depth and bead were measured using a Mitutoyo PJ-300 profile projector. The welds were inspected both visually and using an optical microscope to study weld defects, cracks and the microstructure in the weld region. The parameters used in this experiment for normal welding and the two beam weld geometry are listed in **Table 3.2**. To monitor the relative temperature between the main and the pre-heated beam, temperature measurements were taken throughout the experiments with four thermocouple wires attached onto the specimen surface, 2 mm away from the weld region. Two thermocouple wires (T1 and T2) were arranged adjacent to each other at the beginning of the weld, and the other two thermocouple wires (T3 and T4) were arranged adjacent to each other at the end of the weld, this was the same as for the post-weld heat treatment, as shown in **Figure 3.26**.

3.3.3 Weld Characteristics

3.3.3.1 Hardness profiles

In all cases, the Vicker's hardness tests were performed as a function of depth and transversely across the heat-affected zone, fusion zone and base metals. The laser power for welding was 285 W (including the pre-heating geometry as well). **Figure 3.50** shows the hardness profiles across the weld for the pre-heating and normal welding configurations and different pulse repetition frequencies (PRF). The hardness gradient decreased with increasing PRF. By comparing both weld geometries, it is seen that the pre-heating system produced a lower hardness gradient in the fusion zone and heat-affected zone. This resulted in a reduction in the peak hardness from 568 kg/mm^2 to 521 kg/mm^2 with an increase in the PRF from 6 to 9 Hz. It was seen that for the normal weld the corresponding peak hardness reduced from 1415 to 747.6 kg/mm^2. The hardness was significantly reduced by 59.9 % for a PRF of 6 Hz from 1415 to 568 kg/mm^2. At 9 Hz, the reduction was 30.2 %. **Figure 3.51** shows the hardness profiles across the weldment for different pulse widths, for both weld geometries. Using a preheating beam produced a less brittle weld and this weld geometry was more effective in decreasing the weld hardness characteristics than the normal welding configuration.

From **Figure 3.51**, the preheating configuration resulted in a reduction in peak hardness from 651.6 kg/mm^2 to 531.8 kg/mm^2 with an increase in the pulse width from 6 to 9 ms. It was seen that the normal welding gave the greatest reduction in the peak hardness from 1839.6 to 1278.2 kg/mm^2 with the same in increase pulse width. In both cases, for 6 ms the peak hardness was greatly reduced by 64.6 % from 1839.6 to 651.6 kg/mm^2 for the normal and preheated welds respectively. For a pulse width of 12 ms the reduction was 58.3 %. This results confirmed that, a dual pass welding produced a less brittle weld, this correlates well with the work done by Moon [3.37].

In all cases, it is seen that the Vicker's hardness was much greater for the normal welds than the preheated welds and that the heat-treatment process was effective in reducing the hardness discontinuities. For the normal weld, non-uniform hardness in the welds lead to poor mechanical properties. **Figures 3.52** and **3.53** show the percentage of reduction in the peak hardness for the preheated weld relative to the normal weld at different PRFs and pulse widths, respectively. As the PRF was increased from 6 to 8 Hz, the difference in the peak hardness reduction for the normal welds and treated welds, became lower; this difference was greatest at the lowest PRF of 6 Hz. **Figure 3.52** shows that there was nearly 59.9 % reduction in the peak hardness for a PRF of 6 Hz of the preheated weld. Interestingly, increasing the PRF above 8 Hz, there was a slight increase in the peak hardness reduction from 30 % to 30.2 %.

From **Figure 3.53** shows the dependency of the reduction in the peak hardness of the weld at different pulse widths. It is seen that the percentage reduction in peak hardness was slightly increased and decreased, for the pulse width from 6 ms to 10 ms, respectively. The average percentage reduction in the peak hardness of the weld was 65.1 %. Quite clearly, the reduction in the peak hardness decreased from 64.8 % to 58.3 %, for the pulse width from 10 ms to 12 ms. As the pulse width increased, pre-heating the sample was more effective in improving weld hardness characteristics than the normal weld geometry; this is illustrated clearly **Figure 3.53**. As the pulse width was increased, the greatest reduction in the peak hardness at the fusion zone was achieved.

Hence, with reduced non-uniformities in the hardness profiles, the likelihood of cracking, when subjected to cyclic loading was reduced.

Figures 3.54 and **3.55** show the variation of hardness as a function of depth, for both weld geometries, for different pulse widths and PRF. From these figures and for a given PRF and pulse width, it is seen that for the normal weld the hardness decreased significantly with increasing pulse width and PRF. For a given pulse width or PRF, the preheating geometry showed no significant change in the hardness as a function of depth. However, for a given depth, the hardness decreased with increasing pulse width and PRF. In general, the preheating process produced a uniform hardness along the centre of the fusion zone, these results are similar to the post-weld heat treatment - see Section 3.2.3.2. Foley *et al.* [3.39] reported on the softening effect of dual pass laser weld on armor plates, the effect of second pass weld resulted in a slight reduction of hardness from the top and bottom of the fusion zone.

3.3.3.2 Tensile test

The weld beads for all samples were machined and tested in the transverse direction. Tensile tests were performed, at a crosshead of 0.5 mm/sec, to determine the mechanical properties of the welds done with both geometries. All failures occurred in the fusion zone; this confirms the hardness results discussed previously. **Figure 3.56** shows the tensile strength as a function of pulse width for normal and preheating geometries. It can be seen clearly that the pre-heating configuration produced the welds with greatest strength. In all cases, the tensile strength increased with increasing pulse widths. Furthermore, for the preheating geometry, the tensile strength was 117.83 MN/mm^2 for 12 ms and for the normal welding with the same pulse width, the tensile strength was 81.86 MN/mm^2. This represents difference in tensile strength of 30.5 %.

It is apparent from **Figure 3.57** that, as the pulse width was increased, the difference between the tensile strength for the normal weld and pre-heated weld, became less. The maximum tensile strength of 75.3 %, that was observed at a pulse width of 6 ms, for the pre-heated samples. The rate of percentage difference in tensile strength reduced greatly

with increasing the pulse width from 6 to 12 ms. However, the minimum difference in tensile strength was observed at 12 ms for both normal and pre-heated weld.

The effect of PRF can be seen in **Figure 3.58**, for both normal and preheating geometries. Interestingly, the PRF increased with the tensile strength for both cases. However, the tensile strength was greatest for the preheated welds. For all cases, the difference was minimum at 6 Hz. For the pre-heating geometry at 9 Hz, the tensile strength was 84.44 MN/mm^2 and for normal weld the maximum strength was 55 MN/mm^2. The tensile strength was increased by 53.5 %.

Figure 3.59 shows the maximum and minimum difference in tensile strength, for the normal and pre-heated welds. Increasing the PRF from 6 to 7 Hz resulted in a significant increase in tensile strength by 36.8 %, for the pre-heated weld. For an increase in PRF from 7 and 8 Hz, a slight decrease between tensile strengths was seen. Moreover, above 7 Hz, the difference in tensile strength between the normal and pre-heated weld increased.

3.3.3.3 Aspect ratio

The aspect ratio for both normal and preheated laser welds was taken as dividing the weld penetration by weld width, and the dependency of the aspect ratio on PRF and pulse widths are shown in **Figures 3.60** and **3.61**, respectively. **Figure 3.60** shows that for the normal welding process, the aspect ratio increased with the PRF. Whereas, at a higher PRF, the pre-heated weld produced a wider weld bead than normal weld, this resulted in a lower aspect ratio as compared to the normal weld process. Thus, it can be seen clearly that the aspect ratio decreased with increasing PRF for the pre-heated welds. Despite the lower aspect ratio, for the pre-heated weld geometry, there was an increase in the weld width which resulted in an increase in the tensile strength at a higher PRF.

It can be seen in **Figure 3.61** that the aspect ratio increased with the pulse width from 6 to 10 ms for the normal welding. This is due to the narrow weld bead achieved in the normal welding process over the range of laser parameters investigated. For pre-heated welds, the aspect ratio decreased with increasing pulse width. Moreover, a wider weld width was produced by the pre-heated weld; this resulted in a lower aspect ratio as compared to the normal weld.

3.3.3.4 Weld beads

Figure 3.62 shows that the weld widths for preheating were greater than those for normal weld configuration. For both geometries, the weld widths increased with increasing pulse widths. The smallest difference between both geometries occurred for 6 ms and the greatest difference occurred for pulse widths of 12 ms. **Figure 3.63** shows the effect of weld widths for different PRF, for the normal and preheating configurations. The minimum difference in the weld width occurred at the lowest PRF, and the maximum difference occurred at the highest PRF. From the range of parameters investigated the weld widths increased with increasing PRF. In all cases, for the pre-heated welds, the weld bead was greater than with the normal weld, these results agree with the report made by Chung *et al.* [3.40] in that the pre-heating technique produced a wider weld bead.

3.3.3.5 Weld penetration

Figure 3.64 shows the weld penetration for normal and preheating configuration as a function of pulse widths. Interestingly, over the range of pulse widths investigated, the weld width increased with increasing pulse width from 6 ms to 12 ms. For the preheating geometry, there was no significant difference in the weld penetration. **Figure 3.65** shows the effect of weld penetration as a function of PRF, for the normal weld configuration the penetration depth increased with PRF. For the preheating geometry, the weld depth remained constant throughout the range of parameters investigated.

3.3.3.6 Rate of formation of weld volume

The rate of formation of weld volume was found by multiplying the product of the weld width and weld depth by the translation velocity of 5 mm/sec. The weld volume rate of formation for different pulse widths was calculated, for the normal and pre-heated weld geometries, the results are shown in **Figure 3.66**. The rate of formation of the weld was greatest for the preheating geometry, and in both cases it increased with pulse width. For instance, for a pulse width at 6 ms the weld formation rate was 7.35 mm^3/sec and 3.13 mm^3/sec, for the normal and preheating geometries, respectively. The effect of PRF on the weld volume formation rate is shown in **Figure 3.67** Again, the formation rate was greatest for the preheating geometry, and in both cases it increased with PRF. For example the weld formation rate increased by 19 % for the preheating geometry for an increased in PRF from 6 to 9 Hz.

3.3.3.7 Temperature profiles

The temperature distribution along the welded gauge plate was measured. **Figures 3.68** and **3.69** show the temperature profiles for the normal weld configuration for pulse widths of 6 ms and 12 ms, respectively. Measurements were taken at the beginning (T1 and T2) and end (T3 and T4) of the weld region, four thermocouples were attached to the surface of the specimen. The temperature measurements were normalised so that the highest value was unity. By comparing **Figures 3.68** and **3.69**, a significant difference in the peak normalised temperature occurring at the beginning and end of the weld is seen. With a pulse width of 12 ms, a wider width was produced and a corresponding higher normalised temperature profile at the end of the weld. **Figure 3.70** shows the peak temperature for a pulse width of 12 ms for the preheated weld. With the preheating technique, the temperature reduced at a slower rate than with the normal weld, and it produced a wider and higher normalised peak temperature than the normal weld configuration at the beginning and end of the weld. In general, it was observed that the normal weld produced a uniform temperature profile but the preheating technique developed a non-uniform and wider temperature profile; this geometry leads to a slower rate of cooling. The spatial hardness discontinuities are dependent on the

temperature distribution during the welding process. Moreover, different welding techniques and laser parameters will lead to different heat transfer characteristics and ultimately to different weld characteristics and grain size. There are two possible sources of error in the temperature measurement. The repeatability in the placement accuracy of the thermocouple is difficult and the spatial error may be up to 1 mm. However, in this work it is the relative shape of the temperature profile that is of interest and not the absolute temperature.

3.3.3.8 Microstructure study of fusion zone

Figure 3.71 shows a picture of a typical normal laser weld that had not received any heat treatment. No evidence of micro-cracks was found in the fusion zone for the normal and preheating geometry. During welding the temperature around the weld was greater than the materials melting point, this inevitably leads to the formation of relatively coarse grain in the fusion zone. Moreover, the temperature dropped sharply with increase in distance from the heat-affected zone, and a finer grain size was produced in the heat-affected zone. For all cases, the main fusion region consisted of a martensite, dispersed carbides and retained austenite. This results from higher solubilities of carbon content, and supercooling of the high temperature from the austenite phase; this is caused by the high quenching rate associated with conduction of the heat to surrounding environment, Goswami [3.41]. **Figure 3.72** shows the microstructure for the preheating geometry with the same laser parameters and translation velocity as shown in **Figure 3.71**. Here the grain size was finer in the fusion zone than that observed for the normal weld configuration. The appearance of this microstructure is reflected in the microhardness profile results, see Section 3.3.3.1. **Figures 3.73** and **3.74** show significant differences between the weld beads, for the normal and preheating geometry. However, this shows that preheating the material before a weld permits more laser beam energy to couple into the weld region, this produced a wider bead and a finer grain structure in the fusion zone.

3.3.4 Conclusion of Nd:YAG laser welding with in-line pre-heating process

The investigation of the mechanical properties and microstructure of welded high carbon steels have revealed more details about the pulse laser welding process and the possible advantages that can be achieved with preheating. The weld quality was investigated for different pulse widths and pulse repetition frequencies, and the results were quantified by measuring the hardness profiles, tensile strength, weld beads, weld penetration and thermal profiles, for both normal and preheating geometry.

The hardness profiles measured transverse across the weld direction show in all cases that there was a greater peak reduction in the hardness, at the centre of the weld, for the preheating geometry. The peak hardness was reduced by 36.2 % for a PRF of 9 Hz, and increasing the pulse width to 12 ms gave a peak hardness reduction of 58.3 %. However, this shows an effective significant hardness reduction can be achieved by increasing the pulse width for the preheating technique, a higher temperature profile was achieved for the preheating process with increasing PRF and pulse width. Moreover, the preheating geometry showed no significant change in the hardness as a function of depth. From the tensile test results, the annealing process produced a higher tensile strength at the butt joints than the normal welding. The difference in tensile strength between normal and pre-heated welds decreased with increasing pulse width. Interestingly, increasing the PRF and pulse width, resulted in a greater strength which lead to a lower aspect ratio for the pre-heated weld. Moreover, this produced a wider weld bead than the normal weld for different laser settings. A favourable structure appeared in the weld region for the preheating process. The evidence to support this result and the reduced cooling rate was shown in the thermal distribution profiles of the pre-heated weld geometry as compared to the normal weld configuration.

3.4 Comparison between post-heating and pre-heating techniques

The rate of cooling in the fusion and heat affected zones of laser welded high carbon steel was controlled by using a dual beam delivery system. The tempering process was done simultaneously with propitious selection of pre-heating and post-heating the

welded sample to control the rate of cooling and prevent a rapid quenching rate. Both approaches resulted in considerable improvement in the hardness profiles. **Figures 3.75** and **3.76** show the percentage of reduction in the peak hardness of the weld for the pre-heating and post-heating of the samples, for different pulse widths and PRFs, respectively. For the pre-heated samples, there was nearly more than a 60 % of maximum hardness reduction in the peak hardness at the lowest pulse width and PRF. Additionally, the post-heated samples also achieved a maximum hardness reduction at a pulse width of 6 ms and PRF of 6 Hz. In all cases, as the pulse width and PRF were increased the difference between the Vicker's hardness of the normal, post-heated and pre-heating welds were compared to the hardness of the parent metal, and they became less; this difference was greatest for the pre-heated samples. Thus, pre-heating the sample was more effective in improving the weld hardness characteristics than the post-heating technique; this is clearly illustrated in **Figures 3.75** and **3.76.**

However, the pre-heated welds produced a wider weld bead as compared to the post-heated welds, this resulted in a lower aspect ratio with the pre-heating technique compared to the post-heated welds as shown in **Figures 3.77** and **3.78**. Whereas, it can be seen clearly that the aspect ratio decreased with increasing PRF and pulse width, for the pre-heated weld. Due to the wider weld width which leads to a lower aspect ratio, the rate of weld formation rate was greatest for the pre-heated weld configuration. **Figures 3.79** and **3.80** show that the weld volume formation rate increased with the PRF and pulse width, for both beam delivery configurations.

For the post-heated welds, the mechanical strength of the joint is superior to that of the pre-heated samples as shown by the results in **Figures 3.81** and **3.82**. The post-heated technique had a hardening effect, and it also raised the tensile strength as compared to the pre-heated welds which produced a softer region in the HAZ, which was generally narrow. This softer region produced by the post-heated welds was restrained on both sides by harder material which opposed its deformation. For both approaches, the tensile strength increased with the pulse width, and the strength reduced with increasing

PRF for the post-heated weld, but slightly increased for the pre-heated weld. The spatter loss appeared above the fusion region which resulted in the reduction of the strength for a higher PRF.

CHAPTER THREE REFERENCES

[3.1] Weisman, C. " Welding Handbook". American Welding Society publisher. 7th Edition, **1**, 1981.

[3.2] Thyagarajan, K., Ghatak, A. K. "Laser Theory And Applications". Optical Physics And Engineering, 294-295, 1981.

[3.3] Olsen, F. O. "Pulse Laser Material Processing, Nd:YAG Versus CO_2 Lasers". In: Proc. Annals Of The CIRP. 44, 142-144, 1995.

[3.4] Yoshioka, S. Miyazaki, T. Shirai, J. Miyazaki, N. "Fundamental of Experiments of Nd:YAG Laser Beam Welding For Assesment of Mechanical parts In Miltimeter machine System", The 15th International Congress on Applications of Lsers and Electro-Optics, ICALEO'96, Sect C, 150 - 156.

[3.5] Steen, W. M."Lasers material processing". Springer-Verlag publisher. 1991.

[3.6] Schwartz, M. M. "Source book on electron beams and laser beam welding". American Society For Metals, 343-346, 1981.

[3.7} Gu, H. P., Duley, W. W. "A statistical approach to acoustic monitoring of laser welding". J. Phys. D: Appl Phys. 29, 556-560, 1995.

[3.8] Honeycombe, R. W. K. "Microstructure and Properties". Edward Arnold publisher. 1981.

[3.9] Ng, E. S., Watson, I. A. "Characteristic of CO_2 laser welded high carbon steel guage plate". J of Laser Application. 9, 15-21,1997.

[3.10] Ng, E. S., Watson, I. A., "Nd:YAG Laser Welding of High Carbon Steel with in-line process annealing". Journal of Laser Application, under reviewed.

[3.11] Wang, K. L., Zhu, Y.M., Dong, Z. J., Zhang, R.J. "Microstruture and property of laser Transformation hardening on sheet steel with high carbon content". In: Proc. ICALEO '95. The 14th International Congress on Applications of Lsers and Electro-Optics, San Diego (J. Mazumder, A. Matsunawa and C. Magnusson eds.). Orlando FL: Laser Institute of America, 85-91, 1995.

[3.12] Goswami, G. L., Kumar. D., Pappachan, A. L., Grover, A. K.,Sridhar, k. "Characterisation of chromium bearing surface alloys produced by lase alloying on low carbon shell substrates". Journal of Laser Application. 7, 157-159, 1995.

[3.13] Kajanpa V P, Helin J P and Moisio T J I 1988 Composition and microstructure of laser beam welds between dissimilar metals Proc. 7th International Congress on Applications of Lasers and Electrooptics, 259-70

[3.14] Mimatsu J, Bros J A, Elijah-Kannatey-Asibu Jr and Chan M M. 1995 Determination of energy absorption during laser welding by an iterative conduction methods J. Laser. Appl. **7**, 162-168

[3.15] Poueyo-verwaerde A, Fabbro R and Deshors G 1993 Experimental study of laser induced plasma in welding conditions with continuous CO_2 laser J. Appl. Phys. **74** 5773-5.

[3.16] Milewski J O, Lewis G K and Wittig J E 1993 Microstructural Evaluation Of Low and High Duty Cycle Nd:YAG Laser Beams Welds In 2024-T3 Aluminum Supplement of Welding Journal, 341-342

[3.17] Abdullah H A, Ng E S, Chatwin C R and Watson I A 1995 Process annealing of laser welded high carbon steel Proc. 14th International Congress on Applications of Lasers and Electro-optics, 964-73

[3.18] Pan R and Watt F D 1995 Simulating microstrucutre development in high carbon steel cross-wire welding Welding. Journal, 385-388.

[3.19] Ng E S, Watson I A 1997 Characteristics of CO_2 laser welded high carbon steel gauge plate J. Laser. Appl. **9,** 15-20

[3.20] Scott, A. Frewin, M. "Tandem Nd:YAG Laser Welding", The International Congress On Applications Of Lasers And Electro-optics, ICALEO'97, San Deigo, Nov 1997, Section G, 44-50.

[3.21] Burdekin F M !969 Heat Treatment Of Welded Structure (The Welding Insitute), 8-15.

[3.22] Ng E S, Watson I A, Abdullah H A and Chatwin C R 1996 Improved hardness characteristic of laser welded high carbon steel Proc. CLEO/EUROPE-EQEC Europe Congress, 243

[3.23] Wang K L, Zhu Y M, Dong Z J and Zhan R J 1995 Microstructure and property of laser transformation hardening on sheet steel with high carbon content Proc. ICALEO, 85-88

[3.24] Byer, E. Brenner, B. Poprawe, "Hybrid Laser Welding Techniques For Enhanced Welding Efficiency", The International Congress On Applications Of Lasers And Electro-optics, ICALEO'96, Detriot, Nov 1996, Section D, 157-166.

[3.25] Okorokov L V, Volkov A A and Uglov A A 1989 Laser Preheating turning Of High-Melting Metals Soviet Engineering Research **9,** 117-19

[3.26] Liu N Y and Jr E K 1993 Characteristic Of Elliptical Laser Beam Preheating During Laser Welding Transaction Of ASME **64,** 895-899

[3.27] Liu N Y and Jr E K 1992 Laser Beam Welding With Simultaneous Guassian Laser Preheating Transaction Of ASME **58,** 191-195

[3.28] Goswami G L, Kumar D, Pappachan A L, Grover A K and Sridhar k 1995 Characterisation Of Chromium Bearing Surface Alloys Produced By Laser Alloying On Low Carbon Shell Substrates Journal of Laser Application **7,** 157-159

[3.29] Diehl M J and Messler R W 1995 Using Stress Relaxation Tests For Evaluating And Optimizing Postweld Heat Treatments Of Alloy 625 Welds Supplement of The Welding Journal, 109-114

[3.30] Zheng, M. Tapani, "Weld Metal/Ferritic Steel Interface In Laser Welded Austenitic/Ferritic Dissimilar Steel Joints", Journal of Materials Science Letters, 13(1994), 802-804.

[3.31] Kroos, U. Gratzke, G. Simon, "Toward A Self-Consisted Model of The Keyhole In Penetration Laser Beam Welding", J. Phys. D: Appl Phys. 26 (1993), 474-480.

[3.32] Poueyo, L.Sabatier, G. Deshors, R. Fabbro, A. M. Frutos, D. Bermsjo, J. M. Orza, "Experimental Study of The Laser Induced Plasma In Welding Conditions With Continuous High Power CO_2 Lasers", J. Phys D, Vol 3, 1(Dec 1991), 183-185.

[3.33] Behler, E. Beyer, R. Schafer, "Laser Welding of Aluminium", The 7th International Congress On Applications Of Lasers And Electro-optics, Nov 1988, 249-253.

[3.34] Hussein.A.Abdullah, Eng.S.Ng, Chris.R.Chatwin, Ian.A. Watson, " In Line Process Annealing Of Laser Welded High Carbon Steel ", The 14th International Congress On Applications Of Lasers And Electro-optics, San Diego, Nov 1995, 964-973.

[3.35] Metzbower, H. k. D. H. Bhadeshia, R. H. Phillips, "Microstructures In Hot Wire LaserBeam Welding of HY 80 Steel", J Material Science and Technology, Vol 10, Jan 1994, 57-60.

[3.36] Major, R. Ciach, R. Ebner, F. Jeglitsch, B. Kriszt, K. Rabitsch, "Laser Microstructure Modification of Aluminium Alloys and Steels", Phys. Stat. Sol. (a) 141, 15 (1994), 15-19.

[3.37] Moon, D."A Study of Dual Pass In Laser Welding of Steels", The International Congress On Applications Of Lasers And Electro-optics, ICALEO'87, Nov 1987, 964-973.

[3.38] Brenner, B. Gnann, R. Duschek, C. Lynen, T. Beyer, E. "Laser Induction Welding of Hardenable Steels", The International Congress On Applications Of Lasers And Electro-optics, ICALEO'97, San Deigo, Nov 1997, Section A, 61-70.

[3.39] Foley, J. "Survey of Application of High Power CO_2 Laser in Manufacturing", United Technology Research Centre, Jan 1986.

[3.40] Chung, C. Kim, M. Kim, C. "Comparison of Ultrasonic Weld Width Measurement And Optical Weld Depth Monitoring In Laser Sleeve Welding", The International Congress On Applications Of Lasers And Electro-optics, ICALEO'97, San Deigo, Nov 1997, Section C 44 - 54.

[3.41] L. Goswami, D. Kumar, A. L. Pappachan, A. K. Grover, K. Sridhar, "Characterization of Chromium Bearing surface Alloys produced by Laser Alloying On Low Carbon Steel Substrates", Journal of Laser Application, Vol 7, Sept (1995), 153-161

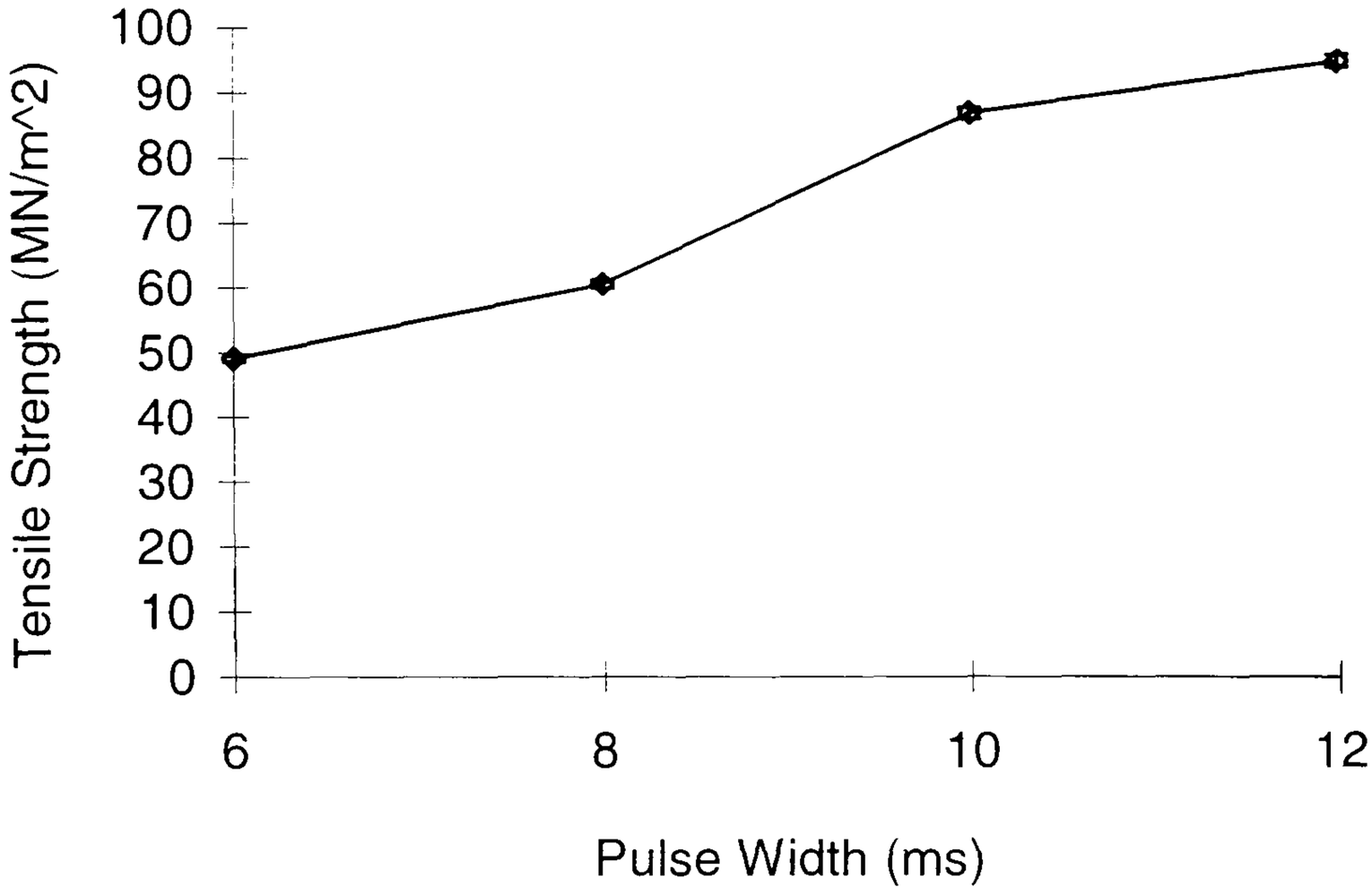

Figure 3.1 Tensile strength as a function of pulse width
(PRF: 10 Hz, translation velocity: 5 mm/s, Power: 200 W)

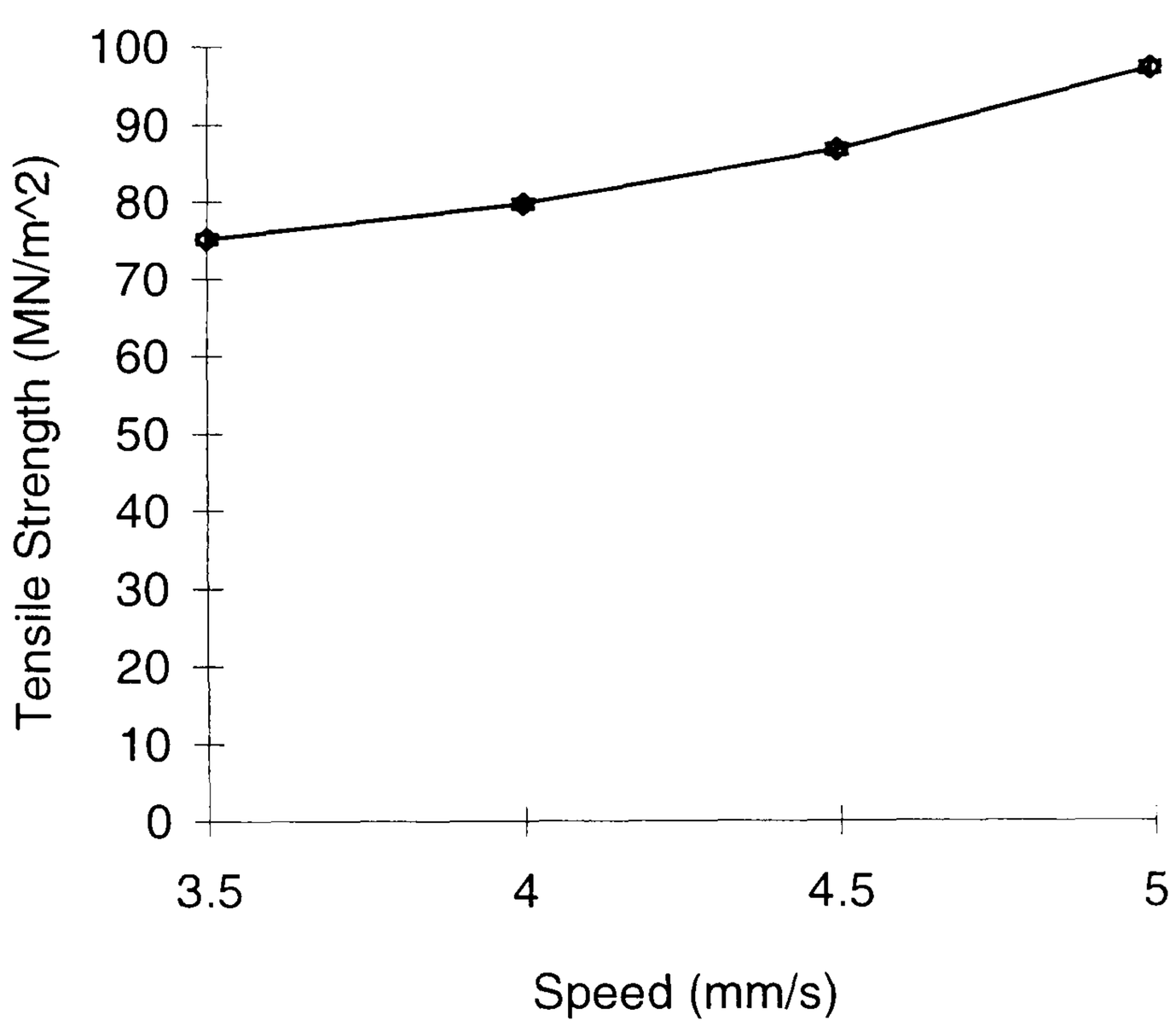

Figure 3.2 Tensile strength as a function of translation velocity
(PRF: 10 Hz, pulse width: 10 ms, Power: 200 W)

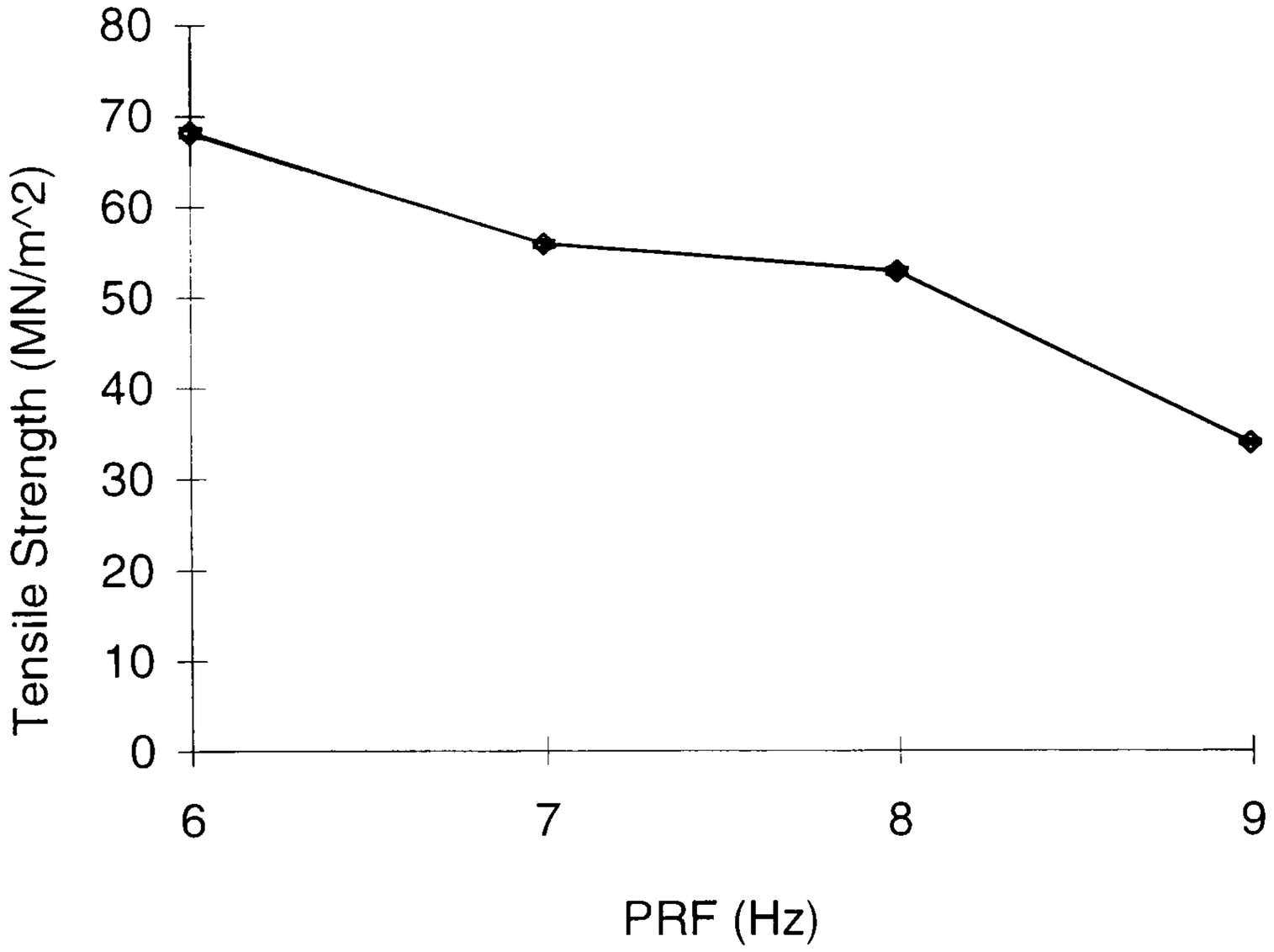

Figure 3.3 Tensile strength as a function of PRF
(Pulse width: 10 ms, translation velocities: 5 mm/s, Power: 200 W)

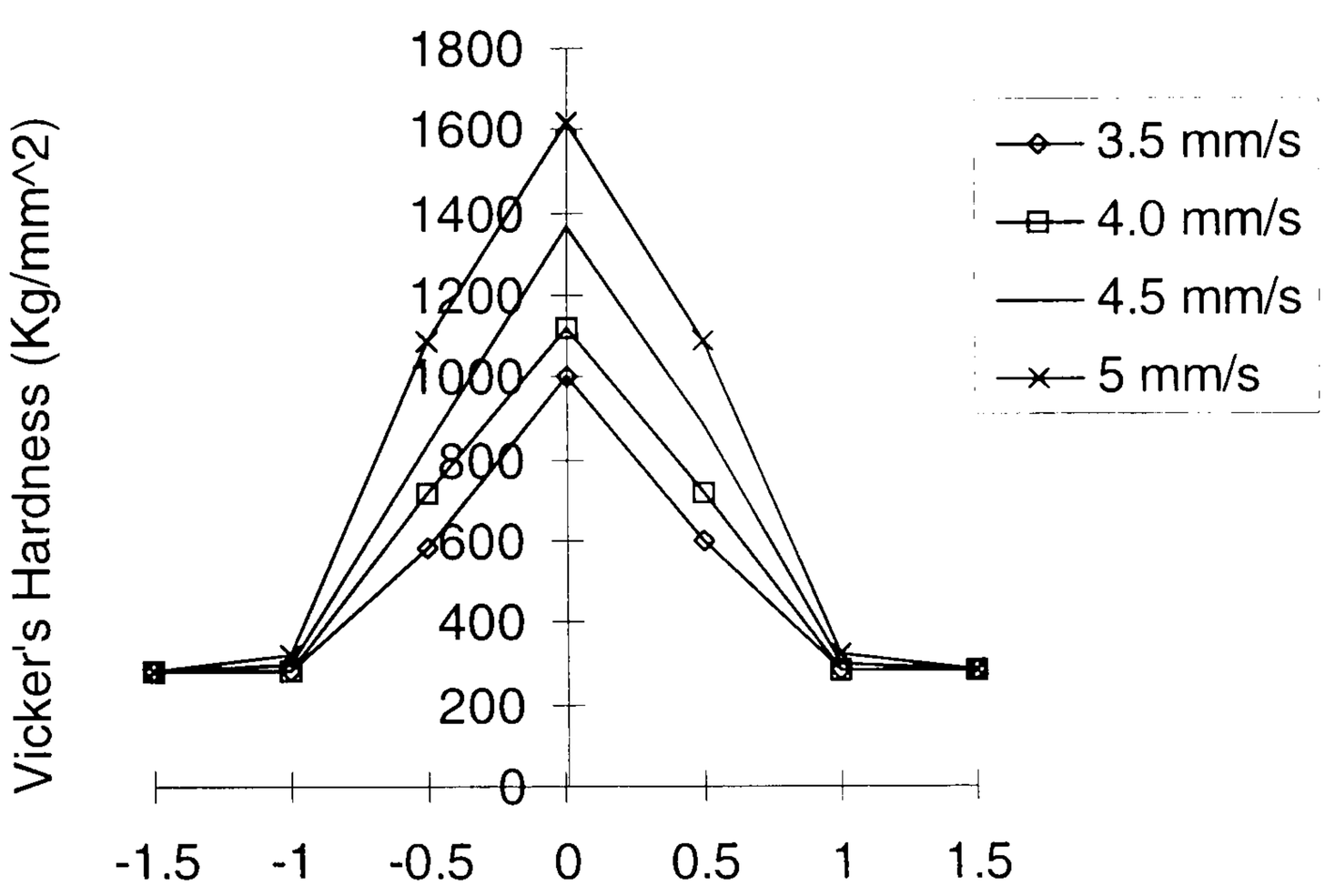

Figure 3.4 Microhardness across the weld for different translation velocity
(Power: 200 W, PRF: 10 Hz, pulse width: 10ms)

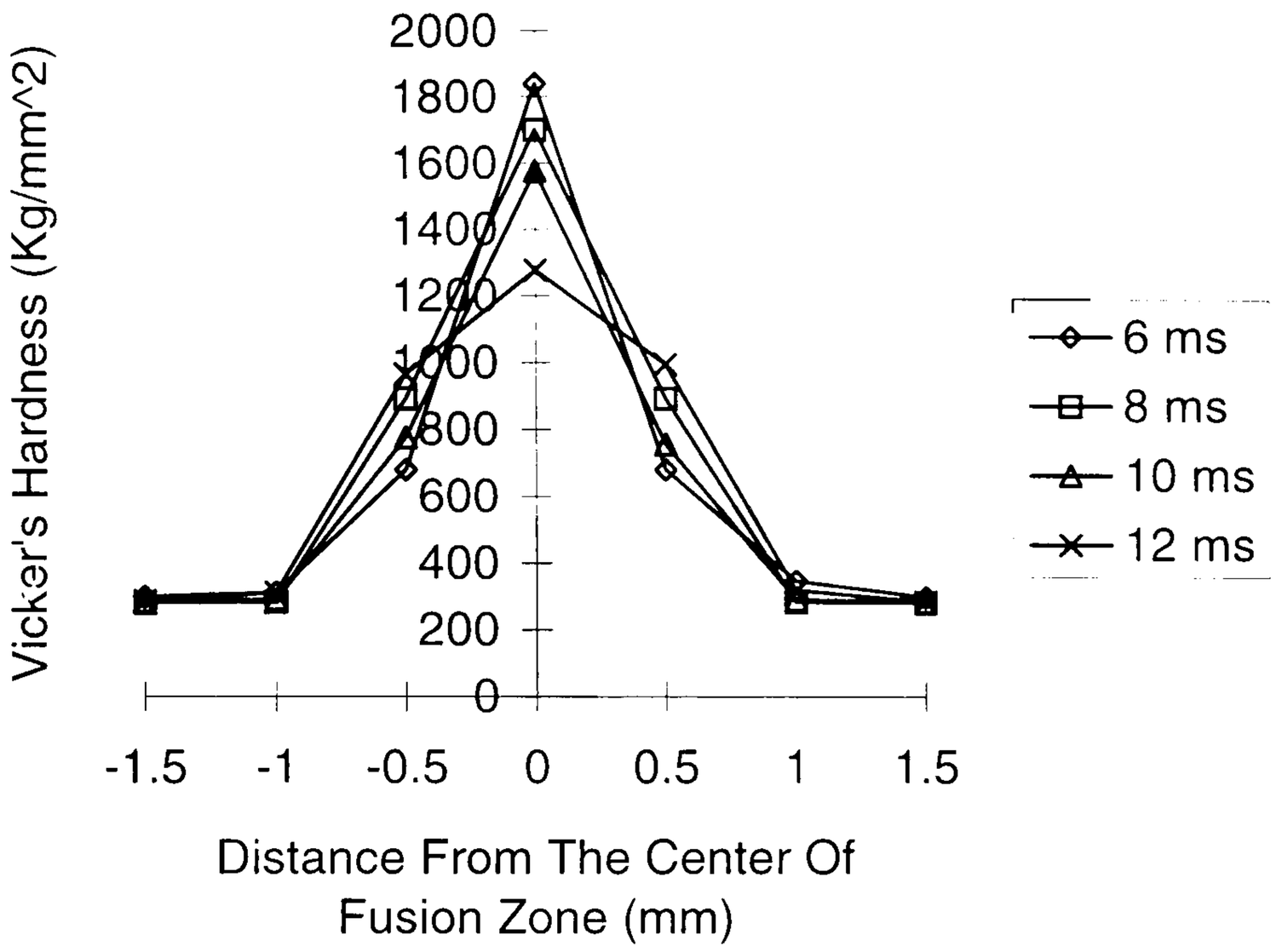

Figure 3.5 Microhardness across the weld for different pulse widths
(Power: 200 W, PRF: 10 Hz, translation velocities: 5 mm/s)

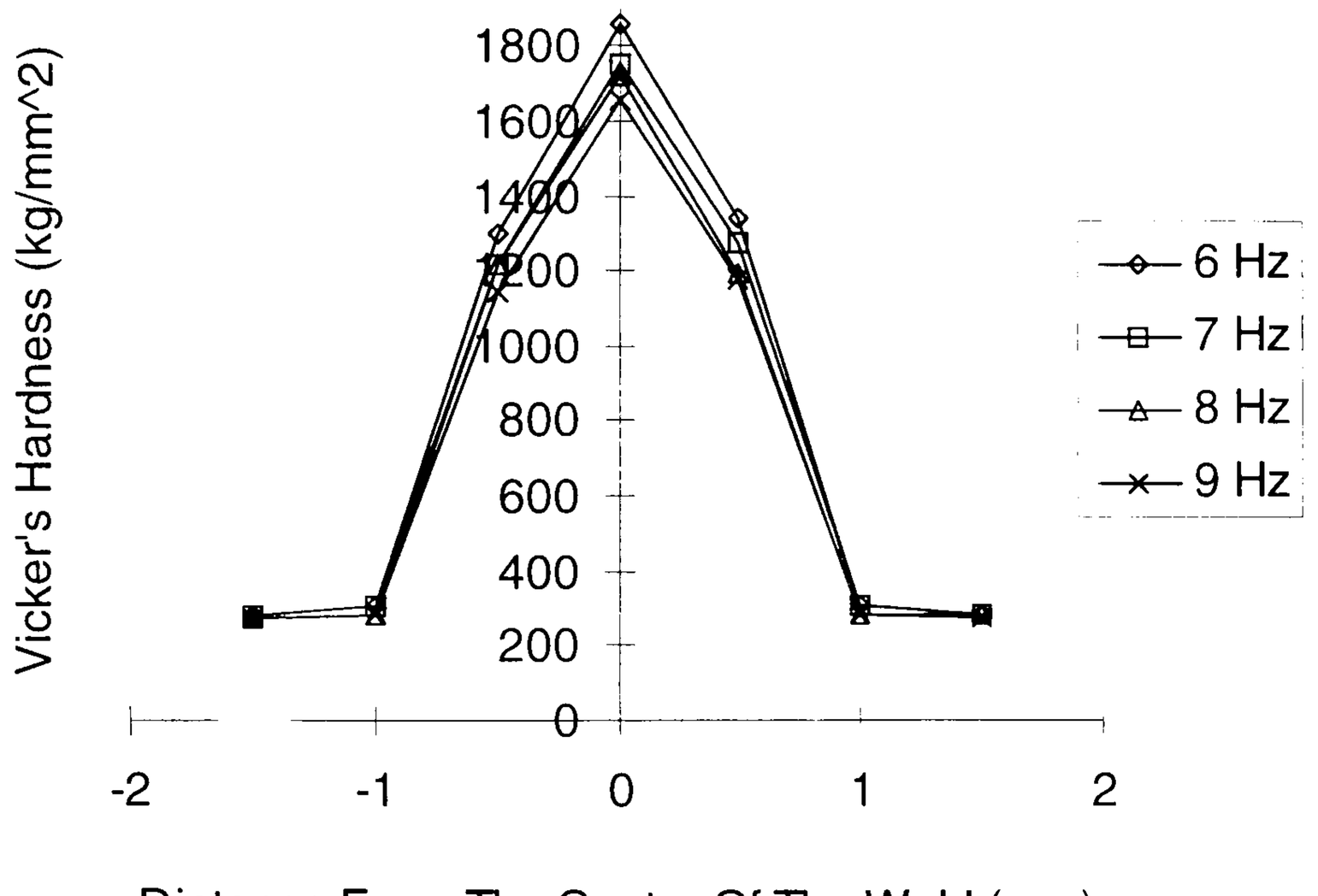

Figure 3.6 Microhardness across the weld for different PRFs
(Power: 200 W, pulse width: 10ms, translation velocities: 5 mm/s.)

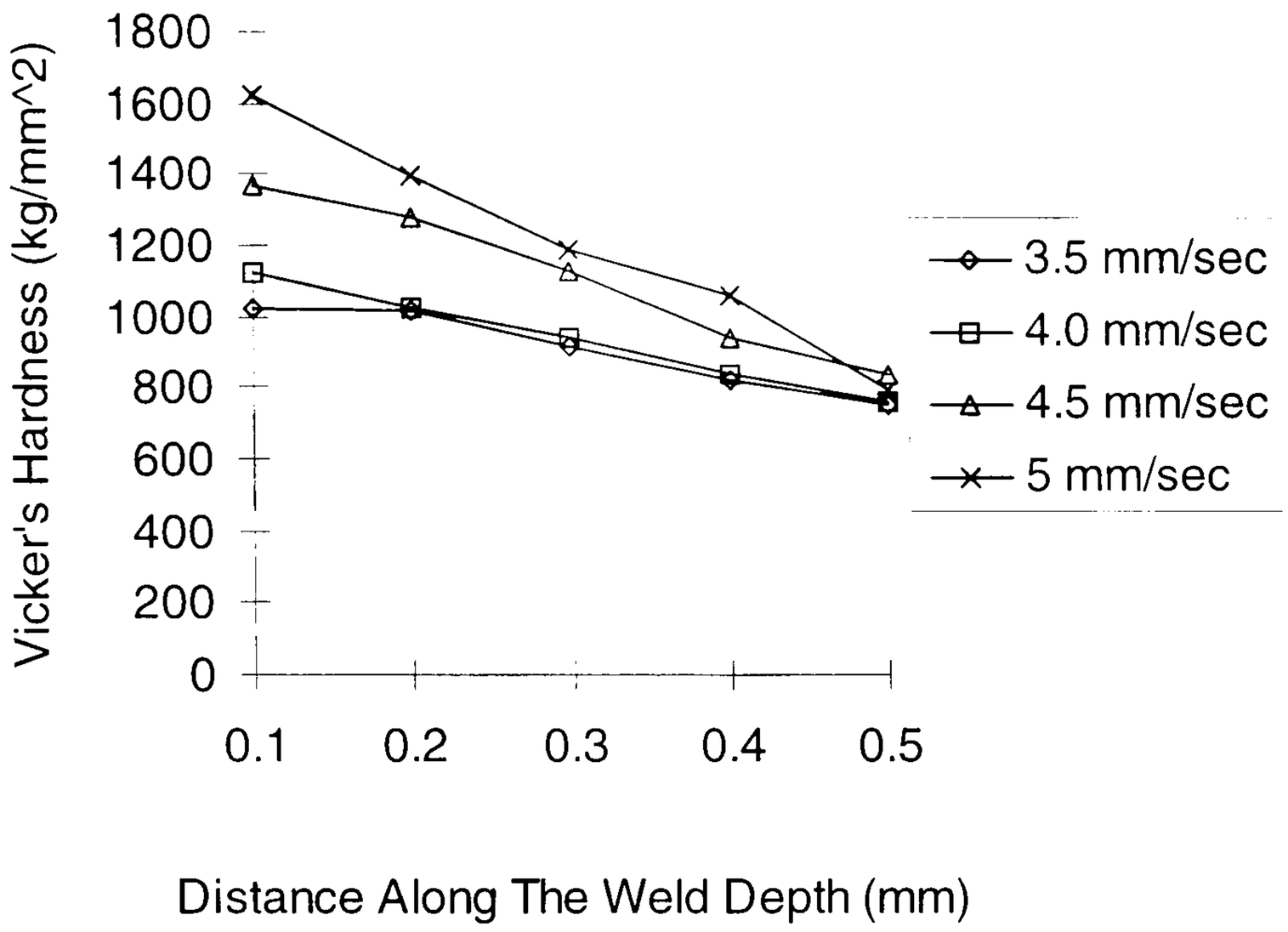

Figure 3.7 Microhardness as a function of weld depth for different translation velocities(Power: 200 W, pulse width: 10ms, PRFs: 10 Hz)

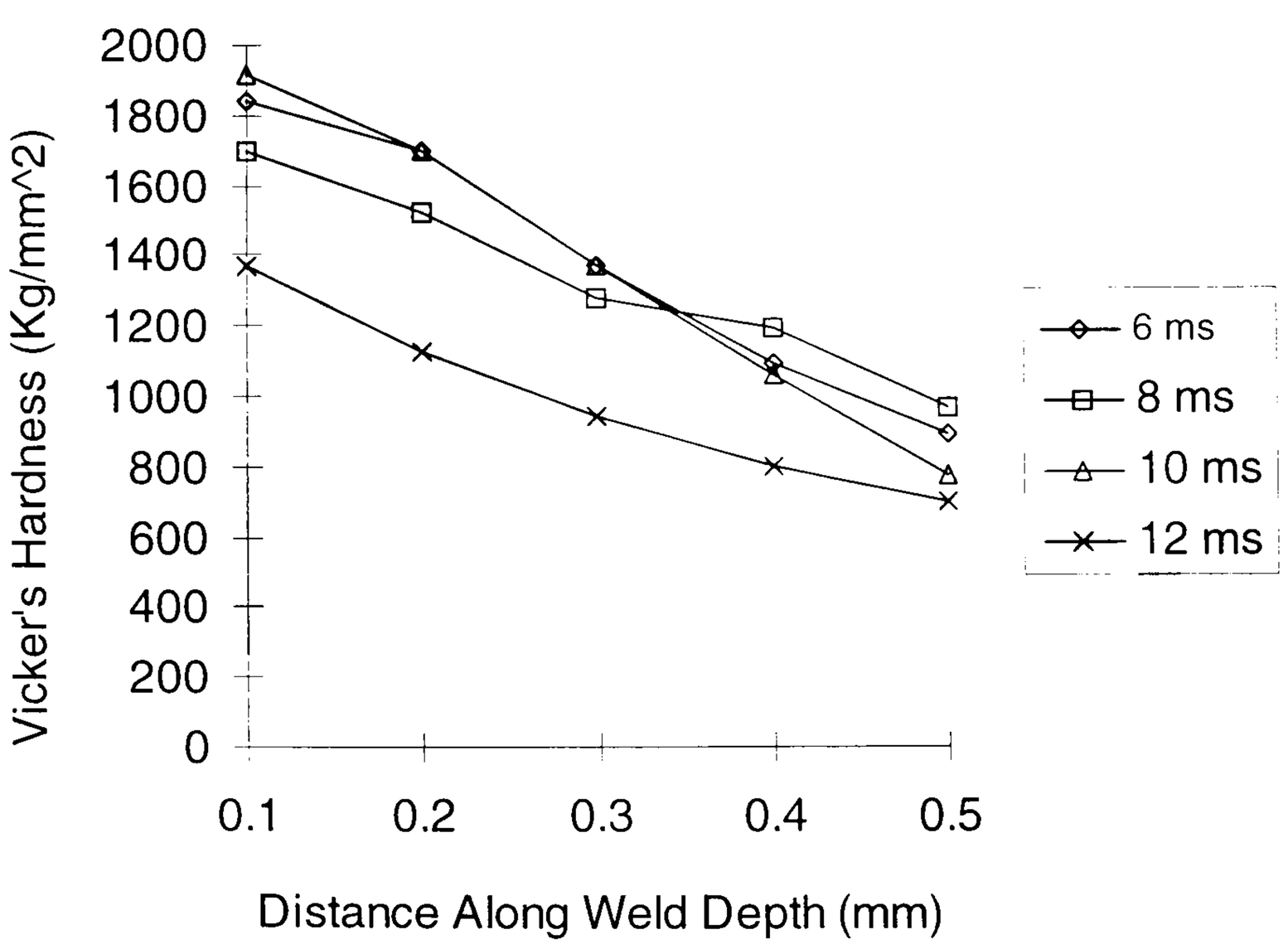

Figure 3.8 Microhardness as a function of weld depth for different pulse widths (Power: 200 W, PRFs: 10 Hz, translation velocity: 5 mm/s)

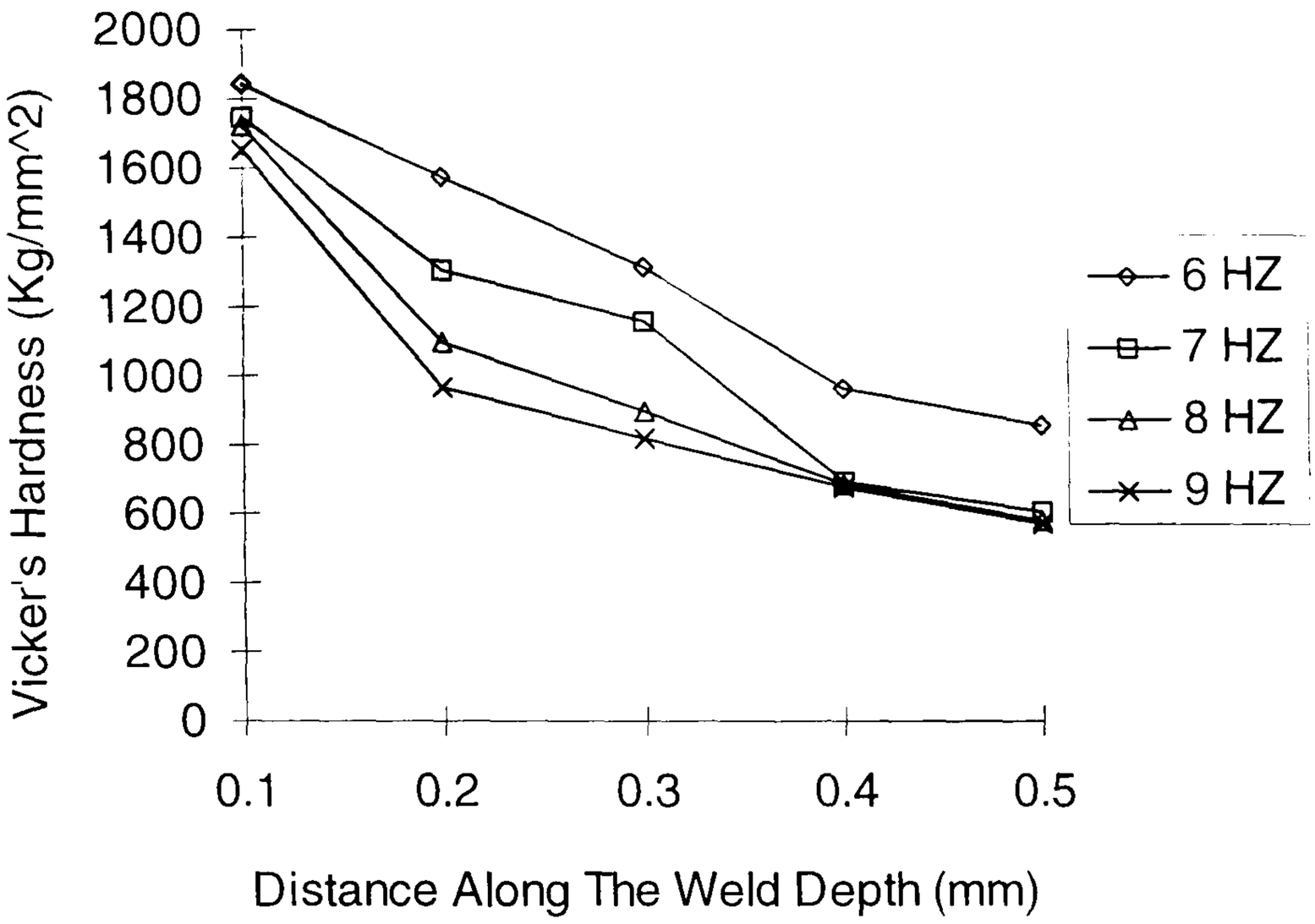

Figure 3.9 Microhardness as a function of weld depth for different PRFs
(Power: 200 W, pulse length: 10 ms, translation velocity: 5 mm/s)

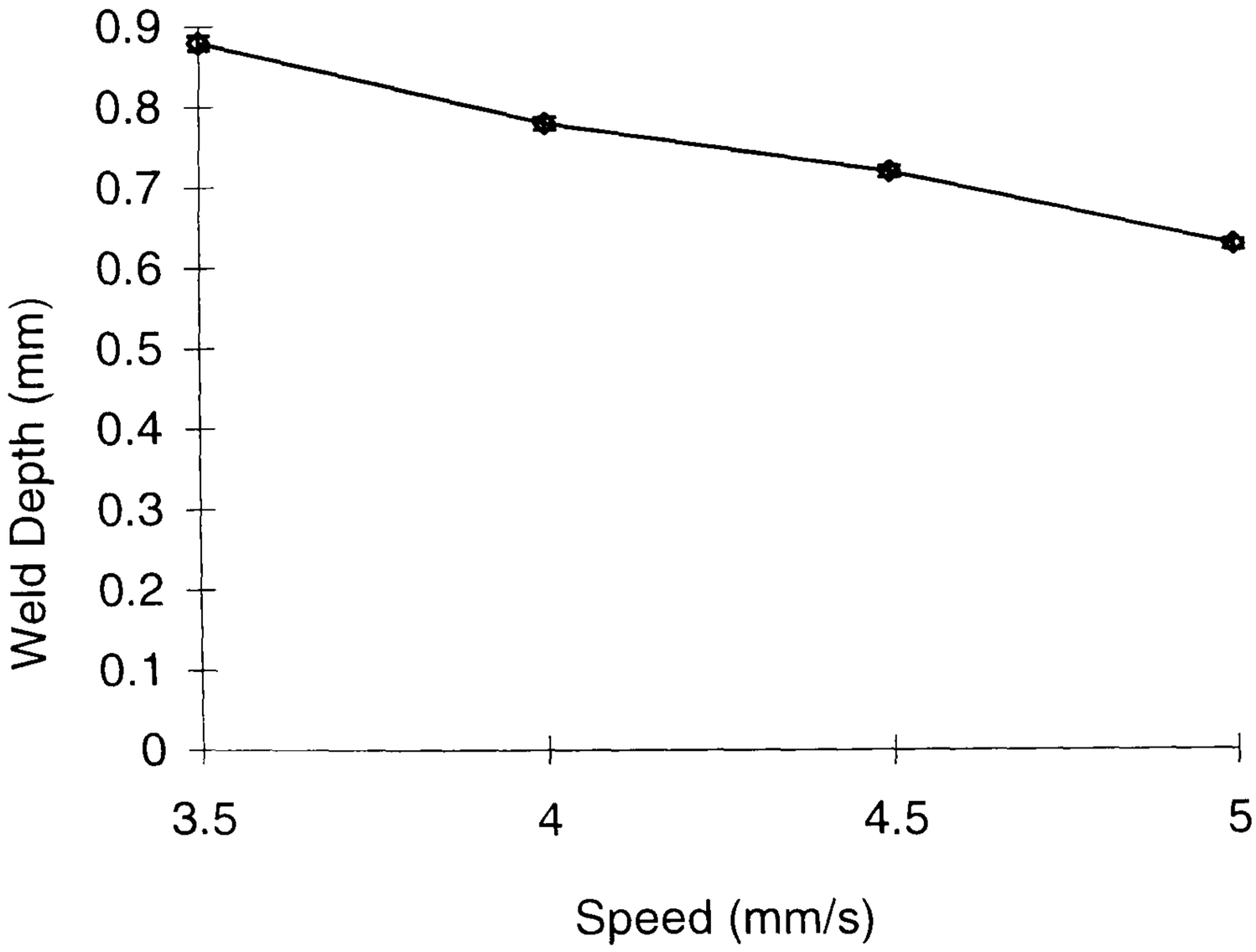

Figure 3.10 Weld depth as a function of translation velocity
(power of 200 W, PRF of 10 Hz, and pulse width of 10 ms)

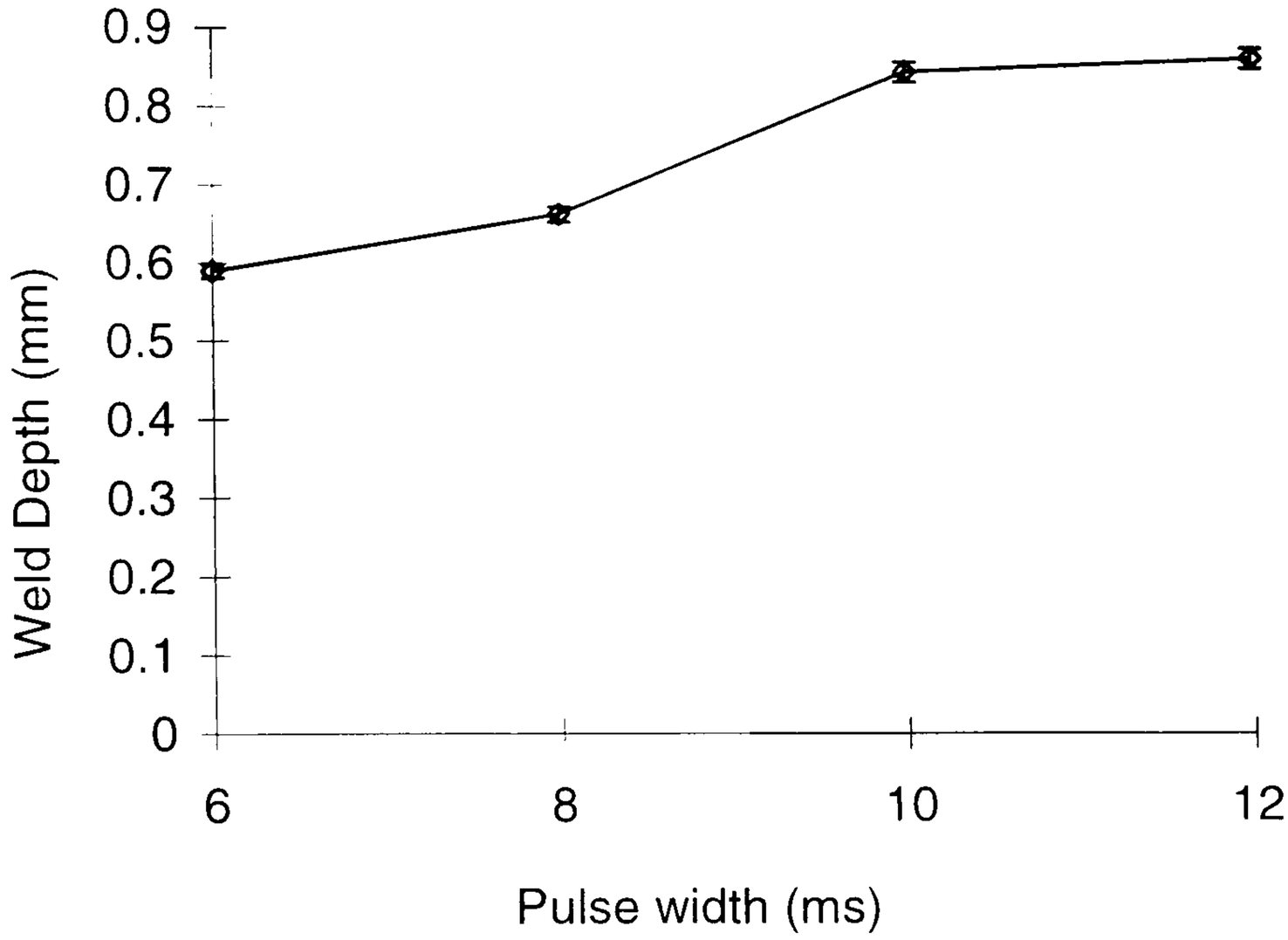

Figure 3.11 Weld depth as a function of pulse width
(power of 200 W, translation velocity of 5 mm/s, and PRF of 10 Hz)

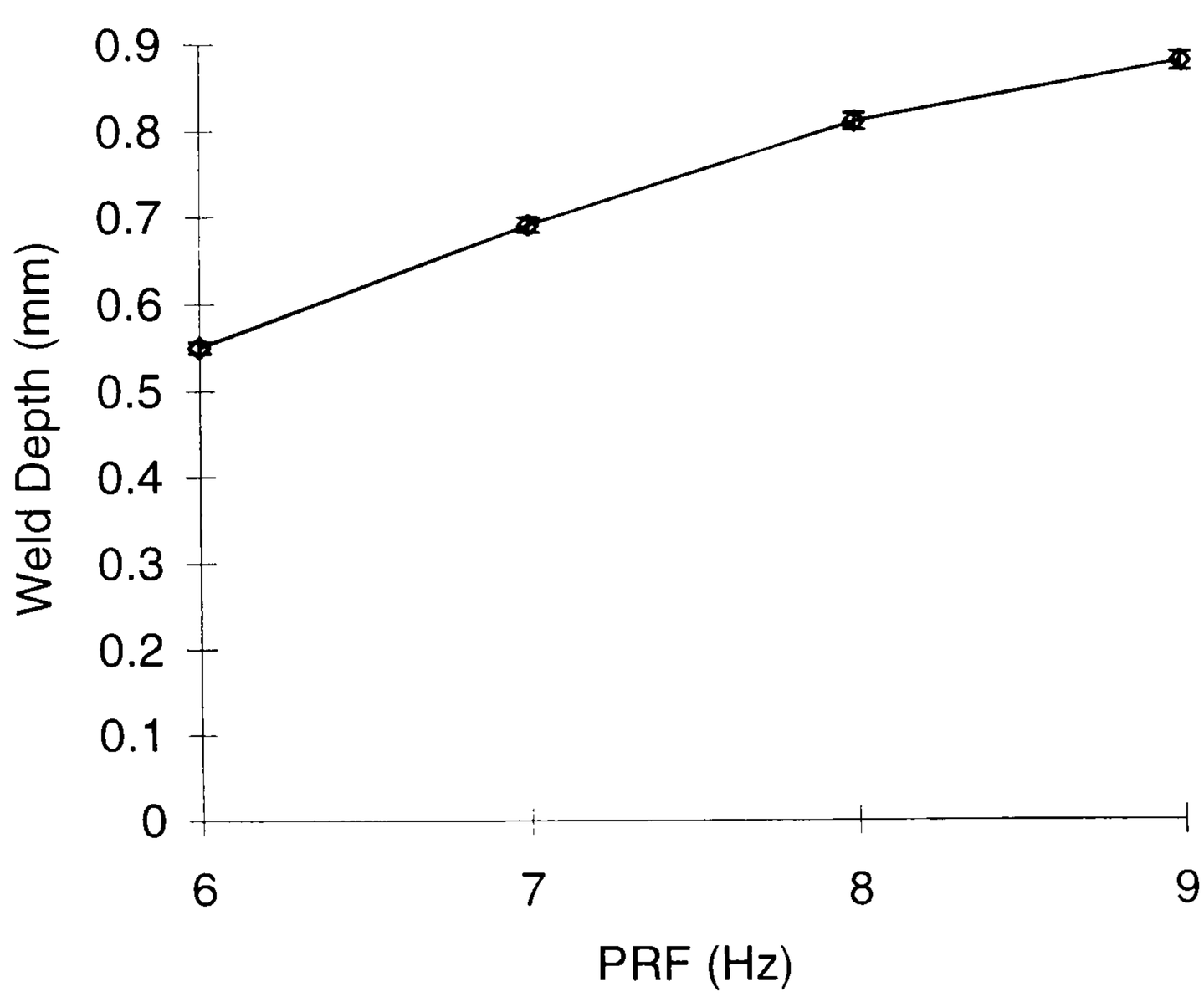

Figure 3.12 Weld depth as a function of PRF
(power of 200 W, translation velocity 5 mm/s, and pulse width of 10 ms)

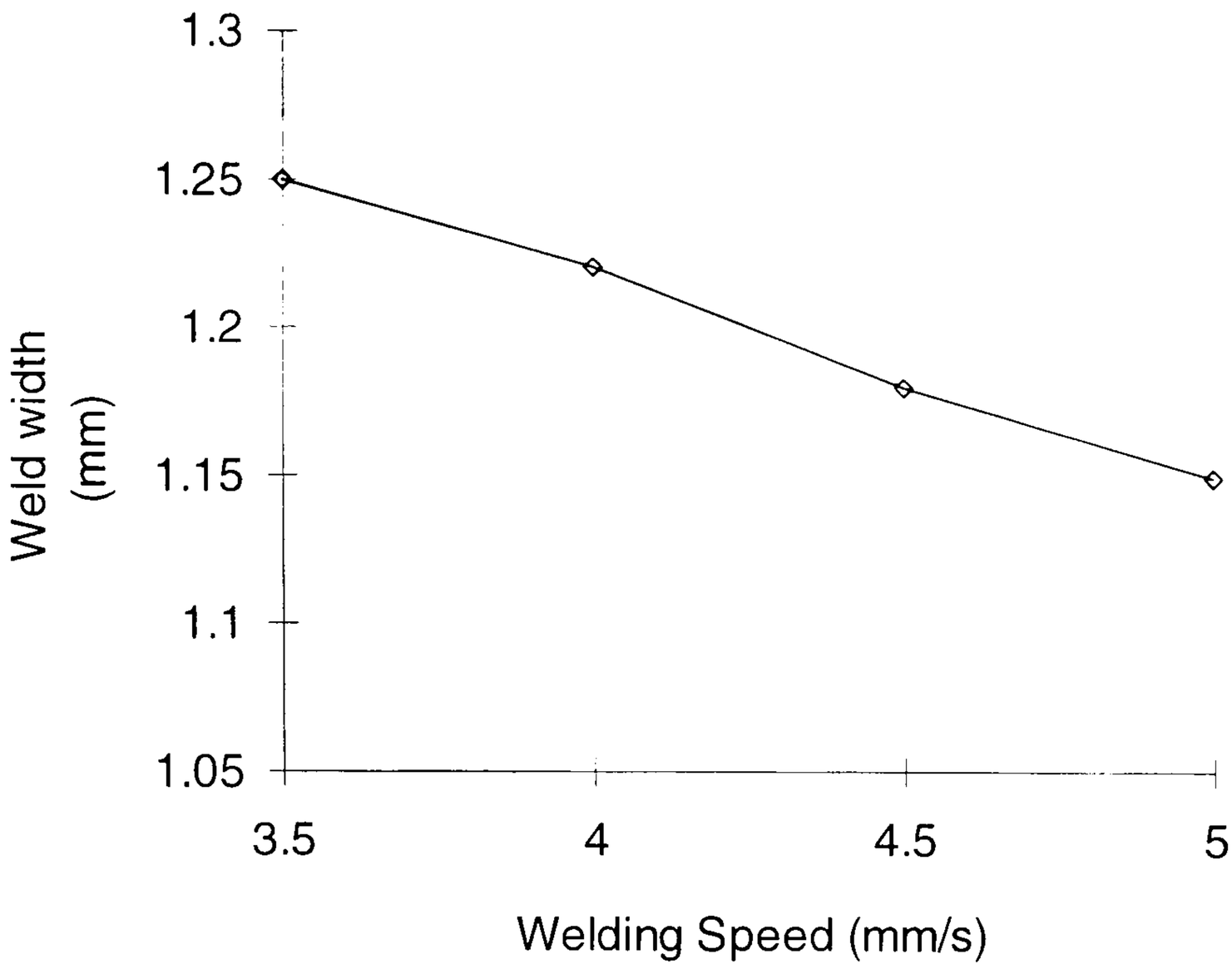

Figure 3.13 Weld width as a function of translation velocity (power of 200 W, PRF of 10 Hz, and pulse width of 10 ms)

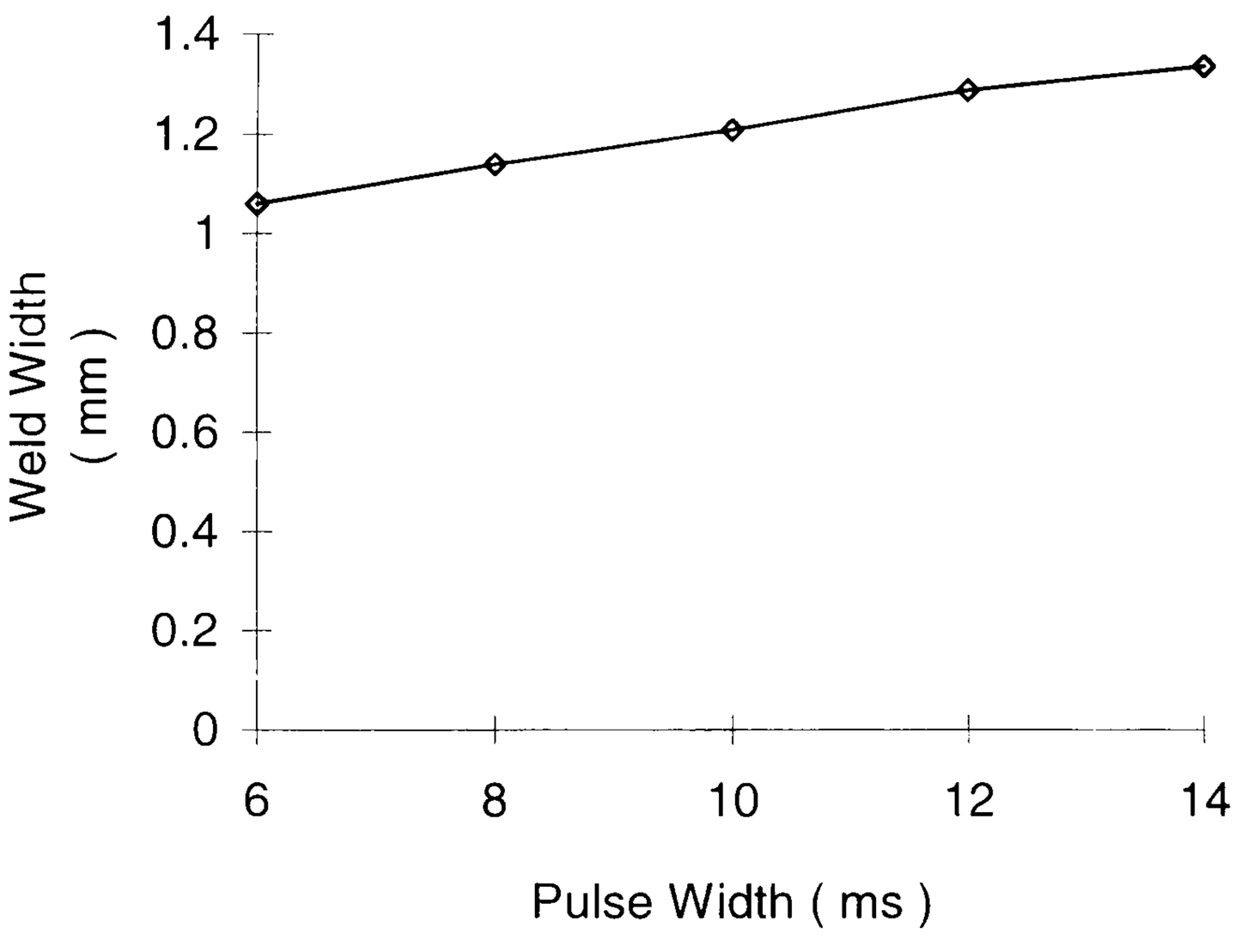

Figure 3.14 Weld width as a function of pulse width (power of 200 W, PRF of 10 Hz, and translation velocity of 5 mm/s)

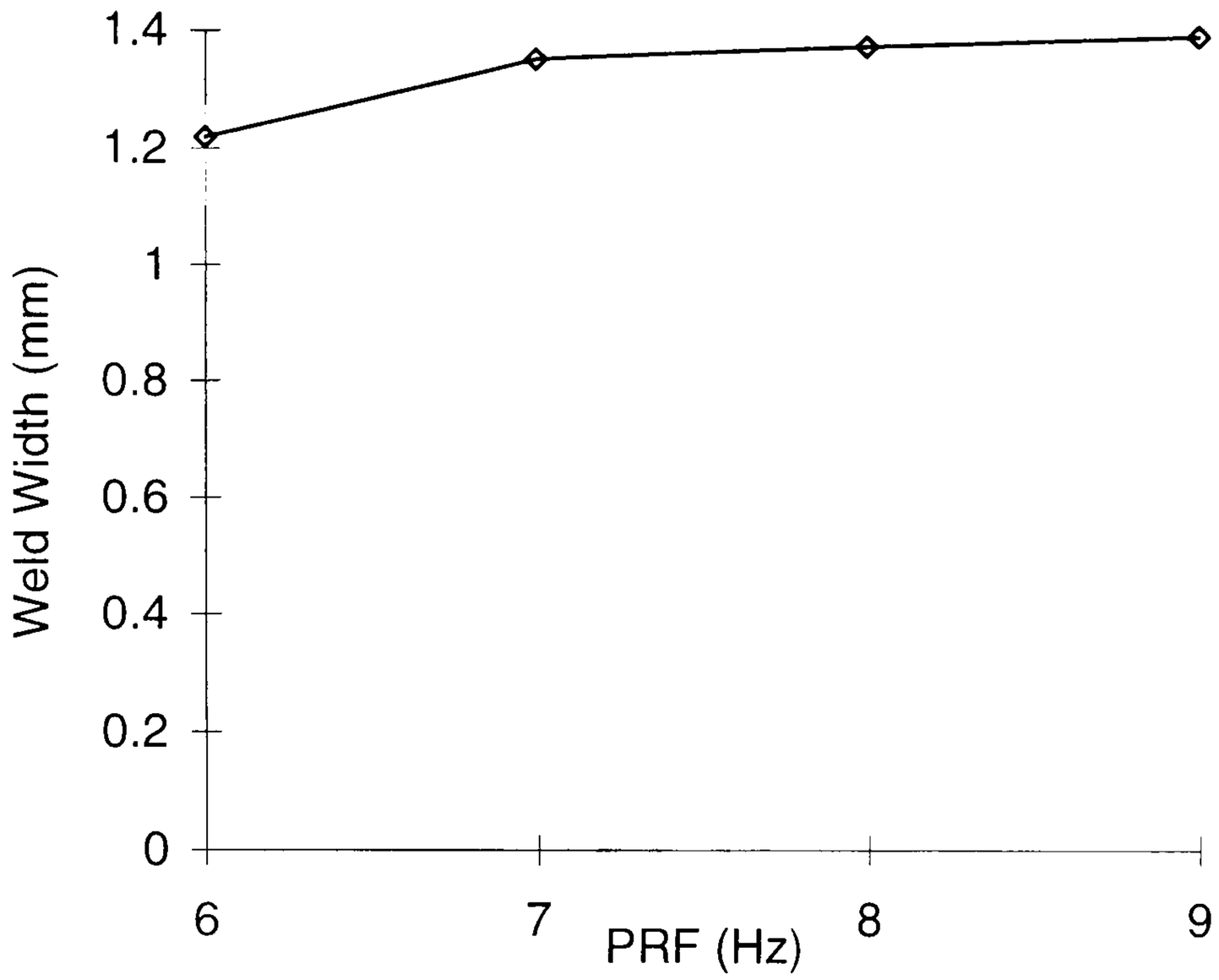

Figure 3.15 Weld width as a function of PRF
(power of 200 W, translation velocity of 5 mm/s, and pulse width of 10 ms)

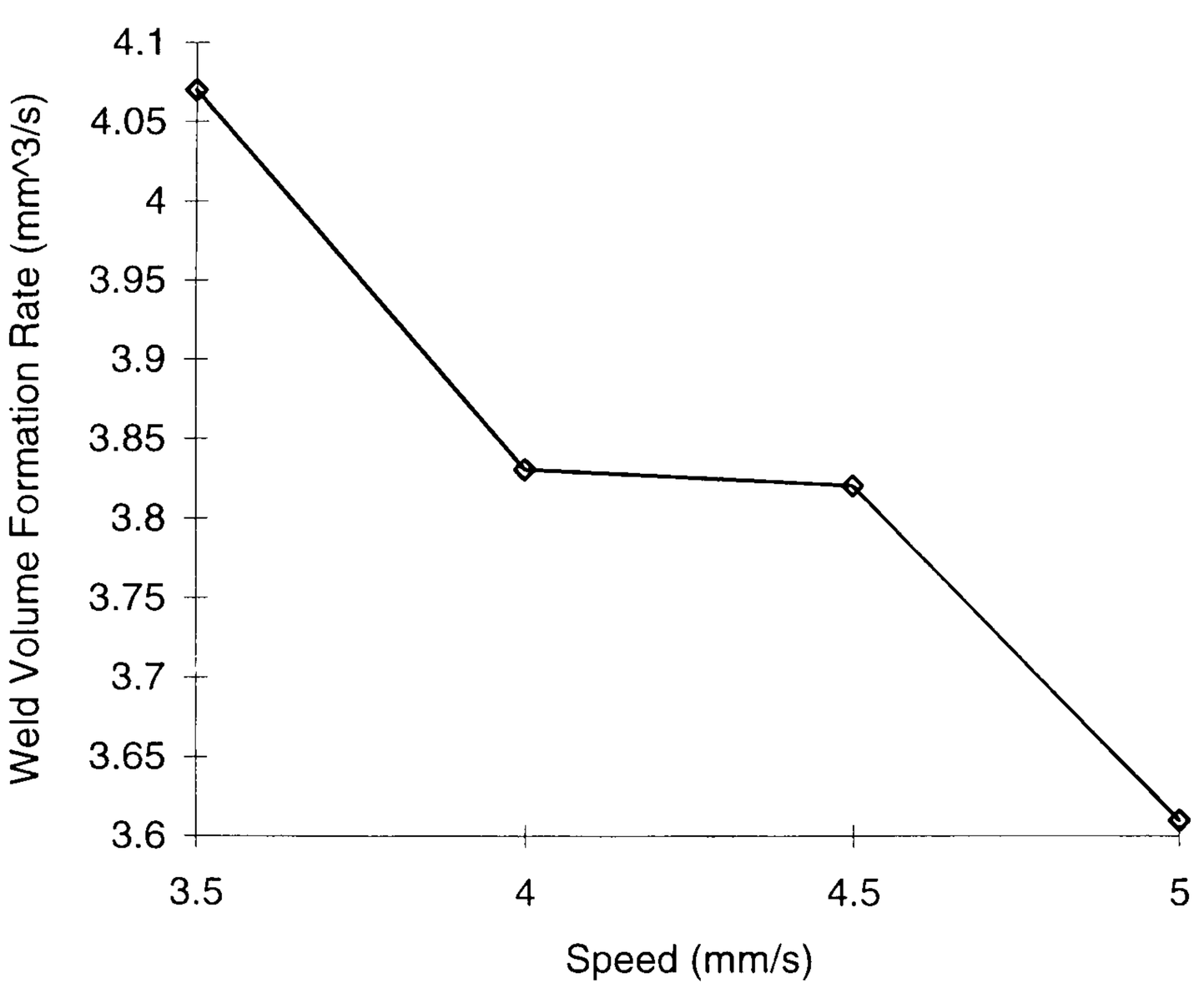

Figure 3.16 Weld volume formation rate as a function of translation velocity
(power of 200 W, PRF of 10 Hz, and pulse length of 10 ms)

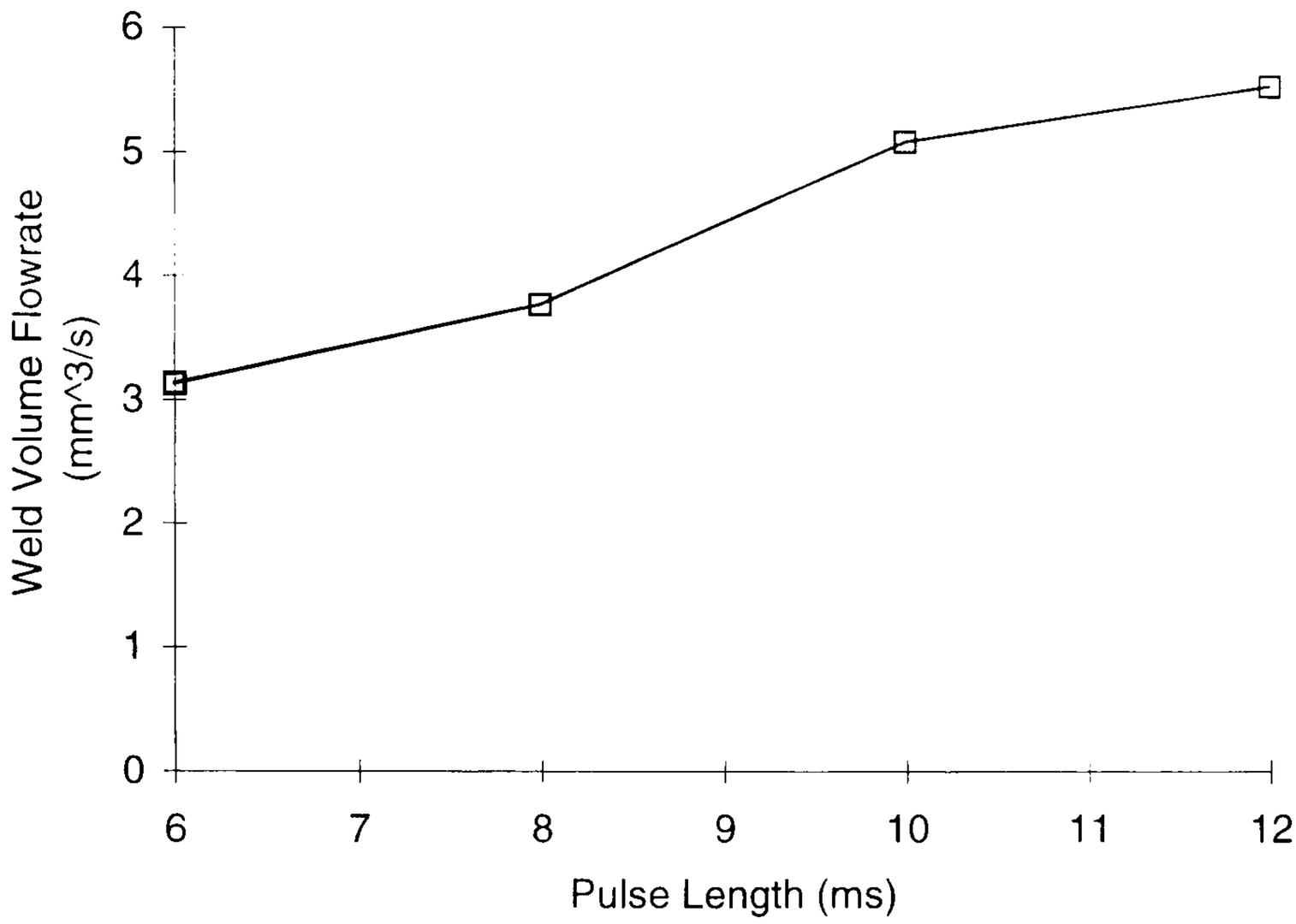

Figure 3.17 Weld volume formation rate as a function of pulse length (power of 200 W, PRF of 10 Hz, and translation velocity of 5 mm/s)

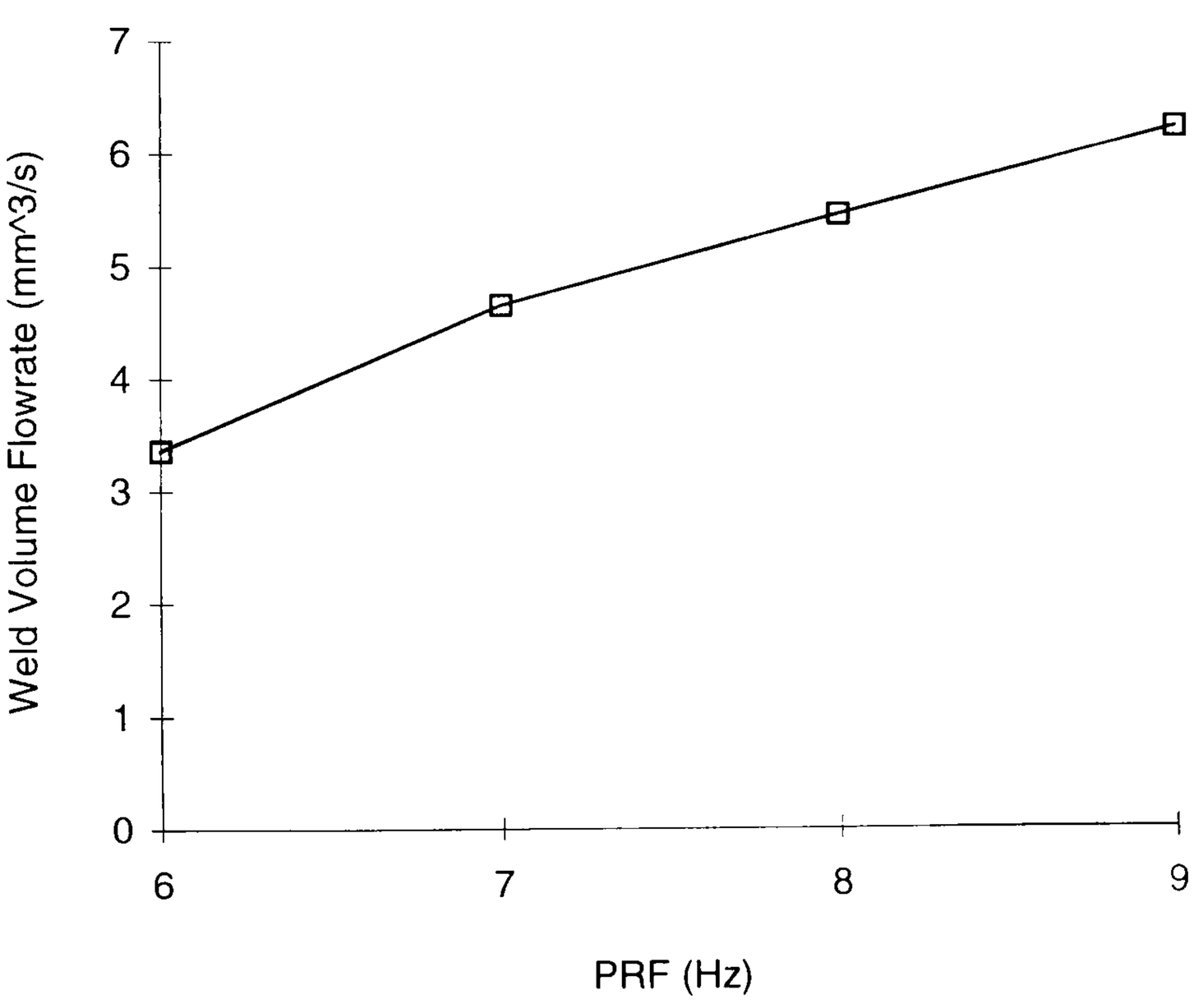

Figure 3.18 Weld volume formation rate as a function of PRF (power of 200 W, Pulse length of 10 ms, and translation velocity of 5 mm/s)

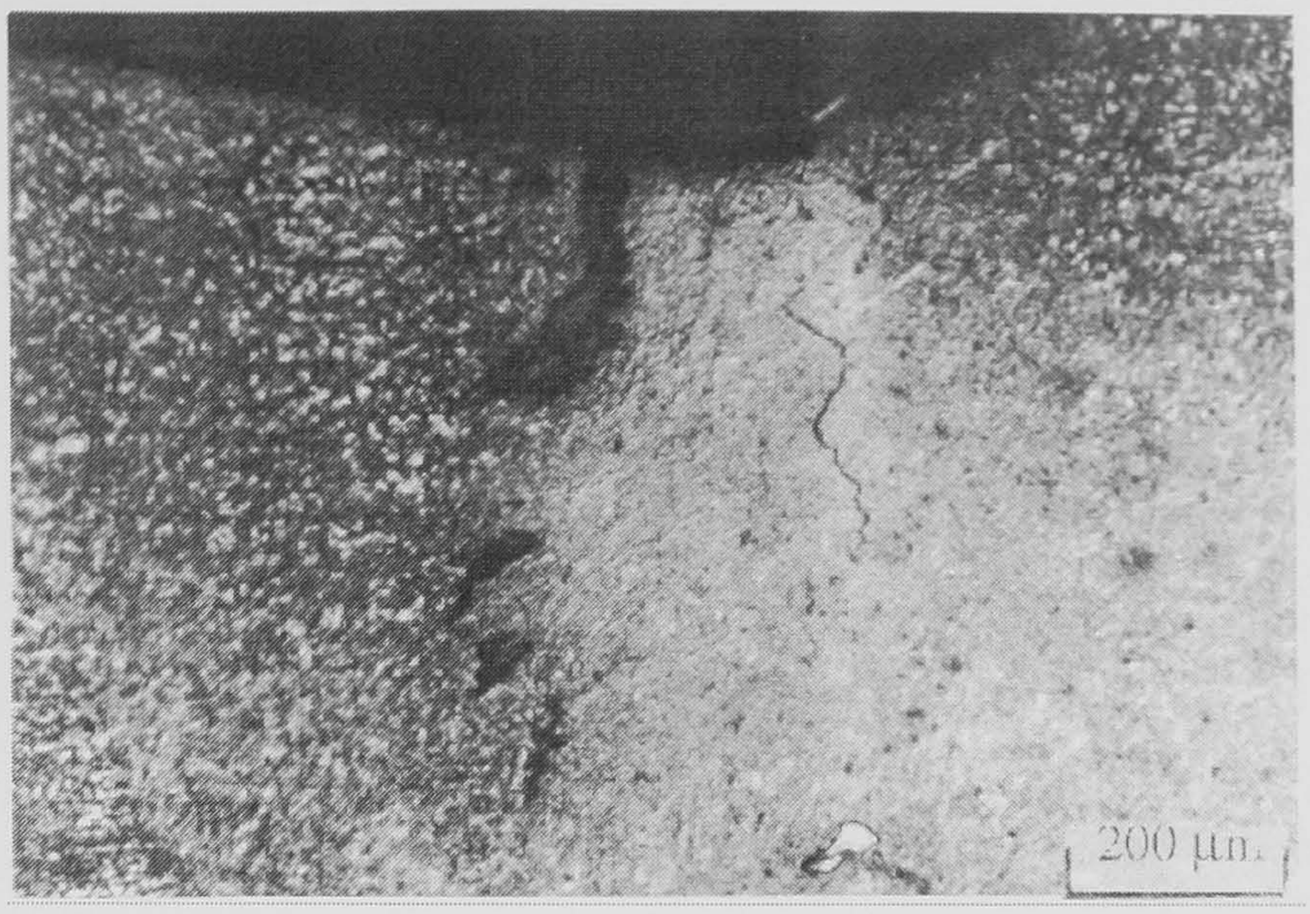

Figure 3.19 Crack evident shown on top of the fusion zone for a normal weld (Power for welding: 200 W, pulse length: 6 ms, PRF: 10 Hz, translation velocity: 5 mm/s): x 225 magnification

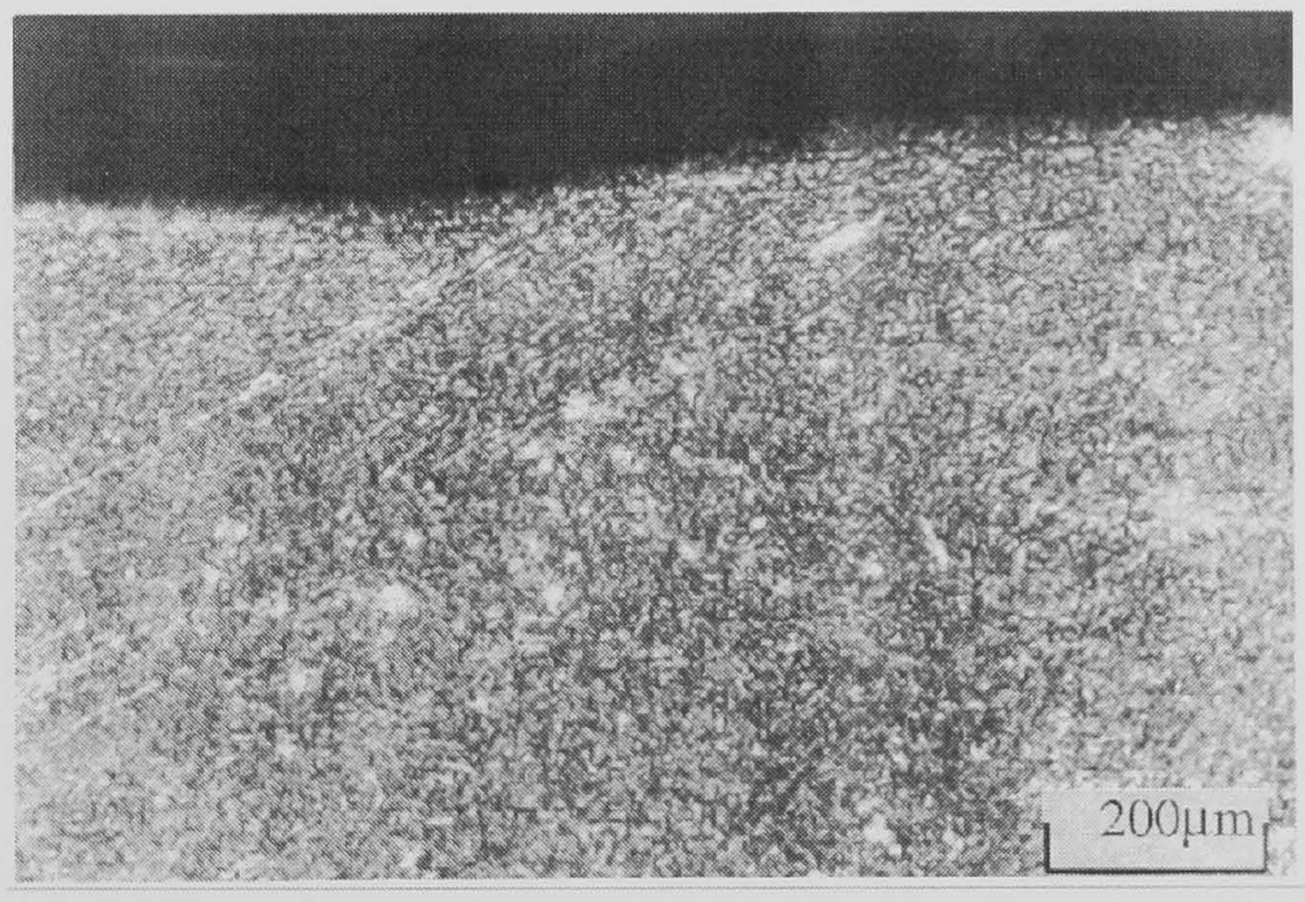

Figure 3.20 No crack evident shown on top of the fusion zone for a normal weld (Power for welding: 200 W, pulse length: 12 ms, PRF: 10 Hz, translation velocity: 5 mm/s): x 225 magnification

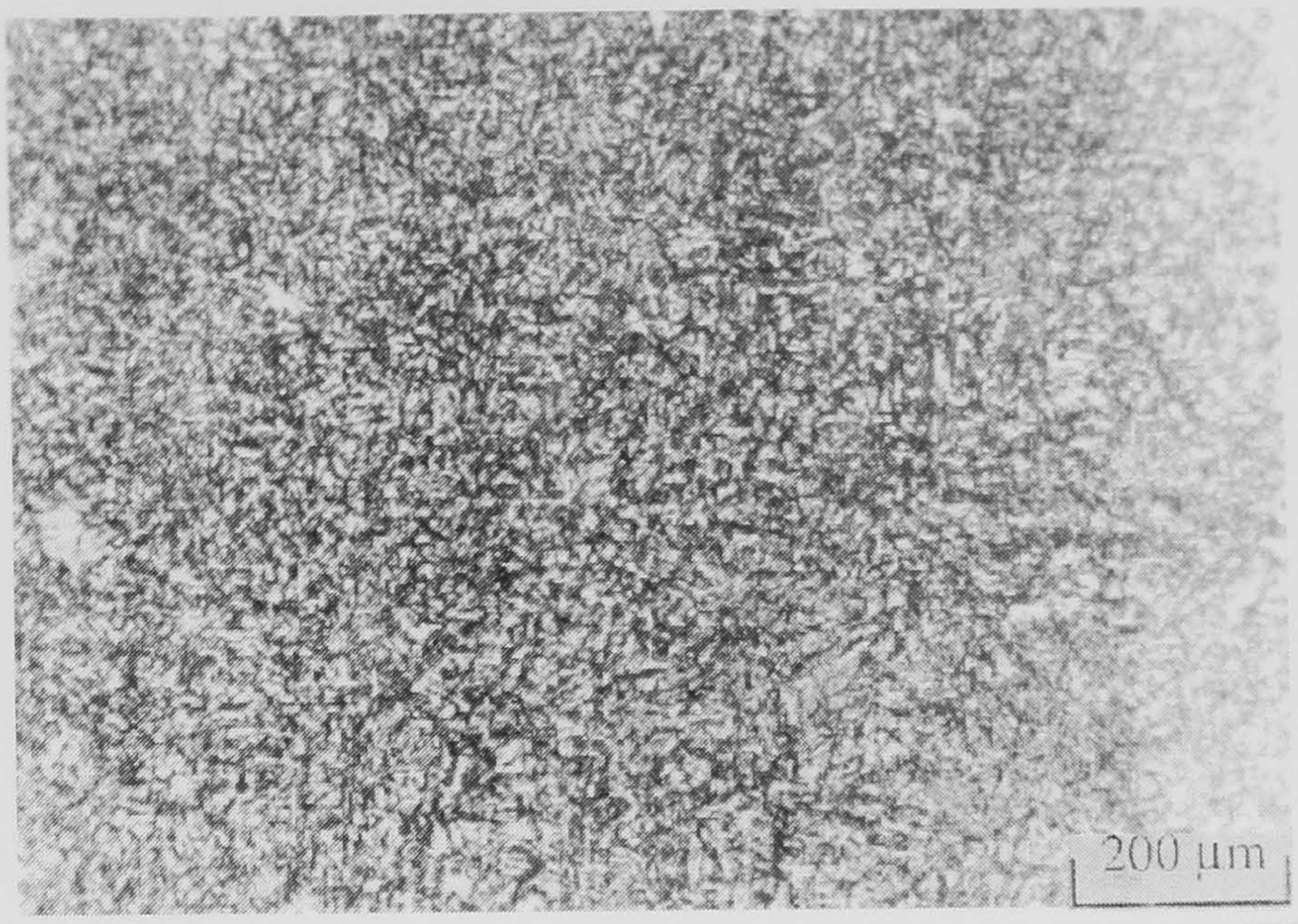

Figure 3.21 Microstructure of fusion zone for a normal weld (Power for welding: 200 W, pulse length: 10 ms, PRF: 6 Hz, translation velocity: 5 mm/s): x 225 magnification

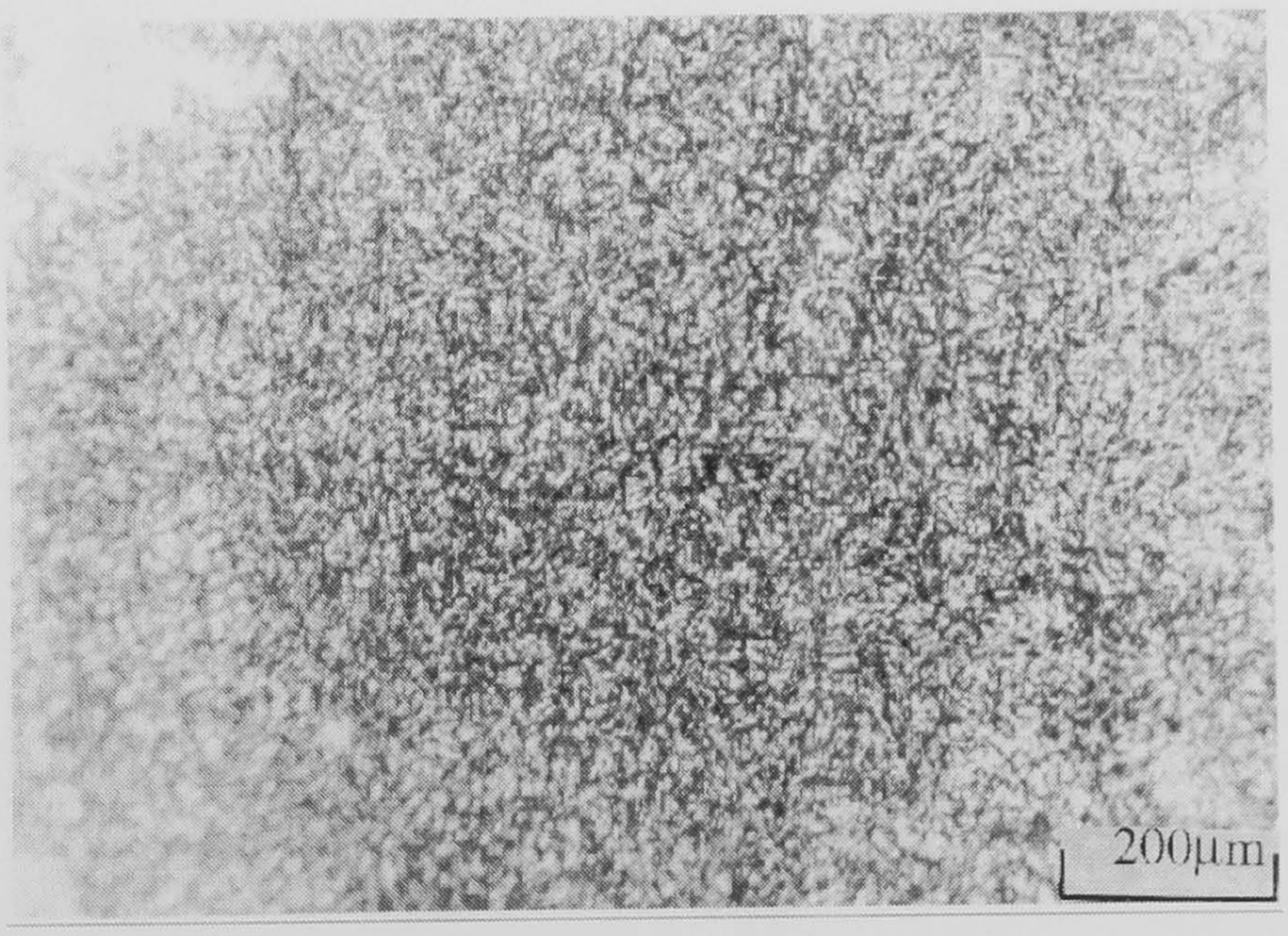

Figure 3.22 Microstructure of fusion zone for a normal weld (Power for welding: 200 W, pulse length: 10 ms, PRF: 10 Hz, translation velocity: 4.5 mm/s): x 225 magnification

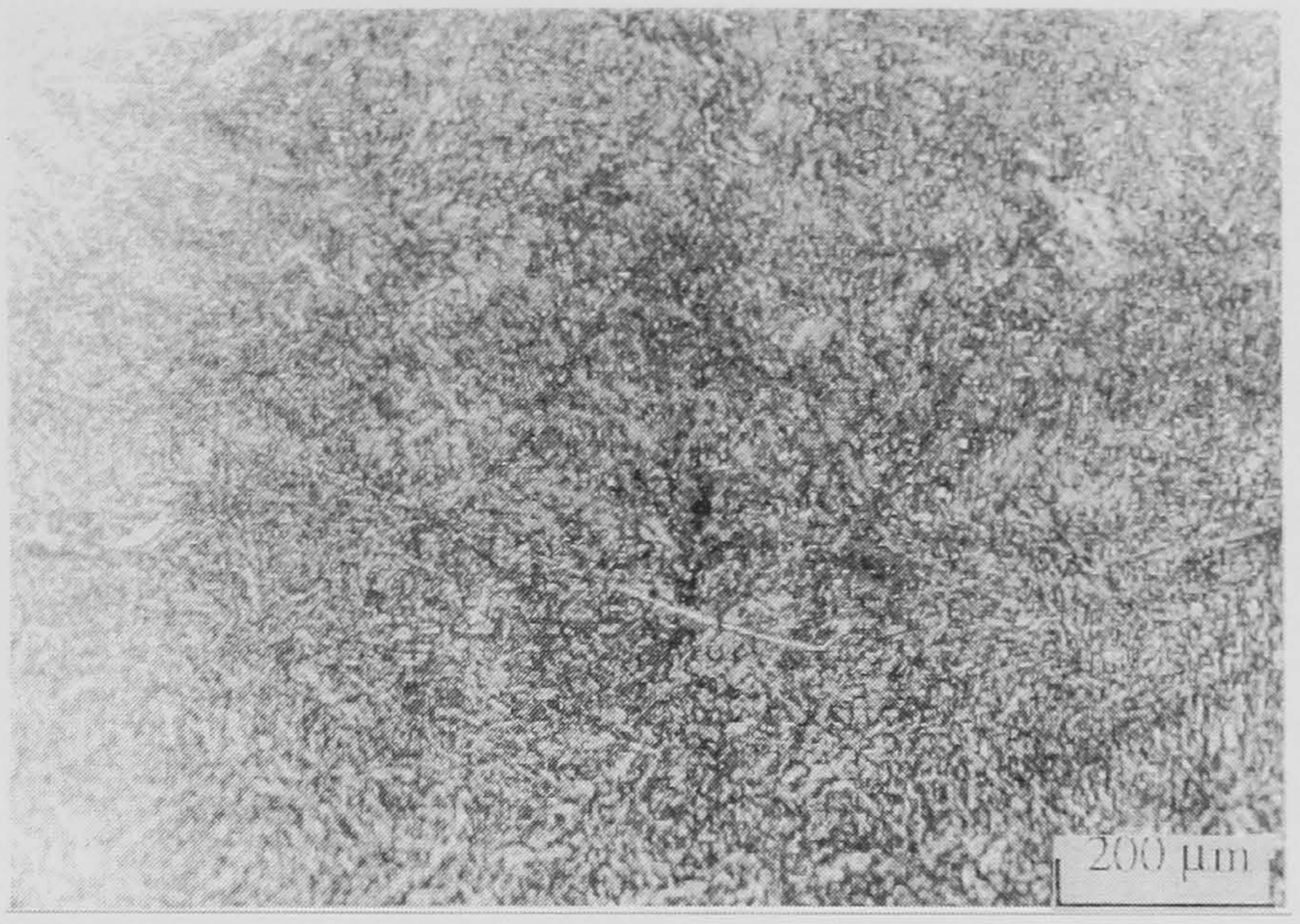

Figure 3.23 Microstructure of fusion zone for a normal weld (Power for welding: 200 W, pulse length: 10 ms, PRF: 9 Hz, translation velocity: 5 mm/s): x 225 magnification

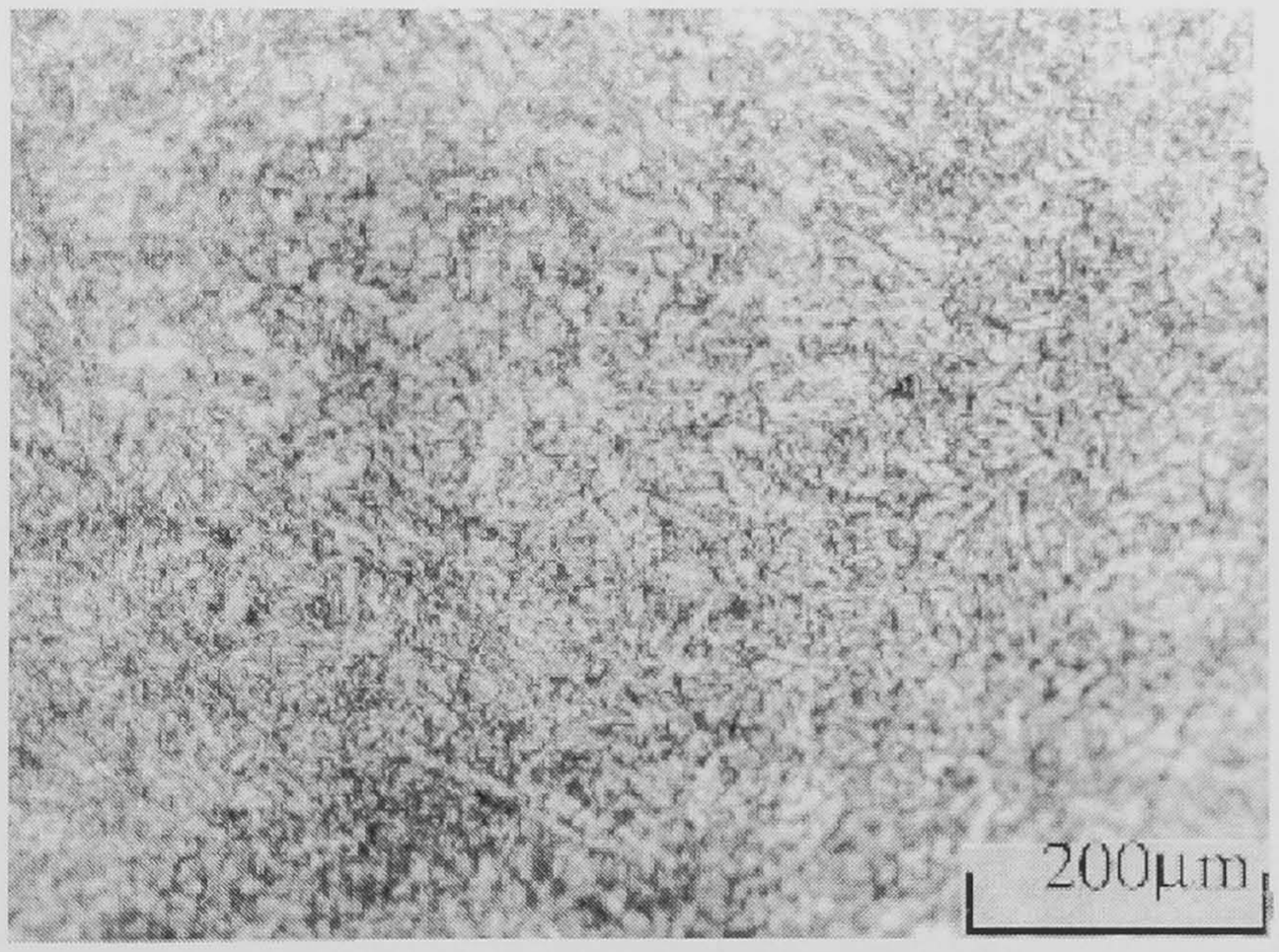

Figure 3.24 Microstructure of fusion zone for a normal weld (Power for welding: 200 W, pulse length: 10 ms, PRF: 10 Hz, translation velocity: 4 mm/s): x 225 magnification

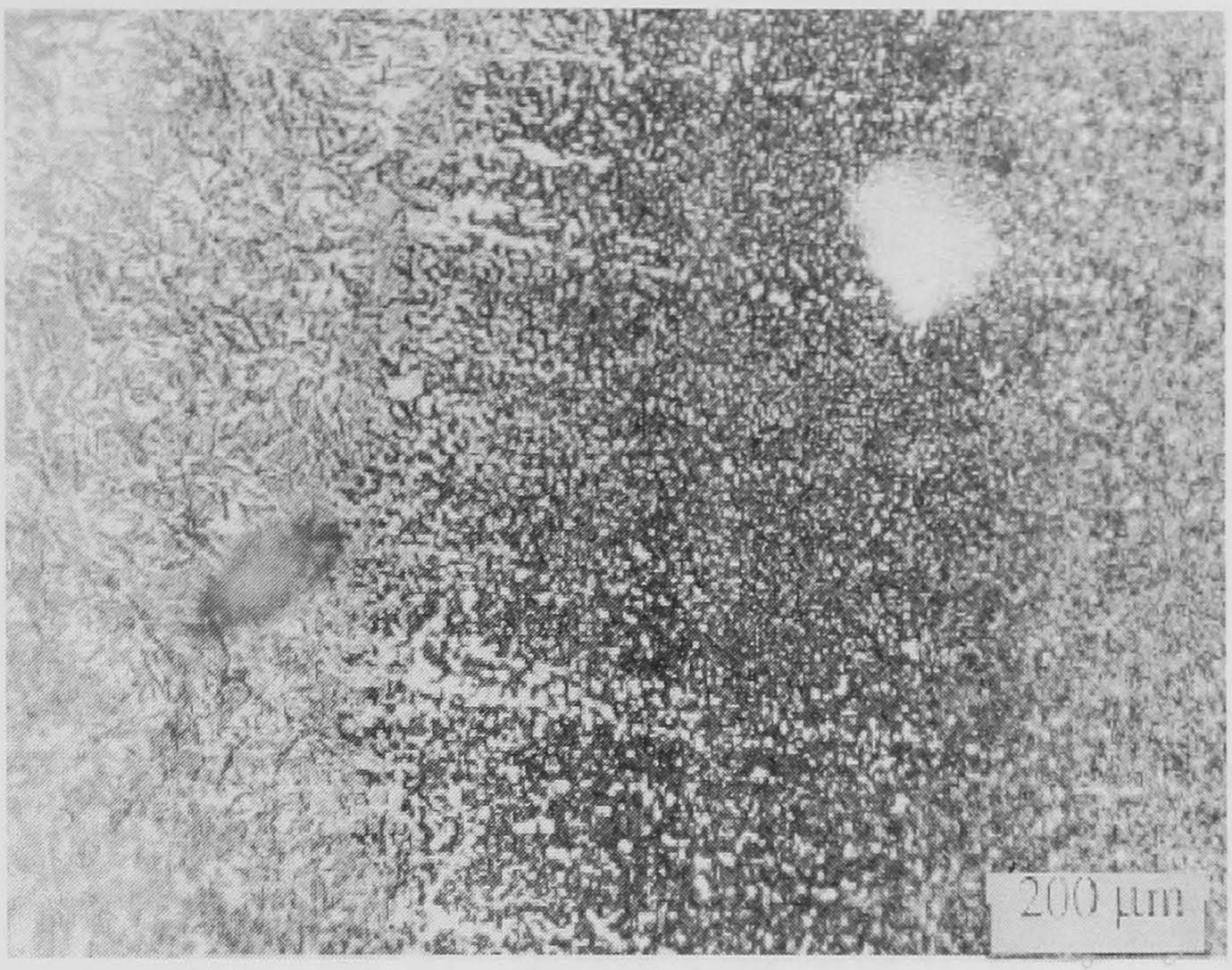

Figure 3.25 a Microstructure of fusion zone (left) and heat-affected zone (right) for a normal weld (Power for welding: 200 W, pulse length: 6 ms, PRF: 10 Hz, translation velocity: 5 mm/s): x 225 magnification

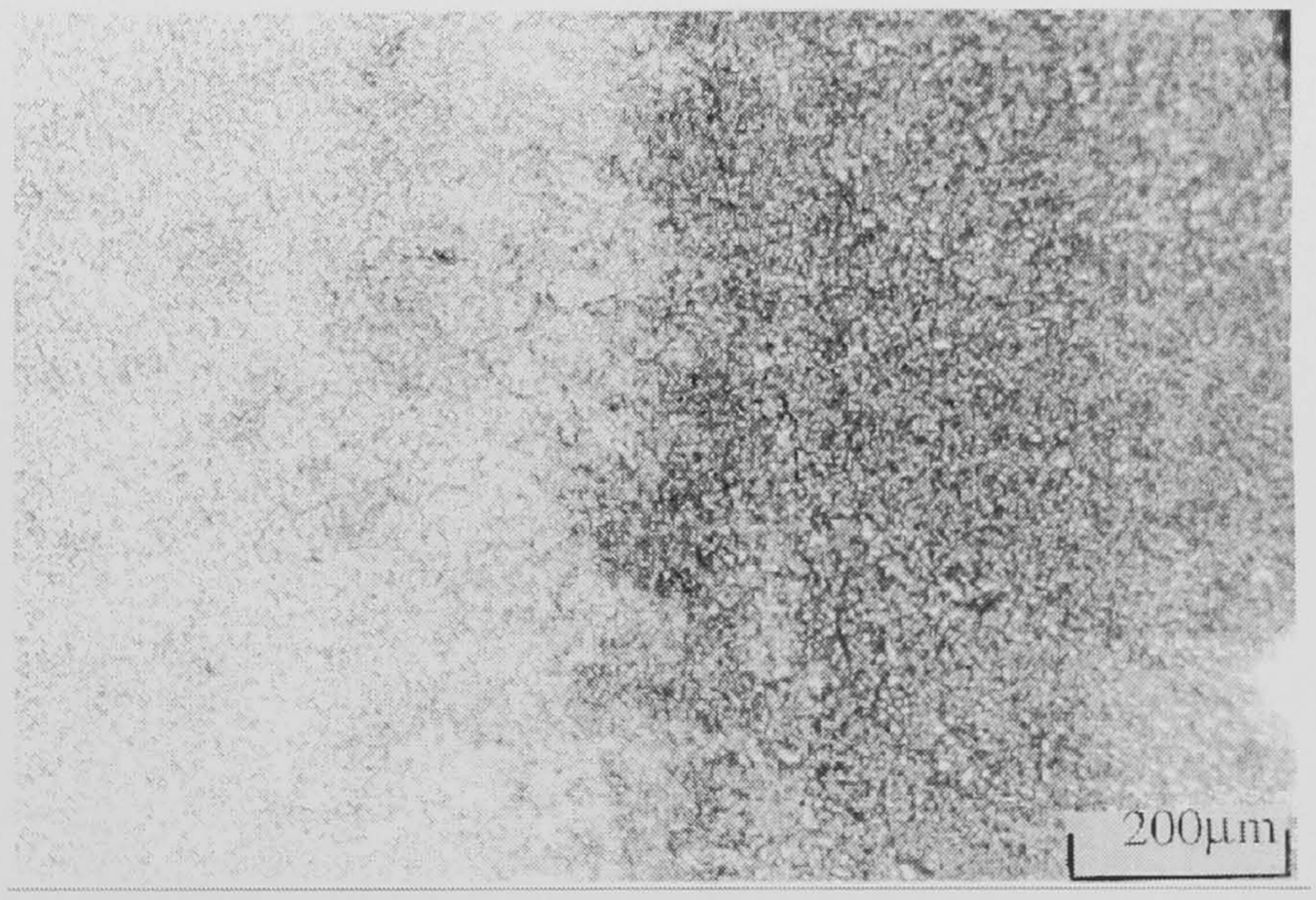

Figure 3.25 b Microstructure of heat affected zone (left) and base metal (right) for a normal weld (Power for welding: 200 W, pulse length: 6 ms, PRF: 10 Hz, translation velocity: 5 mm/s): x 225 magnification

Table 3.1. Parameters for normal welding and post-heating welding

Type Of Welding	Power for welding / Power for Post-heating (W)	Pulse Width (ms)	PRF (Hz)	Speed (mm/sec)	Pulse Energy (Joules)	Peak Power (kW)	Spot Size (mm)	Pulse Shape
Normal	200	6	10	5	20	3.3	2	Top hat
Normal	200	8	10	5	20	2.5	2	Top hat
Normal	200	10	10	5	20	2	2	Top hat
Normal	200	12	10	5	20	1.7	2	Top hat
Normal	200	10	6	5	33.3	3.3	2	Top hat
Normal	200	10	7	5	28.6	2.9	2	Top hat
Normal	200	10	8	5	25	2.5	2	Top hat
Normal	200	10	9	5	22.2	2.2	2	Top hat
Postheating	200 / 85	6	10	5	20/8.5	3.3/1.4	2/20	Top hat
Postheating	200 / 85	8	10	5	20/8.5	2.5/1.1	2/20	Top hat
Postheating	200 / 85	10	10	5	20/8.5	2/0.9	2/20	Top hat
Postheating	200 / 85	12	10	5	20/8.5	1.7/0.7	2/20	Top hat
Postheating	200 / 85	10	6	5	33.3/14.2	3.3/1.4	2/20	Top hat
Postheating	200 / 85	10	7	5	28.6/12.1	2.9/1.2	2/20	Top hat
Postheating	200 / 85	10	8	5	25/10.6	2.5/1.1	2/20	Top hat
Postheating	200 / 85	10	9	5	22.2/9.4	2.2/0.9	2/20	Top hat

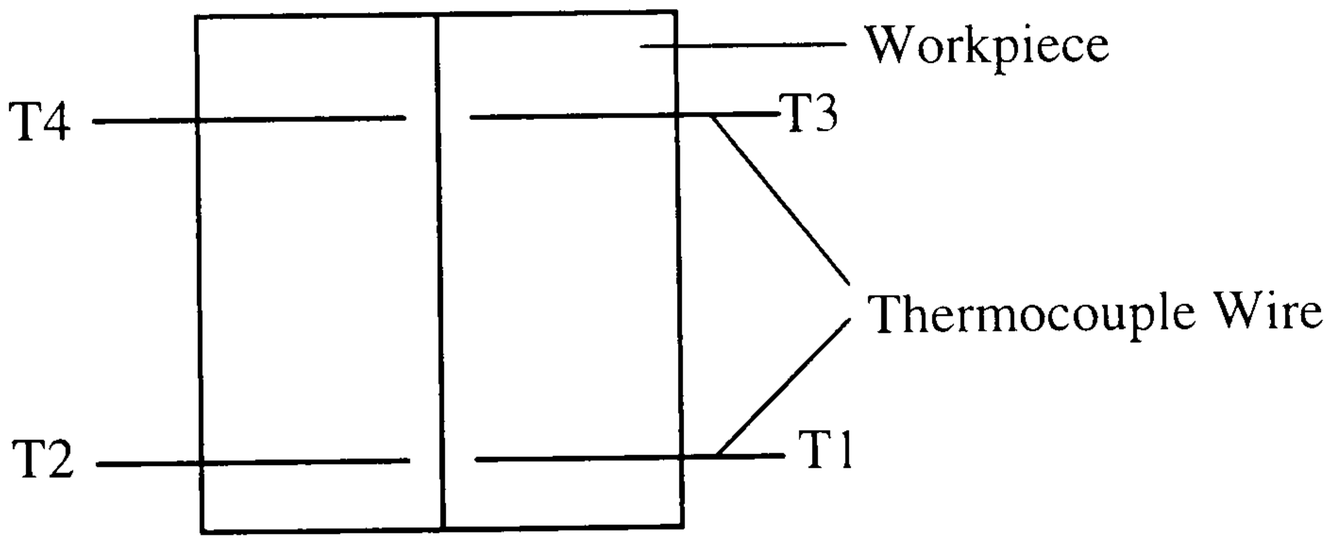

Figure 3.26. Position of thermocouples attached to workpiece

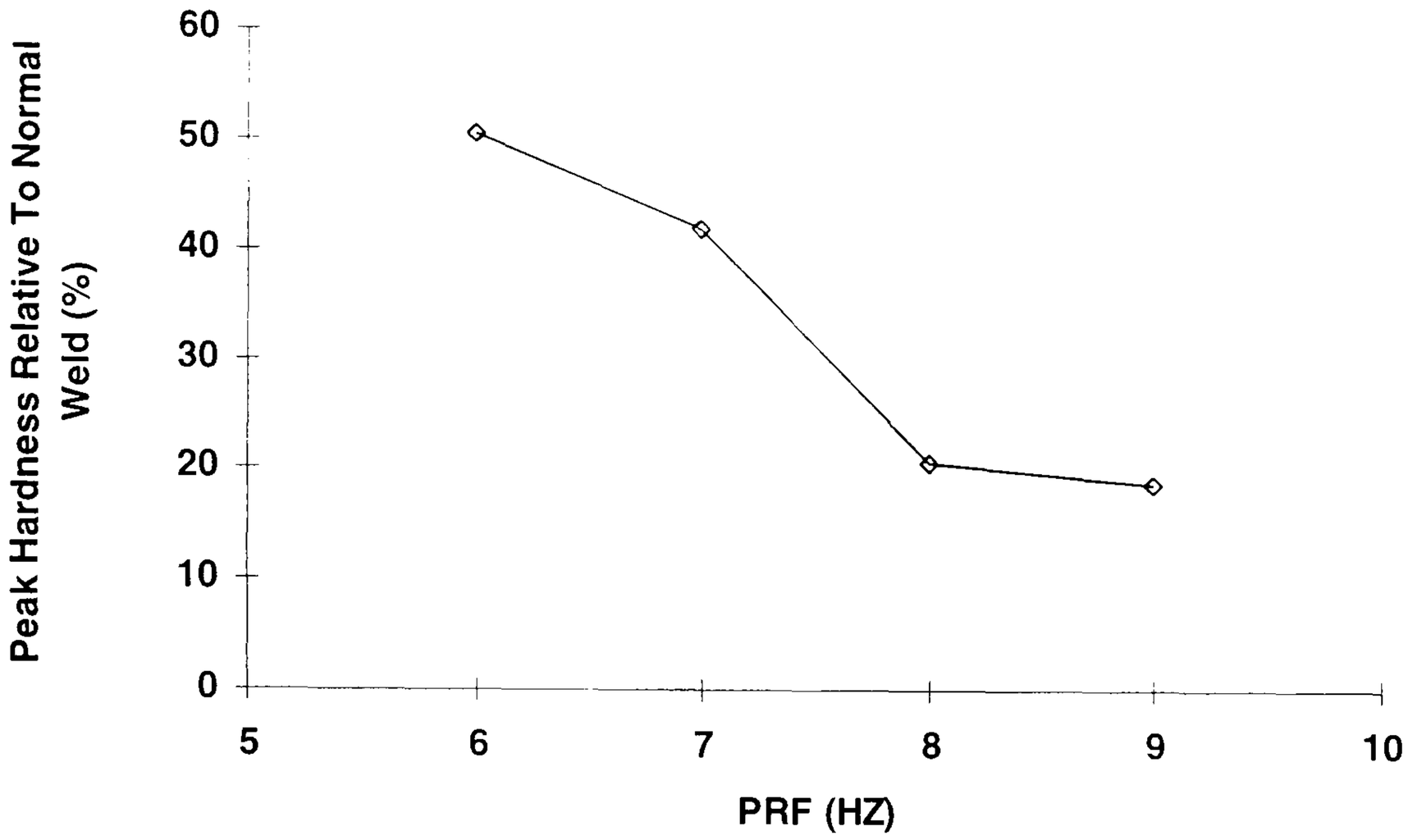

Figure 3.27 Relative peak hardness reduction as a function of PRFs

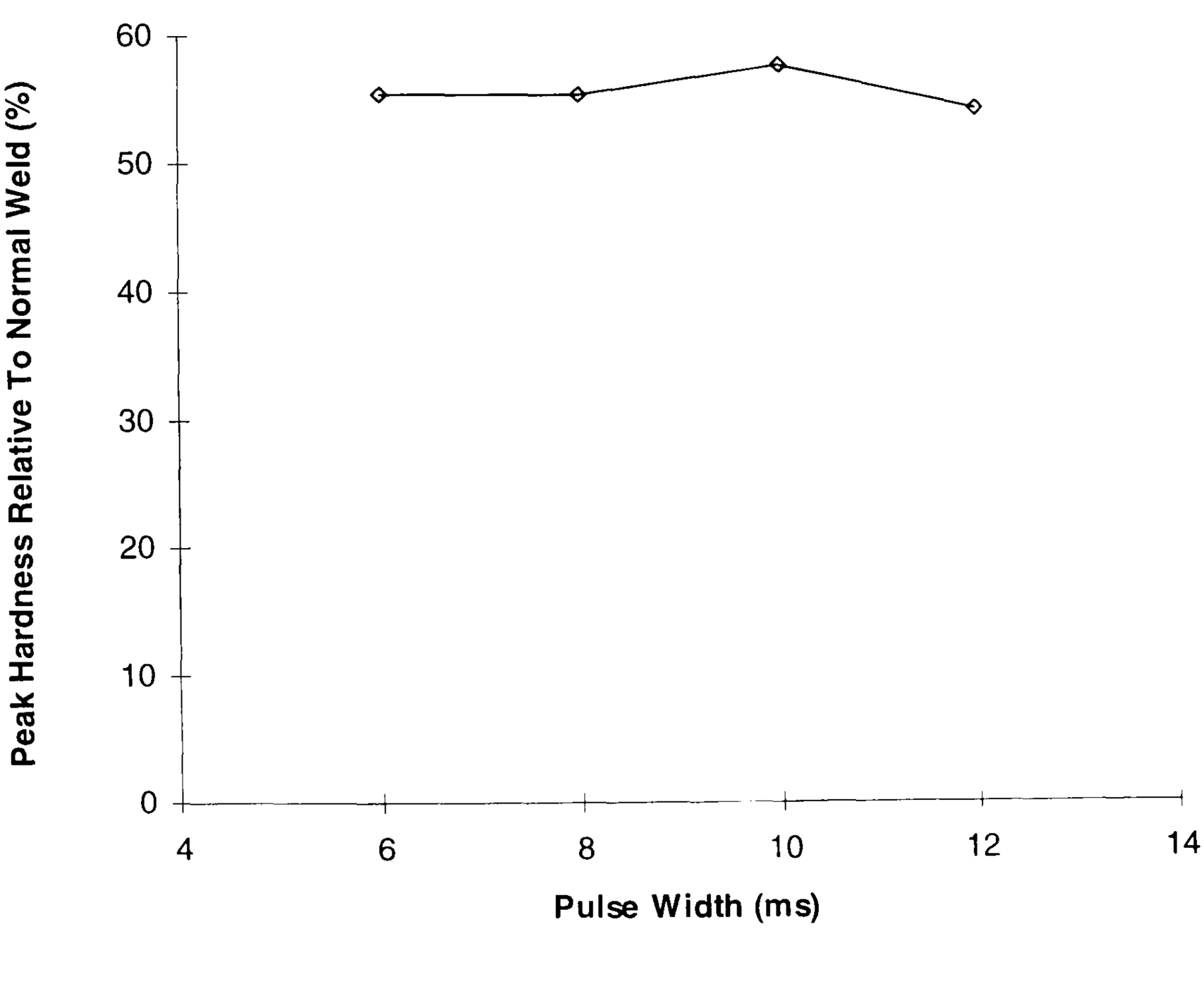

Figure 3.28 Relative peak hardness reduction as a function of pulse widths

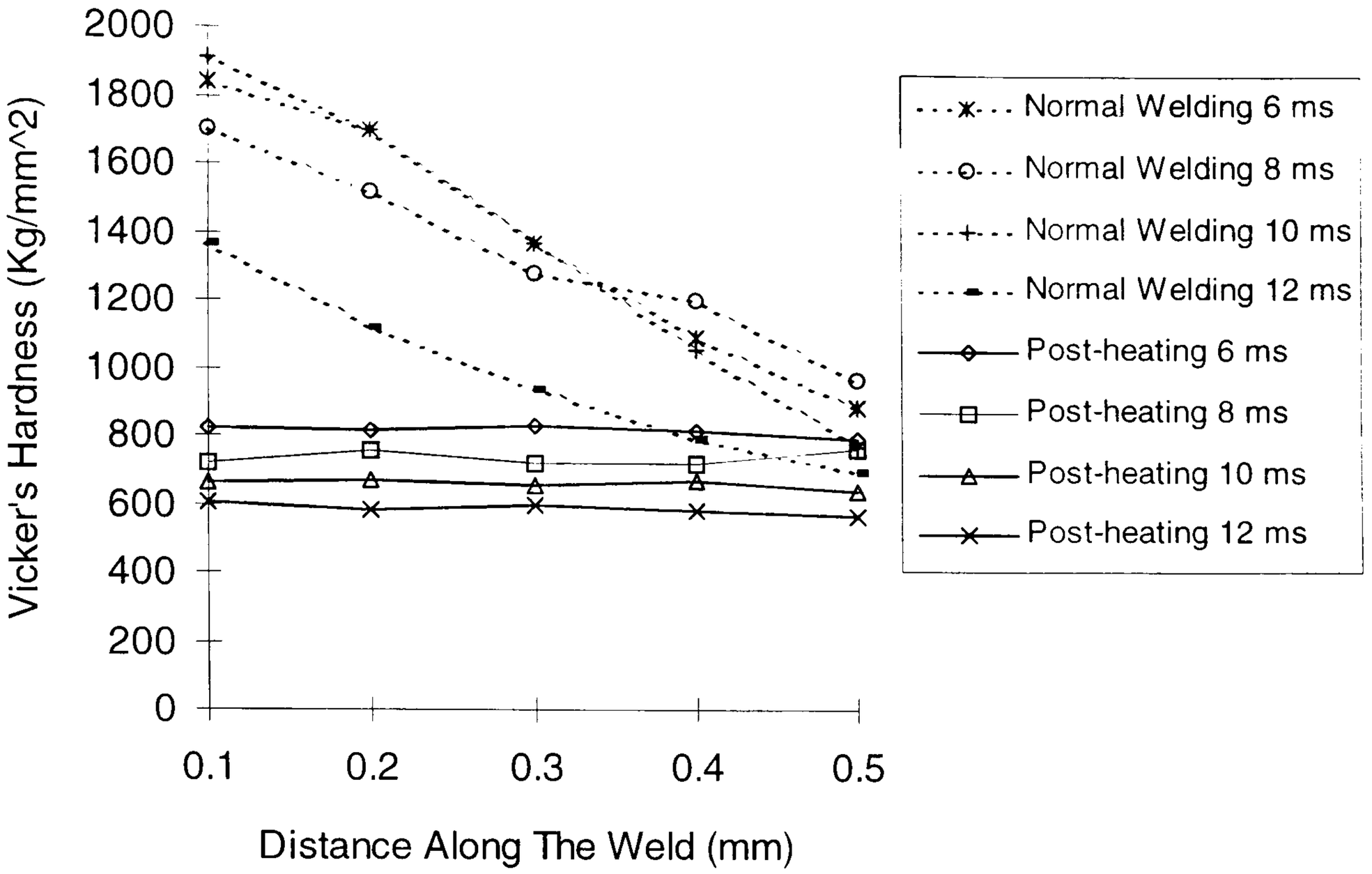

Figure 3.29 Vicker's hardness as a function of depth for different pulse widths

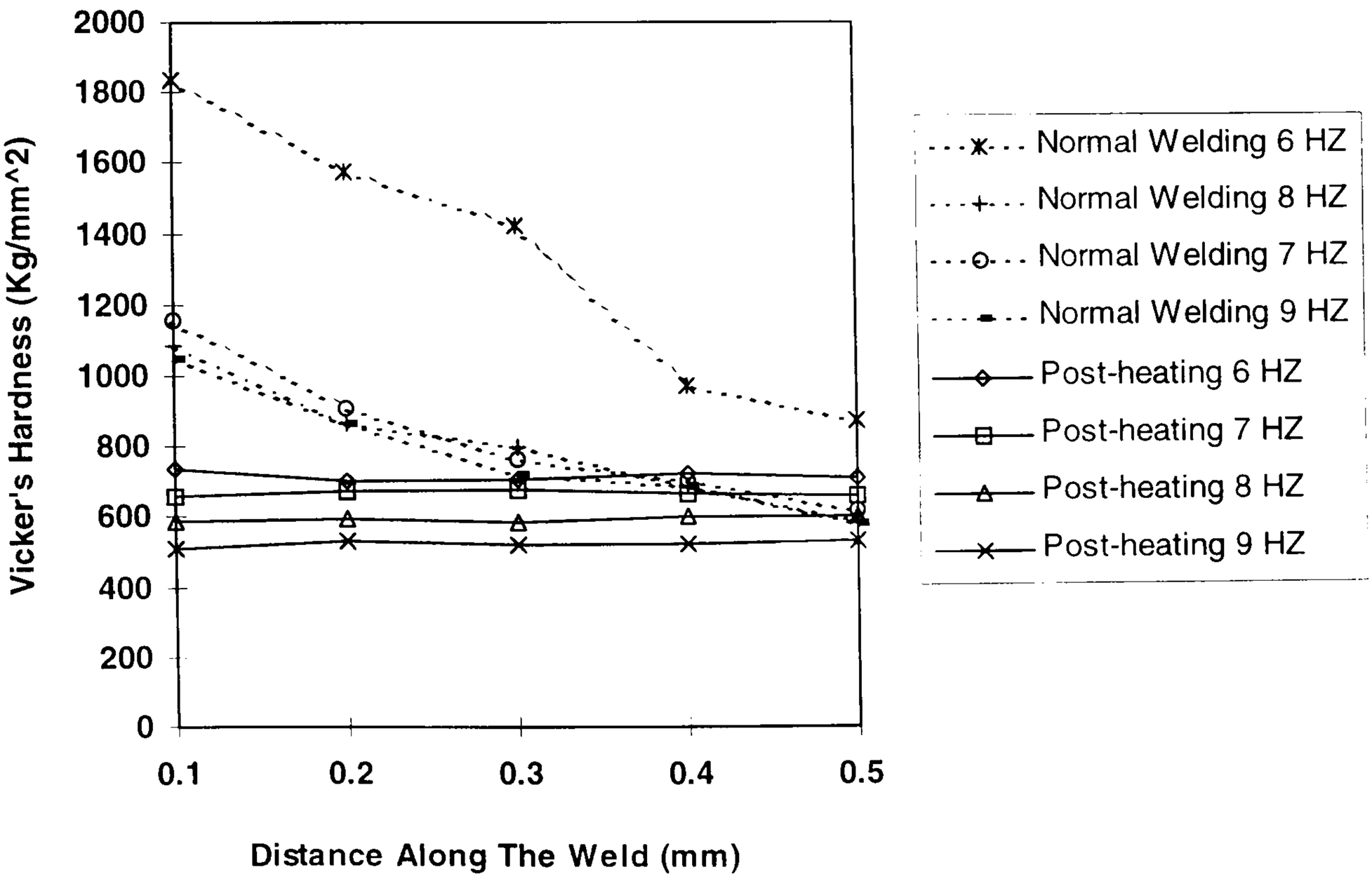

Figure 3.30 Vicker's hardness as a function of depth for different PRFs

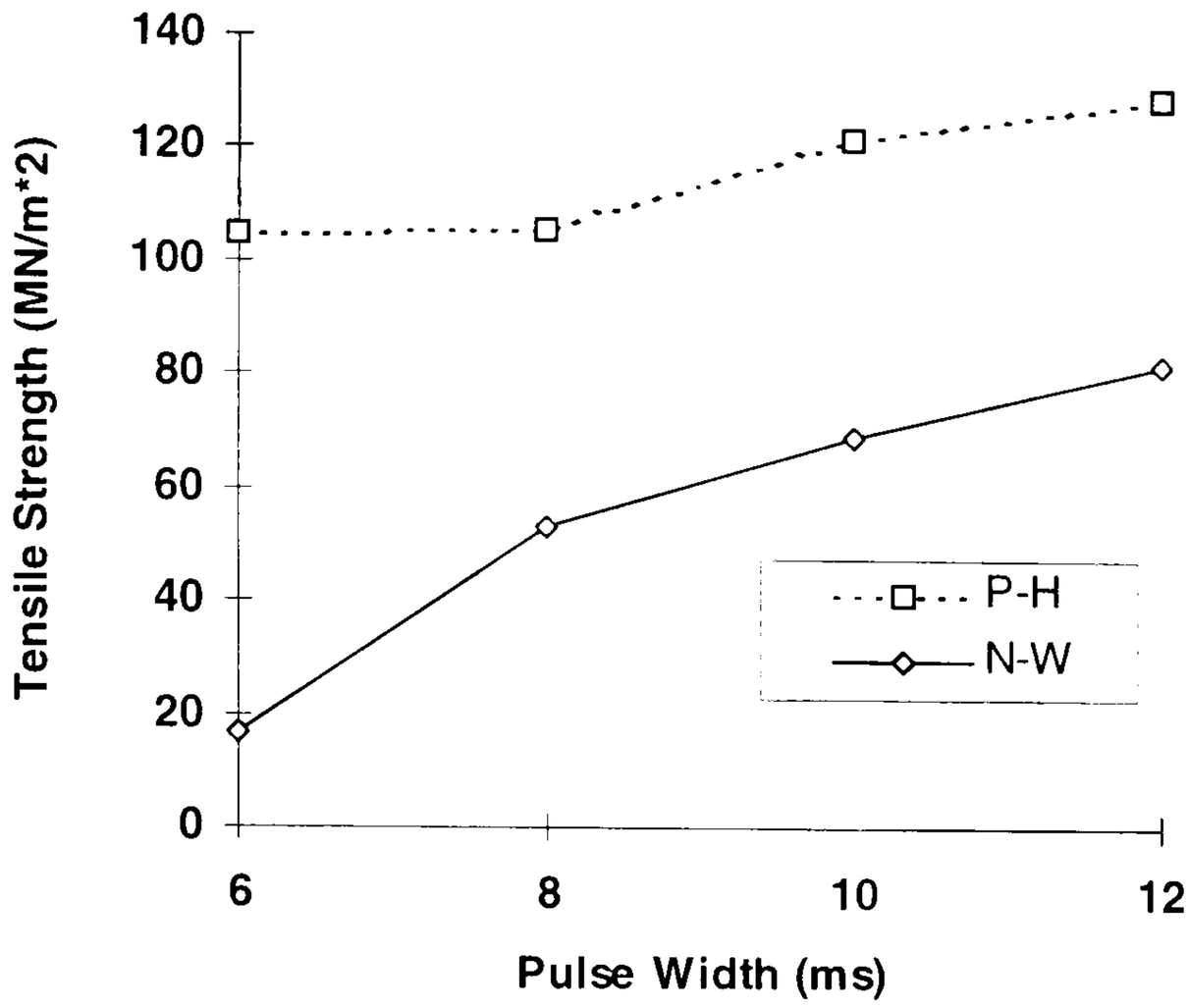

Figure 3.31. Tensile strength for different pulse widths

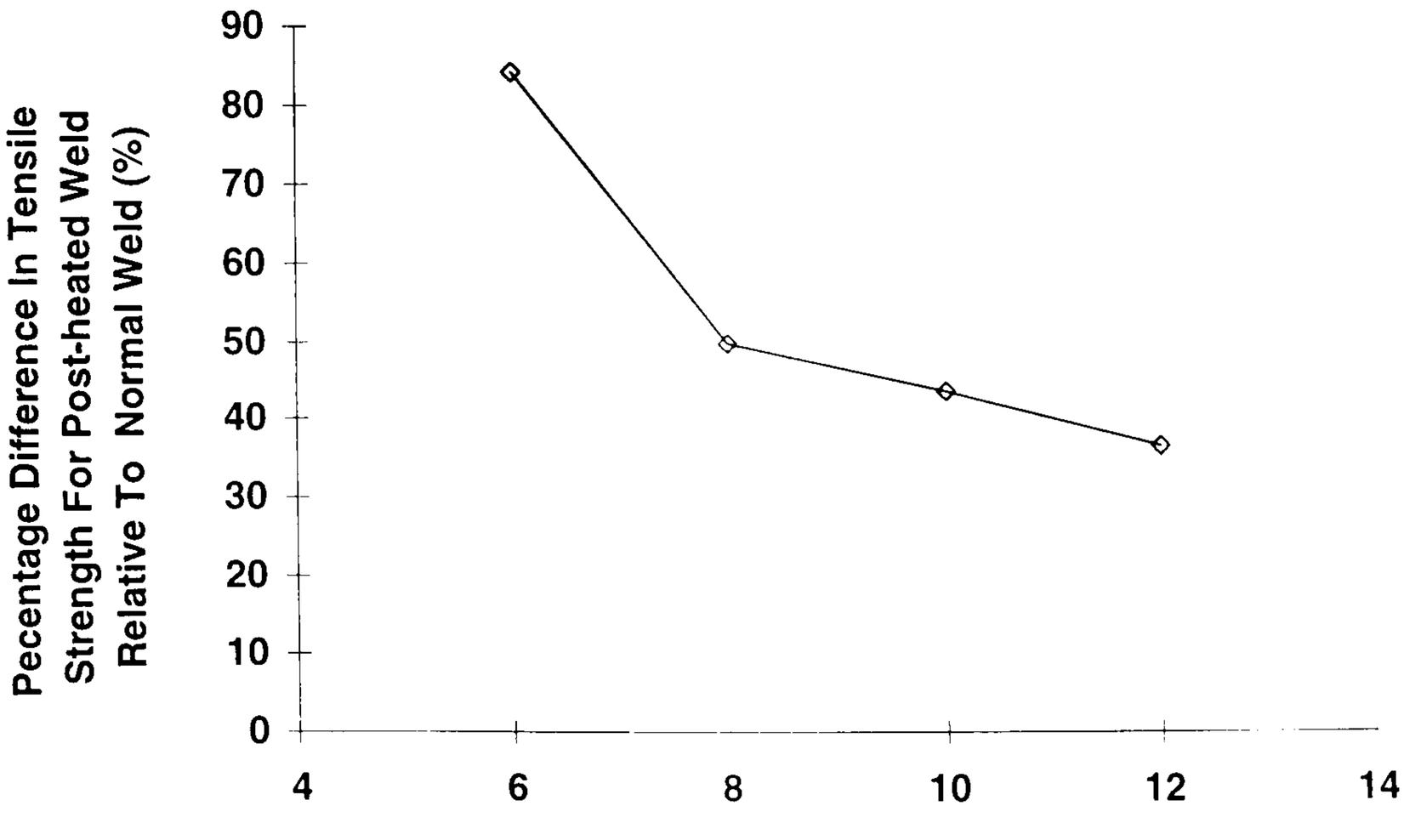

Figure 3.32 Percentage of difference in tensile strength for different pulse widths

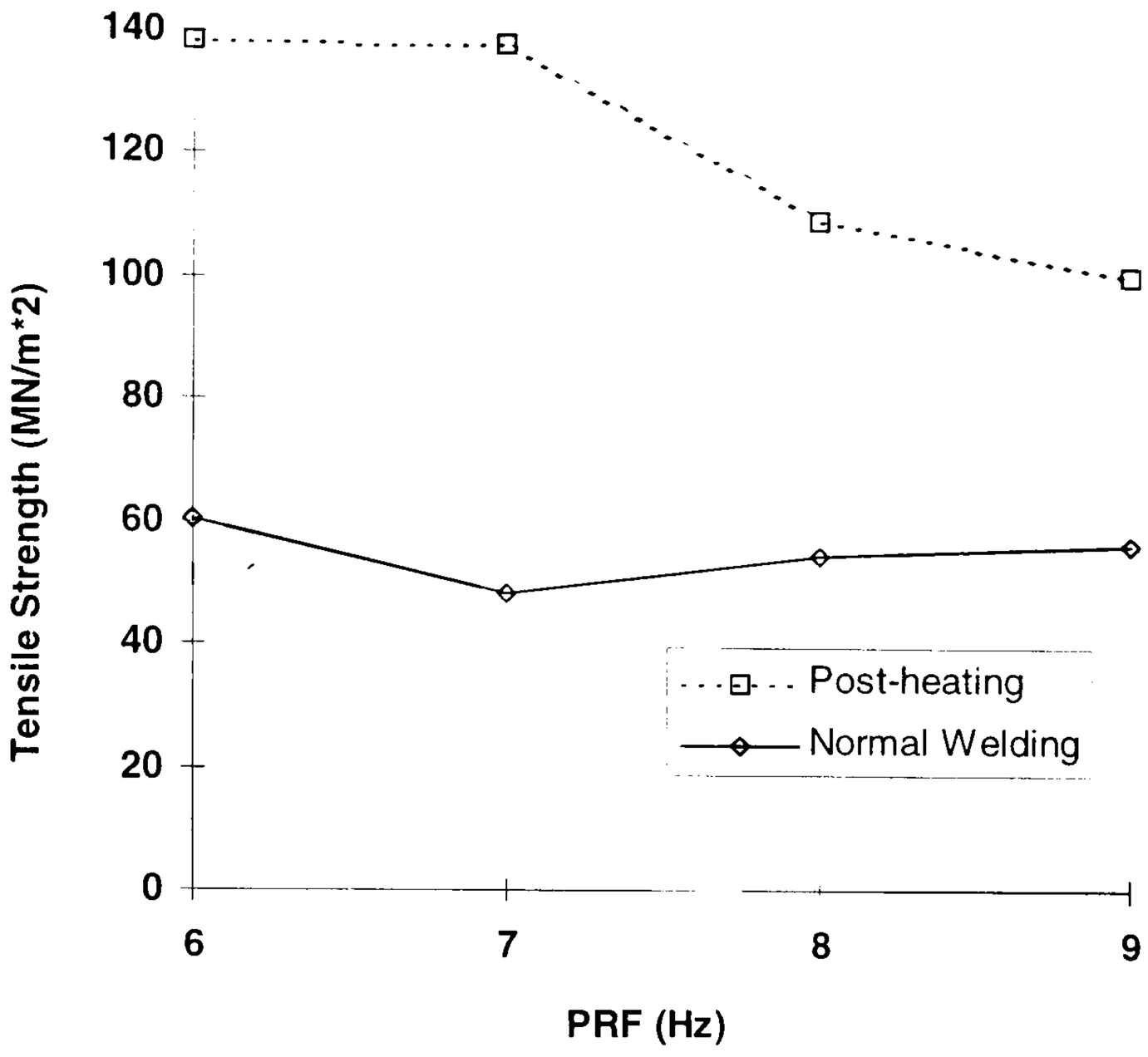

Figure 3.33. Tensile strength for different PRFs

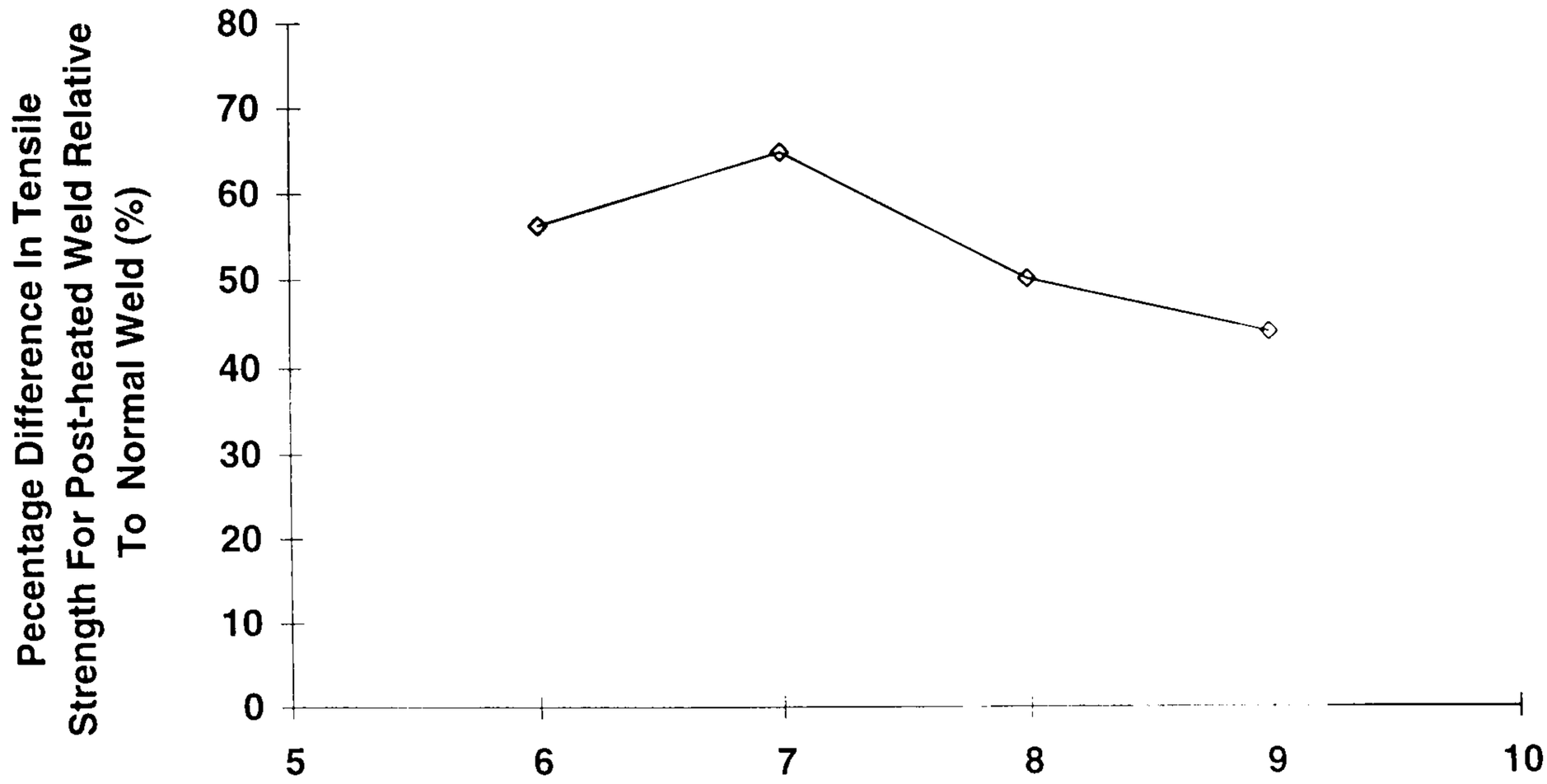

Figure 3.34 Percentage of difference in tensile strength for different PRF

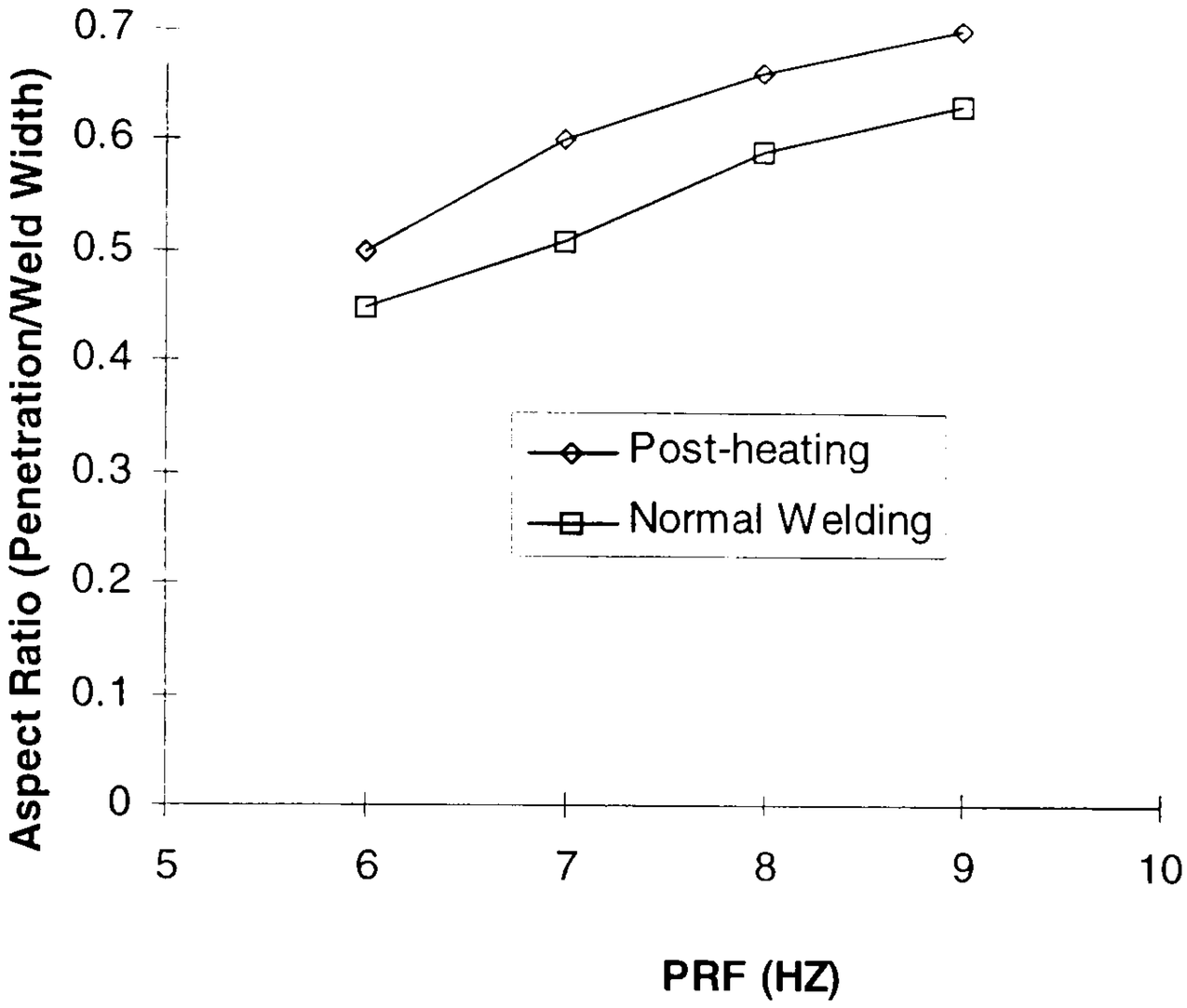

Figure 3.35. Aspect ratio as a function of PRF

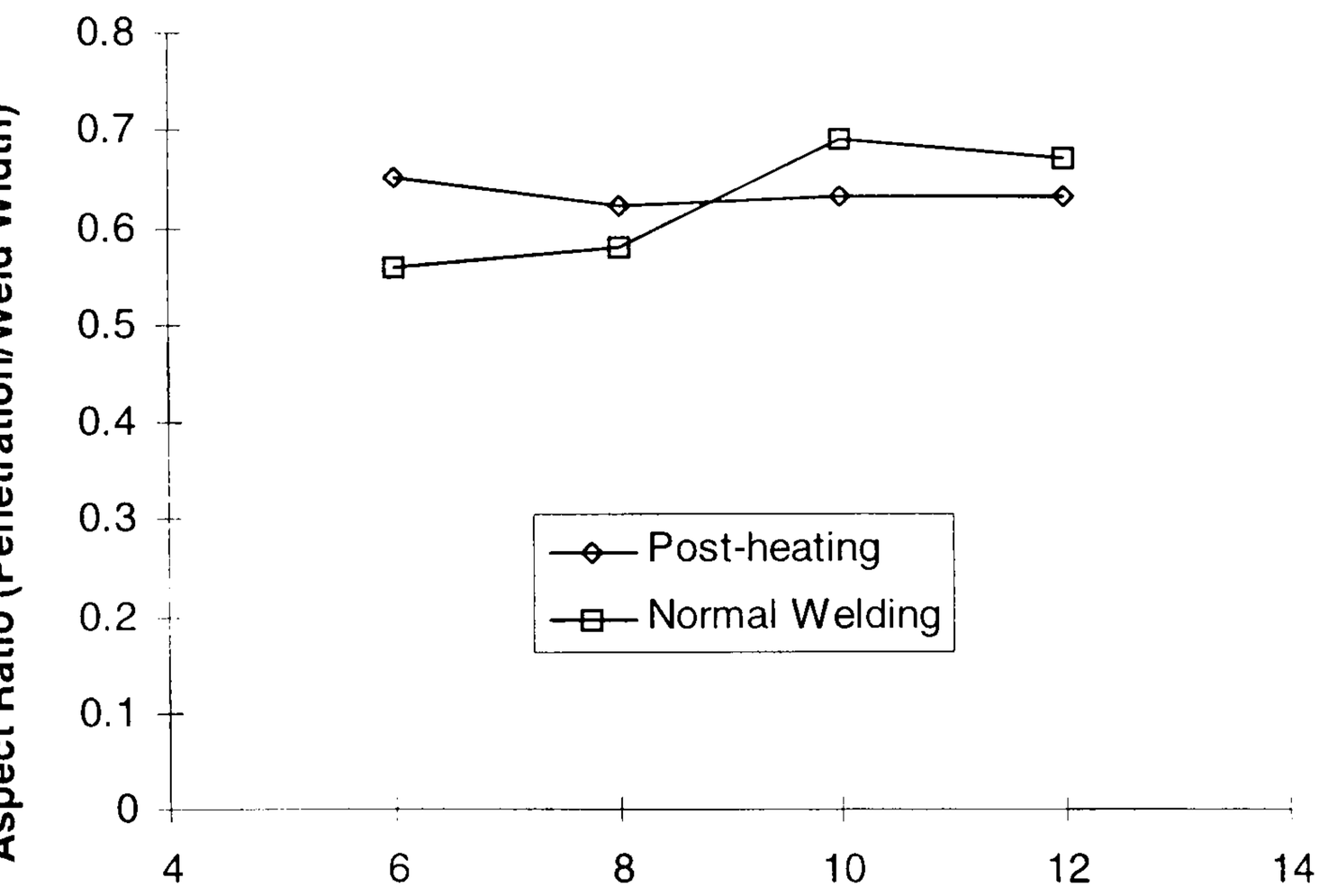

Figure 3.36. Aspect ratio as a function of pulse width

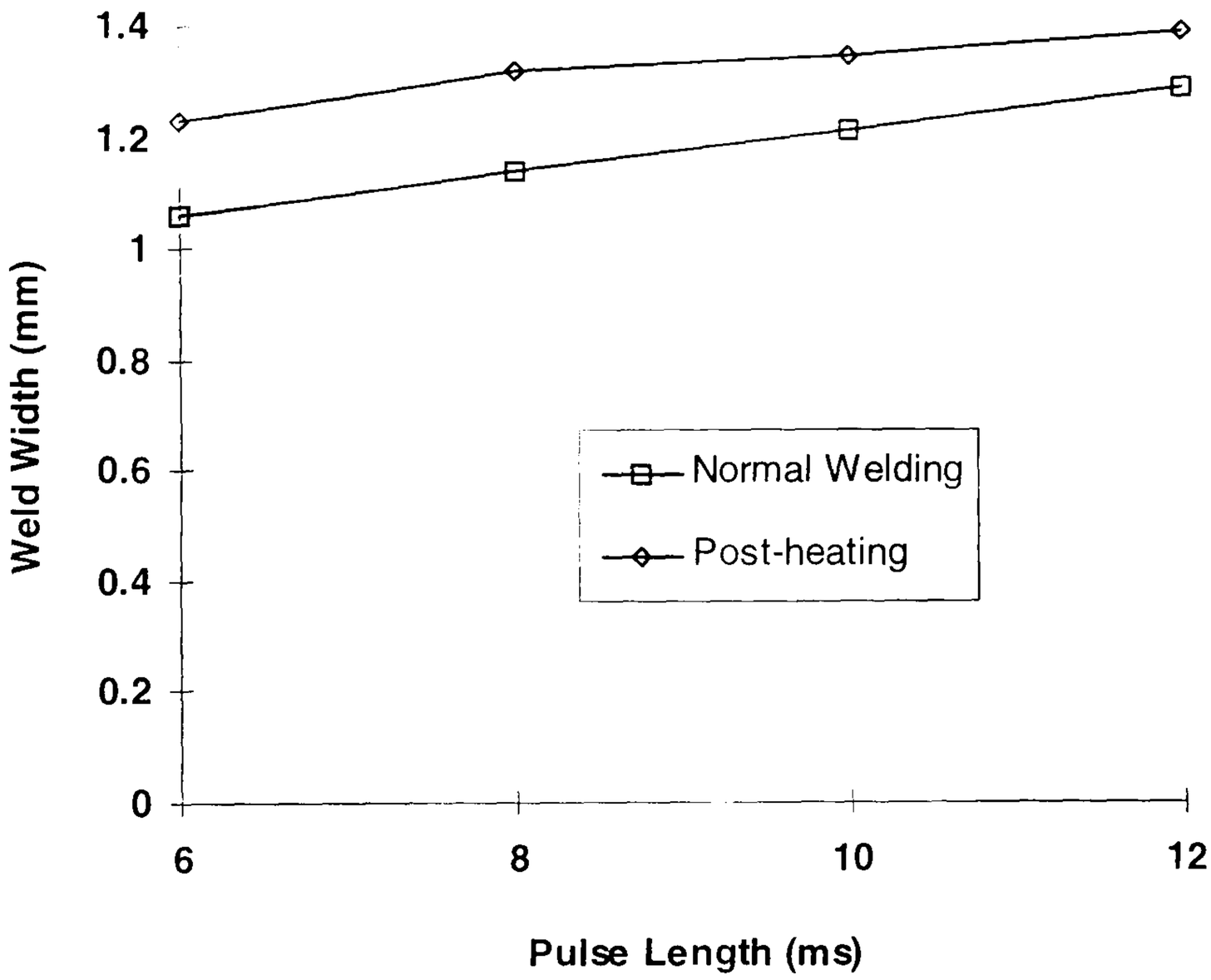

Figure 3.37. Weld Width for different pulse widths

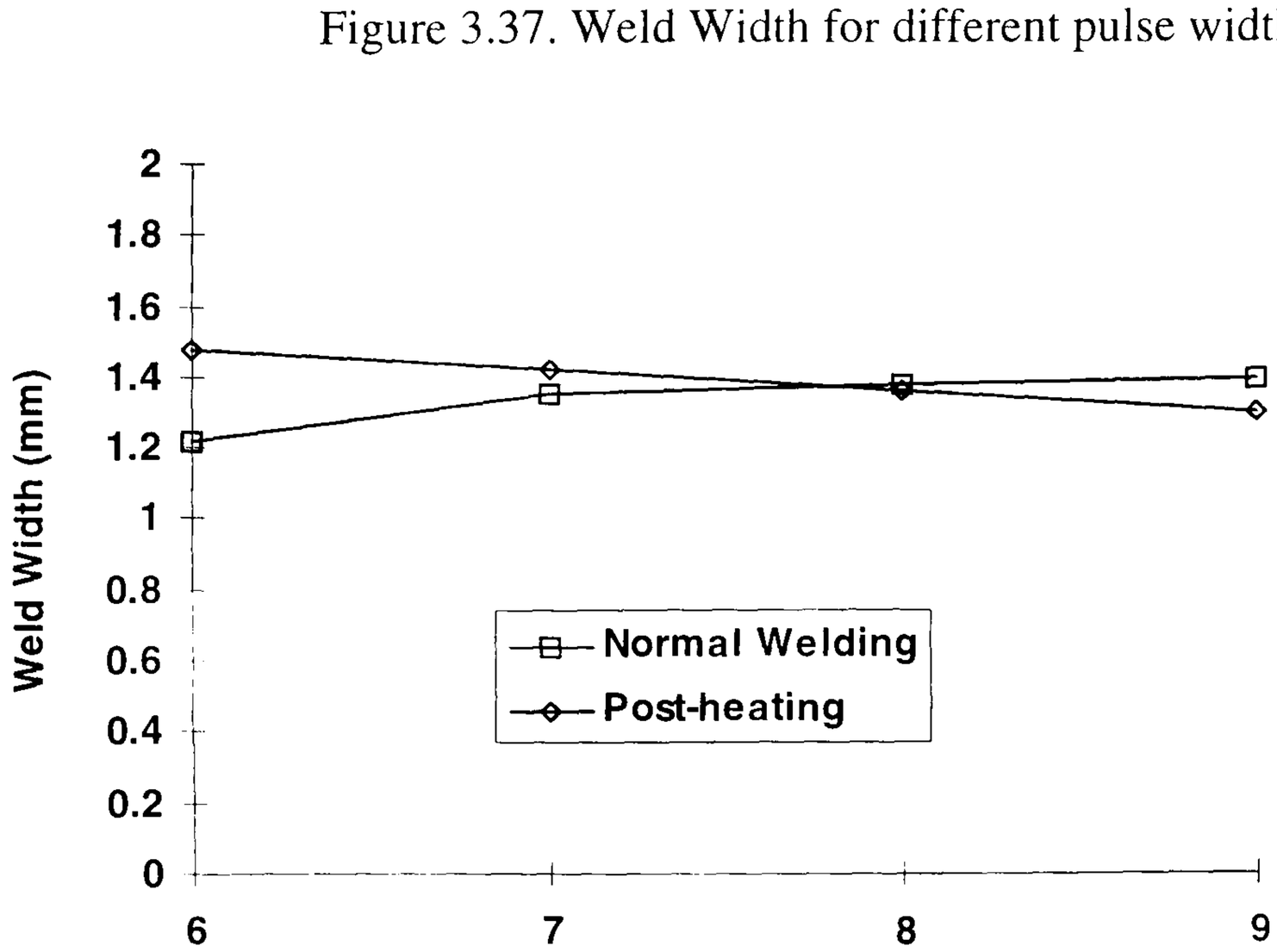

Figure 3.38 Weld width for different PRFs

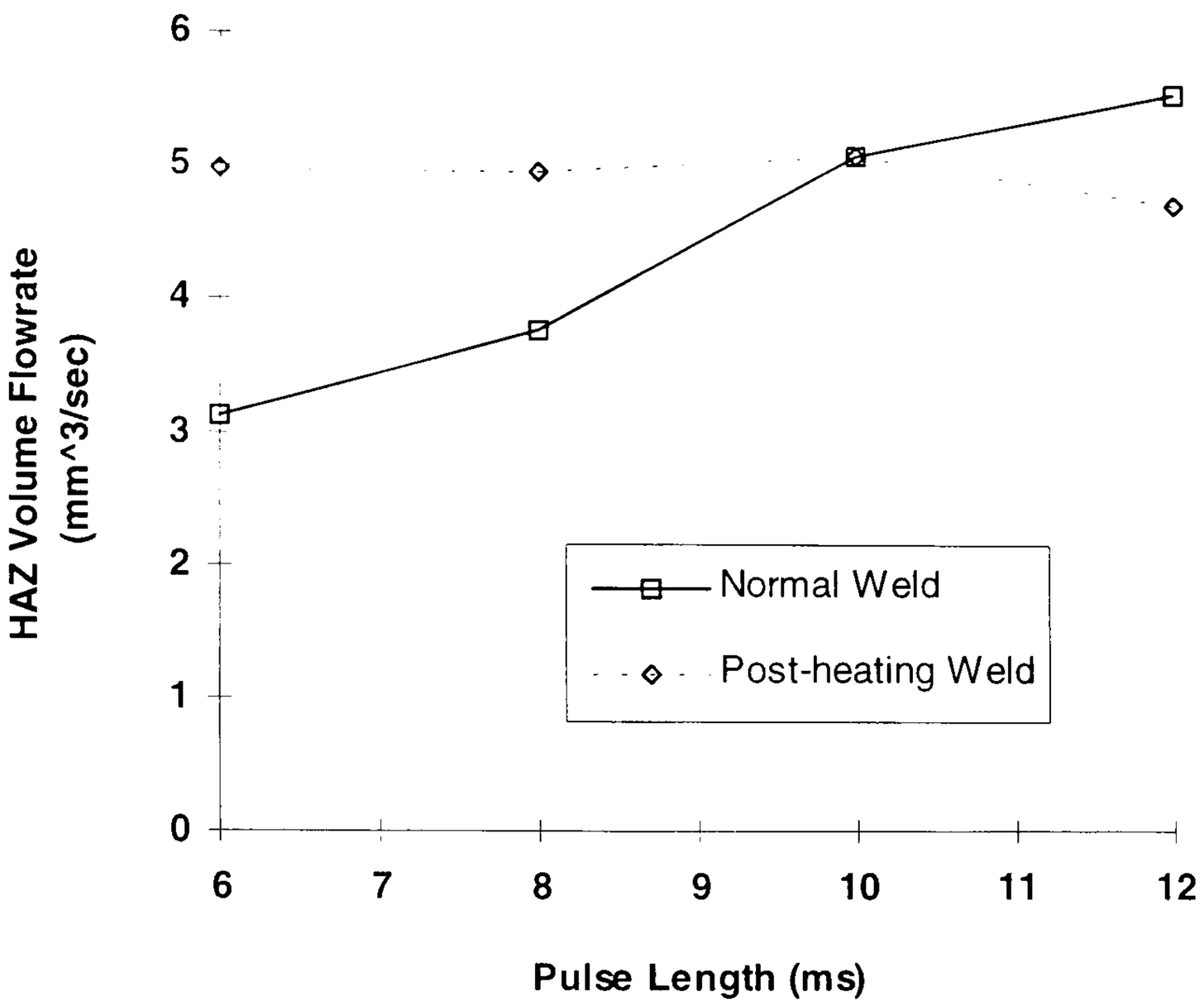

Figure 3.39. Rate of formation of weld volume for different pulse widths

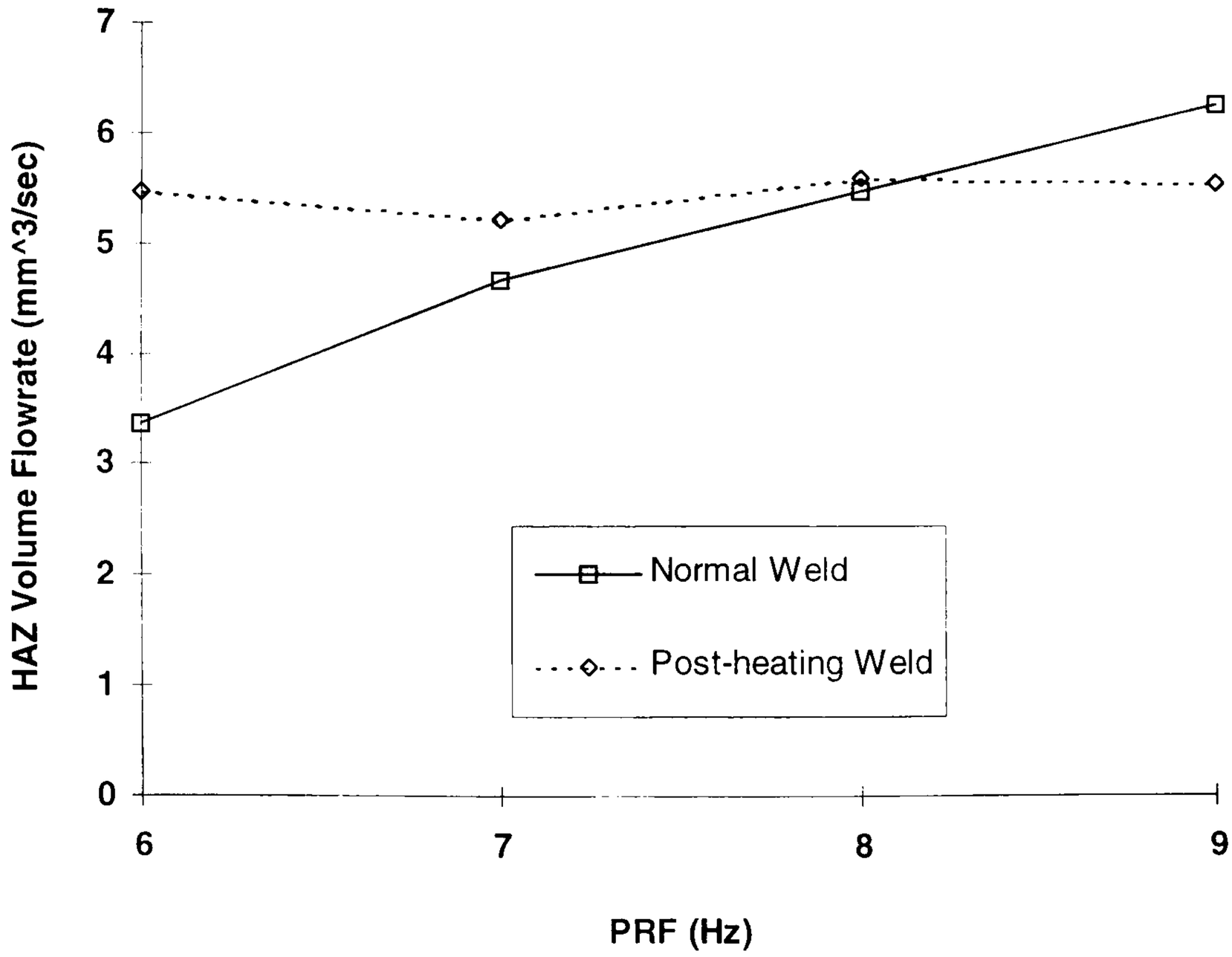

Figure 3.40 Rate of formation of weld volume for different PRFs

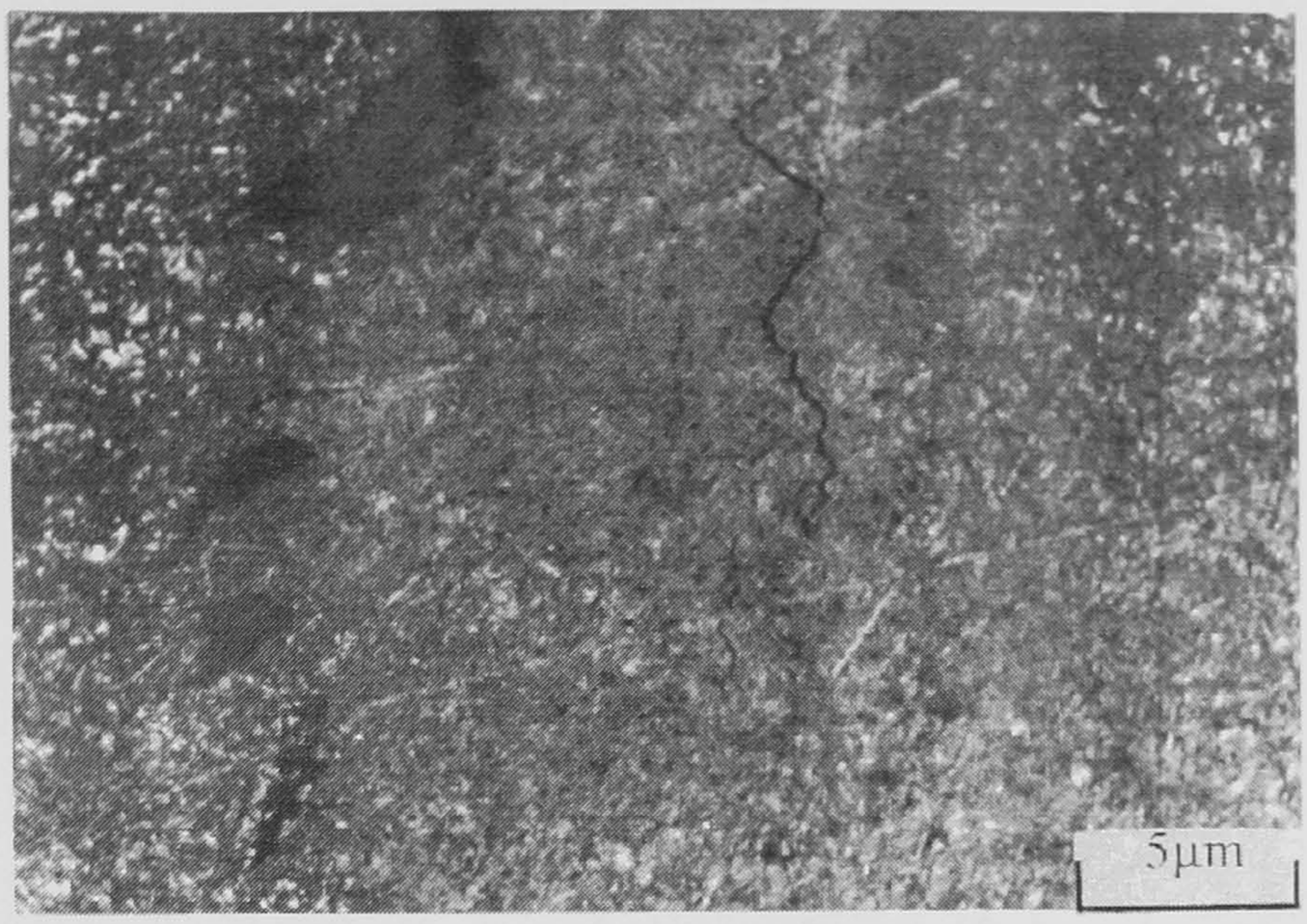

Figure 3.41 Microstructure of fusion zone for normal weld at a magnification of x225 (for a pulse width of 6 ms, PRF of 10 Hz, laser power of 200 W). Cracking can be seen down the middle of the weld

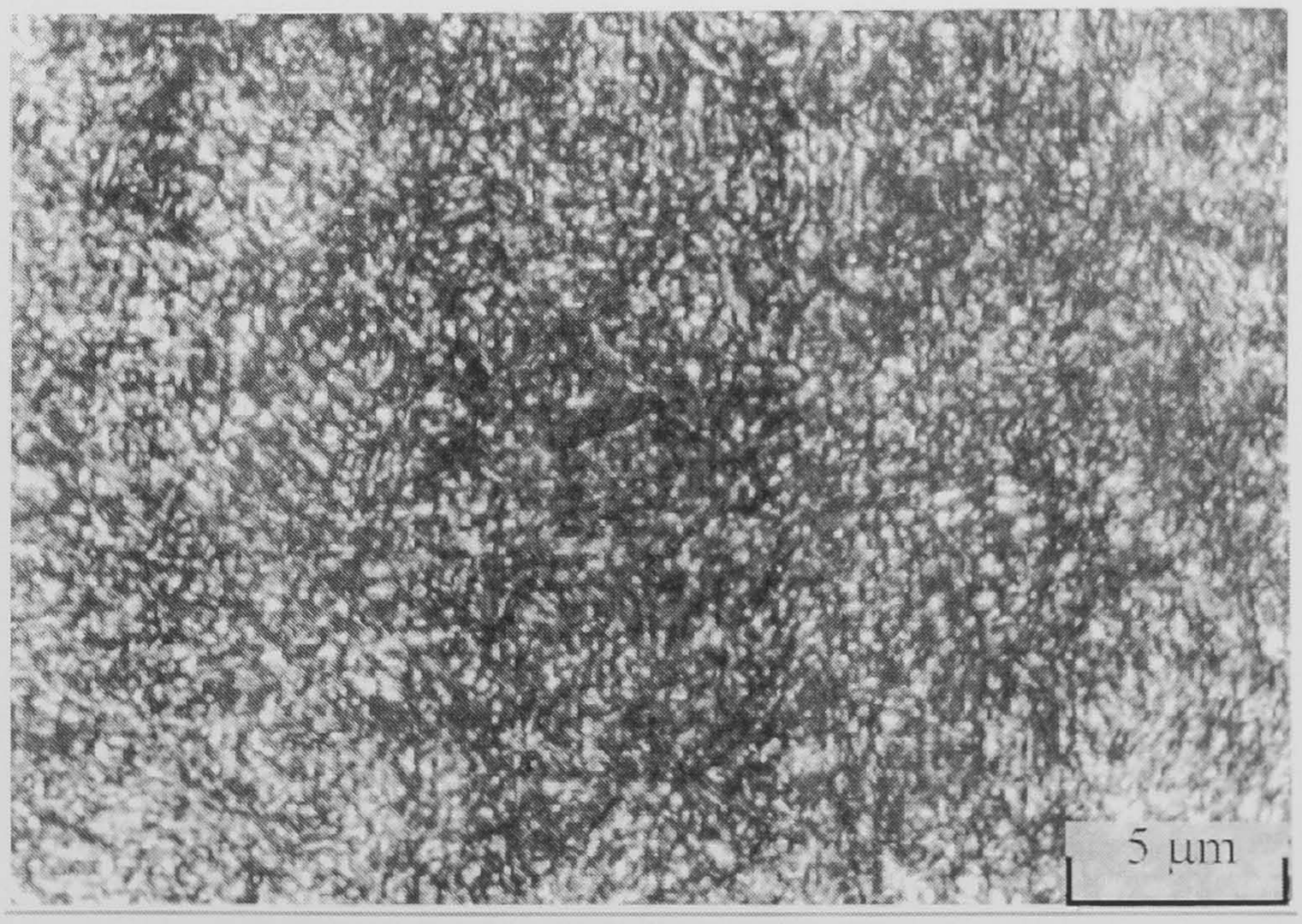

Figure 3.42. Microstructure of fusion zone for post-heated weld at a magnification of x225 (for a pulse width of 6 ms, PRF of 10 Hz, laser power of 285 W)

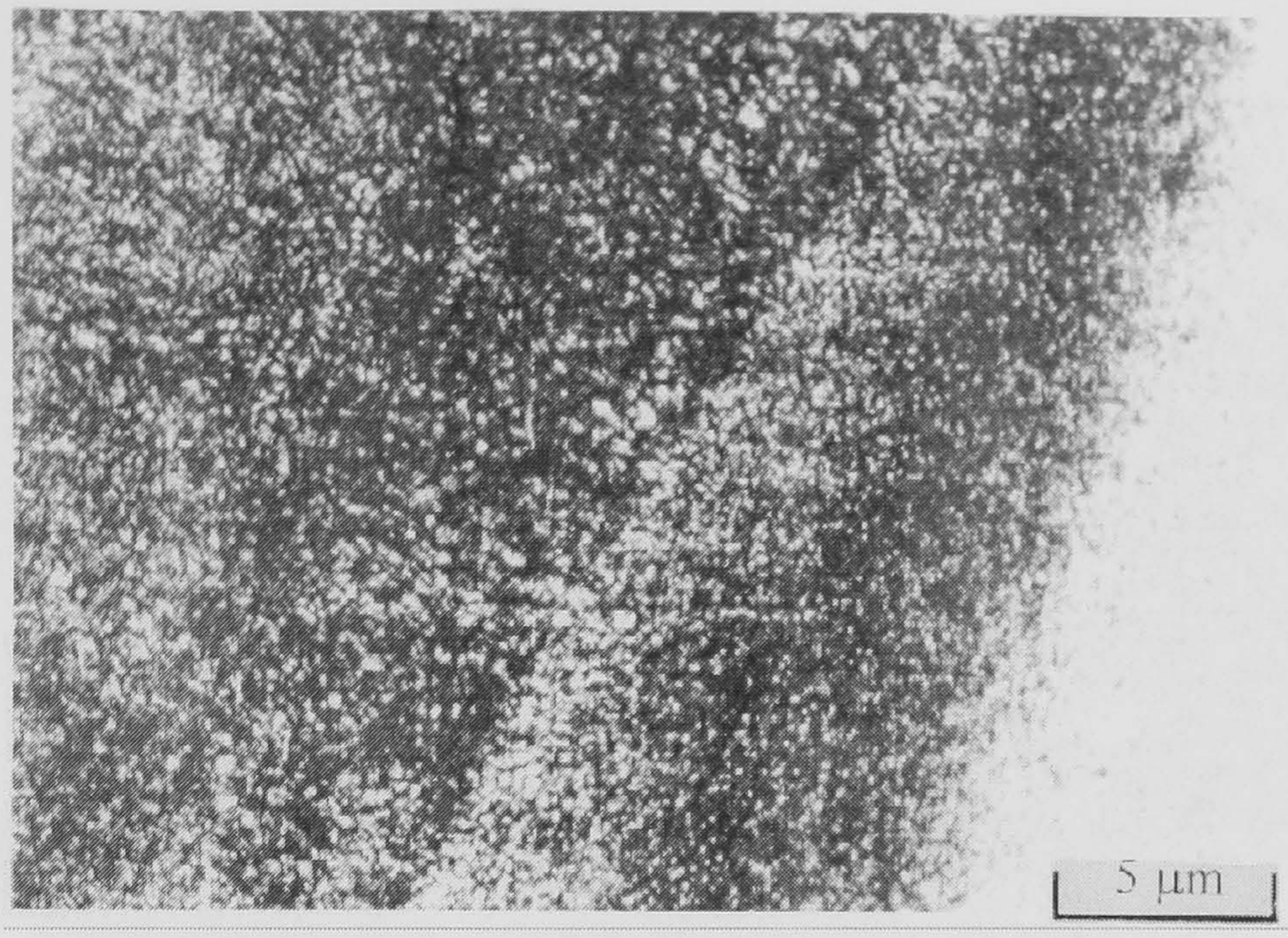

Figure 3.43. Microstructure of fusion zone (right), heat affected zone (centre) and base metal (left) for post-heated weld at a magnification Of x225 (for a pulse width of 6 ms, PRF of 10 Hz, laser power of 285 W)

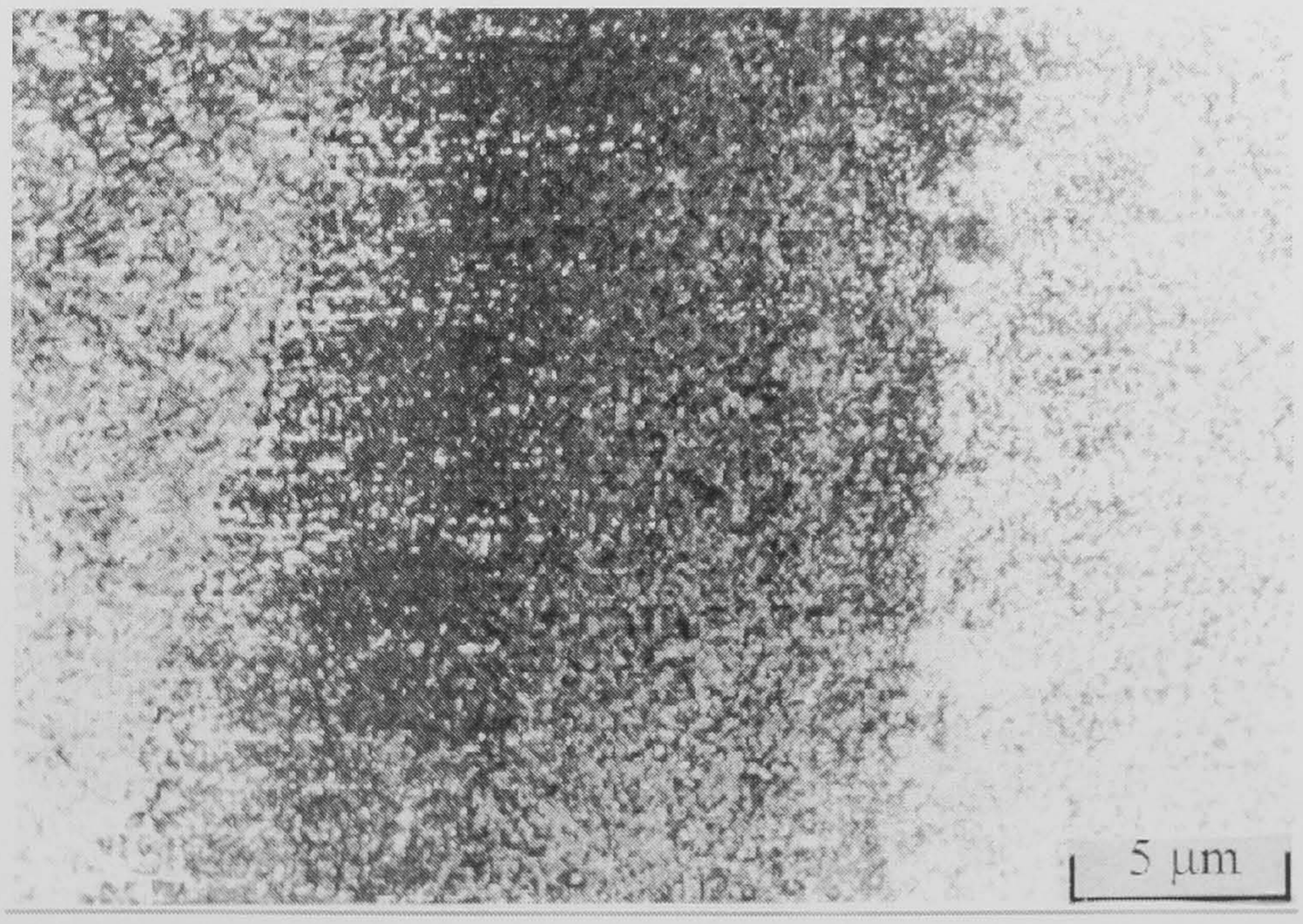

Figure 3.44. Microstructure of fusion zone (right), heat affected zone (centre) and base metal (left) for normal weld at a magnification Of x225 (for a pulse width of 6 ms, PRF of 10 Hz, laser power of 200 W)

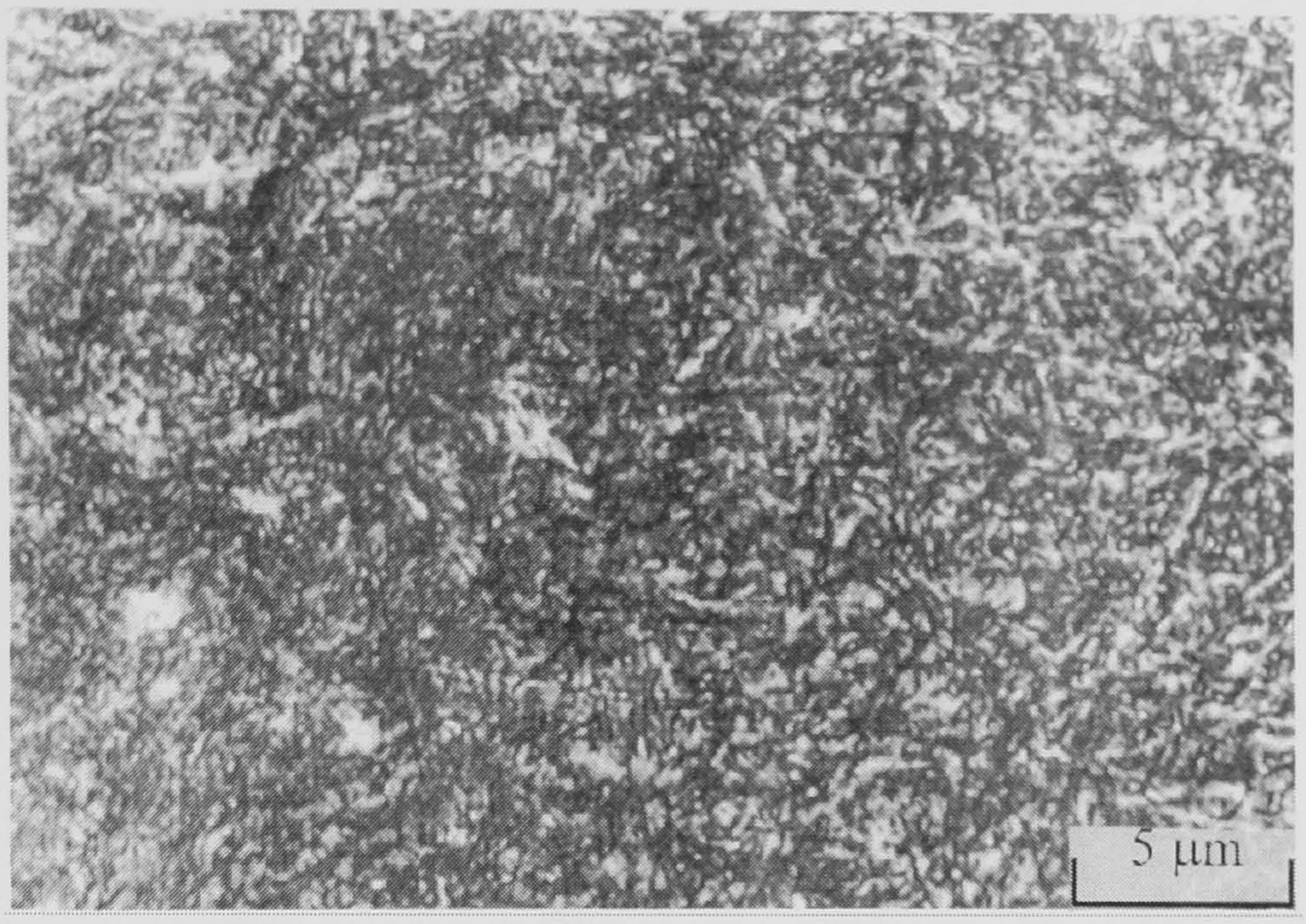

Figure 3.45. Microstructure of fusion zone for normal weld at a magnification of x225 (for a pulse width of 10 ms, PRF of 9 Hz, laser power of 200 W)

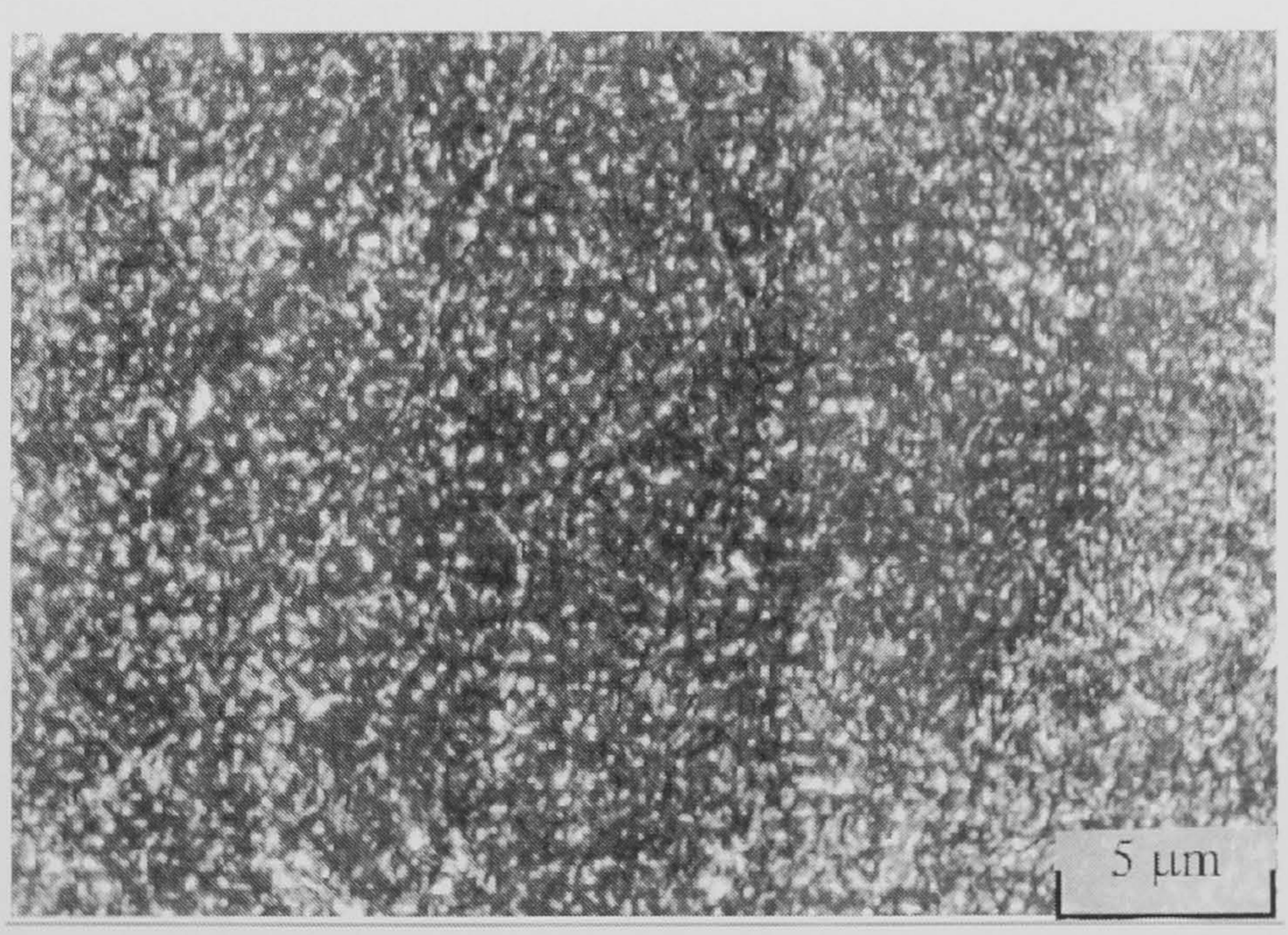

Figure 3.46. Microstructure of fusion zone for post-heated weld at a magnification of x225 (for a pulse width of 10 ms, PRF of 9 Hz, laser power of 285 W)

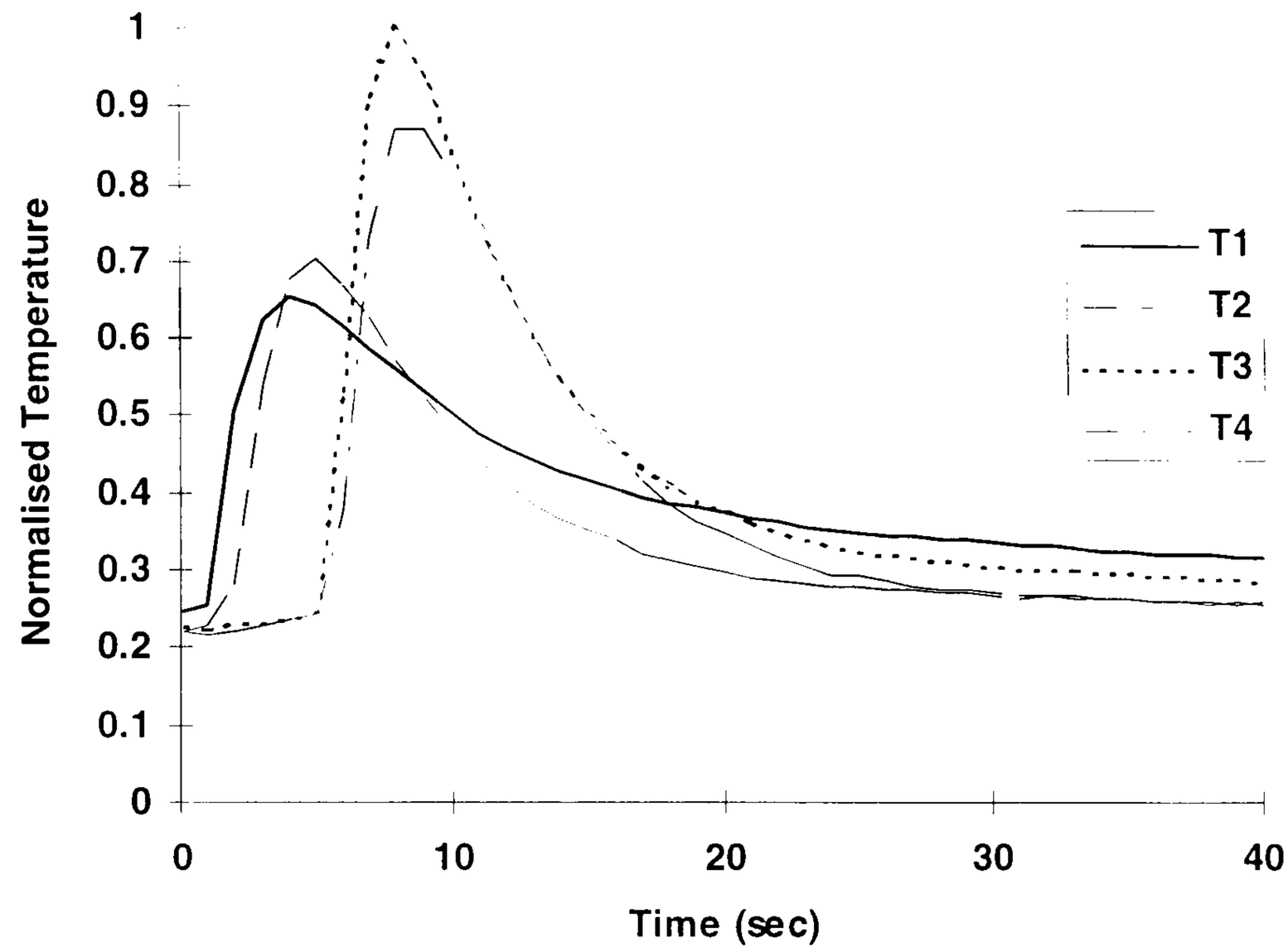

Figure 3.47 Normalised temperature profile for normal weld with a pulse width of 6 ms

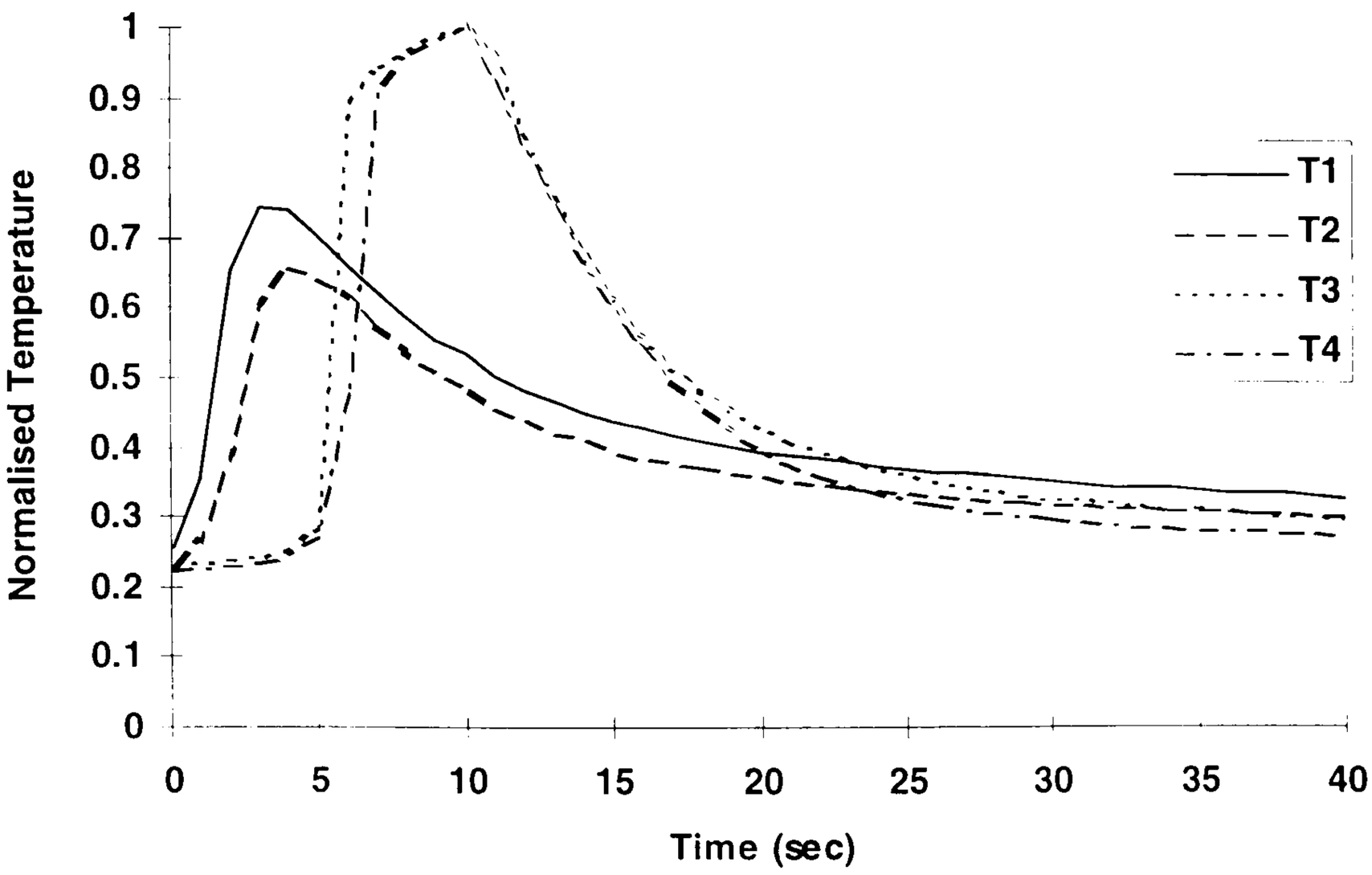

Figure 3.48 Normalised temperature profile for normal weld with a pulse width of 12 ms

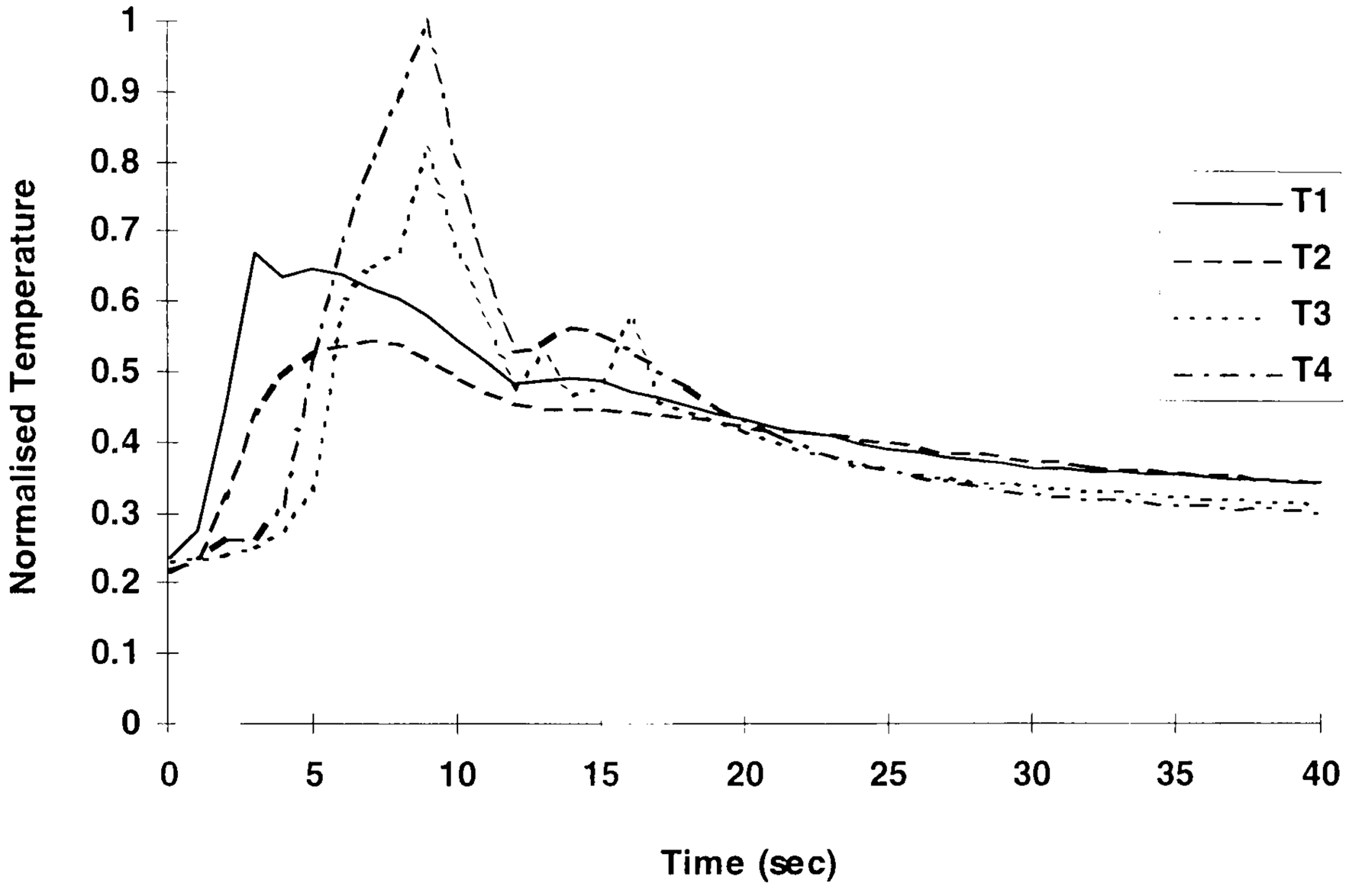

Figure 3.49 Normalised temperature profile for post-heated weld with a pulse width of 12 ms

Type Of Welding	Power for welding / Power for Pre-heating (W)	Pulse Width (ms)	PRF (Hz)	Speed (mm/sec)	Pulse Energy (Joules)	Peak Power (kW)	Spot Size (mm)	Pulse Shape
Normal	200	6	10	5	20	3.3	2	Top hat
Normal	200	8	10	5	20	2.5	2	Top hat
Normal	200	10	10	5	20	2	2	Top hat
Normal	200	12	10	5	20	1.7	2	Top hat
Normal	200	10	6	5	33.3	3.3	2	Top hat
Normal	200	10	7	5	28.6	2.9	2	Top hat
Normal	200	10	8	5	25	2.5	2	Top hat
Normal	200	10	9	5	22.2	2.2	2	Top hat
Pre-heating	200 / 85	6	10	5	20/8.5	3.3/1.4	2/20	Top hat
Pre-heating	200 / 85	8	10	5	20/8.5	2.5/1.1	2/20	Top hat
Pre-heating	200 / 85	10	10	5	20/8.5	2/0.9	2/20	Top hat
Pre-heating	200 / 85	12	10	5	20/8.5	1.7/0.7	2/20	Top hat
Pre-heating	200 / 85	10	6	5	33.3/14.2	3.3/1.4	2/20	Top hat
Pre-heating	200 / 85	10	7	5	28.6/12.1	2.9/1.2	2/20	Top hat
Pre-heating	200 / 85	10	8	5	25/10.6	2.5/1.1	2/20	Top hat
Pre-heating	200 / 85	10	9	5	22.2/9.4	2.2/0.9	2/20	Top hat

Table 3.2: Parameters For Normal Welding And Pre-heating Welding

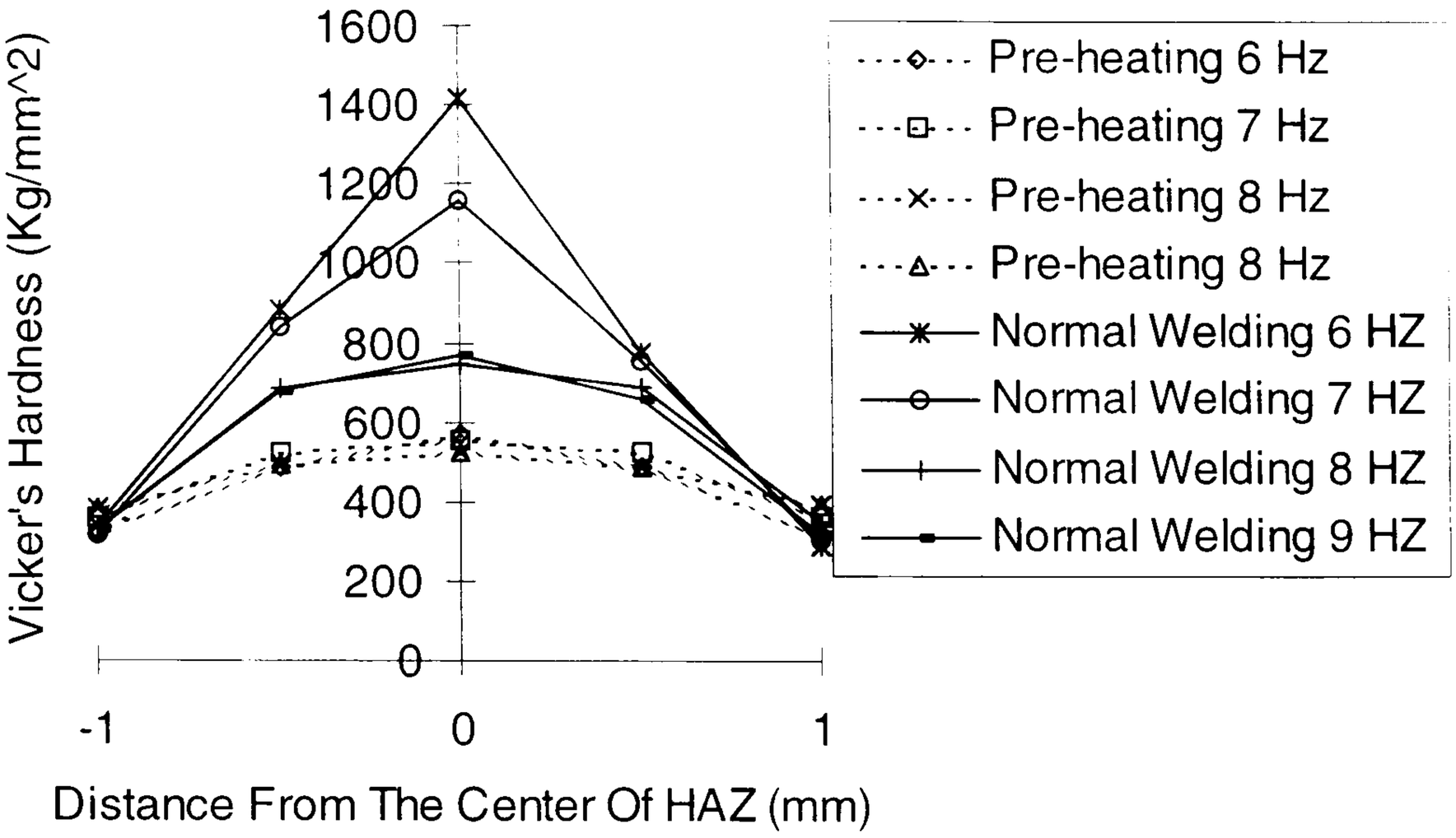

Figure 3.50 Microhardness across the weld for different PRFs

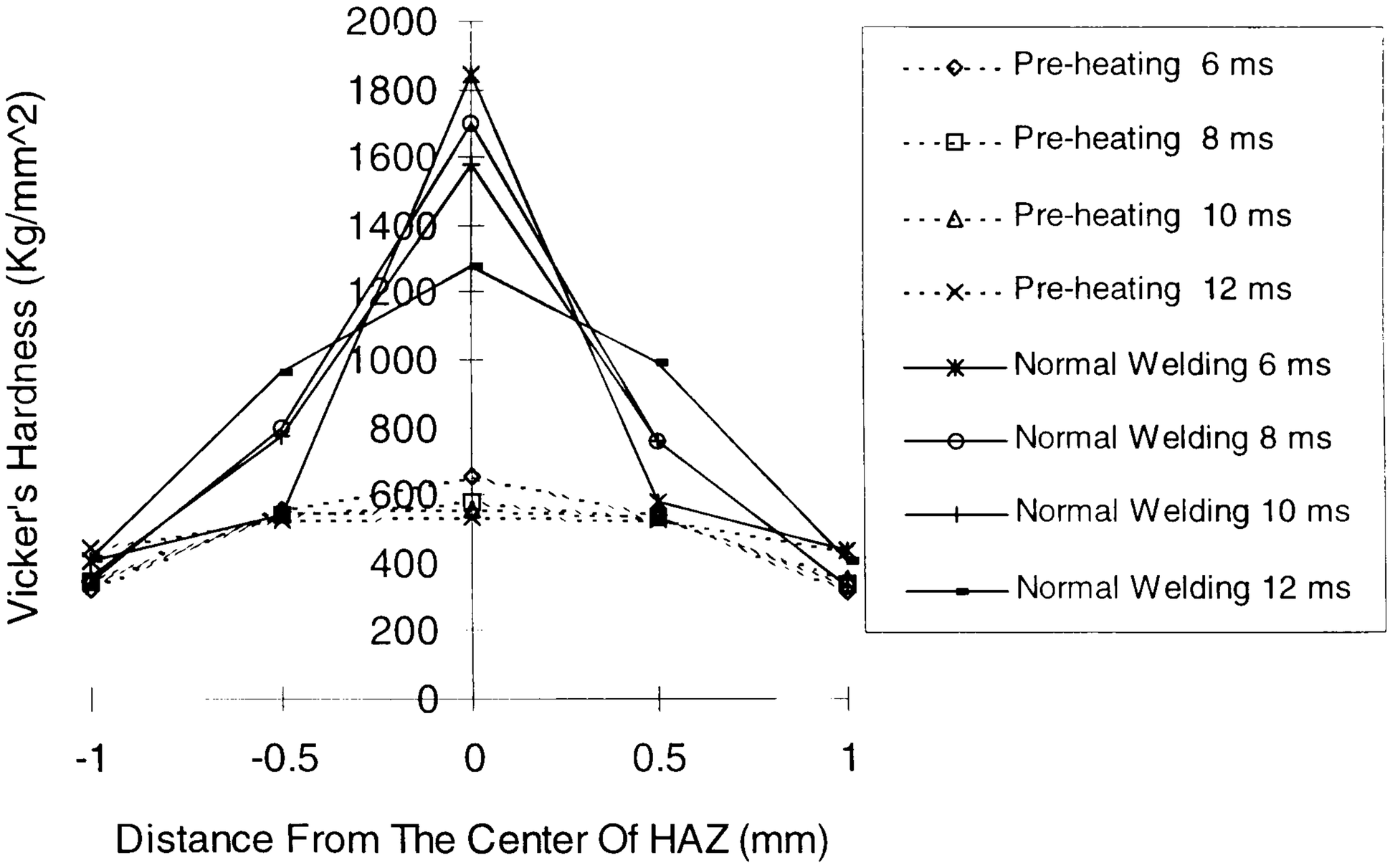

Figure 3.51 Microhardness across the weld for different PRFs

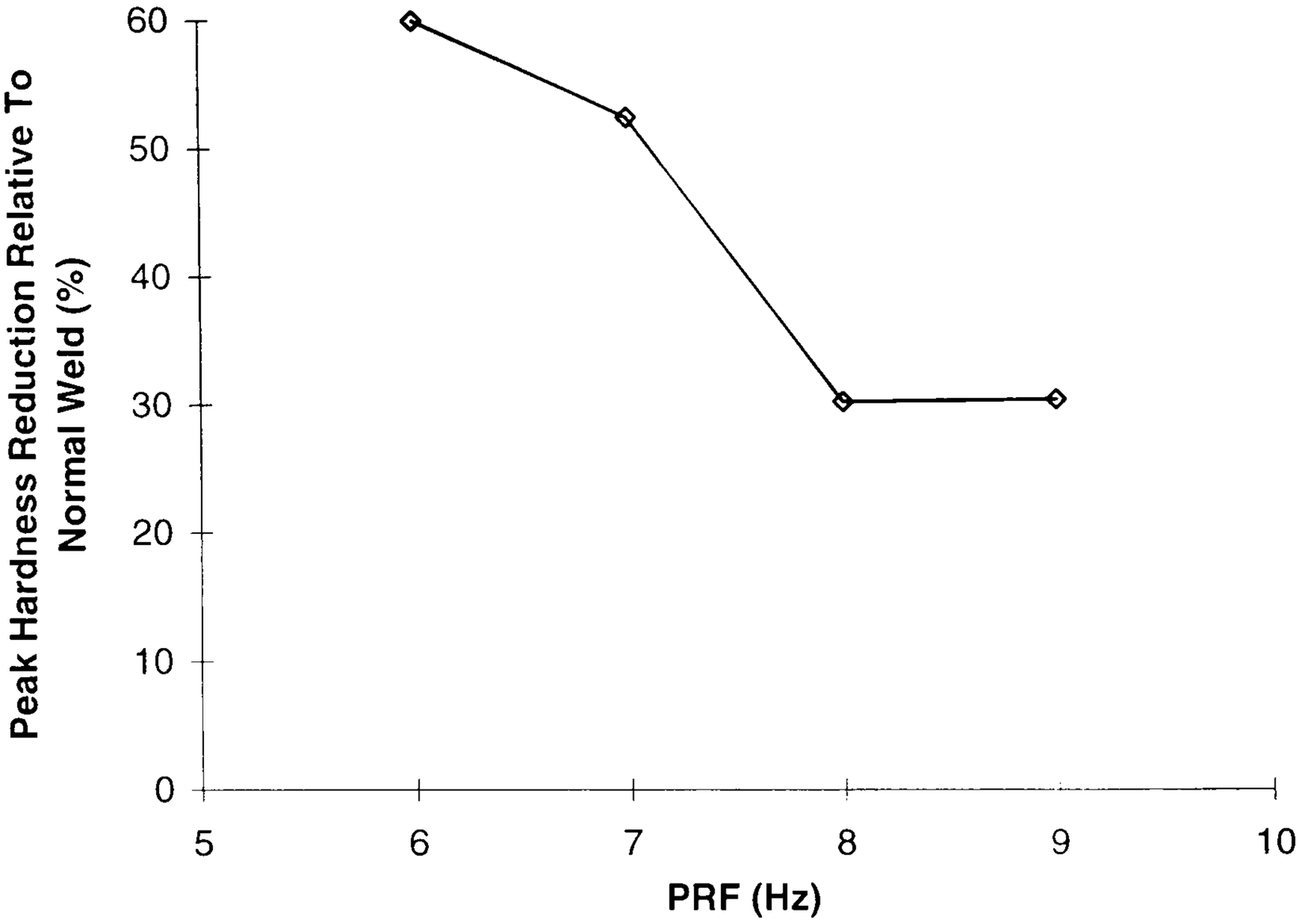

Figure 3.52 Relative peak hardness reduction as a function of PRFs

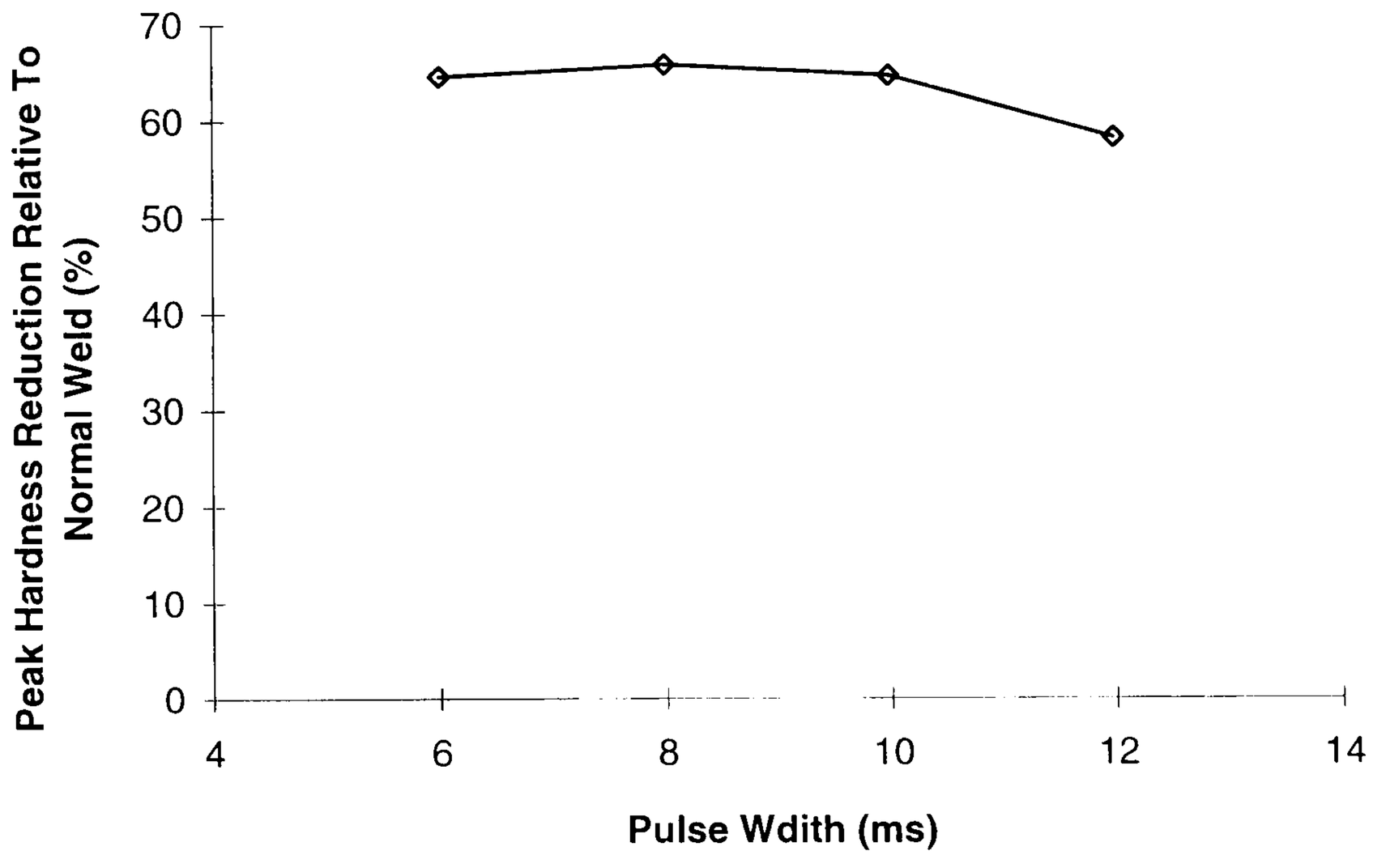

Figure 3.53 Relative peak hardness reduction as a function of pulse widths

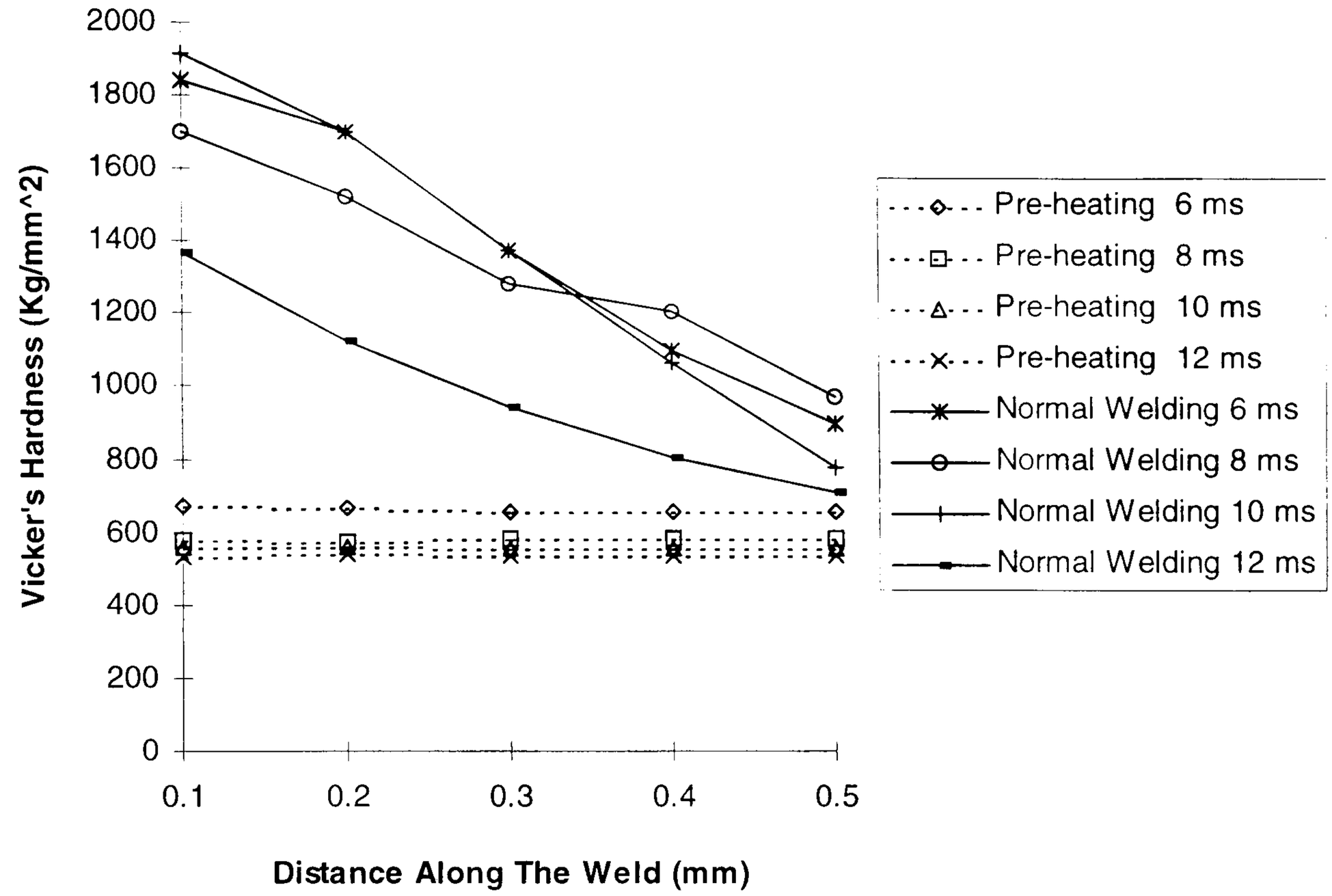

Figure 3.54 Vicker's hardness as a function of weld depth for different pulse widths

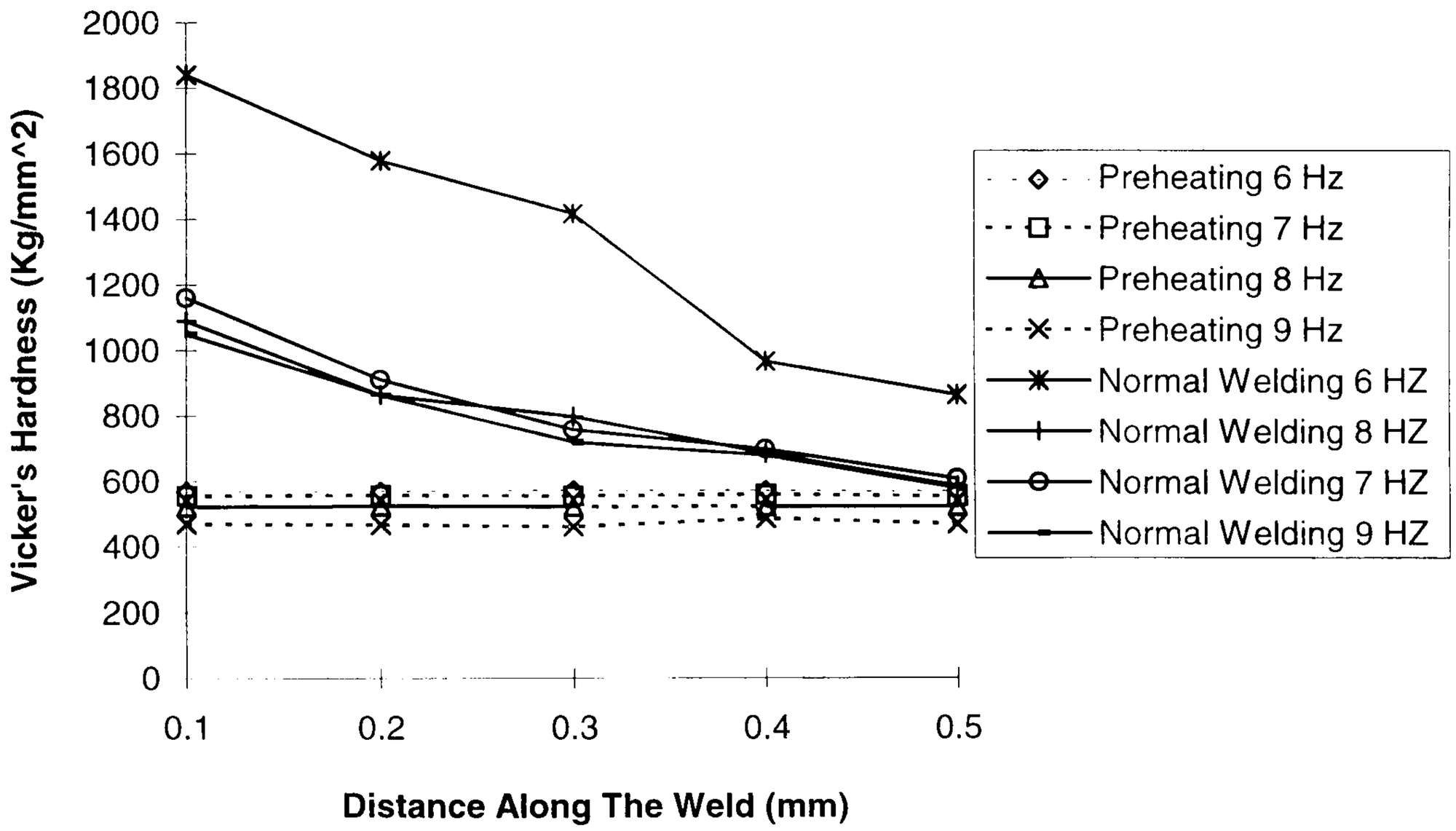

Figure 3.55 Vicker's hardness as a function of weld depth for different PRF

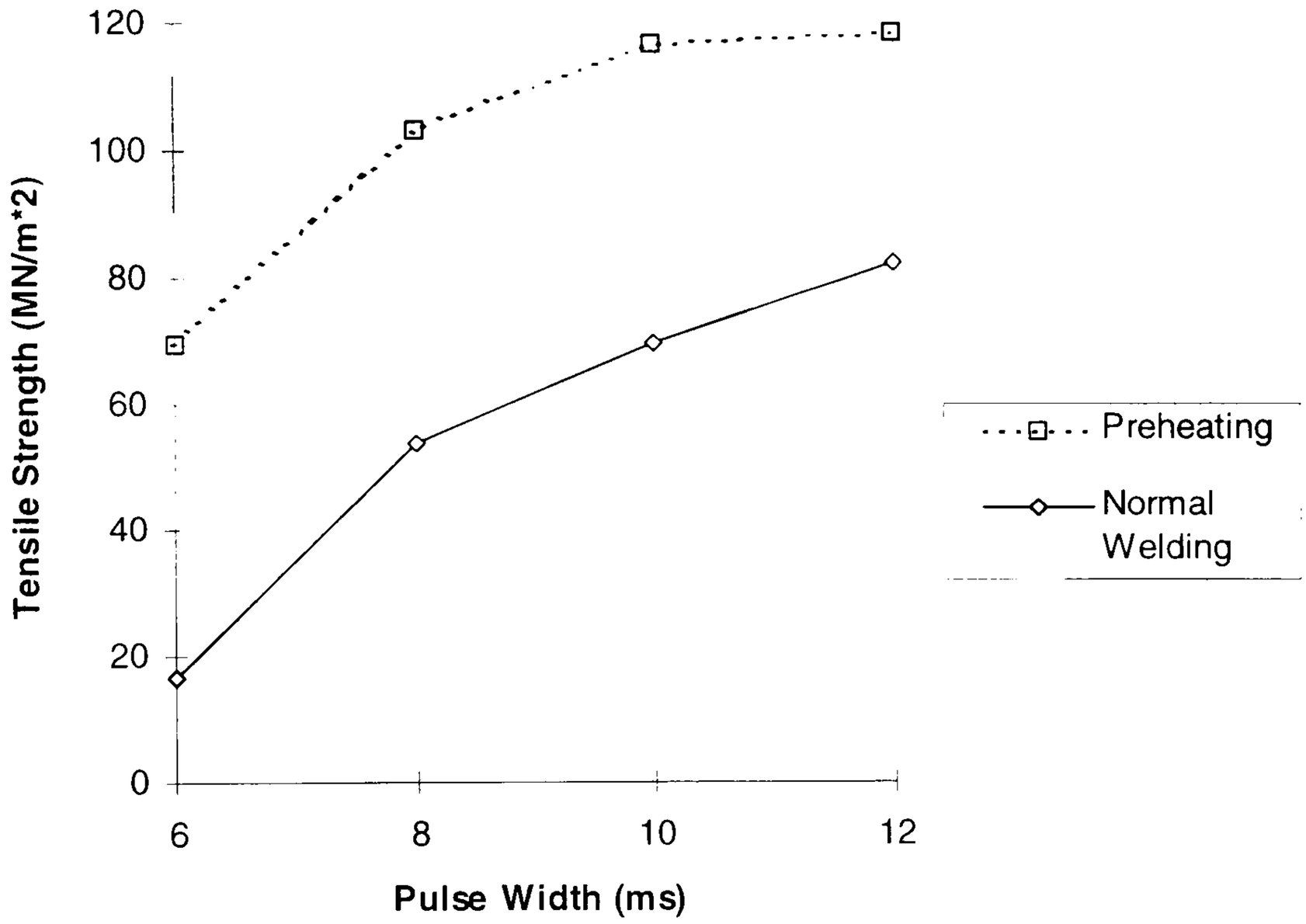

Figure 3.56 Tensile strength as a function of different pulse width

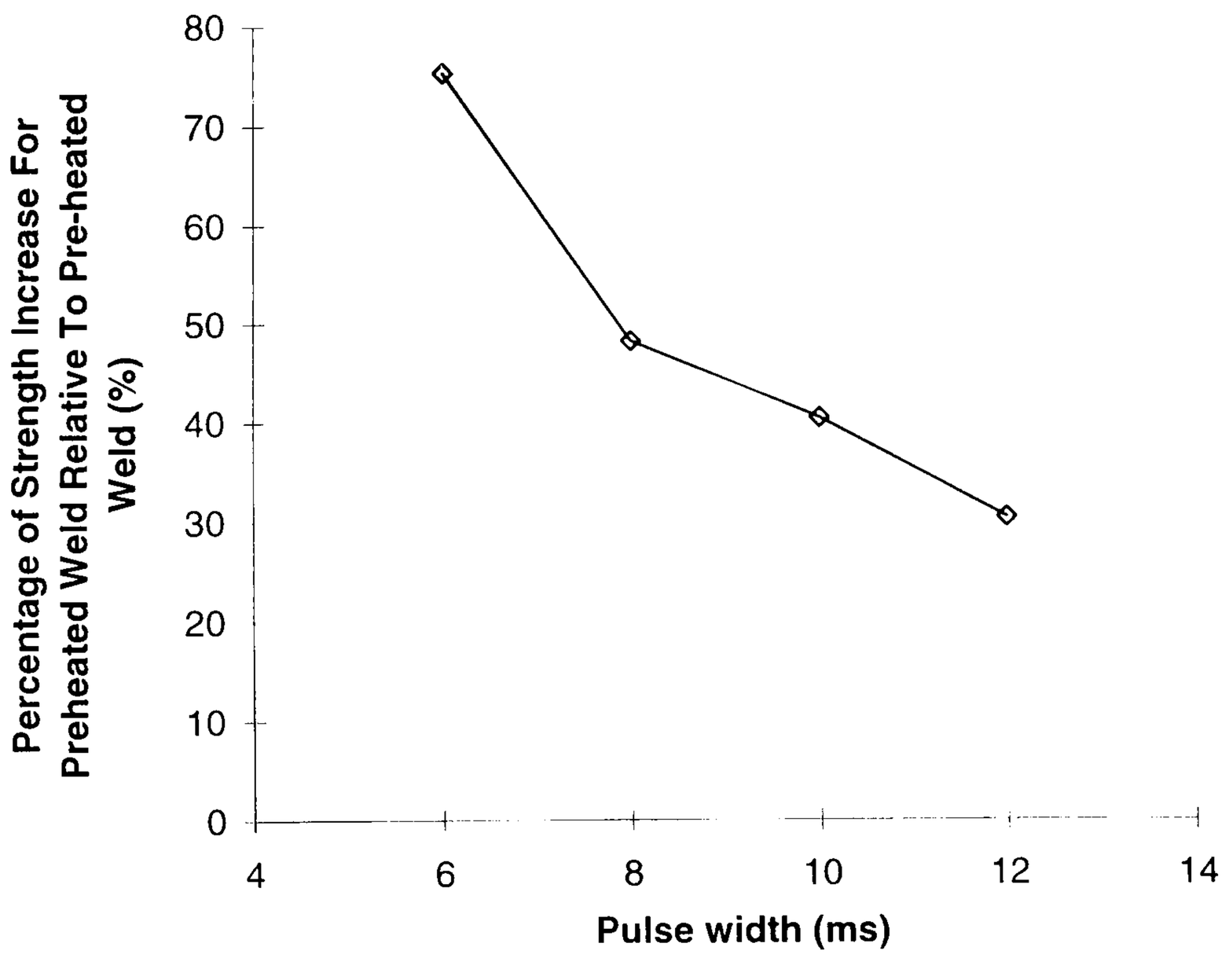

Figure 3.57 Percentage of difference in tensile strength for different pulse widths

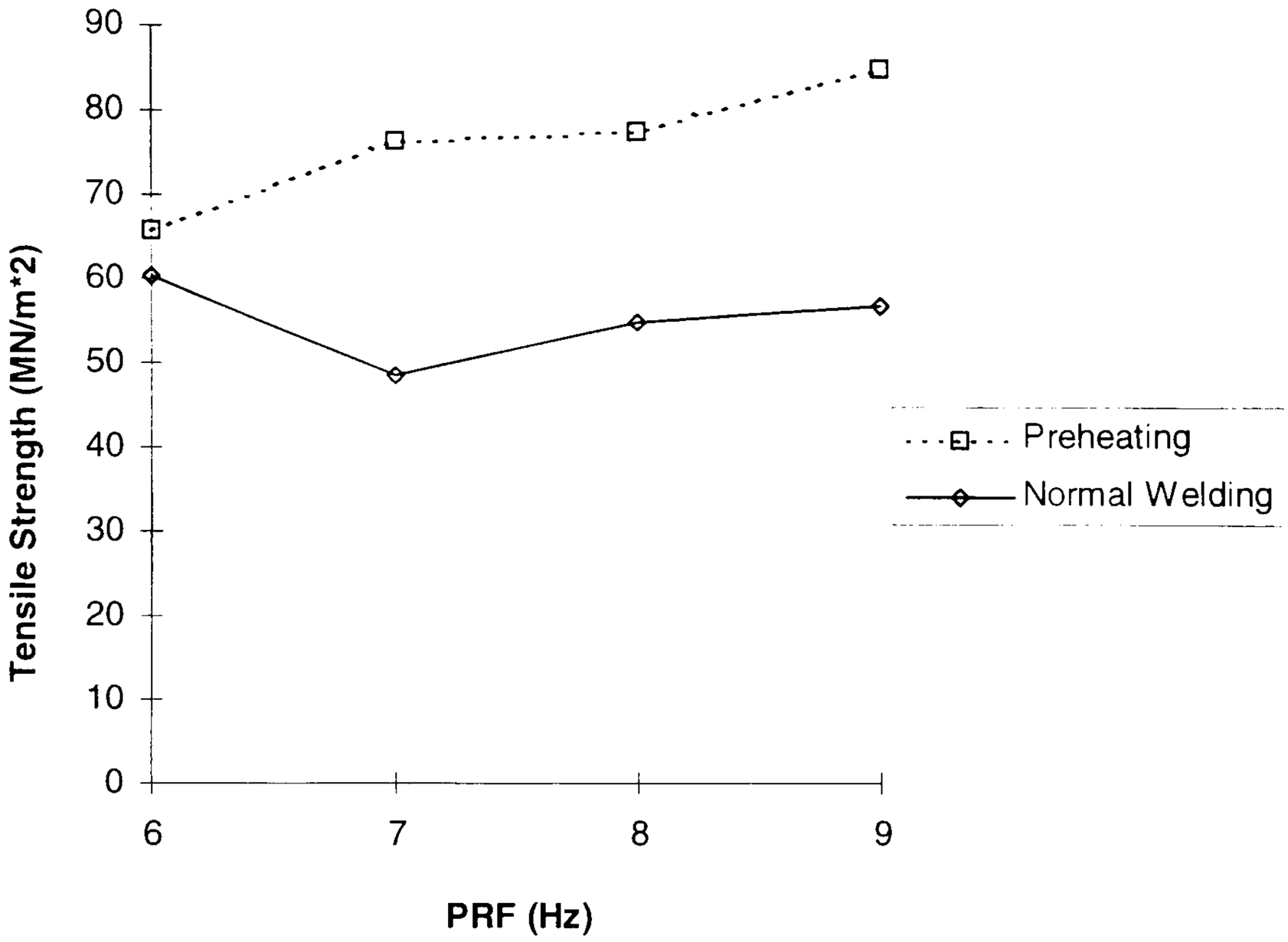

Figure 3.58 Tensile strength as a function of different pulse width

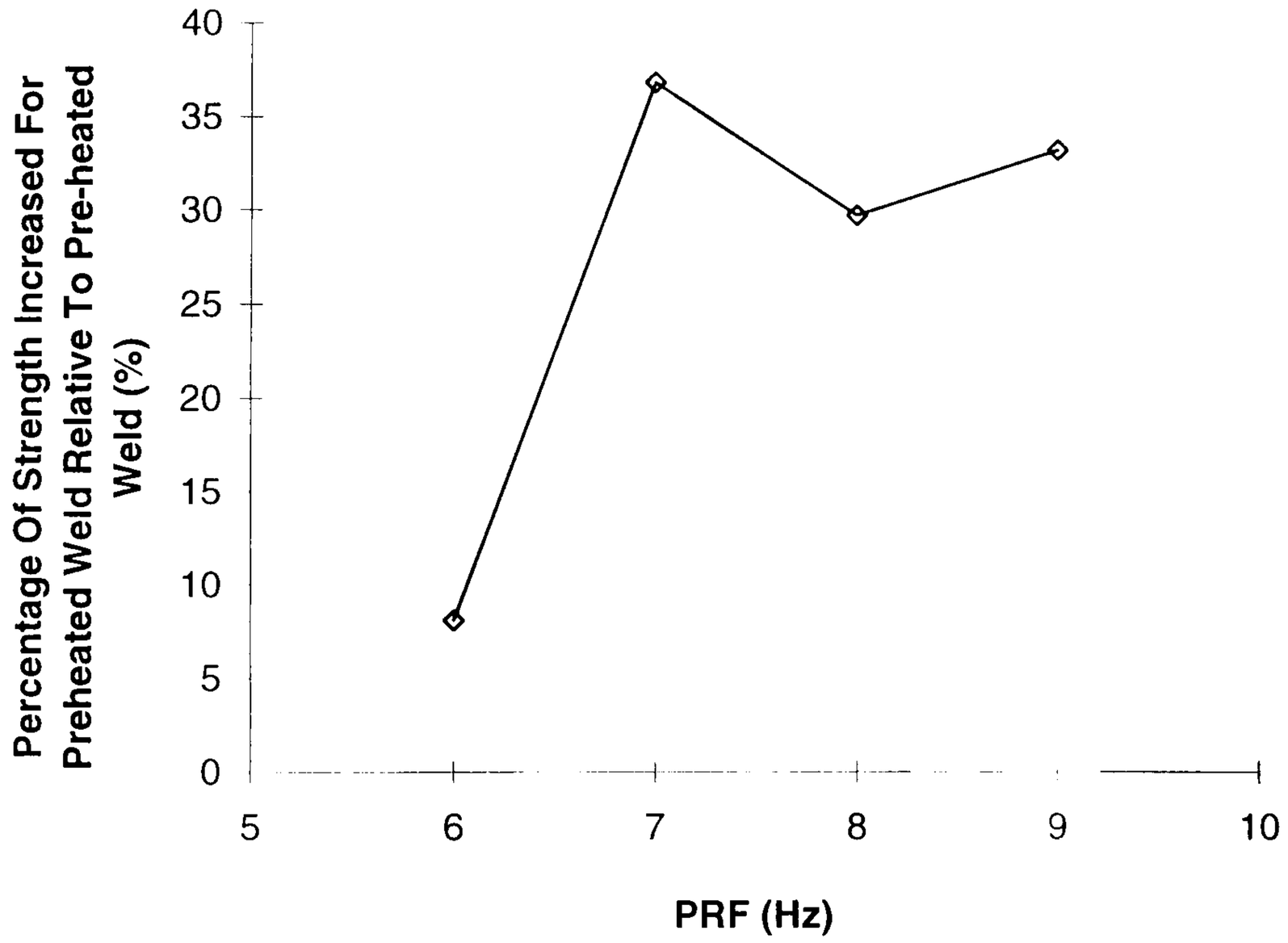

Figure 3.59 Percentage of difference in tensile strength for different pulse widths

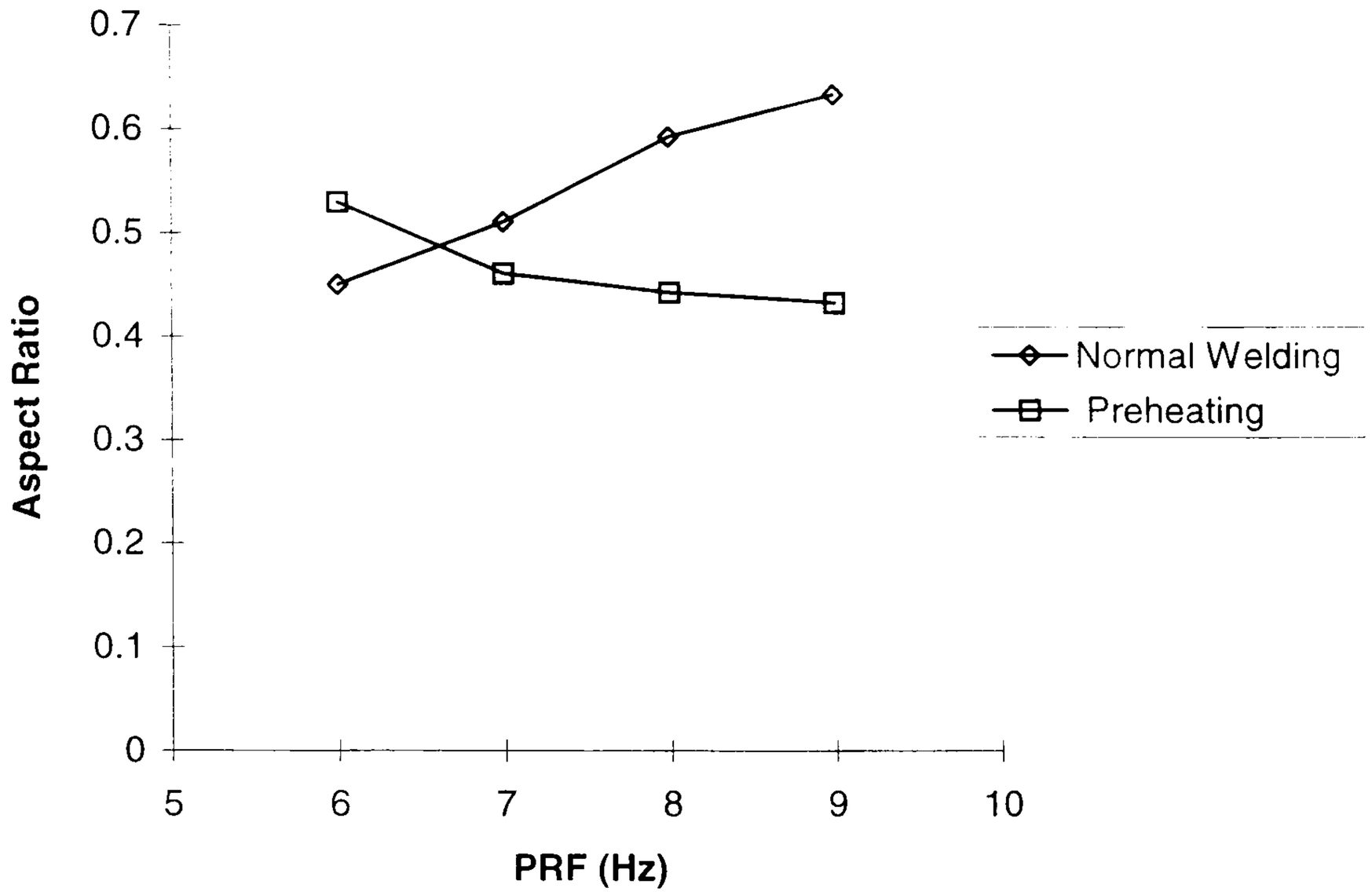

Figure 3.60 Aspect ratio as a function of PRFs

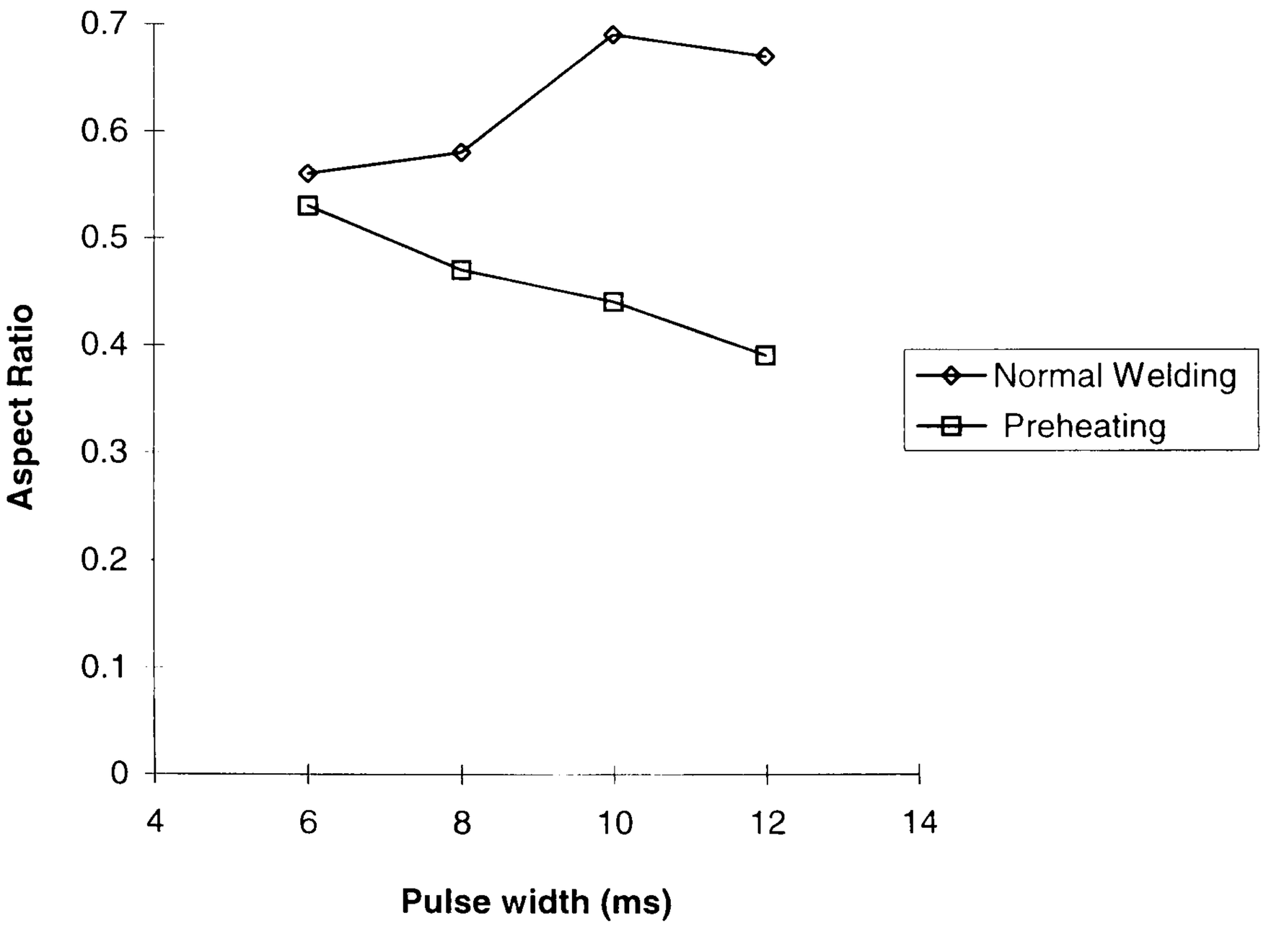

Figure 3.61 Aspect ratio as a function of pulse widths

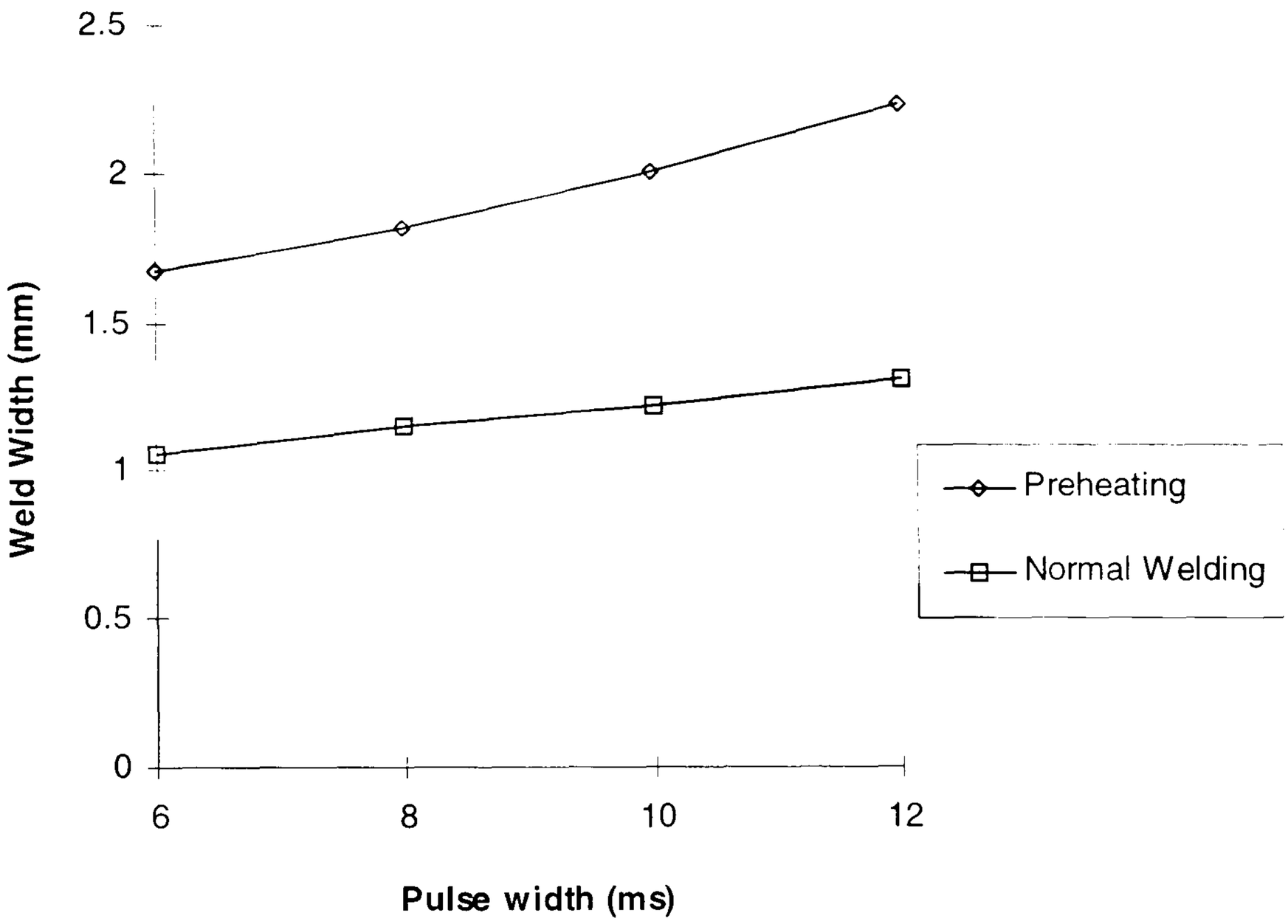

Figure 3.62 Weld width as a function of different pulse widths

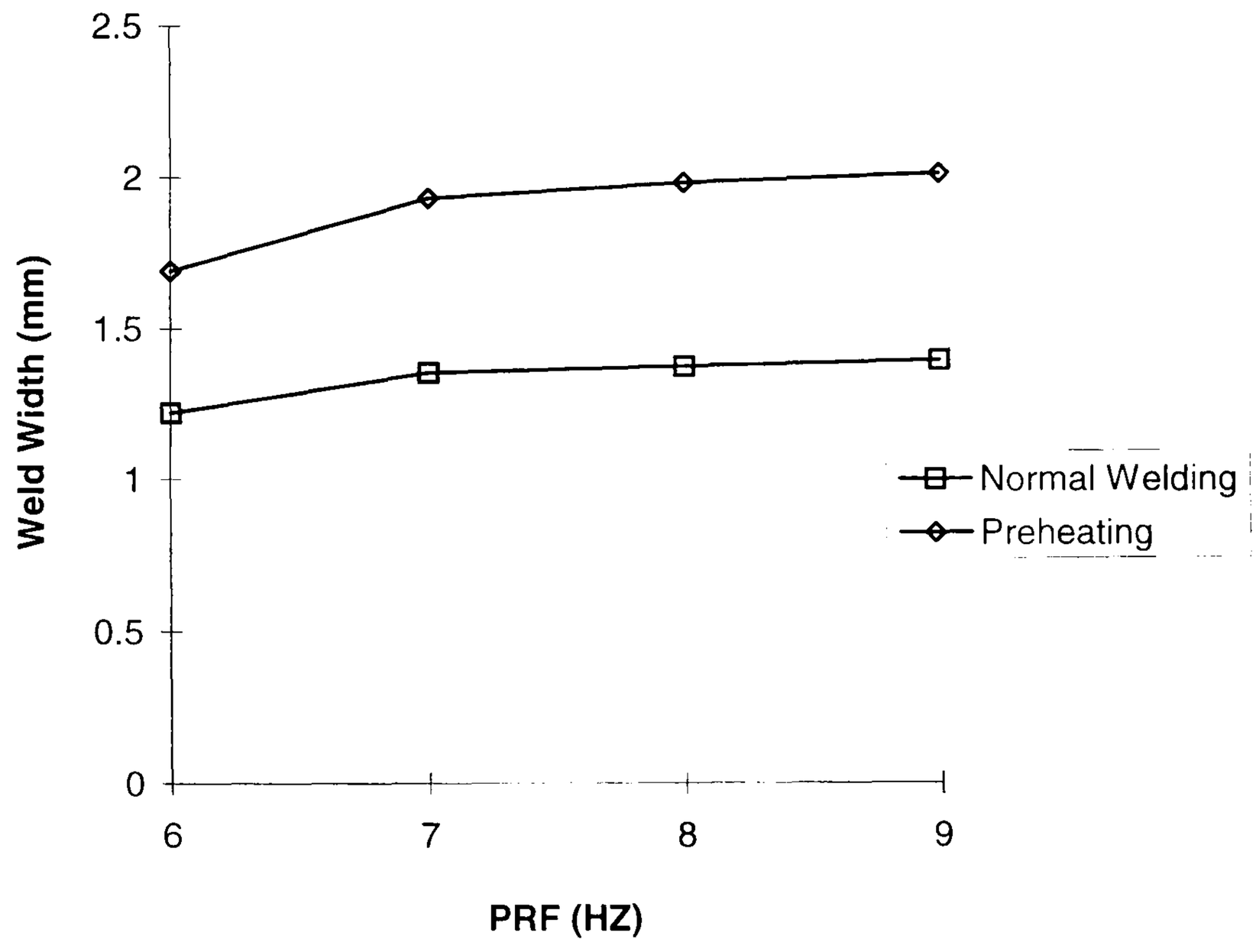

Figure 3.63 Weld width as a function of different PRFs

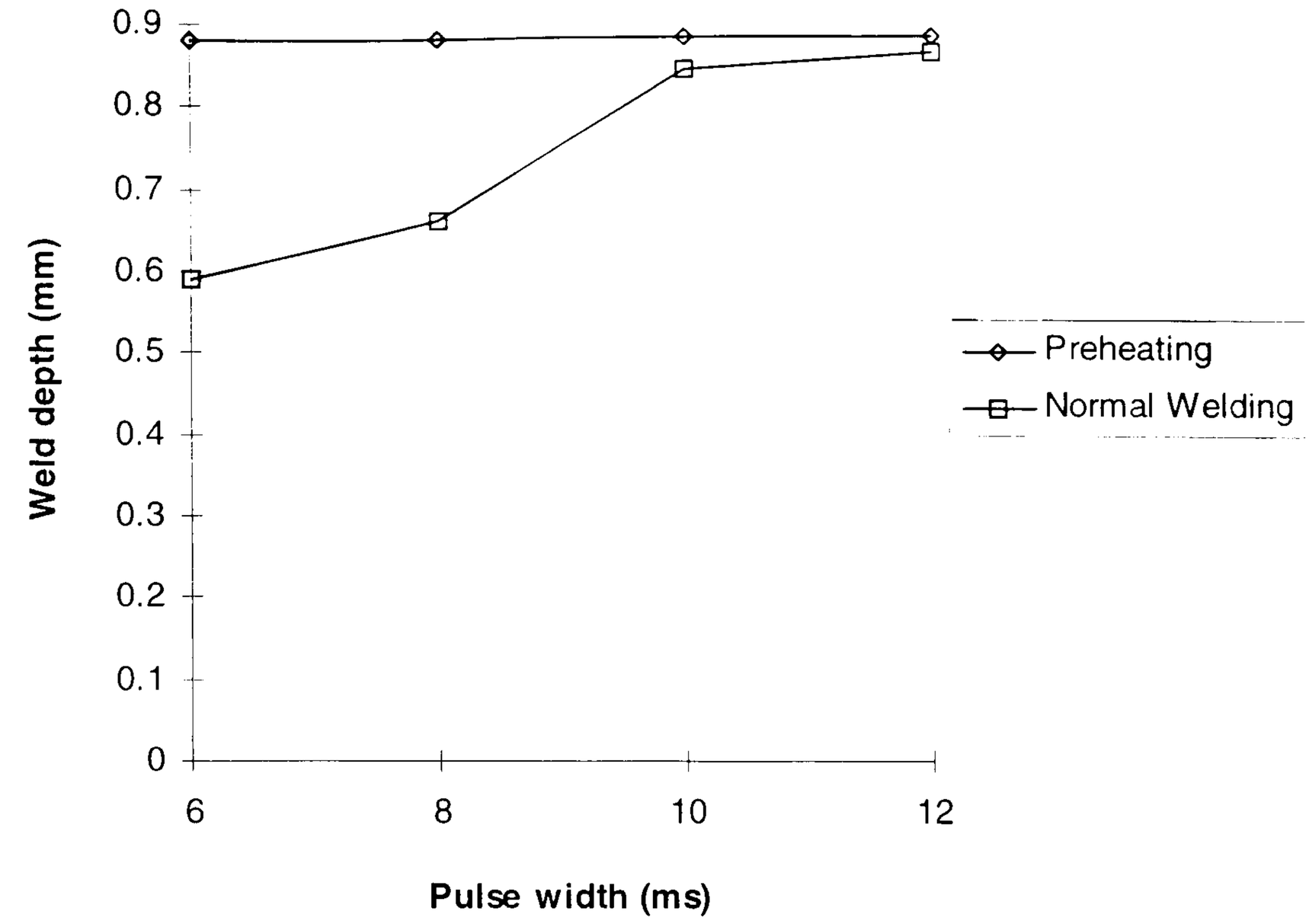

Figure 3.64 Penetration depth as a function of different pulse widths

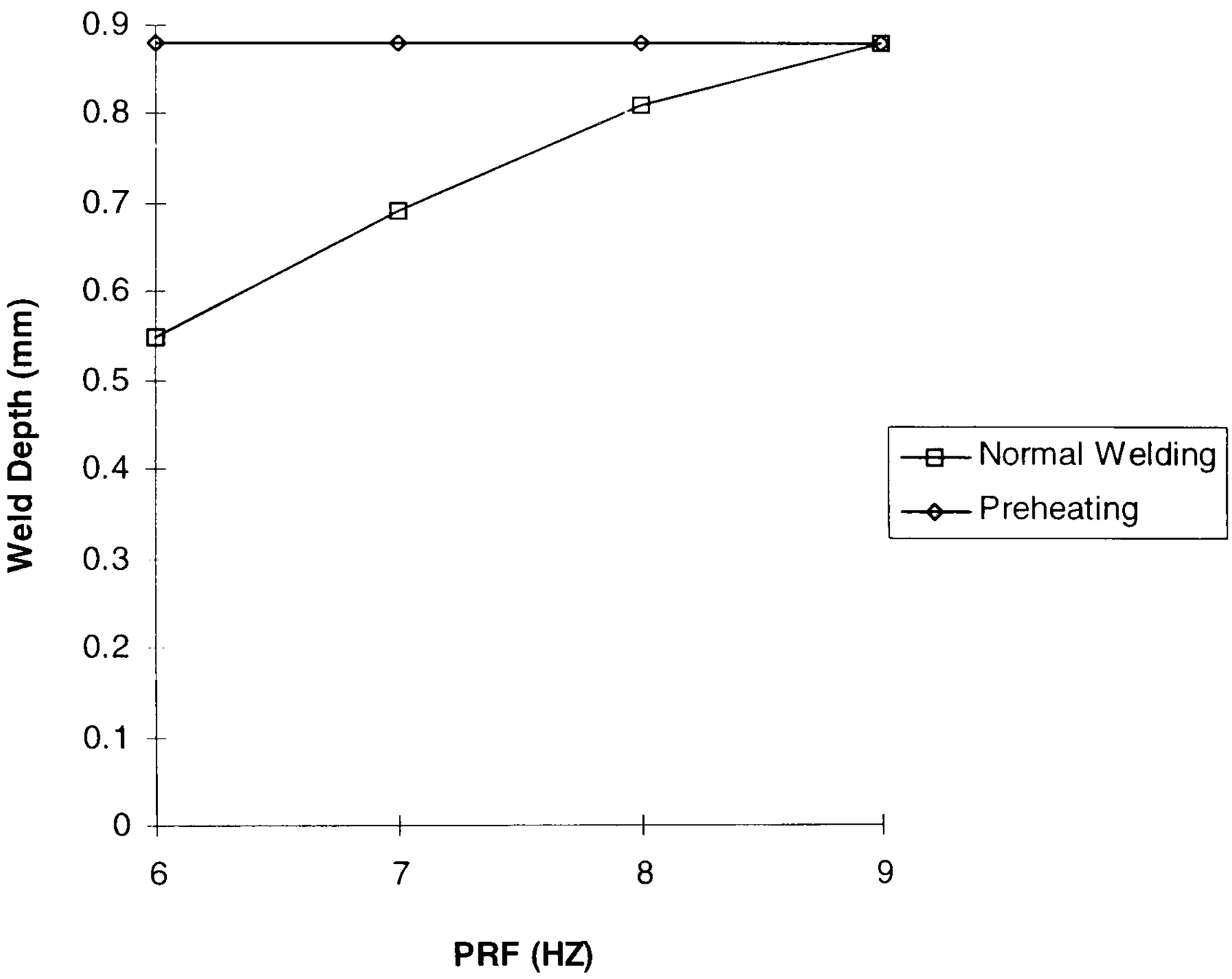

Figure 3.65 Penetration depth as a function of different PRFs

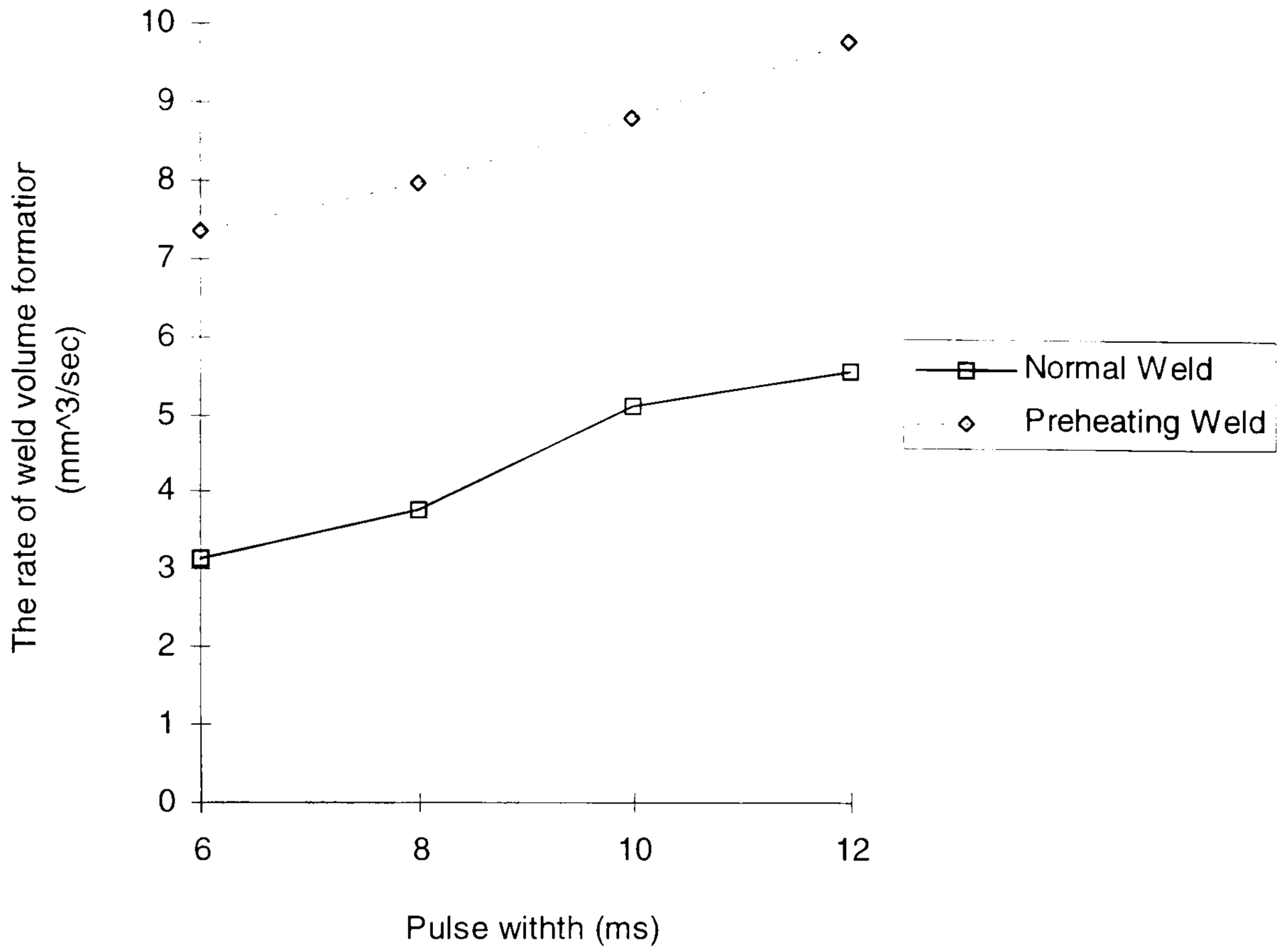

Figure 3.66 The rate of weld volume formation as a function of pulse widths

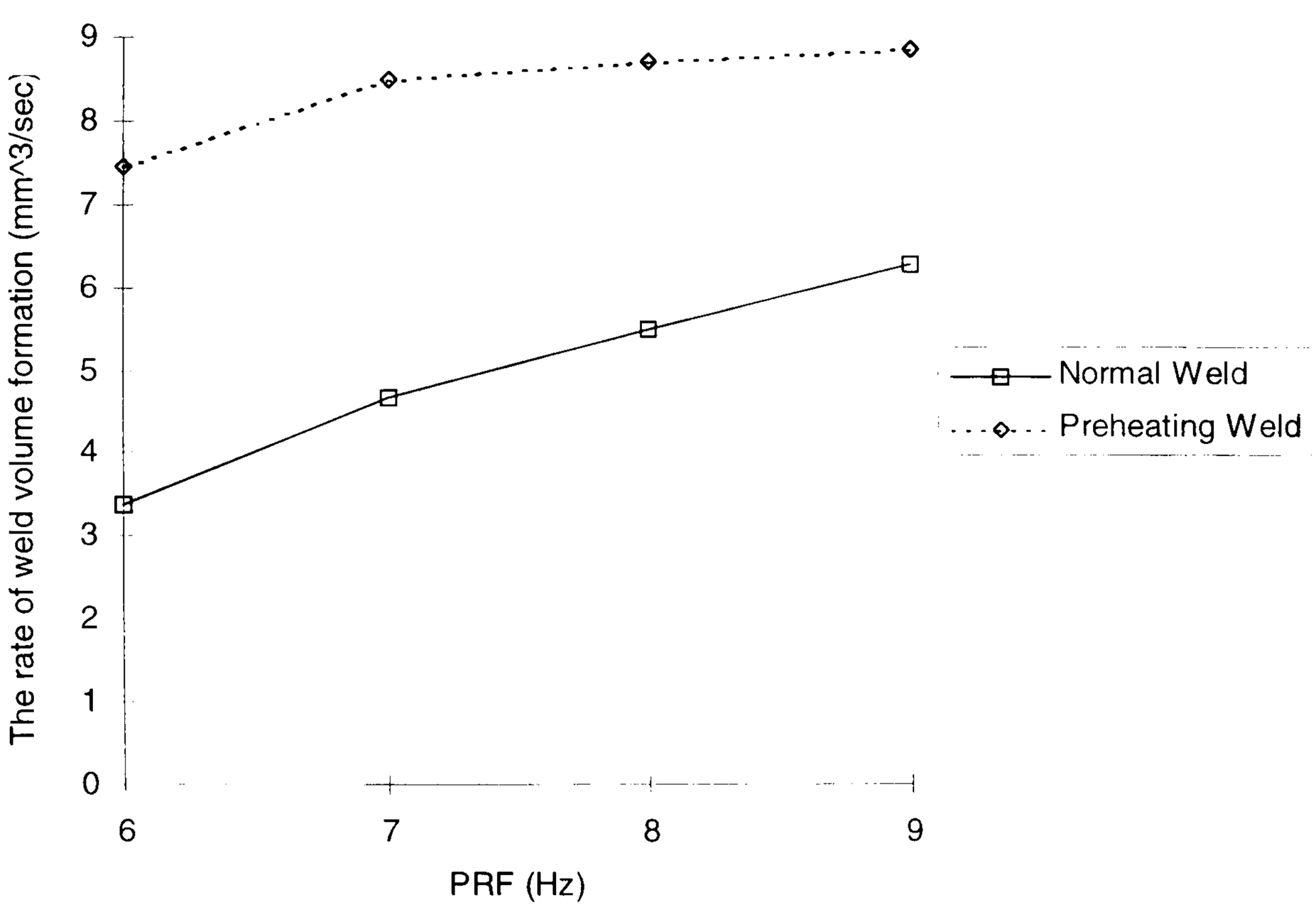

Figure 3.67 The rate of weld volume formation as a function of PRFs

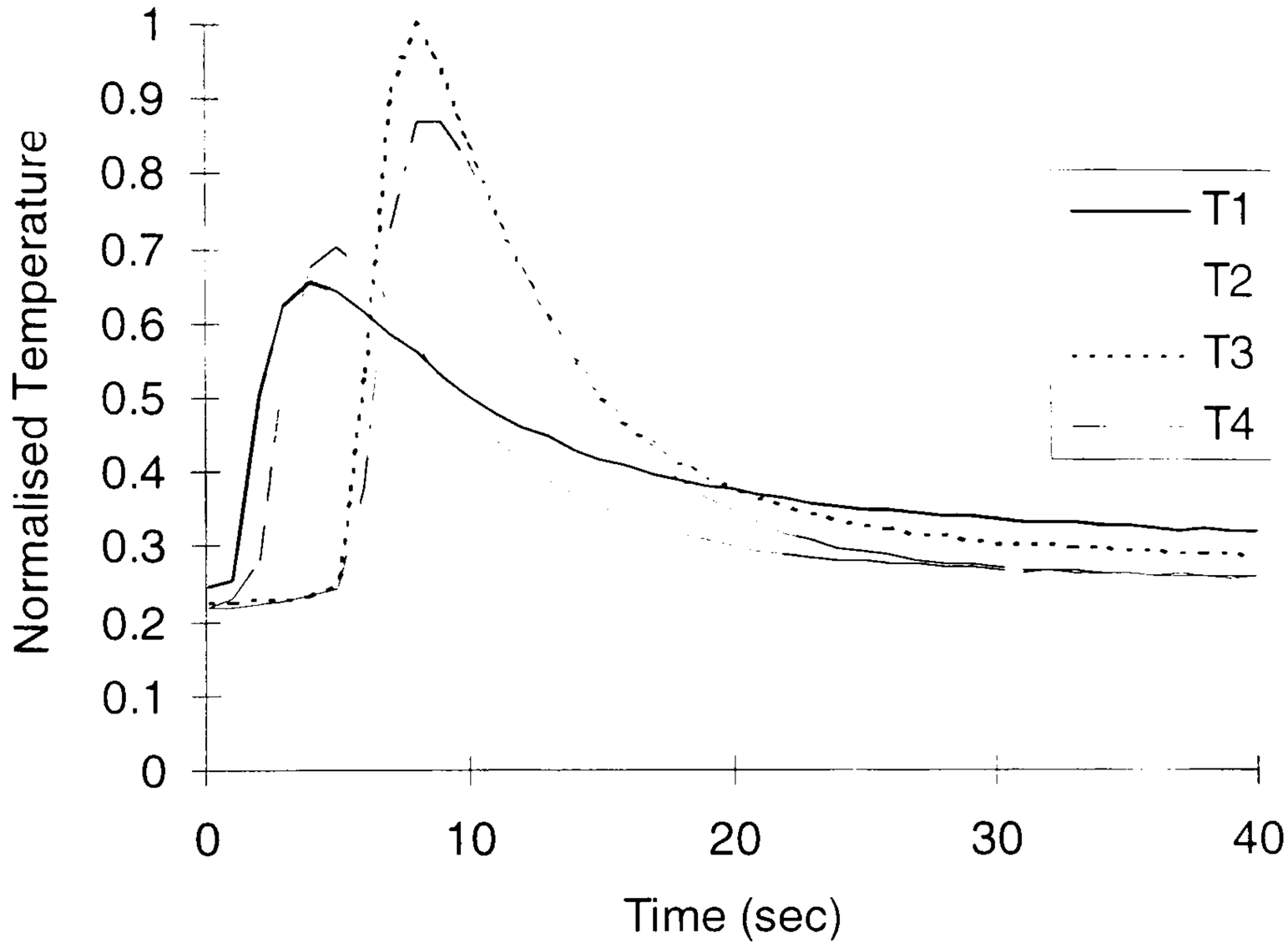

Figure 3.68 Normalised temperature profile for normal weld with a pulse width of 6 ms

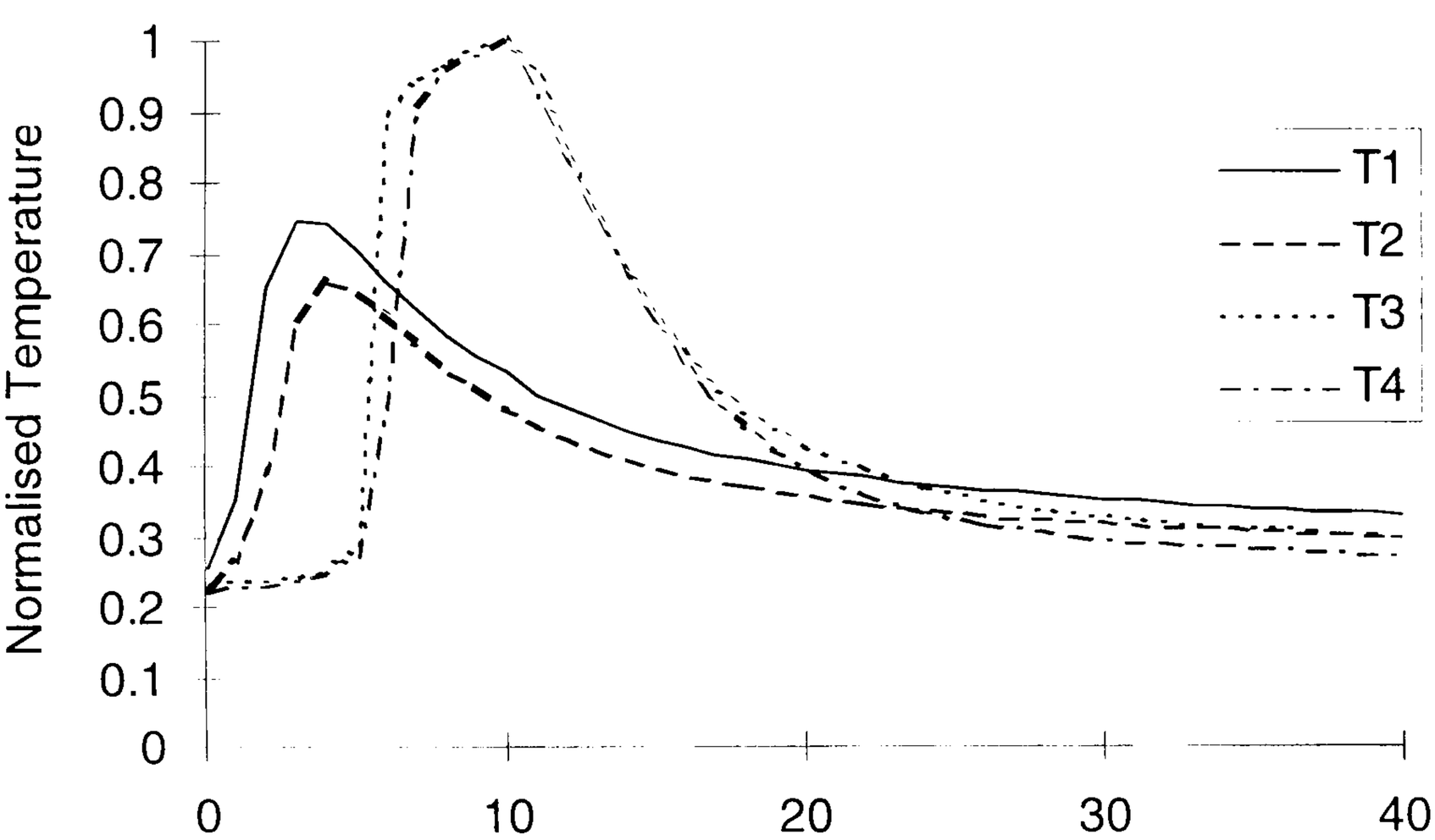

Figure 3.69 Normalised temperature profile for normal weld with a pulse width of 12 ms

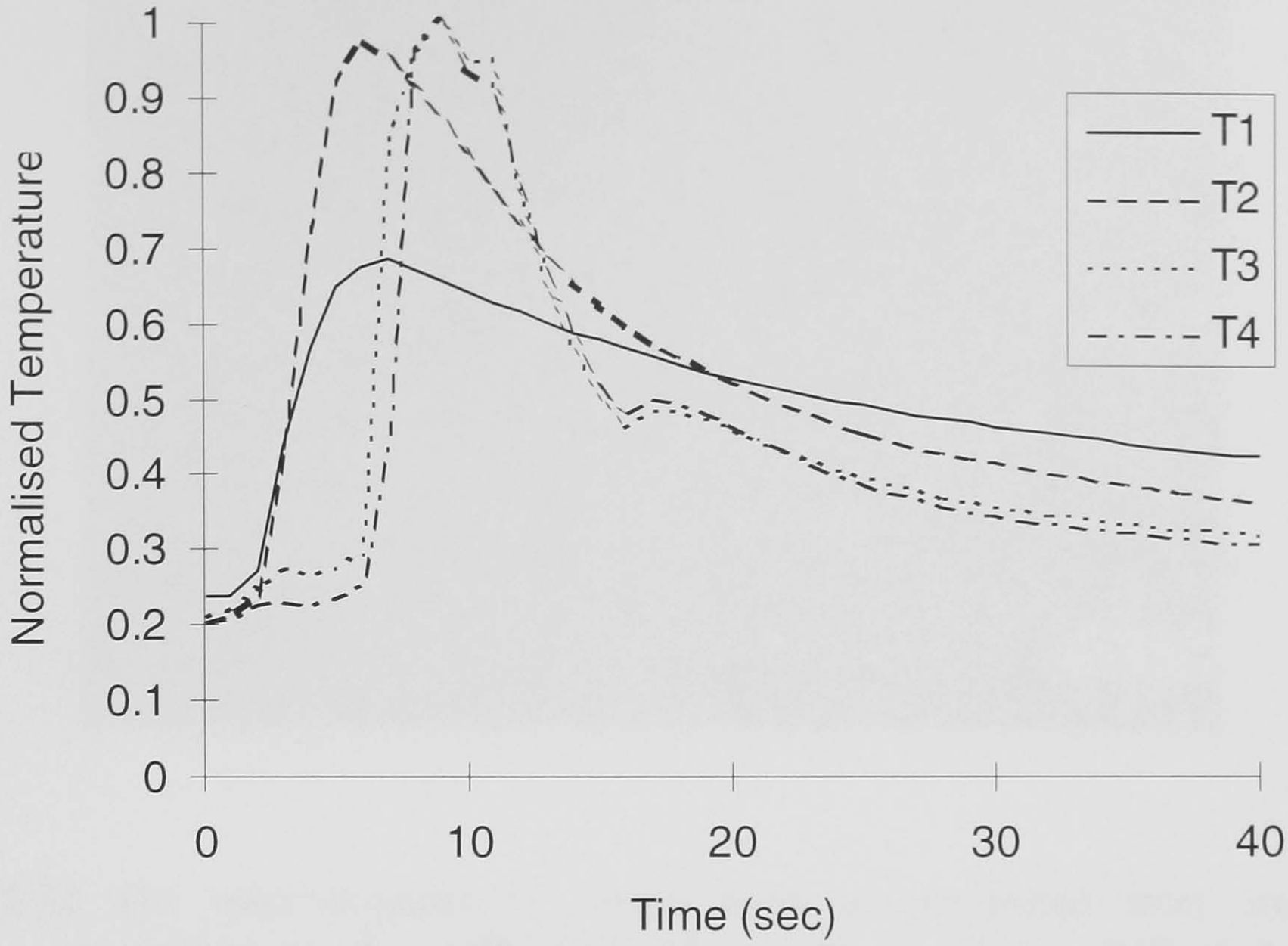

Figure 3.70 Normalised temperature profile for pre-heated weld with a pulse width of 12 ms

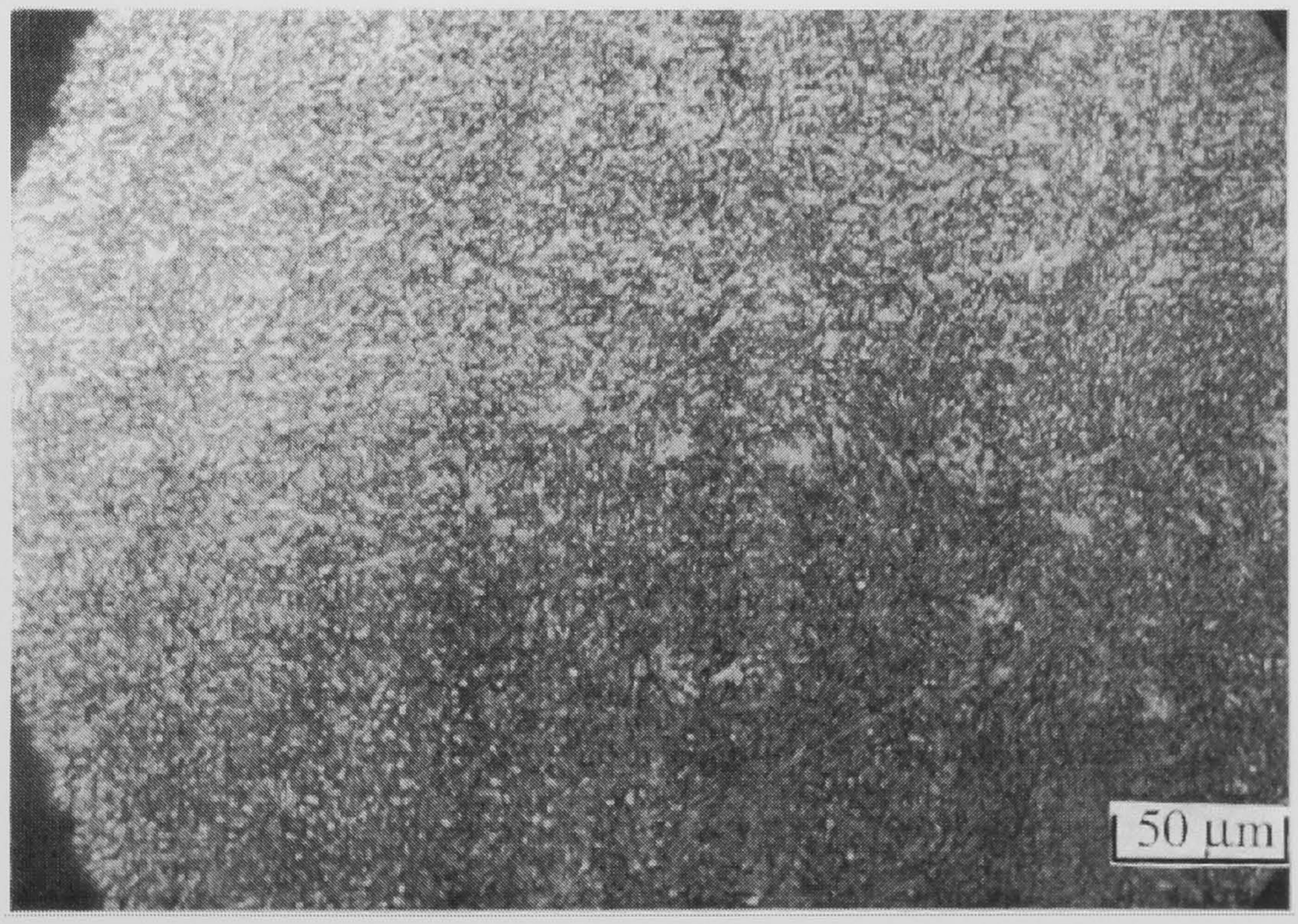

Figure 3.71 The microstructure of fusion zone of normal laser weld at a magnification of x 150(For a pulse width of 10 ms, PRF of 9 Hz, and welding speed of 5 mm/s)

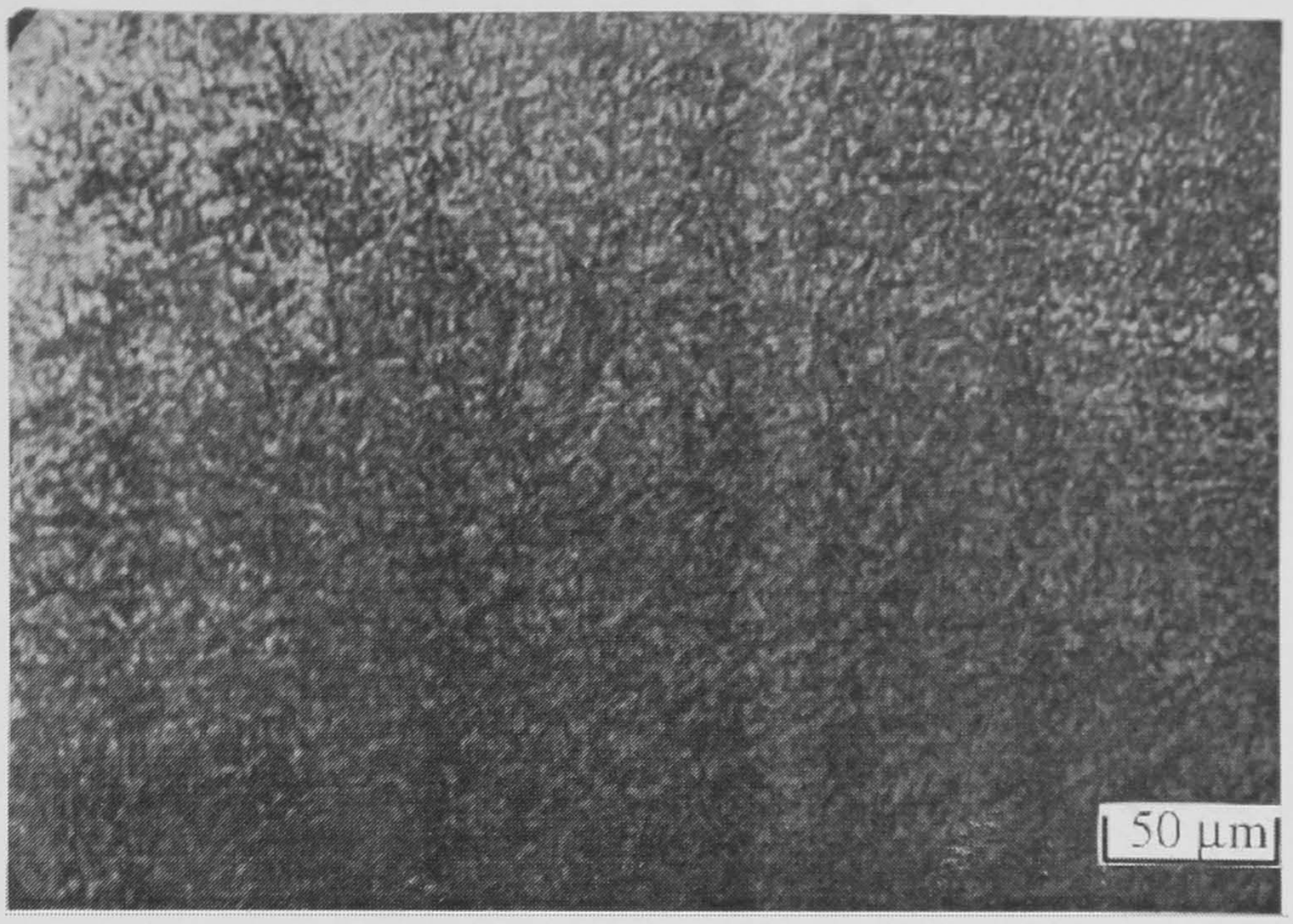

Figure 3.72 The microstructure of fusion zone of pre-heated laser weld at a magnification of x 150(For a pulse width of 10 ms, PRF of 9 Hz, and welding speed of 5 mm/s)

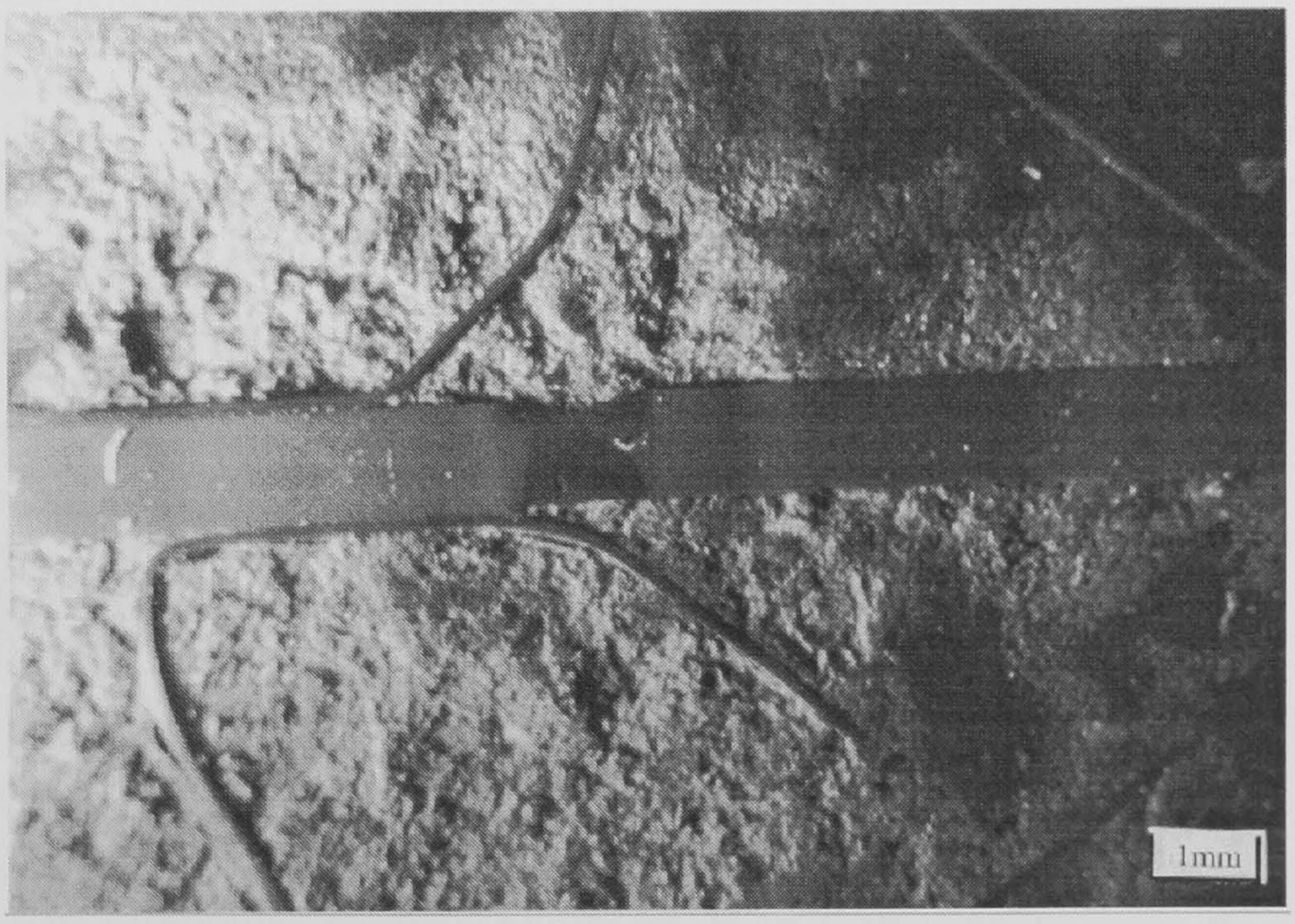

Figure 3.73 The microstructure of weld region for normal laser weld at a magnification of x 3

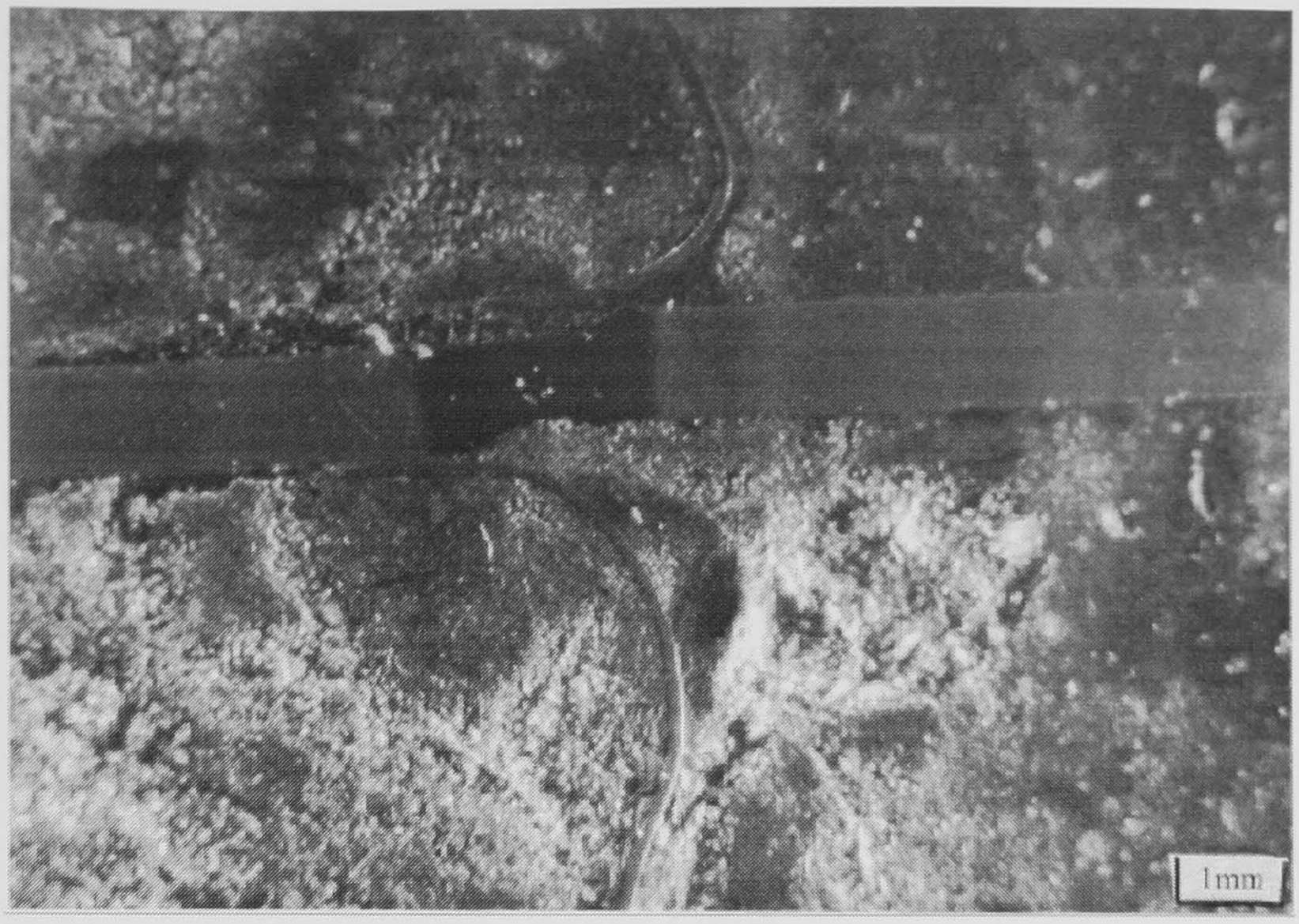

Figure 3.74 The microstructure of weld region for pre-heated laser weld at a magnification of x 3

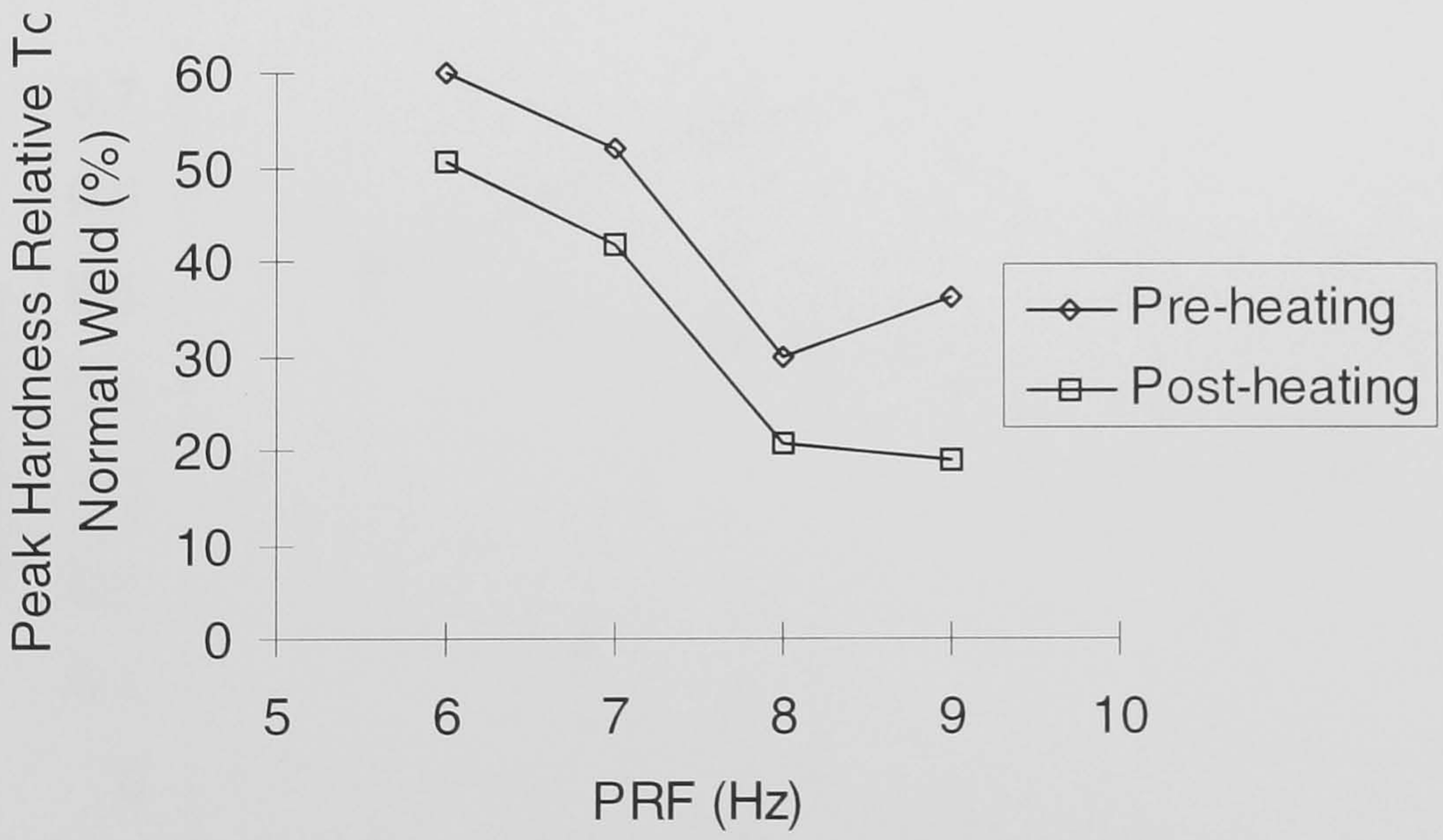

Figure 3.75 The peak hardness relative to normal weld as a function of PRFs.

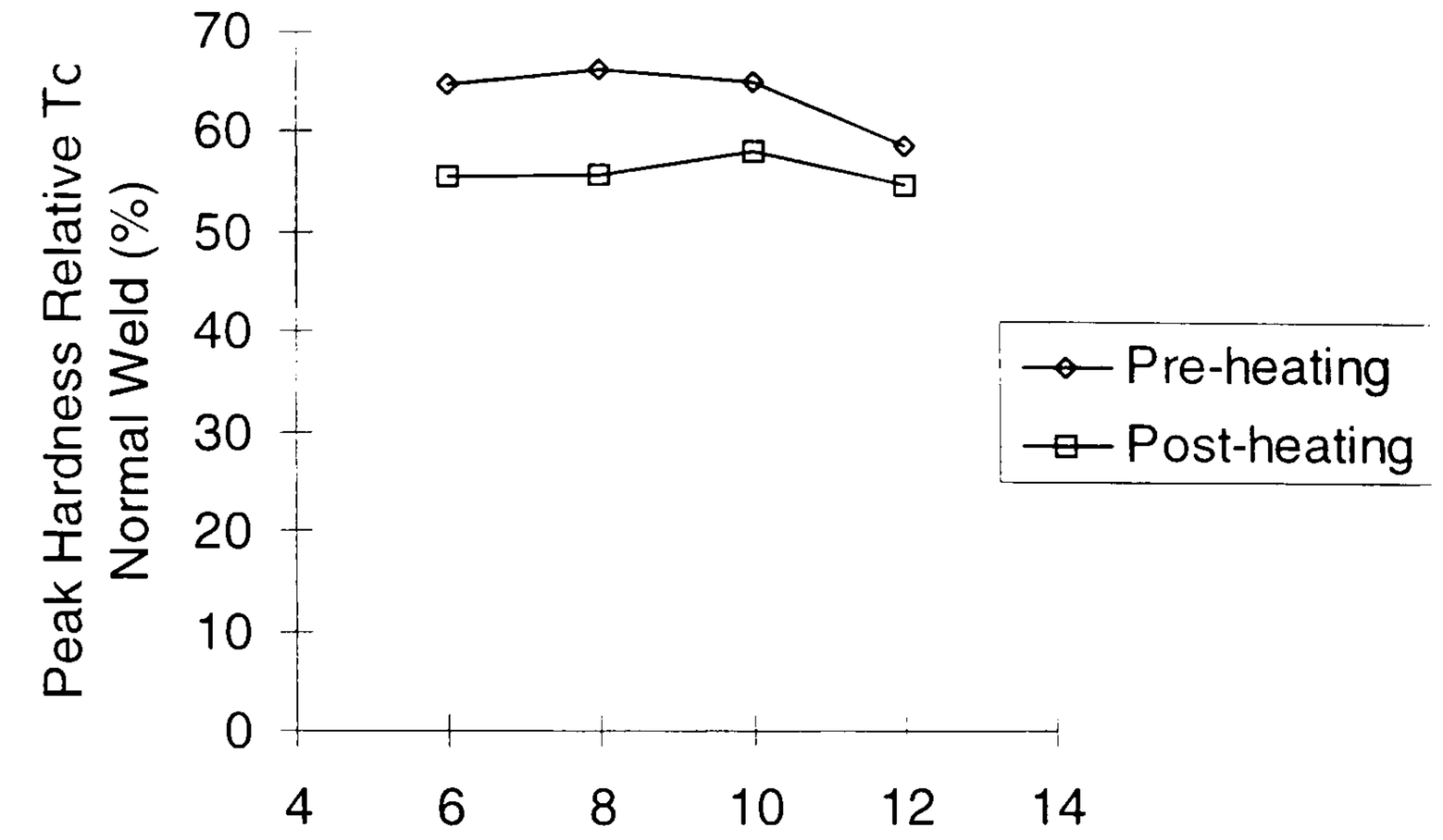

Figure 3.76 The peak hardness relative to normal weld as a function of pulse widths.

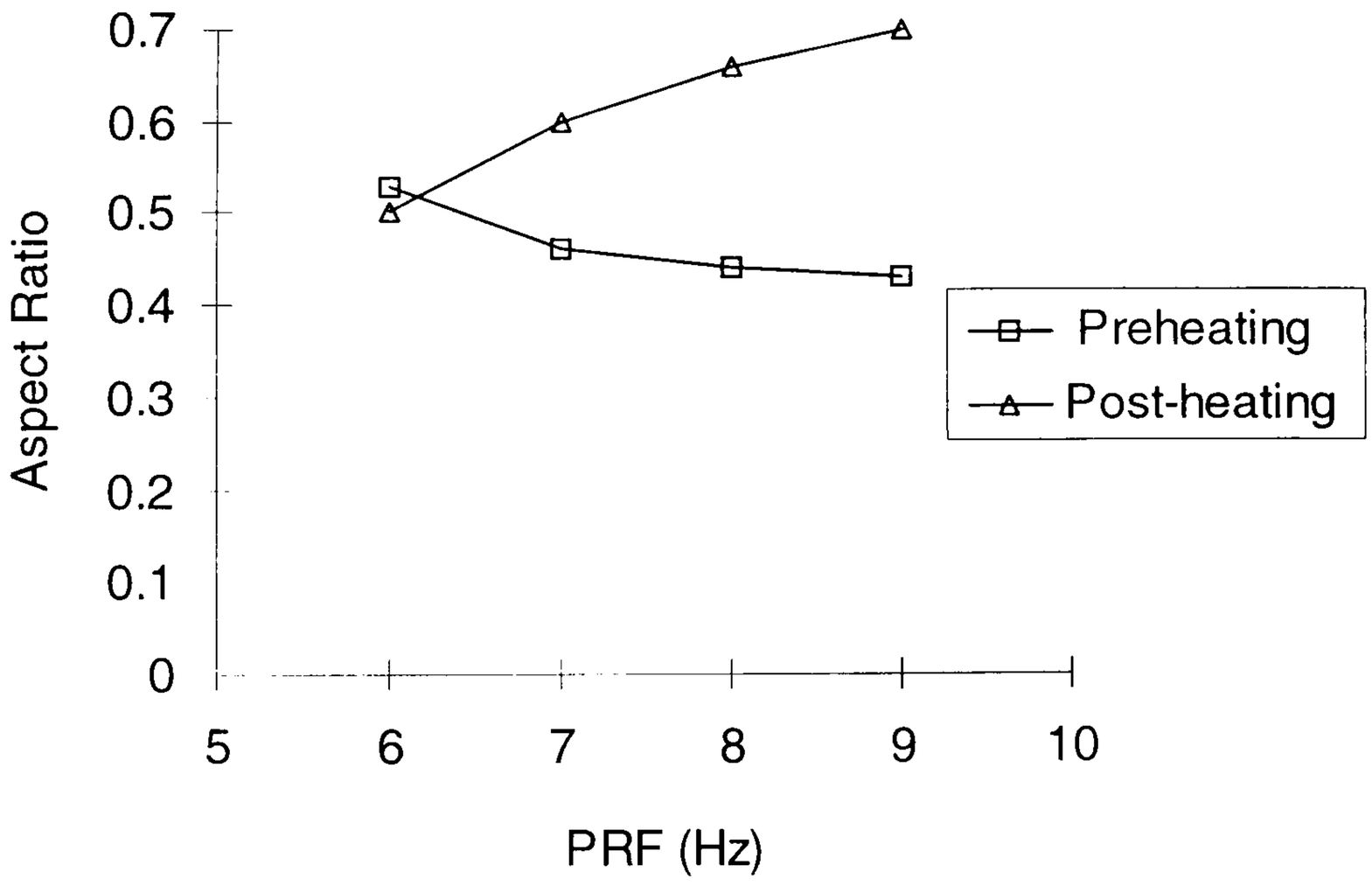

Figure 3.77 Aspect ratio as a function of different PRFs.

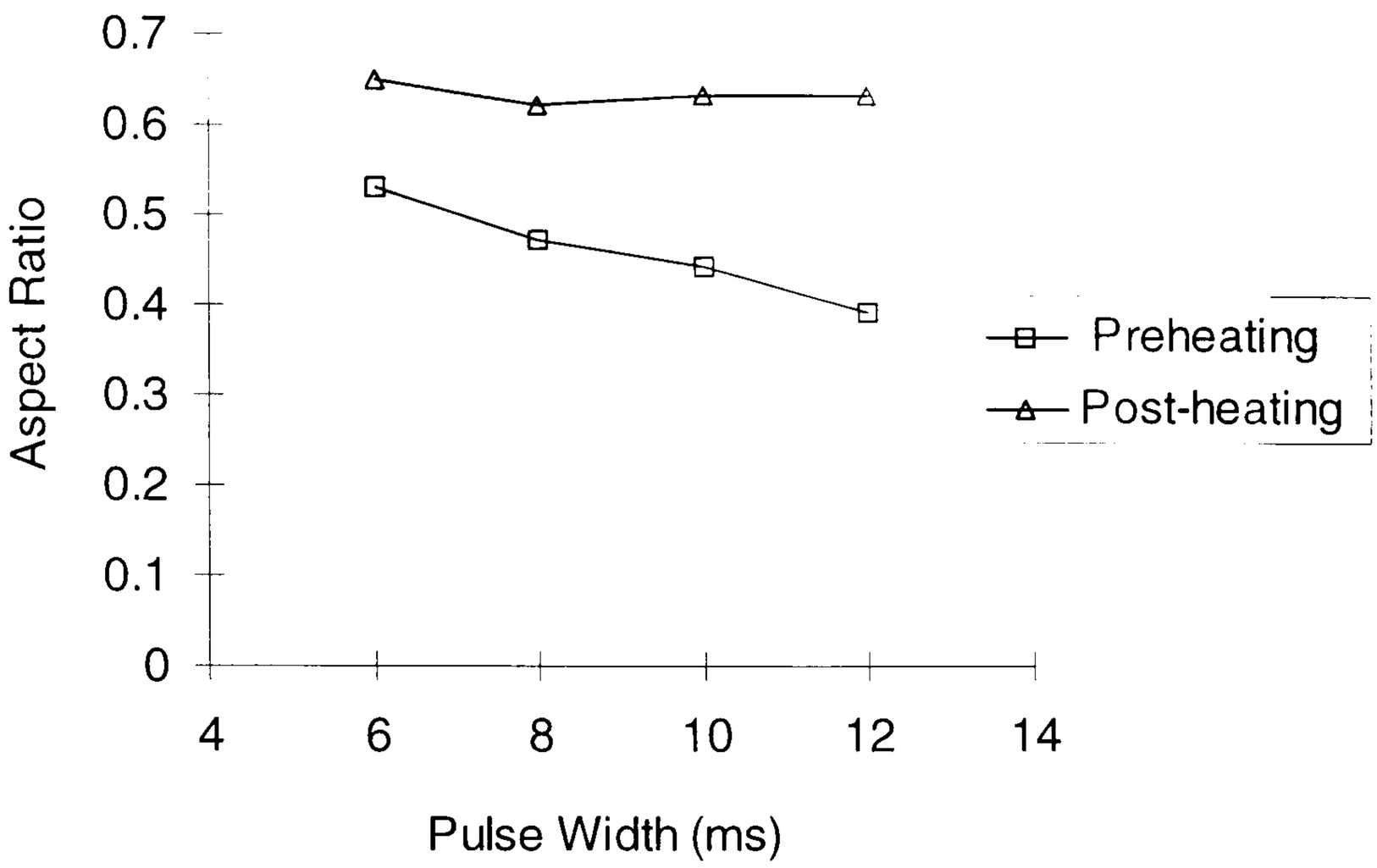

Figure 3.78 Aspect ratio as a function of different pulse widths.

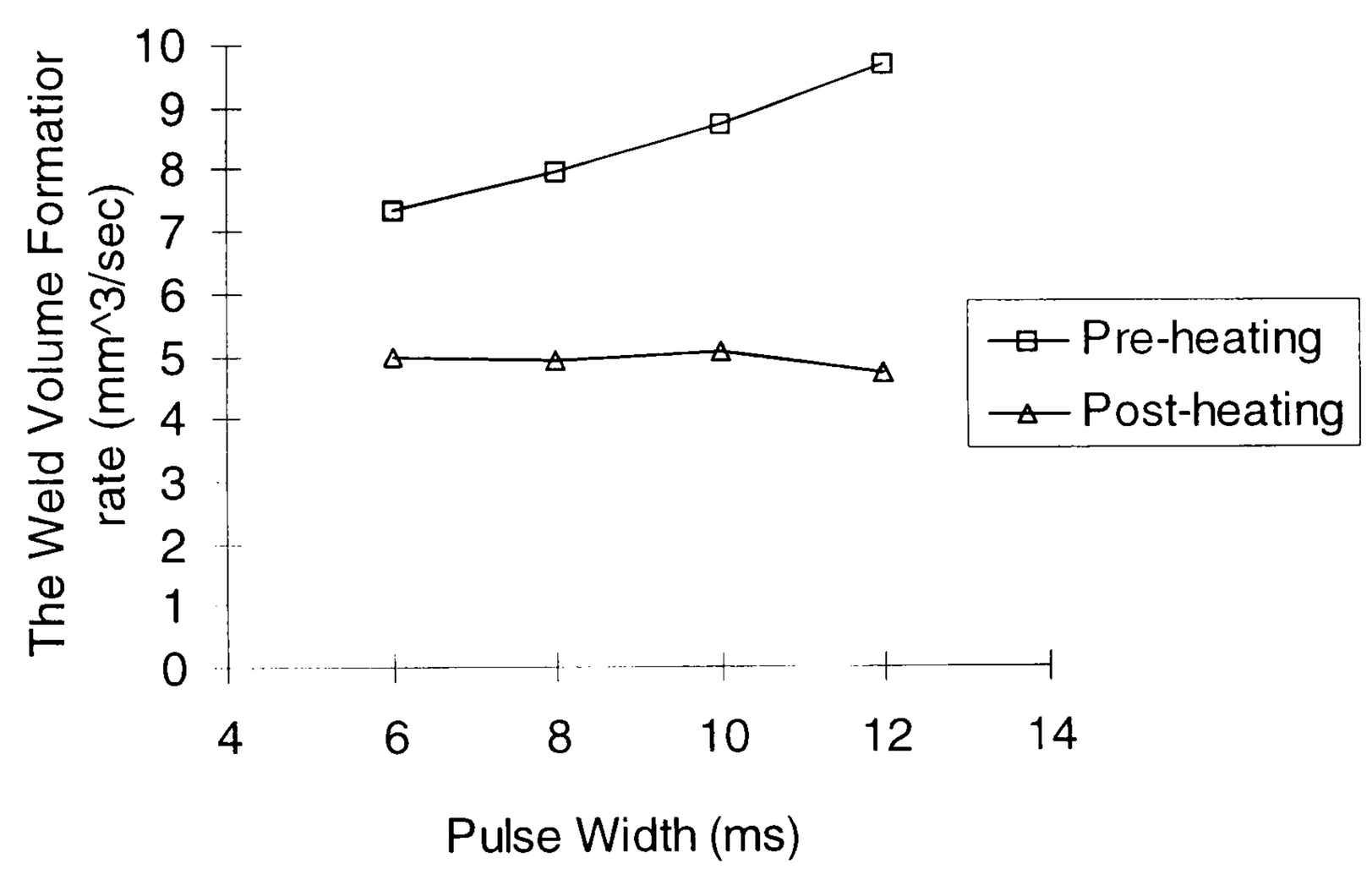

Figure 3.79 The weld volume formation rate as a function of different pulse widths.

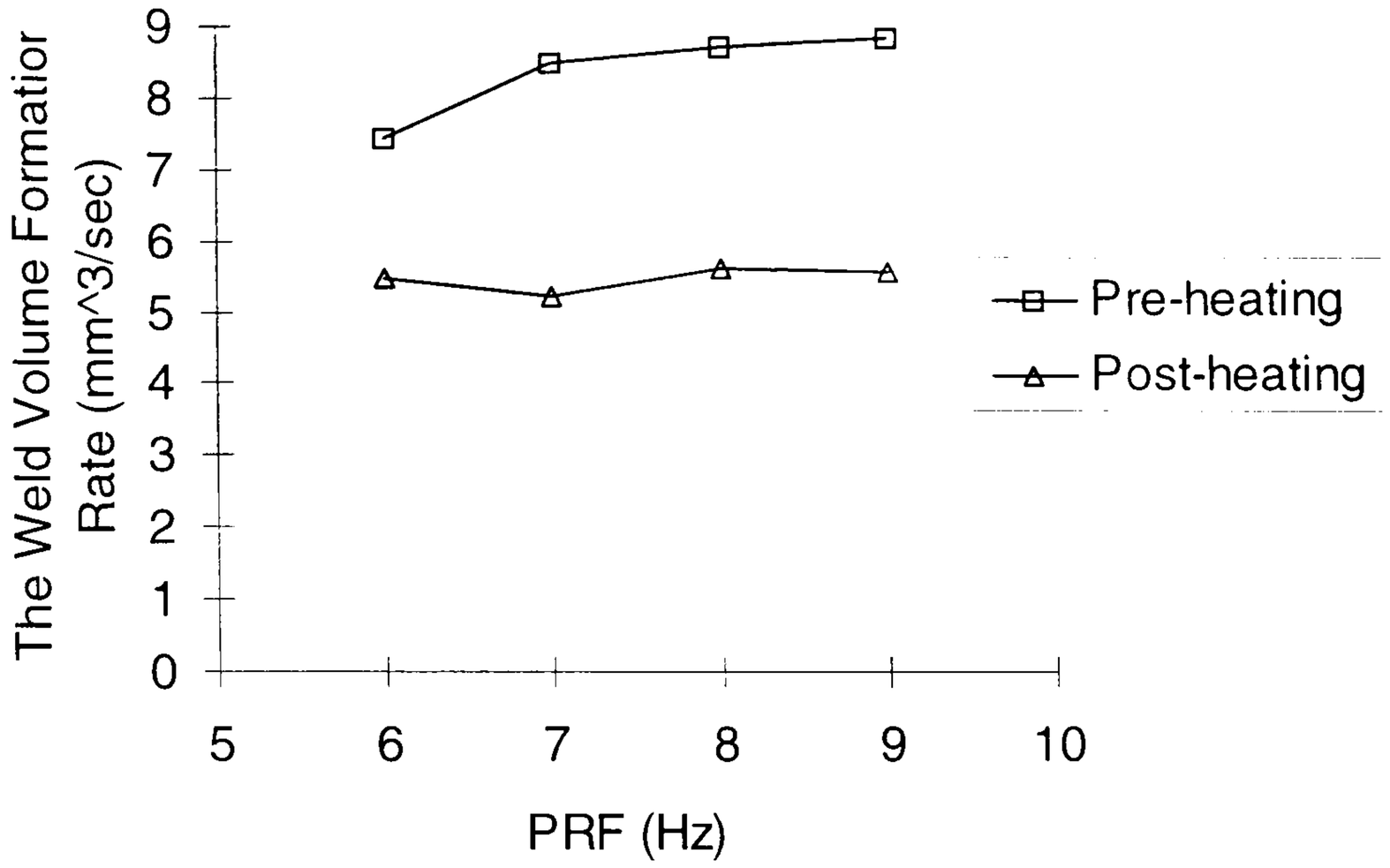

Figure 3.80 The weld volume formation rate as a function of different PRFs.

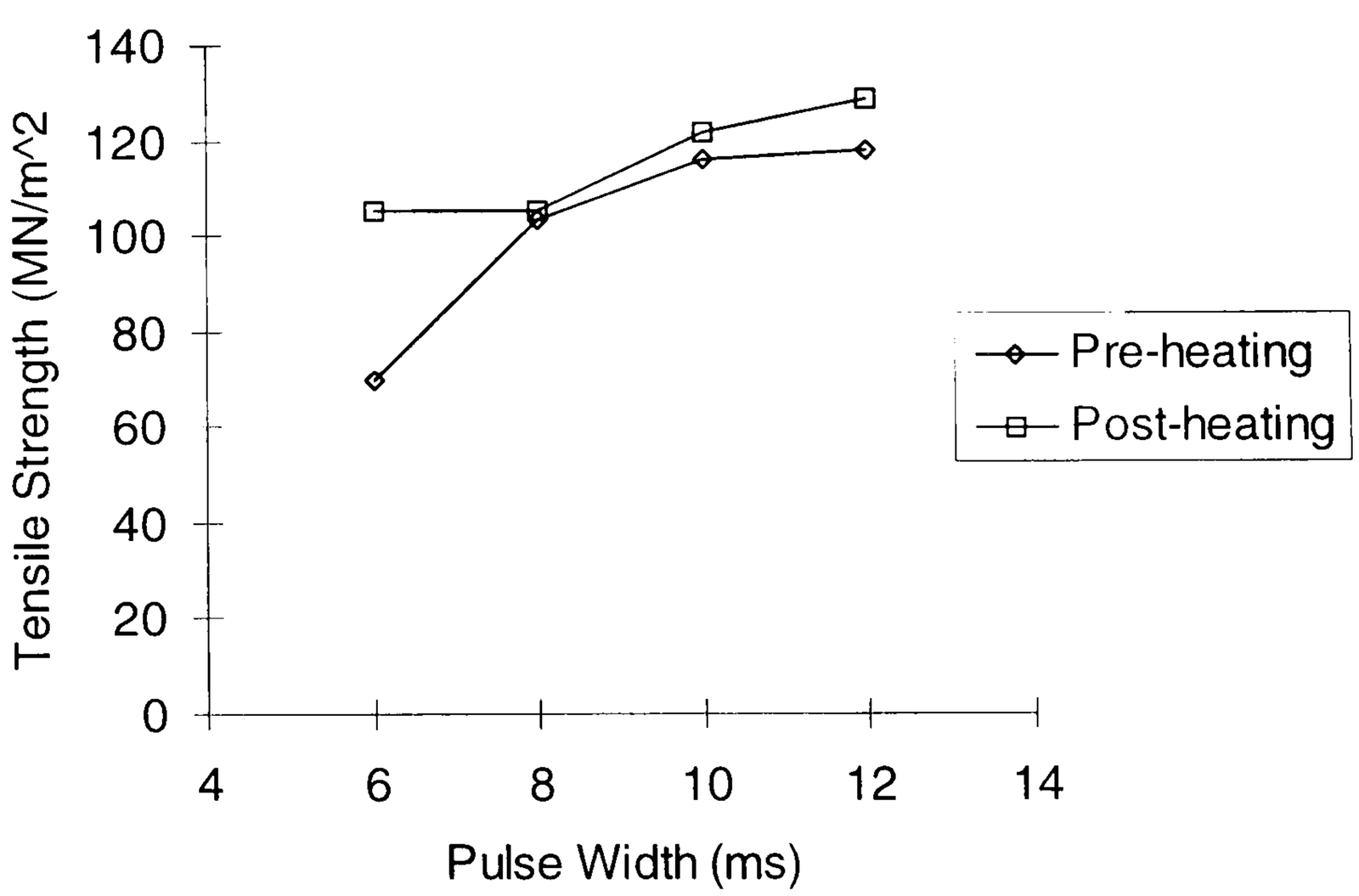

Figure 3.81 Tensile strength as a function of different pulse widths

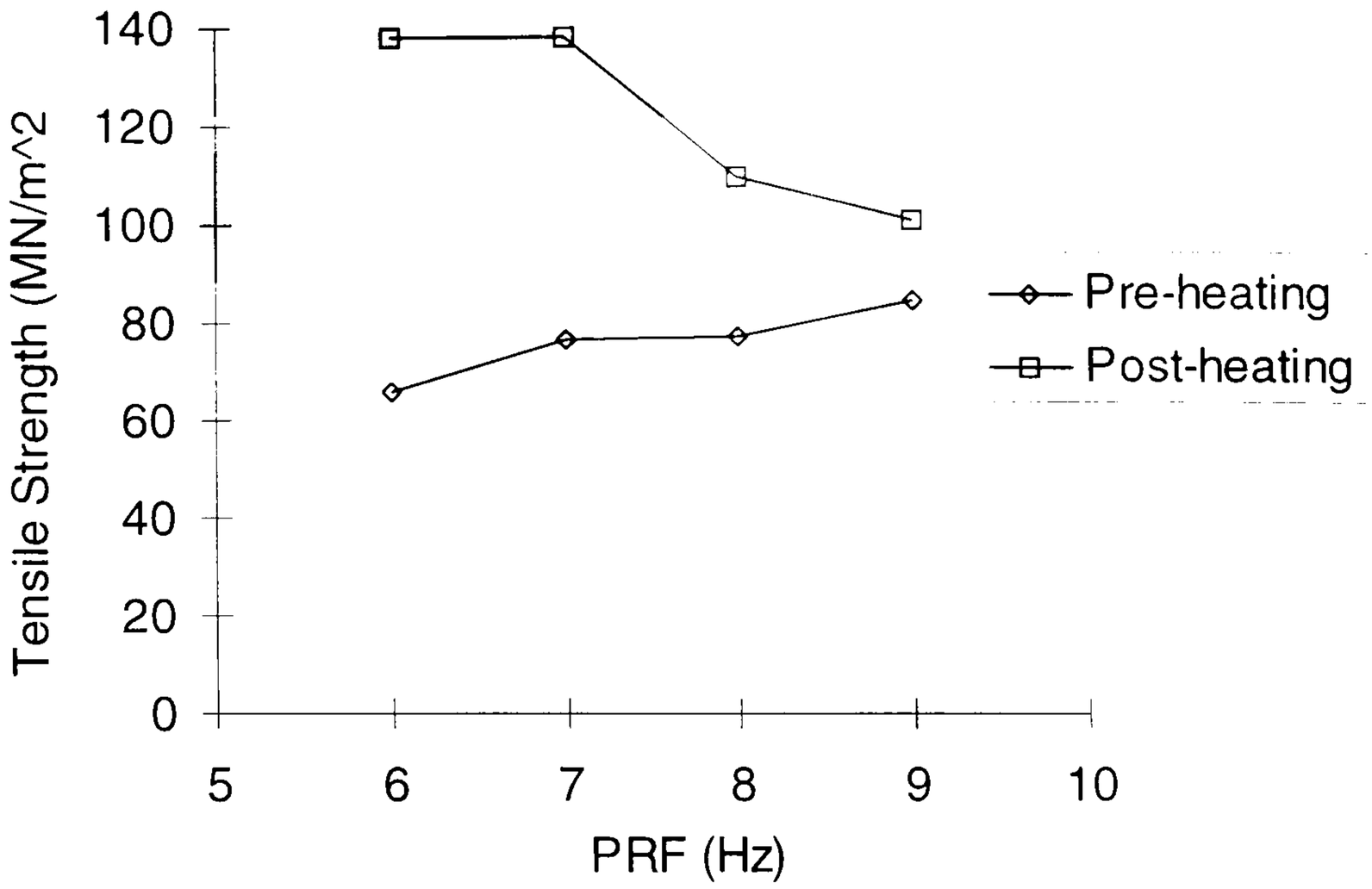

Figure 3.82 Tensile strength as a function of different PRFs.

CHAPTER FOUR
MULTI-FACTORIAL ANALYSIS OF Nd:YAG LASER WELDING

4.1 Effect of laser parameters and welding geometry

4.1.1 Introduction

Nd:YAG lasers have been used successfully for welding applications for many years. Studies focussed primarily on Nd:YAG, Ng *et al* [4.1], and include performance analysis of single and dual beam systems, Ng *et al* [4.2], Okorokov *et al* [4.3] and Liu *et al* [4.4]. Several laser parameters and geometries potentially influence the laser welding process as mentioned in Chapter 3. The laser parameters which affect the weld quality are the welding speed, pulse repetition frequency and pulse width. In addition to the laser parameters, the pre-heat and post-heat treatment was used to improve the weld quality as discussed in the previous chapter. However, to determine the extent to which the parameters and geometries influence the weld quality a multi-factorial designed experiment was done. The number of experiments required to investigate the effect of each parameter can be significantly reduced with the use of a multi-factorial designed experiment, which enabled assessment of the effect of a number of different variables in normal, pre-heated and post-heated welding experiments, Ng *et al* [4.5]. The advantage of this is that the experimental time, and ultimate cost, is considerably reduced. Multifactorially designed experiments can also allow investigation into the interaction between selected parameters, which is difficult to realise with standard experimental procedures. The multifactorial method used in this investigation was the 2^N (or two level) method to analyse and quantify the effect of the selected laser parameters and the beam delivery system. The mechanical properties of the Nd:YAG laser welded joints of high carbon steel gauge plate were chosen as the measurands. In the present case, the maximum and minimum parameters were quantified for use in a multifactorially designed experiment by measuring the aspect ratio, tensile strength and weld volume for the different welding speed, pulse width and PRF.

4.1.2 The 2^N multifactorial method and welding analysis

In the 2^N multifactorial system each parameter, or factor, is limited to two values, or levels - level 0 (lower value) and level 1 (higher value). **Table 4.1** shows the full set of values used in the multi-factorial experiment. The application of this set of parameters in a system governed by three parameters: such as A (speed), B (pulse width) and C (PRF) in **Figure 4.1**. Each of these either has a high or a low value to achieve a measured output M - parameters shown in **Table 4.1**. To provide an overall picture of the influence of each factor, all combinations of the three external factors must be applied and the value for M recorded. As can see, if there are N parameters in the set of data then there are 2^N combinations. Thus, for the three parameters, 8 combinations of the laser parameters are possible as shown in **Table 4.2**. These M values were obtained by measuring the weld width, weld depth, weld volume and tensile strength.

The welding speed, pulse width and PRF that were examined in these experiments fell into three geometries: normal, pre-heated and post-heated welding process. The parameter values used in this experiment were for the welding speed, 3.5 and 5 mm/s, pulse widths were 6 and 12 ms, and PRFs were 6 and 9 Hz. In all cases, the results only show a trend and there is an assumption that response (M-parameter values) varies linearly between the high and low levels within each set of experimental data. The general linear model generated by mini-tab, was implemented to obtain the probability and the significance effect of the individual and combined parameters, for the normal, post-heated and pre-heated welds, at the selected high and low values. The 2 level multifactorial experiment, given an idea about the trends of the data for the high and low value parameter combinations. This assumes linearity between this data. If the data is highly non-linear, then more than two levels should be selected for the multifactorial experiment. This greatly increases the complexity of the experiment and was not warranted in this case, and so only two level experiments were done.

The welding was done with a Lumonic's MS830 Nd:YAG laser, operating at 1.06 μm and with a maximum output power capacity of 400 watts. A dual-beam fiber optic

beam delivery system was used to achieve in-line process pre-heat and post-heat treatment with a constant total power of 285 watts. Here the laser power was divided so that 70% was coupled to the weld beam and 30% was directed into pre-heating or post-heating. The amount of losses taken into account for all the optical lens and fiber optic beam delivery system resulted in a constant power of 154 W and 72 W used to produce the butt weld and post-heating of gauge plates, respectively. For a dual beam delivery system - see **Figure 2.2**, a weld was produced by the weld beam focused to about 2 mm diameter, and the post-heating or pre-heating beam diameter was about 20 mm. For the normal weld geometry, 154 W of laser power was used to produce a weld with a single fiber optic beam delivery system. The focused beam spot size was about 2 mm and normal to the welding direction. In all cases, the focus of the laser beam was brought down to the surface of the workpiece, and a He shielding gas was used at a source pressure of 5×10^4 Pa indicated on the pressure gauge.

For all the measurements, the graphs show an average value of three experiments. The amount of errors observed is less than $\pm$ 0.03%, it is not significant to show up in the graphs. The error limits show in the graphs make it more difficult to distinguish between the normal, post-heating and pre-heating welding process in most of the cases, thus, the error limits is omitted. High carbon steel gauge plate, with a nominal composition of 0.85 wt % C, 0.4 wt % Si, 1.1 wt % Mn, 0.4 wt % Cr, 0.25 wt % V and 0.4 wt % W, was selected for this experimental investigation. All of the samples were machined to the dimension of 75 X 50 X 0.88 mm. The tolerance of the length and width of the samples was $\pm$ 0.1 mm. After machining, the samples were ground (Type J, B.A.60.P.V, medium grain) to ensure smooth, flat surfaces. After welding, the workpieces were sectioned, moulded, etched (2 % nital) and polished. To quantify the weld quality, tensile strengths were measured, with an instron tensile tester machine with a cross-head speed 0.5 mm/s was used to measure the tensile strength along the weld joints. The weld depth and bead width were measured using a Mitutoyo PJ-300 profile projector. The parameters that were used in this experiment for the single and dual beam weld geometries are listed in **Table 4.2**.

4.1.3 Multi-factorial approach on welding analysis

4.1.3.1 Analysis on aspect ratio

The effect of PRF, pulse width and welding speed on the aspect ratio can be seen in **Figures 4.2, 4.3** and **4.4**, for the normal, post-heated and pre-heated weld, respectively. The difference between the dotted and solid lines indicate an increase in the pulse width from 6 to 12 ms, respectively. From this data, the effect of increasing each laser parameters is clearly seen. Interestingly, the aspect ratio decreased with a corresponding increase in the PRF from 6 Hz to 9 Hz. From **Figure 4.2,** it is seen that there is only a slight decrease in the aspect ratio with a lower pulse width (6 ms) compared to the higher value (12 ms). A higher aspect ratio was achieved with the lower pulse width at 5 mm/s. Thus, it is noted a wider weld width can be produced with a lower pulse width at 3.5 mm/s, and as a result the lower aspect ratio was achieved.

However, the graphical representation of **Figures 4.2, 4.3** and **4.4** do not indicate any analysis of variance of the effective variables. The general linear model, therefore, was implemented to obtain the p-values to attribute the significance of individual and interactive effects of the different laser parameters for the normal, post-heated and pre-heated welds. All these results are shown in **Tables 4.4, 4.5** and **4.6**, for the normal, post-heated and pre-heated welds.

The data described in **Tables 4.4, 4.5,** and **4.6** show the probability of proving the null hypothesis that indicate the significant effects in the normal, post-heated and pre-heated weld, due to the changes in respective laser parameters. From the **Tables 4.4, 4.5** and **4.6**, if the p-value drops below 0.05 (5 %) then the individual parameter, or the interaction effect between the different laser parameters is considered to have a significant effect on the aspect ratio. All of the laser parameters and interactions which indicate a significant effect on the aspect ratio are highlighted in bold, as shown in **Tables 4.4, 4.5** and **4.6**. We can clearly see from **Tables 4.4** and **4.5**, as a result of increasing the welding speed, pulse width and PRF, there was a significant effect on the

aspect ratio, for the normal and post-heated welds. For the post-heated weld, the interaction between the welding speed and pulse width had a significant effect on the aspect ratio. Moreover, increasing the pulse width indicated a significant effect on aspect ratio. For pre-heated welds, **Table 4.6**, there was only significant effect for the pulse width.

4.1.3.2 Analysis on tensile strength

Figures 4.5, 4.6 and **4.7** show the maximum and minimum tensile strength as a function of PRF from 6 to 9 Hz. The dotted and solid-lines represent an increase in the pulse width from 6 to 12 ms, respectively.

From **Figures 4.5** and **4.7**, it can be seen that the tensile strength increased with the PRF, pulse width and welding velocity, for the normal and pre-heated weld geometries. The graphs show that a higher tensile strength was achieved with a higher pulse width, PRF and translation velocity. For an increase in PRF, the weld strength slightly increased with a lower pulse width and welding velocity. As reported in Section 3.1.3 a higher PRF and pulse width tended to produce a wider weld width. This leads to a clearer explanation of the increase in tensile strength, for the normal and pre-heated welds. Interestingly, from **Figure 4.6**, a higher tensile strength was easily achieved with a pulse width of 12 ms at 3.5 mm/s.

The data presented in **Tables 4.7, 4.8** and **4.9**, shows the probability of proving the "null hypothesis" which indicates a significant effect of the tensile strength between any two or more laser parameters. When the p-values shown in **Tables 4.7, 4.8** and **4.9** drop below 0.05 (5 %) then the individual and two or three interactive effects between the laser parameters are considered as a significant.

The welding speed and pulse width had a significant effect on the tensile strength for the normal welding process. These has no significant effect for the interaction between any of the parameters. For the post-heated weld geometry, as **Table 4.8**, there was

significant effect on the tensile strength for increasing pulse width and PRF. Both normal and post-heated welds showed no significant effect between any two or all laser parameters. From **Table 4.9**, the welding speed and pulse width was significant as was the interaction between these parameters. No other significant effects were observed.

4.1.3.3 Analysis on the rate of weld volume formation

The rate of formation of weld volume was found by multiplying the weld width, weld depth and translation velocity. The weld volume were calculated as a function of PRF from the range of 6 to 9 Hz, and these results are shown in **Figures 4.8, 4.9** and **4.10**, for the normal, post-heated and pre-heated welds, respectively. The dotted and solidlines represent an increase in the pulse width from 6 to 12 ms, respectively.

From **Figure 4.9**, it can be clearly observed that for the normal welding process, the rate of formation of the weld volume was reduced, at a welding velocity of 3.5 mm/s, for pulse width of 6 ms and PRF of 9 Hz. This was because the spatter losses increased with higher PRF and there was significant loss of the weld material. Thus, for an increased PRF, the weld volume formation rate increased with the pulse width, at a higher welding translation velocity.

Figures 4.9 and **4.10** show the maximum and minimum weld volume formation rate as a function of the PRF. The overall results show that the greatest weld volume formation rate can be achieved with a faster welding speed, higher PRF and pulse width.

The p-values are shown in **Tables 4.10, 4.11** and **4.12**, for the normal, post-heated and pre-heated welds. There were no second order interactions but there was a triple order one (**Table 4.12**) between all the laser parameters. The welding velocity and pulse width is regarded as showing highly significant individual effects. However, **Table 4.12** shows a significant interactive effect between all three parameters which leads to an increase of weld volume formation rate for the pre-heated weld configuration.

4.1.4 Conclusions

A number of multi-factorial experiments were done to investigate the effect of a range parameters that influence the weld quality.

The aspect ratio generally decreased with an increase in PRF for the range of PRF investigated from 6 to 9 Hz. All these results indicate that a higher aspect ratio was achieved with a lower pulse width at 5 mm/s. With a higher pulse width at 3.5 mm/s, a wider weld width was produced which resulted in a lower aspect ratio. Both the main and interaction effects were observed. An increase in individual laser parameters: for instance the welding velocity, pulse width and PRF, within the range of values specified, had significant effects on the aspect ratio, for both normal and post-heated welds. However, these results showed that a lower aspect ratio was achieved at a slower welding speed and higher pulse width. Moreover, for the post-heated weld configuration, the second order interactions were highly significant, and these observations suggested that the double interactive effect of the welding speed and pulse width had a significant effect on the aspect ratio. For a pre-heated weld, only the welding velocity showed significant interaction over the range of values investigated.

As for the normal, post-heated and pre-heated welds, the tensile strength increased linearly with the range of PRF selected, and the greatest weld strength was achieved with a higher pulse length and faster welding velocity. Thus, for the pre-heated geometry, the second order between the welding velocity and pulse width was significant. These experimental observation suggested that the welding velocity and pulse width was a major factor that influenced the weld strength, there was no significant effect of the PRF on the tensile strength, for both normal and pre-heated weld geometries. The results agree with the conclusions in Chapter 3 that a wider weld bead was achieved with a higher pulse width.

The weld volume formation rate increased with PRF over the range of selected parameters, for the normal, post-heated and preheated geometries. As for the normal

weld, there was a slight decrease in the weld volume formation rate with an increase in PRF with a lower pulse width and slower welding velocity. The greatest weld volume formation rate was achieved with a higher pulse width at the faster welding velocity. The significant effect of different laser parameters on the weld volume formation rate was investigated via the general linear model. An increase in the welding velocity, pulse width and PRF, within the specified range, had a significant effect on the weld volume formation rate for all the different welding process. For both the normal and post-heated welding, there was no evidence of a second or third order interaction effect on the weld volume formation rate. The triple interaction effect was observed for the pre-heated geometry, suggesting that this combination had a significant effect on the weld volume formation rate. It should be noted that the null hypothesis was taken at 0.05. It is possible, therefore an apparently observed that significant interaction (first, second or third order) is a 1 in 20 chance observation and is an anomaly.

REFERENCES CHAPTER FOUR

[1] Ng, E.S., Watson, I.A. "Characteristics of CO_2 and Nd:YAG Laser Welded High Carbon Steels", The International Congress On Applications Of Lasers And Electro-optics, Nov 1996, Section D, 141 - 148.

[2] Ng, E.S., Watson, I.A "Characteristics Of Nd:YAG Laser Welded High Carbon Steel", Journal of Laser Application, Vol 9, 1997, 243 - 252.

[3] Okorokov L V, Volkov A A and Uglov A A, "Laser Preheating turning Of High-Melting Metals", Soviet Engineering Research, Vol 9, 1989, 117-19.

[4] Liu N Y, Jr E K, "Characteristic Of Elliptical Laser Beam Preheating During Laser Welding", Transaction Of ASME, Vol 64, 1993, 895-899.

[5] Ng, E.S., Watson, I.A and C. B. Allen. Yeo, "Multi-factorial analysis of Nd:YAG laser welding of high carbon steels: Effect of laser parameters and weld geometry", The International Congress On Applications Of Lasers And Electro-optics, Nov 1998.

Experiments	**A** (Speed)	**B** (Pulse Width)	**C** (PRF)	**M** Values
1	0 (3.5 mm/s)	0 (6 ms)	0 (6 Hz)	M1
2	0 (3.5 mm/s)	0 (6 ms)	1 (9 Hz)	M2
3	0 (3.5 mm/s)	1 (12 ms)	0 (6 Hz)	M3
4	0 (3.5 mm/s)	1 (12 ms)	1 (9 Hz)	M4
5	1 (5 mm/s)	0 (6 ms)	0 (6 Hz)	M5
6	1 (5 mm/s)	0 (6 ms)	1 (9 Hz)	M6
7	1 (5 mm/s)	1 (12 ms)	0 (6 Hz)	M7
8	1 (5 mm/s)	1 (12 ms)	1 (9 Hz)	M8

Tables 4.1 High and low values in each set of experiments (actual values in brackets).1

Experimental Arrangement:

speed	pw	prf
3.5	6	6
3.5	6	9
3.5	12	6
3.5	12	9
5	6	6
5	6	9
5	12	6
5	12	9

=====>>

Index	speed	pw	prf
0	0	0	0
1	0	0	1
2	0	1	0
3	0	1	1
4	1	0	0
5	1	0	1
6	1	1	0
7	1	1	1

=====>>

M1
M2
M3
M4
M5
M6
M7
M8

Table 4.2. Laser parameter values in the multi-factorial experiments

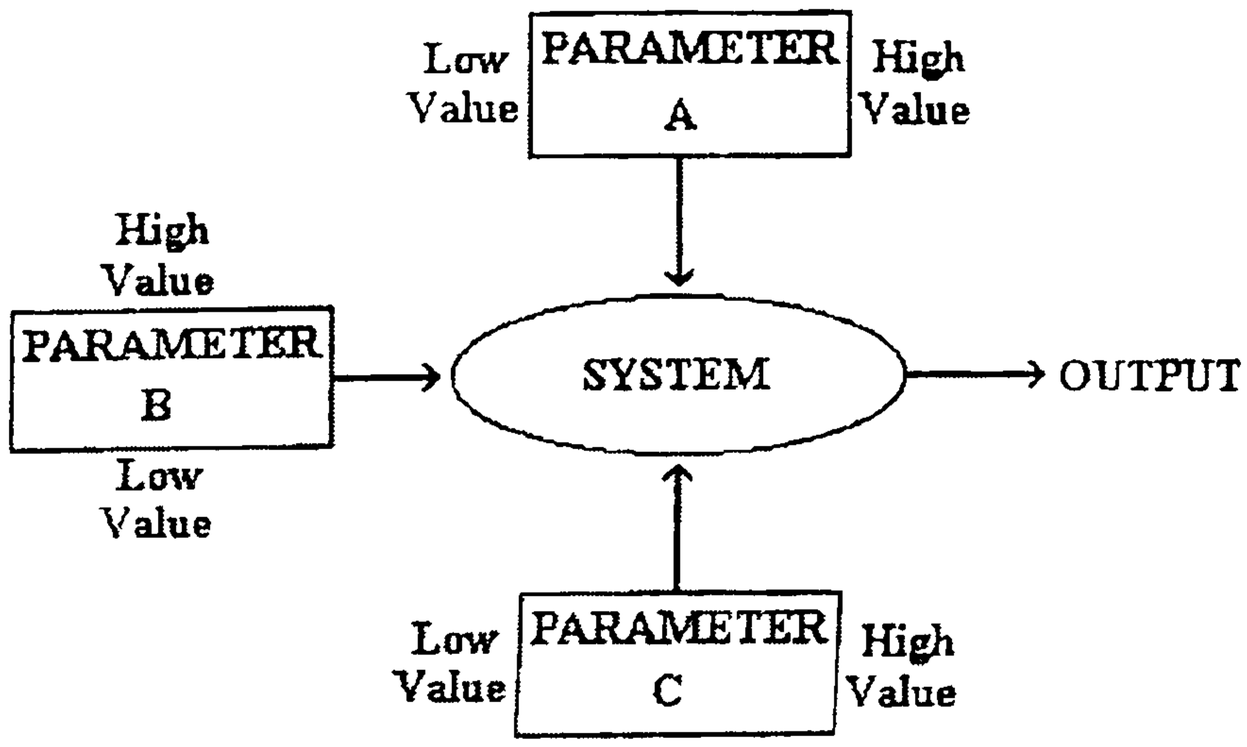

Figure 4.1. A 2^N experimental system influenced by three parameters .

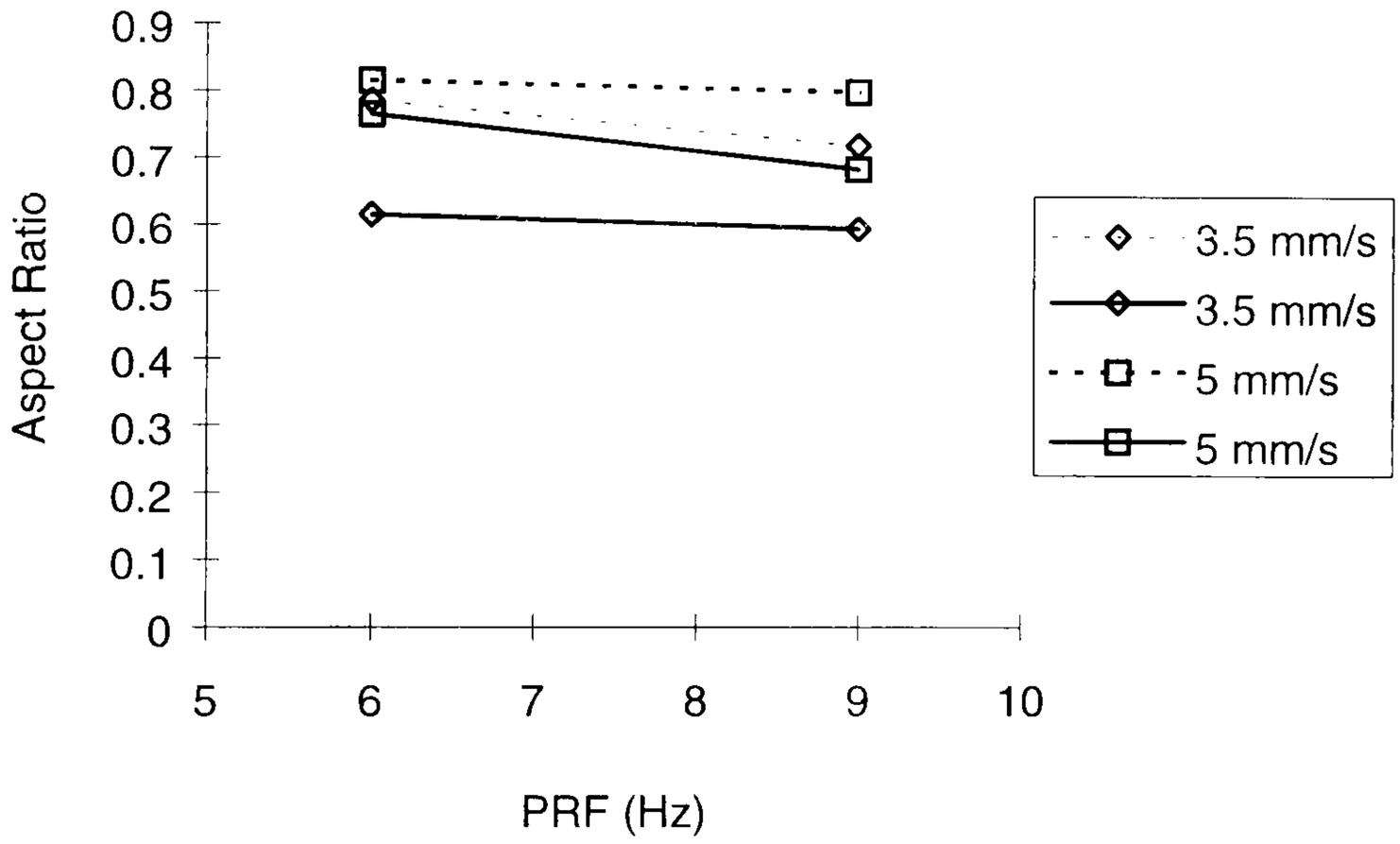

Figure 4.2. Effect of aspect ratio as a function of PRF, for normal welding. The dotted and solid lines indicate the pulse width of 6 and 12 ms, respectively.

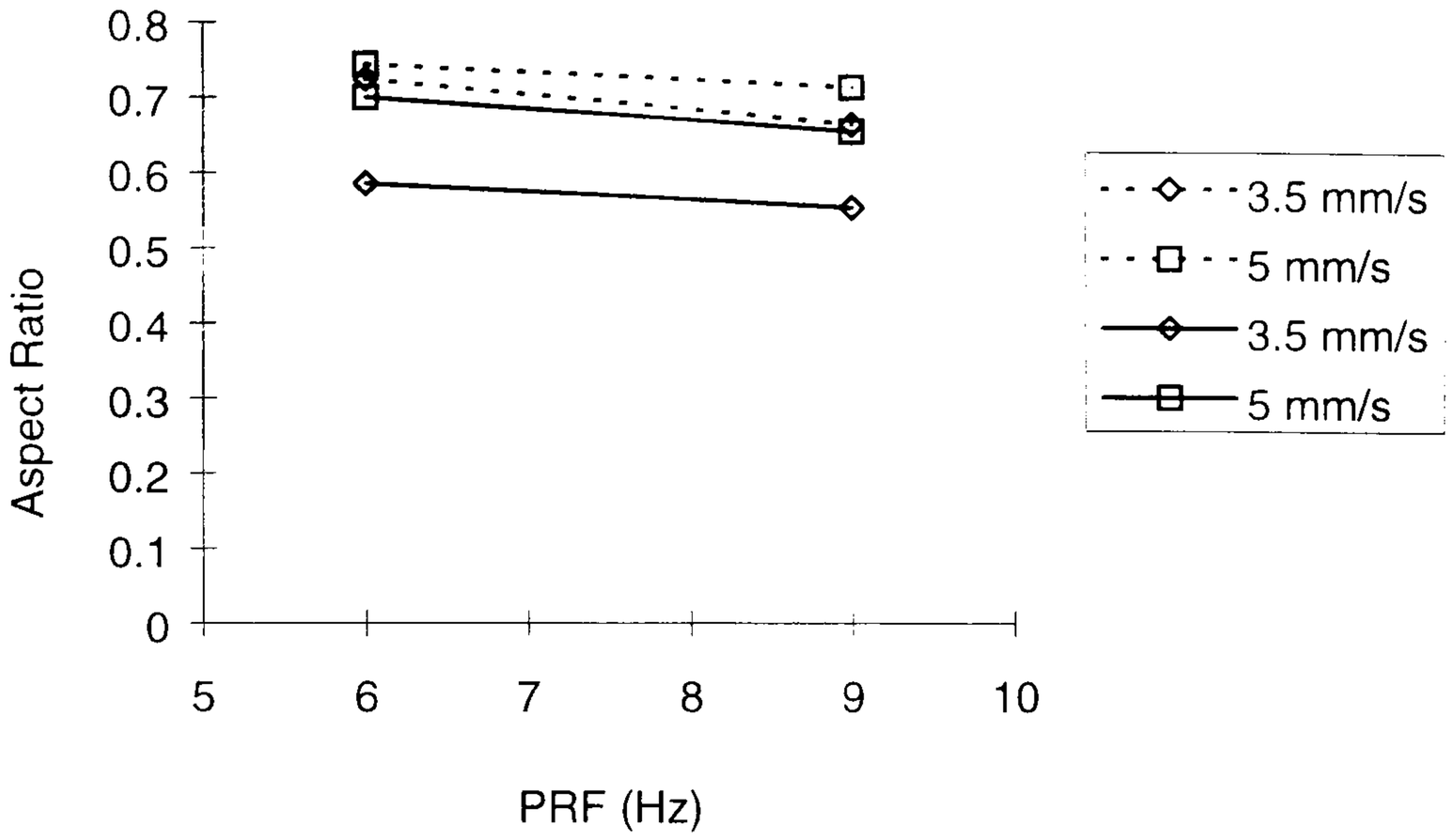

Figure 4.3 Effect of aspect ratio as a function of PRF, for post-heated welding. The dotted and solid lines indicate the pulse width of 6 and 12 ms, respectively.

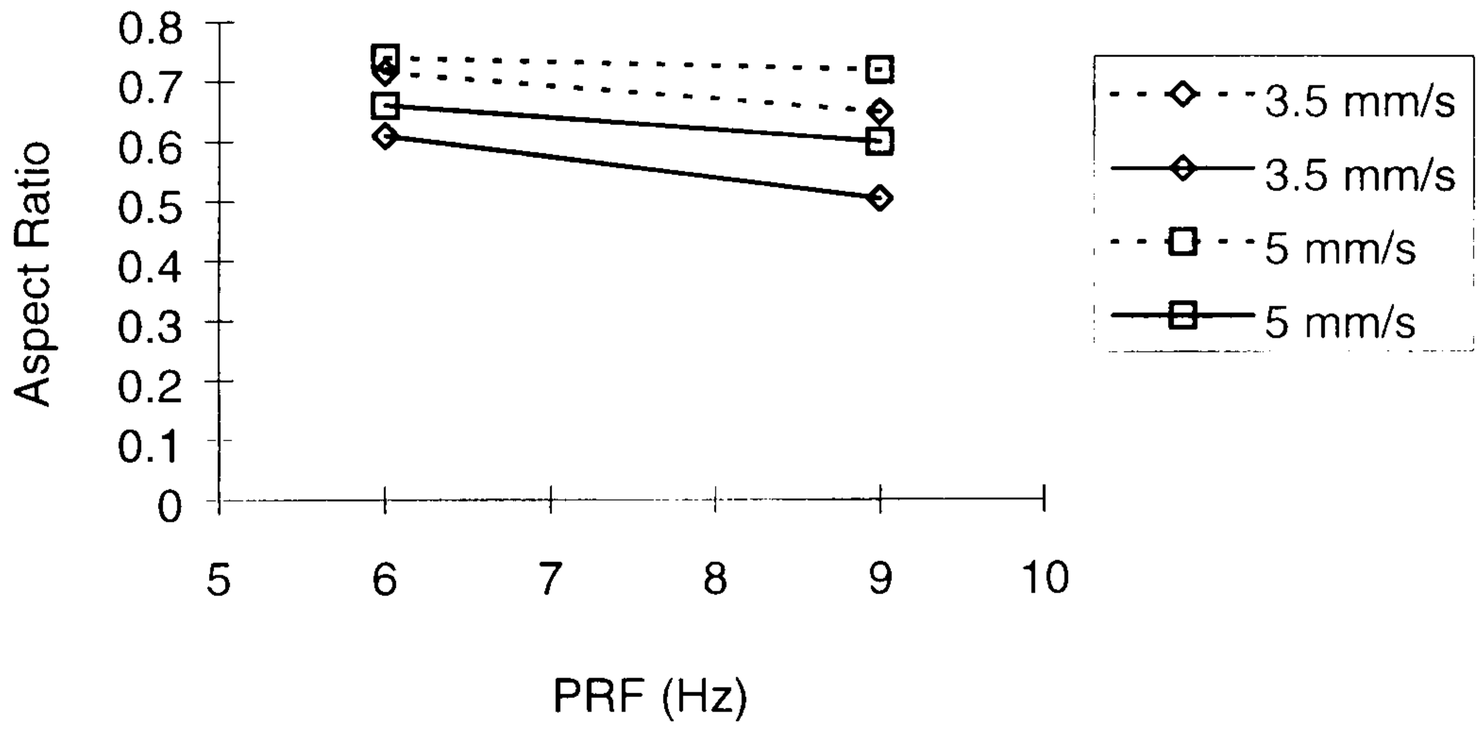

Figure 4.4 Effect of aspect ratio as a function of PRF, for pre-heated welding. The dotted and solid lines indicate the pulse width of 6 and 12 ms, respectively.

Type of Welding	Parameter interactions	P- Values
Normal Welding	Speed	**0.0**
Normal Welding	Pulse Width	**0.0**
Normal Welding	PRF	**0.02**
Normal Welding	Speed*Pulse Width	0.07
Normal Welding	Speed*PRF	0.88
Normal Welding	Pulse Width *PRF	0.76
Normal Welding	Speed*Pulse Width*PRF	0.12

Table 4.4 P-values obtained from the general linear model, the effect of aspect ratio, for different laser parameters. The highly significant effect on the aspect ratio is indicated in bold.

Type of Welding	Parameter interactions	P- Values
Post-heated Welding	Speed	**0.0**
Post-heated Welding	Pulse Width	**0.0**
Post-heated Welding	PRF	**0.0**
Post-heated Welding	Speed*Pulse Width	**0.04**
Post-heated Welding	Speed*PRF	0.67
Post-heated Welding	Pulse Width *PRF	0.67
Post-heated Welding	Speed*Pulse Width*PRF	0.12

Table 4.5 P-values obtained from the general linear model, the effect of aspect ratio, for different laser parameters. The highly significant effect on the aspect ratio is indicated in bold.

Type of Welding	Parameter interactions	P- Values
Pre-heated Welding	Speed	0.08
Pre-heated Welding	Pulse Width	**0.04**
Pre-heated Welding	PRF	0.08
Pre-heated Welding	Speed*Pulse Width	0.66
Pre-heated Welding	Speed*PRF	0.51
Pre-heated Welding	Pulse Width *PRF	0.56
Pre-heated Welding	Speed*Pulse Width*PRF	0.97

Table 4.6 P-values obtained from the general linear model, the effect of aspect ratio, for different laser parameters. The highly significant effect on the aspect ratio is indicated in bold.

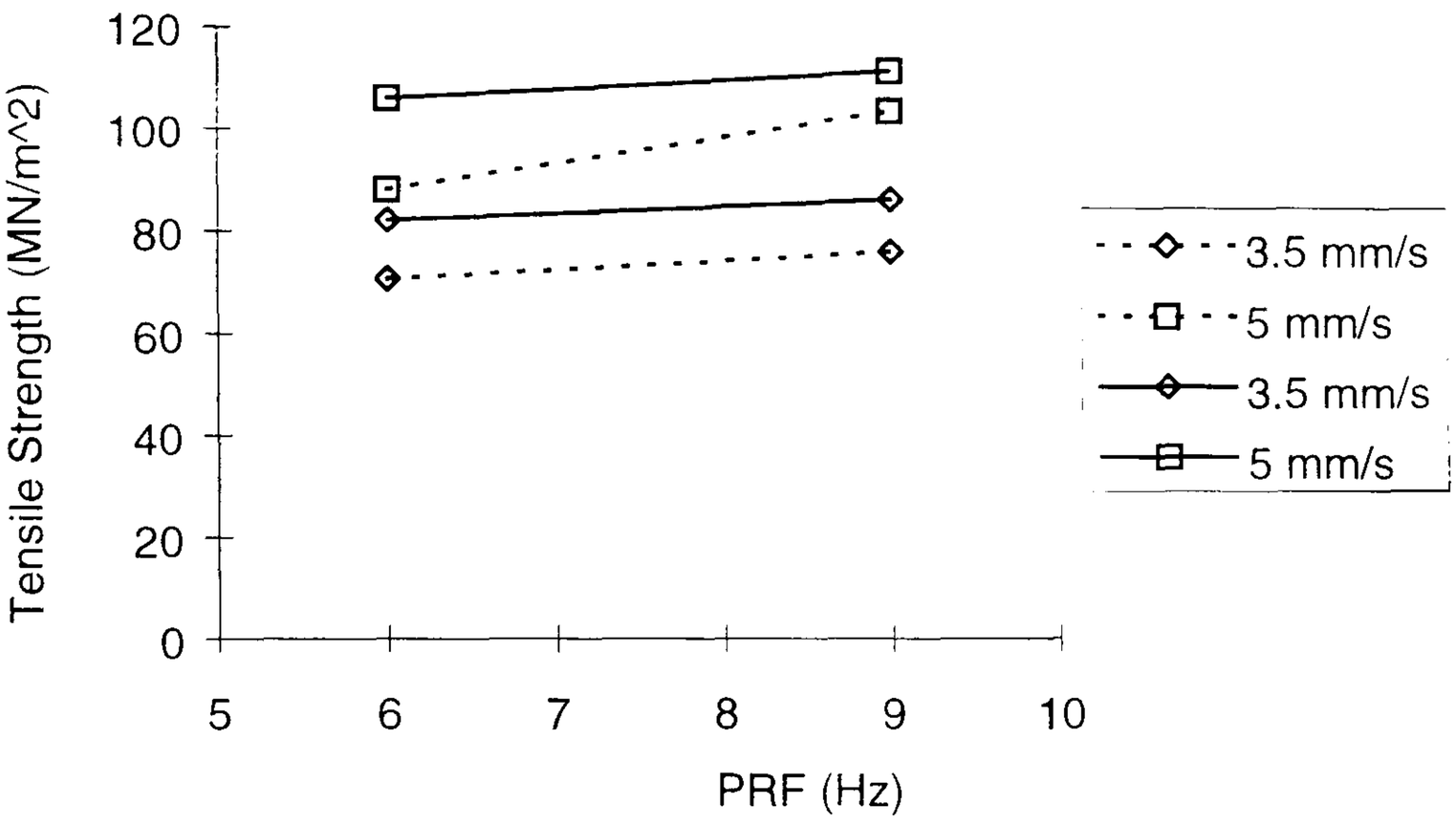

Figure 4.5. Effect of tensile strength as a function of PRF, for normal welding. The dotted and solid lines indicate the pulse width of 6 and 12 ms, respectively.

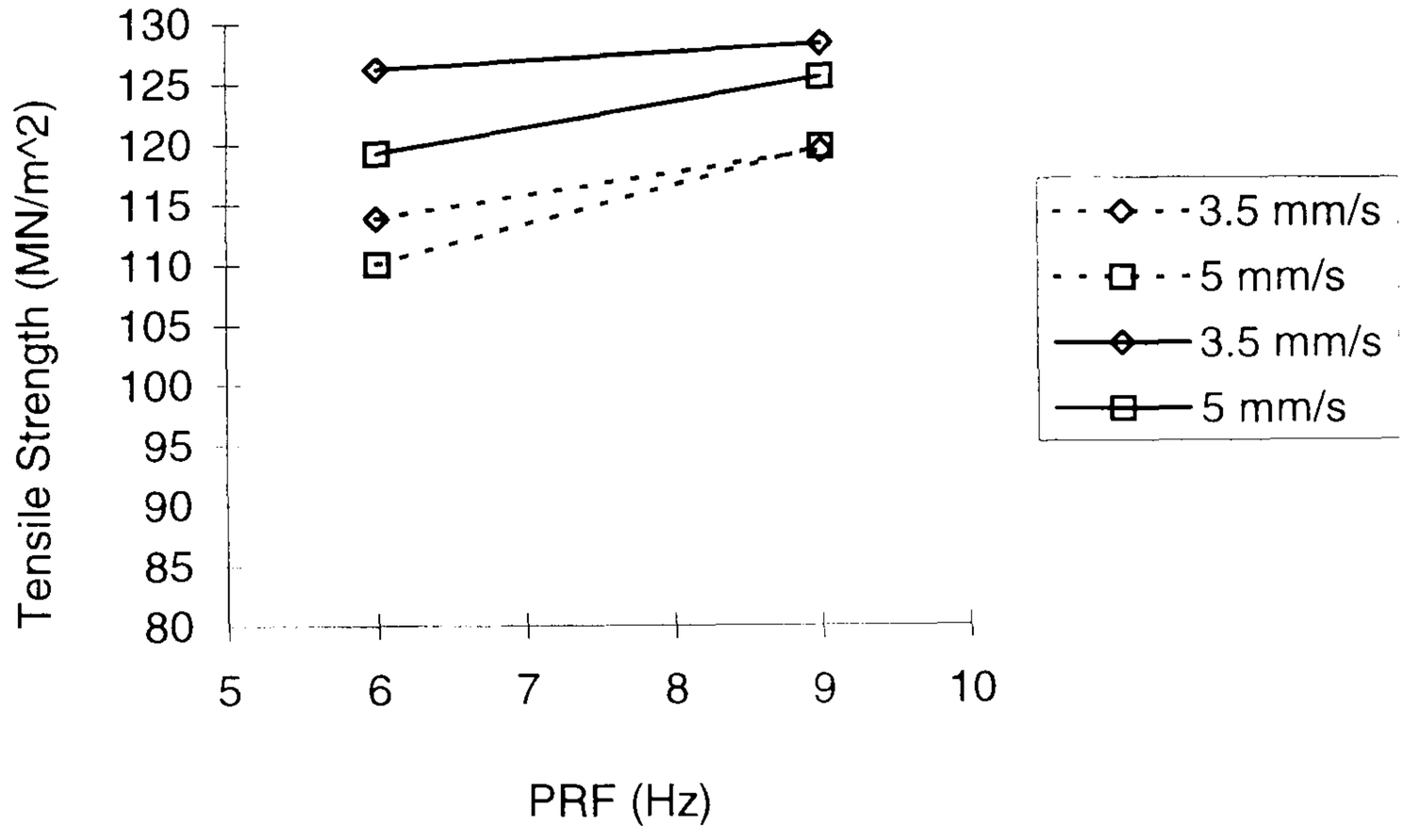

Figure 4.6. Effect of tensile strength as a function of PRF, for post-heated welding. The dotted and solid lines indicate the pulse width of 6 and 12 ms, respectively.

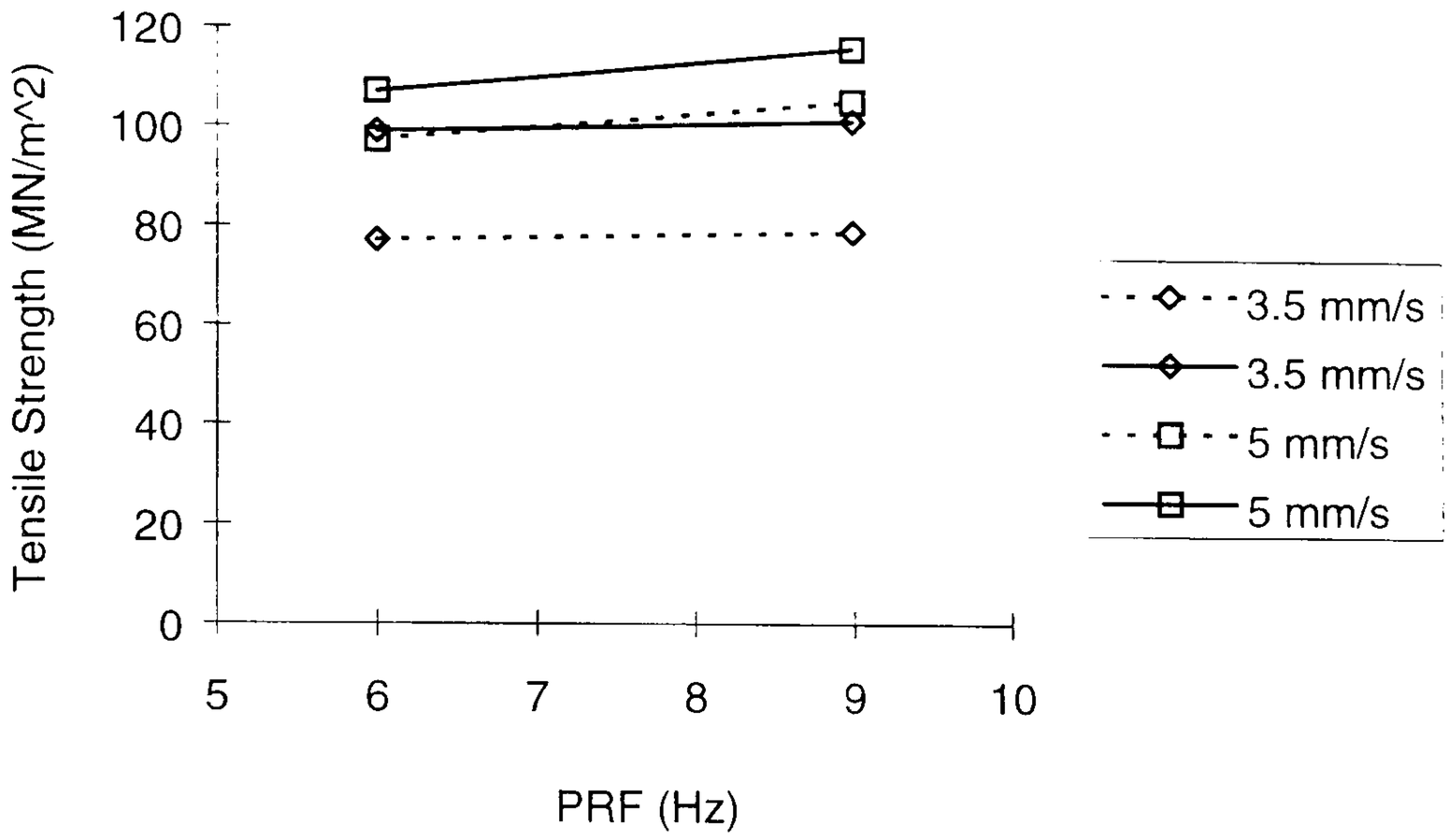

Figure 4.7 Effect of tensile strength as a function of PRF, for pre-heated welding. The dotted and solid lines indicate the pulse width of 6 and 12 ms, respectively.

Type of Welding	Parameter interactions	P- Values
Normal Welding	Speed	**0.0**
Normal Welding	Pulse Width	**0.04**
Normal Welding	PRF	0.19
Normal Welding	Speed*Pulse Width	0.84
Normal Welding	Speed*PRF	0.58
Normal Welding	Pulse Width *PRF	0.59
Normal Welding	Speed*Pulse Width*PRF	0.67

Table 4.7 P-values obtained from the general linear model, the effect of tensile strength, for different laser parameters. The highly significant effect on the tensile strength is indicated in bold.

Type of Welding	Parameter interactions	P- Values
Post-heated Welding	Speed	0.10
Post-heated Welding	Pulse Width	**0.00**
Post-heated Welding	PRF	**0.01**
Post-heated Welding	Speed*Pulse Width	0.39
Post-heated Welding	Speed*PRF	0.32
Post-heated Welding	Pulse Width *PRF	0.42
Post-heated Welding	Speed*Pulse Width*PRF	0.95

Table 4.8 P-values obtained from the general linear model, the effect of tensile strength, for different laser parameters. The highly significant effect on the tensile strength is indicated in bold.

Type of Welding	Parameter interactions	P- Values
Pre-heated Welding	Speed	**0.00**
Pre-heated Welding	Pulse Width	**0.04**
Pre-heated Welding	PRF	0.09
Pre-heated Welding	Speed*Pulse Width	**0.05**
Pre-heated Welding	Speed*PRF	0.25
Pre-heated Welding	Pulse Width *PRF	0.90
Pre-heated Welding	Speed*Pulse Width*PRF	0.96

Table 4.9 P-values obtained from the general linear model, the effect of tensile strength, for different laser parameters. The highly significant effect on the tensile strength is indicated in bold.

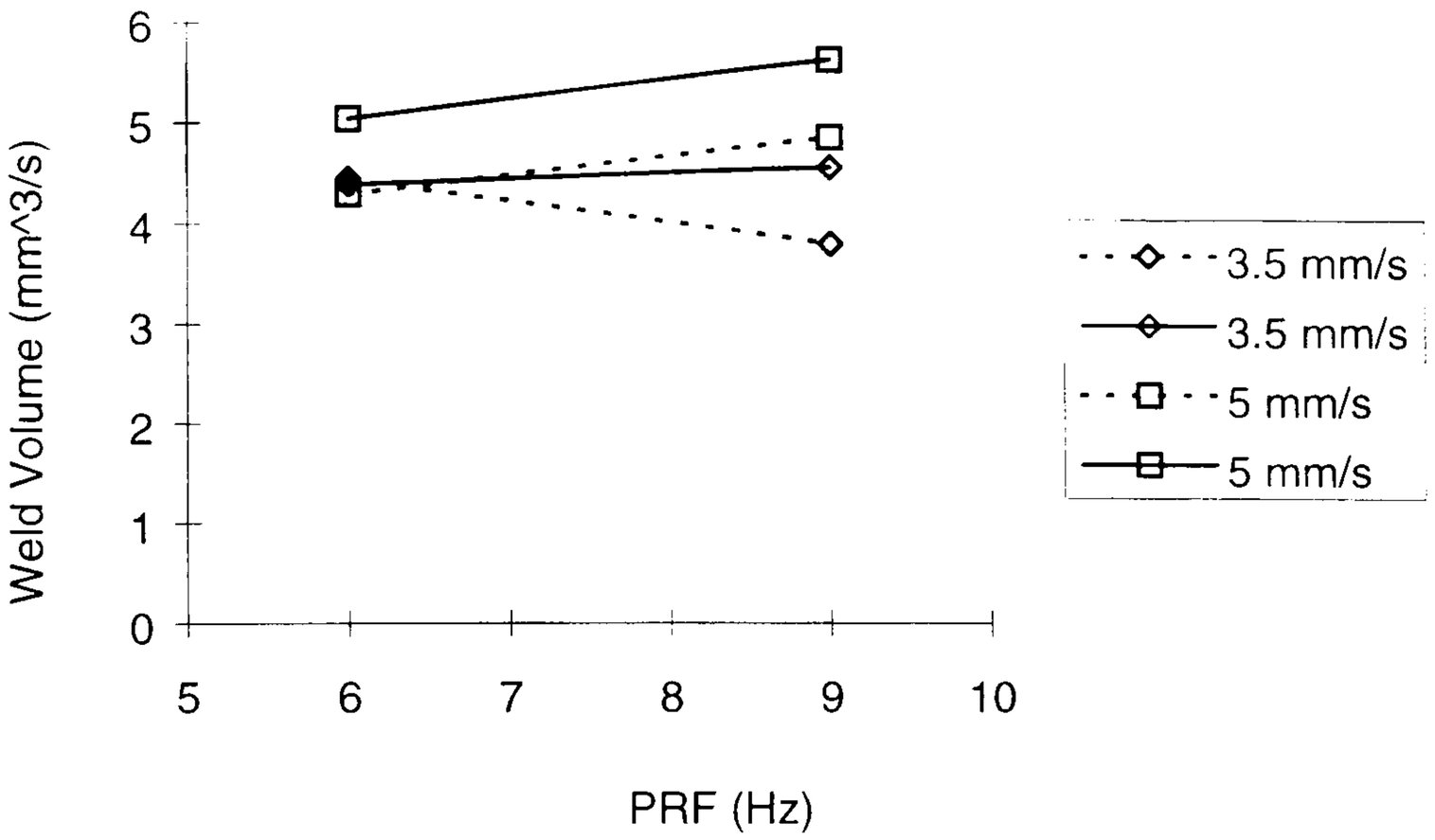

Figure 4.8 Effect of weld volume formation rate as a function of PRF, for normal welding. The dotted and solid lines indicate the pulse width of 6 and 12 ms, respectively.

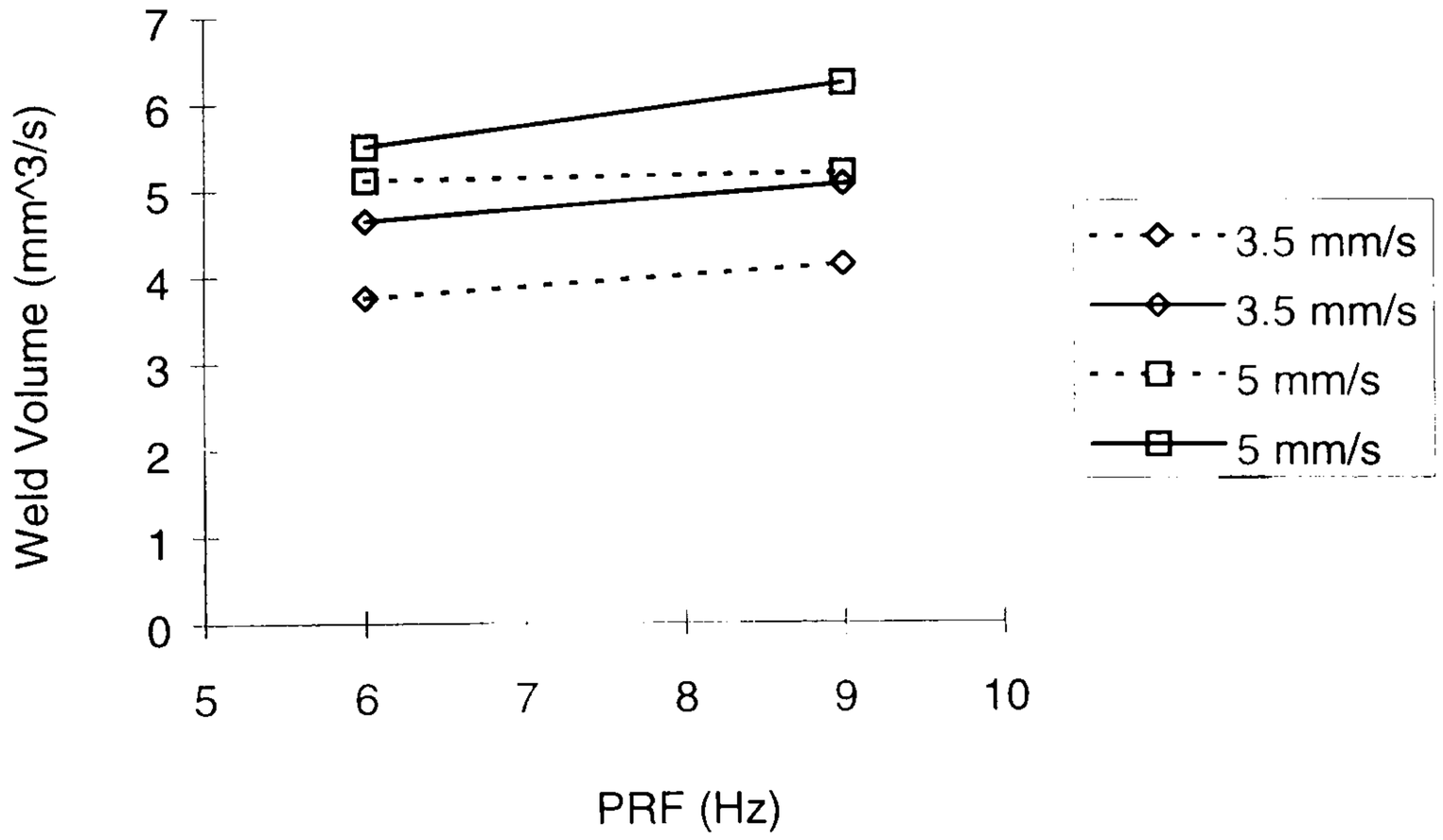

Figure 4.9 Effect of weld volume formation rate as a function of PRF, for post-heated welding. The dotted and solid lines indicate the pulse width of 6 and 12 ms, respectively.

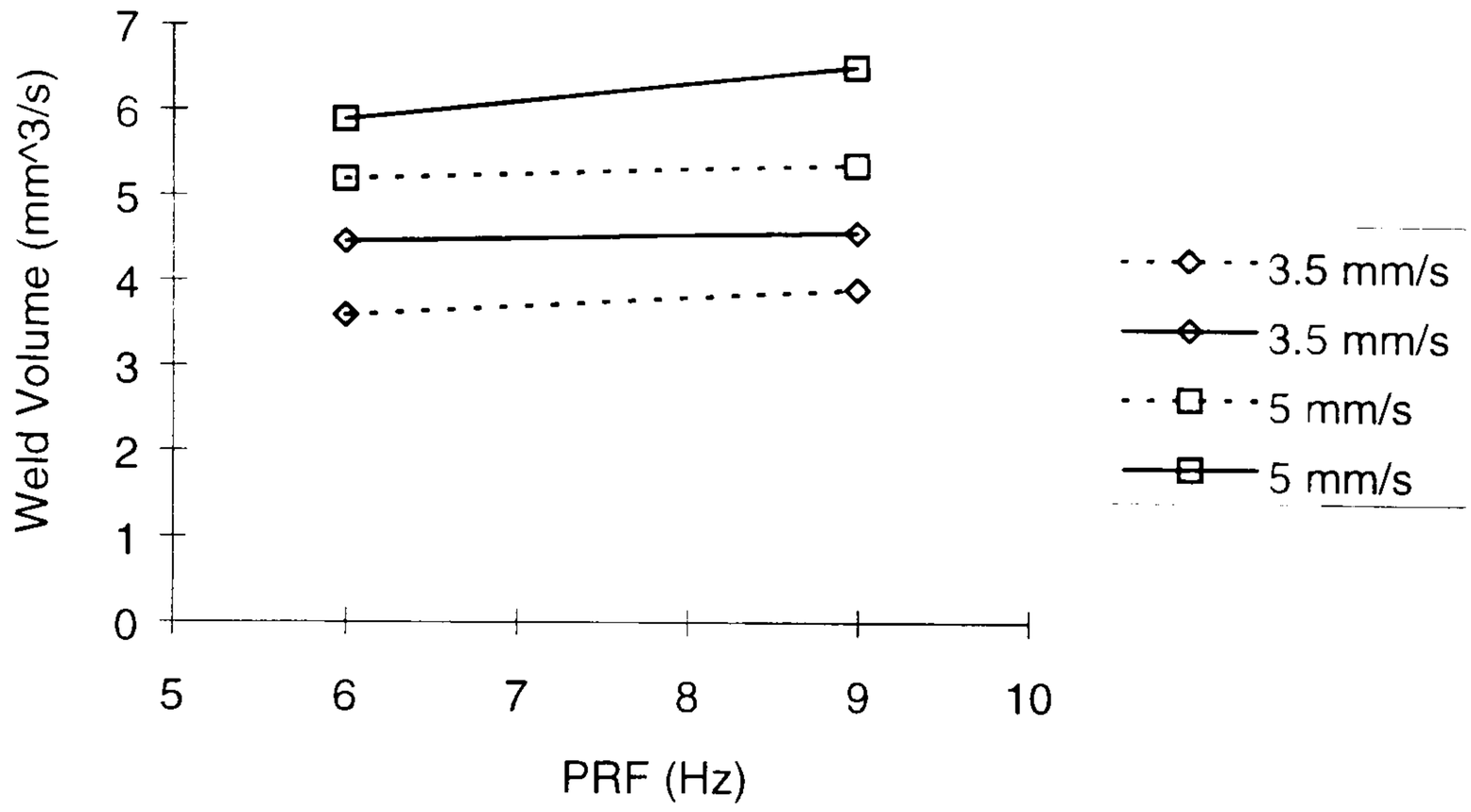

Figure 4.10 Effect of weld volume formation rate as a function of PRF, for pre-heated welding. The dotted and solid lines indicate the pulse width of 6 and 12 ms, respectively.

Type of Welding	Parameter interactions	P- Values
Normal Welding	Speed	**0.00**
Normal Welding	Pulse Width	**0.00**
Normal Welding	PRF	**0.03**
Normal Welding	Speed*Pulse Width	0.75
Normal Welding	Speed*PRF	0.34
Normal Welding	Pulse Width *PRF	0.77
Normal Welding	Speed*Pulse Width*PRF	0.73

Table 4.10 P-values obtained from the general linear model, the effect of weld volume formation rate, for different laser parameters. The highly significant effect on the rate of weld volume formation is indicated in bold.

Type of Welding	Parameter interactions	P- Values
Post-heated Welding	Speed	**0.00**
Post-heated Welding	Pulse Width	**0.00**
Post-heated Welding	PRF	**0.00**
Post-heated Welding	Speed*Pulse Width	0.25
Post-heated Welding	Speed*PRF	0.99
Post-heated Welding	Pulse Width *PRF	0.06
Post-heated Welding	Speed*Pulse Width*PRF	0.09

Table 4.11 P-values obtained from the general linear model, the effect of weld volume formation rate, for different laser parameters. The highly significant effect on the rate of weld volume formation indicated in bold.

Type of Welding	Parameter interactions	P- Values
Pre-heated Welding	Speed	**0.00**
Pre-heated Welding	Pulse Width	**0.00**
Pre-heated Welding	PRF	**0.02**
Pre-heated Welding	Speed*Pulse Width	0.35
Pre-heated Welding	Speed*PRF	0.19
Pre-heated Welding	Pulse Width *PRF	0.35
Pre-heated Welding	Speed*Pulse Width*PRF	**0.03**

Table 4.12 P-values obtained from the general linear model, the effect of weld volume formation rate, for different laser parameters. The highly significant effect on the rate of weld volume formation is indicated in bold.

CHAPTER FIVE
INVESTIGATION OF Nd:YAG LASER WELDING WITH AN ELLIPTICAL BEAM PROFILE

5.1 Characteristics of Nd:YAG Laser Welding With 30° Incident Beam

5.1.1 Introduction

The performance of a dual beam delivery system, as described in Chapter 3, was assessed and compared with the performance of a single beam delivery system. The experiments reported in the previous chapters demonstrate that the hardness discontinuities in a metal structure were dependent on the cooling rate, which for laser welding is dominated by the rapid quenching of the fusion zone via conduction to the surrounding environment. To eliminate these problems and to improve the mechanical properties of the weld, a dual beam delivery system was used, see Section 5.2. Dausinger *et al* [5.1] observed an increase in the welding process stability when a dual-beam technique or Nd:YAG laser (shorter wavelength) was applied. For non-diffusion limited processes, the keyhole can close rapidly. This can lead to high cooling rates especially in the root of the weld, Steen [5.2] and Schwartz [5.3].

Glumann [5.4] concluded that according to the theoretical considerations the combination of beams set at an angle resulted in a higher process stability. Abduallah [5.5] *et al* made a detailed study of a dual beam optical fiber delivery system to deliver focused laser radiation to the workpiece. This work demonstrated the need to have effective control of the cooling rate during laser processing. It is well known that lasers provide a unique source of heat that can be focused onto the workpiece, and the generated irradiance is high enough to permit vaporization and formation of a keyhole, Metzbower *et al* [5.6]. Guitterez *et al* [5.7] made a detailed study on the loss of alloying elements in the weld due to vaporization which may influence the mechanical properties of the weld joints. Pulsed Nd:YAG lasers, allow the heat input into the weld joint and power density to be kept sufficiently high to achieve the desired weld penetration; advantages over CO_2 laser processing are due to its shorter wavelength and greater focussability, as analyzed by Olsen [5.8]. Prokhorov [5.9] *et al* described the heating

rate of a laser welded joint and coupling of laser radiation into the workpiece as being dependent on the base metal absorptivity for a given wavelength and the material's thermal properties. Moreover, how the workpiece is in thermal contact with its surrounding environment plays an important role in the rapid quenching rate and the resultant mechanical properties of the weld.

Miller [5.10] *et al* showed that during laser welding, the laser beam energy was delivered to the welded joints through the plasma plume that was formed above the material surface. The effect of the induced plasma can be reduced and controlled by using the correct shielding gas, Behler *et al* [5.11]. The high cooling rate associated with laser welded high carbon steel, leads to a variation in the transverse hardness profiles, and consequently, results in brittle welds. Additionally, Ng *et al* [5.12] and Honeycombe [5.13] reported that the hardness discontinuities in the fusion region and heat affected zone (HAZ) due to the rapid quenching rate leads to cracking and poor component fatigue life at the fusion zone.

In the present case, a 30° clamping geometry was developed to conduct a series of experiments examining the characteristic of cooling rate with an elliptical beam profile. The samples were clamped at 30° and laser welded to improve the mechanical properties at the weld joints. Preliminary assessment of the weld profiles was conducted by measuring the weld width, weld penetration, hardness characteristic, tensile strength and observing the microstructure, for different laser parameters. The results were compared to the flat welding process discussed in Section 3.1.2.

5.1.2 Welding and Analysis

The laser employed in this study was a Lumonics MS830 Nd:YAG laser, operating at a wavelength of 1.06 μm, its maximum mean power was 400 watts. The power was delivered via a fibre optic system which was robotically manipulated to produce the butt welds with a constant mean power of 154 watts. In all cases, an argon shielding gas at a source pressure of 5×10^4 Pa indicated at the pressure gauge was used for welding.

Focusing was optimised by adjusting the vertical height of the gauge plate, which was clamped in two different ways. Additionally, the effect of using two different angles of incidence (0°,30°) of the laser beam were compared, as were the effects of the pulse width and pulse repetition frequency (PRF) on the mechanical and microscopic properties of the material. **Figures 5.1** and **5.2** show the experimental set-up that was used in the experimental investigation, using flat (0°) and 30° clamped geometries, respectively.

For all the measurements, the errors observed for all the experiments was less than ± 1.1 %, each of the data points plotted in the graph in this thesis is the average of 3 values. The error is not significant and is hardly seen. Thus, the error bars are omitted in most of the cases for clarify. The gauge plates (0.88 mm) that were welded had the same nominal composition that was mentioned in Chapter 3 - see **Table 3.1**. The weld beads were sectioned in the transverse and longitudinal direction and the weld width, weld depth and hardness profiles measured and the microstructure examined. This was done by moulding, polishing and etching in nital (3% nitric acid and 97% methanol). The weld bead that appeared on the moulded surface was also noted for comparison. A Reichiert 1541555 Vicker's hardness testing machine with a diamond indenter was used to measure the hardness profiles across the weld direction and as a function of depth, by applying a 70 gm load. The weld depth and bead width were measured using Mttutoyo PJ-300 profile projector. The tensile tester was an Instron tensile machine, comprising a load of 10 kN; this was applied to the welded specimens with a cross-head velocity of 5 mm/s.

The effect of varying the laser parameters was quantified by measuring the hardness transverse to the weld direction, tensile strength, aspect ratio, weld volume formation rate and examining the phase transformation.

5.1.3 Weld Characteristics

5.1.3.1 Tensile Test

All of the welds were tested in the longitudinal direction. Compared to normal flat welding, the welds done at 30° all required a higher tensile load before failure occurred in the weld region. **Figures 5.3** and **5.4** show, the tensile strengths that resulted in the failure of the butt welded joints, as a function of the pulse width and PRF, respectively. **Figure 5.3** clearly shows that the tensile strength increased with increasing pulse width, for both welding process. It can be seen that the tensile strength was greatest for the welds done at 30°. No full penetration was achieved with the flat welding process. For a partial weld, the tensile strength increased from 49 MN/m^2 to 95 MN/m^2 for a corresponding pulse width from 6 to 12 ms. Whereas, full penetration welds were achieved using the 30° clamped geometry for all welds. This is due to the laser beam was set welding above the gap of the welded joints, thus, the gravity of the molten pool tends to sink and fill up the welded joint The tensile strength increased from 64.1 to 165.5 MN/m^2, for corresponding increase in the pulse width from 6 to 12 ms.

For the flat and 30° welding process, the effect of PRF on the tensile strength can be seen in **Figure 5.4**. Interestingly, increasing the PRF reduced the tensile strength for the flat welding process, but the tensile strength increased with PRF for the 30° welding geometry only partial welds were achieved with the flat welding. The tensile strength decreased from 68 MN/m^2 to 53 MN/m^2 for a corresponding increase in the PRF from 6 Hz to 8 Hz. This represents a decrease of 22.5 %. This reduction was due to the spatter loss above the fusion zone (see Section 5.1.3.5). Toru *et al.* [5.14] mentioned that the spatter loss could be prevented and/or reduced by using a defocused laser beam, where the optics and welding direction were optimised to obtain a deep penetration. For a flat welding geometry, a full penetration weld was achieved with a PRF of 9 Hz and in this case the tensile strength was 34.14 MN/m^2. The tensile strength increased from 120 to 195 MN/m^2 for an increase in the PRF from 6 to 9 Hz, for 30° weld geometry. This represent an increase in the tensile strength of 62.5 %. Full penetration was achieved

with the 30° clamped geometry, however, this process produced a wider weld bead which resulted in the molten material dropping out in the fusion region. However, in all cases, the greatest tensile strength was achieved by welding with the 30° clamped geometry (using an elliptical beam) as compared to the flat welding (using a focussed beam) results, for the range of parameters investigated.

5.1.3.2 Hardness Characteristics

Vicker's hardness profiles were performed across the heat-affected zone, fusion zone and base metal to characterize the strength across the weld joints. A diamond pyramid indenter with a load of 70 gm was used to measure hardness transverse across the weld and as a function of depth, for both the flat and 30° clamped geometry. In all cases, the hardness profile gradually increased towards the fusion zone boundary. **Figure 5.5** shows the hardness profiles transverse to the weld. It is seen that the hardness across the weld decreased with increasing PRF for both the flat and 30° clamped geometries. The peak hardness was greatest for the flat welding process and the lowest PRF, such a weld would be liable to fracture if it is subjected to cyclic loading. For a PRF of 6 Hz, the peak hardness was 1855 kg/mm^2 for the flat welding geometry; this reduced by 43.1 % to 1055 kg/mm^2 for the 30° clamping geometry. However, at 9 Hz the reduction was 62.1 %.

Figure 5.6 shows the hardness profiles at the HAZ region greatly reduced with increasing pulse width, for both flat and 30° welding geometries. The major advantage of using the 30° clamping geometry is that it creates an elliptical beam profile, produces a greater HAZ than flat welding but also a reduced rate of cooling, as discussed in Chapter 3. In this cases, the flat welding geometry had large hardness gradients transverse to the weld. These were suppressed by using an elliptical beam. The hardness across the weld was greatest for the lowest pulse width for both weld geometries. For example, with a pulse width of 6 ms, the peak hardness was 1839 kg/mm^2 for flat welding geometry, however, this was reduced by 44.3 % to 1024 kg/mm^2 for the 30° welding geometry. In all cases, the maximum peak hardness was

observed for a pulse width of 6 ms and PRF of 6 Hz for both geometries. The large hardness gradients were attributed to the rapid cooling rate which produced poor mechanical joints due to the hardness discontinuities. Whereas, the lowest peak hardness at the centre of the HAZ was observed for a pulse width of 12 ms and PRF of 9 Hz.

Figures 5.7 and **5.8** show the hardness profiles, at the centre of the weld and as a function of depth for both geometries, at different PRFs and pulse widths. From these figures, it can be seen that the rate of change of hardness as a function of depth reduced with increasing pulse width and PRF, for both flat and 30° welding configurations. With the flat welding geometry, the hardness decreased with the depth into the sample. Here, the largest variation was observed for the flat welding geometry. Whereas, for the 30° clamped geometry, there was no significant difference in the hardness over the depth investigated. In all cases, and for a given depth, the hardness decreased with increasing pulse length and PRF with the flat welding geometry. In general, the 30° welding configuration produced a uniform hardness into the weld.

5.1.3.3 Aspect Ratio

The aspect ratio for both flat and 30° clamped geometries was found by dividing the weld penetration depth by the weld width. The aspect ratio dependence on different PRFs and pulse widths are shown in **Figures 5.9** and **5.10**, respectively. **Figure 5.9** shows that, for flat welding process, the aspect ratio increased with the PRF. Whereas, the aspect ratio decreased with increasing PRF for the 30° welding configurations. Welding with the 30° clamped geometry produced a larger and wider HAZ and resulted in a lower aspect ratio as compared to the flat welding results. For the 30° clamped geometry, a full penetration was achieved, but the slow welding velocity lead to the drop out in the centre of the fusion region, for further explanation of this see Section 5.1.3.5.

It can be seen in **Figure 5.10**, that the aspect ratio increased with the pulse width for the flat welding process. At less than 10 ms, the aspect ratio was lower than for the flat welding configuration, and above 10 ms the aspect ratio was higher. This is due to the lack of penetration and increased weld width that was achieved with the flat welding process at the higher pulse width. Whereas, for the 30° clamped geometry, the aspect ratio decreased with increasing pulse width. Full penetration was achieved over the entire range of pulse widths investigated. An increase in the pulse width produced a lower aspect ratio as compared to the normal weld, because of the wider weld bead.

5.1.3.4 Rate of Formation of the Weld Volume

The rate of formation of the weld volume was taken as the product of the weld width, penetration depth, and the translation velocity (5 mm/s), for the flat and 30° welding systems. The dependency of the weld volume formation rate on the pulse width for both geometries can be seen in **Figure 5.11**.

For the both geometries, the weld volume increased with the pulse width. The weld volume formation rate was greatest for the 30° welding geometry. From **Figure 5.11**, it is clearly observed that the maximum weld volume formation rate was achieved at a higher pulse width of 12 ms, and minimum weld volume formation rate was observed at a pulse width of 6 ms, for both geometries. For instance, for the flat welding geometry, with pulse width of 6 ms the weld formation rate was 3.13 mm^3/s, this increased by 96 % to 6.14 mm^3/s for the 30° welding configuration. Moreover, for a pulse width of 12 ms, the weld formation rate for the flat welding was approximately 5.55 mm^3/s, and this was increased by 33 % to 7.4 mm^3/s, for the 30° welding geometry.

The weld volume formation rates at different PRFs for the flat and angular welding geometries are shown in **Figure 5.12**. From this figure, it is clearly seen that the rate of weld volume increased with PRF, and the largest rate of formation was observed at a higher PRF for both geometries. For instance, with a PRF of 6 Hz, the weld formation rate was 3.36 mm^3/s for flat welding geometry, this was increased by 91 % to 6.4 mm^3/s

for 30° welding geometry. The weld volume formation rate was increased by 22 % for the higher PRF (9 Hz).

5.1.3.5 Microstructure study of the weld

The microstructure of a welded region depends on the rate at which the sample is cooled from the elevated temperature. Moreover, Burdekin [5.15] described that the different cooling rates determine the different types of microstructure that arise in the fusion zone and heat-affected zone. Wang [5.16] *et al* discovered that a general feature of laser welded high carbon steel is the formation of a martensite structure in the fusion zone, due to the rapid quenching rate, and finely dispersed carbides. In all of the present cases, martensite and carbide structures appeared between the ferrite with some retained austenite. **Figure 5.13** shows the fusion zone of flat welded sample, a fine grain structure was found in this region, which resulted in the high hardness discontinuities and brittleness. **Figures 5.14** shows, a typical picture of the fusion zone for the same set of laser parameters and the 30° clamping geometry. It is obvious that welding with the 30° clamped geometry leads to a reduction in the cooling rate, so that the grain size becomes coarser and more refined in form. For the 30° clamping geometry, as shown in **Figure 5.15,** a wider weld width was achieved, this resulted in a slower cooling rate as compared to the flat welding. Formation of porosity occurs through bubbles becoming trapped by the fast solidification front due to the intense evaporation and unstable vibration of the molten pool, Katayama *et al.* [5.17]. It was observed with 30° geometry that bubbles were trapped from the bottom and tip of the keyhole, due to the influence of the laser beam irradiation angle relative to the weld specimen. However, due to the periodic evaporation the shielding gas, sometimes air can become entrained in the keyhole, due to the sudden collapse of an unstable keyhole after laser termination; this leads to the formation of pores. Matsunawa *et al.* [5.18] concluded that it is necessary to close the keyhole gradually during the solidification process, and Arata *et al* [5.19] showed that a dual beam delivery system can suppress porosity. This dual beam system is later discussed in Section 5.2. **Figure 5.16** shows the narrow fusion and heat-affected zones produced by flat welding, the formation of a fine grain structure was attributed to

the rapid cooling rate, and lower strength was achieved compared to the 30° welding. spatter loss above the fusion region is clearly observed, as discussed in Section 5.1.3.1. For both welding processes, the grain size significantly became more dense and coarser close to the heat-affected zone. **Figure 5.15** clearly shows the grain structure was completely modified in the fusion zone, the drop-out for the 30° welding, can be clearly seen, and under-cut was found on the top view of the fusion zone. By appropriate selection of the laser parameters, the desired characteristics of the material can be achieved.

5.1.4 Conclusion of laser welding with 30° incident beam

These fundamental investigation have demonstrated the influence of two different welding geometries (0°,30°) and optimizing a range of laser parameters to improve the weld quality. The weld quality was quantified by: measuring the sample's hardness profile transverse across the weld region, as a function of depth, tensile strength, aspect ratio, weld volume formation rate and examination of its microstructure.

The above welding results demonstrated that welding at 30° produced a higher tensile strength in the weld region than the flat welding geometry for different pulse widths and PRF. For the 30° welding geometry, the results have shown that the tensile strength greatly increased with the pulse length and PRF. The increased in tensile strength of 74 % was achieved at a pulse width of 12 ms.

The hardness profiles decreased with increasing PRF and pulse width for both geometries, however, the hardness gradients were less for the 30° welding configurations. For a PRF of 6 Hz, the hardness at the fusion zone reduced from 1855 kg/mm^2 for the flat welding geometry to 1055 kg/mm^2 for the 30° weld geometry. Furthermore, a maximum hardness reduction of 62.1 % was achieved at the weld center for a PRF of 9 Hz with the 30° welding geometry. For a pulse width of 6 ms, the peak hardness was reduced by 44.3 % with an 30° incident welding beam as compared to the flat welding configuration. Interestingly, for the flat welding geometry, the rate of

change of hardness as a function of depth reduced along the weld depth. For the 30° welding geometry, the hardness as a function of depth exhibited little fluctuation along the weld centre; thus, the hardness did not differ significantly as a function of depth for a given PRF or pulse width. For both geometries, the hardness reduced with increasing PRF and pulse width.

For the 30° weld geometry, the aspect ratio decreased with increasing PRF and pulse width. Compared to the flat welding geometry, full penetration and wider weld widths were achieved with welding at 30°, thus, the drop out in the fusion zone could be eliminated with a higher welding speed, for 30° welding geometry. For flat welding, the aspect ratio increased below 10 ms, above this value there was a slight decrease in the aspect ratio.

The rate of formation of the weld volume increased with pulse width and PRF for both geometries. For the 30° weld geometry, the maximum weld formation rate was achieved at the highest PRF and pulse width.

Because of the rapidly cooled high carbon steel, the main weld region consisted of a martensitic structure. The hardness profile was dependent on the thermal distribution around the fusion zone, moreover, in the present case, the cooling rate was greatly reduced due to the elliptical beam profile on the workpiece, for 30° welding geometry. Therefore, a slower cooling rate was achieved in the fusion zone for 30° welding geometry. A general feature of all the specimens was that the main weld region consisted of cementite and carbides structures. For the flat weld geometry, the grain size was coarser and less dense near the fusion zone, moreover, for welding at 30°, the structure was completely modified at the fusion zone. The rate of cooling was slower, so this lead to a less brittle weld. The grain structure that appeared in the fusion zone was typically more refine and granular.

5.2 Study on the performance of single and dual beam system in Nd:YAG laser welding with a 30° incident beam

5.2.1 Introduction

The preliminary experiments examined the effect of the rate of cooling influencing the mechanical properties of a welded joint for different clamped geometries. The single and dual pass welding are compared in Chapter 3. It was found that for dual pass welding, the mechanical properties of the welded samples were improved compared to that with a single pass weld. A dual beam delivery system is discussed in Chapter 3 - see Section 3.2 and 3.3, this system allowed a heat transfer mechanism to control the material processing. Oslen [5.20] stated that the temperature between the melting point and boiling point was maintained long enough to allow heat conduction to a certain depth.

Laser processing of materials has been the subject of intensive experimental and theoretical studies since the invention of the laser. The need of knowing the precise relationship between the processing parameters, different geometries and induced plasma effects is crucial, it is also necessary to understand the underlying thermal distribution over the weld region in order to optimize this process. The heating rate of a welded joints depends on the parent metal absorptivity, moreover, the base metal in contact with the surrounding environment can plays a major role in the cooling process via conduction. See appendix A for a detailed discussion on the rate of heating and cooling of the welded samples.

During laser welding, the plasma plume generated forms near the workpiece, it can prevent optical energy from reaching the weld surface, as reported by Miller *et al.* [5.17] and Verwaerde *et al.* [5.21]. Later Fabbro *et al* [5.22] generated a model to predict the behaviour of the laser beam energy, as a unique heat source which was high enough to permit vaporization to take place in the weld pool, and it was then deposited along the keyhole in the molten region. Metzbower *et al.* [5.23] and Gu *et al.* [5.24] conducted a series of experiments, and concluded that it was critical to maintain the keyhole during

the welding process because any disturbance to the keyhole can lead to poor penetration and reduction of the weld strength.

The high cooling rate of the laser weld leads to a variation in the transverse hardness profiles, consequently, resulting in brittle welds. However, Ng *et al* [5.25] had investigated the hardness discontinuities in the fusion region and heat affected zone (HAZ), which leads to cracking and poor component fatigue life. It was noted that inorder to achieve a lower hardness profile across the weld, a pre-heat or post-heat treatment had to be conducted. This was achieved simply by an additional pass following the first pass as discussed in chapter 3 - see Section 3.2 and 3.3. Moon [5.26] concluded that this was simple and economic way of heat-treating the weldments compared to the conventional processing. Therefore, to ameliorate these poor mechanical characteristics, this work investigated normal, preheating and post-heating. Welds were done on a 30° clamped geometry which previous experiments had shown retarded rate of cooling and prevented rapid quenching. With multiple beam delivery systems, the workpiece and temporal temperature distribution can be controlled to generate desired weld properties, without losing the benefits of this low distortion joining process. In this Chapter, the results of this detailed investigation compared the weld quality for the normal laser welding and those welded with post-heated or pre-heated treatments. The results were quantified in the same manner as before by measuring the weld depth, weld bead widths, hardness characteristics and tensile strengths.

5.2.2 Welding and analysis

A Lumonic's MS830 Nd:YAG laser (1.06 μm), with a maximum output power capacity of 400 watts was used to weld 0.88 mm thick gauge plate. In the present case, a dual beam fibre optic delivery system was used to achieve in-line process annealing (pre-heating or post-heating) with a constant power of 285 watts. **Figure 5.2** shows the schematic diagram of single beam system - see Section 5.1.2, and **Figure 5.17** shows the dual-beam delivery system used in this experiment. The amount of losses taken into

account for all the optical lens and fiber optic beam delivery system resulted in a constant power of 154 W and 72 W used to produce the butt weld and post-heating of gauge plates, respectively. The gauge plate was clamped at an angle of 30° to the incident beam, this created an elliptical beam which was focused and used for welding. A defocused beam was used before or after welding to produce heat-treatment simultaneously. In the case of post-heating, the laser power was divided so that 70 % of the power was coupled to the weld beam, and the remaining 30 % was directed into the weld region to provide heat treatment. The elliptical welding beam was 3 mm diameter, and the pre-heating or post-heating beam was approximately 25 mm diameter. The processing method was designed to heat treat the material before welding with the main beam, this allows more beam energy to couple into the carbon steel gauge plate during welding.

In all cases, the errors observed for all the experiments was less than ± 1.2 %, each of the data points plotted in the graph in this thesis is the average of 3 values. The error is not significant and is hardly seen. Thus, the error bars are omitted in most of the cases for clarify. High carbon steel gauge plate, with a nominal composition as discussed in Chapter 3 - see Section 3.2.2 was selected for this experimental investigation. After welding, the workpieces were sectioned, moulded, polished, etched (2 % nital) and photographed. To quantify the weld quality, the Vicker's hardness was measured, transverse along the weld direction and as a function of depth. Furthermore, an Instron tensile tester machine was used to measure the tensile strength along the weld joints with a cross-head speed 0.5 mm/sec. The weld depth and bead were measured using a Mitutoyo PJ-300 profile projector. The welds were inspected both visually and using an optical microscope to study weld defects, cracks and the microstructure in the weld region. The parameters used in this experiment for normal welding and the dual beam weld geometries are listed below in **Table 5.1**. Temperature measurements were taken throughout the experiments with thermocouples attached onto the specimen surface, 2 mm from the weld region. **Figure 5.18** shows attachment of two thermocouple wires

(T1 and T2) at the beginning of the weld, and the other two thermocouples (T3 and T4) were arranged adjacent to each other at the end of the weld.

5.2.3 Weld characteristics

5.2.3.1 Hardness Profiles

The hardness characteristics for both the normal and pre-heating geometry was quantified by measuring the hardness transverse across the weldment and as a function of depth at the fusion zone centre. **Figure 5.19** shows the Vicker's hardness profiles transverse across the weld region, heat affected zone and parent metals, for different pulse repetition frequency (PRF) from 6 Hz to 9 Hz for the normal, post-heating and pre-heating geometries. It is seen that the peak hardness at the centre of the weld was 1056 kg/mm^2 for a PRF of 6 Hz for normal weld geometry. Interestingly, the peak hardness was greatly reduced at the centre of the weld with the pre-heating and post-heating weld geometries as shown in **Figure 5.19**. The post-heated weld achieved the lower peak hardness compared to the pre-heated weld geometry, at different PRFs. In all cases, the hardness profiles transverse across the weld decreased with increasing PRF. **Figure 5.20** shows the hardness profiles for the normal, post-heated and pre-heated weld geometries, for different pulse widths. In all cases, the hardness transverse to the weld direction decreased with increasing pulse widths. Increasing the pulse width from 6 ms to 12 ms, the peak hardness reduced from 1024.66 kg/mm^2 to 736.61 kg/mm^2 for normal weld geometry. For the pre-heating geometry, the hardness reduced from 676.73 kg/mm^2 to 573.98 kg/mm^2 with an increase in pulse width from 6 to 12 ms. The lowest peak hardness was achieved with the pre-heating geometry. **Figures 5.19** and **5.20**, clearly indicate that a less brittle weld was achieved with a dual pass weld.

Figure 5.21 shows the hardness profile as a function of depth for the normal and pre-heated weld geometries and different PRFs. **Figure 5.21** shows no significant difference in the hardness along the fusion zone, approximately over a depth of 0.5 mm. In general, the hardness profiles decreased with increasing PRFs for the normal and pre-heated welding configurations. However, for the pre-heating geometry there was a

lower hardness as a function of depth than the normal weld configuration. Both techniques produced a uniform hardness through the weld depth. For the normal and pre-heating geometries, the hardness as a function of depth for different pulse widths is shown in **Figure 5.22.** In all cases, the hardness was slightly reduced by increasing the pulse width. In general, the hardness as a function of depth exhibited little fluctuation along the fusion zone, and the hardness showed no significant difference along the weld depth (0.5 mm) over the range of pulse widths investigated. For the normal weld geometry, the hardness along the weld depth was lower than the post-heated weld geometry, at a pulse width of 12 ms.

Figures 5.23 and **5.24** show the hardness profiles, at the centre of the weld and as a function of depth, for the normal and post-heated weld geometries and for different PRFs and pulse widths. From **Figure 5.23**, it can be seen that the rate of change of hardness as a function of depth reduced with increasing PRF, for the normal and post-heating geometries. Moreover, a slight variation was observed over the range of depths investigated for different PRFs. In general, the hardness decreased with increasing PRF for both the normal and post-heated weld configurations. From **Figure 5.24**, it can be seen that the hardness profiles as a function of depth decreased with increasing pulse width for both geometries. Here, the largest variation was observed over the range of depth investigated for the normal weld geometry. However, for a post-heating geometry, there was a slight variation in the hardness profiles for the range of pulse widths from 6 ms to 8 ms, and the hardness profile as a function of depth remained constant above 8 ms. In all cases, the hardness as a function of depth exhibited a little fluctuation along the fusion zone for the normal weld geometry, but the hardness profiles as a function of depth showed significant change for the post-heating geometry. For a pulse width above 8 ms, the normal weld geometry showed a lower hardness profile along the weld depth than post-heated weld, for a pulse width above 8 ms.

5.2.3.2 Tensile test

Tensile tests were performed to determine the strength of the laser welded gauge plates done with the normal, pre-heating and post-heating weld configurations. It can be seen that the tensile failure occurred in the welded region. Deformation of the welded region was evident, indicating brittle fracture due to the sample's high hardness had resulted from the rapid quenching rate of the laser welded gauge plates. The weld strength was significantly inferior to those of the parent metal. **Figure 5.25** shows the tensile strength as a function of pulse widths, for the normal, pre-heating and post-heating weld geometries. For the normal weld geometry, the tensile strength increased from 40 to 95 MN/m^2 with an increase in the pulse width from 6 to 12 ms. This represents an increase in the tensile strength of 58.7 % for the normal weld geometry over the post-heated welds, for a pulse width above 8 ms. Whereas, for the pre-heating geometry, the tensile strength increased from 61 to 67 MN/m^2 with an increase in pulse width from 6 to 8 ms. Moreover, the pulse width was increased from 8 to 12 ms, the tensile strength started decreased from 67 to 46 MN/m^2 at the higher pulse width. **Figure 5.25** shows clearly that for the post-heating system, the tensile strength decreased from 63 to 48 MN/m^2 for an increased in the pulse width from 6 to 12 ms.

Figure 5.26 shows the tensile strength as a function of PRF, for the normal, pre-heating and post-heating weld configurations. It can be seen clearly that the tensile strength was greatest for the normal weld geometry over the range of PRF investigated, and the strength increased with PRF. For the normal weld geometry, the tensile strength increased from 120 to 195 MN/m^2 for an increase in PRF from 6 to 9 Hz. This represents an increase of tensile strength of 62.5 % for the normal weld geometry. Whereas, for the pre-heating geometry, the tensile strength increased from 37 MN/m^2 to 59 MN/m^2 for an increase in the PRF from 6 to 9 Hz. For the post-heating configuration, the tensile strength increased from 44 MN/m^2 to about 65 MN/m^2 with increasing PRF from 6 Hz to 9 Hz. For a post-heated weld, drop out occurred in the fusion zone resulting in a lower strength, see Section 5.2.3.6.

5.2.3.3 Aspect Ratio

The aspect ratio for both the normal, pre-heated and post-heated welds was found by dividing the penetration depth by the weld width. In all cases, full penetration welds were achieved. The dependency of the aspect ratio on the PRF and pulse width is shown in **Figures 5.27** and **5.28**. **Figure 5.27** shows that for the normal, pre-heated and post-heated welds, the aspect ratio decreased with an increase in the PRF. Compared to the normal weld, the aspect ratios for the dual beam welding was lower because of the wider weld beads produced by the pre-heated and post-heated weld geometries. The greatest aspect ratio was achieved at a lower PRF, for all weld configurations. Comparing both post-heating and pre-heating geometries, it can be seen that the post-heating weld geometry produced a wider weld bead, this was clearly shown in **Figure 5.27**. However, this leads to a slower rate of cooling which agrees with the results discussed in Section 5.2.3.1; in that, a less brittle weld was achieved with the post-heating and pre-heating weld geometries. In **Figure 5.28**, it is seen that the aspect ratio was measured a function of pulse width. In all cases, the aspect ratio decreased with increasing pulse width, moreover, the greatest aspect ratio was achieved with the normal weld geometry. Whereas, for the dual beam system, a wider weld bead was produced with the pre-heated geometry than the post-heated one, this is clearly illustrated in **Figure 5.28**. In all cases, the pre-heated geometry produced a wider weld width than the normal and post-heated weld, and the same results were achieved for flat welding process, discussed in Chapter 3 - see Section 3.4.

5.2.3.4 Temperature Profile

The relative temperature of the gauge plate during the weld process has been monitored. **Figures 5.29** and **5.30** show the temperature profiles along the weld direction for the post-heated weld configurations at PRF of 7 Hz and 8 Hz, respectively. Measurements were taken near the beginning (T1 and T2) and end (T3 and T4) of the weld with four thermocouples attached to the surface of the specimen. By comparing **Figures 5.29** and **5.30**, it can be seen that a significantly different peak in the normalised temperature occurs at the beginning and end of the weld. This was due to the overall temperature of

the specimen rising due to the greater integrated energy input near the end of the weld. A PRF of 8 Hz produced a wider width and a higher normalised temperature profile. **Figure 5.31** shows the temperature variation for the pre-heating weld geometres, at a PRF of 8 Hz and pulse width of 10 ms, respectively. Here the profile was wider for the post-heating geometry, the cooling process was reduced to greater overlapping of the elliptical post-heating and welding beams; this permits more energy absorption onto the weld region. The post-heating technique allowed the temperature to drop at a slower rate than the pre-heating weld geometry, for an increase of PRF. Thus, this technique produced a less brittle weld, seen Section 5.2.3.1. The spatial hardness discontinuities are dependent on the temperature distribution during the welding process, the details are discussed in Section 5.2.4. Moreover, different beam delivery systems and laser process parameters will lead to different heat transfer characteristics and ultimately to different weld characteristics and grain size. Two possible sources of error in the temperature measurement could be involved. Firstly, there may temperature differences within the thermocouple itself so that the thermo-electric e.m.f. developed does not correspond to the temperature at the point of contact with the specimen but spatially averaged value. Secondly, the accuracy of the positioning of the thermocouple wires on the sample. These errors will contribute to errors in the magnitude of the sample, whereas, this measurement was taken to determine the relative temperature for the different beam delivery systems.

5.2.3.5 Rate of Formation of the Weld Volume

Characterizing the rate of formation of weld volume for the normal, pre-heating and post-heating weld geometries was found by multiplying the product of the weld width and weld penetration by the constant translation velocity (5mm/s). the results are shown in **Figures 5.32** and **5.33,** over the range of PRFs and pulse widths investigated. Comparing the three different welding techniques over the selected range of PRF, the pre-heated welds gave the largest rate of formation of the weld volume. For instance, for a PRF of 6 Hz, the weld formation rate was about 5.41 mm^3/s for the normal weld configuration and this was reduced by 19 % to 6.41 mm^3/s with increasing PRF from 6

Hz to 9 Hz. Interestingly, for the preheating geometry the minimum weld rate was 7.31 mm^3/s, and then began to increase slightly for a higher PRFs. This represent an increase of 11 % to 8.14 mm^3/s for a PRF increase from 6 to 9 Hz. Whereas, for the post-heating geometry, the weld volume was increased by 14 % to 7.4 mm^3/s.

The dependency of the weld volume formation rate on the pulse width for the normal, pre-heated and post-heated weld geometries can be seen in **Figure 5.33**. For the normal weld geometry, the formation rate was about 4.73 mm^3/s and this was increased by 39 % to 6.58 mm^3/s with an increase of pulse width from 6 to 12 ms. Interestingly, the weld volume formation rate increased by 14 % to 8.4 mm^3/s, for the pre-heated geometry. Moreover, for the post-heating weld geometry, the weld formation rate was 6.64 mm^3/s for a pulse width of 6 ms. As would be expected, the largest weld formation rate was observed at higher pulse widths. For the post-heating geometry the weld formation rate approximately increased by 10 % to 7.4 mm^3/s. The maximum weld volume formation rate was achieved with a pre-heating weld geometry at the maximum PRF and pulse width.

5.2.3.6 Microstructure study of the weld

Figure 5.34 shows a typical picture of a normal laser weld that had not received any heat treatment or annealing. A general feature of all the specimens was that the weld region consisted of a martensitic structure. Abdullah *et al.* [5.27] stated that the characteristics of rapidly cooled high carbon steel resulted in a fine dispersed carbides, typical of hardened and untempered steel, found in the fusion zone. The grain structure was smaller in the fusion zone and coarser near the heat affected zone. Moon *et al.* discussed [5.28] that this was due to different cooling rates between the fusion and heat affected zones. With a pre- heated weld, this produced a pre-run onto the weld region with a defocused beam, and followed by a focused beam to run a weld. Thus, Lancaster [5.29] suggested that multi-passes over the weld is beneficial in reducing the hardness profiles. Due to the thermal cycle, the structure is completely modified near the weld region, for the post-heated and pre-heated weld geometries. **Figures 5.35** and **5.36**

show the fusion zone of the pre-heated and post-heated welds, respectively, with the same laser parameters. Here, the grain structure in the fusion zone was transformed to a fine and equi-axed grain. A narrow weld interface between the fusion and parent metal was found in the normal laser weld as shown in **Figure 5.37**. Additionally, the pre-heated weld specimen exhibited a wider heat affected zone at the conjunction between the fusion zone and parent metal, see **Figure 5.38**. In general, the dual beam system (see Chapter 6) reduced the rate of cooling forming a favorable mechanical structure, as discussed in Chapter 3. No evidence of micro-cracking was observed in either the pre-heated or post-heated welds. For both weld geometries, the heat affected zone had a slightly coarser and denser structure.

5.2.4 Conclusions of the performance of single and dual beam system in Nd:YAG laser welding with 30° incident beam

These fundamental investigation have demonstrated the influence of welding at 30° and optimizing a range of laser weld parameters to improve the weld quality. The beam geometries comprised a single-beam and dual-beam delivery system. The weld quality was quantified by: measuring the sample's hardness profiles transverse across the weld region, as a function of depth, tensile strength, aspect ratio, temperature profiles, weld volume formation rate and microstructure examination.

The hardness profiles were greatly decreased with increasing PRF and pulse width for the normal, pre-heating and post-heating weld geometries. **Figures 5.19** and **5.20** show clearly the peak hardness of the weld for the normal, pre-heating and post-heating of samples, ie. at different pulse widths and PRFs. In all cases, the peak hardness decreased with increasing pulse width and PRF - this can be seen in Section 5.3.2.1. For increasing pulse width, it was found that pre-heating the workpiece was more effective in improving the hardness characteristics than normal and post-heating techniques, this is illustrated clearly by **Figure 5.23** - detailed this discussed in Section 5.3.2. Post-heating produced the greatest reduction in the peak hardness with increasing PRF from 6 Hz to 9 Hz. Moreover, both post-heating and pre-heating techniques resulted in reduced non-uniformities in the hardness profiles, the likelihood of cracking,

when subjected to cyclic loading therefore, is greatly reduced. Thus, the normal, pre-heating and post-heating geometries were compared, and the hardness profiles decreased as a function of depth with increasing of PRF and pulse width. However, the pre-heated and post-heated weld geometries produced a lower hardness profile as a function of depth than the normal weld, but both techniques gave a uniform hardness along the weld depth.

The tensile strength was measured as a function of pulse width and PRF for the normal, pre-heating and post-heating weld configurations. The tensile strength increased with the pulse width and PRF for the normal weld geometry, and the strength decreased with increasing pulse width for the dual beam system. Whereas the tensile strength increased with PRF for the dual beam system. But the normal weld geometry produced a higher weld strength than the post-heated and pre-heated weld geometries. It was concluded that for the dual beam system, the tensile strength of the welded joints was lower compared to the single beam system, this is due to the severe drop-out problem that occurred in the fusion zone as reported in Section 5.1.3.5. The drop-out reduced with an increase in the translation velocity.

The aspect ratio decreased with increasing pulse width and PRF for the normal, pre-heated and post-heated weld configurations. A lower aspect ratio was achieved with the pre-heated weld geometries. Whereas the pre-heated weld technique produced a wider weld width than the normal and post-heated weld, for an increase in the pulse width.

The measured temperature profiles explain the observed characteristics of the laser welded specimens, for the post-heated and pre-heated weld geometries. The rate of cooling, for instance, was slower for the dual-beam delivery system. This lead to a lower hardness induced in the fusion zone, and increasing the pulse length produced a wider temperature profile, and the cooling rate was effectively reduced.

The rate of formation of the weld volume was dependent on the PRF and pulse width, for the normal, pre-heated and post-heated weld geometries. In all cases, the largest weld volume formation rate was produced by the pre-heated weld geometry. Thus, the weld volume formation rate increased with the pulse width and PRF, for the dual beam system.

For an increased pulse width and PRF, the structure was completely modified at the fusion zone , for the dual beam system. Moreover, for the pre-heated and post-heated welds, the grain structure found in the fusion zones consisted of refine and granular grain, as compared to the single beam system.

REFERENCES CHAPTER FIVE

[5.1] Dausinger, F. Faisst, F. Hack, R. Rapp, J. Hugel, H. "Welding of aluminum: Challenge and chance for laser technology", The 14th International Congress On Applications Of Lasers And Electro-optics, San Diego, Nov 1995, 1059-1067.

[5.2] Steen, W. M."Lasers material processing". Springer-Verlag publisher. 1991.

[5.3] Schwartz, M. M. "Source book on electron beams and laser beam welding". American Society For Metals. pp 343-346, 1981.

[5.4] Glumann, C. Rapp, J. Dausinger, F. Hugel, H. "Welding with a combination of CO_2 lasers - advantages in processing and quality", The 12th International Congress On Applications Of Lasers And Electro-optics, Orlando, 1993, 672.

[5.5] Hussein.A. Abdullah, Chris.R. Chatwin, Ian.A. Watson, "Hardness Characteristic Of Laser Welded Joints", Technical Digest, CLEO/Pacific Rim'95, July 1995, 298.

[5.6] Metzbower, D.W. Moon, "Mechanical Properties, Fracture Toughness And Microstructure Of Laser Welds Of High Strength Alloys", Applications Of Lasers In Material Processing, American Society For Metals, April 1979, 83-85.

[5.7] Guitterez, G. Neye, E. Zschech, "Microstructure, Hardness Profile And Tensile Strength In Welds Of AA6013 T6 Extrusions", Welding Research Supplement, Journal Of Welding, April 1996, 115-120.

[5.8] Olsen, 1995, "Pulse Laser Material Processing, Nd:YAG Versus CO_2 Lasers", Annals of The CIRP, Vol 44/1, 142-144.

[5.9] Prokhorov, V.I. Konov, I. Ursu, I.N. Mihailescu, "Laser Heating Of Metals", Publish 1990, ISBN 0-7503-0040-X , 1-4.

[5.10] Miller, T. Debroy, "Energy Absorption By Metal-Vapour-Dominated Plasma During CO_2 Laser Welding Of Steels", Journal Of Applied Physic, Vol 68(5), Sep 1995, 2047-2050.

[5.11] Behler, E. Beyer, G. Herziger, "Using tThe Beam Polarisation To Enhance The Energy Coupling In Laser Beam Welding, Proceeding Of 7th International Congress On Applications Of Lasers And Electrooptics ICALEO'88, 98-101.

[5.12] S. Ng, I. A. Watson, "Characteristics Of CO_2 Laser Welded High Carbon Steel Gauge Plate", Journal Of Laser Application, Vol 9, 1997.

[5.13] Honeycombe, R. W. K. "Microstructure and Properties". Edward Arnold publisher. 1981.

[5.14] Toru, N. Hiroshi, M. Shigeki, F. Akira, O. Katsuori, T. Kudo, T. "Welding Characteristic With Two YAG Laser Beams", The International Congress On Applications Of Lasers And Electro-optics, ICALEO'97, San Deigo, Nov 1997, 181-184.

[5.15] Burdekin, " Heat Treatment Of Weld Structures", The Welding Institute, 1969, 1-6.

[5.16] Wang, K. L., Zhu, Y.M., Dong, Z. J. and Zhang, R.J. Microstruture and property of laser Transformation hardening on sheet steel with high carbon content. In: Proc. ICALEO '95, The 14th International Congress on Applications of Lsers and Electro-Optics, San Diego (J. Mazumder, A. Matsunawa and C. Magnusson eds.). Orlando FL: Laser Institute of America, 1995, 85-91.

[5.17] Katayama, S. Seto, N. Kim, J. Matsunawa, A. "Formation Mechanism And Reduction Method of Porosity In Laser Welding of Stainless Steel", The International Congress on Applications of Lsers and Electro-Optics, ICALEO'97 San Diego, Section G 83 - 89.

[5.18] Matsunawa, A. Kim, J. Katayama, J. "Porosity Formation In Laser Welding - Mechanism and Suppresion method, The International Congress on Applications of Lsers and Electro-Optics, ICALEO'97 San Diego, Section G 73 - 80.

[5.19] Arata, Y. "Plasma, Electron and Laser Beam Technology", ASM International, 1986.

[5.20] F. O. Olsen, "Pulse Laser Material Processing, Nd:YAG Versus CO_2 Lasers", Annals Of The CIRP, Vol 44, 142-44.

[5.21] R. Miller, T. Debroy, "Energy Absorption By Metal-Vapor-Dominated Plasma During Carbon Dioxide Laser Welding Of Steels", Journal Appl Physic, 68 (5), 1 Sep 1990, 2045-47.

[5.22] A. Verwaerde, R. Fabbro, "Experimental Study Of Continuous CO_2 Laser Welding At Subatmospheric Pressure", Journal Appl Physic, 78 (5), 1 Sep 1995, 2981-83.

[5.23] R. Fabbro, A. Poueyo-Verwaerde, "Modelling Of Deep Penetration Laser Welding Process: Application To The Analysis Of Energy Coupling Inside The Keyhole", The 14th International Congress On Application Of Lasers And Electro-Optic, San Diego, Nov 1995.

[5.24] E. A. Metzbower, D. W. Moon, "Mechanical Properties, Fracture Toughness And Microstructure Of Laser Welds Of High Strength Alloys", Applications Of Lasers In Material processing", American Society For Metals, April 1979, 83-85.

[5.25] H. P. Gu, W. W. Duley, "A Statistical Approach To Acoustic Monitoring Of Laser Welding", Journal Of Physic D: Appl. Phys, 29, 1996, 556-57.

[5.26] E. S. Ng, I. A. Watson, "Characterisation Of CO_2 Laser Welded High Carbon Steel Gauge Plate", Journal Of Laser Application, Vol 9, 1997.

[5.27] D. W. Moon, "A Study of Dual Pass In Laser Welding of Steels", The Proceeding of 6th International Congress on Application of Laser and Electro-optics", ICALEO'87, 1987, 67- 63.

[5.28] H. A. Abdullah, C. R. Chatwin, I. A. Watson, "Hardness Characteristic Of Laser Welded Joints", Proceeding Technical Digest, CLEO/Pacific Rim, 1995, 298.

[5.29] D. W. Moon, C. R. Feng, H. H. Chaskelis, V. E. Merchant, "Characterization of laser beam welds of β 21S-Ti", Journal Lasers In Engineering, 1995, 4, 34-40.

[5.30] J.F. Lancaster, "Metallurgy Of Welding", Allen And Unwin (Publisher) Ltd, 4th Edition, 1987, 167-72.

Table 5.1 Parameters for normal, post-heating and pre-heating welding

Type Of Welding	Power for welding / Power for Post-heating (W)	Pulse Width (ms)	PRF (Hz)	Pulse Energy (Joules)	Peak Power (kW)	Spot Size (mm)	Pulse Shape
Normal	200	6	10	20	3.3	3	Top hat
Normal	200	8	10	20	2.5	3	Top hat
Normal	200	10	10	20	2	3	Top hat
Normal	200	12	10	20	1.7	3	Top hat
Normal	200	10	6	33.3	3.3	3	Top hat
Normal	200	10	7	28.6	2.9	3	Top hat
Normal	200	10	8	25	2.5	3	Top hat
Normal	200	10	9	22.2	2.2	3	Top hat
Postheating	200 / 85	6	10	20/8.5	3.3/1.4	3/25	Top hat
Postheating	200 / 85	8	10	20/8.5	2.5/1.1	3/25	Top hat
Postheating	200 / 85	10	10	20/8.5	2/0.9	3/25	Top hat
Postheating	200 / 85	12	10	20/8.5	1.7/0.7	3/25	Top hat
Postheating	200 / 85	10	6	33.3/14.2	3.3/1.4	3/25	Top hat
Postheating	200 / 85	10	7	28.6/12.1	2.9/1.2	3/25	Top hat
Postheating	200 / 85	10	8	25/10.6	2.5/1.1	3/25	Top hat
Postheating	200 / 85	10	9	22.2/9.4	2.2/0.9	3/25	Top hat
Preheating	200 / 85	6	10	20/8.5	3.3/1.4	3/25	Top hat
Preheating	200 / 85	8	10	20/8.5	2.5/1.1	3/25	Top hat
Preheating	200 / 85	10	10	20/8.5	2/0.9	3/25	Top hat
Preheating	200 / 85	12	10	20/8.5	1.7/0.7	3/25	Top hat
Preheating	200 / 85	10	6	33.3/14.2	3.3/1.4	3/25	Top hat
Preheating	200 / 85	10	7	28.6/12.1	2.9/1.2	3/25	Top hat
Preheating	200 / 85	10	8	25/10.6	2.5/1.1	3/25	Top hat
Preheating	200 / 85	10	9	22.2/9.4	2.2/0.9	3/25	Top hat

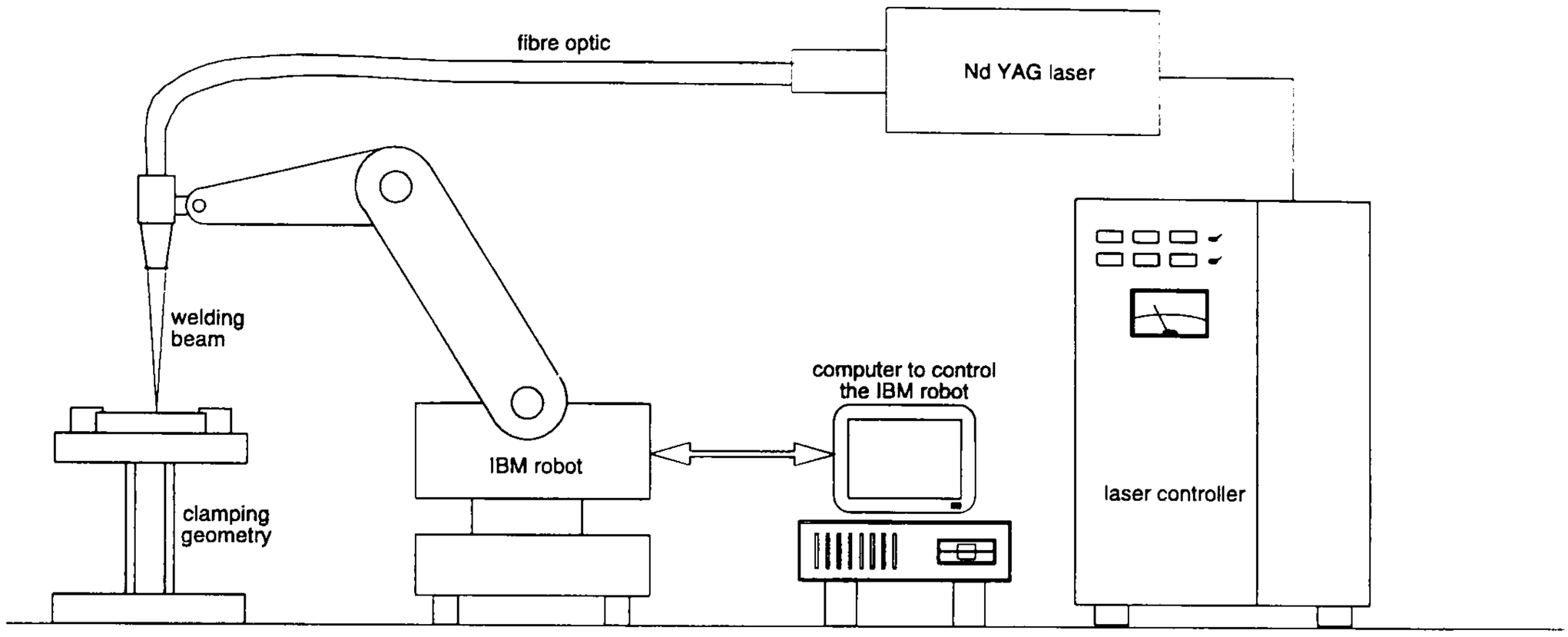

Figure 5.1. Nd:YAG fibre optic beam delivery system (Flat welding Geometry)

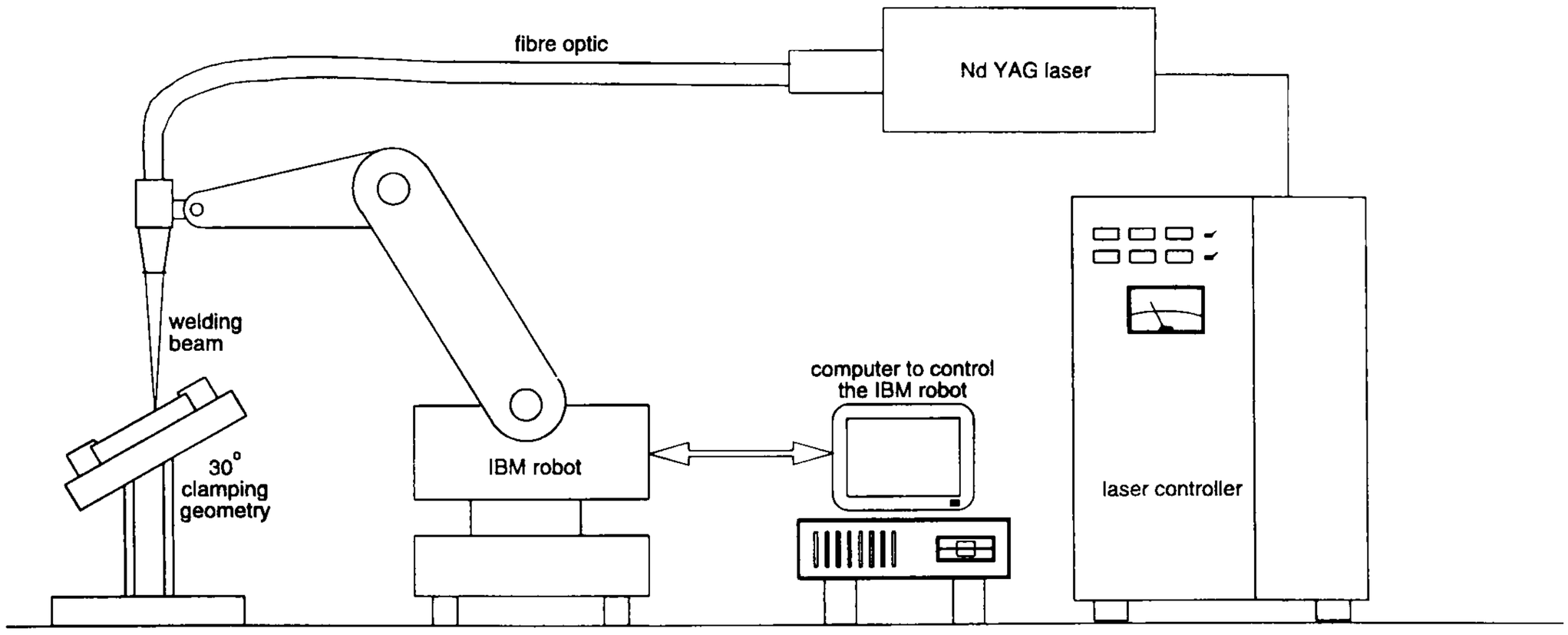

Figure 5.2. Nd:YAG fibre optic beam delivery system (30° Welding Geometry)

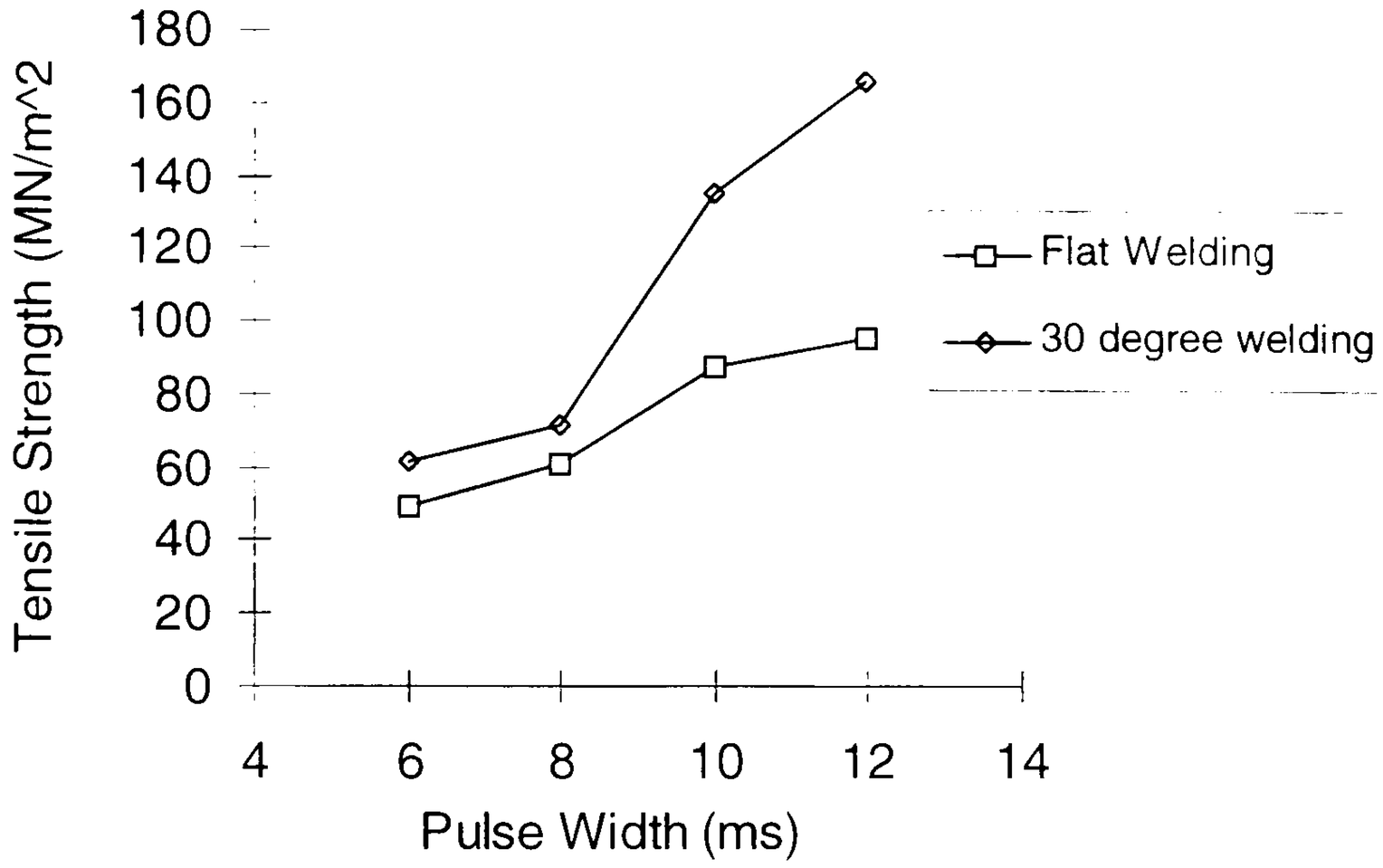

Figure 5.3 Tensile strength as a function of pulse width

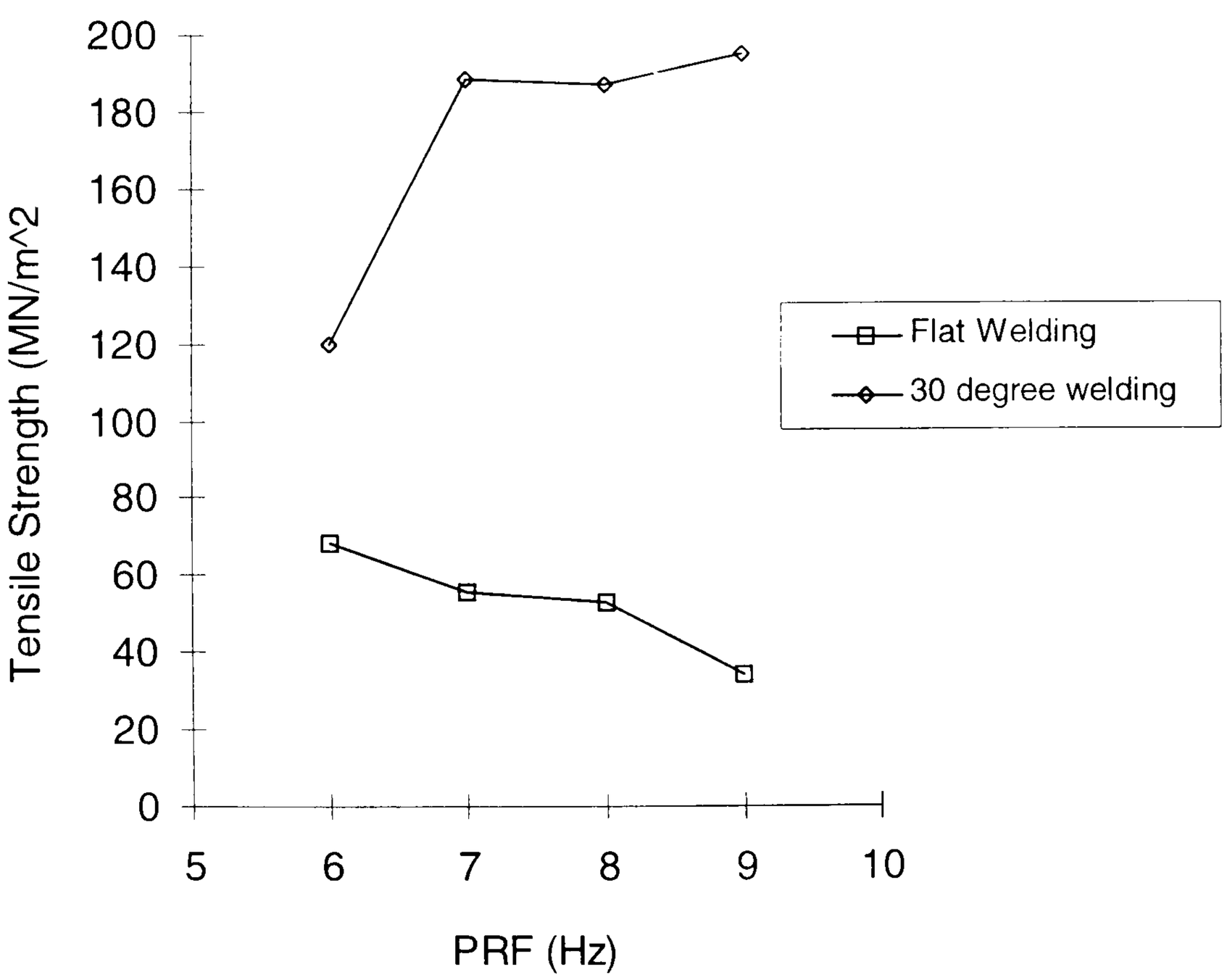

Figure 5.4 Tensile strength as a function of PRF

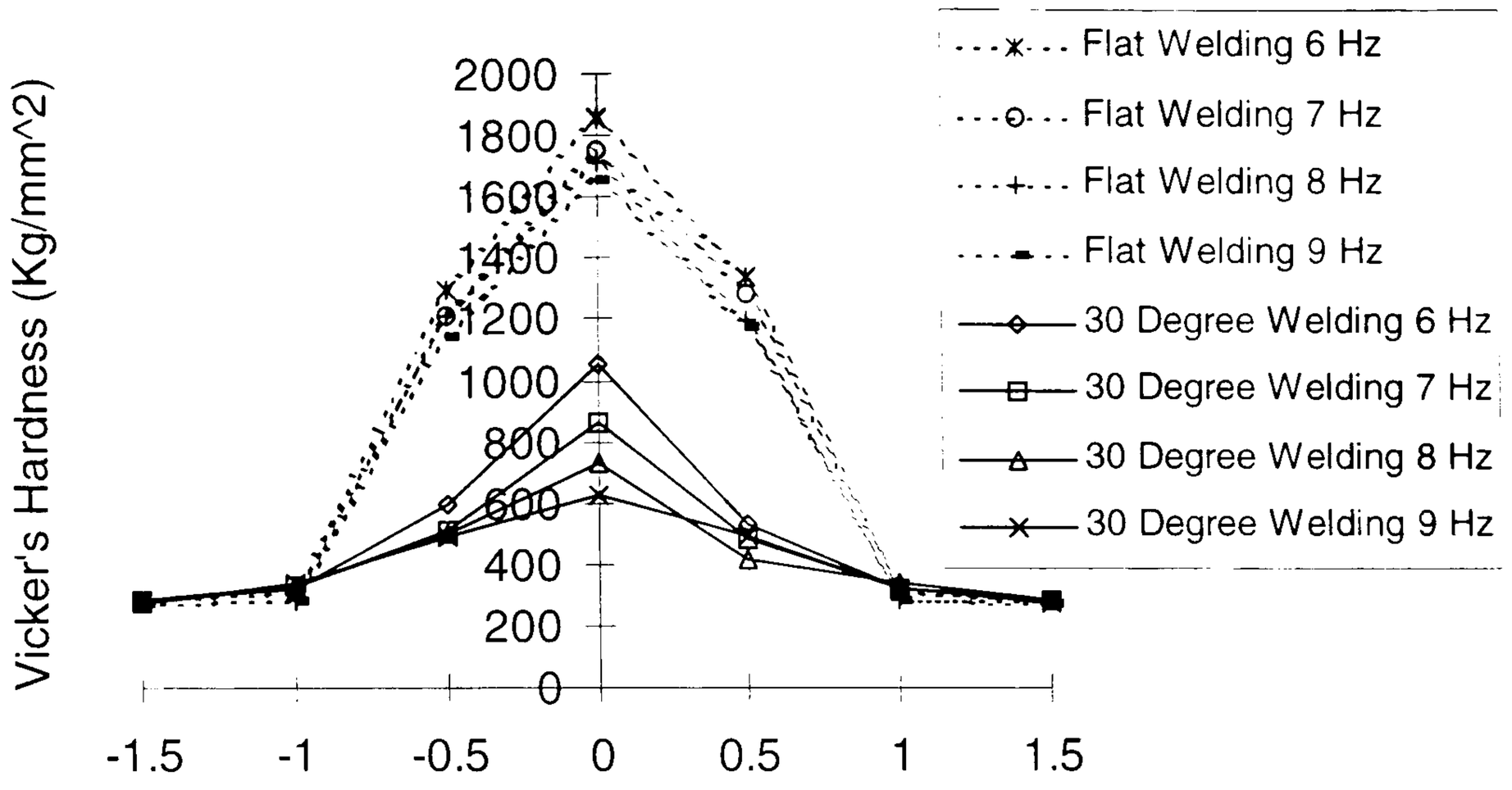

Figure 5.5 Microhardness across the weld for different PRFs

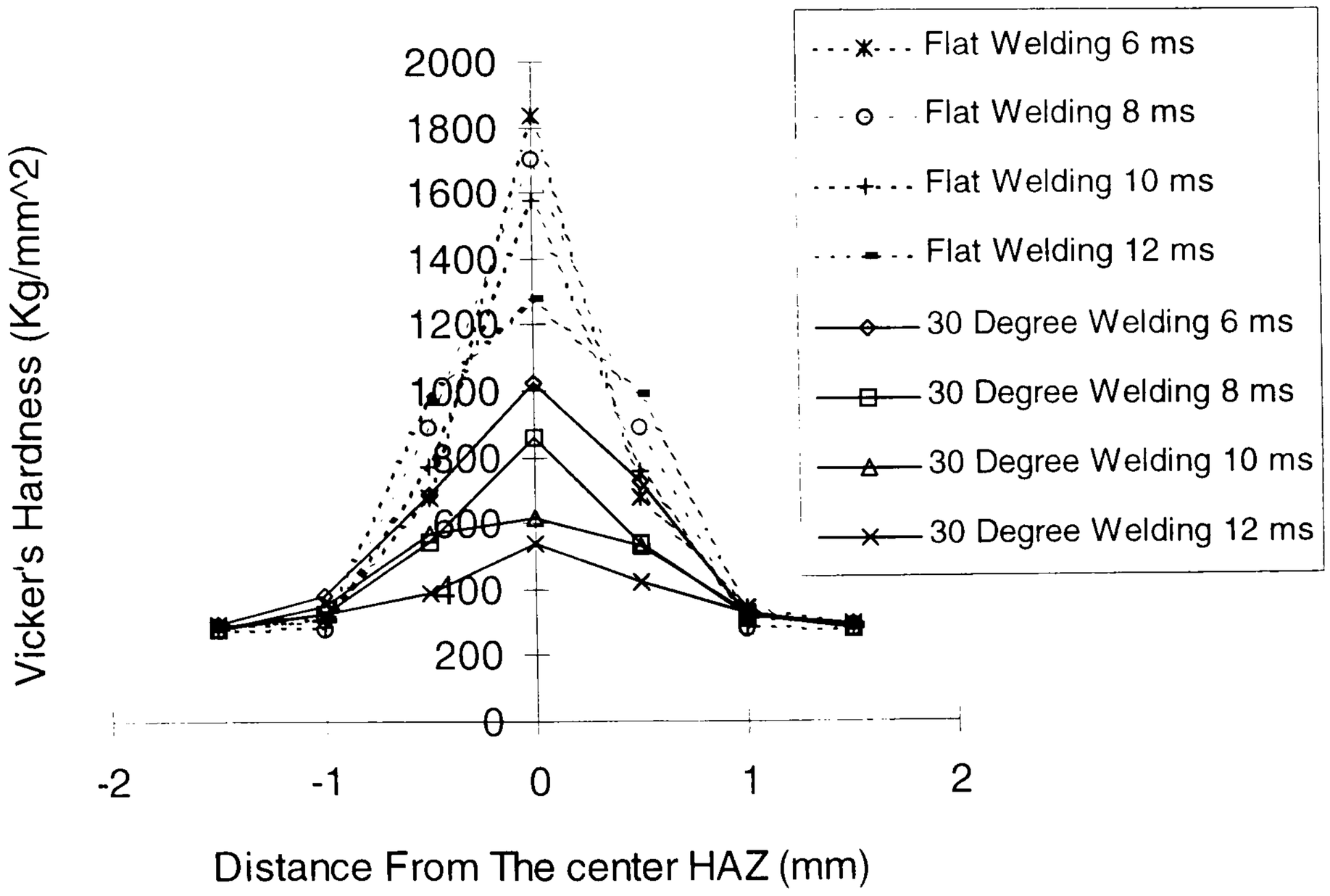

Figure 5.6 Microhardness across the weld for different pulse widths

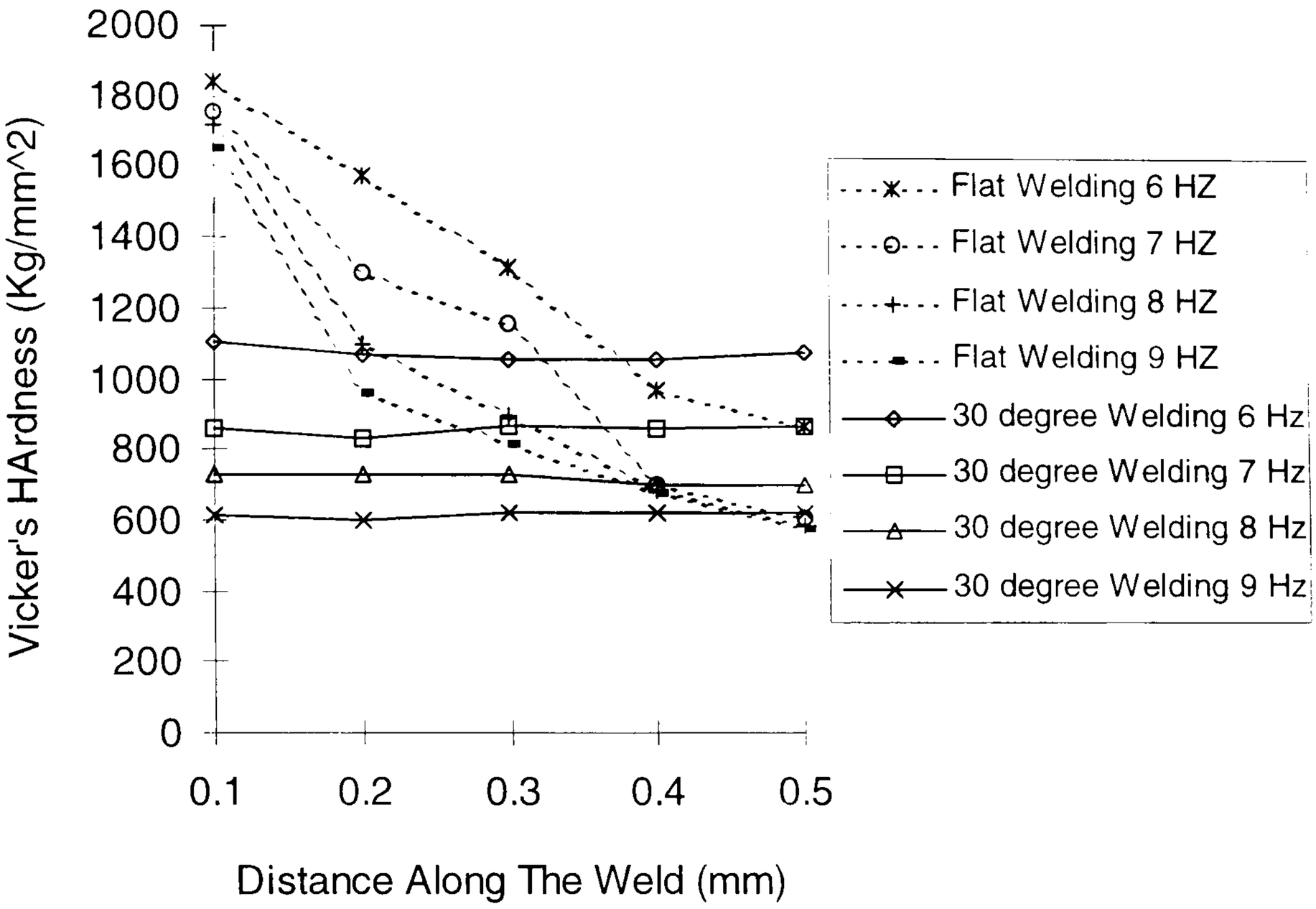

Figure 5.7 Microhardness as a function of weld depth for different PRFs

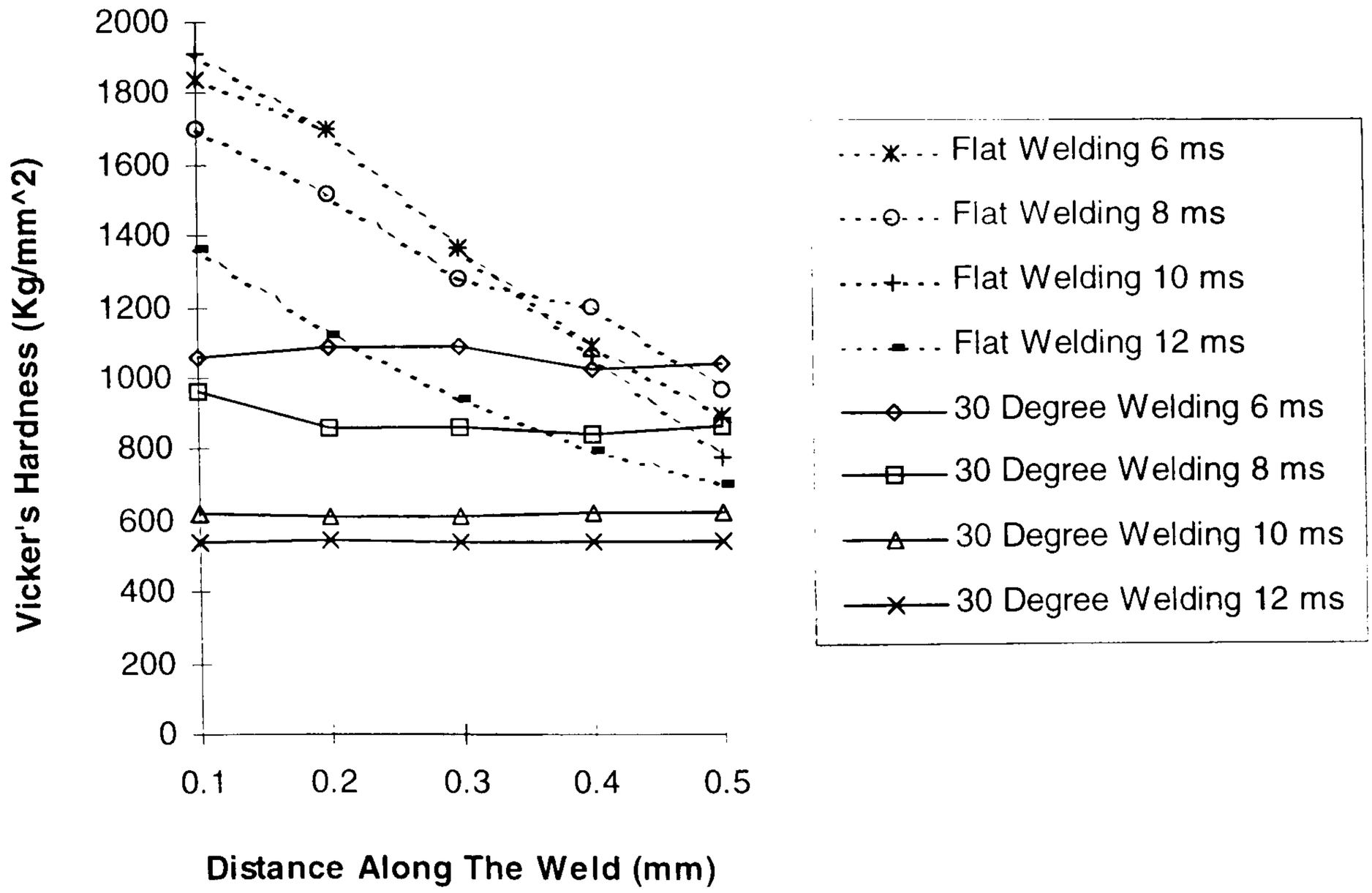

Figure 5.8 Microhardness as a function of weld depth for different pulse widths

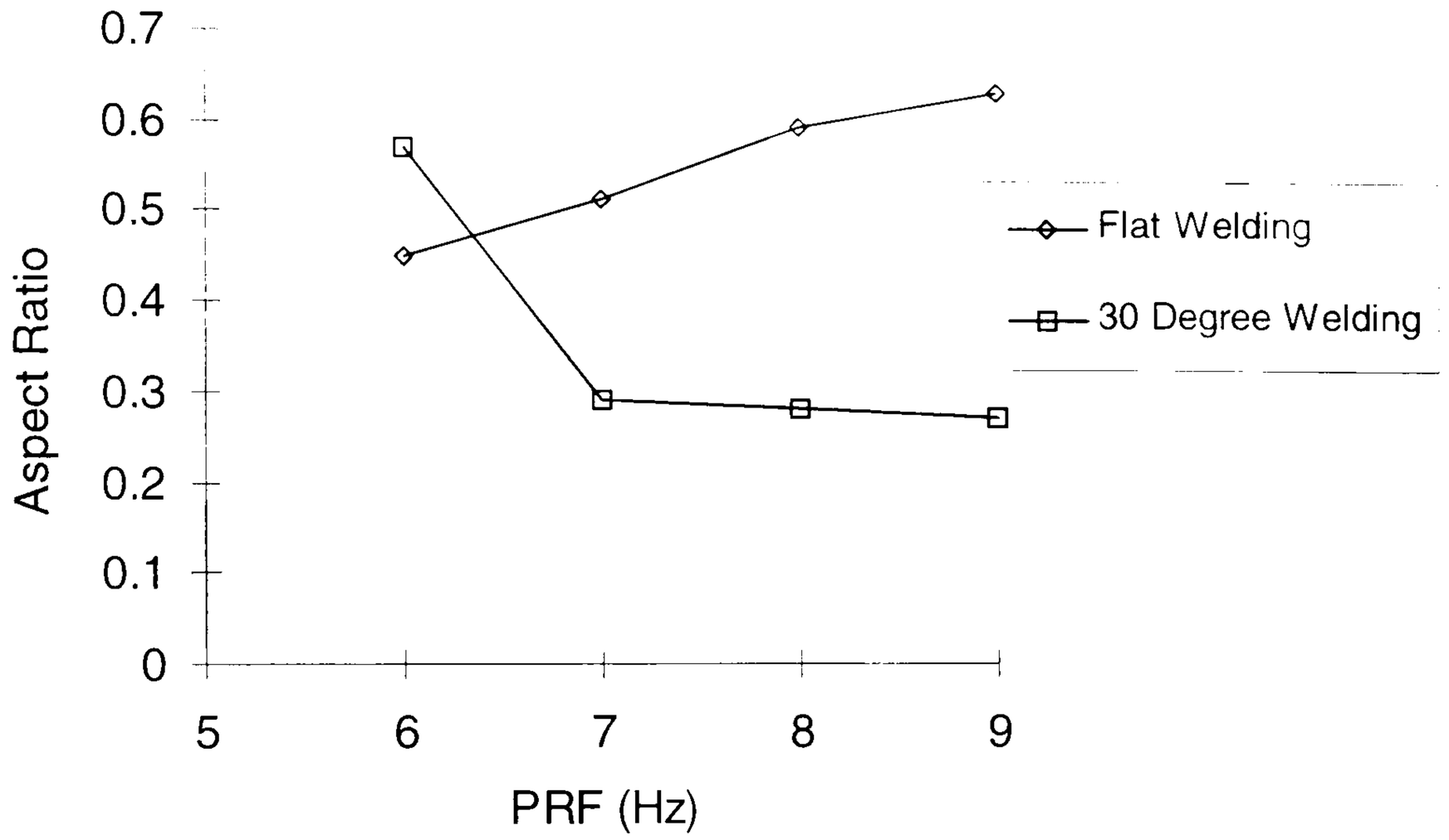

Figure 5.9 Aspect ratio as a function of PRF

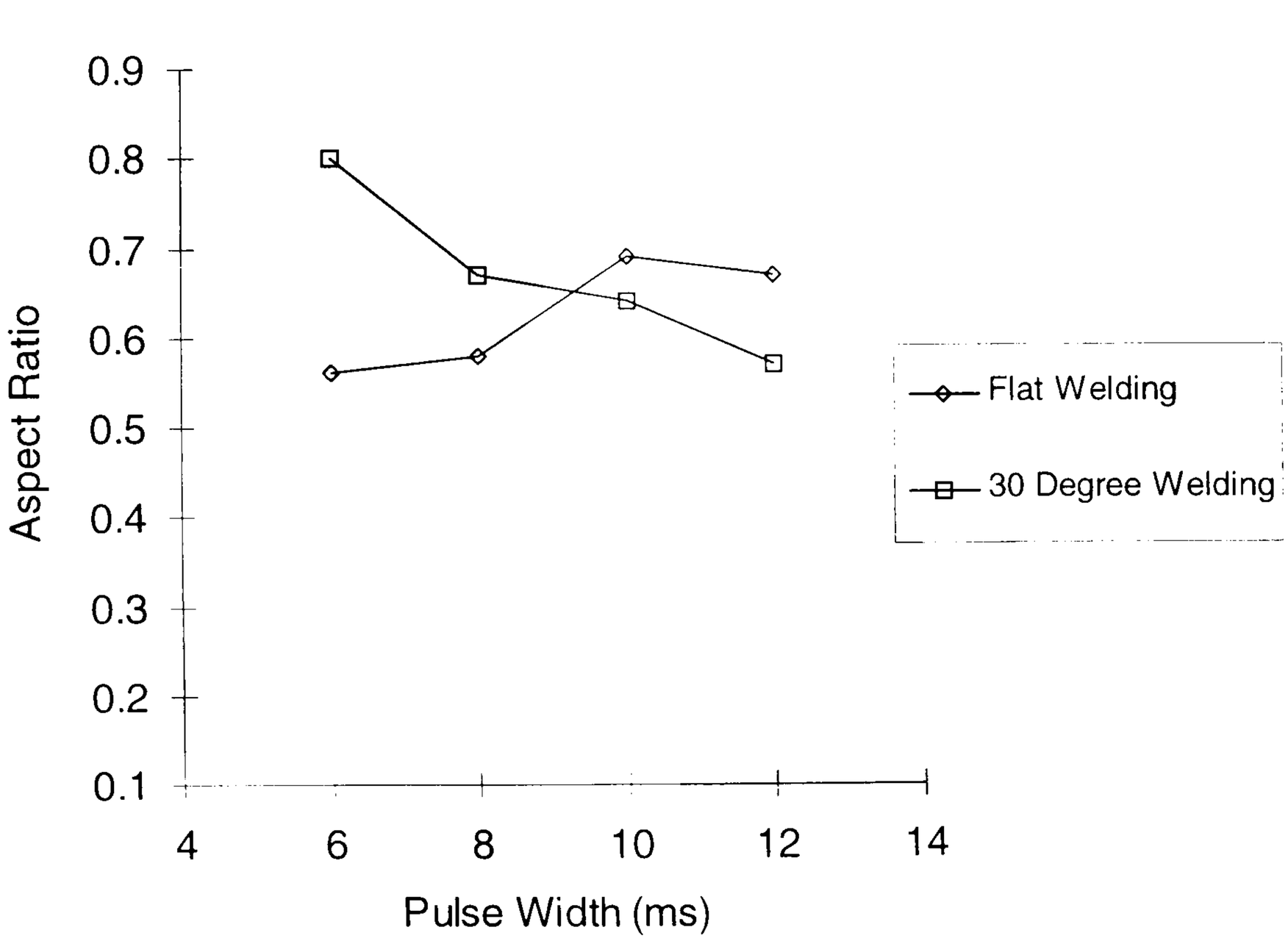

Figure 5.10 Aspect ratio as a function of pulse width

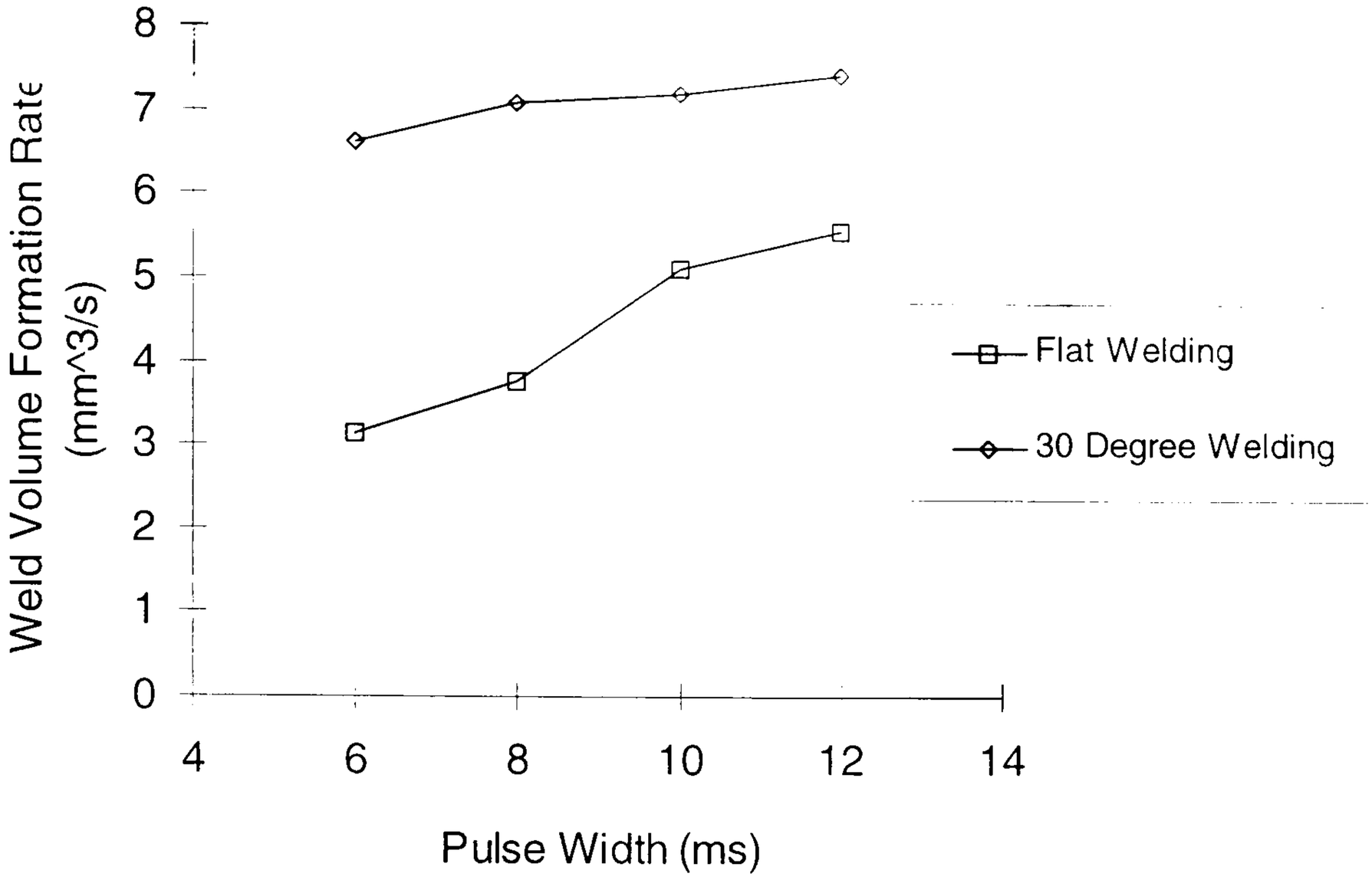

Figure 5.11 Rate of formation of weld volume for different pulse widths

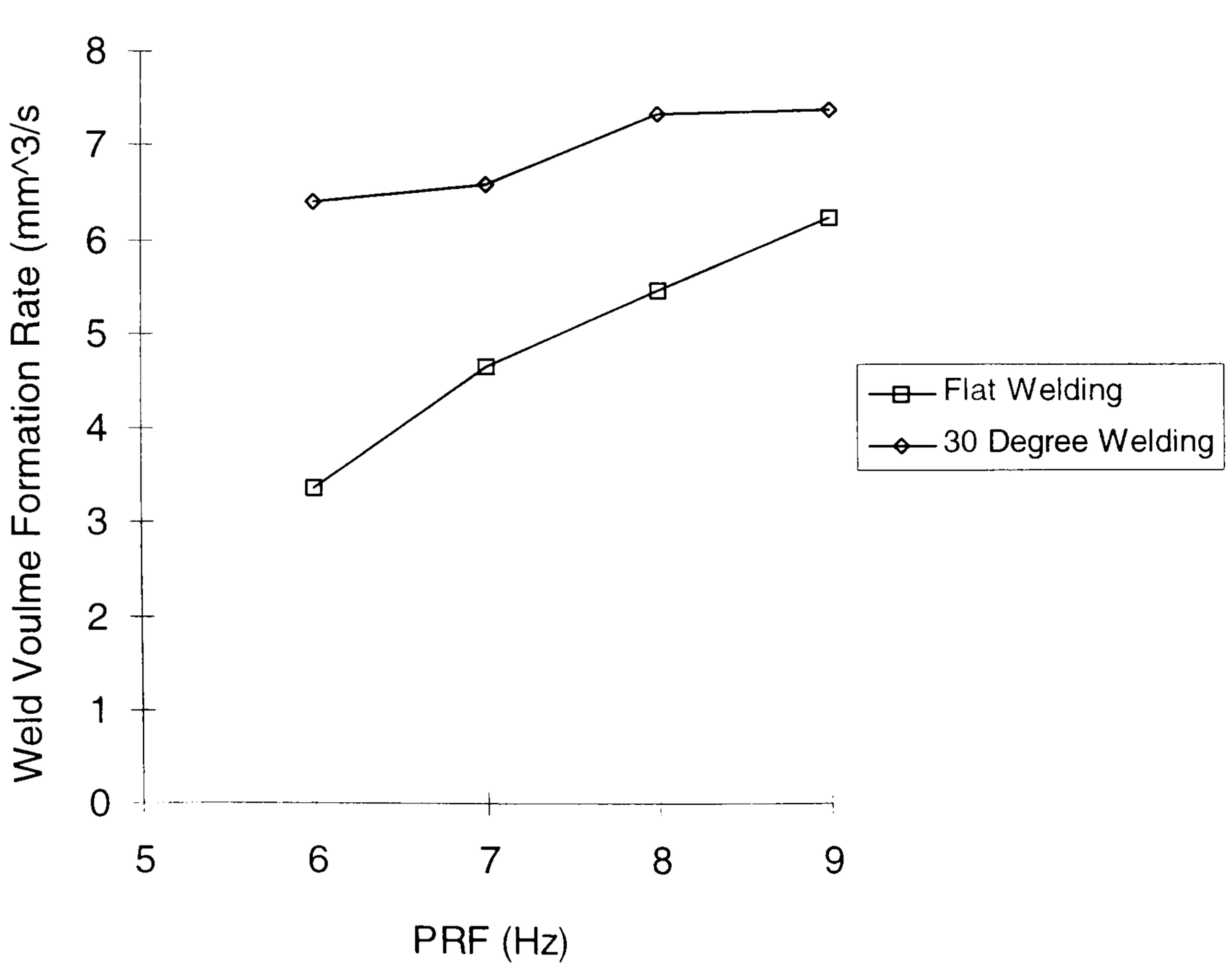

Figure 5.12 Rate of formation of weld volume for different PRFs

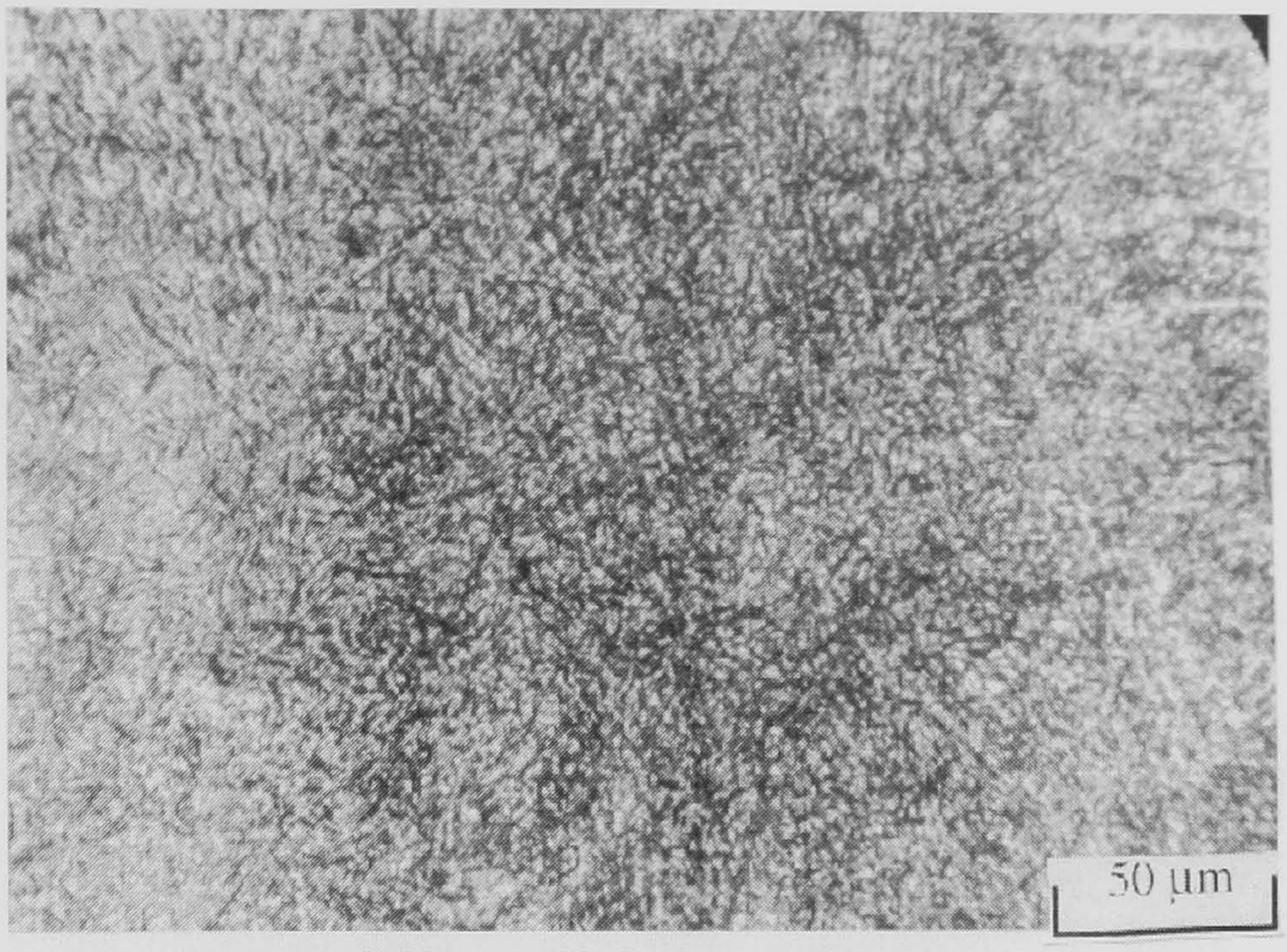

Figure 5.13 Microstructure of fusion for flat welding at a translation velocity of 5 mm/s, pulse width of 8 ms and PRF of 10 Hz: x125 magnification

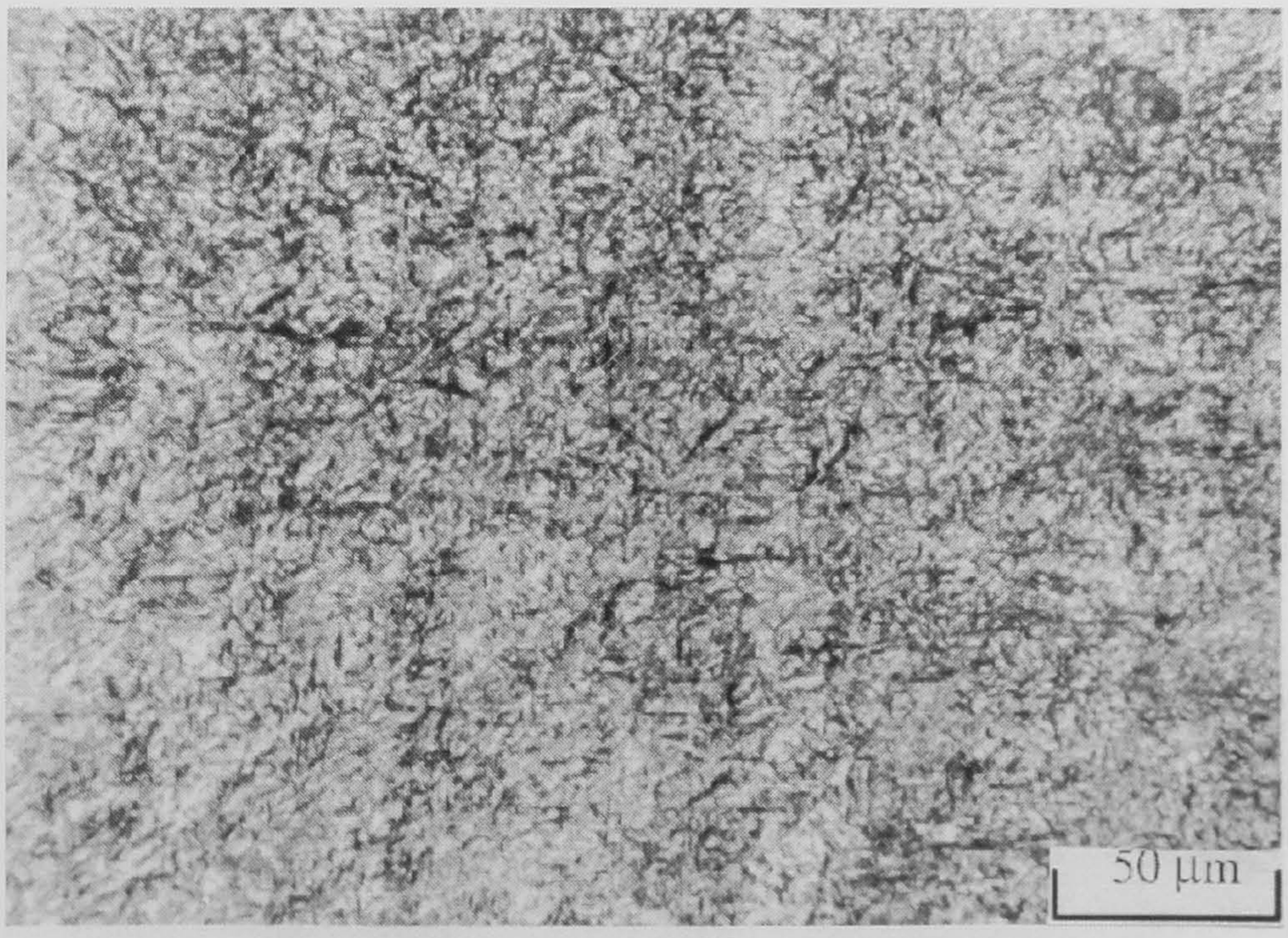

Figure 5.14 Microstructure of fusion for 30° welding at a translation velocity of 5 mm/s, pulse width of 8 ms and PRF of 10 Hz: x125 magnification

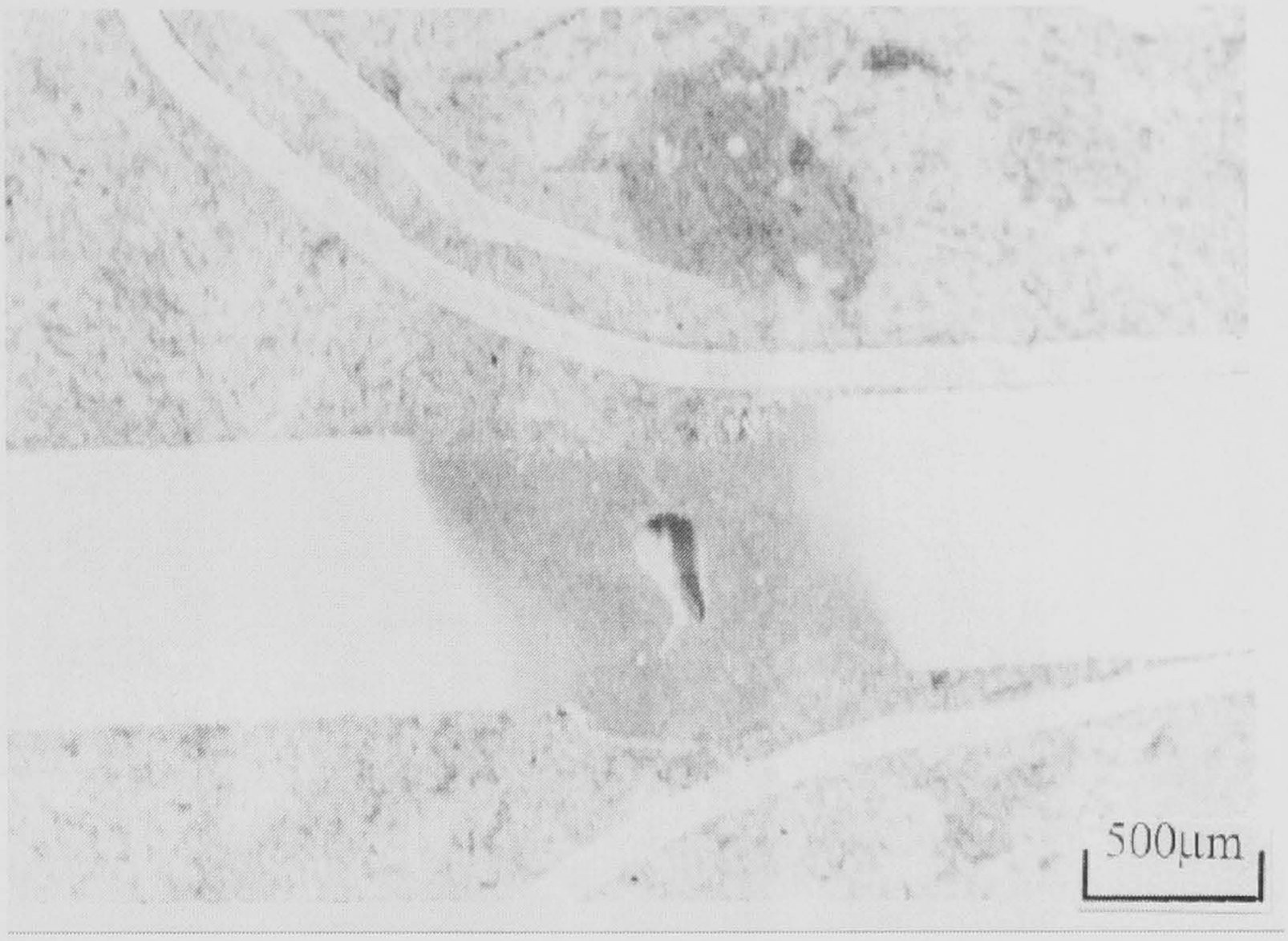

Figure 5.15 Micrograph of the weld width of 30° welding at a translation velocity of 5 mm/s, pulse width of 8 ms and PRF of 10 Hz: x8.5 magnification

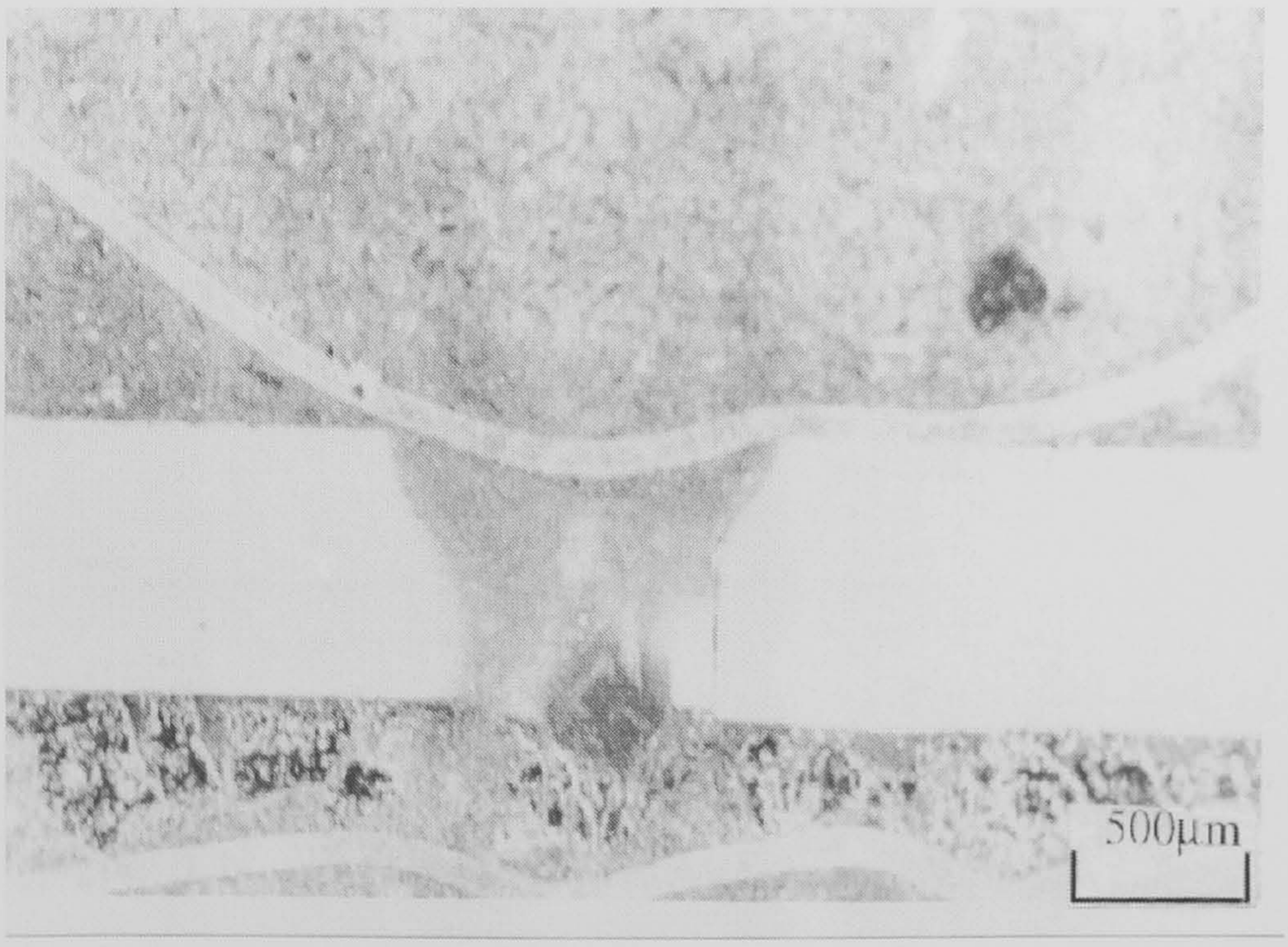

Figure 5.16 Micrograph of the weld width of flat welding at a translation velocity of 5 mm/s, pulse width of 8 ms and PRF of 10 Hz: x8.5 magnification

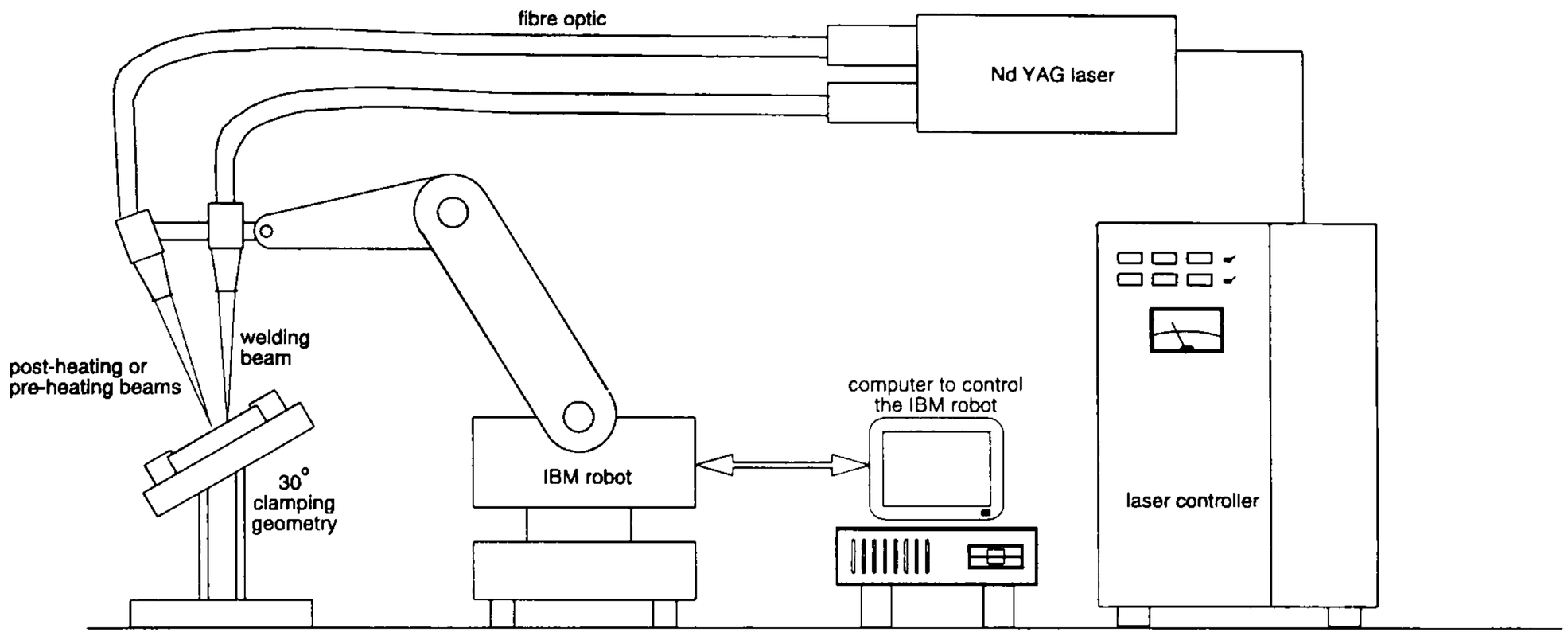

Figure 5.17 Nd:YAG dual-beam delivery system

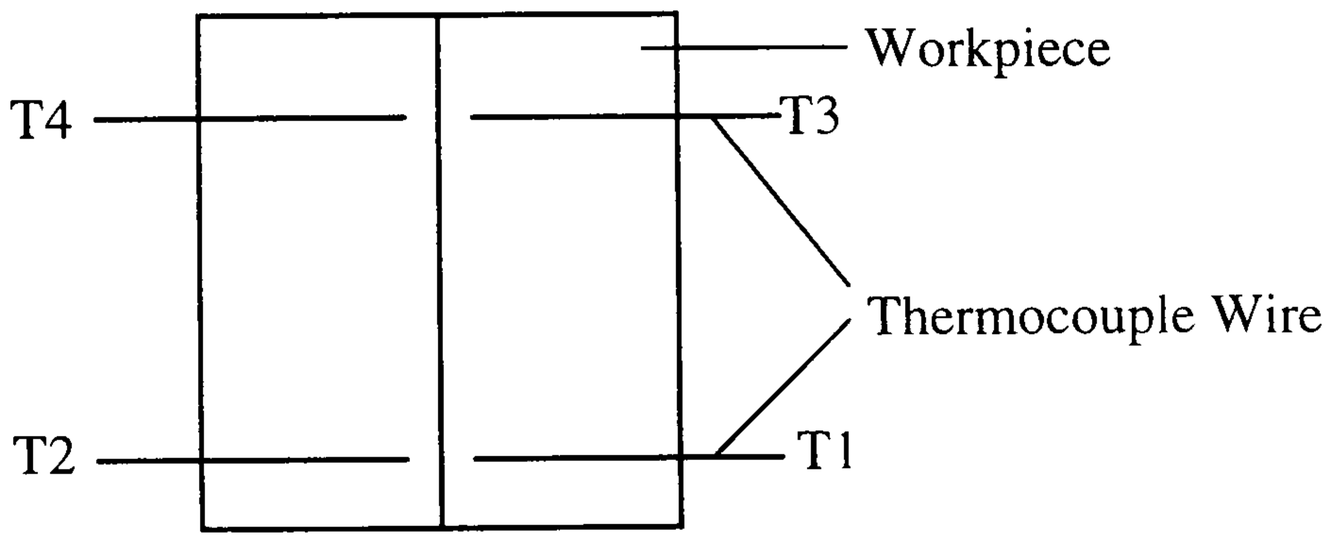

Figure 5.18 Thermocouples attached onto the workpiece

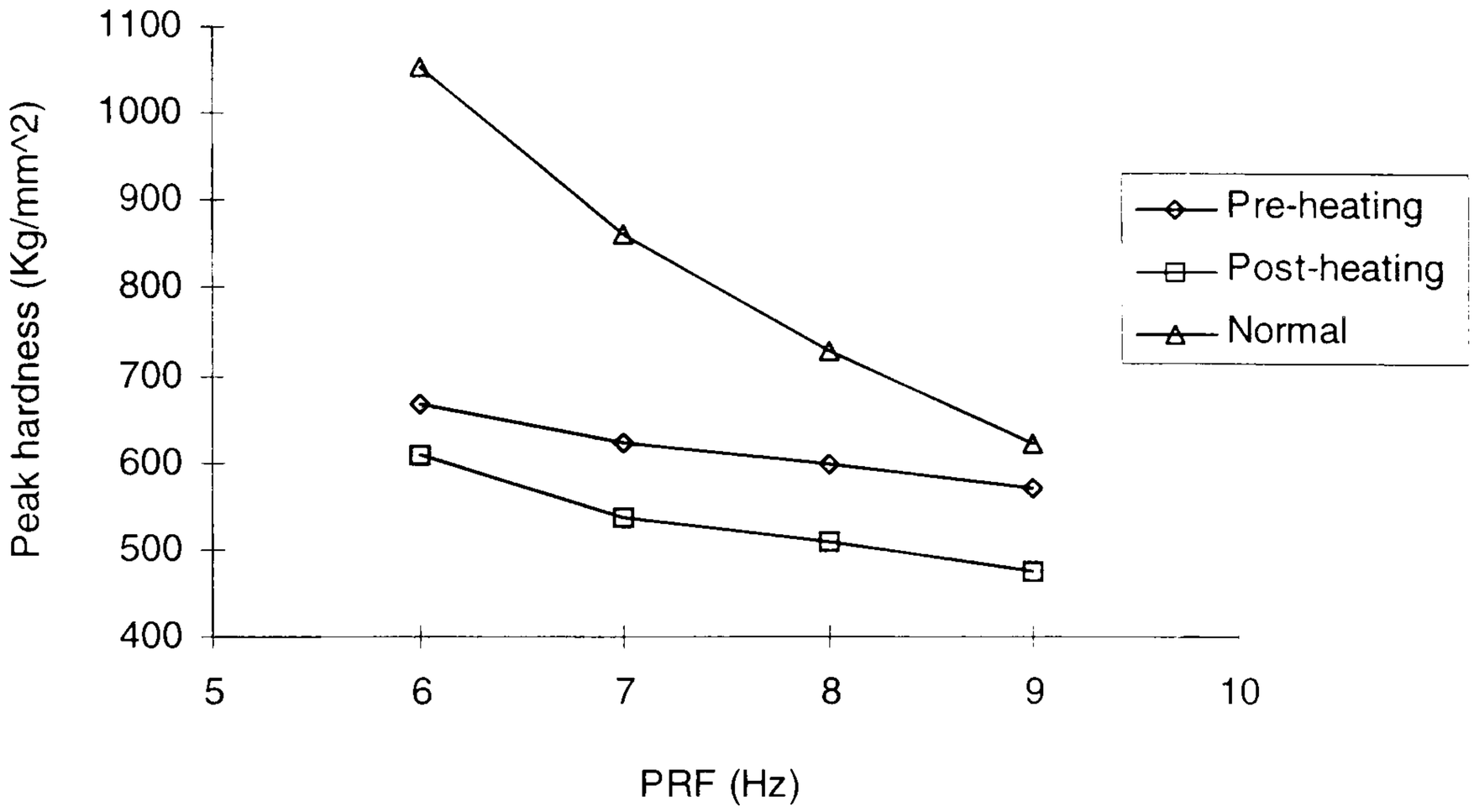

Figure 5.19 Peak hardness as a function of PRF

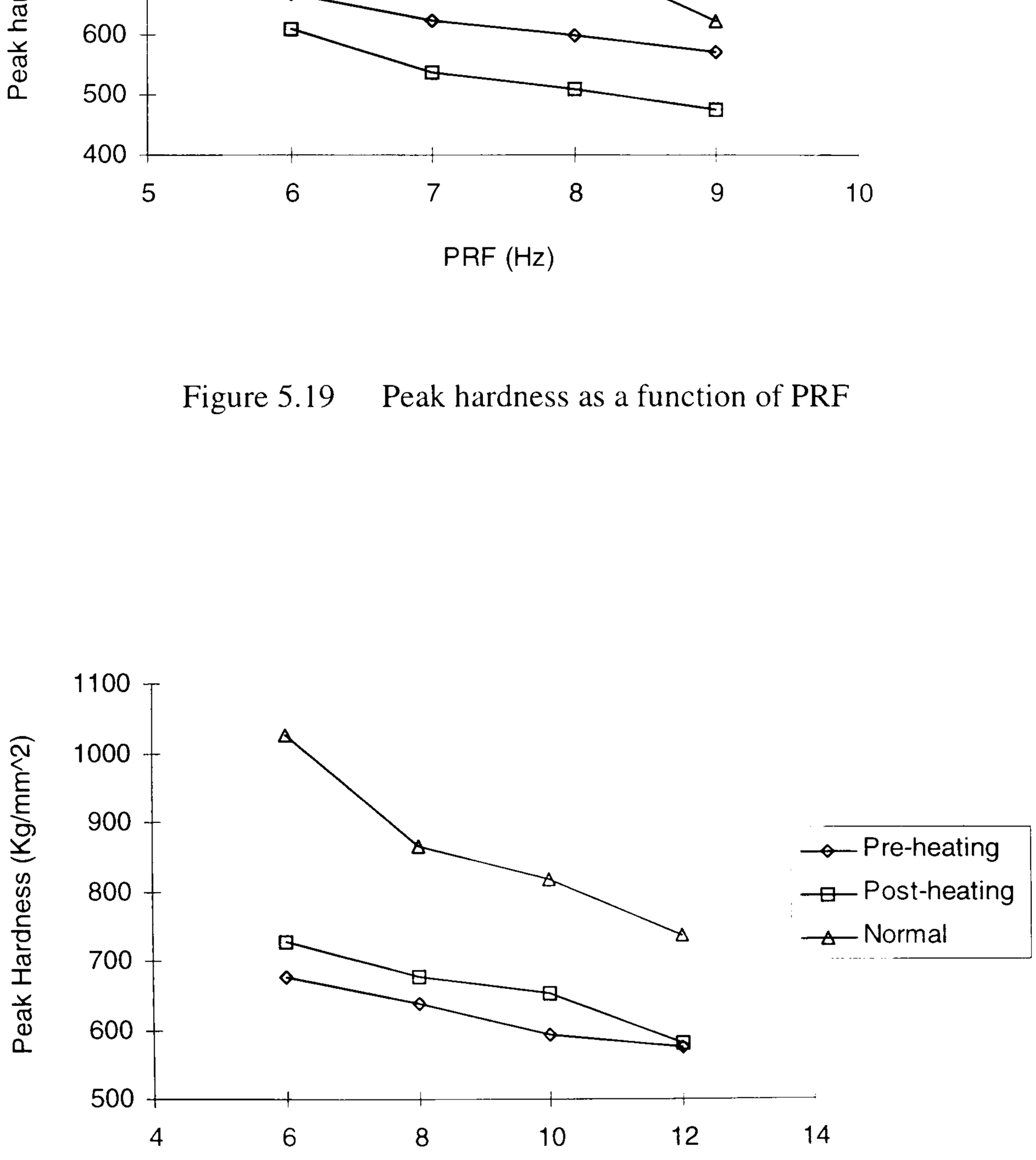

Figure 5.20 Peak hardness as a function of pulse width

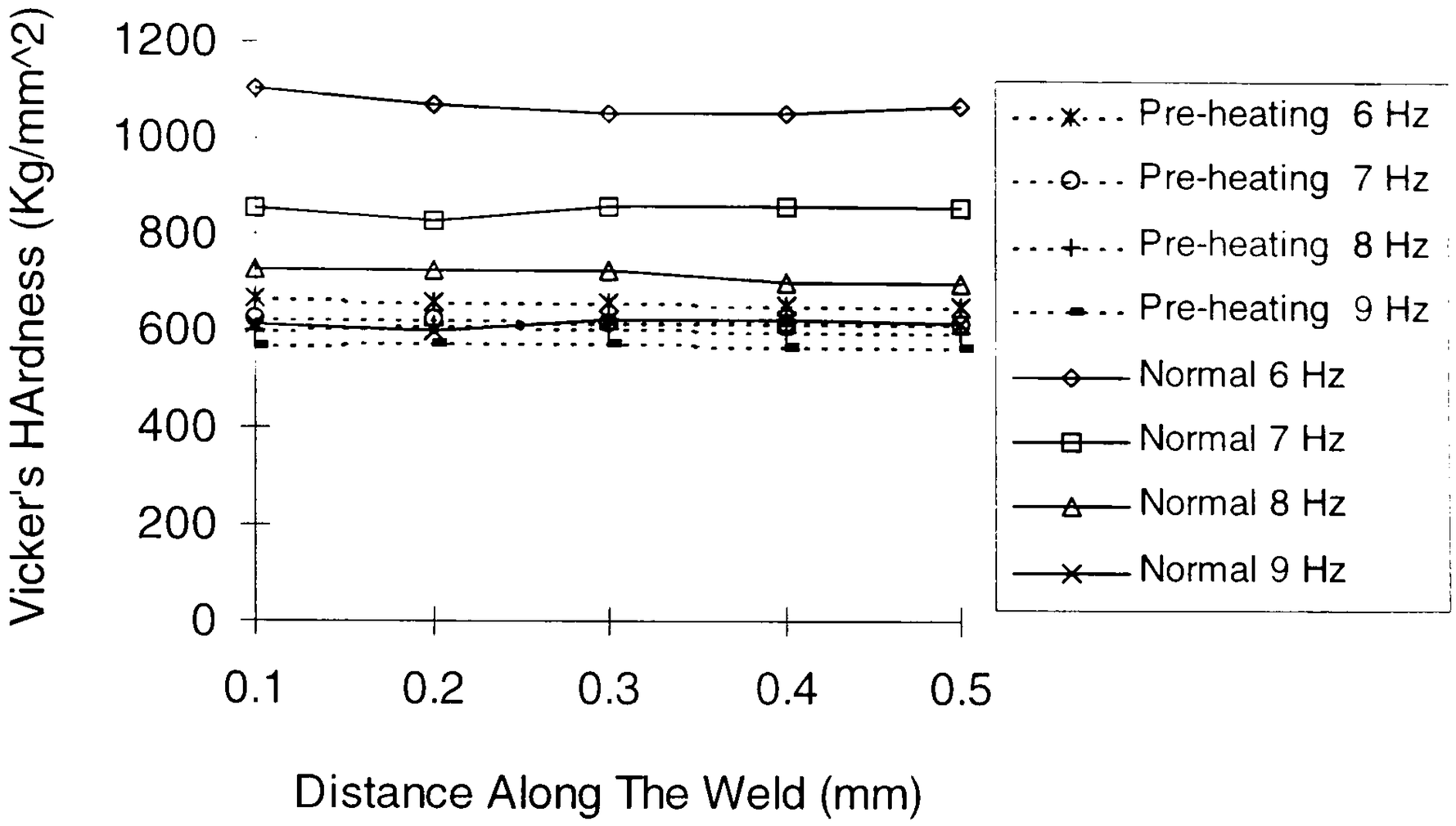

Figure 5.21 Hardness as a function of weld depth for different PRFs

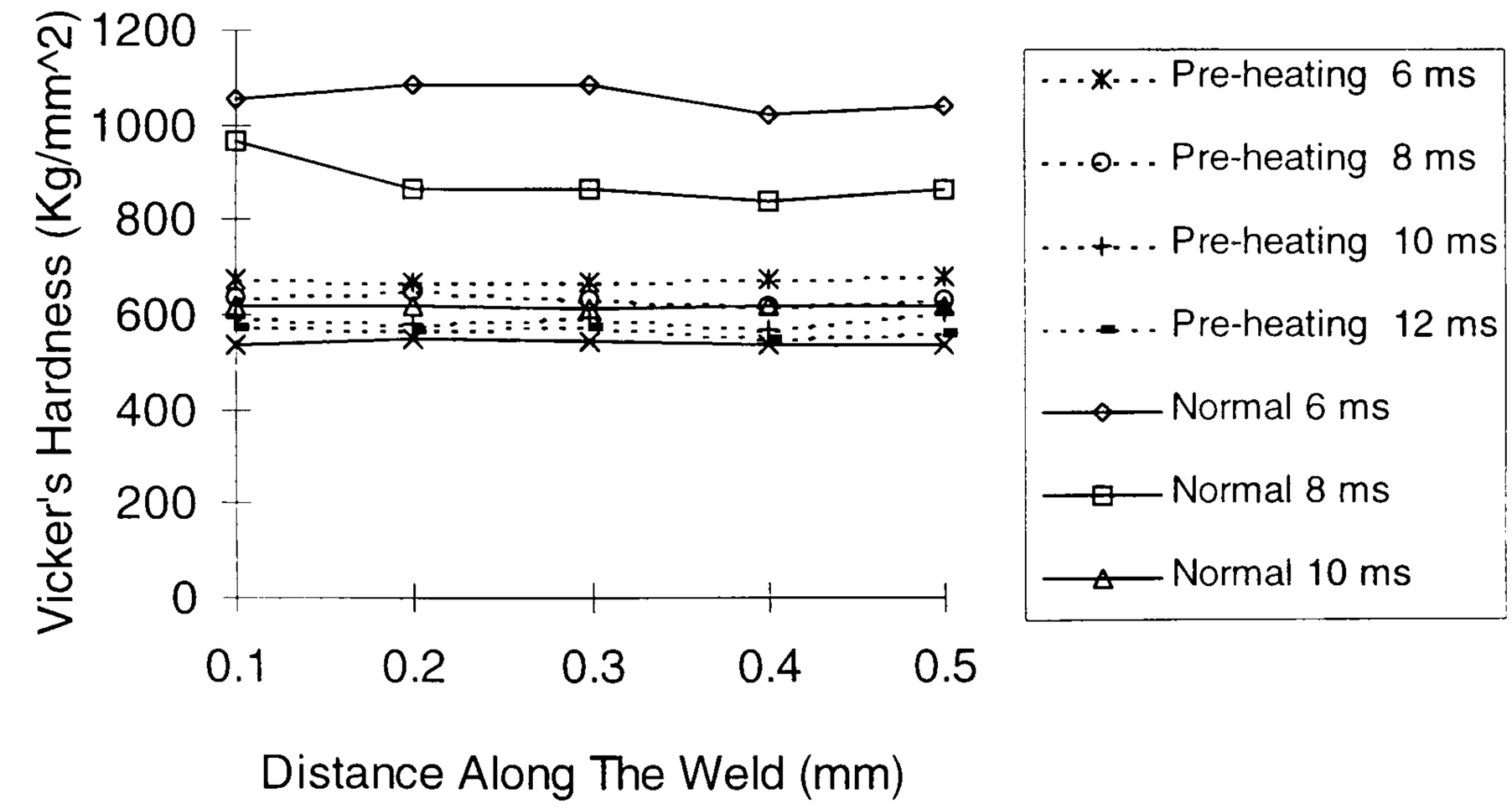

Figure 5.22 Hardness as a function of weld depth for different pulse widths

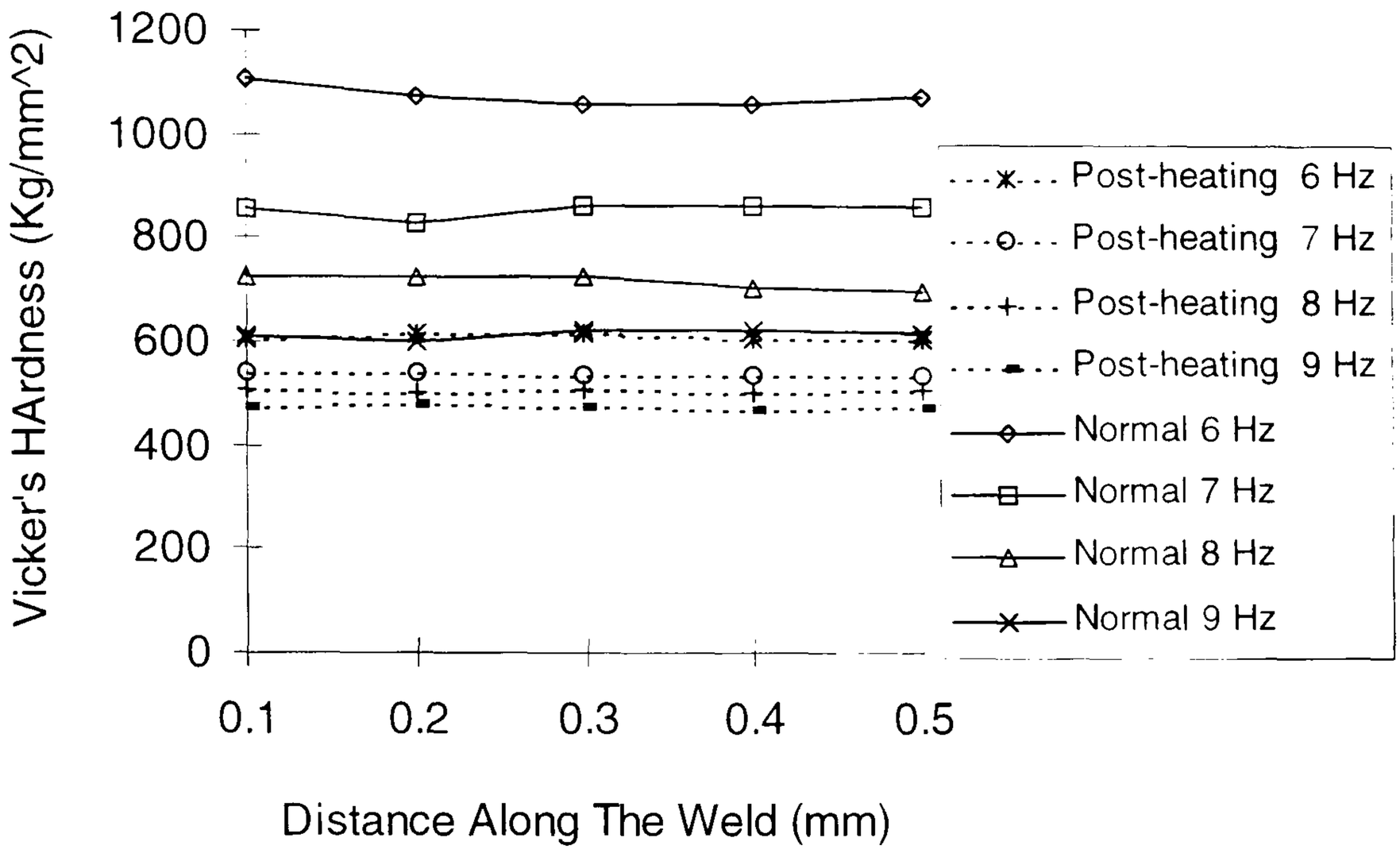

Figure 5.23 Hardness as a function of weld depth for different PRFs

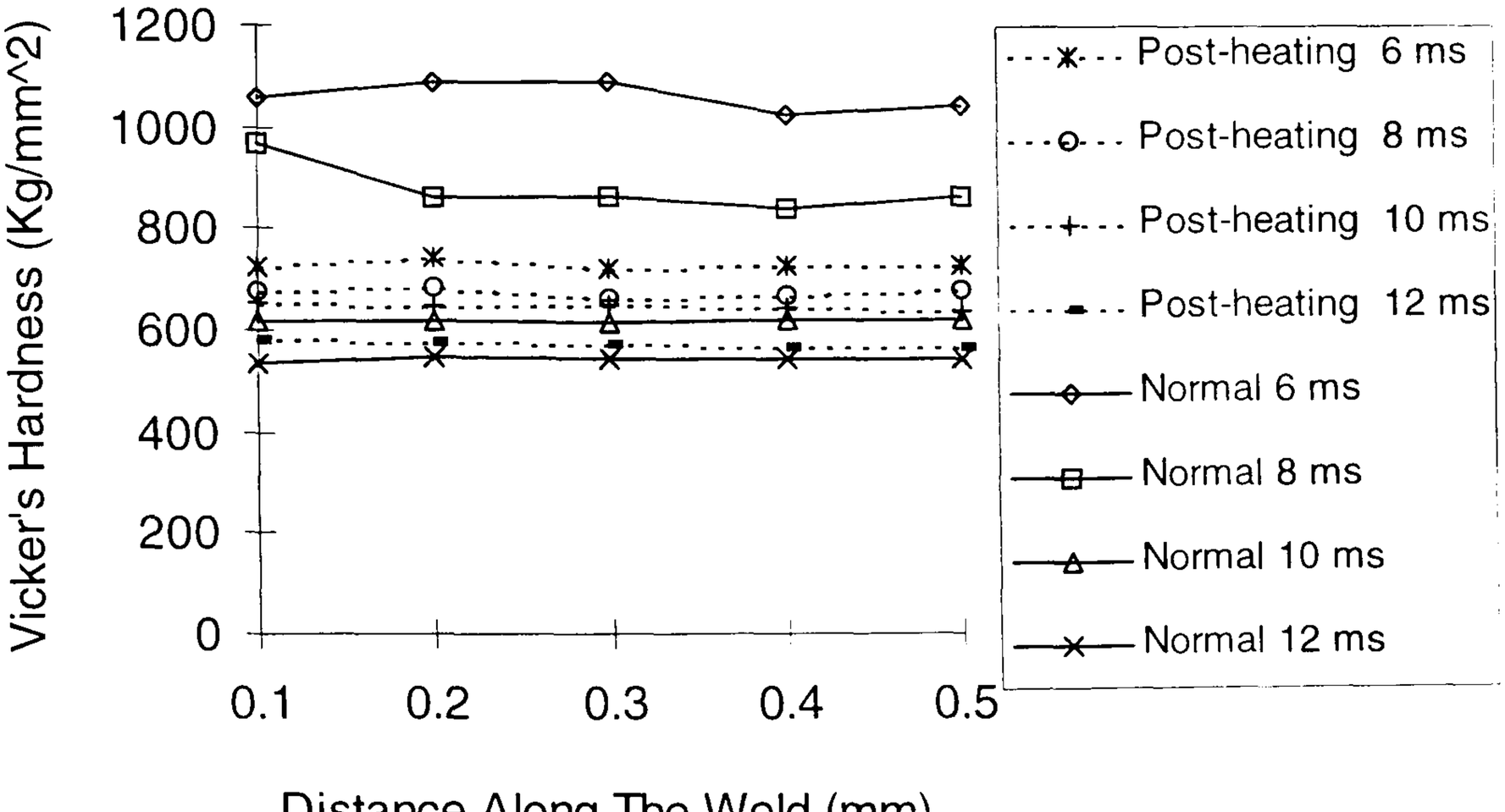

Figure 5.24 Hardness as a function of weld depth for different pulse widths

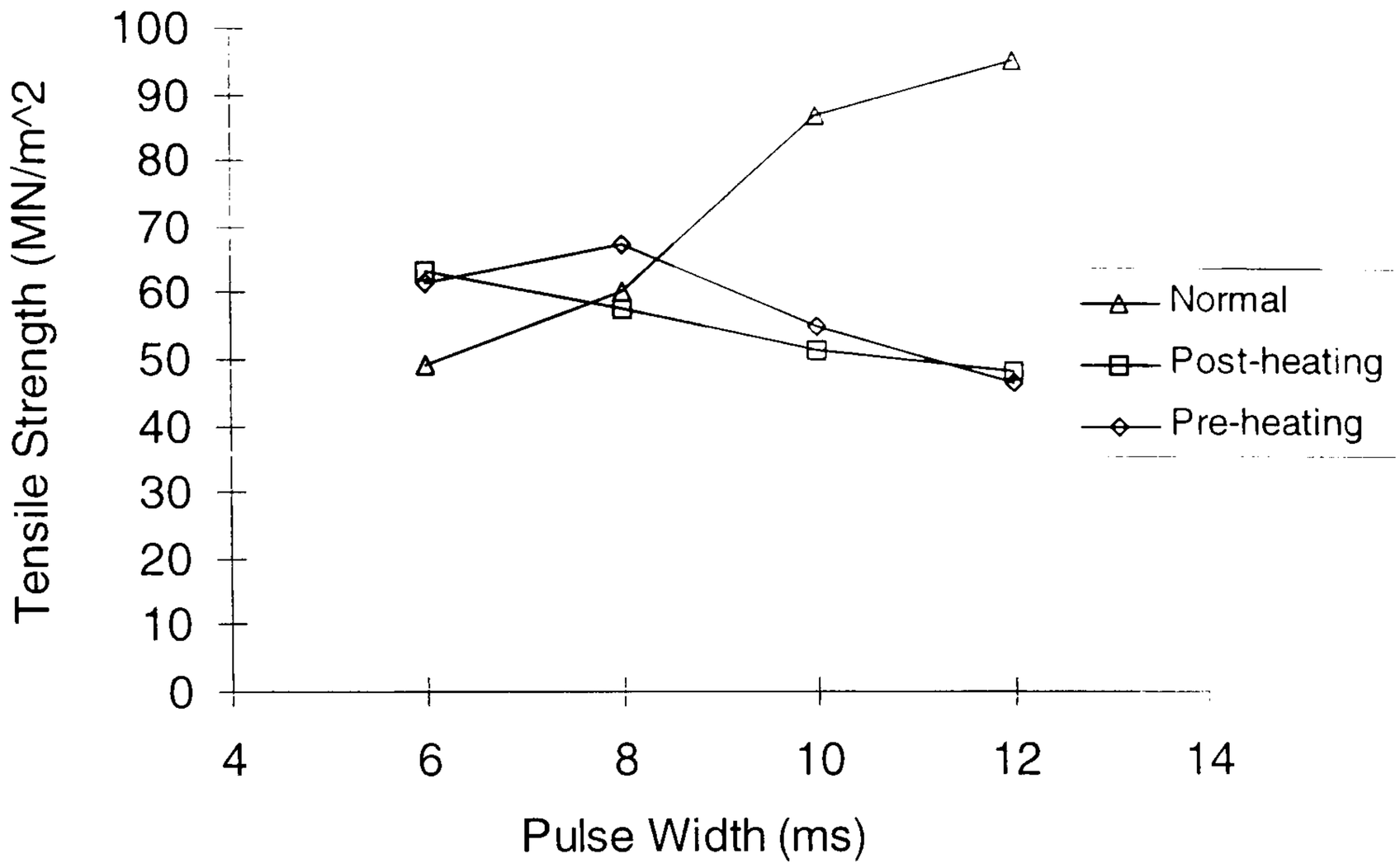

Figure 5.25 Tensile strength as a function of pulse widths

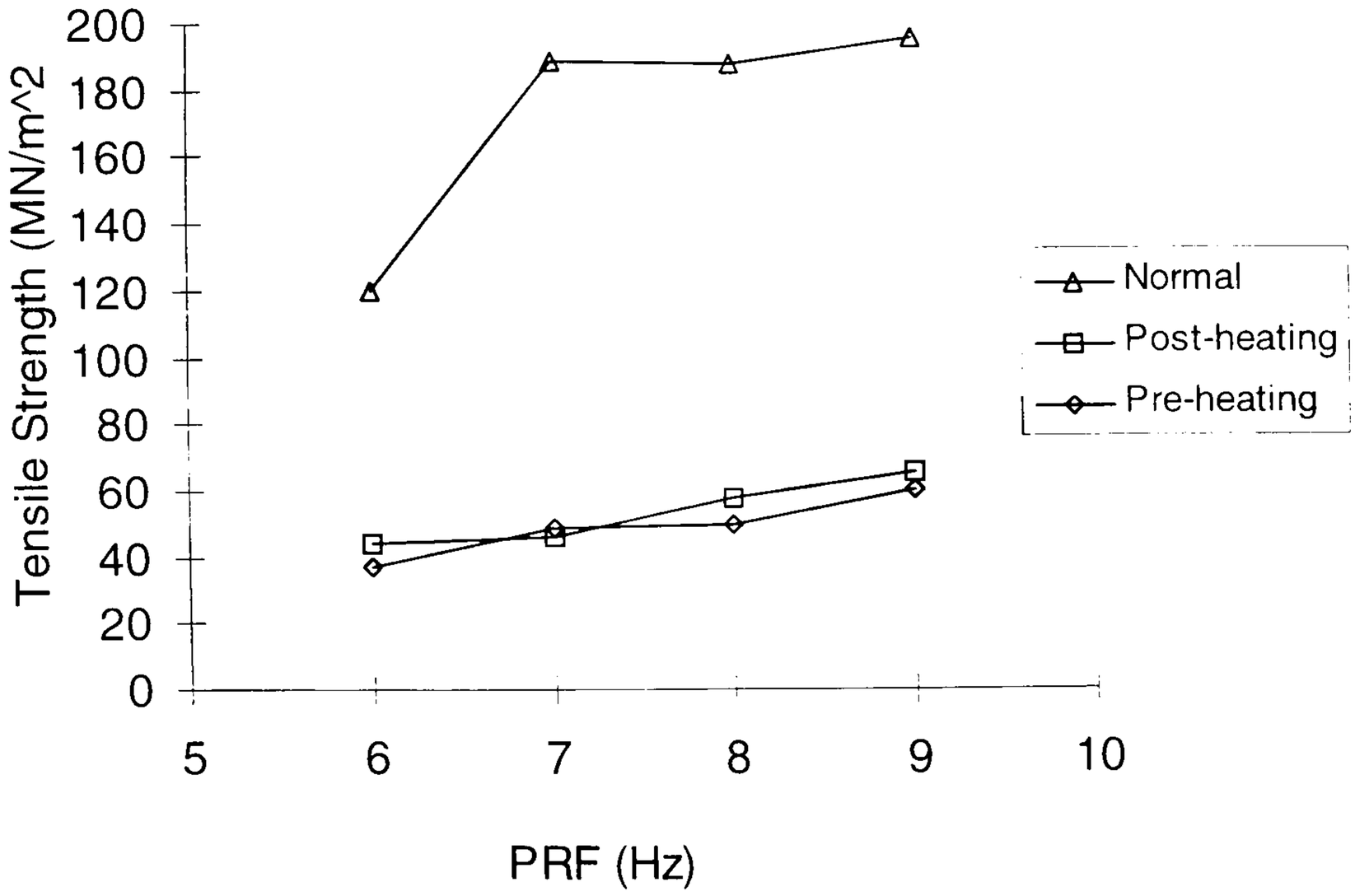

Figure 5.26 Tensile strength as a function of PRFs

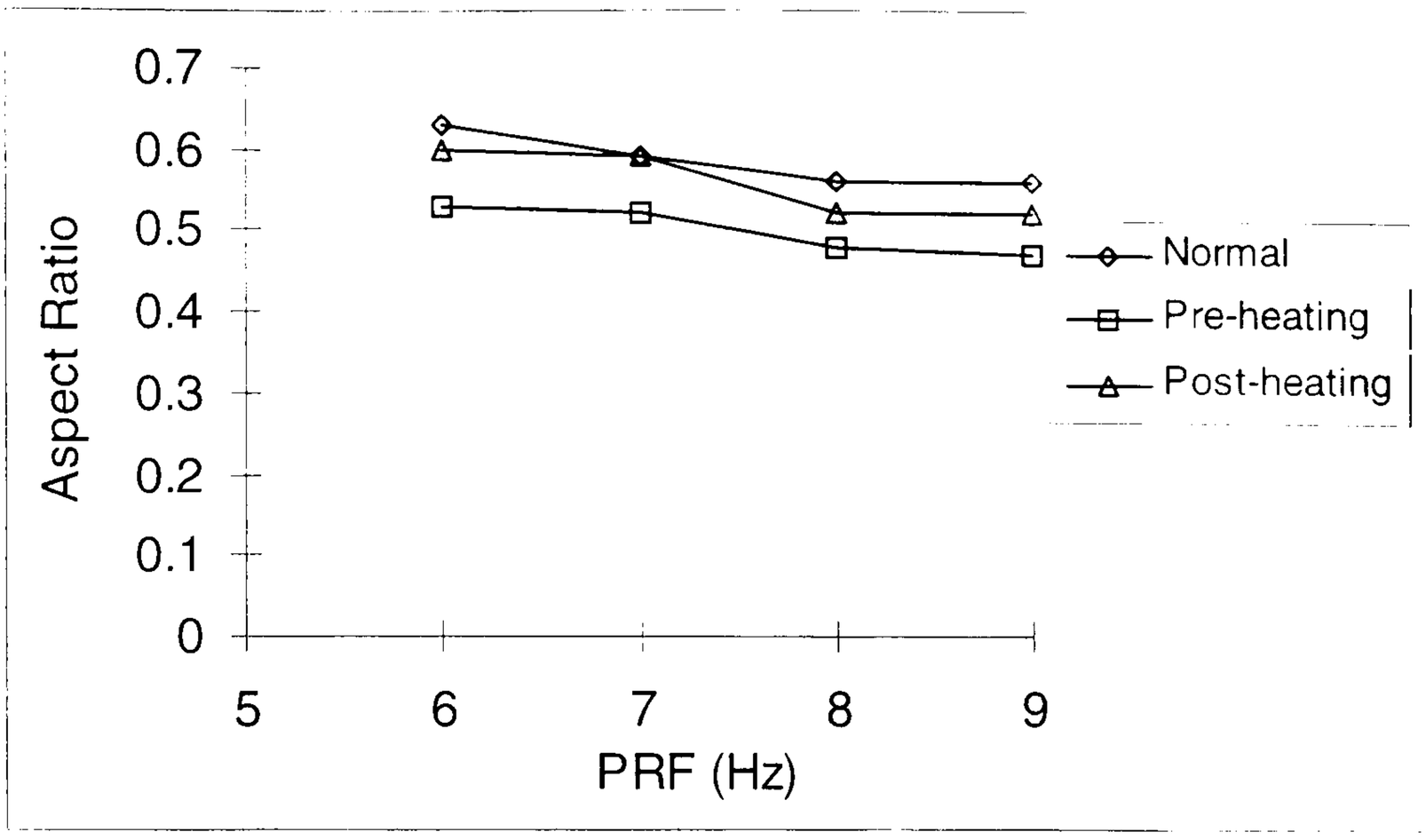

Figure 5.27 Aspect ratio as a function of PRFs

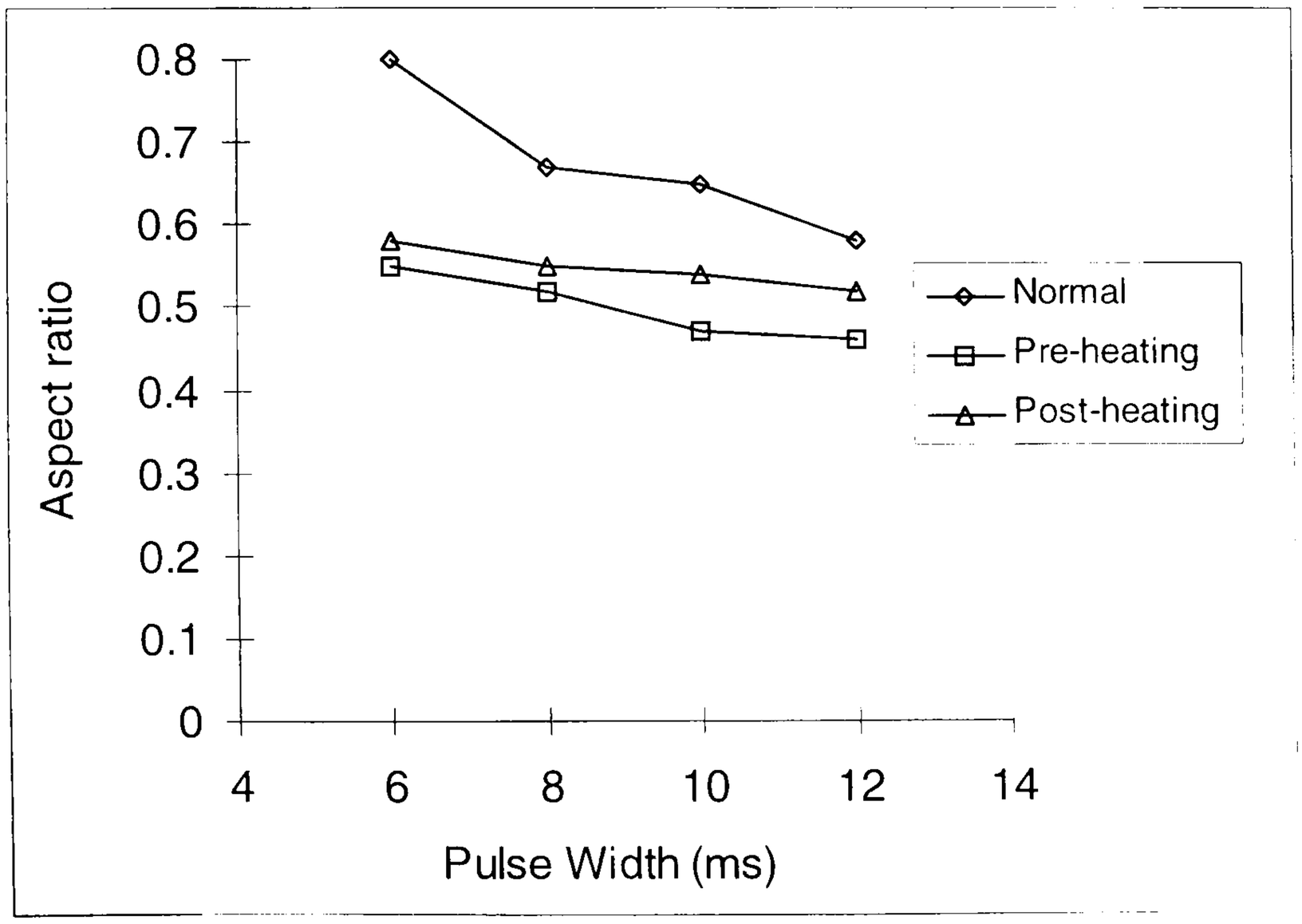

Figure 5.28 Aspect ratio as a function of pulse widths

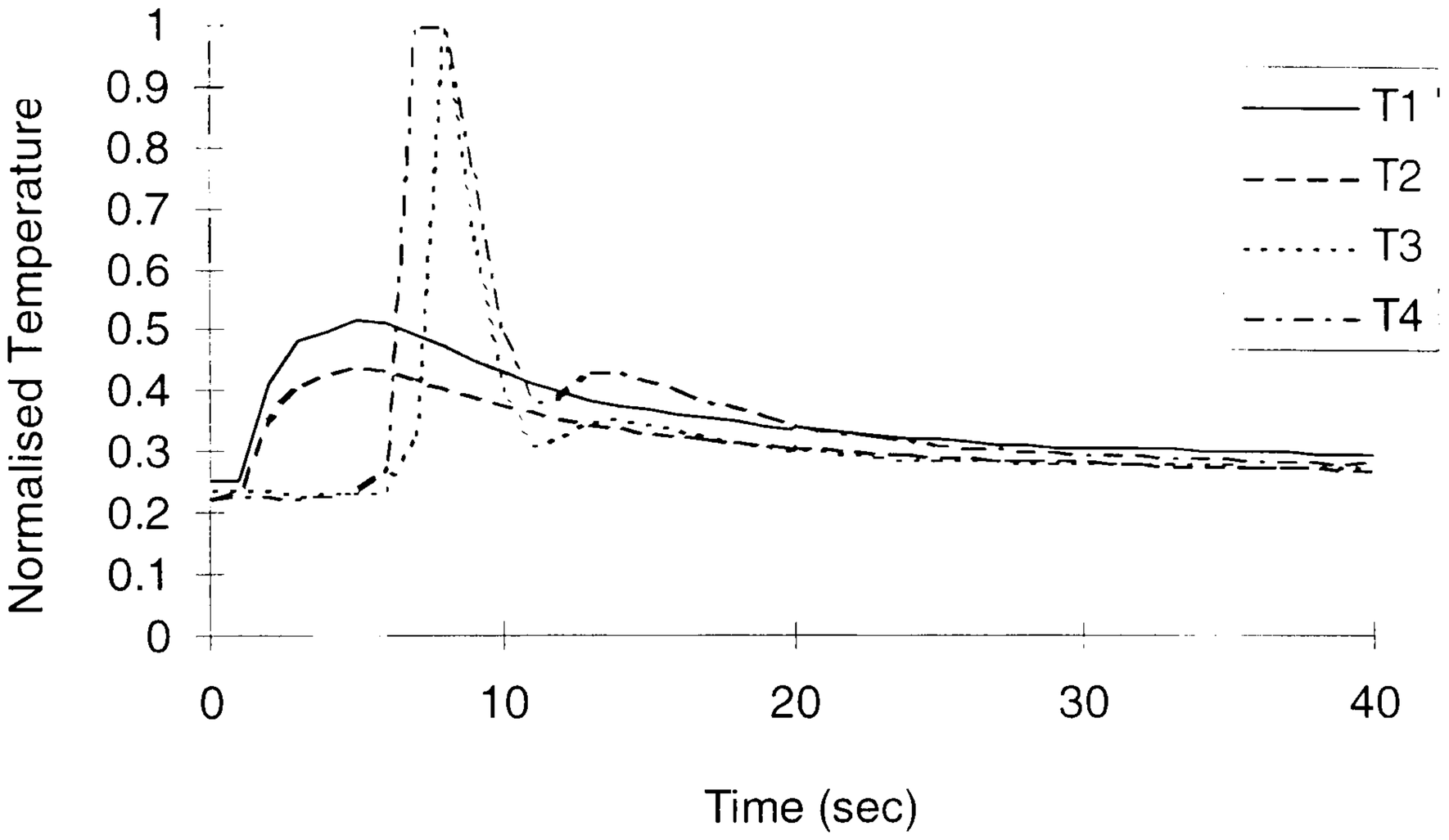

Figure 5.29 Normalised temperature for the post-heated welds with a PRF of 7 Hz

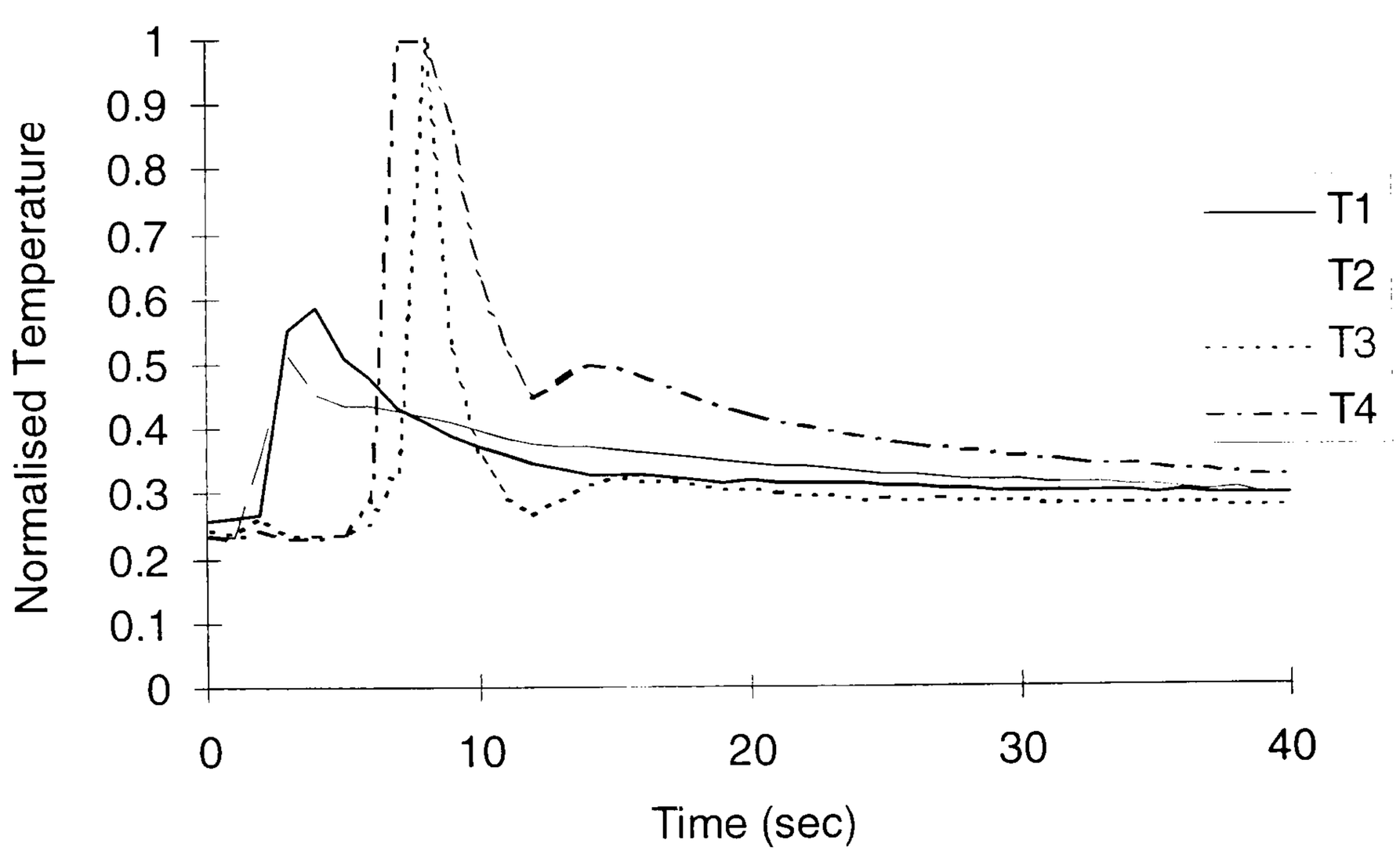

Figure 5.30 Normalised temperature for the post-heated welds with a PRF of 8 Hz

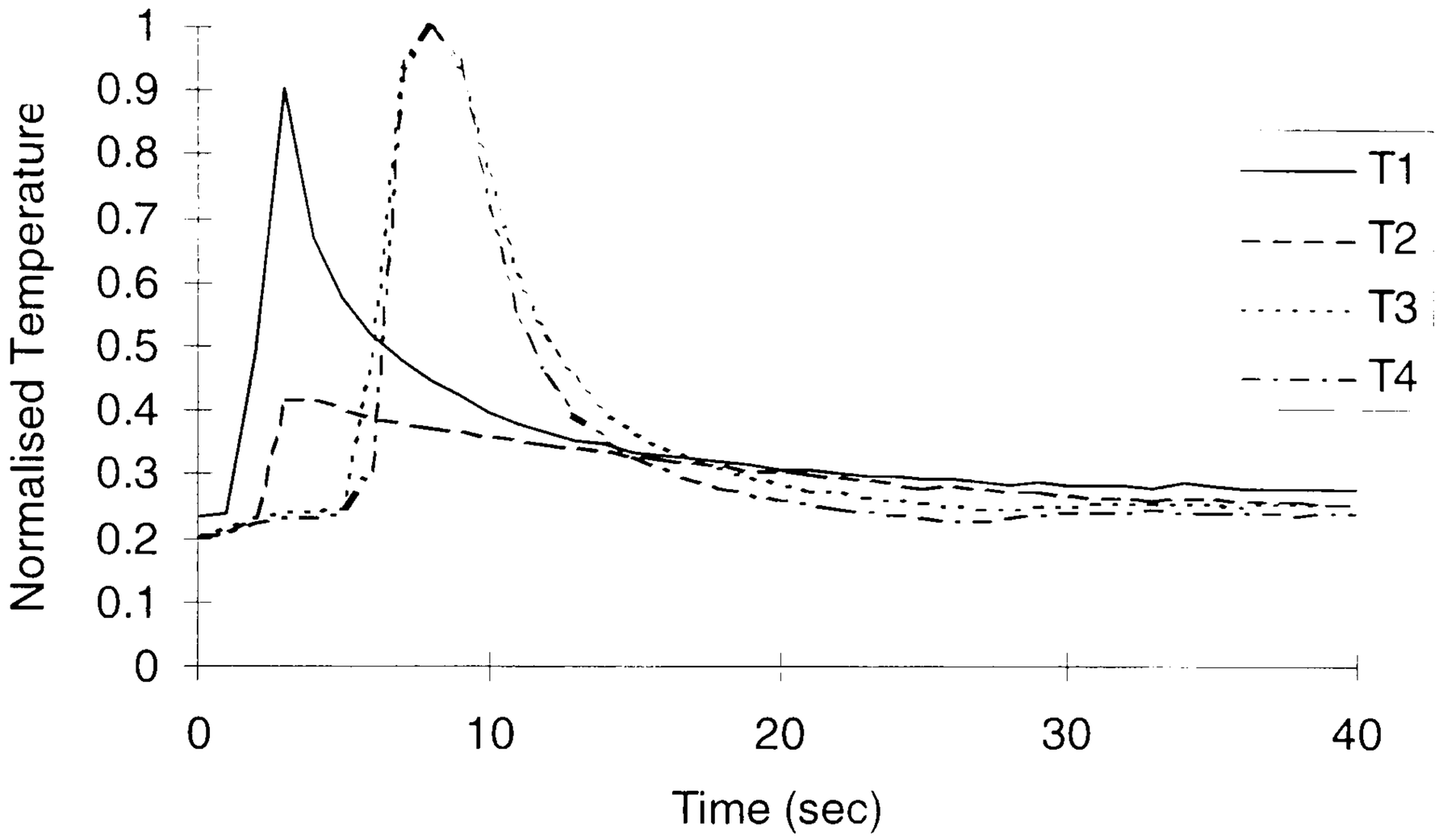

Figure 5.31 Normalised temperature for the pre-heated welds with a PRF of 8 Hz

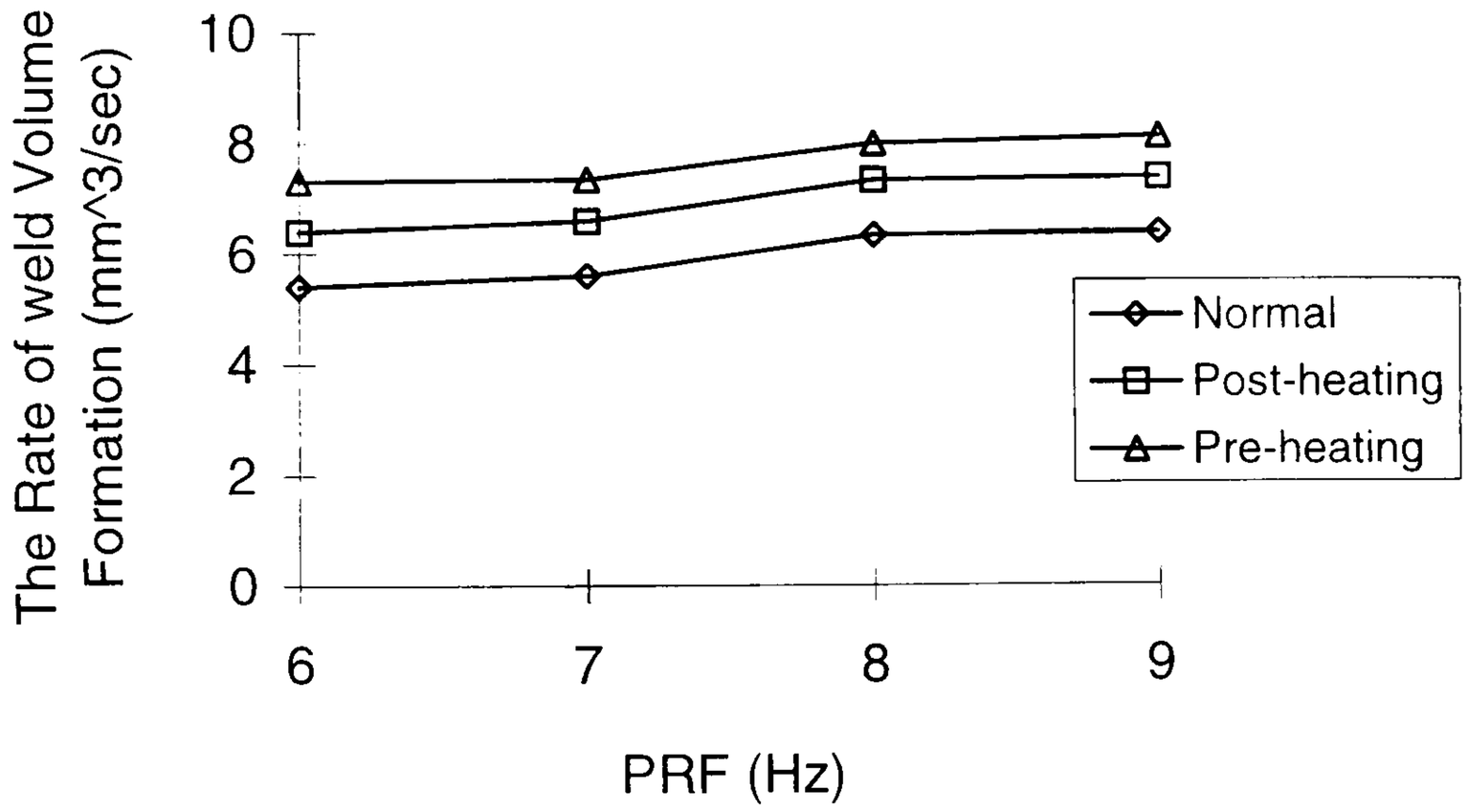

Figure 5.32 The rate of weld volume formation as a function of PRFs

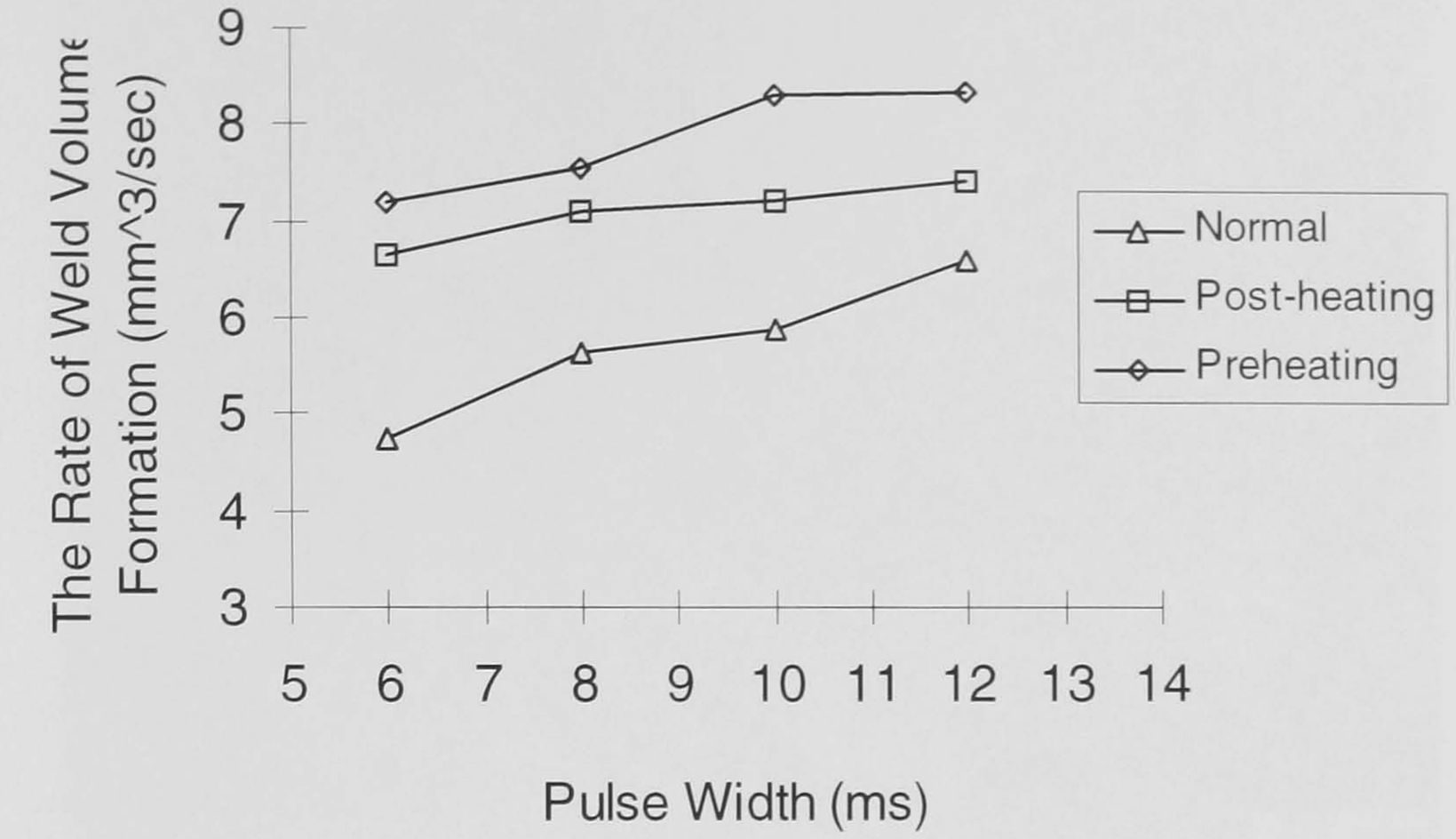

Figure 5.33 The rate of weld volume formation as a function of pulse widths

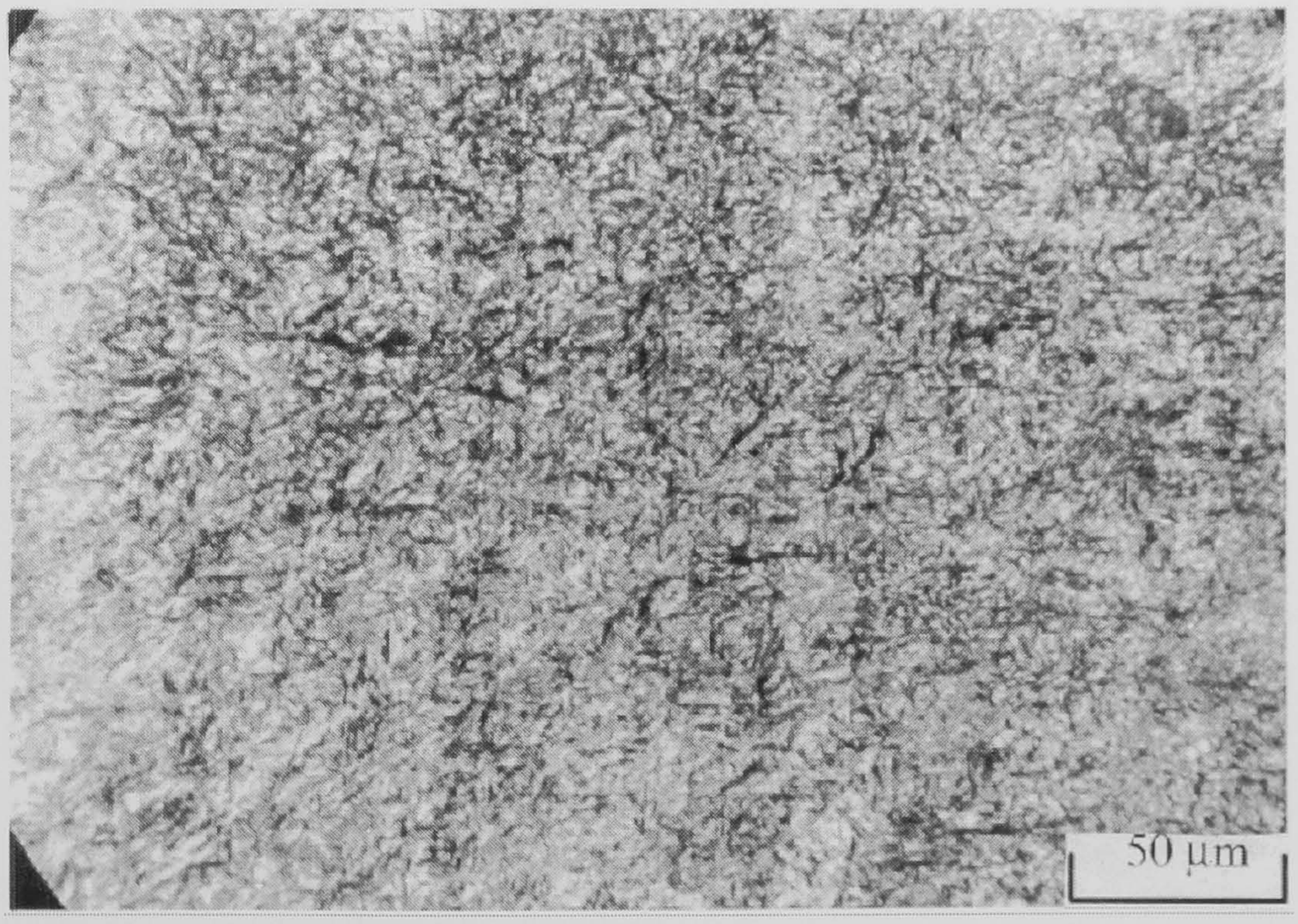

Figure 5.34 The Microstructure of fusion zone of normal laser weld at a magnification of x150. (For a pulse width of 10 ms, PRF of 9 Hz, and welding speed of 5 mm/s)

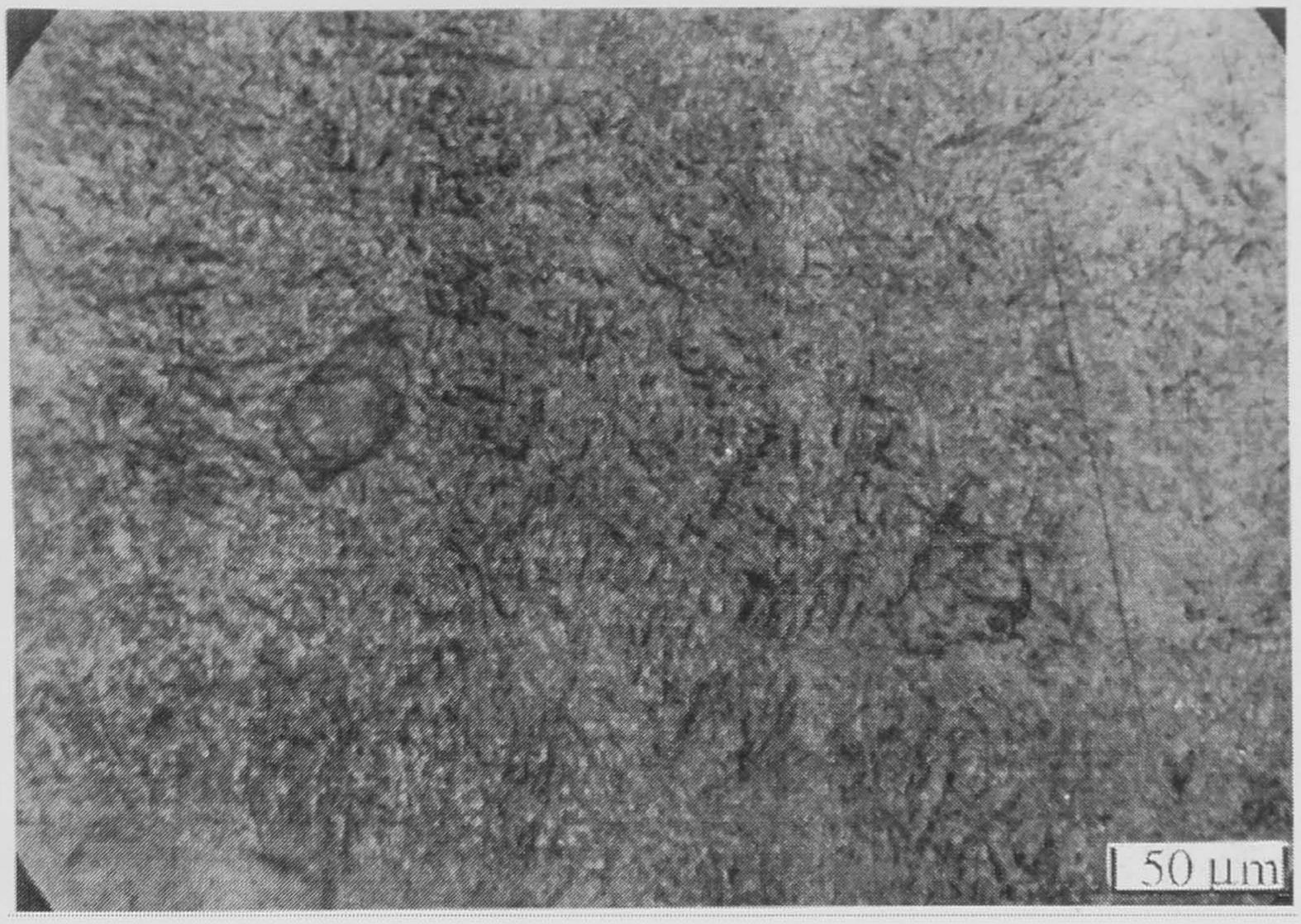

Figure 5.35 The Microstructure of fusion zone of pre-heated laser weld at a magnification of x150. (For a pulse width of 10 ms, PRF of 9 Hz, and welding speed of 5 mm/s)

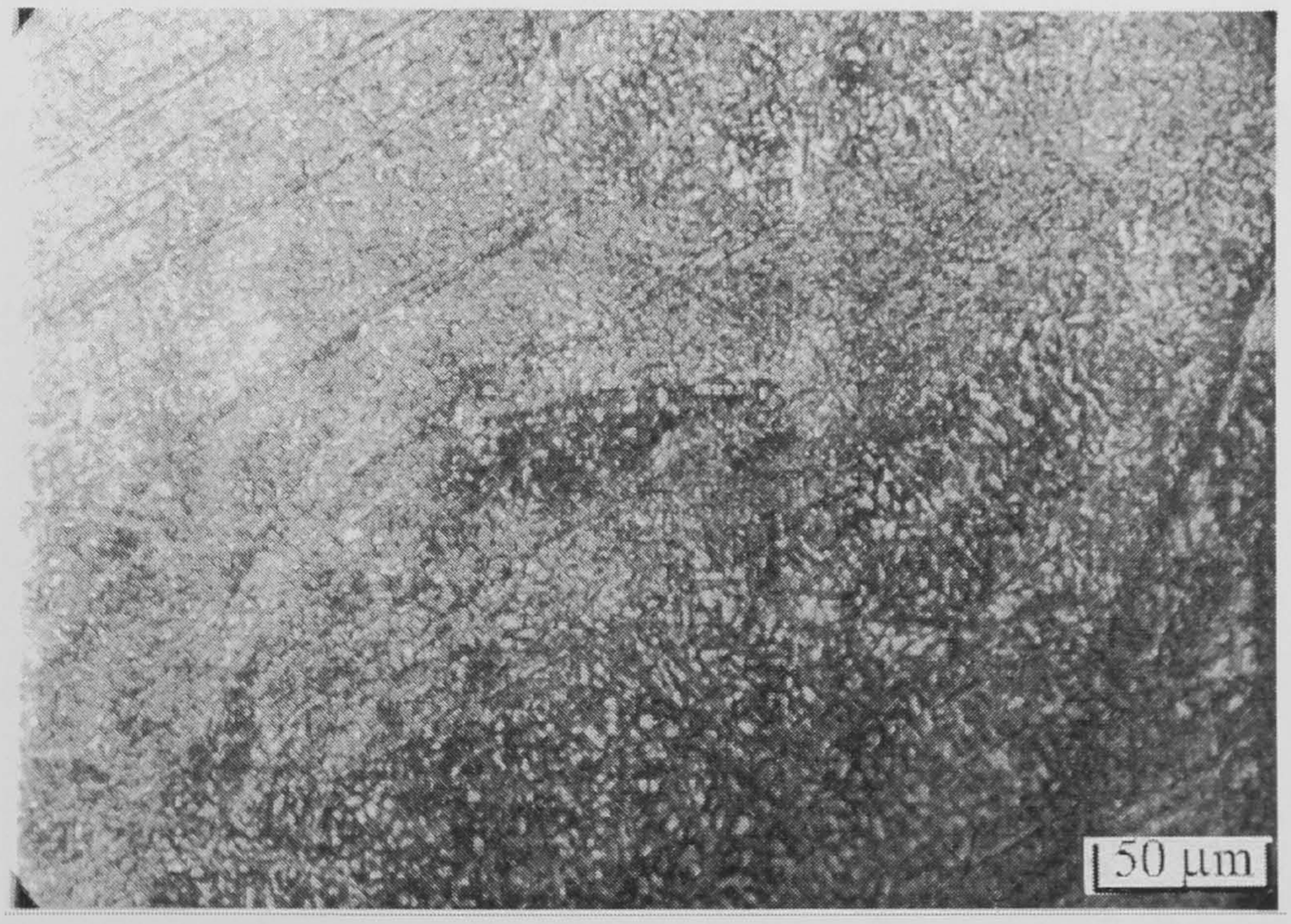

Figure 5.36 The Microstructure of fusion zone of post-heated laser weld at a magnification of x150. (For a pulse width of 10 ms, PRF of 9 Hz, and welding speed of 5 mm/s)

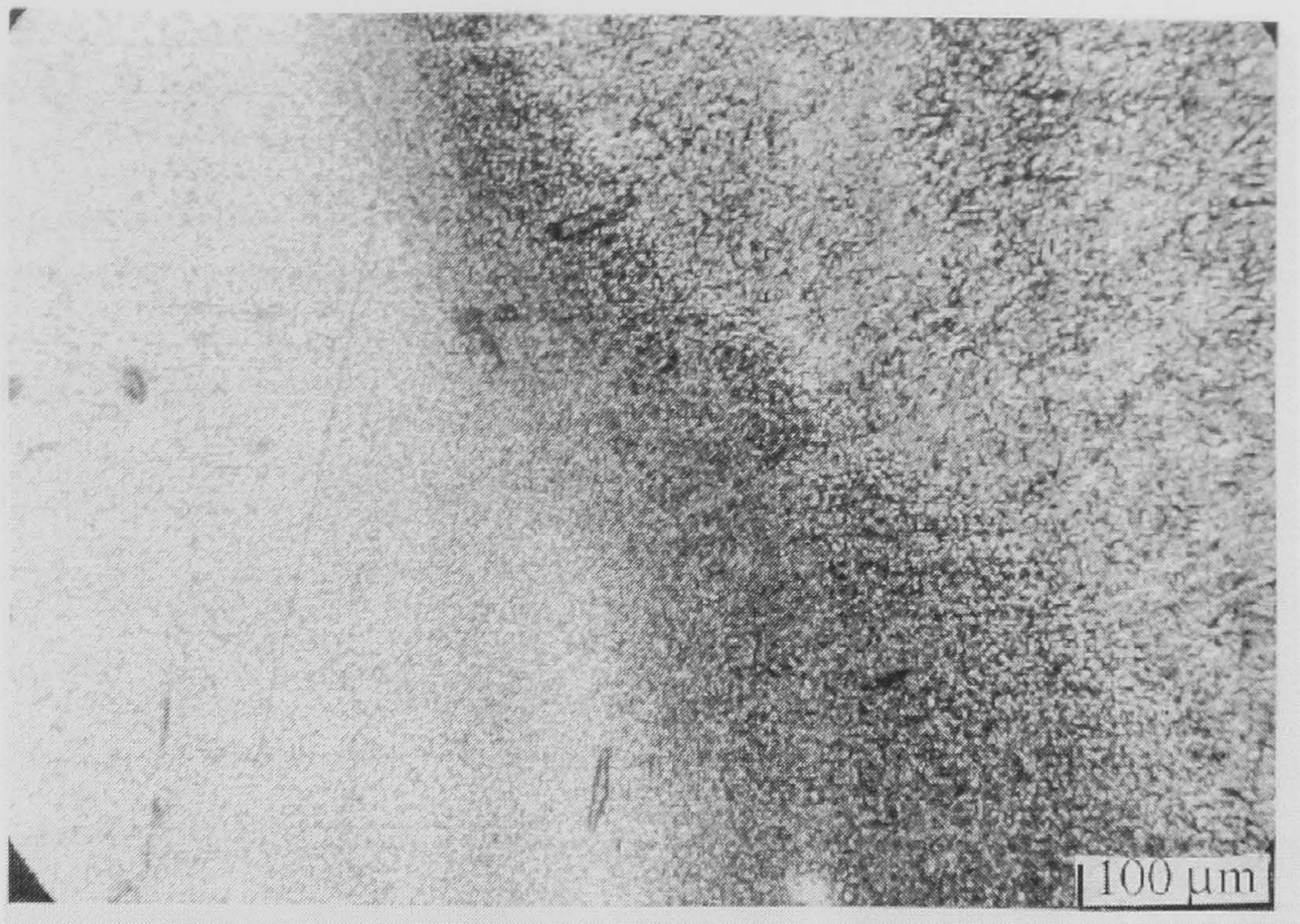

Figure 5.37 The Microstructure of fusion zone (right), heat affected zone (centre), and base metal (left) for normal laser weld at a magnification of x75. (For a pulse width of 10 ms, PRF of 9 Hz, and welding speed of 5 mm/s)

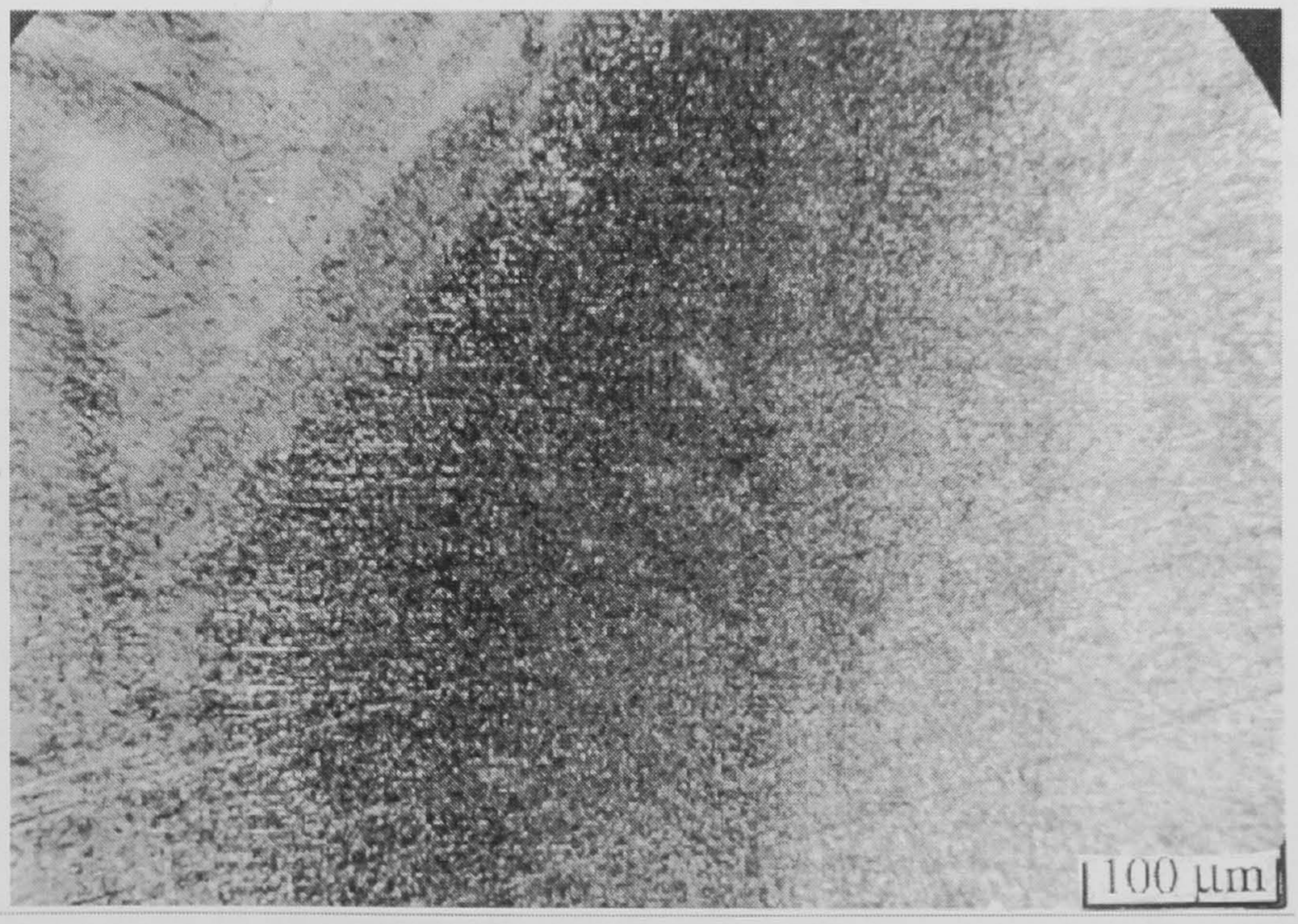

Figure 5.38 The Microstructure of fusion zone (left), heat affected zone (centre), and base metal (right) for pre-heated laser weld at a magnification of x75. (For a pulse width of 10 ms, PRF of 9 Hz, and welding speed of 5 mm/s)

CHAPTER SIX
CO_2 LASER WELDING OF HIGH CARBON STEELS

6.1 Characteristics of CO_2 laser welded high carbon steels with different geometries - 90° incident laser beam

6.1.1 Introduction

The use of lasers in welding of metals has a number of decisive advantages over conventional techniques these include, for example: the weld and heat affected zones adjacent to the weld are very narrow, deep penetration welding of material is possible, and unlike with electron beam welding, a vacuum is not needed, Kroos *et al.* [6.1]. The coupling of laser radiation into the workpiece is dependent on the materials emissivity and the transmission properties of the laser induced plasma. In general for metals, both of these properties increase with wavelength. The formation of the plasma can be controlled by pulsing the laser with pulse lengths less than the plasma formation, Watson *et al.* [6.2], or modifying the local atmosphere with assist shielding gases, Poueyo *et al.* [6.3]. In the latter case, Carlson *et al.* [6.4] observed at the shielding gases should have a higher ionization potential than normal air. Moreover, assist gases can improve the weld quality by reducing the porosity in the weld region. Recent interest in welding aluminium alloys with a 1 kW CO and CO_2 laser was demonstrated by Mehmetli *et al.* [6.5], CO lasers, operating at 5μm, could achieve a deeper penetration weld than the CO_2 device. This was principally because of the lower threshold power needed for processing due to the higher emissivity of the material at the shorter wavelength.

Unfortunately, there are a number of problems with laser welded joints, particularly for those that may be subjected to cyclic loading, where the high hardness induced in both the fusion and heat affected zones can lead to component fatigue. By employing high welding speeds, the time to complete the weld is reduced and welding productivity is increased. If the welding speed is too fast, however, a full penetration weld will not be achieved; and with a welding speed that is too slow, a wide bead width will result, this is discussed in more detail in Section 6.4. The cooling rate of laser welds are high as a consequence of the low heat input per unit length of weld and the high diffusivity of the material. In the present case, a 1kW,

CW, CO_2 laser (Ferranti, MFKP) was used to weld high carbon steels with a He shielding gas at a pressure of 0.5 Bar. The weld quality was examined for different translation velocities and geometries, and quantified by measuring the sample's hardness characterisics (both transverse to the weld direction and as a function of depth), weld width and penetration depth.

6.1.2 Welding and analysis

Gauge plate (2 mm thick) with a nominal composition of: 0.85 - 1.2 wt % C, 0.4 wt % Si, 1.1 wt % Mn, 0.4 wt % Cr, 0.25 wt % V and 0.4 wt % W, was welded, sectioned, photographed and examined. For all the measurements, the errors observed for all the experiments was less than ± 1.1 %, each of the data points plotted in the graph in this thesis is the average of 3 values. The error is not significant and is hardly seen. Thus, the error bars are omitted in most of the cases for clarify. **Figure 6.1** shows a schematic diagram of a single beam delivery system. The material was welded in a clamped and unclamped geometry, shown in **Figures 6.2** and **6.3**, and welded with translation velocities from 800 to 1500 mm/min. The unclamped geometry had a larger area of the sample in thermal contact with the workpiece table (50%). Whereas the clamped geometry had approximately 25% of its surface area in contact with the table. Before measuring the hardness profile and performing microscopic examinations, the welded specimens were sectioned, moulded, polished, etched in nital (3% nitric acid and 97% methanol), and photographed at various magnifications. The Vicker's microhardness profile of the weld was measured transverse to the weld direction and as a function of depth, using a Reichiert 1541555 Vicker's hardness testing machine. The weld depth and bead width were measured using a Mitutoyo PJ-300 profile projector.

6.1.3 Characteristics for different weld geometries and translation velocities

6.1.3.1 Hardness profile

Figures 6.4 and **6.5** show the Vicker's hardness profiles transverse to the weld direction for the unclamped and clamped configurations, respectively, for translation velocities from 800 to 1500 mm/min. In all cases, the rate of cooling process was more strongly dependent on the weld geometry than the welding speed. A slower

translation welding speed resulted in greater contact of the material to the work surface, and resulted in a faster rate of cooling. It is seen in **Figure 6.4** that the peak hardness at the centre of the weld was greatest for a translation speed of 800 mm/min and, in general, increasing the welding speed reduced the hardness profile at the centre of the weld. Interestingly, the hardness increased away from the weld centre with increasing translation velocity. Because welds that are subjected to cyclic loading are liable to fracture if there are large spatial hardness gradients or discontinuities, increased welding speeds, over the range investigated, produced less brittle welds. From **Figure 6.5**, it can be seen that for the clamped geometry, the hardness transverse to the weld direction decreased with increasing translation velocity. However, this effect was observed across the entire weld. By comparing **Figures 6.4** and **6.5**, it can be seen that there was a greater reduction in peak hardness for the unclamped configuration, but the initial peak hardness was about twice as high as it was for the clamped geometry. This can be explained in terms of the rate of cooling, where for the unclamped geometry, the material was distorted and moved away from the workpiece table. This significantly reduced the rate of cooling, providing the reduction in the hardness profile.

During welding the temperature distribution around the weld is greater than the materials melting point and the temperature drops sharply as the distance is increased away from the heat affected zone. The spatial hardness discontinuities are dependent on the temperature distribution during the welding process, moreover, different welding geometries will lead to different thermal heat transfer characteristics and ultimately lead to different weld characteristics (**Figures 6.2** and **6.3**). The unclamped geometry had a greater surface area contact with the worktable; this resulted in a faster cooling rate and a higher hardenability in the fusion and heat affected zones as compared to that achieved with the clamped geometry. In each case, because the same material was used for the weld, the different characteristics were due to the different geometries and translation velocities. The thermal distribution within the sample is dependent on the material diffusivity. The greater the thermal conductivity of the sample, then the faster heat is dissipated from the sample.

Figure 6.6 shows the hardness profile as a function of depth for the unclamped geometry for different welding speeds. The hardness decreased with depth up to about 0.5 mm, and increasing translation velocity. At depths greater than about 0.5 mm, the hardness increased with decreasing translation velocity. It can be seen from **Figure 6.7** that a similar effect was observed when the workpiece was clamped. However, for a given velocity there was a lower reduction in the hardness as a function of depth for the clamped geometry. The lowest rate of change of hardness with respect to depth was observed with the clamped geometry and maximum velocity. These hardness characteristics, as a function of depth determine the bulk hardness of the material and affect the weld quality and its strength. **Figure 6.8** shows how the hardness varied at specific depths for the clamped and unclamped geometries, as a function of translation velocity. The largest variation was observed on the surface of the material for the unclamped geometry, where the hardness decreased from 2271.12 kg/mm^2 to about 1235.83 kg/mm^2 for an increase in the translation velocity of 800 mm/min to 1500 mm/min respectively. At a depth of 0.4 mm into the clamped sample, there was no significant variation in the hardness for the range of translation velocities investigated, even though the weld depth was greater than this value. The spatial variation in the hardness gradient reduced most dramatically for the unclamped configuration. On the weld surface, the modulus gradient reduced from 4.75 kgmin/mm^3 to 0.22 kgmin/mm^3 for a velocity of 800 mm/min and 1500 mm/min respectively. At a depth of 0.2 and 0.4 mm into the sample, the hardness gradient varied by less than 66.1% and was typically 0.76 kgmin/mm^3. Interestingly, for the clamped configuration, the spatial variation in the gradient was much less, the greatest value observed on the surface was 1.86 kgmin/mm^3 for a translation velocity of 800 mm/min. At a depth of 0.2 and 0.4 mm into the sample, the gradient hardly changed and was between 0 to ± 0.5 kgmin/mm^3.

Characterizing the hardness profiles as a function of translation velocity provides information on the optimum laser parameters to reduce hardness gradients throughout the material. Thus identifying how to achieve welds with greater strength by minimizing these gradients.

6.1.3.2 Weld penetration

Figure 6.9 shows the weld penetration for the clamped and unclamped configurations as a function of welding speed. Interestingly, over the range of speeds investigated, a greater penetration was achieved with an unclamped geometry, even though this geometry had greater thermal contact with workpiece translation stage. For a welding speed of 1000 mm/min, the weld depths were 1.3 and 1.7 mm for the clamped and unclamped geometries respectively. These were the maximum depths that were observed. For translation velocities above this value, the penetration depth decreased for both welding configurations.

6.1.3.3 Bead width

It can be seen in **Figure 6.10** that the weld width for the unclamped workpiece was slightly greater than that obtained with the clamped geometry. For lower (less than 1000mm/min) and higher (1200 mm/min) translation velocities there was a greater difference between the weld width for the two geometries. In all cases, however, the weld width reduced with increasing welding speed.

6.1.3.4 Rate of formation of weld volume

The rate of formation of the weld volume for the clamped and unclamped geometries was found by multiplying the product of the weld width and weld depth by the translation velocity, the results are shown in **Figure 6.11**. The unclamped geometry gave the largest rate of formation of HAZ. For example, for a translation velocity of 1000 mm/min the weld formation rate was about 2944 mm^3/min for clamped configuration and this was increased by 14.5% to 3445 mm^3/min for unclamped geometry. Interestingly, the weld formation rate was at a minimum for a translation velocity of 1200 mm/min (for the clamped and unclamped configuration respectively) and then began to increase slightly for higher translation velocities. This increase was greater for the unclamped geometry.

6.1.3.5 Microstructure study of fusion zone

Figure 6.12 shows a picture of a typical normal laser weld for the unclamped workpiece. A general feature of all the specimens was that the weld region consisted

of a martensitic structure, which is characteristic of rapidly cooled high carbon steel, and finely dispersed carbides typical of hardened and untempered steel, and this was also observed by Abdullah *et al* [6.6]. Honeycombe [6.7] concluded that above 0.8 wt % carbon concentration, cementite forms a hyper-eutectoid phase and a similar variation in volume fraction of cementite and pearlite occurs on this side of the eutectoid composition. **Figure 6.13** shows the microstructure for the clamped workpiece with the same settings for the laser parameters and translation velocity as shown in **Figure 6.12**. Here the grain size was finer in the fusion zone than it was for the unclamped workpiece. For the higher speed, there appeared to be a slightly denser and coarser grain structure; Meiheisel [6.8] discovered that this is consistent with a higher cooling rate. The thermal cycle with varying the translation velocity for the clamped welding configuration was such that the structure was completely modified in the fusion zone.

6.1.4 Conclusions of CO_2 laser welded high carbon steels with different geometries

These fundamental investigations have demonstrated the influence of using clamped and unclamped geometries and of optimizing the translation velocity to improve the weld hardness profiles and maximize the weld penetration depth. The effect of cyclic loading on a weld can lead to a poor fatigue life due to the high hardness discontinuities in the fusion and heat-affected zones. Less brittle were produced with increased welding speeds for the clamped geometry. A large number of welds were fabricated, on 2 mm thick gauge plates, with a range of translation speeds from 800 mm/min to 1500 mm/min. The weld quality was quantified by measuring the weld width, weld penetration, and the hardness profiles transverse to the weld direction and as a function of depth. The hardness transverse to the weld direction decreased from 1277.7 kg/mm^2 to 765.7 kg/mm^2 with an increase translation velocity from 800 mm/min to 1500 mm/min for the clamped geometry. A smaller decrease was observed for the unclamped workpiece. These results showed that the hardness decreased with depth for both weld geometries, and that the decrease was greatest for the unclamped geometry. The unclamped geometry produced a deeper weld penetration and a wider bead width. With the clamped geometry, the difference in hardness across the weld was reduced. By increasing the translation

velocity and using the clamped geometry, a denser and coarser grain structure was observed in the fusion zone.

Because the hardness gradients were lower for the clamped geometry by approximately 61 %, these welds were less likely to crack under cyclic loading. The weld material in the unclamped configuration had a lower thermal contact with the surrounding material than the clamped configuration. This would help to contribute to the slower rate of cooling observed for the clamped configuration. The advantage of using the unclamped geometry is that a greater weld depth and a slightly wider bead width were achieved. Furthermore, a more detail investigation on different clamping gemetries (0° and 30°) was used to study the relationship between the rate of cooling and the mechanical properties of the laser welded high carbon steel, see Section 6.4.

6.2 CO_2 laser welded high carbon steels with in-line post process tempering - using a multiple pass system

6.2.1 Introduction

Most recent advances in manufacturing applications of lasers have been due to their high precision, high productivity, flexibility and the effectiveness with which they can be incorporated into automated manufacturing environments. There are however a number of problems associated with this process; for instance: the formation of pores in the weld in the interior of welded material, covered in more detail in Chapter 5, thus, reducing the strength of the completed weld. Dowden *et al.* [6.9] has described how an analysis of the composition of entrapped gas in the pores proves helpful in understanding the keyhole plasma vapour composition. Steen *et al.* [6.10] and Cline *et al.* [6.11] have developed models to study the heat input to the surrounding material to improve the understanding of laser material interaction processes. Due to the low integrated energy input laser welds are often quenched too rapidly in the fusion zone via conduction to the surrounding environment. Zerroukat *et al.* [6.12] developed a model to investigate the heat flow characteristics. Weisman [6.13] and Ashby *et al.* [6.14] described the hardness discontinuities in the fusion and heat affected zone, which leads to cracking and poor component fatigue life. An advantage of the low workpiece energy requirements for laser welding is that

distortion of the workpiece is minimal when compared to conventional arc or gas welding. Continuous laser welding of high carbon steel results in a martensitics structures which can lead to very brittle welds. Roessler *et al.* [6.15] reported that it can be much cheaper to use a laser to modify the surface characteristics such as hardness and temperature stability. Thus, using a multiple beam delivery systems the workpiece spatial and temporal temperature distribution can be controlled to generate the desired mechanical properties without losing the benefits of this low distortion joining process.

To alleviate the poor mechanical characteristic, Ng *et al.* [6.16] investigated the factors which would control the rate of cooling to prevent rapid quenching; this is dependent on different laser parameters and weld geometries discussed in this Chapter. In the earlier work presented herein, a preliminary analysis of dual beam laser process was undertaken. Two beam interactions were modeled by Liu *et al* [6.17,6.18]. To improve the welding characteristics, the dual beam delivery system for the CO_2 laser was designed for welding, but no further experimental work was carried out in this particular area. Therefore, propitious selection of pre-heating and post-heating control parameters are effective in controlling the weld mechanical properties, as discussed more detail in Chapter 3 for Nd:YAG processing. A beam scanning technique was developed for pre-heating or post-heating CO_2 laser welds; this allowed control over the sample's phase transition properties to deliver specific weld characteristics. Whilst not precluding it, this obviated the need of multiple beam delivery systems and is an ideal approach for industrial users with small batch job requirements. The major advantage of the beam scanning technique is that it is a simple and cleaner approach than using a dual beam assembly to achieve in-line process heat. A CO_2 dual beam system was designed, see **Figure 2.7** in Chapter 2, and the final multiple beam system has been fabricated to provide heat-treatment simultaneously during welding. In the following section, two possible problems that were found in this particular design of dual beam system are discussed. Besides this, the current activities in high power diode laser (HPDL) technology and applications to welding showed clearly the effect of different laser welding performance and discussion on the characteristics of HPDL welding of high carbon steel is presented in Section 6.3.

6.2.2 Experimental equipment and welding analysis

For all the measurements, the errors observed for all the experiments was less than ± 1.2 %, each of the data points plotted in the graph in this thesis is the average of 3 values. The error is not significant and is hardly seen. Thus, the error bars are omitted in most of the cases for clarify.. The present study investigated a multi-pass scanning technique, using a 1.2 kW CO_2 laser (Ferranti, MFKP) operating at 10.6 μm, for pre-heating or post-heating the workpiece. For all cases, the laser power was 1.2 kW, the He shielding gas was at a source pressure of 0.5 Bar indicated at the pressure gauge, and the carbon content of the material was 0.85 % and 0.5 %. A schematic of the scanning beam delivery system to achieve in-line process tempering is shown in **Figure 6.1**, and **Figure 6.14a** shows the clamping geometry used in these experiments. This processing method was designed to slow down the rate of cooling of the sample before or after welding with a defocused beam. The laser beam was controlled by the CNC machine to traverse across the material a number of times, at a range of selected translation velocities from 600 mm/min to 1700 mm/min; either before or after welding. In the case of the pre-heating geometry, 10 passes of the beam were made to heat up the base metal with a power of 0.5 kW; this was followed by an additional pass to weld the sample with 1.2 kW laser power. The post-heat treatment was achieved by performing a number of passes after the weld. Both processing methods were designed to slow down the cooling rate and reduce the hardness profiles, without complicating the beam delivery system.

High carbon steel gauge plate, with a nominal composition was mentioned in Section 6.1.2 was selected for this experimental investigation. The mechanical properties of the sample are given in **Table 3.1.** All of the samples were machined to the dimension of 75 x 50 x 0.88 mm^3. The tolerance of the length and width of the samples was ± 0.1 mm. After machining, the samples were ground (Type J, B.A.60.P.V, medium grain) to ensure smooth, flat surfaces. After welding, the workpieces were sectioned, moulded, polished, etched (2 % nital) and photographed. The Vicker's hardness profile of the weld was measured, transversed to the weld direction, using a Reichiert 154155 Vicker's testing machine. These micrographs were examined to establish the effect of pre-heating and post-heating on the weld

quality. The weld depth and bead width were measured using a Mitutoyo PJ-300 profile projector. The welds were inspected using an optical microscope to study any weld defects or cracks and the microstructure in the weld region. The effect of varying the workpiece translation velocity, ie. the degree of post-heating and pre-heating, was quantified by measuring the hardness profiles, weld width, penetration depth and examining the microstructures. These results are shown in Section 6.2.4.

6.2.3 Welding analysis for CO_2 laser dual beam delivery system

The results from the scanning technique (see Section 6.1.2, **Figure 6.1**) were used to develop a multiple beam system to improve the process. There were several problems that were identified for this system due to the cooling of the optics. For the beam splitter, **Figure 6.14b**, the heat flow is predominantly radial, in this edge cooling case. Under this condition, the system faced serious thermal distortion which lead to the distortion of the beam splitter, arising from the heat input from the beam. Dyson [6.10] previously reported that thermal distortion may in part be responsible for changes in the output beam characteristics, during the first few seconds from when a laser is first switched on. With the beam delivery system installed, there were variations in the laser output power. However, attempts to measure these affected the system such that these power fluctuations vanished. Other possible causes of this may be: the reflection of the laser beam from the workpiece back into the laser cavity affected the laser output power; the optics may have been of poor quality; or interference effects may have been occurring at the workpiece. The dual beam system was sucessfully employed to cut 2 mm thick glass, using a Synrad 15 W CW CO_2 laser. The power requirements for the glass cutting were substantially lower than those required for welding and thermal distortion of the optics would have been less likely to occur.

To investigate the effect of the delay between the first and second beam, and optimise the design of the dual beam system, welds were done on the material by using a multiple pass system. For pre-heating, the first pass of the beam was travelling at 4 mm/s (500W), and the second pass (in the same direction as the first) was for welding and the speed was 8 mm/s (1.2kW). In this way, the spatial quality

of the weld in the direction of the weld, could be quantified and correlated to the time delay between the pre-heat and weld. Similar experiments were done for post-heating the weld (4mm/s, 500W), where the weld was done first (8 mm/s, 1.2 kW). The hardness profiles achieved with this system are described in Section 6.2.4.1, see **Figure 6.20**.

6.2.4 Mechanical properties of welds

6.2.4.1 Weld hardness characteristics

Figures 6.15 and **6.16** show the Vicker's hardness profiles transverse to the weld direction for the normal welding condition, pre-heating and post-heating. In this cases, the laser power was 1 kW, and the carbon content of the material was 0.85 %. **Figure 6.15** shows the effect of different welding configurations with a translation velocity of 1000 mm/min, **Figure 6.16** and **6.17**, at 800 mm/min and 600 mm/min, respectively. It is seen that in all these cases, the Vicker's hardness is much greater for the untreated weld and laser tempering is very effective in reducing the hardness discontinuity. The untreated-weld hardness non-uniformity results in the weld having poor mechanical properties.

Figure 6.18 shows the hardness profiles for a sample with 0.5 % carbon content and a translation velocity of 1700 mm/min, all of the other system parameters were identical to those indicated in the previous figures. As the translation velocity was decreased the difference between the Vicker's hardness for the normal weld and treated welds, compared to the hardness of the bulk material, became greater; this difference was greatest for the post-heated samples. **Figure 6.19** shows the percentage reduction in the peak hardness of the weld for pre-heating and post-heating of the different samples, i.e. those with 0.85 % and 0.5 % carbon content. For the post-heated samples, there was nearly 80 % reduction in the peak hardness for a welding velocity of 600mm/min with the 0.85 % carbon content sample; for the same reduction in the hardness, the 0.5 % carbon content material could be processed at a higher translation velocity of 1500 mm/min. Post-heating of the workpiece was more effective in improving the weld characteristics than pre-heating, this is clearly illustrated by **Figures 6.15** to **6.19**. Post-heating produced a

greater reduction in the peak hardness: hence, with reduced non-uniformities in the hardness profiles the likelihood of cracking with the sample subjected to cyclic loading is reduced.

The experiments revealed the benefits that arise over conventional techniques to achieve heat-treatment simultaneously during the welding process. The effect of the time delay between the two beams is illustrated in **Figure 6.20** which shows the effect of pre-heating and post-heating. It should be noted that for the case the welding or heat treatment was always in the same direction (Section 6.2.3). The hardness along the weld seam was dependent on the time delay between the two passes of the laser beam. For the post-heating and pre-heating technique, the hardness increased with the time delay between two passes of the laser beams. Different microstructure transformations occurred for different time delay, see Section 6.2.3.3. This results is what is expected from the simple assessment of the multi-pass system that was used for welding, where the rate of cooling was largely dependent on the post-heating or pre-heating technique. The rapid cooling rate was most effectively suppressed by using the post-heating technique; this gave the greatest hardness reduction, the rate of cooling was significantly reduced compared to the normal and pre-heated welds.

6.2.4.2 Weld bead and penetration depth

Table 6.1 shows the weld width and penetration dependency on the weld geometry and translation velocity. In all cases, the pre-heated welds gave a greater weld penetration than the post-heated or normal welds, for the gauge plates of 0.85 % and 0.5 % carbon content. Also, it is seen that the weld width was greatest for the post-heated geometry. As would be expected, for a lower translation velocity of 800 mm/min, a greater weld width and penetration depth was achieved than for higher translation velocities, for all normal, pre-heated and post-heated welds. The post-heated geometry tended to produce a wider weld width, probably because of the reduced rate of cooling. This ultimately leads to the greater peak hardness reduction as shown in **Table 6.2.**

6.2.4.3 Microstructure analysis

Figure 6.21 shows a picture of a typical normal laser weld that had not received any in-line pre-heating or post-heating. The crack formation is evident at the top and bottom of the weld area. **Figure 6.22** shows the effect of pre-heating the sample. Quite clearly, no cracking was observed. Another general feature of all the specimens was that the main weld region consisted of a martensitic structure, which is characteristics of rapidly cooled high carbon steel, and finely dispersed carbides typical of hardnened and tempered steel. Additionally, the pre-heated weld specimens exhibited complex transformation structures in sharply defined narrow bands comprising a heat affected zone at the junction between the weld and parent metal, shown in **Figure 6.23**. These zones contained fine globular carbide particles, typical of sorbite structures. Also a post-weld heat treatment, shown in **Figure 6.24**, appeared to produce no changes in the metal structure of the bulk weld but did yield interesting structural changes, just below the beam contact point. This was in the form of 5 distinct bands with different metallurgical structures. This is the subject of continuing study, but it appears to include some transformation products similar to those found at the weld/parent metal interface. It is probably due to the multiple passes of the laser beam over the material and the different heat waves penetrating into the samples from each pass of the beam.

It is notable in the two pass geometry, the microstructure in the fusion zone was considerably different from that of the normal, post-heated and preheated welds with the multiple passes, as shown in **Figures 6.25, 6.26** and **6.27**, respectively. In general, the welded specimens were cooled to room temperature rapidly at the fusion and heat affected zones. In all cases, it was found that the austenite transforms to fine martensite rapidly and some retain to room temperature, moreover, the weld region consisted of fine martensite, retained austenite and finely dispersed carbides. As the carbon content increased, both the M_s (martensite start) and M_f (martensite finish) temperature decreased. A fine grain size is clearly seen in **Figure 6.25** for the normal weld. In **Figure 6.26,** the grain size in the fusion region was found to be more refine and coarser than the normal and pre-heated welds, for the post-heated weld. For the pre-heated treatment, a globular grain size was clearly observed in the

fusion zone, **Figure 6.27**. **Figures 6.28, 6.29** and **6.30** show distinct narrow bands at the junction between the weld and parent metal interface, for the normal, post-heated and pre-heated welds, respectively.

6.2.5 Conclusion of CO_2 laser welding of high carbon steel using a multiple pass system

A beam scanning system was used to either pre-heat or post-heat gauge plate with 0.85 % and 0.5 % carbon content. The hardness profiles were measured transverse to the weld direction and showed that there was a greater reduction in the hardness at the centre of the weld for the post-heating geometry. The hardness was reduced by nearly 80 % for a translation velocity 600 mm/min for the sample with 0.85 % carbon content, and by the same amount with a translation velocity of 1500 mm/min with the 0.5 % sample. For a similar reduction in the hardness for both materials, a greater translation velocity was achieved with the 0.5 % sample.

As expected, the weld width and penetration depth was dependent on the welding translation velocity. In all cases, a lower translation velocity produced a wider weld bead and greater penetration depth than a higher welding translation velocity. The pre-heated geometry gave greater penetration than the normal and post-heated geometries. Whereas, the post-heating geometry produced a wider weld bead and resulted in a reduced cooling rate and greater peak hardness reduction.

A complex transformation structure was shown for the pre-heating geometry, comprising a heat affected zone with sharply defined narrow bands at the junction between the weld and parent metal. The post-heated specimens had 5 narrow bands of different metallurgical structure. To optimise the dual beam delivery system and analyse the effect of the delay between pre-heating or post-heating, welds were performed with a time delay between two laser beams (post-heating or preheating) to achieve in-line process tempering, simultaneously with the weld. In all cases, a fine martensite and retained austensite was found in the fusion zone.

6.3 Comparison of CO_2 and diode laser welding of high carbon steels

6.3.1 Introduction

Because laser diode manufacture relies on electronic fabrication techniques they have the potential to be mass produced, and become an extremely inexpensive laser material processing tool. Present technology dictates the limits the minimum beam size can be achieved from laser diode arrays.

In general, laser welding provides a non-contact means of getting high concentrations of heat to specific location without affecting the surrounding environment; this makes it highly reliable and suitable for fusion joining in many engineering applications. For example: automotive, aerospace and electronics industries. Industrial high power laser diode development has progressed rapidly within the last decade and several commercial systems are now offered in the medium or high power regime. Zediker [6.19] has demonstrated the capability of welding carbon sheet. He discovered that the efficiency of welding with HPDL is low and a larger heat-affected zone is obtained compared to other conventional lasers. This is due to the poor beam quality.

Li *et al* [6.20] reported the rapid and continuous enhancement of diode laser materials and fabrication technology and a commercially available CW HPDL with an output power up to 100 W with fibre optical delivery system and a 5 kW CW diode laser stack. Bachmann [6.21] reported that high power diode lasers can be used for welding and surface hardening. The unique features of diode lasers are their portability and their potential cost. Piening *et al.* [6.22] reported that the difficulties in minimising the focused spot size used for industrial applications. For industrial tasks such as cutting and drilling, where a high beam quality is often required, the spatial properties of the processing beam need further improvement. Tabata *et al.* [6.23]. However, the low beam quality from some high power diode lasers is sufficient for some applications; for instance: heat-treatment and welding as investigated by Beckett *et al.* [6.24]. Laser material processing is currently dominated by CO_2 (see Section 6.1.1 and 6.2.1) and Nd:YAG lasers (see Chapter 3). The characteristics of materials welded with diode laser have many differences to

those done with CO_2 laser. Mostly CO_2 lasers have been employed in the field for deep penetration welding, steel plate cutting and surface modification. Moreover, HPDL allow the potential to design highly versatile processing systems with fibre optic beam delivery systems, which is still not commercially available for the conventional CO_2 laser. A major advantage of HPDL processing is its shorter wavelength; consequently, because of the dependency of the material's emissivity on the wavelength, energy is absorbed more readily than for the CO_2 lasers.

Through preliminary studies, an initial understanding of the high power diode laser and CO_2 laser beam processing of high carbon steels has been gained. Both diode and CO_2 lasers, were used to weld gauge plates, that were sectioned, moulded, polished, etched and photographed, allowing examination of the sample's microstructure. The quality of the weld was quantified by assessing the weld's mechanical properties, and size and distribution of the microstructures in the fusion and heat affected zones. A systematic investigation to characterise the weld quality as a function of weld velocity was done. The effect of varying the weld velocity was quantified by measuring the hardness profiles, tensile strength, weld width, aspect ratio, the rate of weld volume formation rate and microstructure examination, for both the diode and CO_2 lasers.

6.3.2 Lasers and analysis of welds

The present study used a 1 kW, CW, CO_2 laser (Ferranti MFKP), operating at 10.6 μm, to weld 1.5 mm thick gauge plate. The translation velocity was changed from 8 to 11 mm/s, with a He shielding gas at a source pressure of 0.5 bar indicated at the pressure gauge and a nozzle diameter of 5 mm. A schematic of the CO_2 laser beam delivery system used in this study is shown in **Figure 6.1**. For the CO_2 laser system, the weld beam was focused to a spot size of 1 mm.

A high power diode laser, comprising a large number of single laser diodes, were incoherently coupled together to deliver laser power up to 2 kW, the system is shown in **Figure 6.31.** For most experiments, the laser head was mounted onto the gantry positioning system shown in **Figure 6.32**; the maximum power was 1.4 kW, CW, operating at 810 nm, and a He shielding gas at a source pressure of 0.5 bar

indicated at the pressure gauge was used. The focal area of HPDL was 3.8 x 1.8 mm^2, which leads to a maximum power density of 2 x 10^6 W/cm^2 compared to 1.3 x 10^7 W/cm^2 with the CO_2 laser.

High carbon steel gauge plate, with a nominal composition of 0.85 wt % C, 0.4 wt % Si, 1.1 wt % Mn, 0.4 wt % Cr, 0.25 wt % V and 0.4 wt % W, was selected for this experimental investigation. The mechanical properties of the sample are shown in Table 3.1. All of the samples were machined to the dimension of 75 x 50 x 0.88 mm^3. The tolerance of the length and width of the samples was ± 0.1 mm. After machining, the samples were ground (Type J, B.A.60.P.V. medium grain) to ensure smooth, flat surfaces. After welding, the workpieces were sectioned, moulded, polished, etched (2 % nital) and photographed. To quantify the weld quality, the hardness profiles were measured, with a Reichiert 154155 Vicker's hardness testing machine, transverse along the weld direction and as a function of depth. An Instron tensile tester machine with a cross-head speed 0.5 mm/sec was used to measure the tensile strength along the weld joints. The weld depth and bead width were measured using a Mitutoyo PJ-300 profile projector. The welds were inspected using an optical microscope to study any weld defects or cracks and the microstructure in the weld region.

6.3.3 Welding analysis

6.3.3.1 Hardness profiles

Transverse cross sections of the weldments were sectioned for the microhardness test. Using a diamond pyramid indenter with a 70 gm load, the hardness was measured from one side of the parent metal across the weld metal to the other side of the parent metal. The hardness was much higher at the centre of the weld, and the hardness across the fusion and heat affected zones in the welded samples is higher than the parent metal, as shown in **Figures 6.33** and **6.34**, for the CO_2 and diode laser welding, respectively. The effect of welding velocity was investigated and the transverse hardness across the weld was found. **Figure 6.35** shows the peak hardness of the weld for the CO_2 and diode laser welding for different welding velocities. The peak hardness increased with the welding velocities for both welding

configurations. For a welding velocity below 10 mm/s, the diode laser produced a higher peak hardness than CO_2 laser welding. Interestingly, for the CO_2 laser welding, the peak hardness was greater compared to that from the diode laser welding for a welding velocity above about 10 mm/s. The CO_2 laser welding produced a wider weld bead, as discussed in Section 6.1, this resulted in slowing down the rate of cooling and was more effective in improving the weld hardness characteristics than the diode laser welding. Hence, a less brittle weld was produced compared to that with the diode laser.

The hardness profiles as a function of depth can be seen in **Figures 6.36**, for the CO_2 and diode laser welding. This figure shows the variation in the depth-hardness for different welding velocities. In this case, using a CO_2 laser for welding, the hardness slightly decreased with depth into the sample. Interestingly, for the diode laser welding, uniform hardness profiles along the weld depth are clearly observed. In general, for both welding configurations, the hardness was reduced with decreasing welding velocity.

6.3.3.2 Tensile strength

Tensile tests aimed at determining the mechanical properties of laser butt welded plates were significantly inferior to those of the parent metal. Tensile test were performed, at a cross-head velocity of 0.5 mm/s, to determine the mechanical properties of the welds done with the different types of laser. In all cases, the tensile failure occurred in the welded region, no deformation of the weld was evident, indicating that brittle fracture, due to the sample's high hardness discontinuities, had been the likely cause of failure.

Figure 6.37 shows the tensile strength, which resulted in failure of butt welded joints, as a function of the welding velocity. It is clearly observed that CO_2 laser welding, the tensile strength decreased from 105 MN/mm^2 to 100 MN/mm^2, for a corresponding welding velocity from 8 mm/s to 9 mm/s. However above 9 mm/s, the tensile strength increased with the welding velocity to a maximum of 11mm/s. For the diode laser welding, when the welding velocity was increased from 8 mm/s to 10 mm/s, the tensile strength decreased from 97 MN/mm^2 to 69 MN/mm^2. The

poor mechanical properties, especially the low tensile strength, was attributed to the presence of centre-line cracks in the fusion zone at welding velocities above 10 mm/s, which were evident on the fusion zone, see Section 6.3.3.6. In general, the welded joints are further weakened by the weld discontinuities. **Table 3.1** shows the strength of the base metal, thus, this indicates that the strength of the welded samples was considerably lower than the base metal. In all cases, full penetration welds were achieved with the two different type of lasers. For a welding velocity of 11 mm/s, the tensile strength was 127 MN/mm^2 for CO_2 laser welding and 69 MN/mm^2 for the diode laser welding. This represents an increase in the tensile strength of 84 % for a full penetration weld with the CO_2 laser.

6.3.3.3 Weld bead

The weld widths was measured as a function of welding velocity, and the results can be seen in **Figure 6.38**. For a welding velocity of 8 mm/s, a maximum weld width of 5.9 mm and 4.1 mm were achieved, for the CO_2 and diode laser welding respectively. Interestingly, for the CO_2 laser, the weld width reduced by 46 % to 3.1mm, for an increase in the welding velocity from 8 mm/s to 11 mm/s. Increasing the welding velocity from 8 mm/s to 11 mm/s for the HPDL resulted in the weld width reducing by 27 %. From **Figure 6.38**, it is clearly seen that at 10 mm/s the diode laser produced a slightly wider weld bead than the CO_2 laser weld. In all other cases, the CO_2 laser welding produced a wider weld bead than with the diode laser. This was significant for velocities below 9 mm/s.

6.3.3.4 Aspect ratio

The aspect ratio for both the CO_2 and diode laser welds was found by dividing the weld penetration by the weld width. In all velocities, a full penetration weld was achieved for both welding configurations. The dependency of the aspect ratio on the welding velocity is shown in **Figure 6.39**, the aspect ratio increased with the welding velocity for both lasers. Compared to the CO_2 laser, the aspect ratio for the diode laser was lower at a welding velocity of 10 mm/s; this was because of the wider weld bead, see **Figure 6.38**. In other cases, a higher aspect ratio was achieved with the diode laser than the CO_2 device.

6.3.3.5 The rate of weld volume formation rate

The rate of formation of weld volume was defined by multiplying the weld width, penetration depth and welding velocity. The rate of weld volume formation was calculated as a function of weld velocity, and these results are shown in **Figure 6.40**. For the CO_2 laser weld geometry, the weld volume decreased with an increase welding velocity, whereas, for the diode laser weld geometry, the weld volume was independent of the weld velocity over the range of values investigated. The average weld volume formation rate for the diode laser welding was 50.1 mm^3/s. For the CO_2 laser welding, the largest rate of weld volume formation was for a translation velocity of 8 mm/s where the formation rate was about 70 mm^3/s. The formation rate for the HPDL at this velocity was 30 % less at 49 mm^3/s. The diode laser welding produced a slightly higher weld volume formation rate than CO_2 laser welding, at a welding velocity of 10 mm/s.

6.3.3.6 Microstructure study of the welds

The microstructures of each of the welded samples were examined in the regions of the fusion zone, heat affected zone (HAZ) and parent metal. The transverse sections of the weldments were prepared for the microstructural examination and analysis. In all cases, no signs of porosity nor of any other voids or inclusions were evident in the microscopic examination. **Figure 6.41** and **6.42** show the typical pictures of the weld seam appearance for the CO_2 and diode laser welding, respectively. It is obvious that a better weld seam was achieved with the diode laser welding than with the CO_2 laser welding, but a wider weld bead was achieved with the CO_2 laser weld for the same welding velocity. The centre-line cracking in the fusion zone is dependent on the cooling pattern as discussed in Section 3.2.3.6. Compared to the CO_2 laser welds, narrow heat affected zones were produced by the diode laser. However, this resulted in a faster cooling rate in the fusion zone, and the weld was last to solidify and hence is much weaker; this leads to cracking at the higher welding velocities. **Figures 6.43** shows, the diode laser welds done at a higher welding velocities at 10 mm/s. The crack evident is clearly observed in the fusion zone. **Figure 6.44** shows the effect of the CO_2 laser weld at the same welding velocity, no cracks were observed. In all cases, martensitie and carbide structures

appeared between the pearlite grains with some retained austenite. **Figures 6.45** and **6.46** show typical pictures of the fusion zones from the CO_2 and HPDL welding respectively. Compared to CO_2 laser weld, the diode laser welding produced a fine grain structure at the same welding velocity; this is due to the low heat input of the diode laser weld which produced a narrow weld width compared to CO_2 laser weld. as shown in **Figures 6.47** and **6.48** discussed in the earlier Section 6.3.3.

6.3.4 Conclusions of CO_2 and diode laser welding of high carbon steels

In general, a number of welds were done for a range of welding velocities from 8 to 11 mm/s with both a CO_2 and a high power diode laser. The weld quality was quantified by measuring the sample's hardness characteristics, tensile strength, weld width, aspect ratio, the rate of weld volume formation rate and examination of its microstructure.

The high hardness values indicated a fast cooling rate for both fusion and heat affected zones. For both welding configurations, the peak hardness increased with the welding velocities. Compared to the diode laser weld, a lower hardness values was achieved with CO_2 laser, and the heat affected zones were wider and the microstructure corresponded to a slower cooling rate than the diode laser welding. For the CO_2 laser welds, this resulted in effectively reducing the cooling rate, and the hardness decreased as a function of weld depth. Interestingly, for the diode laser welding, a uniform hardness profile as a function of weld depth was clearly observed.

For a CO_2 laser weld, the weld strength increased with welding velocity, and a greater tensile strength was achieved. Because of the rapid cooling rate, the diode laser welds at the faster welding velocity, centre-line cracking was found in the fusion zone which resulted in reduced of weld strength.

For both laser welding configurations, the weld width decreased with increasing weld velocity. The greatest weld width was achieved with the CO_2 laser. However, this provides a good explanation and agreement on the greatest weld strength achieved with the CO_2 laser. Under these condition, for CO_2 laser welding, the

aspect ratio was lower than the diode laser welding. At the welding velocity of 10 mm/s, the aspect ratio was lower than the CO_2 laser, this is due to the wider weld bead achieved with the diode laser.

The rate of formation of the weld volume decreased with an increasing welding velocity. Interestingly, for the CO_2 laser welding at a velocity of 8 mm/s, the weld volume formation rate 70 mm^3/s, this was reduced by 30 % to 49 mm^3/s, for the diode laser weld at the same velocity. The diode laser welds produced an average weld volume formation rate of about 50.1 mm^3/s. The centre-line cracking was a definite problem for the diode laser welding, which probably can be alleviated by using CO_2 laser welding. The fine grain size and wider heat affected zone contribute significantly to the lower hardness characteristics for the CO_2 laser welds. It should be noted, however, that the irradiance of the laser diode and CO_2 lasers were 2×10^6 W/cm^2 and 1.3×10^7 W/cm^2. From these difference in the irradiances, it is perhaps surprising that the laser diode array achieves a weld that is almost comparable to the CO_2 laser. This is at least in part due to the more favourable optical properties of the material at its operating wavelength.

6.4 Characteristics Of Elliptical and Focused Laser Beam During CO_2 Laser Welding

6.4.1 Introduction

The significant different mechanical properties observed for different beam delivery system has been discussed in Chapter 3. The work presented in this Section is for welding done with the beam incident on the sample at 30°. The advantages of using an elliptical Nd:YAG laser beam for welding are presented in more detail in Chapter 5. Liu *et al* [6.18] investigated the effect of varying the ratio of the major and minor axes of an elliptical beam, and concluded it should have a significant impact on the transverse temperature profiles. Glumann [6.25] concluded that the theorectical combination of beams set at an angle resulted in a higher process stability. The effects of processing conditions and variable properties upon the pool shape, cooling rate, and absorption coefficient in laser welding was investigated by Chande *et al* [6.26], and he found that the absorption of laser energy in the keyhole affected the depth of penetration more than the width of the weld. Temperature profiles induced

by an elliptical scanning continuous laser beam was studied by Moody *et al.* [6.27], he concluded that an elliptical beam can be used to scan and anneal large areas. Moreover, Nissim *et al.* [6.28] investigated the effect of temperature distribution produced by an elliptical scanning CW laser beam. Whitaker *et al* [6.29] observed that the grain size and microhardness clearly illustrated that the weld properties can be optimised by adopting a slow heating rate. The rapid cooling rates and temperature gradients that result during laser beam welding of high carbon steel is reported in Section 6.1 and 6.2. To eliminate these problems, a 30° clamped geometry was used for welding, this geometry provide an elliptical beam profile on the weld and was used to prevent the formation of brittle microstructures; these results were compared to the flat welding geometry - ie. normal welding.

6.4.2 Experimental Set-Up

High carbon steel gauge plate, with a nominal composition as discussed in Section 6.2.2, was welded. The mechanical properties of the parent metal are shown **Table 3.1**. All samples were machined to dimensions of 75 x 50 x 0.88 mm^3. The tolerance of the length and width of the samples was ± 0.1 mm. After machining, the samples were ground (Type J, B.A.60.P.V, medium grain) to ensure smooth, flat surfaces. After welding, the workpieces were sectioned, moulded, polished, etched (2 % nital) and photographed.

For all the measurements, the errors observed for all the experiments was less than ± 1 %, each of the data points plotted in the graph in this thesis is the average of 3 values. The error is not significant and is hardly seen. Thus, the error bars are omitted in most of the cases for clarify. The gauge plate was welded using a 1 kW, CW, CO_2 laser (Ferranti MFKP), operating at 10.6 μm, to weld 1.5 mm thick gauge plate. The welding speed was changed from 8 mm/s to 11 mm/s, a He shielding gas at a source pressure of 0.5 bar indicated at the pressure gauge was used with a nozzle diameter of 5 mm. A schematic of CO_2 laser beam delivery system was used for flat welding is shown in **Figure 6.1**. For the flat welding geometry, the weld beam was focused to a spot size of 2 mm, whereas for elliptical beam welding a 30° clamped

geometry as shown in **Figure 6.49** was used, the beam size was approximately 22 mm.

To quantify the weld quality, the hardness profiles were measured, with a Reichiert 154155 Vickers hardness testing machine, transverse along the weld direction and as a function of depth. Furthermore, the tensile strength along the weld joints was measured with an Instron tensile tester machine with a cross-head speed 0.5 mm/sec. The weld depth and bead width were measured using a Mitutoyo PJ-300 profile projector. The welds were inspected using an optical microscope to study any weld defects or cracks and the microstructure in the weld region.

6.4.3 Welding Analysis

6.4.3.1 Hardness Profile

Welds were sectioned transversely and subjected to hardness tests transverse across the welds using a microhardness tester (70 gm). The measurements were made from the parent metal, across the weld and heat affected zones into the parent metal on the opposite side of the weld. These result are shown in **Figure 6.50**. It is seen that the peak hardness increased with the welding speed for both the flat and 30° welding configurations. The high hardness for the flat welding was attributed to high cooling rate depressing the transformation temperature, thereby producing hard transformation products. Both the fusion and heat affected zones were excessively hard compared to the parent metal. In this case, for the flat and 30° welding geometries, the peak hardness was lowest and highest, at a welding speed of 8 mm/s and 11 mm/s, respectively. The hardness gradient was less for the 30° welding, this matched the results discussed in Chapter 5, for Nd:YAG laser welding - see Section 5.1.3.2. **Figure 6.51** shows, the hardness profiles as a function of depth, for the flat and 30° welding configurations. These figures illustrate that the hardness decreased with welding speed for both welding geometries. In all cases, the hardness was highest at the top of the fusion zone, also the hardness profiles were less for the 30° welding compared to the flat welding geometry.

6.4.3.2 Tensile Strength

Tensile tests were done on a wide variety of laser welding speeds for the flat and 30° welding geometries. These tests were performed at a crosshead velocity of 0.5 mm/sec, inorder to determine the strength between the two different types of welding process, at different welding speeds. In contrast to the results shown in **Table 3.1** - see Section 3.1.2, the strength of the welded regions were significantly inferior to those of parent metal. **Figure 6.52** demonstrates the tensile strength that resulted in failure as a function of welding speed, for the flat and 30° welding. In all cases, full penetration welds were achieved for both welding geometries. It can be seen clearly the flat welding configuration produced the weld with the greater strength compared to welding at 30°, and this is due to the wider weld bead that was achieved with a flat welding, this is discussed in more detail in Section 6.4.3.3. Moreover, welding done with a 30° clamped geometry, the top surface showed rippling caused by the sinking of the molten pool; this is resulted in a turbulent keyhole and irregular weld bead being formed. This was clearly revealed with an optical monitoring system that is discussed in Chapter 7. These results indicated how sensitive the mechanical properties were to the weld quality, and this is covered more detailed in Chapter 7. Interestingly for the 30° welding configuration, the weld strength was slightly greater than the flat welding, however, in this case, the tensile strength was 127 MN/m^2 for flat welding and 146 MN/m^2 for the 30° welding geometry.

6.4.3.3 Weld Bead

The weld width was measured as a function of welding speed, for both the flat and 30° welding, these result can be seen in **Figure 6.53**. It can be seen that the weld width decreased with an increase in the welding speed, for both welding configurations. In this case, the flat welding geometry produced a wider weld width than the normal weld. It is clearly observed that the maximum difference in the weld width occurred at a welding speed of 8 mm/s, and this difference decreased with increasing welding speed.

6.4.3.4 Aspect Ratio

The aspect ratio for both the flat and 30° welding geometries was found by dividing the weld penetration by the weld width. In all cases, full penetration was achieved. Results of plotting the aspect ratio as a function of welding speed for both welding are shown in **Figure 6.54**. For the flat and 30° welding, the aspect ratio increased with the welding speed, resulting in a higher aspect ratio for higher welding speeds; this is due to the decrease in the weld bead as discussed in Section 6.4.3.3. Compared to 30° welding geometry, the aspect ratio was lower because of the wider weld bead - See Chapter 7, for the flat welding. Despite this disadvantage, the 30° welding however suffered a lower distortion area even with movement of the melt pool.

6.4.3.5 The rate of formation weld volume

The rate of formation of weld volume was taken as the product of the weld width, weld depth, and the weld speed, for the flat and 30° welding geometries. The dependency of the weld volume formation rate on different welding speeds, for the flat and 30° welding is shown in **Figure 6.55**.

The largest rate of formation of weld volume was observed for the flat welding geometry. For instance, for a welding speed of 8 mm/s the weld volume formation rate was 43.2 mm^3/s for the 30° welding configuration, and this was increased by 63 % to about 70.2 mm^3/s for the flat welding geometry. For both cases, the rate of weld volume formation decreased with increasing welding speed from 8 to 10 mm/s. Interestingly, the weld formation rate was at a minimum for a welding speed of 10 mm/s, for both welding configurations, and then began to increase slightly for a higher welding speed above 10 mm/s.

6.4.4 Microstructure Analysis

The transverse cross sections of the weldments were prepared for microstructural examination and solidification structure analysis. The microstructure of each material were examined in the fusion region. A general feature of all the specimen was that the main welded region consisted of retained austenite, pearlite, and martensitics structure, which is the characteristic of rapidly cooled high carbon

steel, and finely dispersed carbides were also found. **Figure 6.56** shows a picture of a typical 30° welding geometry, at a welding speed of 8 mm/s. and **Figure 6.57** shows the microstructure of a specimen at a higher weld speed of 10 mm/s. for 30° welding configuration. Due to the thermal cycle. the microstructure was completely modified, thus, the specimen had received a greater heat input at a slower welding speed. This resulted in reducing the rate of cooling which gave the austenite time to transform to a refined and coarser grain size, compared to the fusion zone of higher welding speed of 10 mm/s shown in **Figure 6.57**. The same features were observed at the same welding speed (10 mm/s) . compared to 30° welding configuration (see **Figure 6.57**), the grain structure was transformed to a refined, globular and coarser structure, as shown in **Figure 6.58** for the flat welding geometry. **Figures 6.59** and **6.60** show the weld region of flat (0°) and 30° welding, respectively. It is seen from these figures that the flat welding geometry reduced the rate of cooling, forming a favourable structure, this was due to a wider heat affected and fusion zones which resulted in reducing the rate of cooling as compared to the 30° welding geometry.

6.4.5 Conclusion of CO_2 laser welding with Flat (0°) and 30° welding geometries

For the flat and 30° welding geometries, the hardness profiles increased with welding speed, however, the hardness gradients were less for the 30° welding configuration. Less brittle welds were produced with slower welding speeds for both welding geometries. These results also show the hardness profiles decreased with weld depth, for both weld angles and the decrease was greater for the flat welding. A small decrease was observed for the 30° welding geometry.

The tensile strength increased with the welding speed for the flat and 30° welding configurations. For the flat welding geometry, the tensile strength was greater than 30° weld geometry when the welding speed was increased from 8 to 10 mm/s. For with welding speeds above 10 mm/s. the 30° weld geometry tended to produce a slightly greater strength compared to the flat welding configuration.

Because the welded strengths were greater for the flat welding geometry, these welds tended to produce a wider weld bead than the 30° welding geometry, moreover, for both cases, the hardness gradients were lower at the slower welding speed, and these welds were less likely to crack under cyclic loading, which resulted in a wider weld bead at a lower welding speed, for both welding geometries. In all cases, the weld width decreased with increasing welding speed.

For the flat and 30° welding, the aspect ratio increased with the welding speed, however, the 30° welding geometry produced a greater aspect ratio. The flat welding geometry produced a larger rate of weld volume formation compared to 30° welding, but the rate of weld volume formation was at a minimum for a welding speed of 10 mm/s, for both welding geometries.

REFERENCES CHAPTER SIX

[6.1] Kroos, J. Gratzke, U. Vicanek, M. Simon, G. "Dynamic Behaviour Of The Keyhole In Laser Welding", Journal of Phys D:. Appl. Phys. **26**, 1993, 481-486.

[6.2] Watson, I. Chatwin, Chris. "Segmented Ballasted Electrodes For A Large-Volume, Sub-atmospheric, Transversely Excited Pulsed Laser", Journal Phys. D. **28**, 1995, 258-260 .

[6.3] Poueyo, A. Sabatier, L. Deshors, G. Fabbro, R. De Frutos, A. Bermejo, D. Orza, J. "Fundamenatal Study Of The Parameters Of The-Induced Plasma bserved In Welding Of Iron Targets With Continuous High Power CO_2 Lasers", SPIE Vol 1502, Industrial And Scientific Uses Of High Power Lasers, 1991, 140-147.

[6.4] Carlson, K. Gregson, V. "Characteristics Of Deep Penetration Laser Welds At Various Sectioned Thickness", ICALEO 88, The 7th International Congress On Applications Of Lasers And Electrooptics, 1988, 223-225.

[6.5] Mehmetli, B. Takahashi, K. Sato, S. "Comparision Of Aluminium Alloys Welding Characteristics with 1kW CO And CO_2", Journal of Lasers Applications, **8**, 1996, 25.

[6.6] Abdullah, A. Ng, S. Chatwin, C. Watson, I. "In Line Process Annealing Of Laser Welded High Carbon Steel", ICALEO 95, The 14th International Congress On Applications Of Lasers And Electro-optics, 1995, 964 - 973.

[6.7] Honeycombe, R. "Microstructure And Properties",.Metallurgy And Materials Science Series, Edward Arnold (Publishers), 1981 .

[6.8] Meiheisel, G. "High Speed Welding Of Deep Drawing Low Carbon Steel", ICALEO 88, Proceedings Of The 7th International Congress On Applications Of Lasers And Electrooptics, 1988, 357-370.

[6.9] Dowden, J. Kapadia, P. "The Instabilities of The keyhole and The Formation of Pores in The Weld In Laser Keyhole Welding", The 14th International Congress On Applications Of Lasers And Electro-optics, San Diego, Nov 1995, 961-963.

[6.10] Steen, W. Dowden, J. Davis, M. Kapadia, P. "A Point of Line Source Model of Laser Keyhole Welding", Journal of Physic: Appl Phys D, **21**, 1988, 1255 - 1260.

[6.11] Cline, H. Antony, T. "Heat Treating and Melting of Material With a Scanning Laser or Electron-Beam", Journal of Physic: Appl Phys D, **48**, 1977, 3895 - 3900.

[6.12] Zerroukat, M. Chatwin, C. "Heat Flow Computations For CW-Laser-Material Interactions", Journal of Lasers In Engineering, **3(2)**, 1994, 113 - 123.

[6.13] Weisman, C. "Welding Handbook", American Welding Society, **7(1)**, 1981.

[6.14] Ashby, M. Easterling, K. "The Transformation Hardening of Steel Surfaces by Laser Beam", Actal Metall, **32**, 1984, 1935 - 1948.

[6.15] Roessler, D. Coady, M. "Lasers In Automotive Materials Processing and Microelectronics Manufaacturing", Trends In Optic and Photonics - Laser and Optics for Manufacturing, 9, OCT 1996, 51 - 53.

[6.16] Ng, S. Watson, I. "Characteristics Of CO_2 Laser Welded High Carbon Steel Gauge Plate", Journal of Laser Application, **9**, 1997, 15 - 20.

[6.17] Lui, Y. Jr, E. "Laser Beam Welding With Simultaneous Gaussian Laser Pre-heating", American Society of Mechanical Engineering - Production Engineering Division, ASME 1992, 191 - 197.

[6.18] Liu, Y. Jr, E. "Characteristics of Elliptical Laser Beam Pre-heating During Laser Welding", Manufacturing Science and Engineering, Vol 64, ASME 1993, 895 - 988.

[6.19] Zediker, S. "Direct Diode Laser Competes with Nd:YAG and CO_2", Industrial Laser Review,1993, 17.

[6.20] Li, L. Lawrence, J. Spencer, J. "Material Processing With a High Power Diode Laser", The 15h International Congress On Applications Of Lasers And Electro-optics, Nov 1996, Sect E 38 - 40.

[6.21] Bachmann, F. "Application of High Power Diode Laser", The 17th International Congress On Applications Of Lasers And Electro-optics - Laser application overview , San Diego, Nov 1998.

[6.22] Piening, A. Watson, I. "Minimising The Focus Spot Size From a 15 Watt Laser Diode Array", The 16th International Congress On Applications Of Lasers And Electro-optics, San Diego, Nov 1997, Sect A 207 - 209.

[6.23] Tabata, S. Yagi, H. "Present and Future of Lasers For Fine Cutting of Metal Plate", Journal of Material Processing Technology 62, 1996, 304 - 306.

[6.24] Beckett, M. Fleming, A. Foster, M. Gilbert, j. Whitehead, D. "The Application of Semi-conductor Diode Laser to The Soldering Electronic Components", Opical and Quantum Electronic 27, 1995, 1303 - 1311.

[6.25] Glumann, C. Rapp, J. Dausinger, F. Hugel, H. "Welding with a combination of CO_2 lasers - advantages in processing and quality", The 12th International Congress On Applications Of Lasers And Electro-optics, Orlando, 1993, 672.

[6.26] Chande, T. Mazumder, J. "Estimating the effect of Processing Conditions and Variable Properties Upon Pool Shape, Cooling Rates and Absorption Coefficient in Laser Welding", Journal of Applied Physic, Vol 56 (**1**), 1984, 1981 -1986.

[6.27] Moody, J. and Steen, W. "Heat Transfer Model for CW Laser Material Processing", Journal of Applied Physic, Vol 53 (**6**), 1982, 4367 - 4374.

[6.28] Nissim, Y. Hendel, R. "Temperature Profiles Induced By Scanning CW Laser Beam", Journal of Applied Physic, Vol 51 (**1**), 1980, 274 - 279.

[6.29] Whitaker, I. Calder, N. Mccartney, D. Steen, W. "Influence of Heat Treatment On The Microstructure And Properties of Laser Welds in 8090", Journal of Applied Physic, Vol 3, Nov 1993, 1053 -1055.

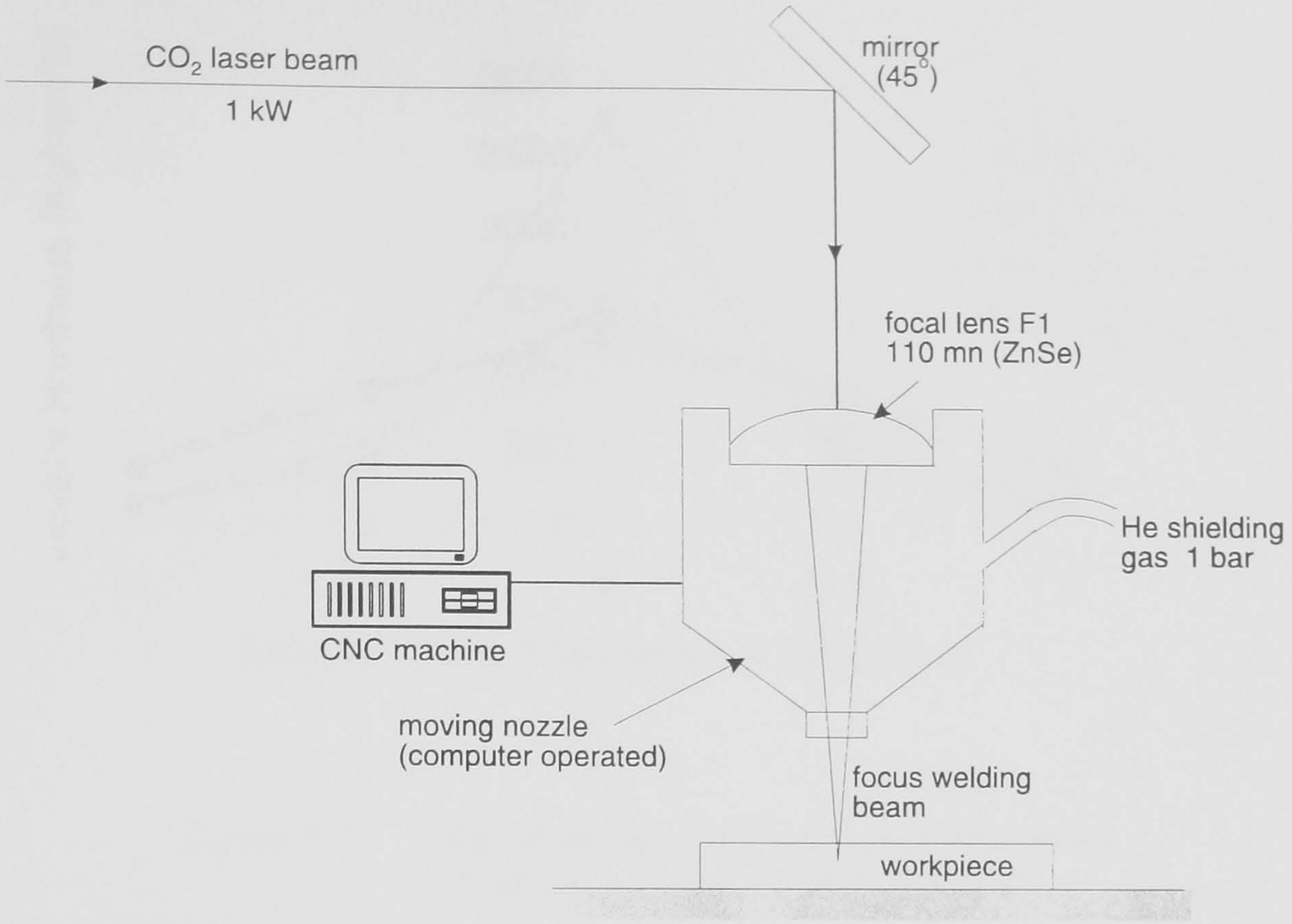

Figure 6.1 A schematic diagram of single beam delivery sytem

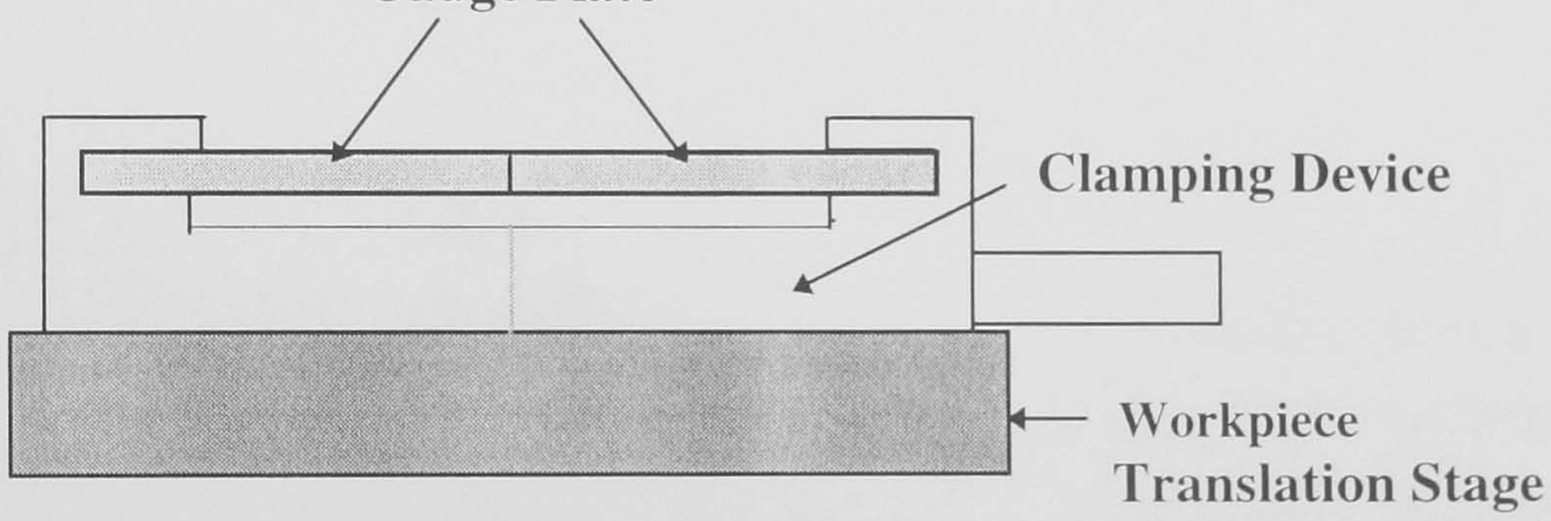

Figure 6.2 Clamped Geometry For Laser Welding

Figure 6.3 Unclamped Geometry For Laser Welding

Figures 6.2 and 6.3 Clamped And Unclamped Geometry For Laser Welding

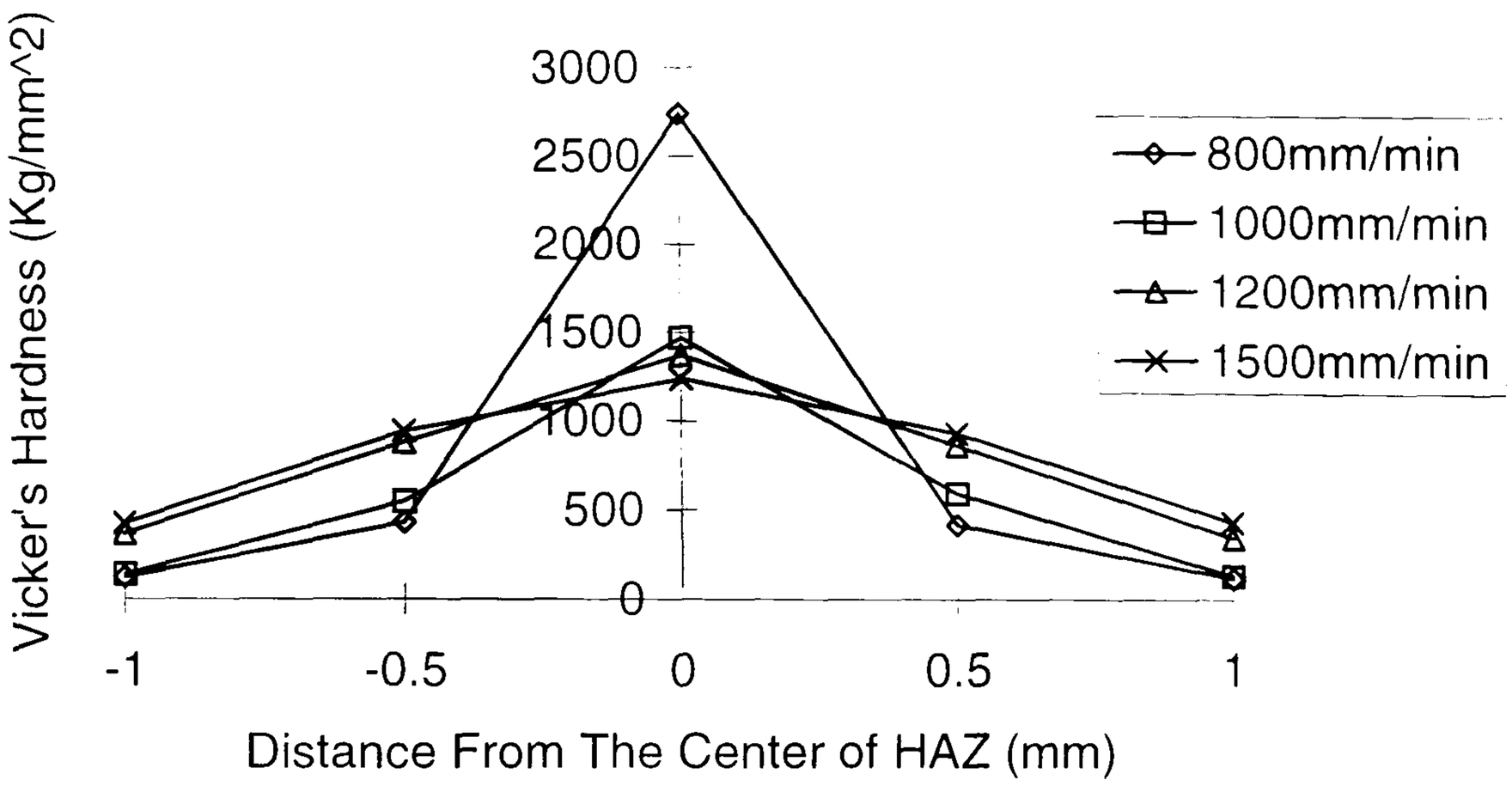

Figure 6.4 Microhardness Of Unclamped Workpiece
(2 mm guage plate of 0.85 WT % C)

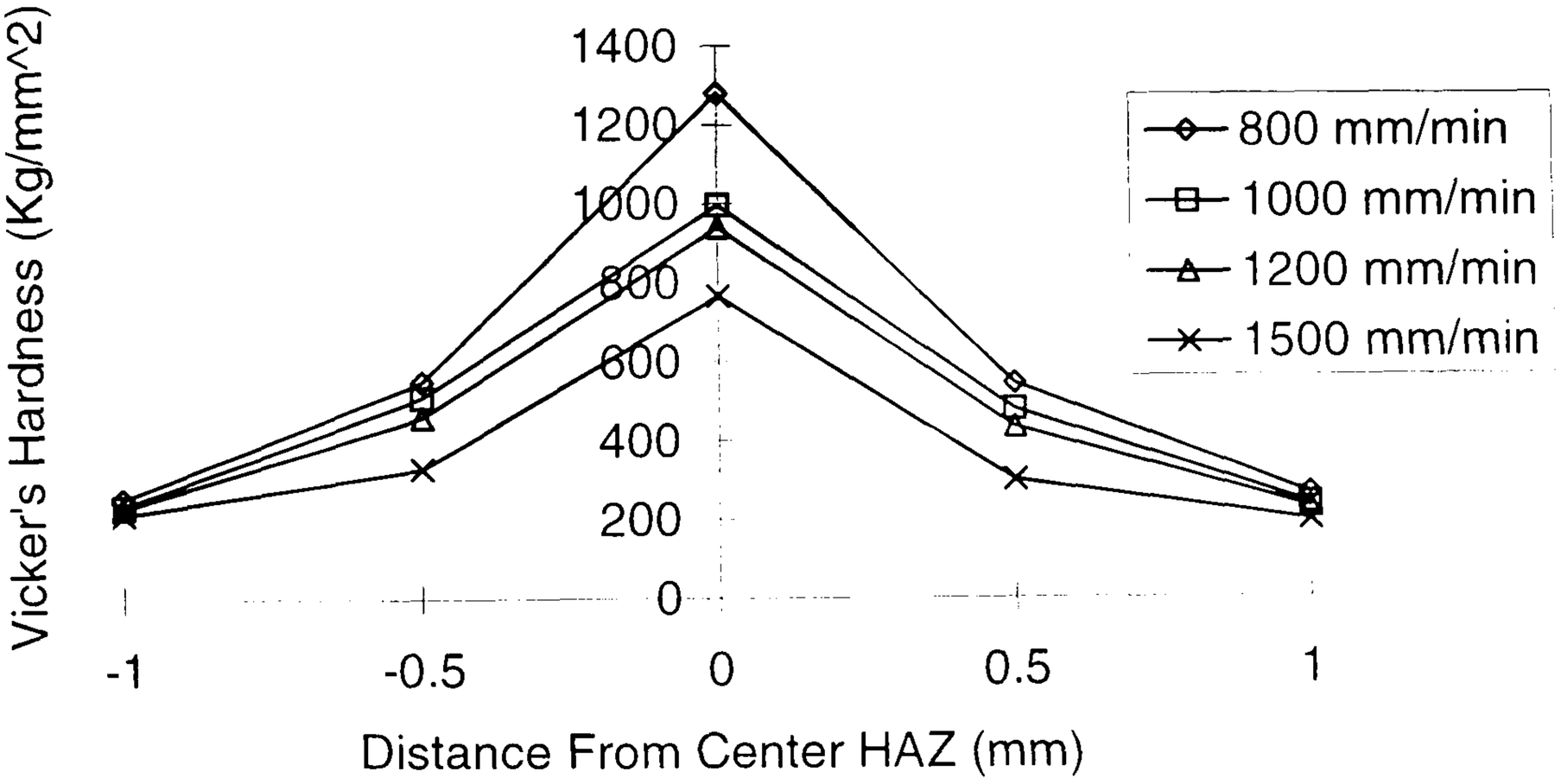

Figure 6.5 Microhardness Of Clamped Workpiece
(2 mm guage plate of 0.85 WT % C)

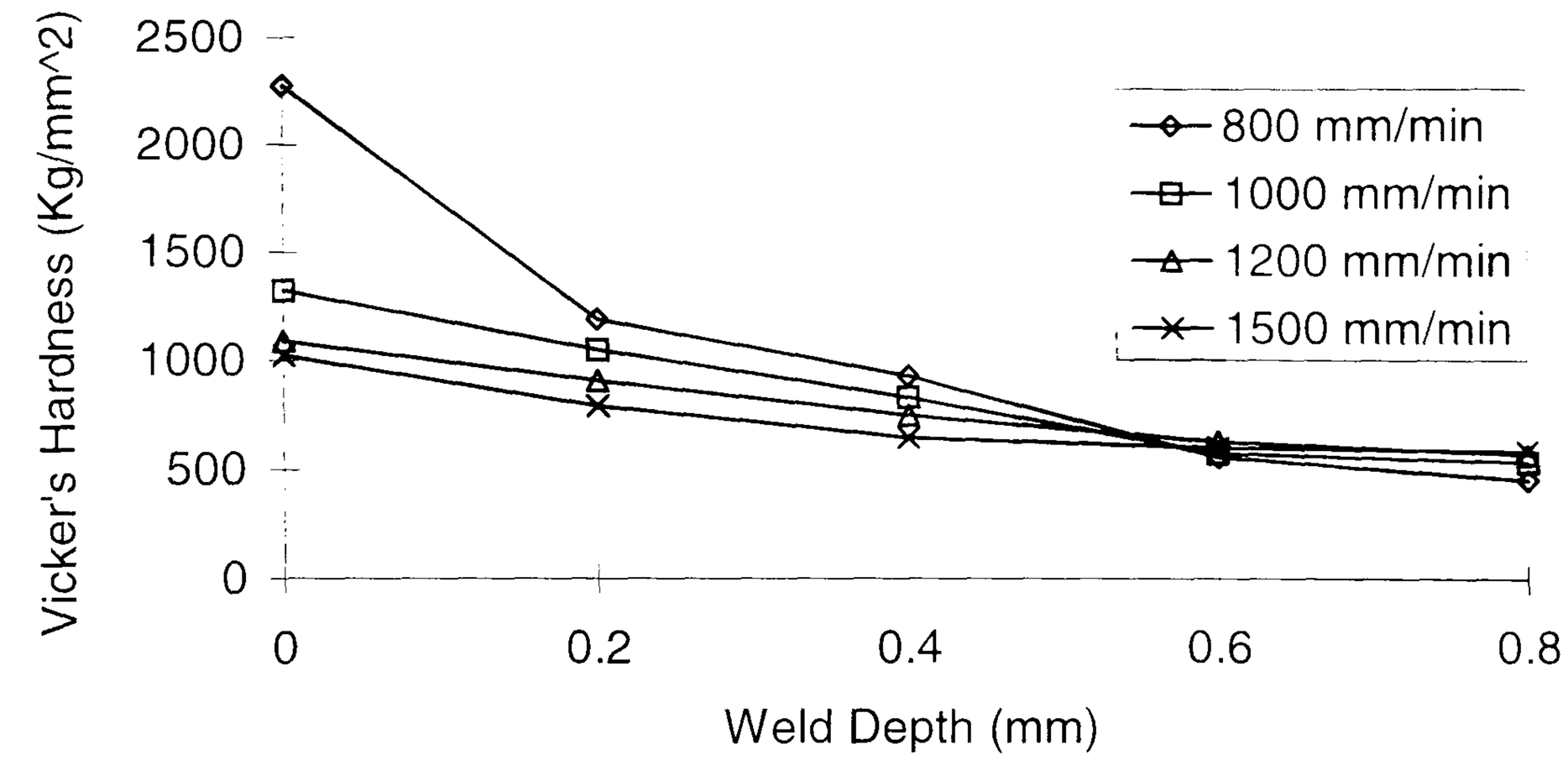

Figure 6.6 Hardness as a Function of Depth for Unclamped Workpiece (2 mm guage plate of 0.85 WT % C)

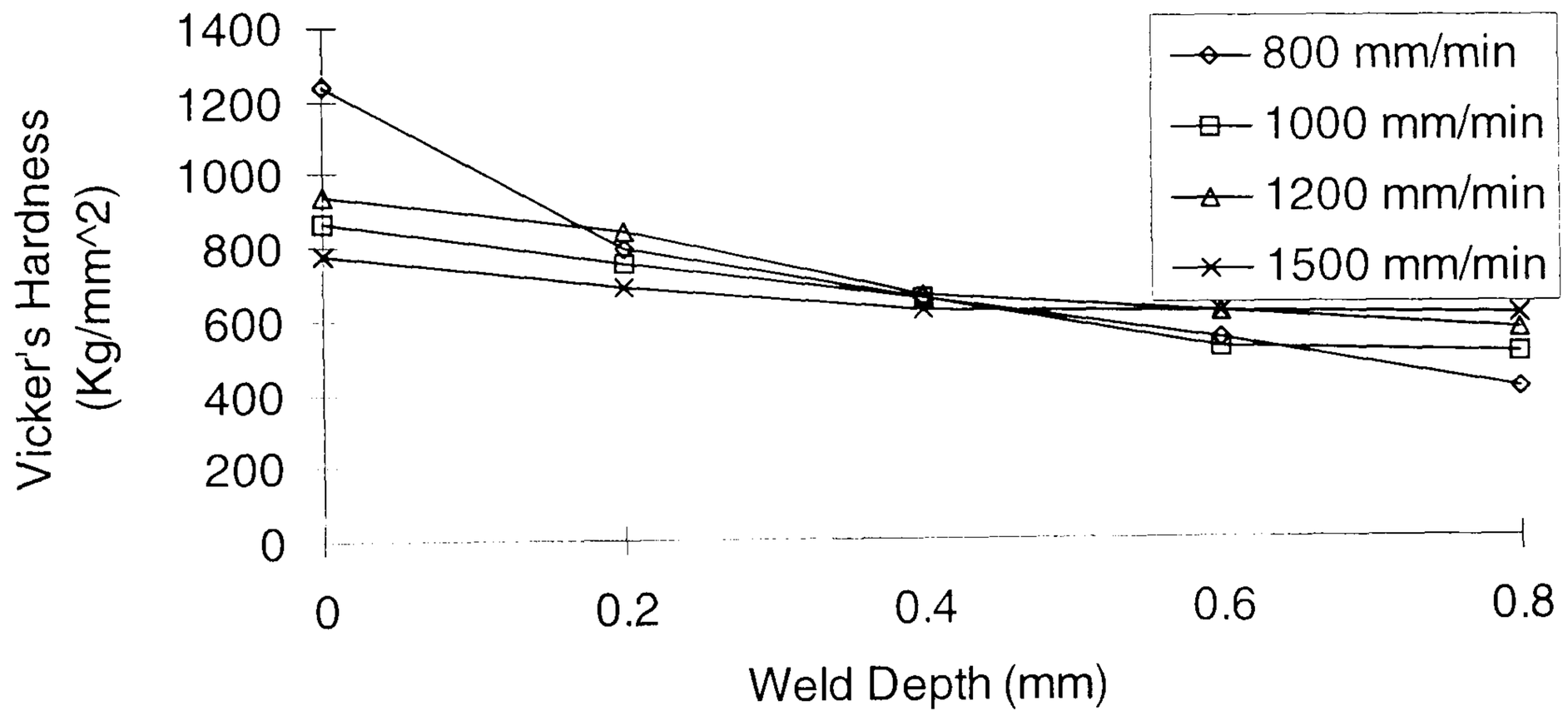

Figure 6.7 Hardness As A Function Of Depth For Clamped workpiece (2 mm guage plate of 0.85 WT % C)

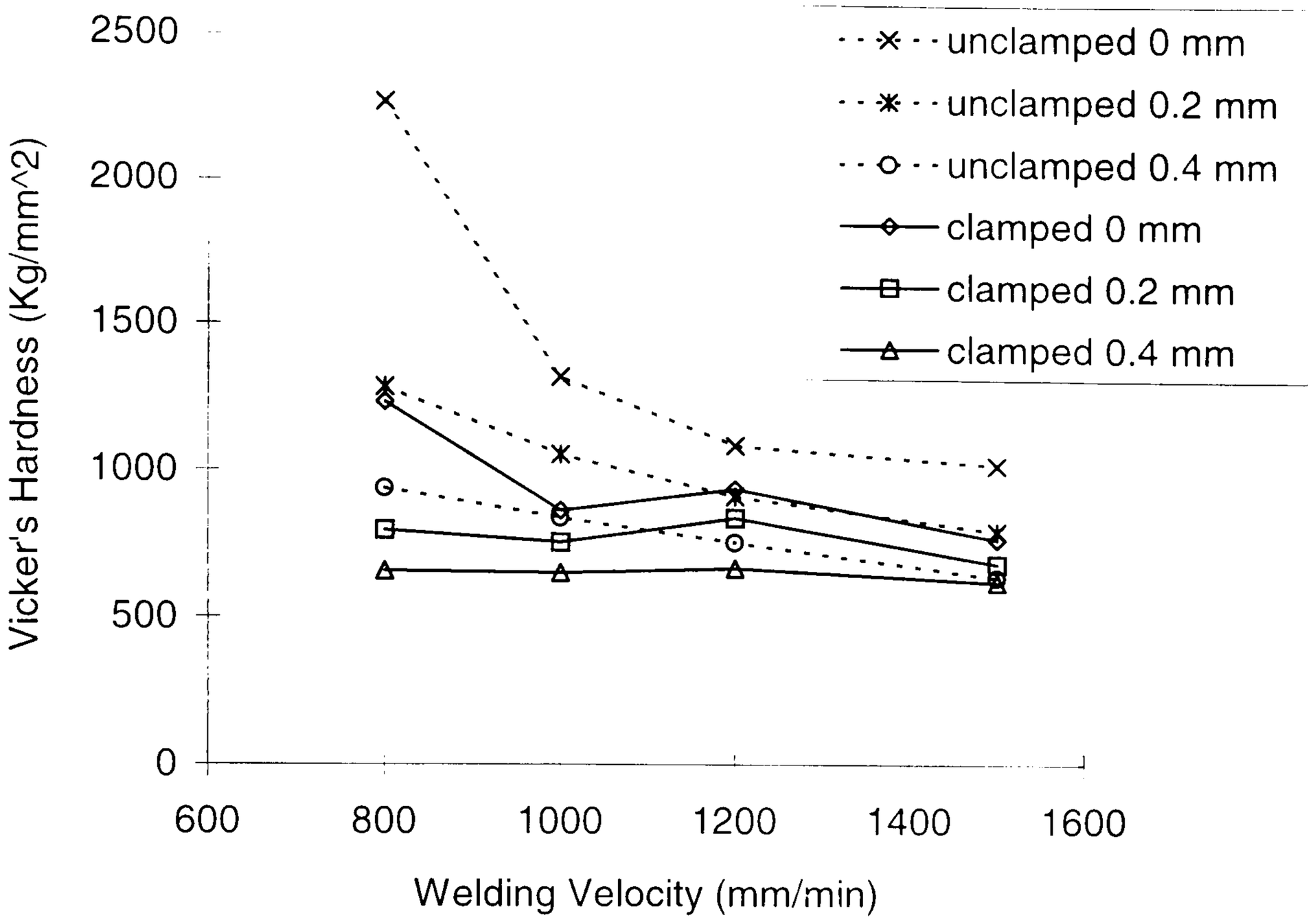

Figure 6.8 Hardness As A Function Of Certain Depth Versus Translation speeds (2 mm guage plate of 0.85 WT % c)

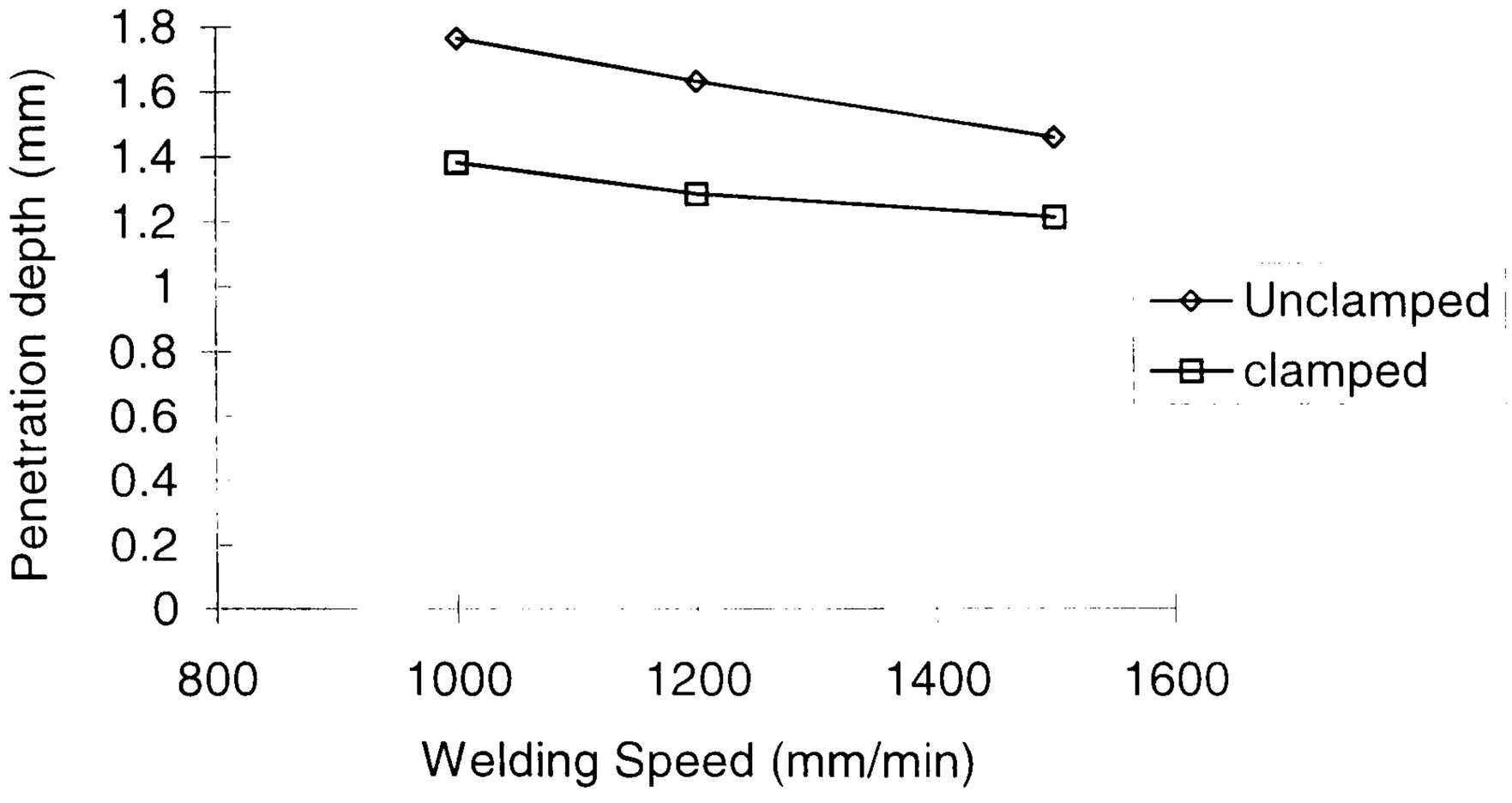

Figure 6.9 Weld Penetration Versus Welding Translation Velocity

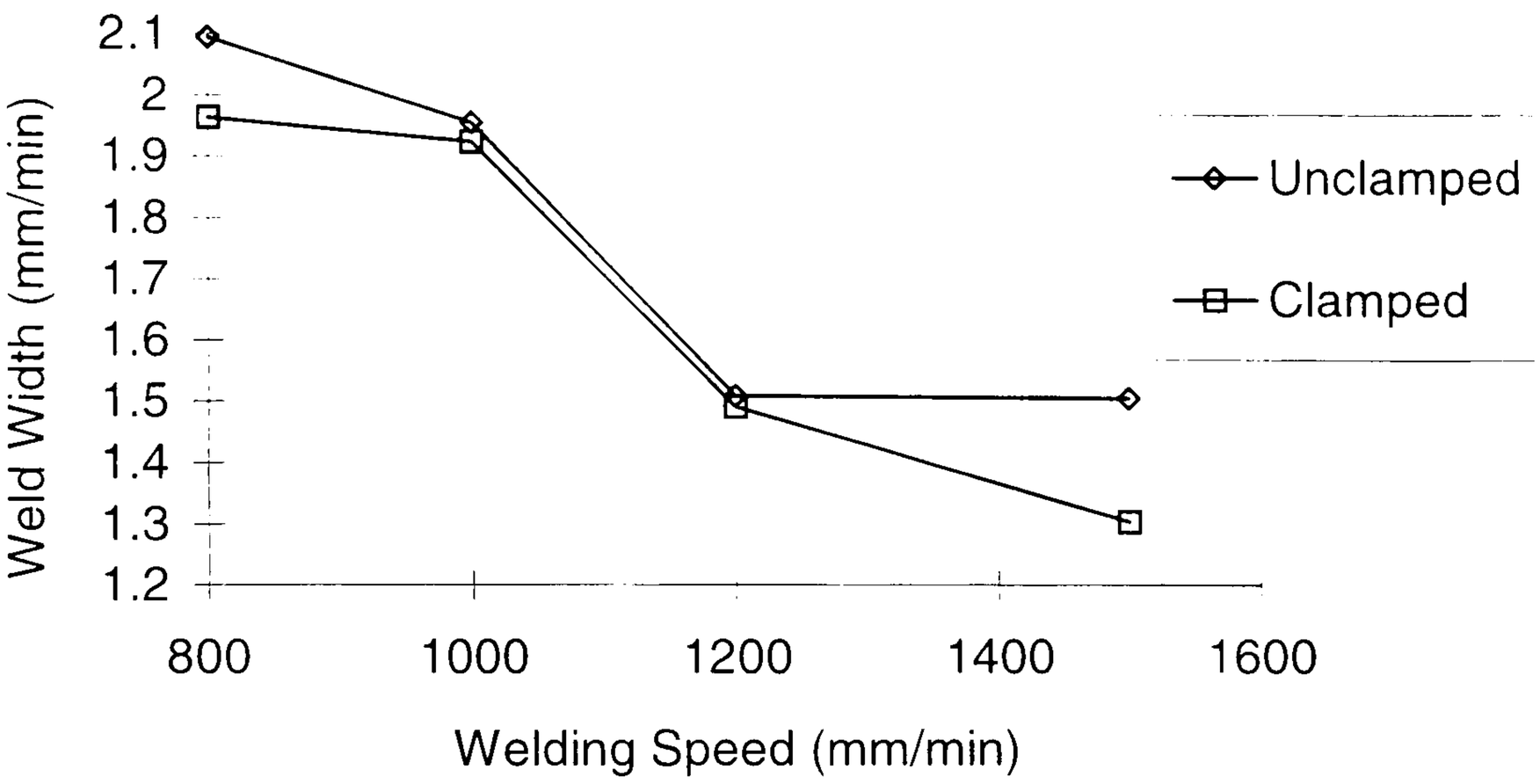

Figure 6.10 Weld Width Versus Welding Translation Velocity

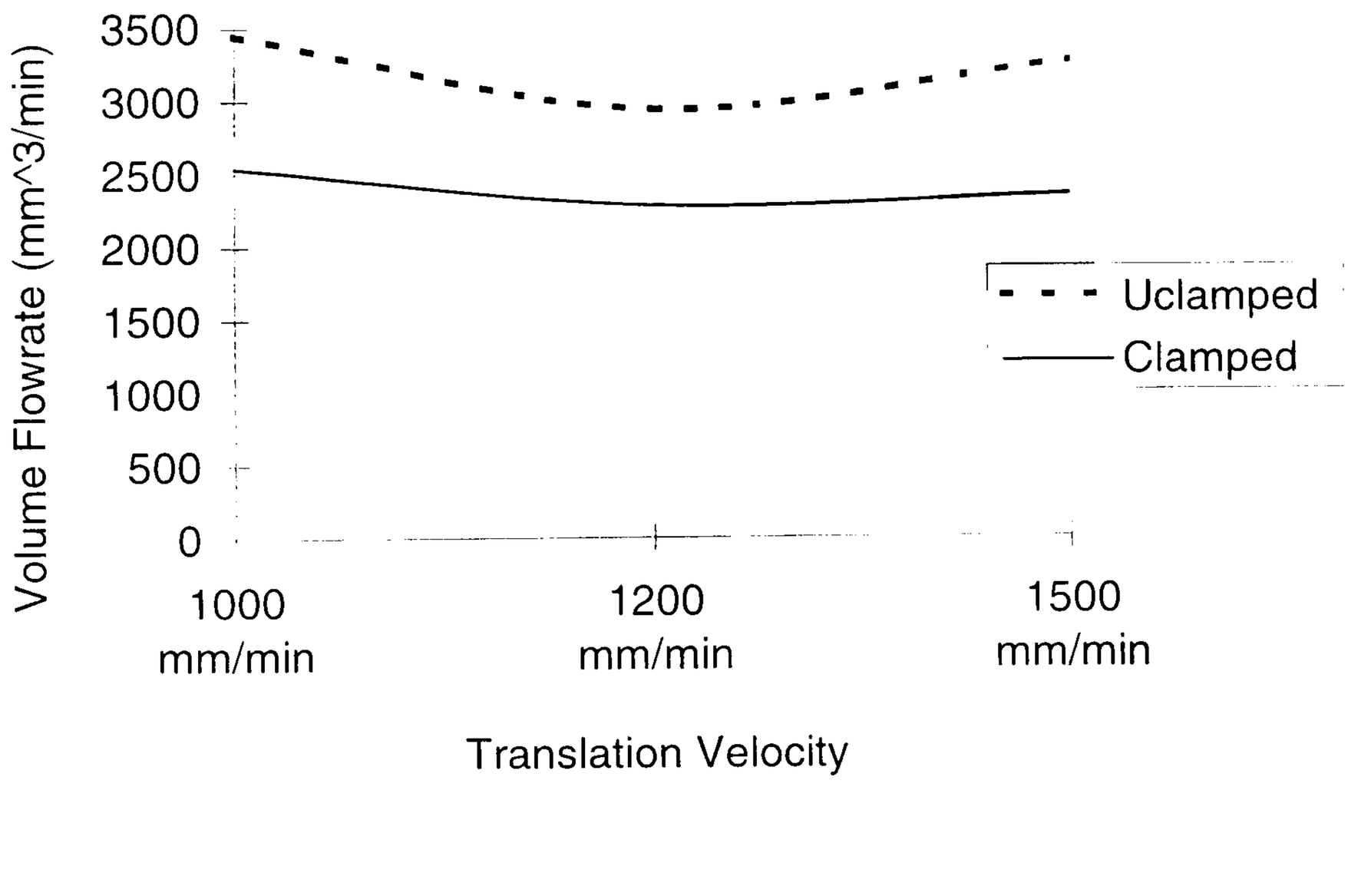

Figure 6.11 HAZ Volume Flowrate Versus Translation Velocity

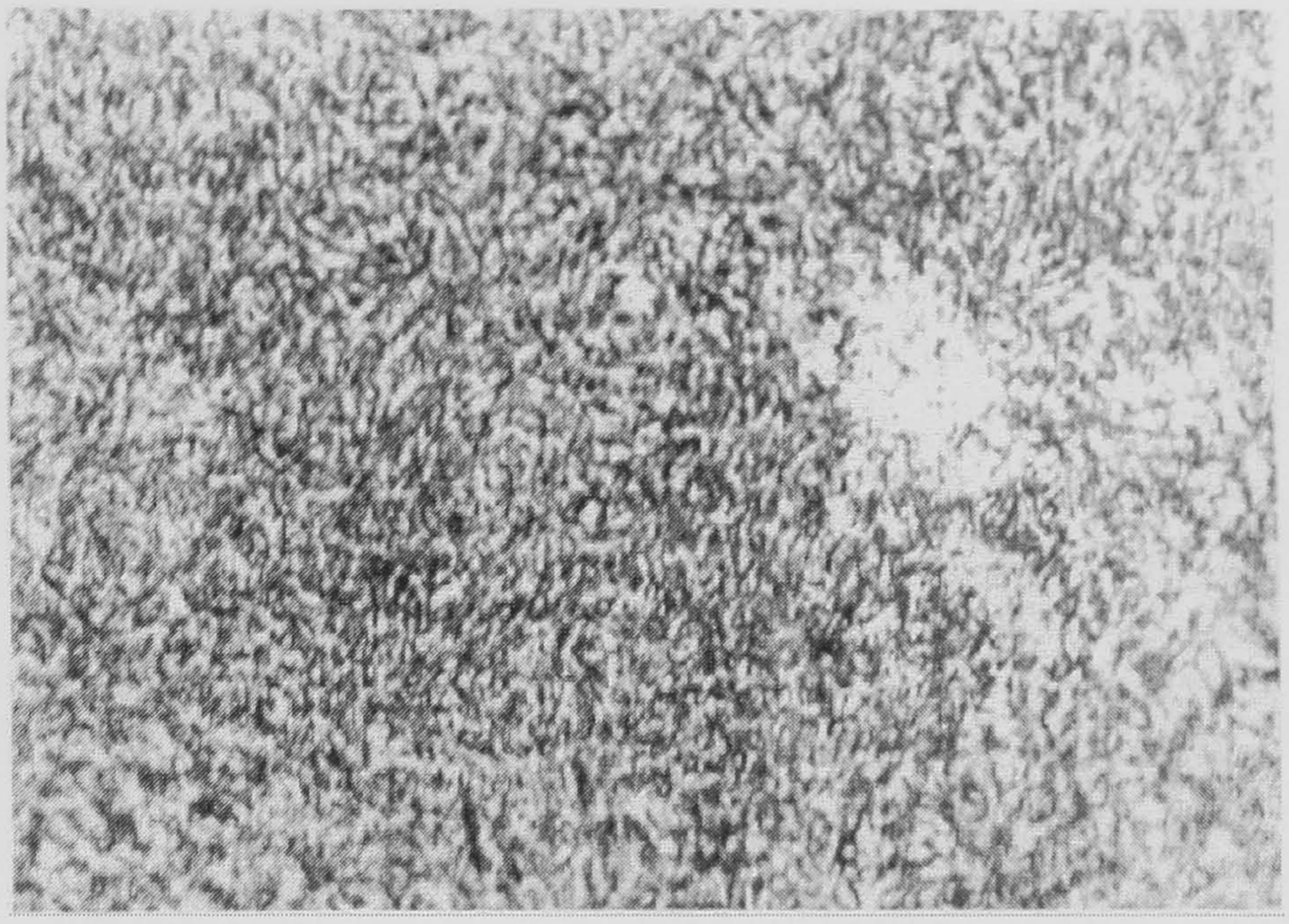

Figure 6.12 Microstructure Of Fusion Zone For Unclamped Workpiece At a Translation Velocity of 800 mm/min : 500X Magification

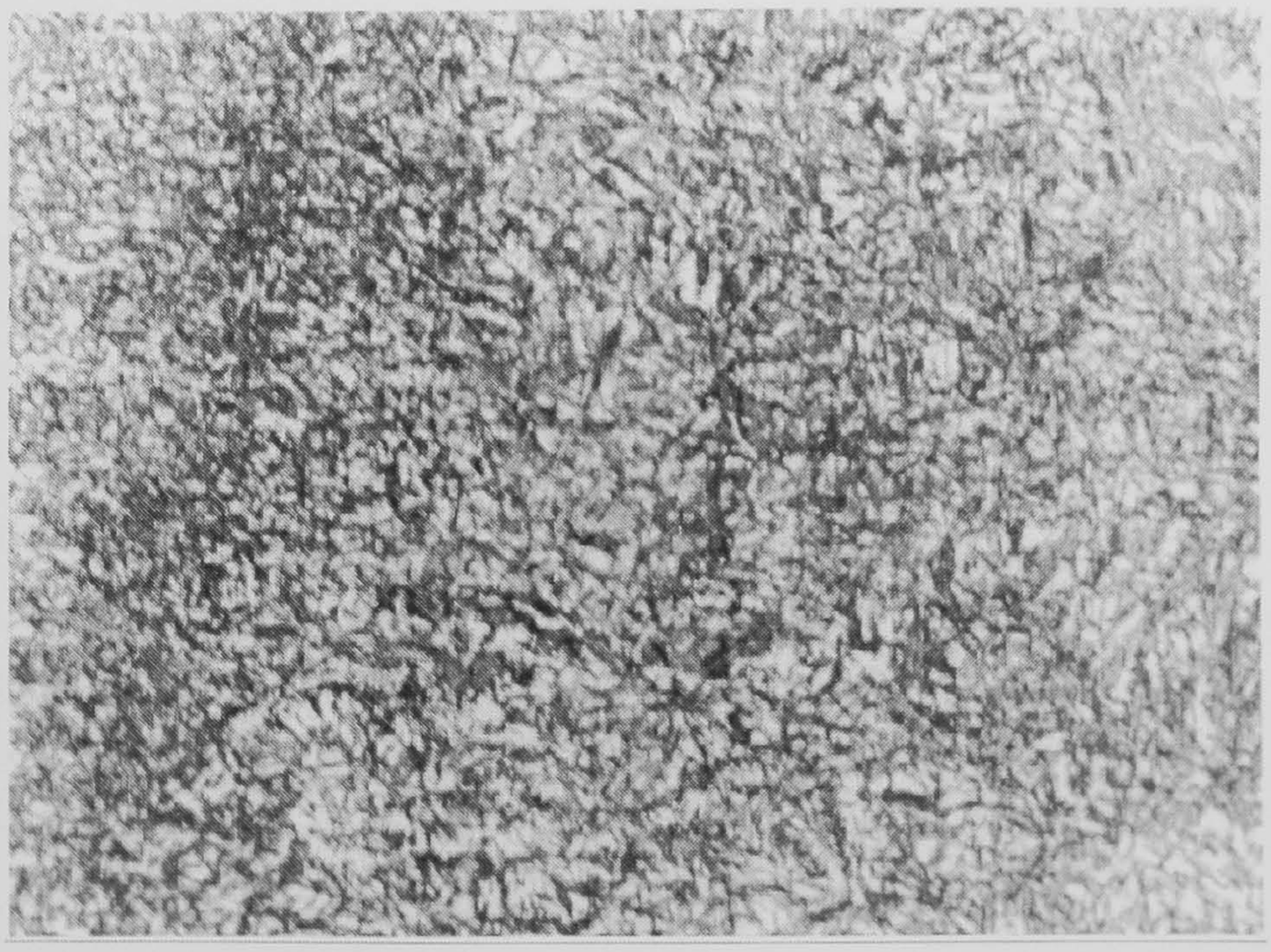

Figure 6.13 Microstructure Of Fusion Zone For Clamped Workpiece At A Translation Speed Of 800 mm/min: 500X Magification

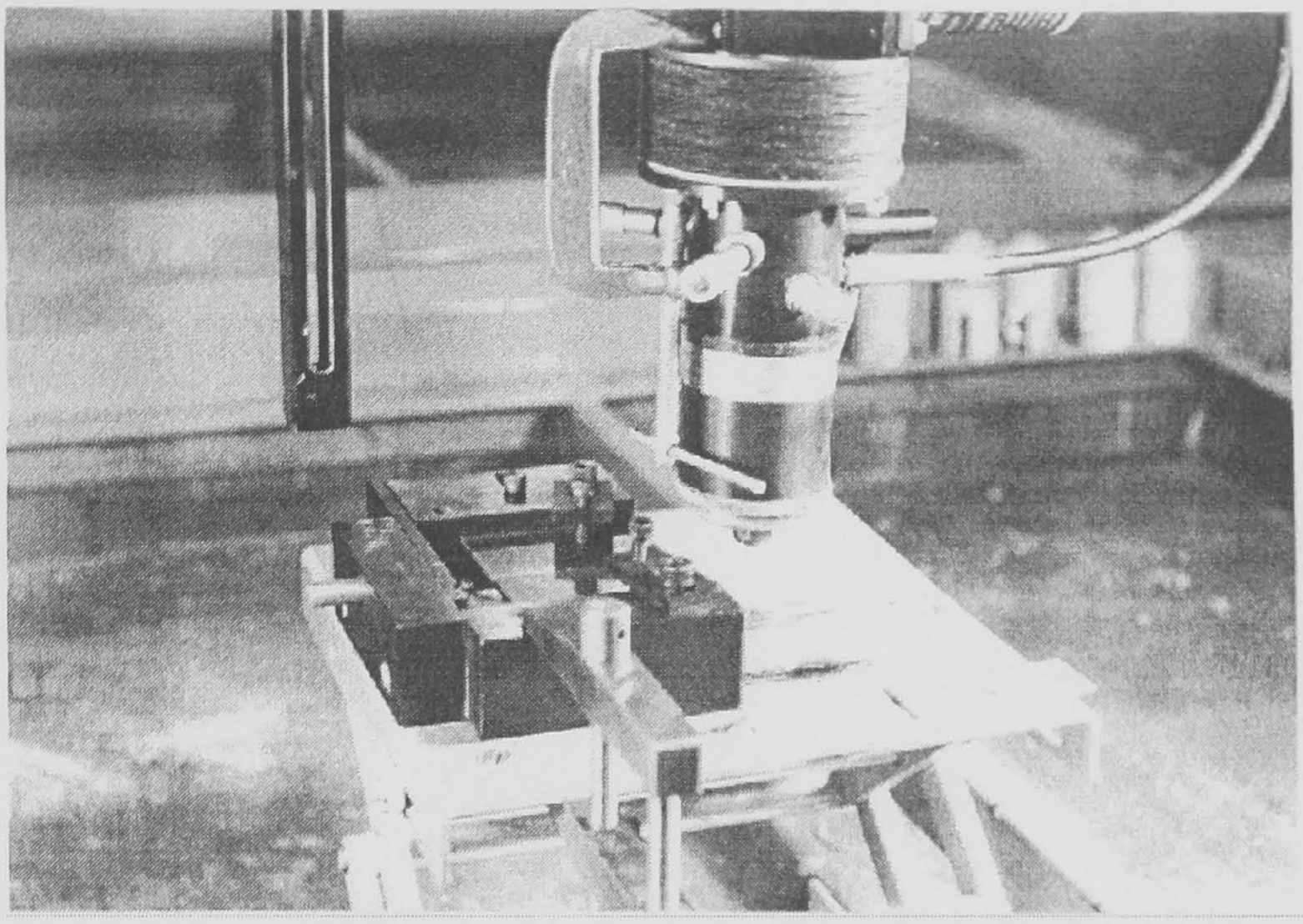

Figure 6.14a An improved clamped geometry used for CO_2 laser welding

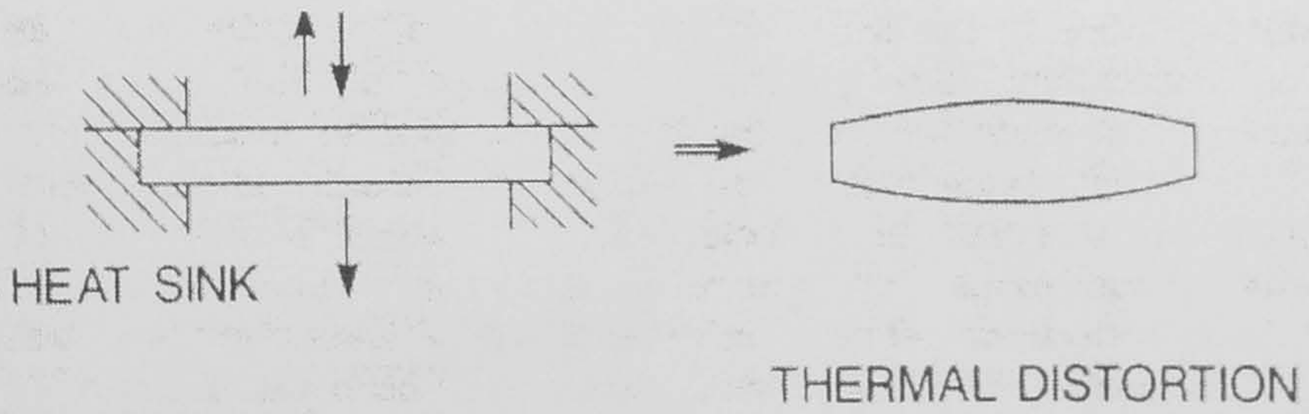

Figure 6 14b. The beam splitter holder for dual beam delivery system

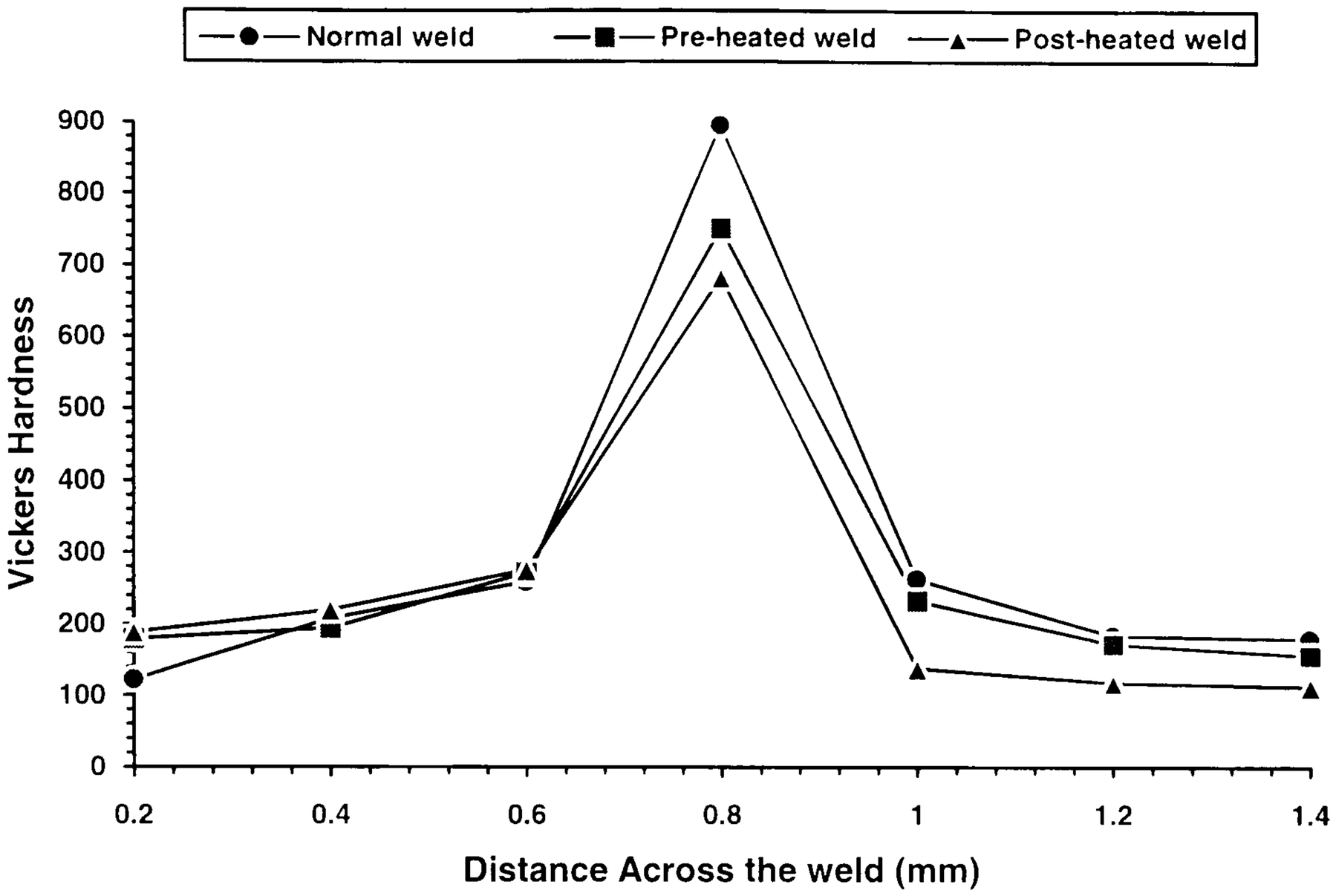

Figure 6.15 CO_2 Laser Weld On 0.85 % C Steel
(Feedrate = 1000 mm/min, Power = 1 kW, Gas = 0.5 bar)

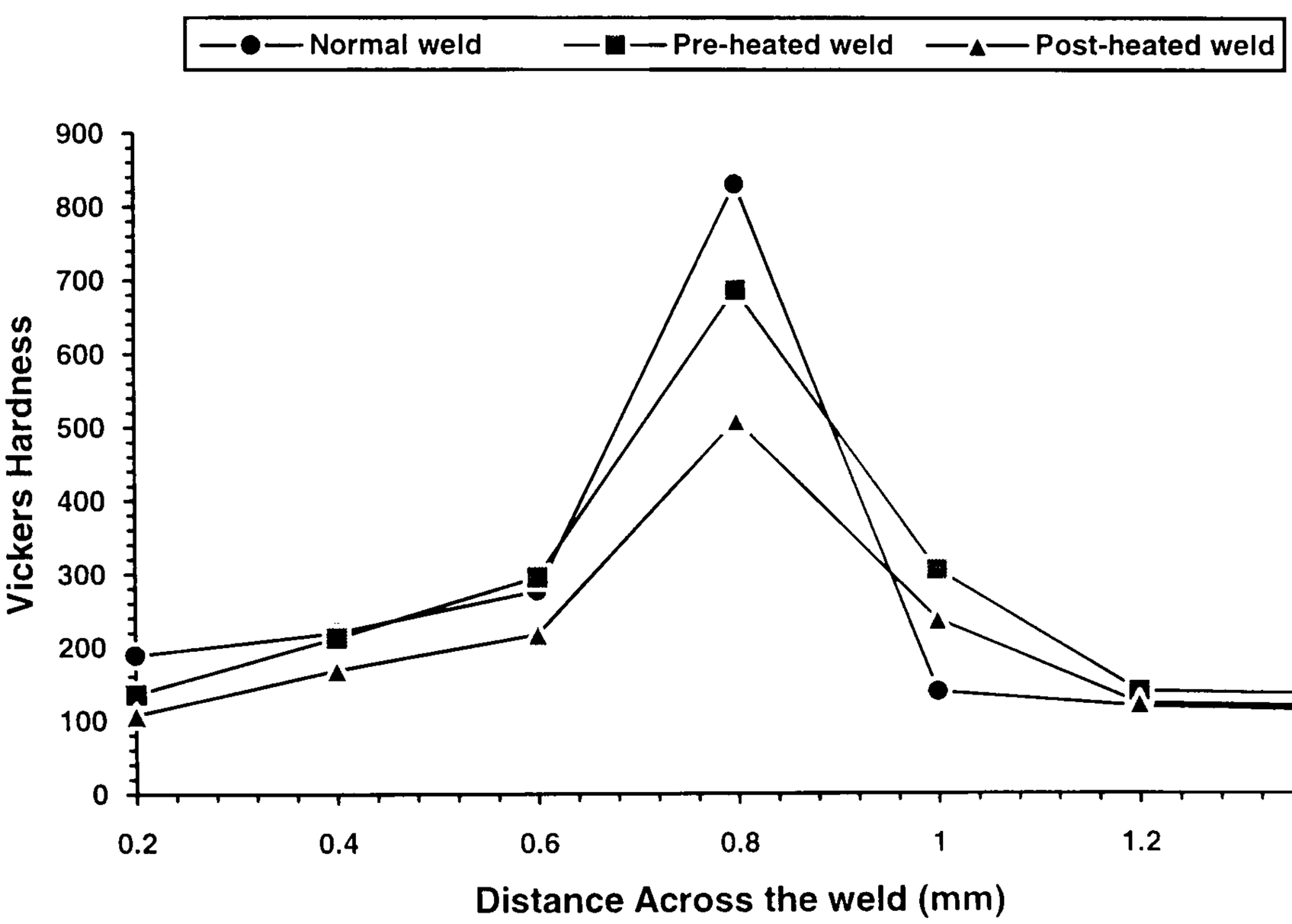

Figure 6.16 CO_2 Laser Weld On 0.85 % C Steel
(Feedrate = 800 mm/min, Power = 1 kW, Gas = 0.5 bar)

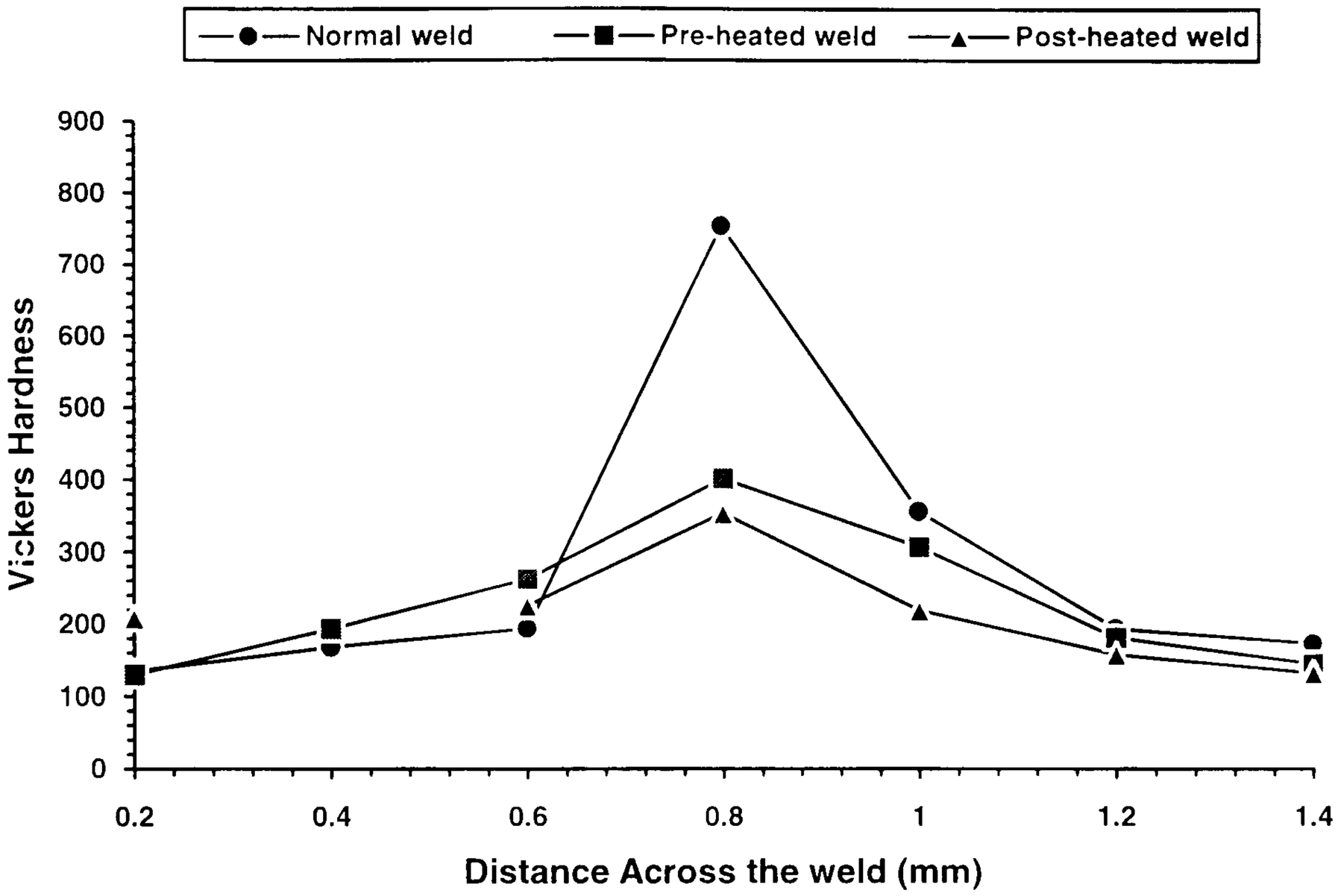

Figure 6.17 CO_2 Laser Weld On 0.85 % C Steel
(Feedrate = 600 mm/min, Power = 1 kW, Gas = 0.5 bar)

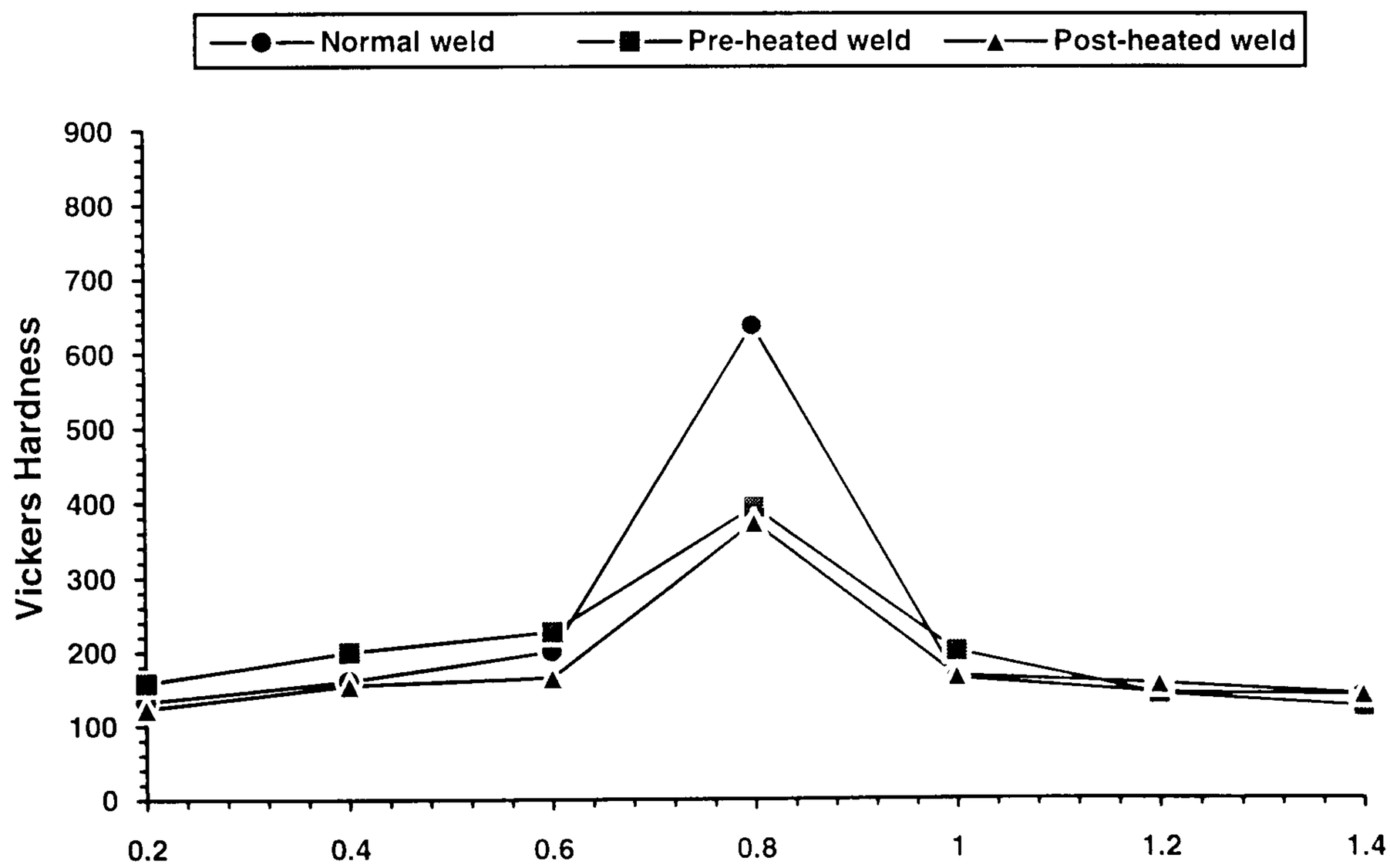

Figure 6.18 CO_2 Laser Weld On 0.5 % C Steel
(Feedrate = 1700 mm/min, Power = 1 kW, Gas = 0.5 bar)

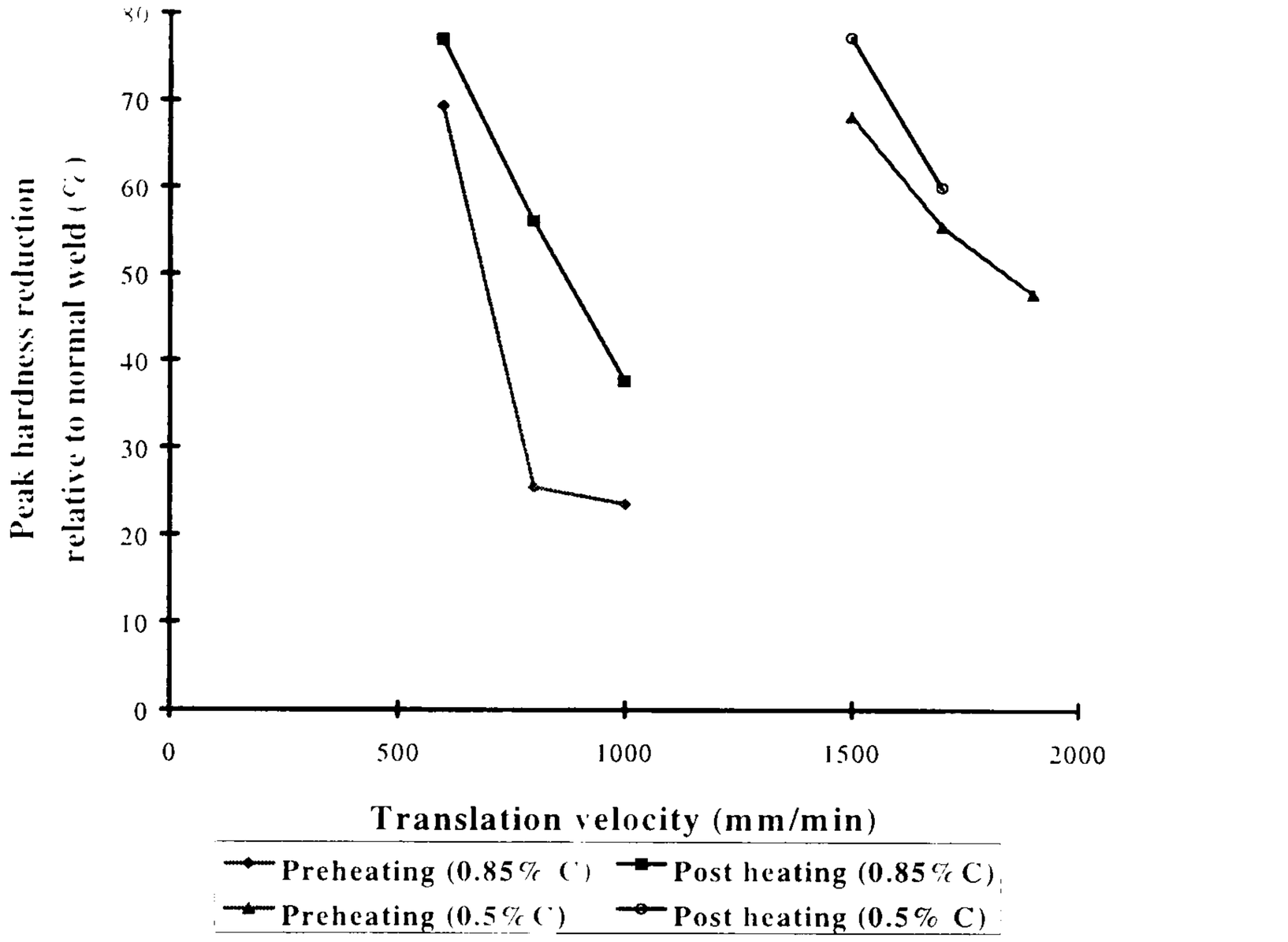

Figure 6.19 Relative Peak Hardness Reduction as A Function of Translation Velocity

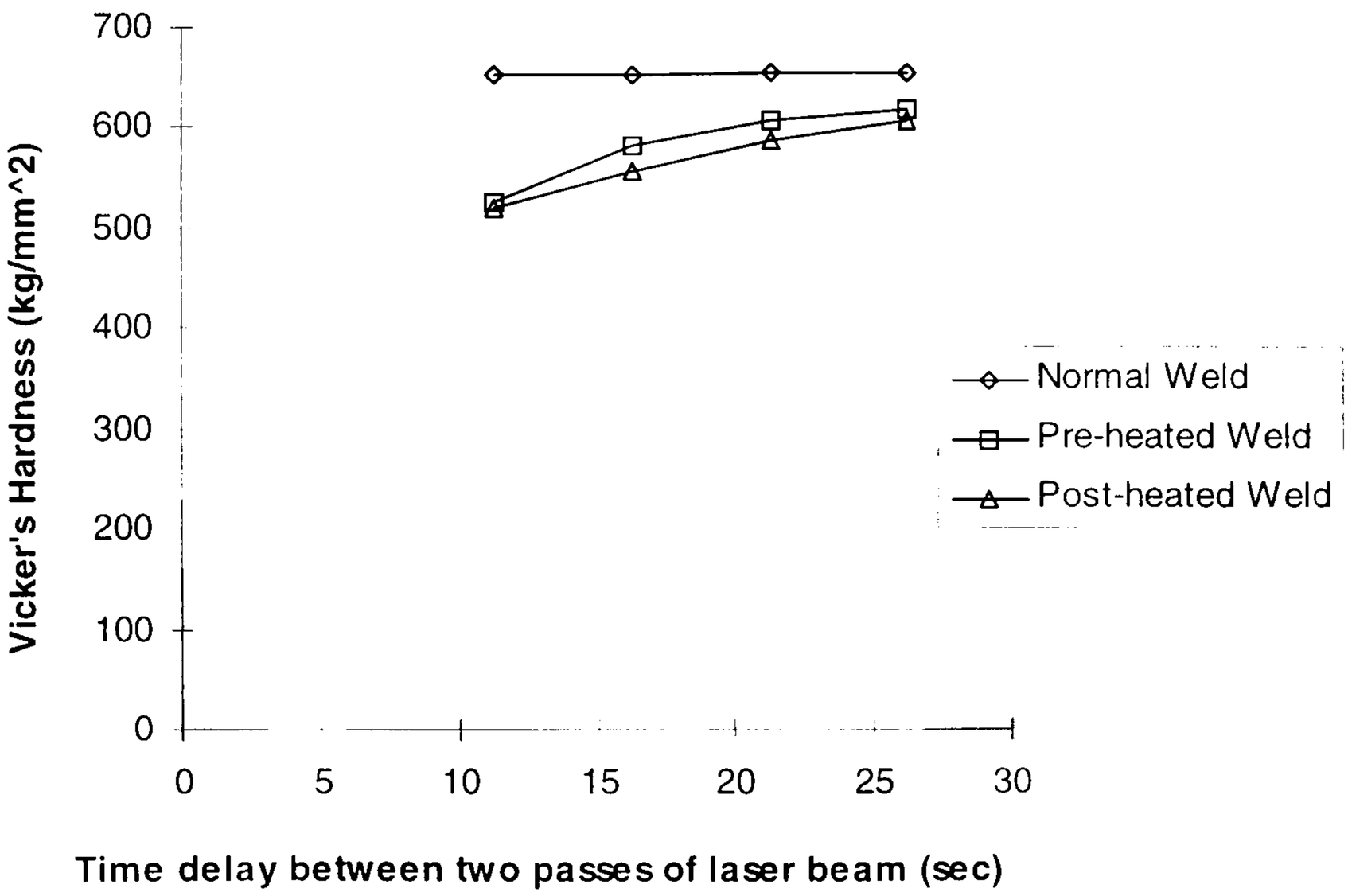

Figure 6.20 Relative Peak Hardness as A Function of Time Delay Between Two Beam

Translation speed (mm/min)	Carbon Content (%)	Welding Methodology	Weld Width (mm)	Weld Penetration (mm)
1500	0.5	Normal Weld	1.371	1.483
1500	0.5	Pre-heated Weld	1.401	1.513
1500	0.5	Post-heated Weld	1.408	1.503
800	0.85	Normal Weld	2.110	1.741
800	0.85	Pre-heated Weld	2.131	1.821
800	0.85	Post-heated Weld	2.156	1.749

Table 6.2 The Weld Width and Penetration Depth, For the Normal, Pre-heated and Post-heated Welds

Figure 6.21 Micrograph of Normal Laser Weld (x16)

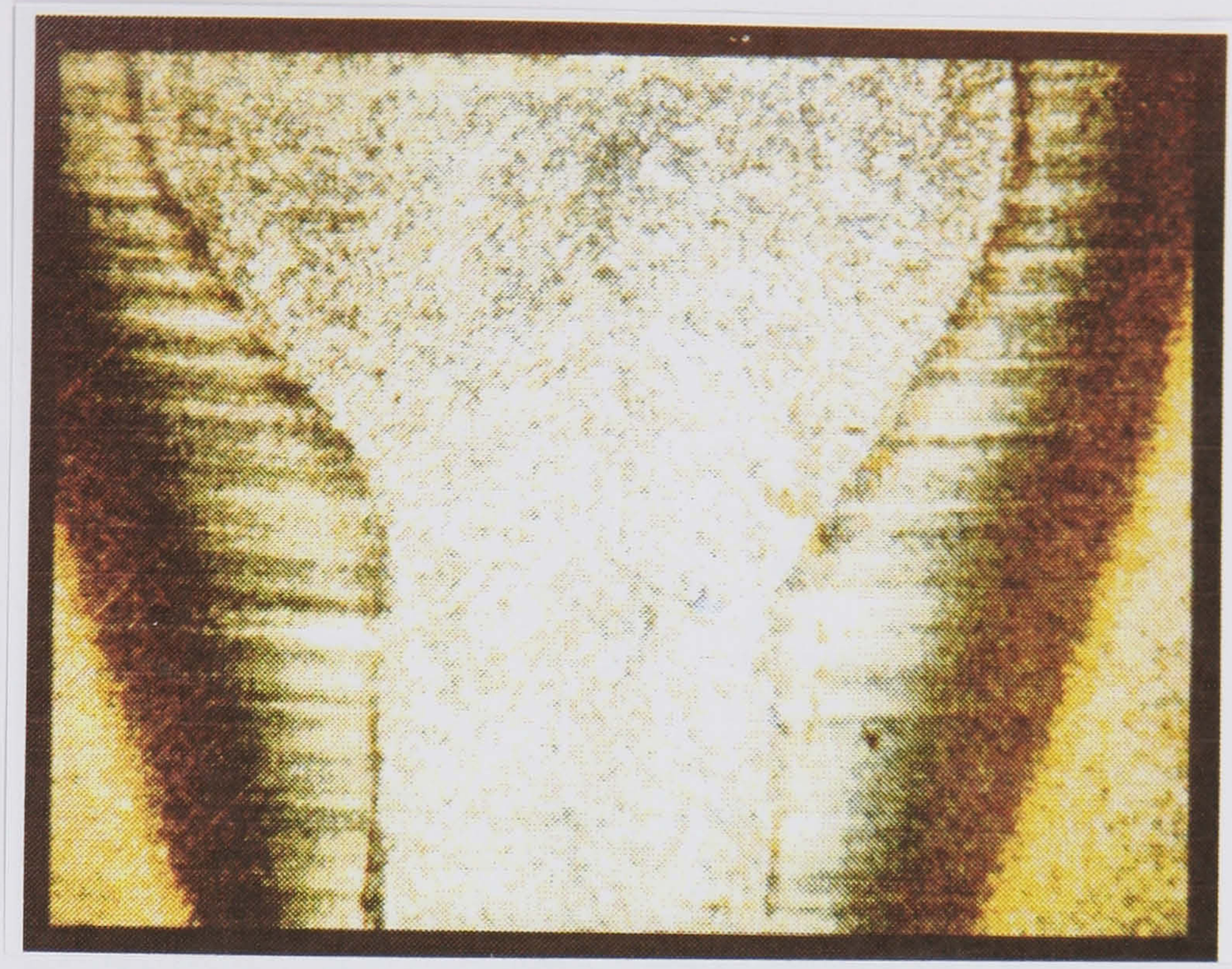

Figure 6.22 Micrograph of Pre-heated Weld (x63)

Figure 6.23 Micrograph of Complex Transformation Structure With Pre-heating (x63)

Figure 6.24 Micrograph of Post-heated Sample showing Banding (x63)

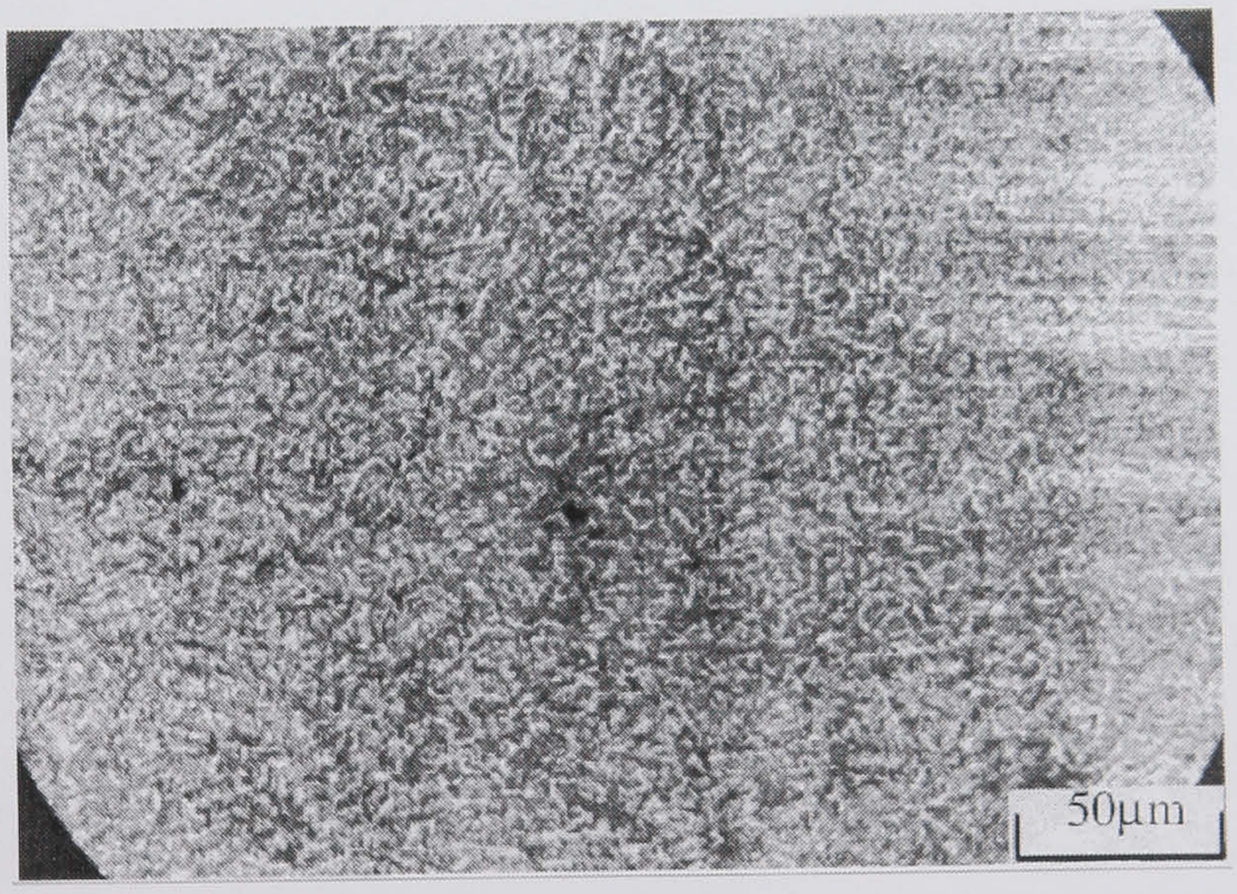

Figure 6.26 Micrograph of normal weld Sample (x63) using time delay of two passes of laser beams

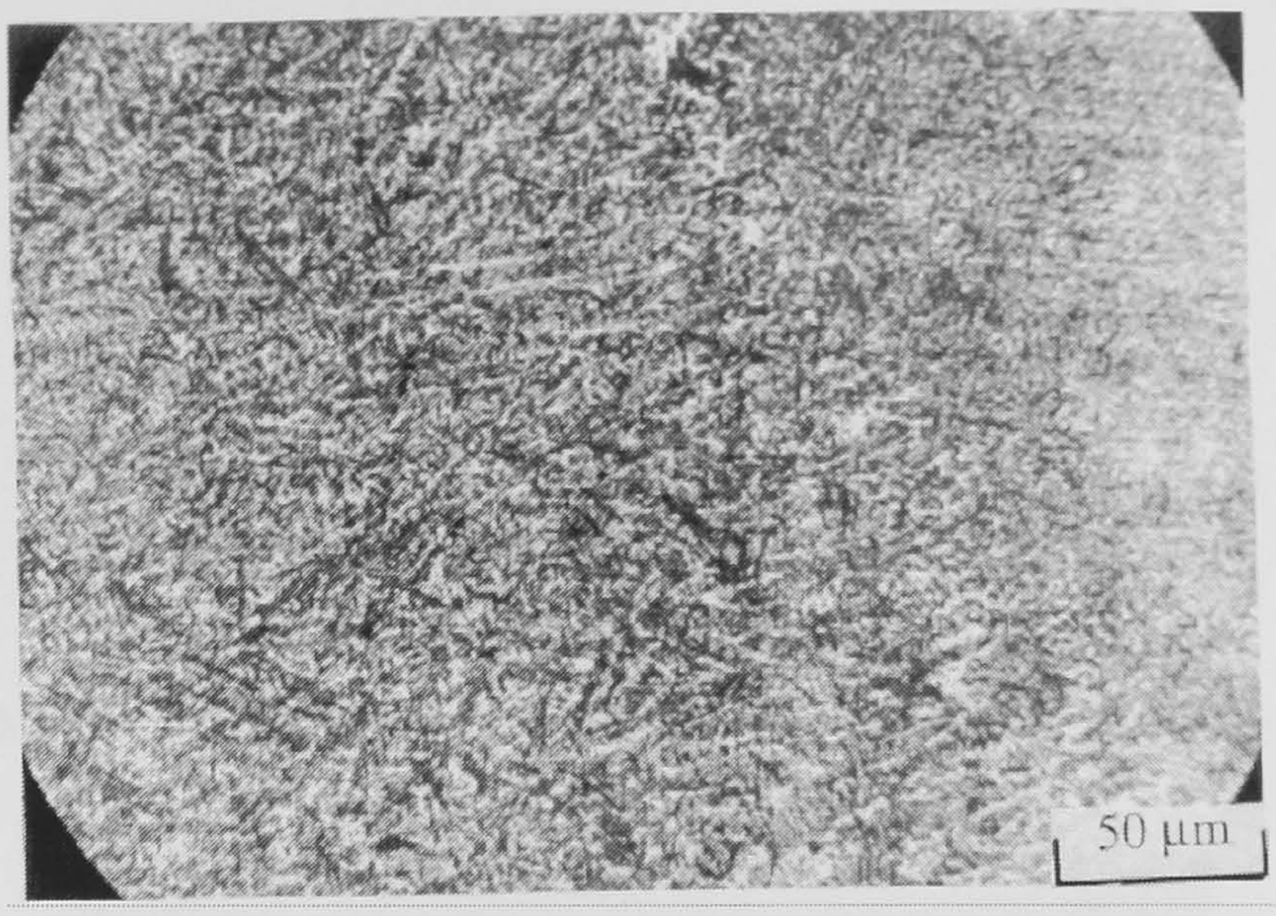

Figure 6.26 Micrograph of post-heated weld Sample (x63) using time delay of two passes of laser beams

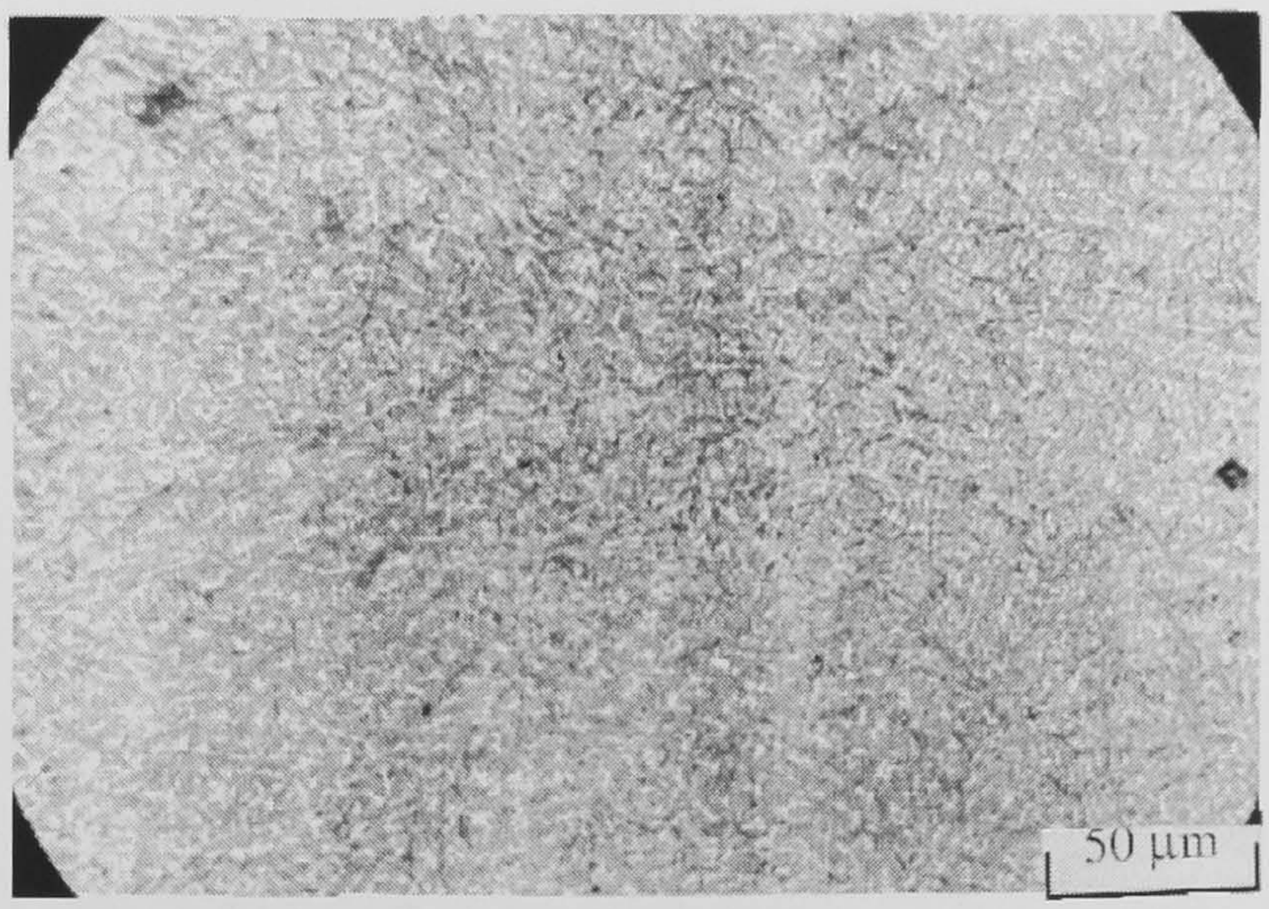

Figure 6.27 Micrograph of pre-heated weld Sample (x63) using time delay of two passes of laser beams

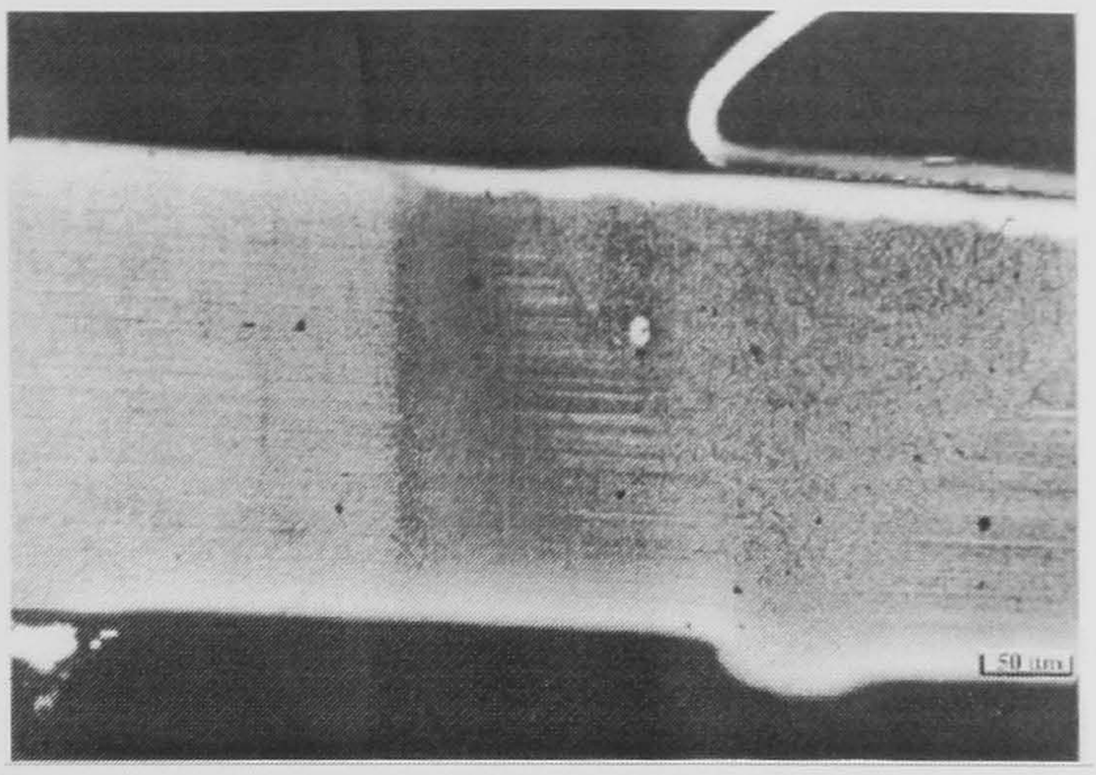

Figure 6.28 Micrograph showing transformation structure of normal weld (x15.6)

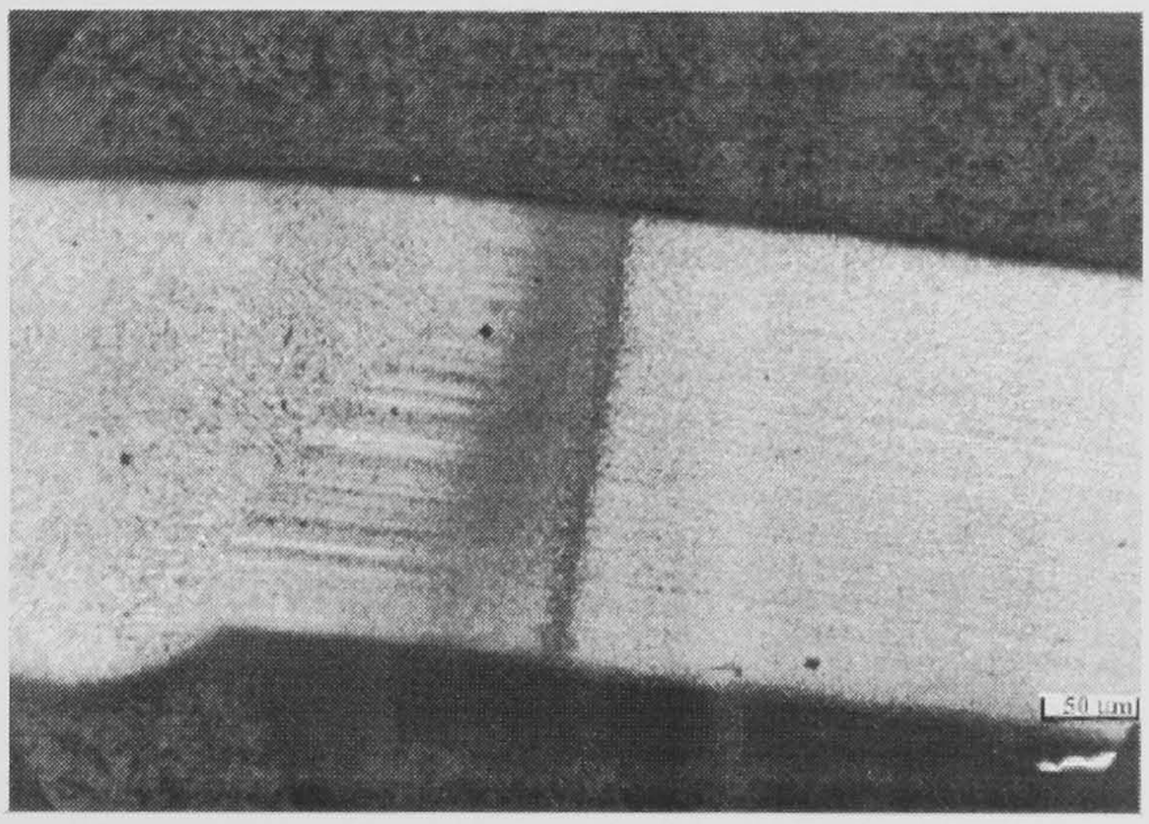

Figure 6.29 Micrograph showing transformation structure of post-heated weld (x15.6)

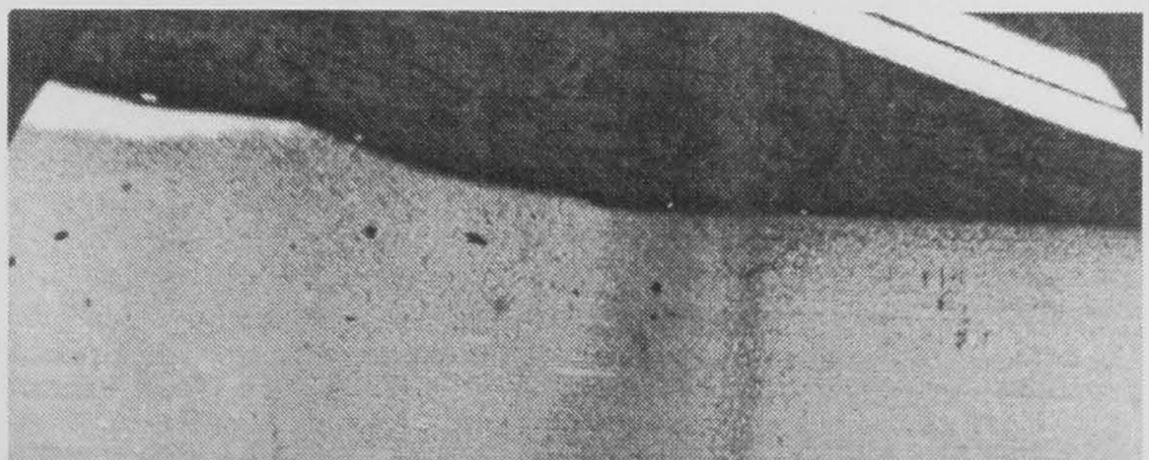

Figure 6.30 Micrograph showing transformation structure of pre-heated weld (x15.6)

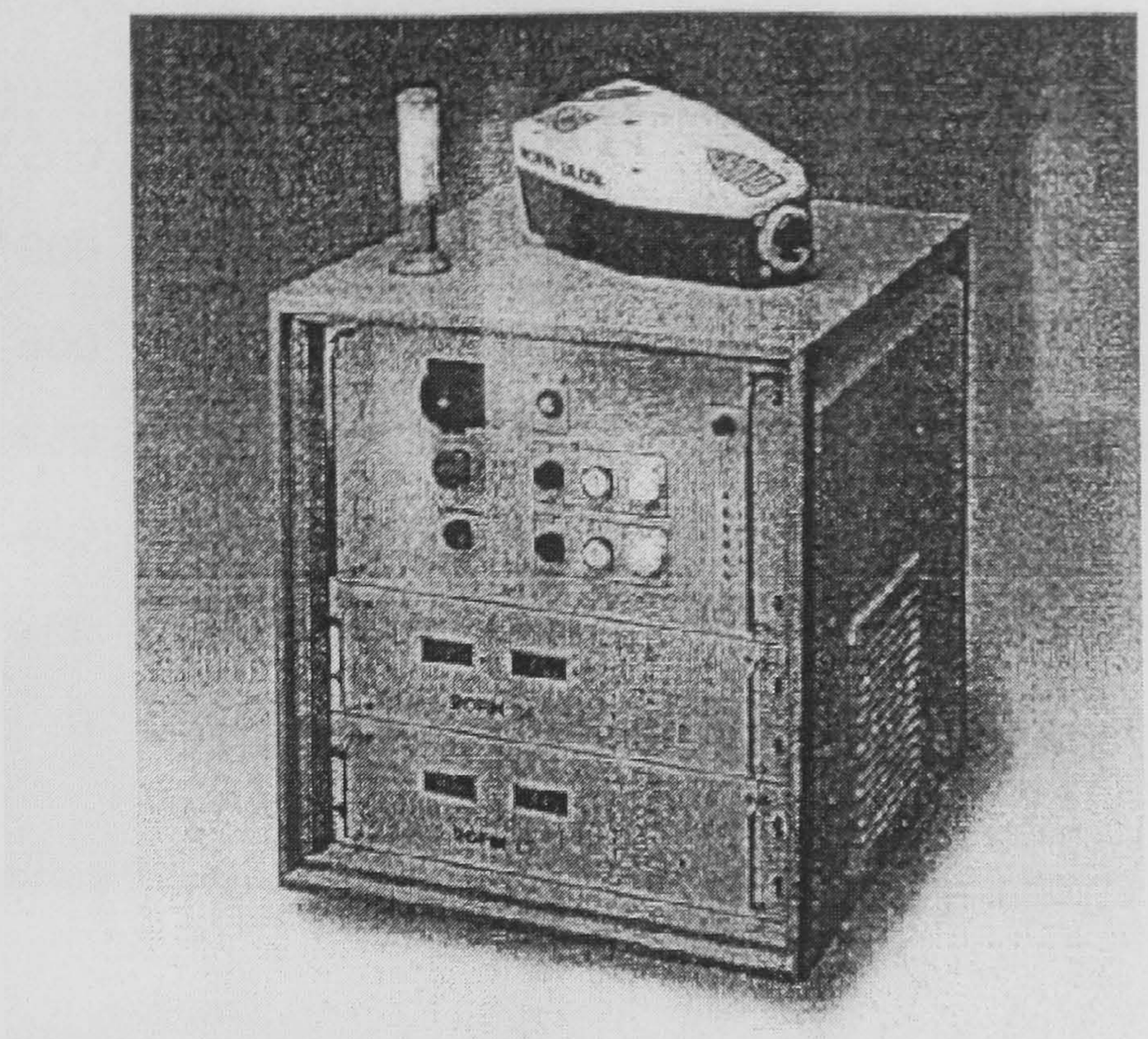

Figure 6.31. Industrial high power diode laser system Rofin DL 015 (1.5 kW)

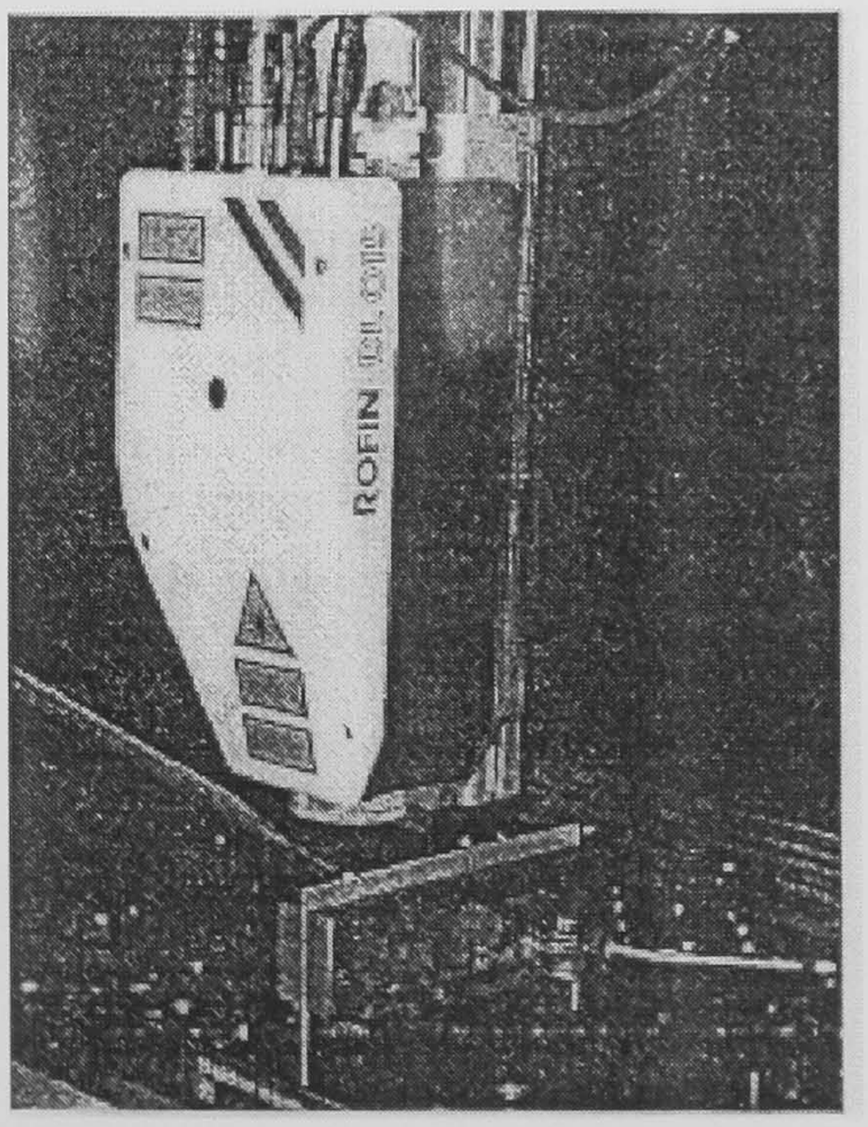

Figure 6.32 High power diode laser head mounted on a gantry system

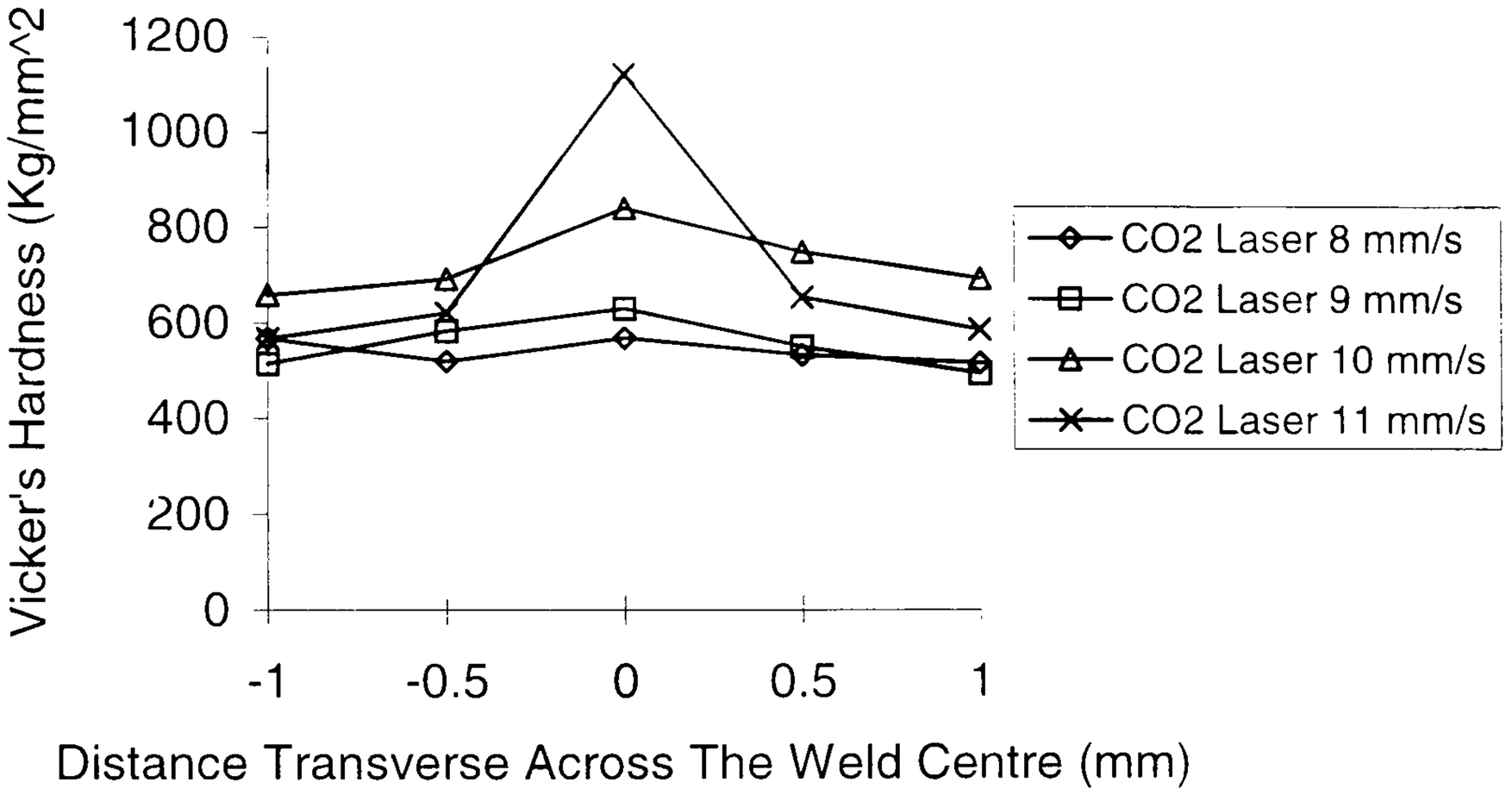

Figure 6.33 Microhardness transverse across CO_2 laser welded samples (2 mm gauge plate of 0.85 - 1.2 wt % C)

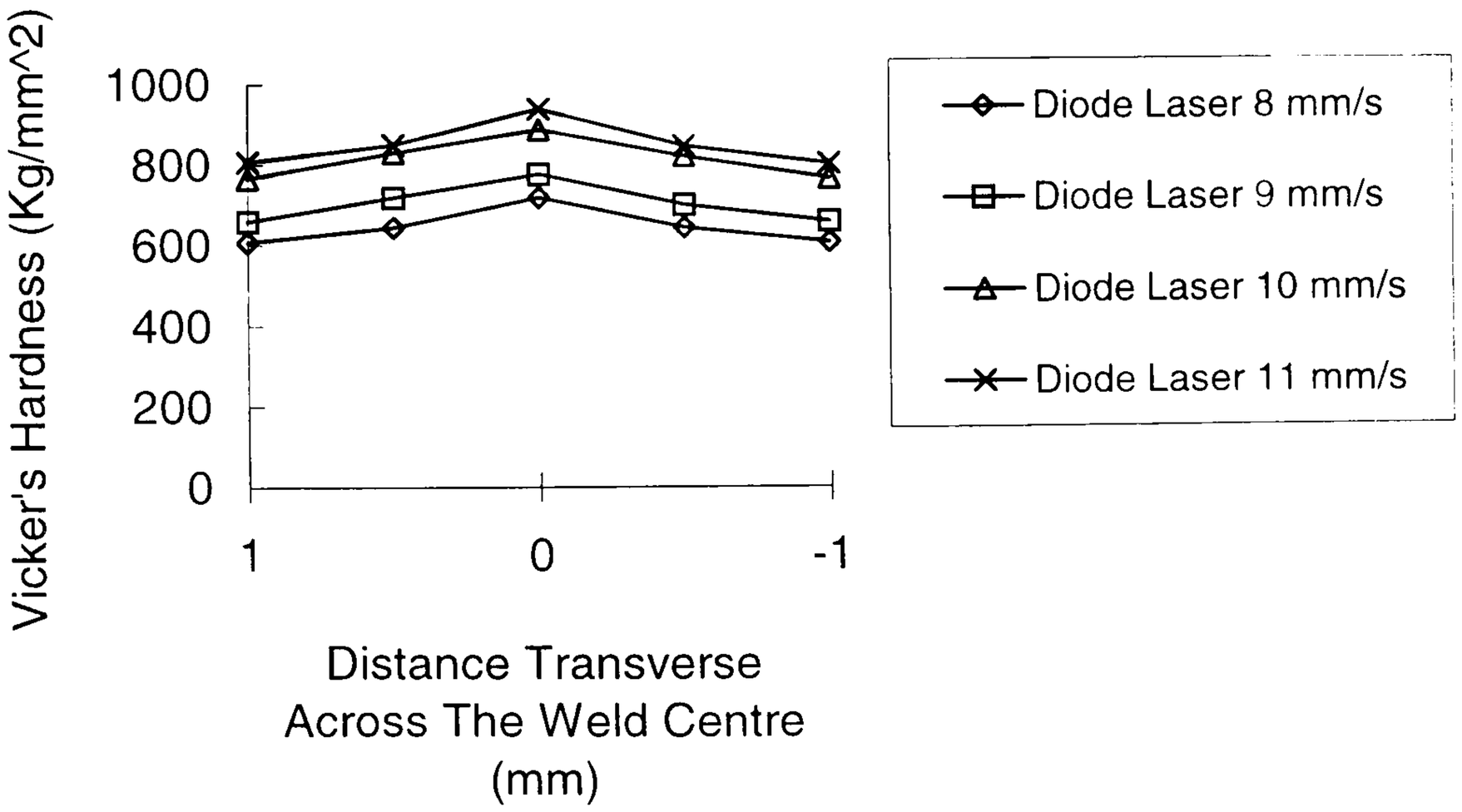

Figure 6.34 Microhardness transverse across diode laser welded samples (2 mm gauge plate of 0.85 - 1.2 wt % C)

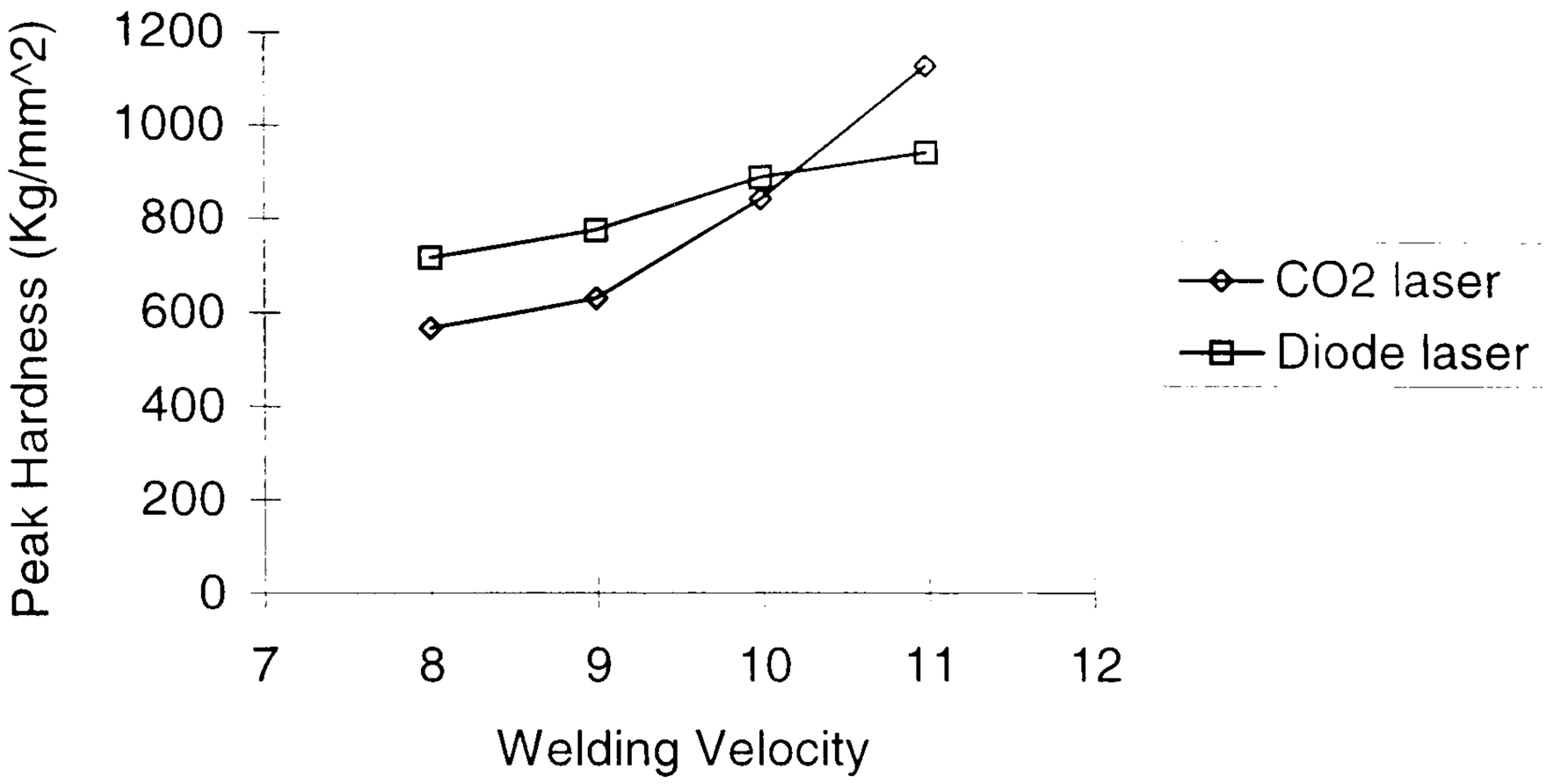

Figure 6.35 Peak hardness as a function of welding velocity

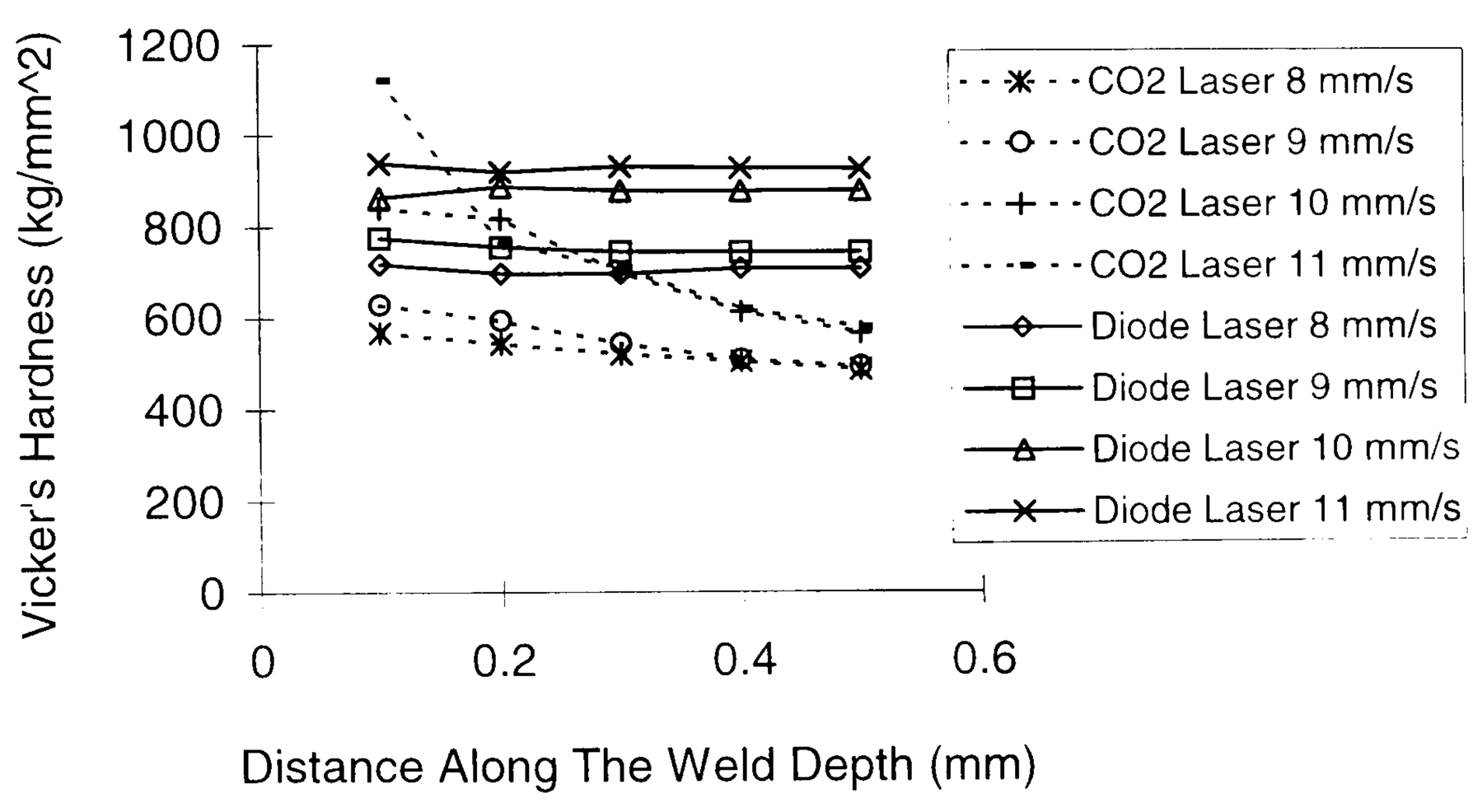

Figure 6.36 Vicker's hardness as a function along weld depth, for CO_2 and diode laser welds

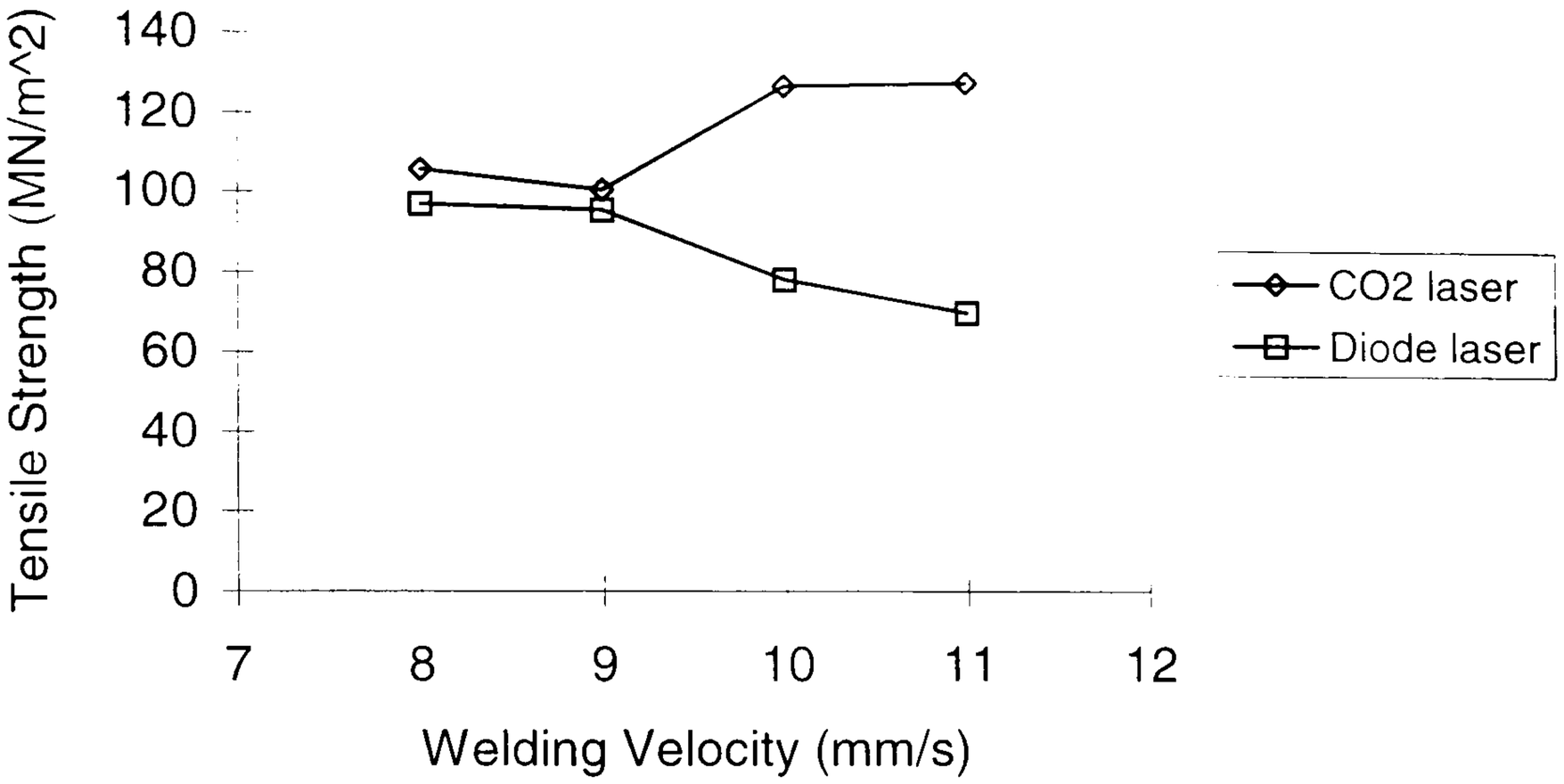

Figure 6.37 Tensile strength as a function of welding velocity

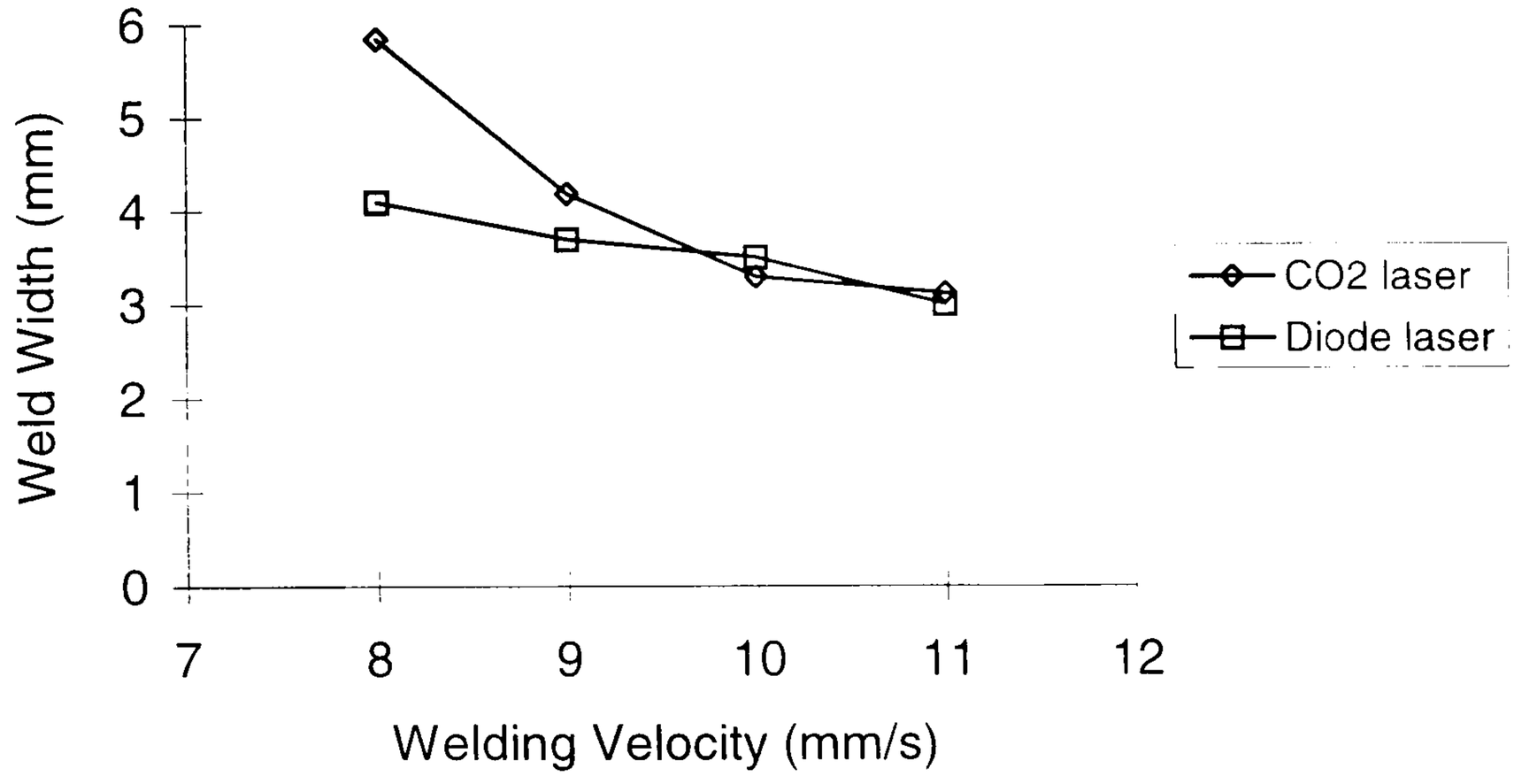

Figure 6.38 Weld width as a function of welding velocity

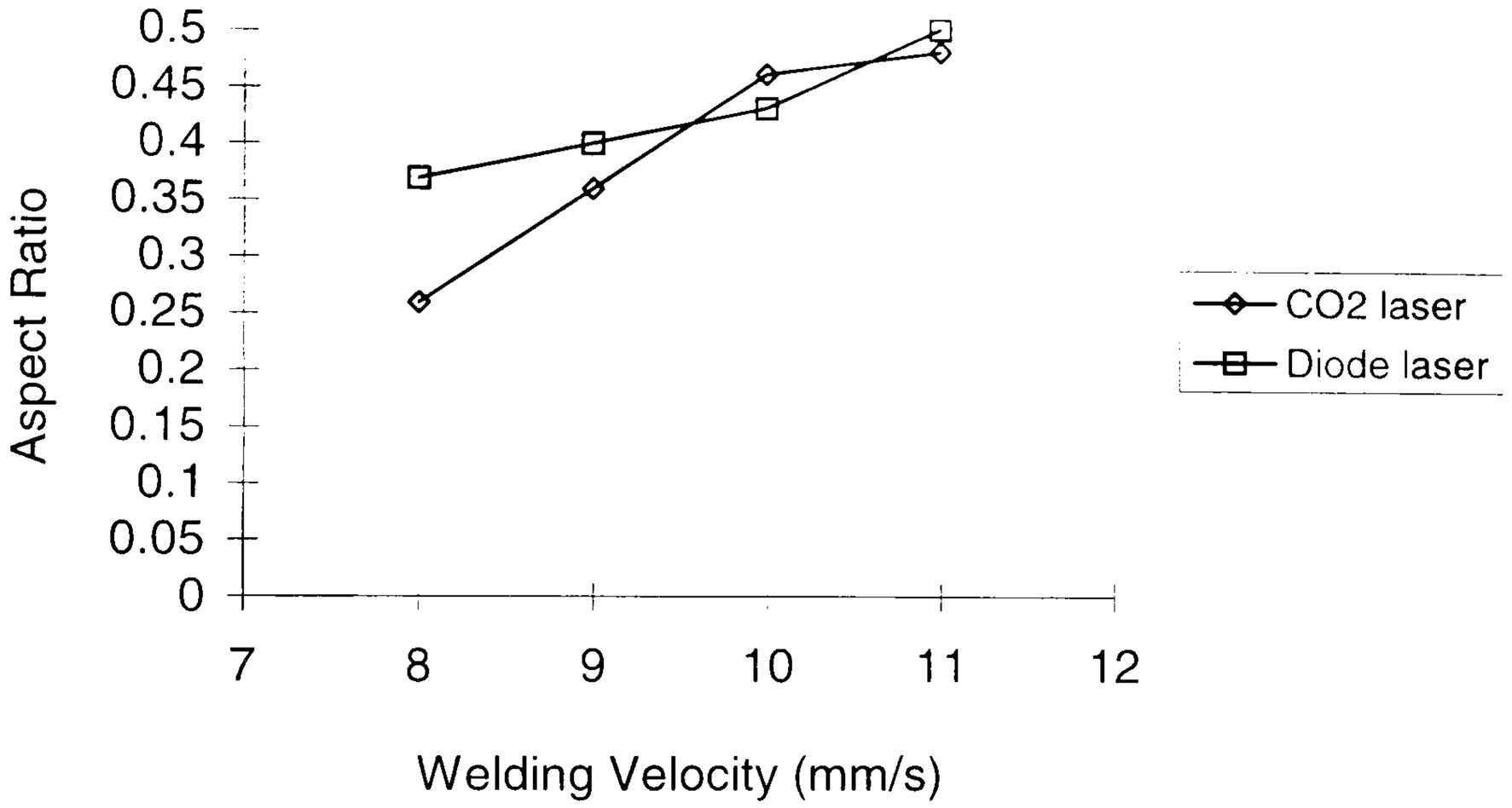

Figure 6.39 Aspect ratio as a function of welding velocity

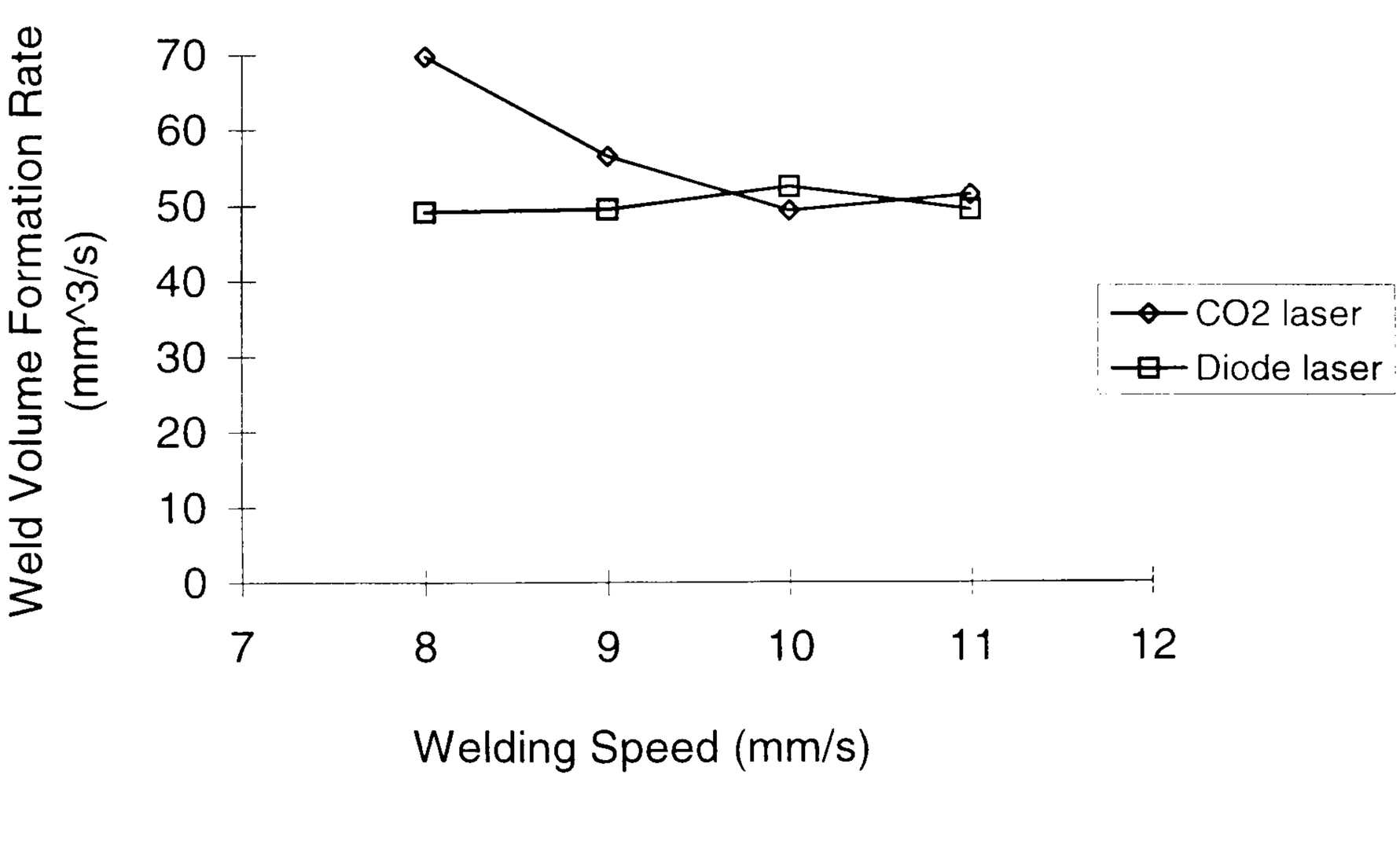

Figure 6.40 The rate of weld volume formation as a function of welding velocity

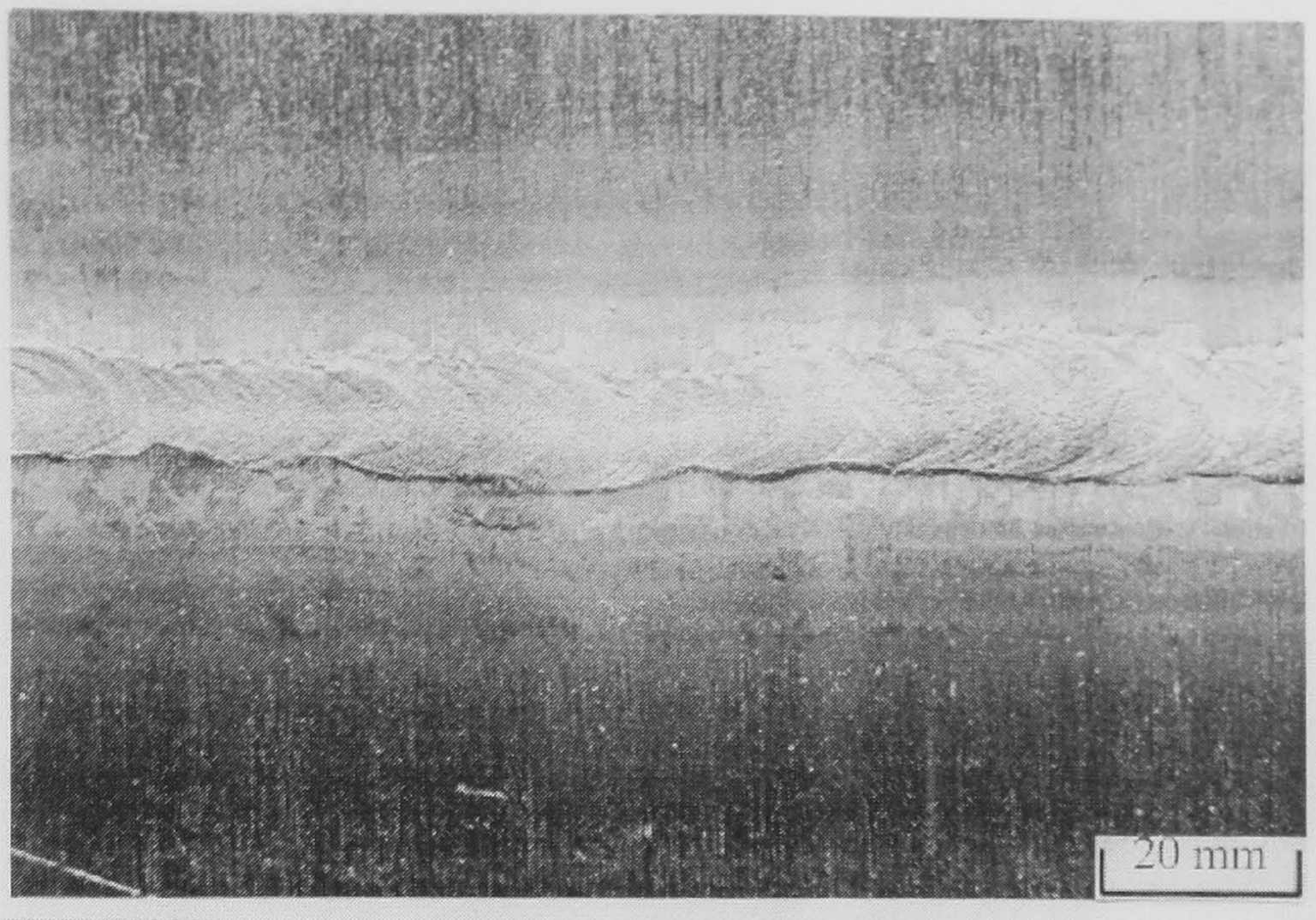

Figure 6.41 Weld seam appearance for CO_2 laser weld at a welding velocity of 7 mm/s

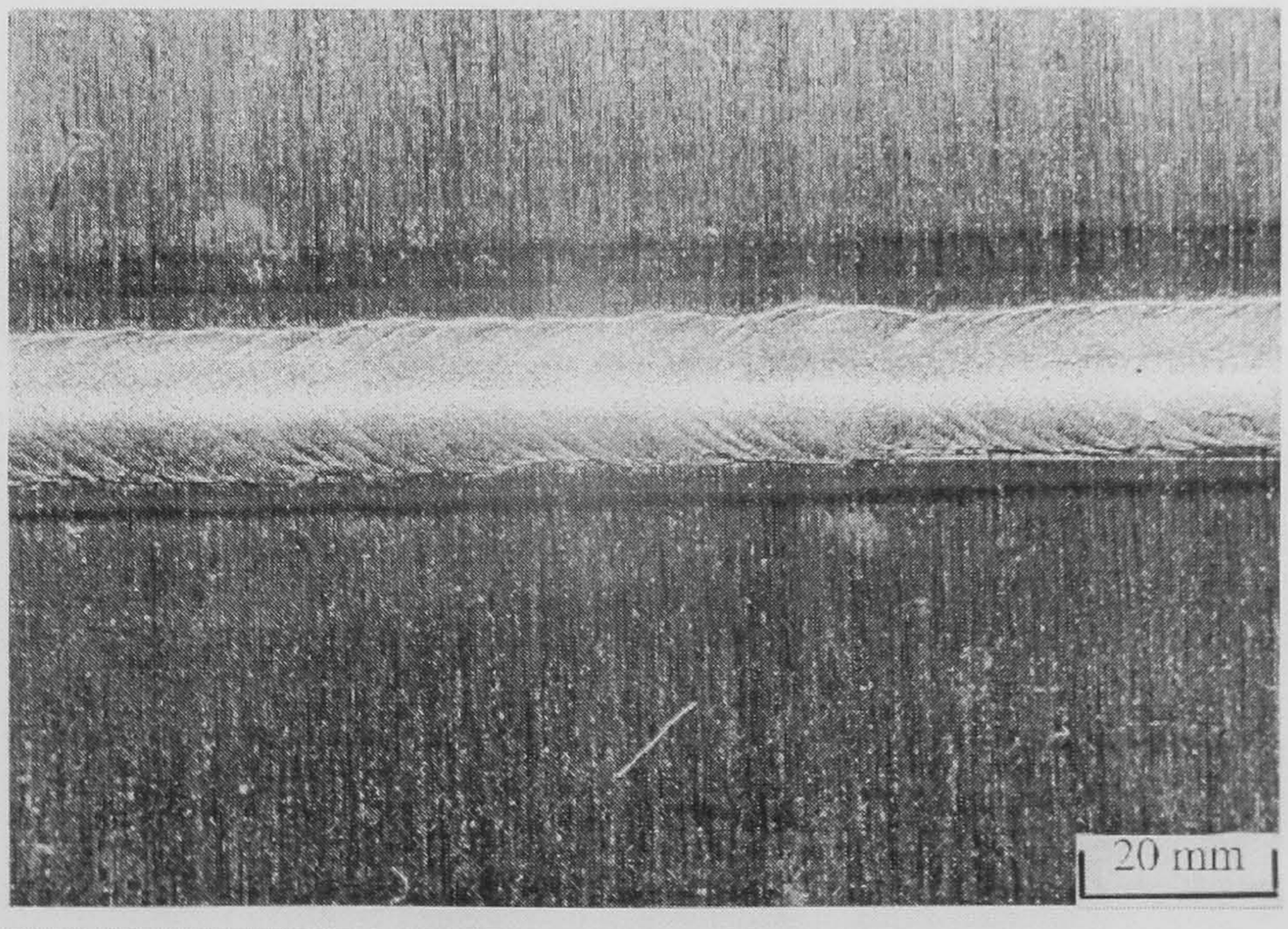

Figure 6.42 Weld seam appearance for diode laser weld at a welding velocity of 7 mm/s

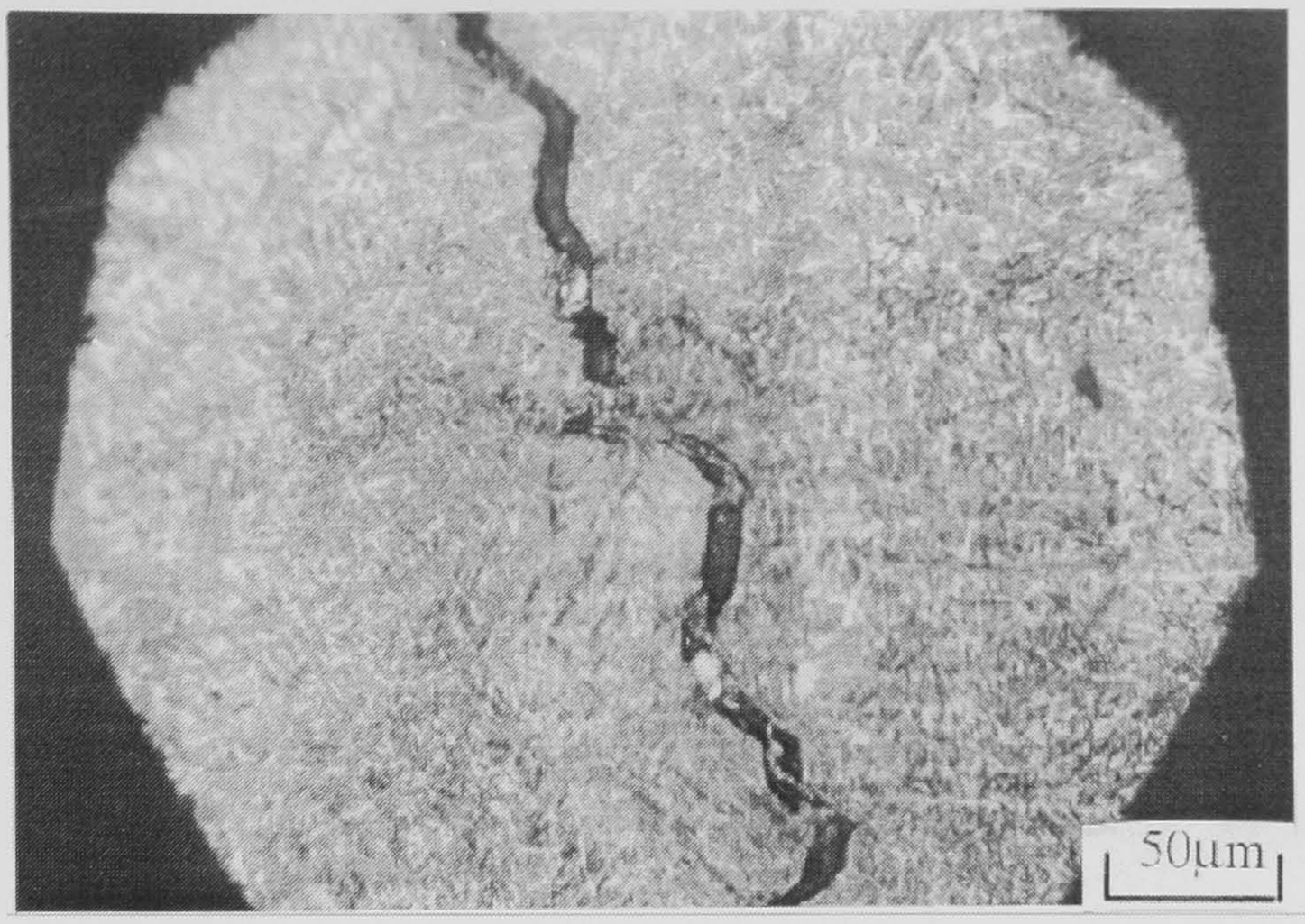

Figure 6.43 Crack evident was clearly observed in the fusion zone, for diode laser welding at a welding velocity of 10 mm/s

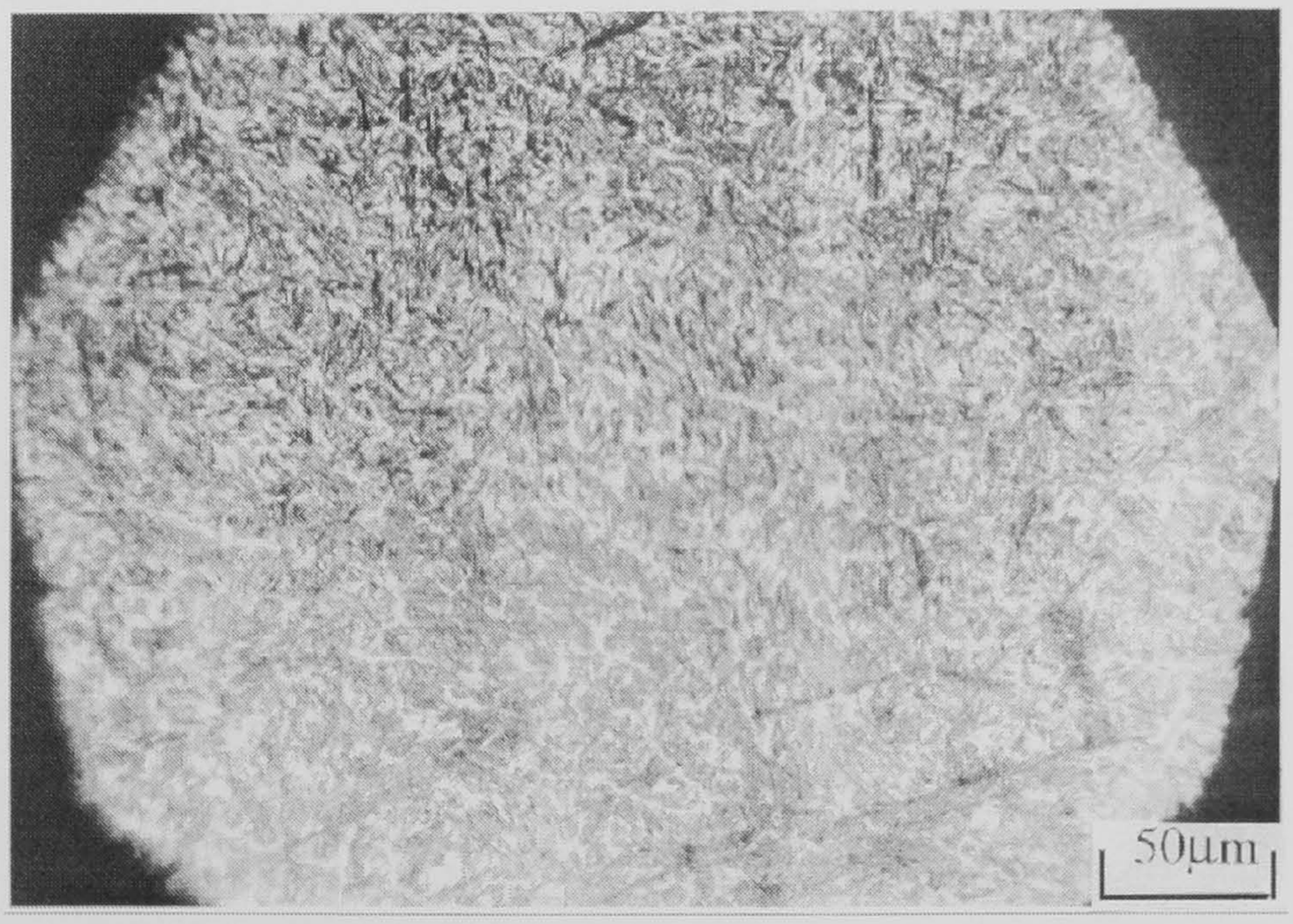

Figure 6.44 No crack evident was found in the fusion zone of CO_2 laser weld at a welding velocity of 10 mm/s

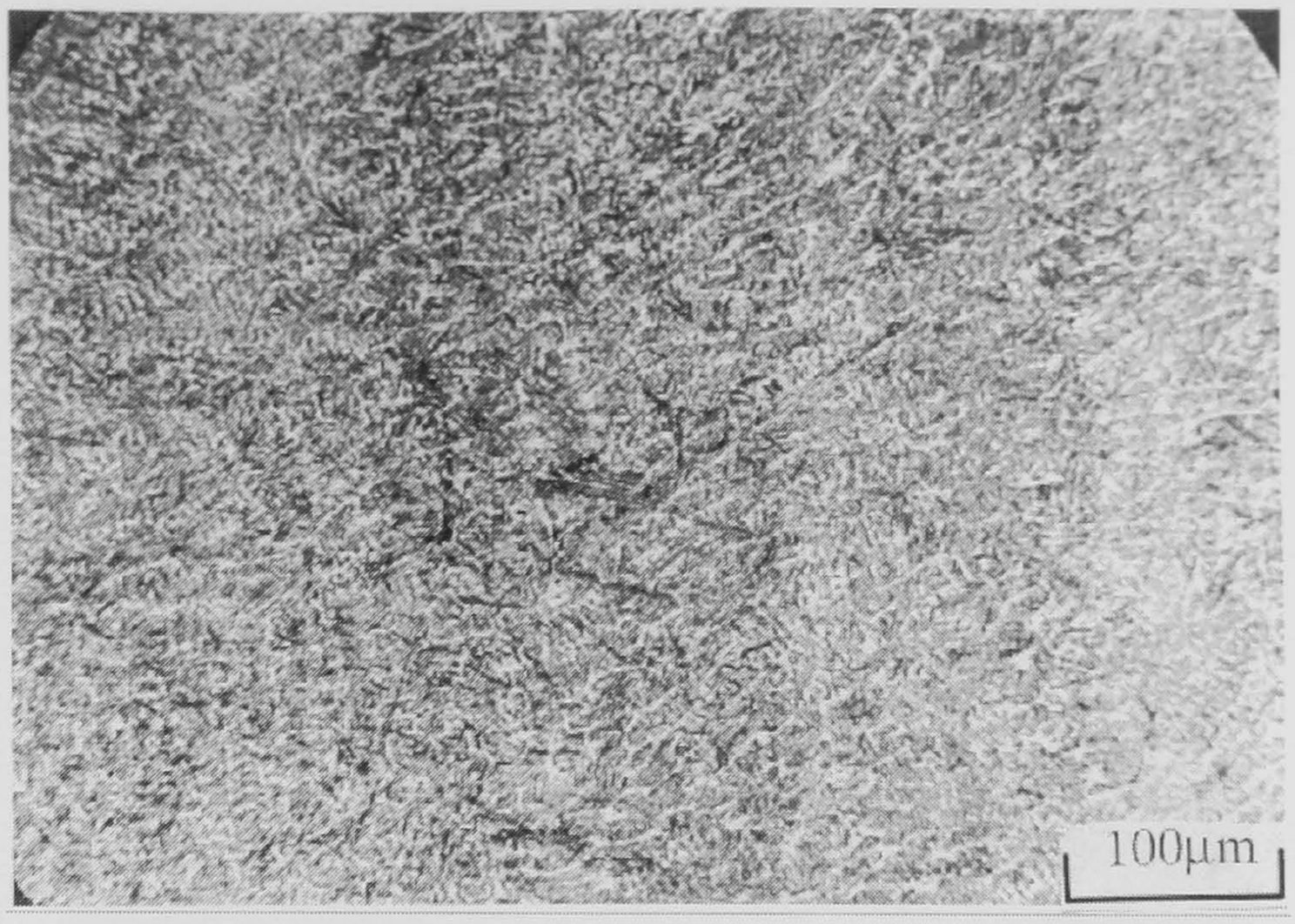

Figure 6.45 Microstructure of fusion zone for diode laser weld at a welding velocity of 10 mm/s

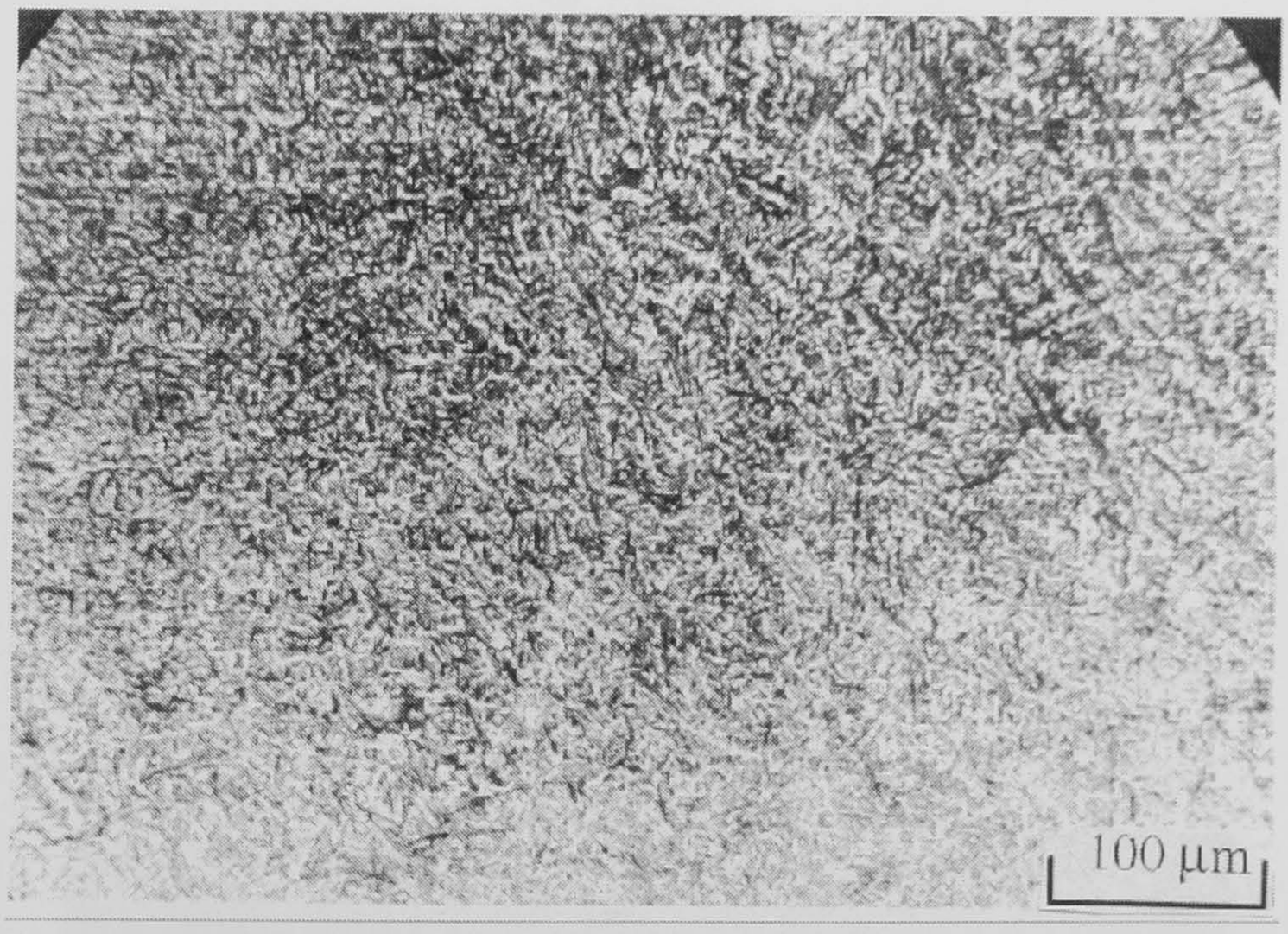

Figure 6.46 Microstructure of fusion zone for CO_2 laser weld at a welding velocity of 10 mm/s

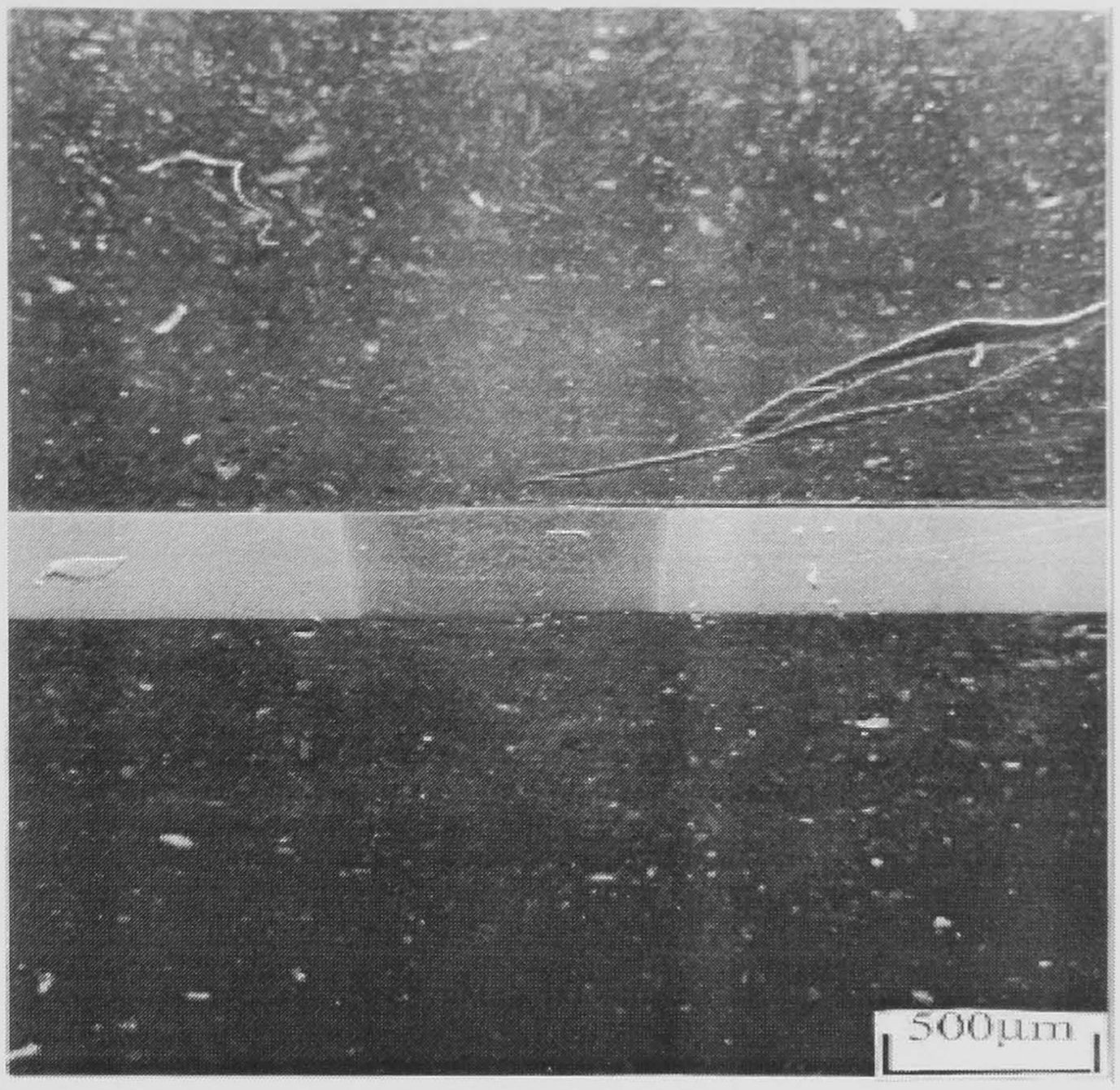

Figure 6.47 Micrograph of the weld width for diode laser weld at a welding velocity of 9 mm/s

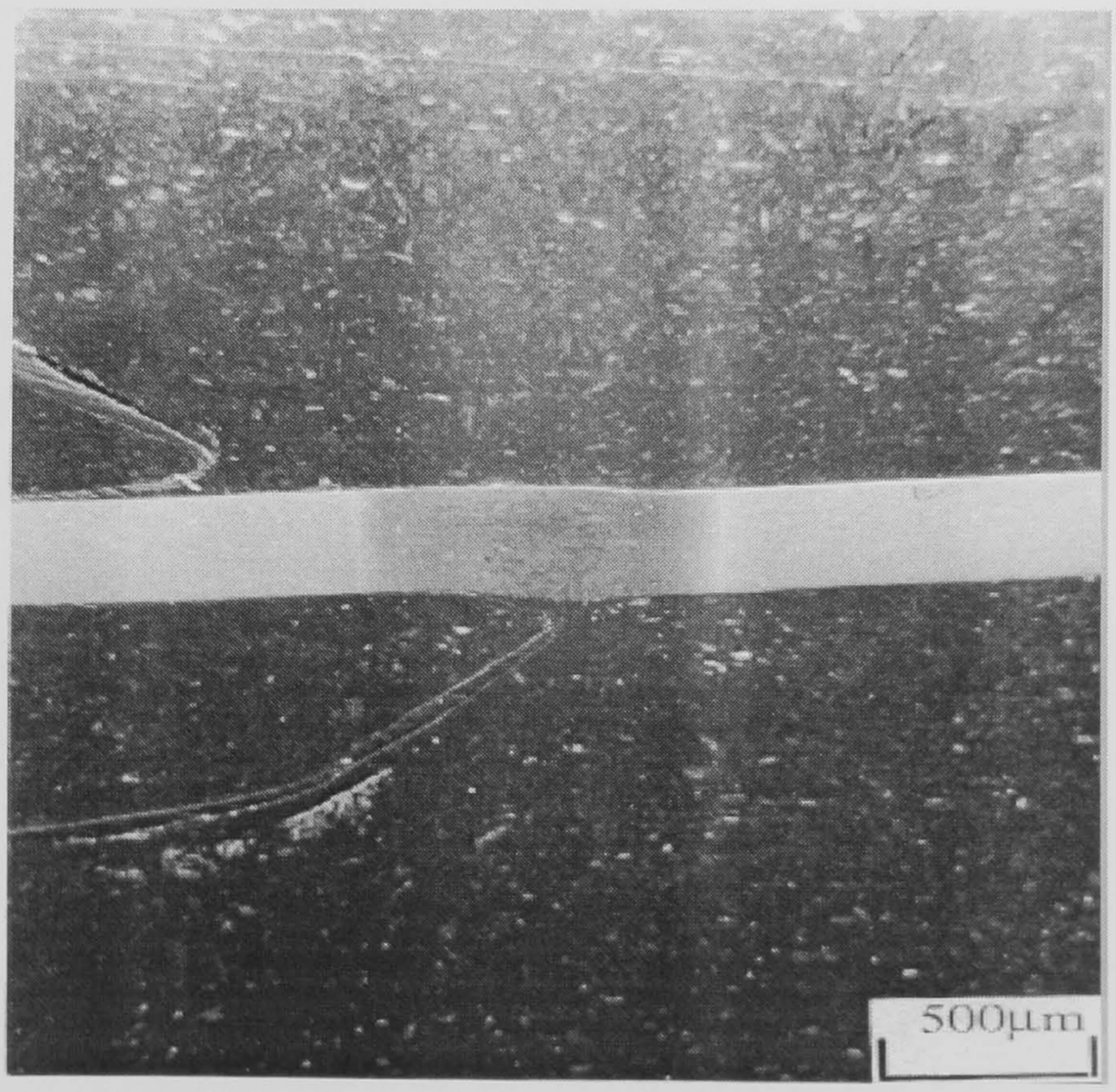

Figure 6.48 Micrograph of weld width for CO_2 laser weld at a welding velocity of 9 mm/s

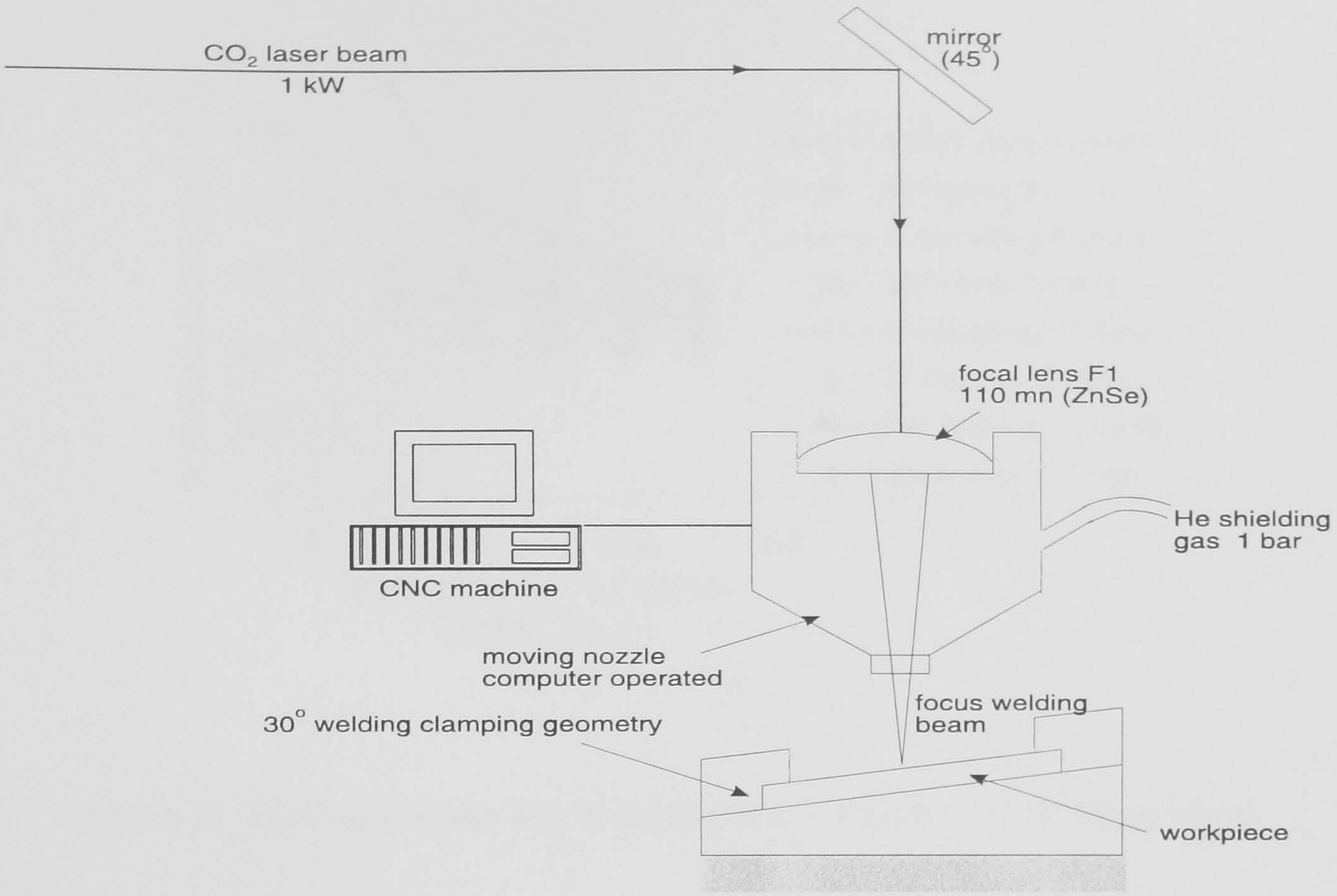

Figure 6.49 A Schematic Diagram of Welding With 30° Clamped Geometry

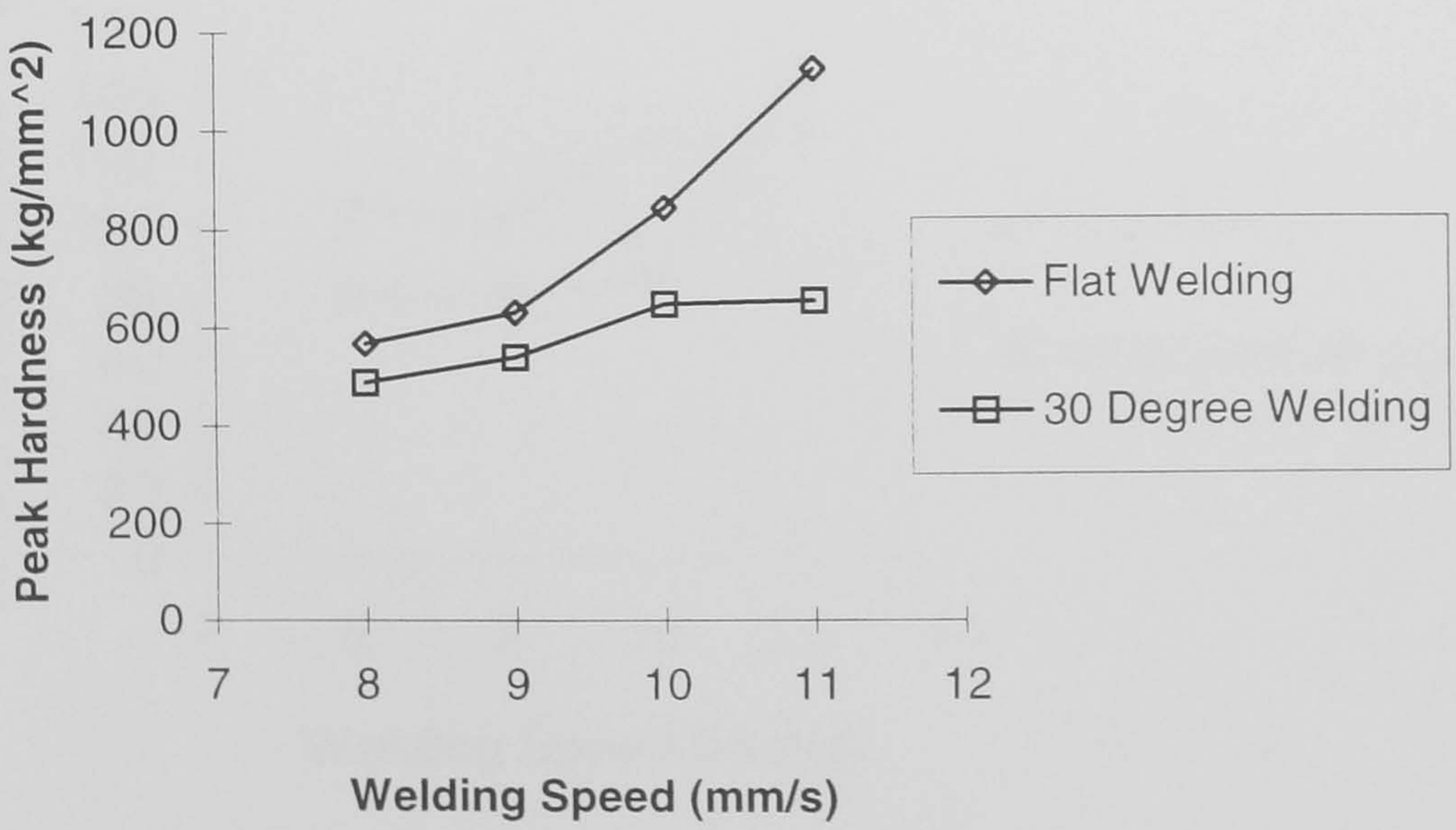

Figure 6.50. Peak Hardness as a Function of Welding Speed

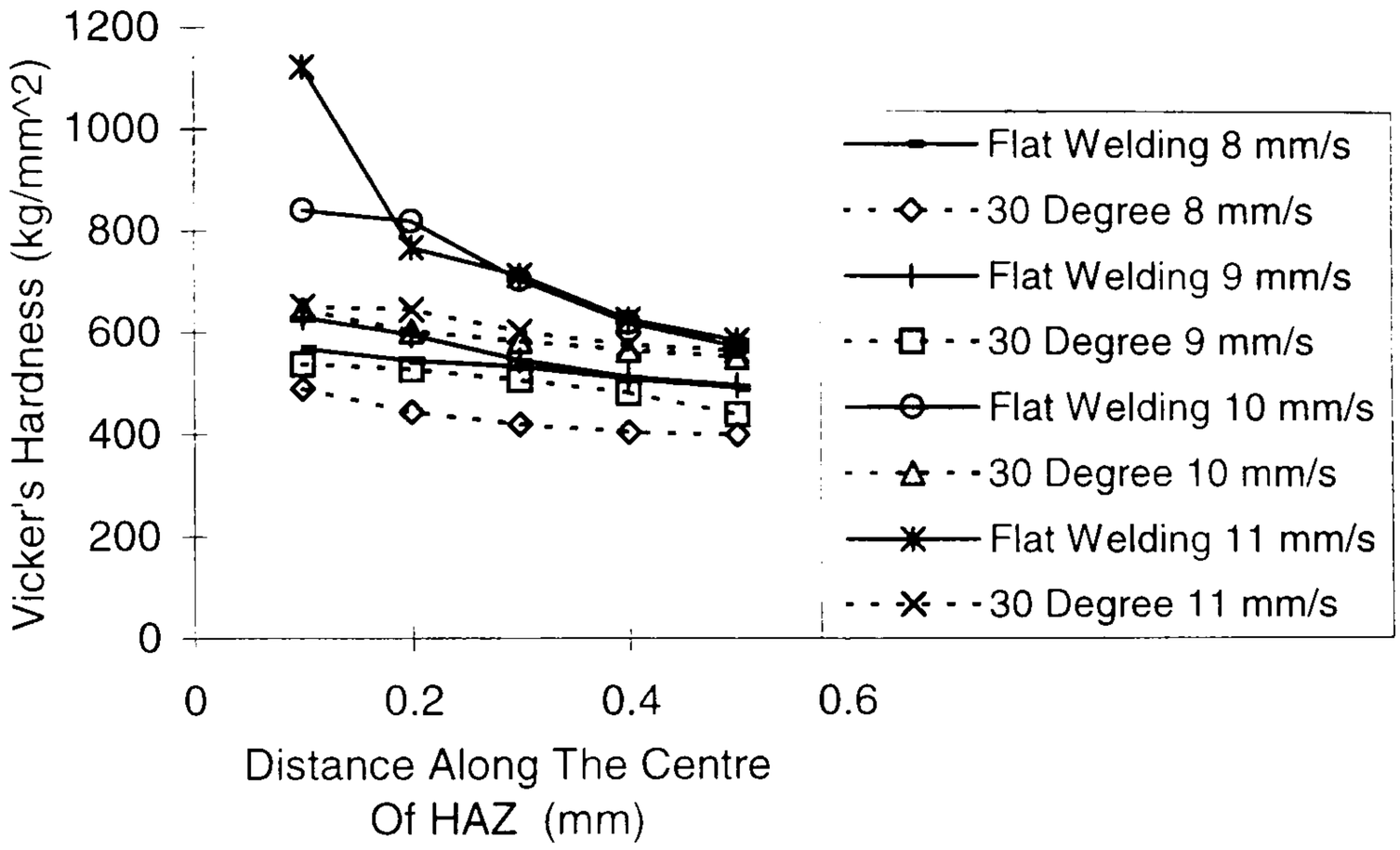

Figure 6.51. Hardness Along The Weld Depth as a Function of Welding Speed

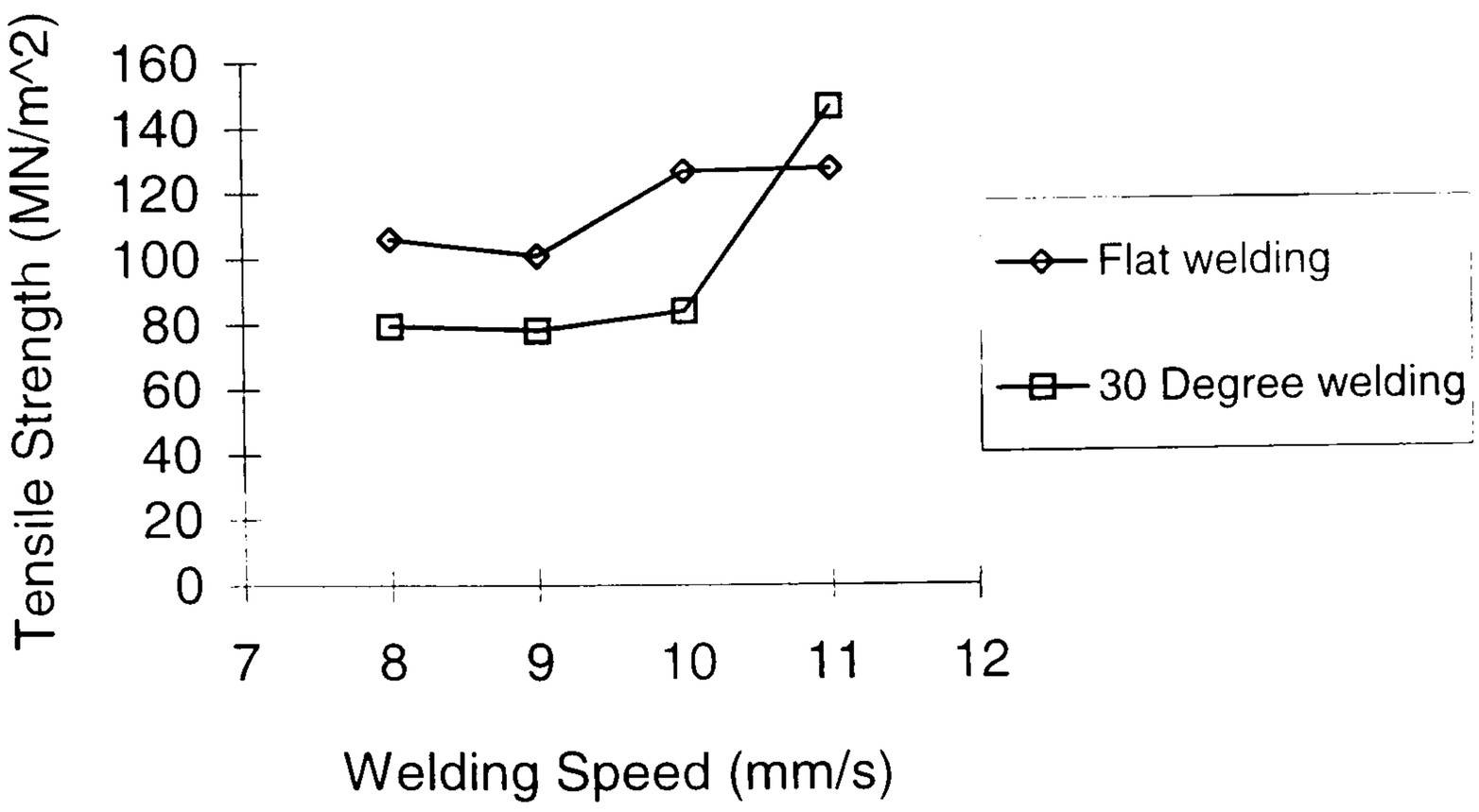

Figure 6.52. Tensile Strength as a Function of Welding Speed

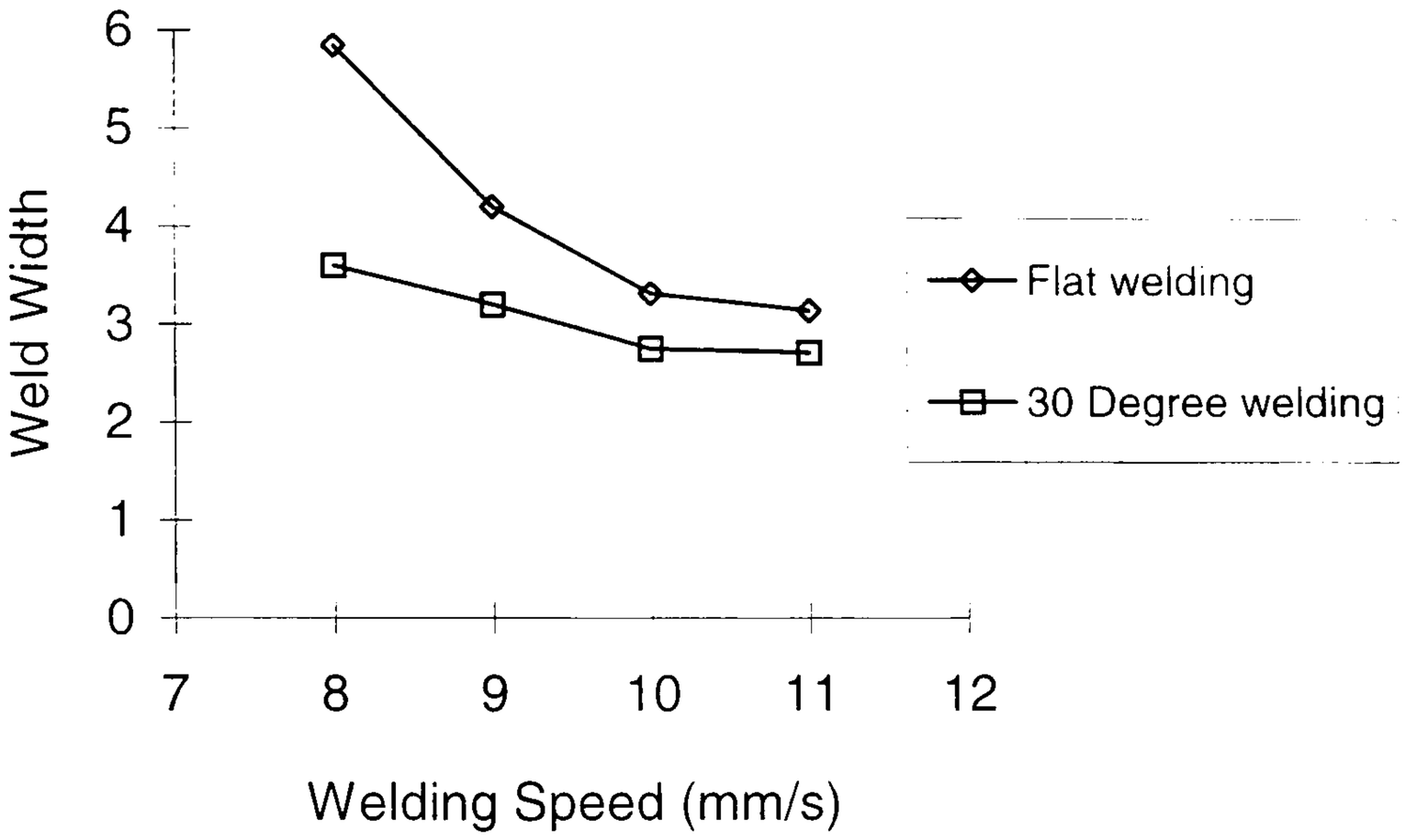

Figure 6.53. Weld Width as a Function of Welding Speed

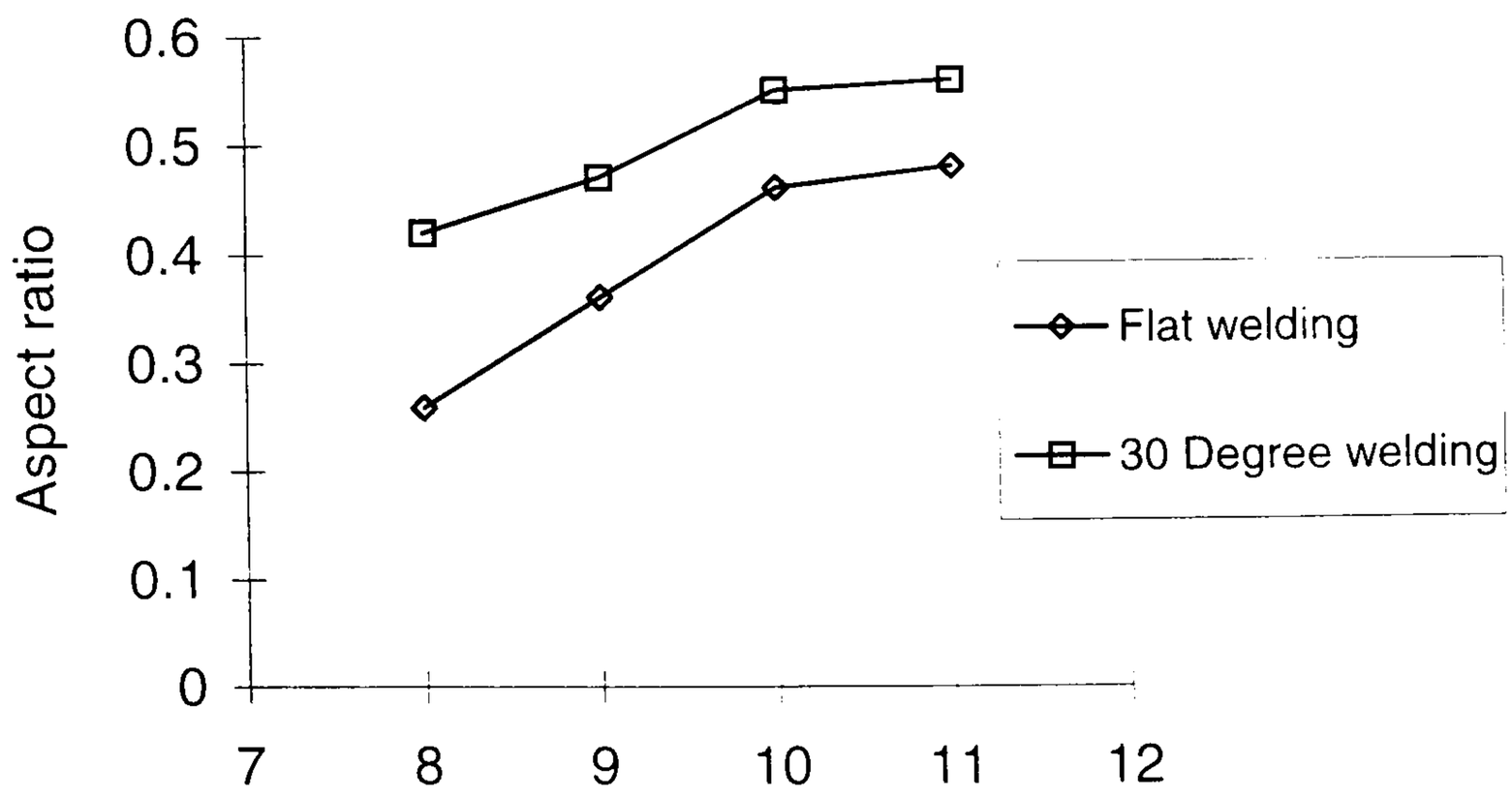

Figure 6.54. Weld Width as a Function of Welding Speed

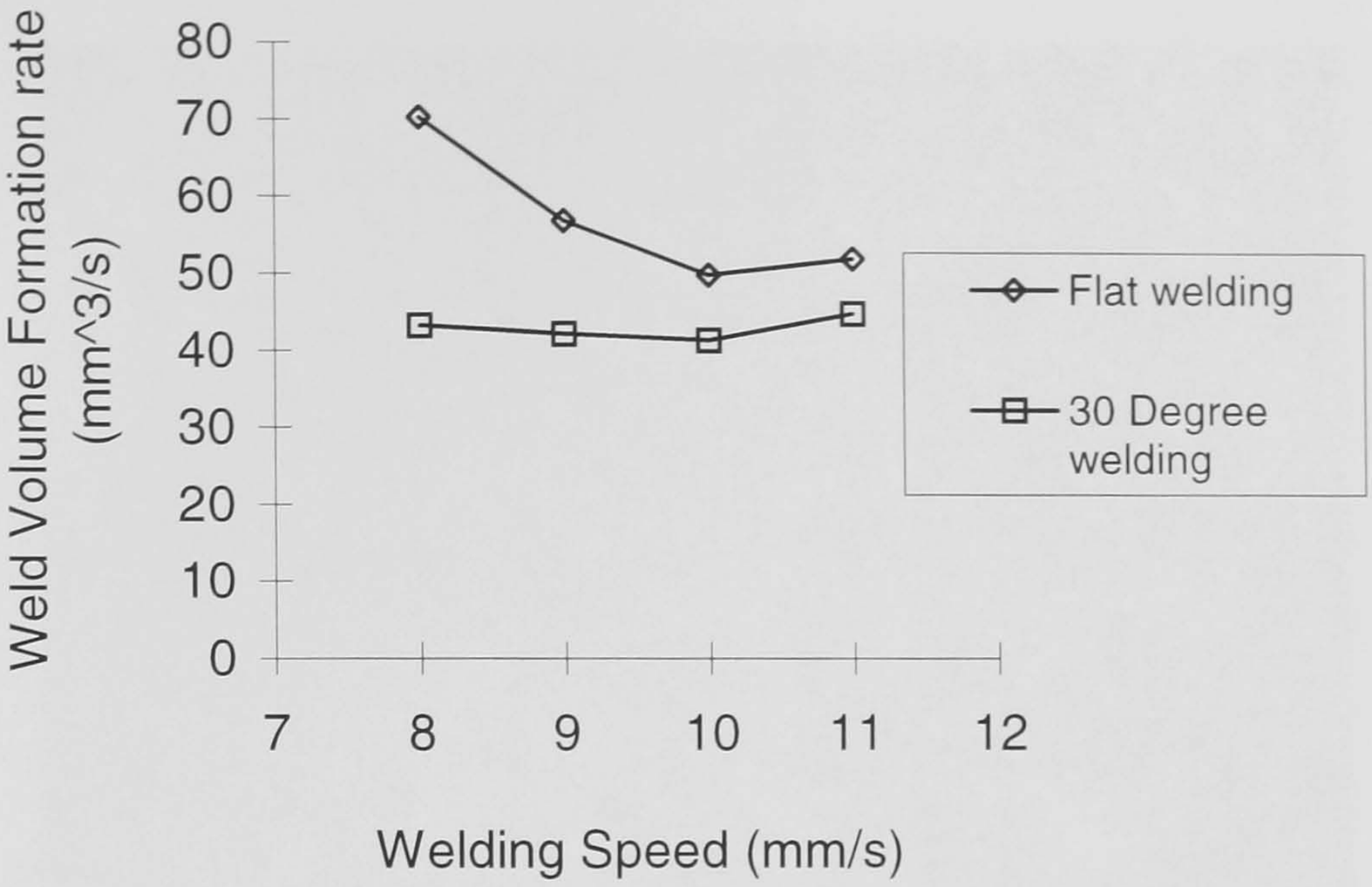

Figure 6.55. The Rate of Weld Volume Formation as a Function of Welding Speed

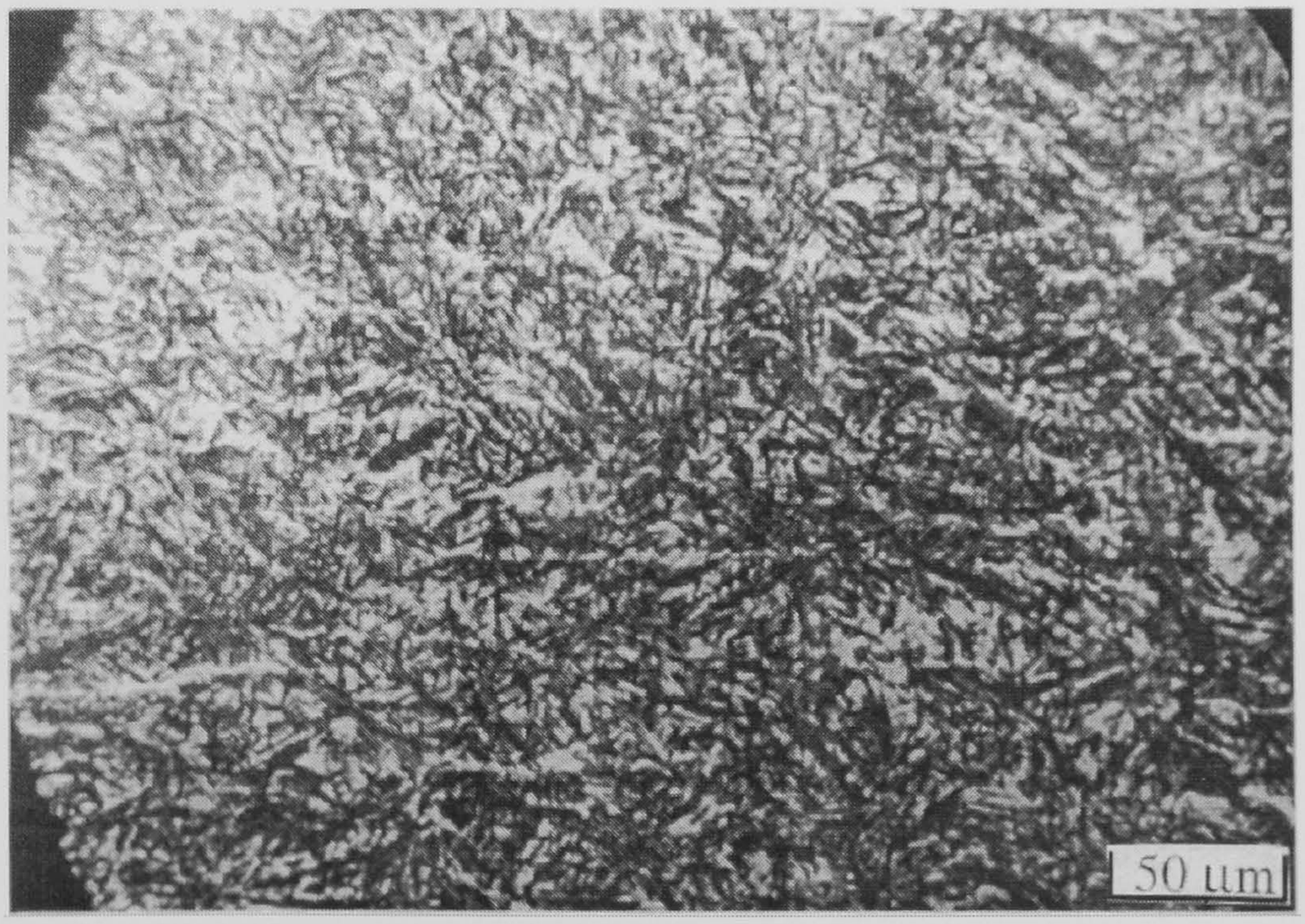

Figure 6.56 Microstructure of fusion zone of 30° laser weld at 8 mm/s.(x 150)

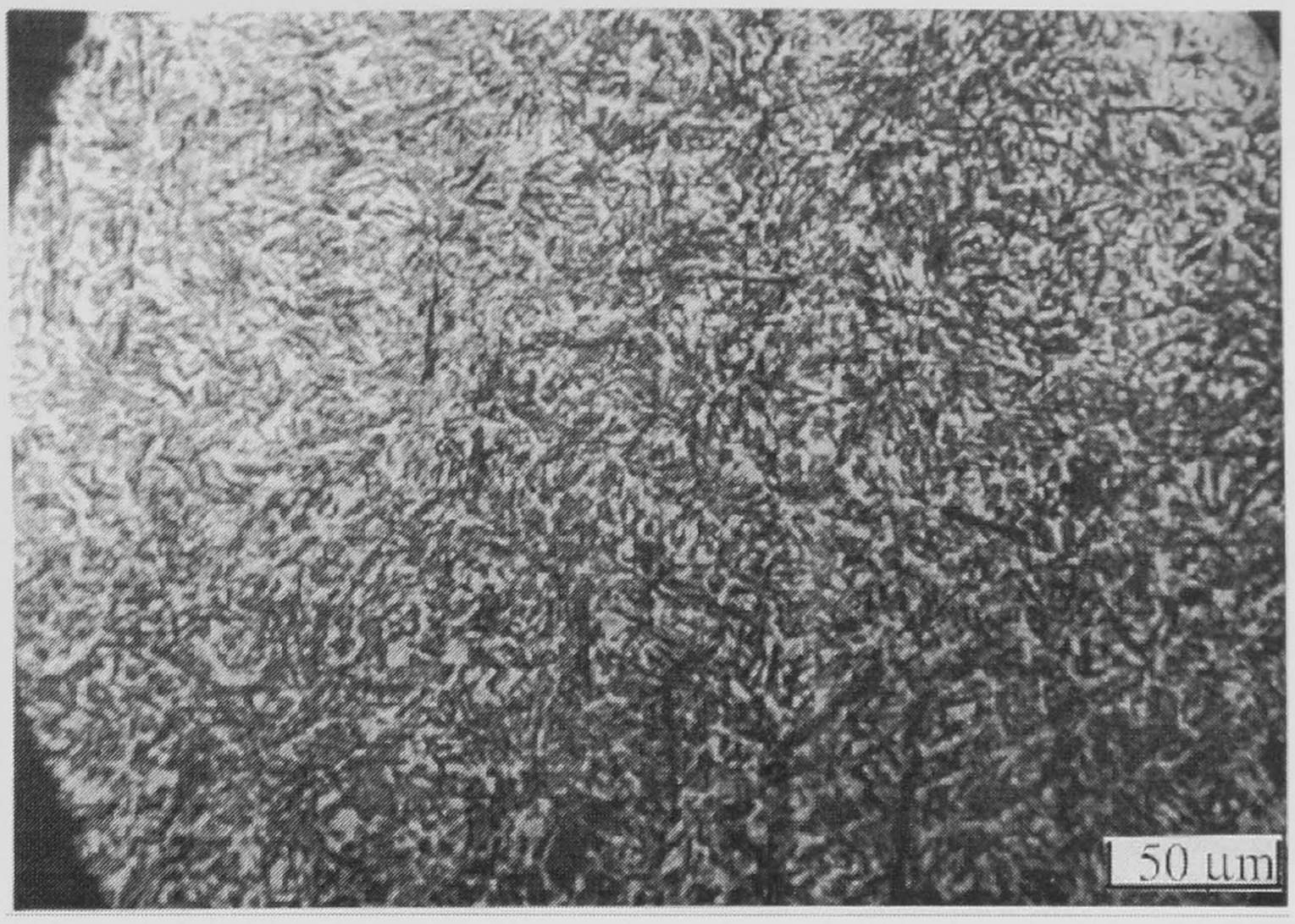

Figure 6.57 Microstructure of fusion zone of 30° laser weld at 10 mm/s (x 150)

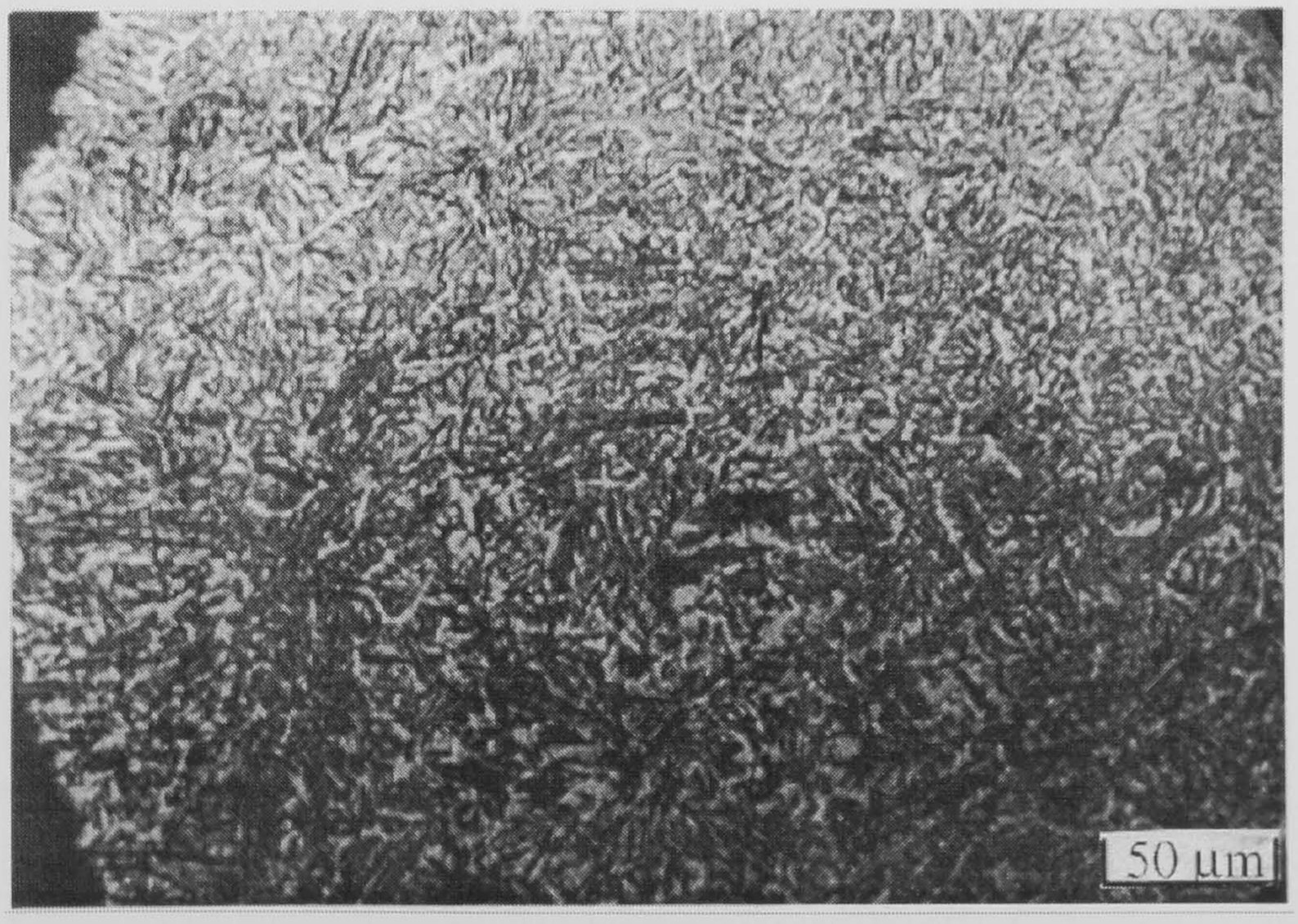

Figure 6.58 Microstructure of fusion zone of flat laser weld at 10 mm/s. (x 150)

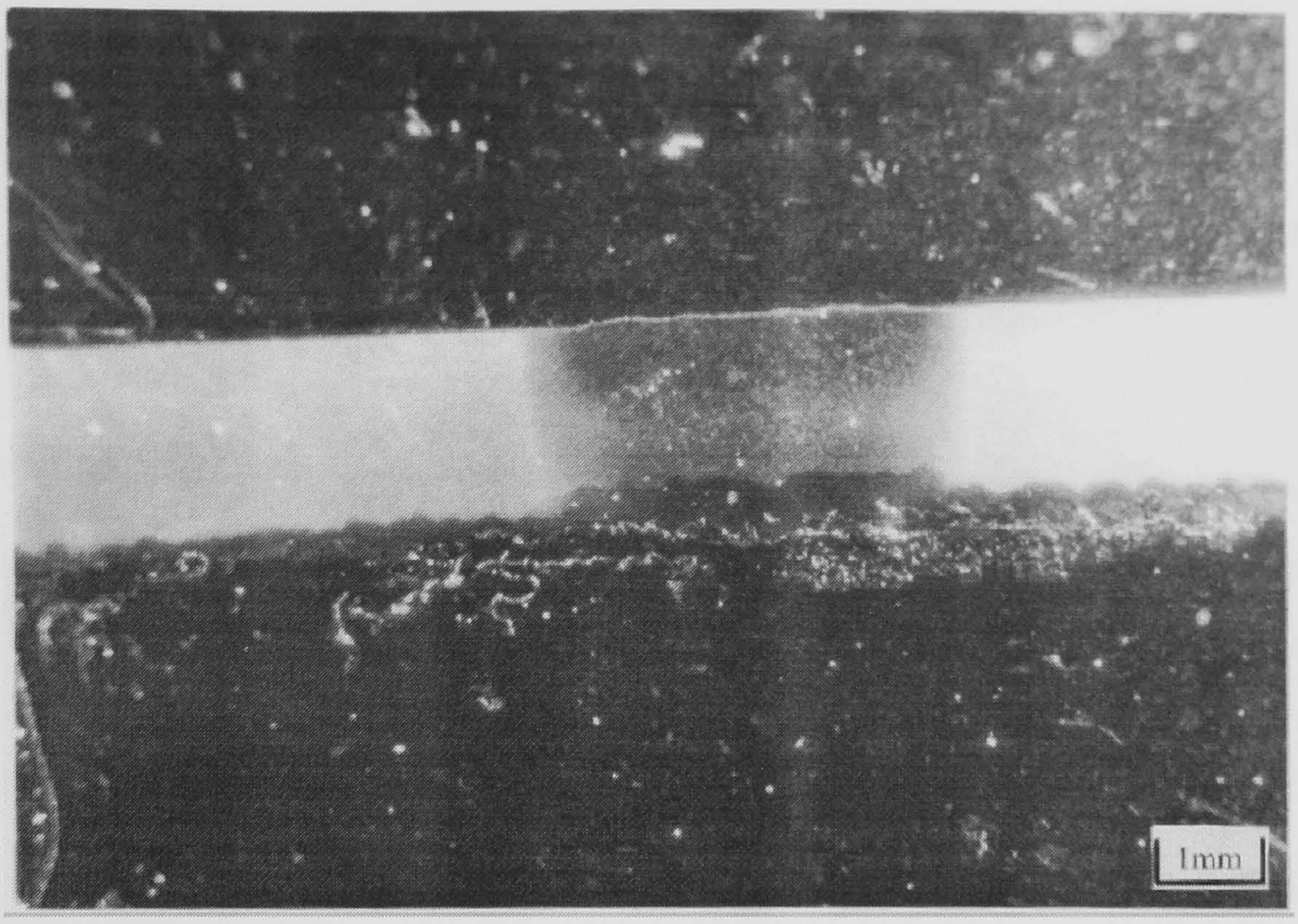

Figure 6.59 Microstructure of weld region of flat laser weld at 10 mm/s. (x3)

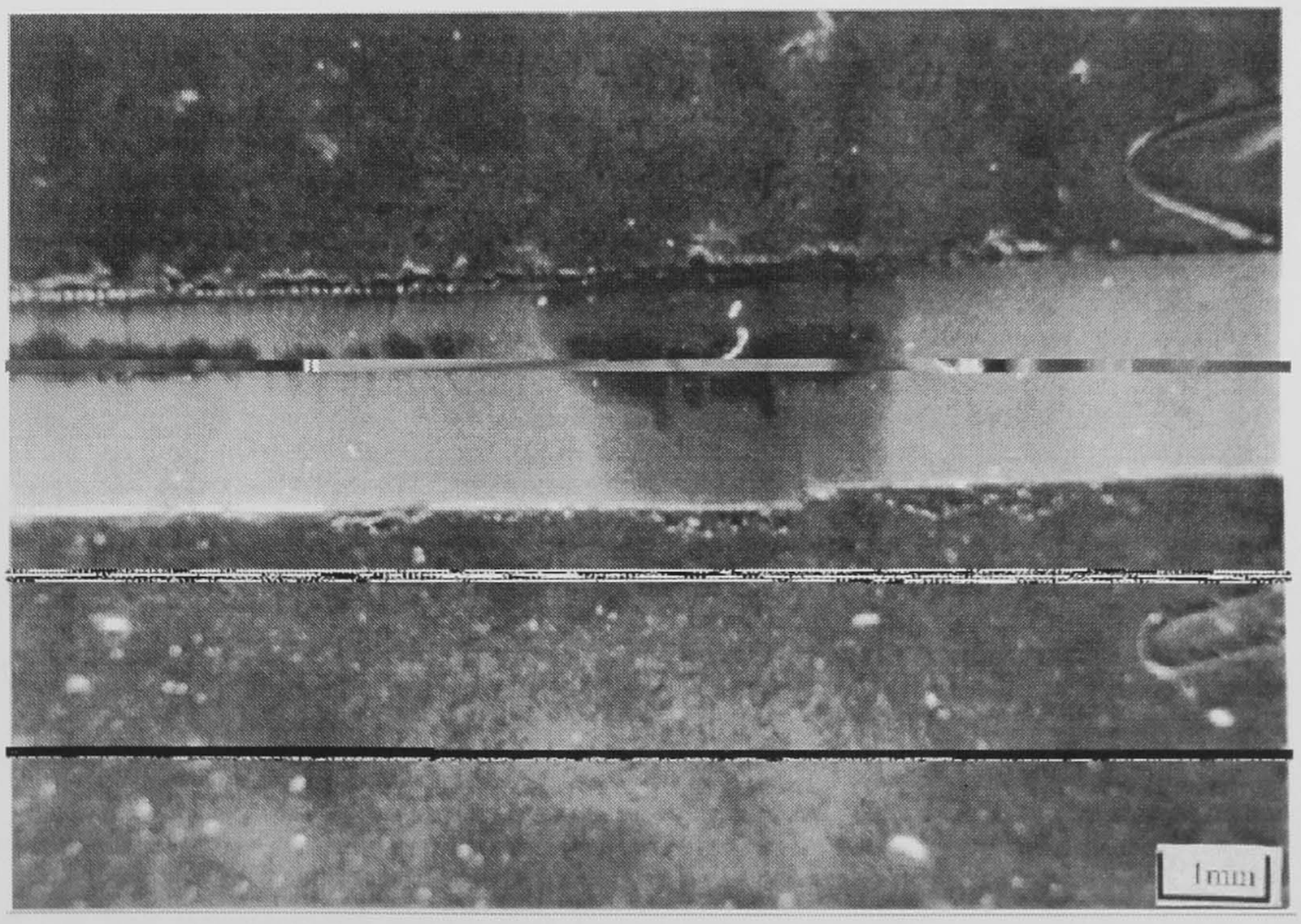

Figure 6.60 Microstructure of weld region of 30° laser weld at 10 mm/s. (x3)

CHAPTER SEVEN
QUALITY ASSURANCE ANALYSIS ON CO_2 LASER WELDING

7.1 Monitoring CO_2 laser weld quality - Comparison between 30° and 90° incident beam

7.1.1 Introduction

Weld quality assurance procedures often utilise destructive testing: this can become extremely wasteful and it is cheaper to meet the weld quality assurance by monitoring the welding process through non-destructive methods. Quality inspection of laser welds is especially difficult since visual inspection is often inadequate to determine the weld quality, non-destructive tests are commonly used to determine the weld penetration and the integrity of a laser weld, Chang [7.1]. Recently, systems have been developed based on the absorption and transmission of infrared signals to monitor and interpret key-hole formation occurring at the weld, Griebsch *et al* [7.2] and Kroos *et al* [7.3]. Haran *et al* [7.4] discovered that spectral analysis of the optical signals has the potential of being a very powerful tool for monitoring the weld process, and it has been exploited for seam tracking applications. Weerasinghe *et al* [7.5] has reported that a low signal is generated when a keyhole is formed, and it is necessary to employ an optical signal to observe plasma formation generated above the weld pool, Willmott *et al* [7.6]. Mazumder [7.7] concluded that the absorbed energy and dissipation rate are the two main factors that significantly influence the welding process.

Recently, ultrasonic signals have been used to monitor the weld penetration. The major drawback of this system is that when developing a closed-loop control system the measuring probes have to be kept away from the key-hole to avoid damage by the weld spatter. Several weld depth monitoring methods have been proposed by Lankalapalli et al [7.8] and Hand *et al* [7.9]. Chung *et al* [7.10] has made a comparison on the prediction accuracy of the weld depth between the optical signals and ultrasonic signals. Mao *et al* [7.11] and Gu *et al* [7.12] have investigated a number of systems to monitor and detect welding processes; including acoustic monitoring. The preferable approach is to develop a system to achieve on-line monitoring of the weld process. Laser welding quality control can be improved by

developing sensors that accurately record the weld characteristics and provide a feedback signal that allow the laser output to be controlled appropriately. A number of solutions to this problem have been developed by Neipold *et al* [7.13] and Stone *et al* [7.14].

In the present study, an image processing system was developed that offered real time capability to determine the weld quality via measurement of the weld width and surface irregularity and the fusion zone. The system comprised an inexpensive CCD camera acquisition and processing boards to capture the image of the welded specimen, and a trace line scan from the camera, the output of which was correlated to the weld seam to analyse the quality of the weld seam.

7.1.2 Optical set-up for monitoring laser welded quality

In the present case, an image processing system was developed that offered real time capability to determine the weld quality via measurement of the weld width and surface roughness. The weld quality from two different angles of incidence (0°,30°) of welding were compared for a range of selected welding velocities from 8 to 11 mm/s. The gauge plates that were welded had a nominal composition of 0.85 wt % C, 0.4 wt % Si, 1.1 wt % Mn, 0.4 wt % Cr, 0.25 wt % V and 0.4 wt % W. The system comprised an inexpensive CCD camera (625 x 380), acquisition and processing boards. The weld was imaged onto the CCD with a 135 mm focal length lens mounted in bellows. The performance of a single line detector was evaluated and compared to the CCD camera to analyse the weld seam appearance produced by the Nd:YAG pulsed laser and CW CO_2 laser. The CCD camera offered the capability to scan an area of the welded specimen without adjusting the specimen's position. The lens was about 0.4 m from the workpiece. Butt welds were done on 1.5 mm thick high carbon steel with 1 kW, CW, CO_2 lasers, operating at 10.6 μm, and analysed with this system.

Figure 7.1 shows the configuration of the monitoring device used in this study. It comprised a CCD camera, and a PC to drive an oscilloscope and capture the images within a particular time. Two sources of white light were inclined at 2° from the

horizontal base to illuminate the diffuse source onto the welded specimen that was placed onto the translation stage. A digital LeCroy 9310 oscilloscope was used. After placing the specimens onto the translation stage, the oscilloscope was set and both light sources illuminated the welded region. To measure the intensity distribution over the welded specimen, every fifth line was recorded and saved onto the hard-disk of the PC as a binary file; this reduced the data and size of the file without significant loss in detail. The data was used to build-up 3 D images for the weld bead. In all cases, the line scan traces and 3-D images were generated by the commercial software package.

7.1.3 Weld quality analysis

7.1.3.1 Analysis of the effect of optics on the weld signature

The sensor system was capable of detecting geometric defects and surface quality across the weld seam. **Figures 7(a)** to **7(d)** show the effect of different methods of illumination on the weld seam - the trace corresponding to a line scan taken from the CCD camera was normalised to unity. The reflected light increased or decreased proportionately with the trace, and this depended on the surface quality of the weld seam. For a bad weld seam, the reflectance of light into the camera reduced and there was not a significantly high signal. **Figure 7(b)** shows the trace without illumination. **Figures 7 (c)** and **7 (d)** show the typical trace with the light illuminating across the left or right border of the weld seam, respectively. It is clearly observed that the left and right illumination are independent of each other.

Figures 7(e) to **7(h)** show the intensities as a function of distance across the weld seam with different angles of incidence for the light source. In all cases, the traces correspond to the line scan of the same welded specimen and the weld seam is illuminated by the left light source. Higher intensities were achieved on the left border of the weld seam than the right border, with light incident at 88°. Moreover, the angle of incidence of the left light source decreased, the intensities on the right weld border increased. In all cases, the distance between the peak intensities correlated with the width of the fusion zone.

7.1.3.2 Evaluating the performance of different detectors

Figure 7.2 shows typical results of Nd:YAG pulsed laser welds. The weld seam appearance correlated to the traces captured by the CCD camera and the single line detector: **Figure 7.2** (a) shows the weld appearance of Nd:YAG pulsed laser weld, (b) the trace captured by the single line detector and (c) the trace captured by the CCD camera. However, the traces indicate that the light reflected and detected are dependent on the detector. In the case of a CW, CO_2 laser weld, **Figure 7.3** shows the weld seam and trace: (a) the weld appearance of CW CO_2 laser weld, (b) the trace captured by the single line detector and (c) the trace captured by the CCD camera. In contrast, both **Figures 7.2** and **7.3** indicate that the CCD camera was able to differentiate between the pulsed Nd:YAG and continuous wave CO_2 welding. With the Nd:YAG welding, the output from the camera was saturated due to the increase in specular reflection from the rough surface. The output from the line scan detector was not sufficiently sensitive to give enough detailed information on the weld quality. In all cases, the traces corresponding to a line scan taken from the CCD camera and single line detector were normalised to unity.

Figure 7.4a shows the effect of illuminating the Nd:YAG laser weld with two light sources. **Figures 7.4b** and **7.4c** show pictures and traces of high and low quality welds respectively, done with the 1 kW CO_2 laser. The high spatial frequencies in **Figure 7.4c** indicate a poor weld. This trace was typical of those observed for poor welds because of the irregularities on the weld seam.

7.1.3.3 Analysis of the weld seam and surface roughness

Figures 7.5 and **7.6** show the pictures and corresponding traces of high and low quality welds for different welding velocities, the welding was done with a 90° incident beam. **Figures 7.5(a)** and **7.6(a)** show the appearance of the respective weld seams, at 8 and 10 mm/s, respectively, for the flat welding configuration. It can be clearly observed that the width of the weld seam decreased with an increased welding velocity. The width of the weld seam was correlated with the peak-peak distance. The variation in the trace between the peaks is representative of the

surface roughness profile across the fusion zone. The high spatial frequencies in **Figure 7.6** indicates a poor weld. This trace was typical of those observed for poor welds because of the irregularities on the weld seam. A groove started to form between the solidified pool ripples along the weld bead for a higher welding velocity.

The weld signatures shown in **Figures 7.7** and **7.8** are representative of the typical weld seam appearance and trace for the 30° welding configuration at different welding velocities. In the sequence of images illustrated in **Figures 7.7(a)** and **7.8(a)**, the weld seam decreased slightly with increasing welding velocity, and the weld seam correlated to the traces between the peak-peak distance. The traces correlated and were matched in phase with the appearance of the weld seam.

For both welding techniques, the variation in the trace between the peaks limits of the trace are representative of the surface roughness profile across the fusion zone. The high spatial frequencies in **Figure 7.7** indicate a poor weld. This trace was typical of those observed for poor welds because of the irregularities on the weld seam; this can clearly be observed on the 3-D scan shown in **Figure 7.9(a)**. **Figures 7.9(a)** and **7.9(b)** represent the 3-D weld profiles at a welding velocity of 8mm/s. They were used to quantify the weld peak characteristics for the 30° and flat welding geometries, respectively. **Figure 7.9(a)** clearly shows, the narrow irregularities on the weld bead along the fusion zone, and welding at 30° resulted in weld pool tending to flow transverse across the weld before solidification. Thus, a deep groove started to form between the solidified pool ripples along the weld bead. **Figure 7.9(b)** represents the 3-D weld profiles for the flat welding configuration, it is clearly observed that a more uniform and wider weld bead occurred along the fusion zone, and this further agreed with the traces between the peak-peak intensities in comparison to **Figures 7.5(b)** and **7.7(b).** The weld width and the aspect ratio see Section 6.4.3 (**Figures 6.53** and **6.54**) agreed with the peak to peak traces as discussed.

7.1.4 Conclusions of quality assurance analysis on CO_2 laser welding

A non contact, non destructive optical method and system used for monitoring the weld quality of laser welding has been developed and tested successfully. This monitoring system can also be used to analyse the weld quality in real time. This system was based on analysing the reflected light, which increased or decreased proportionately with the weld roughness. The peak traces on the periphery of the scan correlated to the fusion region; this was dependent on the intensities of the light sources, angle of incidence of the light sources, and the surface quality of the weld seam. The variation in the trace between the peaks was representative of the surface roughness profile across the weld. The characteristics of the peak were quantified for different welds. The variation of traces between the peak-peak for the two different angles of incidence (0°,30°) for welding were compared, as were effects of using different welding velocities, from 8 to 11 mm/s.

The traces and appearance of the high and low quality weld seams were compared at different welding velocities, and welding was done with a normally incident beam. In this case, it was clearly observed that the weld seam and the width of the trace between the peak-peak decreased with increased welding velocity. Furthermore, increasing the welding velocity showed a significant variation in the trace between the peak-peak, and high spatial frequencies indicated poor surface quality on the weld seam. Whereas, for 30° welding, the weld seam and the trace between peak-peak decreased slightly with increased welding velocity, and the trace indicated poor welds because of the irregularities on the weld seam. This trace was typical of those observed for poor welds because of the irregularities on the weld seam. The weld width was calculated by measuring the peak-peak time and converting to the spatial domain from knowledge of the object size and the line scan time. The variation in the trace between the peaks is representative of the surface roughness profile across the weld, and the 3-D scan evaluation further showed the narrow and irregular surface occurred in 30° welding conditions. Moreover, for the flat welding condition, a wider and better weld seam surface was produced. The characteristics of the peak were quantified for different welds.

CHAPTER SEVEN REFERENCES

[7.1] Chang, D. "Real-time Quality Monitoring System For Laser Welding", Laser Optic For Manufacturing - Trends in Optics and Photonics, New York, **9**, Oct 1996, 110 -115.

[7.2] Griebsch, J. Hugel, H. Dausinger, F. Jurca, M. "Quality Assurance in Pulsed Laser Welding", The 14th International Congress On Applications Of Lasers And Electro-optics, San Diego, Nov 1995, 603-605.

[7.3] Kroos, J. Gratzke, U. Vicanek, M. Simon, G. "Dynamic Behaviour of The Keyhole in Laser Welding", Journal of Physic D: Appl. Phys, **26**, 1993, 481-486.

[7.4] Haran, F. Hand, D. Peters, C. Jones, J. "Real-time Focus Control in Laser Welding ", Meas. Sci. Technol, **7**, 1996, 1095-1098.

[7.5] Weerasinghe, M. Steen, W. "In-process Monitoring of Laser Process", The 5th International Congress On Applications Of Lasers And Electro-Optics, 1985.

[7.6] Willmott, N. Hibberd, R. Steen, W. "Keyhole/Plasma Sensing System for Laser Welding Control System", The 7th International Congress On Applications Of Lasers And Electro-optics, Santa Clara, Nov 1988, 109-111.

[7.7] Mazumder, J. "The-State-of-The-Art of Laser Material Processing", Interdisciplinary Issues In Material Processing and Manufacturing, **2**, Dec 1987, 599-630.

[7.8] Lankalapalli, K. Tu, J. "Penetration Depth Estimation For Monitoring CO_2 Laser welding Process", The International Congress On Applications Of Lasers And Electro-optics, San Diego, Nov 1995, 573-582.

[7.9] Hand, D. Haran, F. Peters, C. Jones, J. "Full Penetration Detection in Nd:YAG Laser Welding By Analysis of Oscillatory Optical Signal: Application to Overlap Weld seam Tracking", Proceeding of XI International Symposium on Gas Flow and Chemical Lasers and High Power Laser Conference, Spie Proceeding, **3092**, APR 1997, 534-537.

[7.10] Chung, M. Kim, S. Kim, J. "Comparison of Ultrasonic Weld-width Meaurement and Optical Weld-depth Monitoring in Laser Sleeve Welding", The International Congress On Applications Of Lasers And Electro-optics, San Diego, Nov 1997, Sect C 47-51.

[7.11] Mao, L. Kinsman, G. Duley, W. "Real-time Fourier Transform Analysis of Acoustic Emission During CO_2 Laser Welding of Materials", Journal Laser Application, **5**, 1993, 17-22.

[7.12] Gu, H. Duley, W. "Resonant Acoustic Emission During Laser Welding of Metals", Journal of Phys: Appl. Phys. **29**, 1996, 550-555.

[7.13] Neipold, R. Bruemmer, F. "A Visual Sensor For Seam Tracking and On-line Process Parameter Control In Arc-welding Applications", Fraunhofer Institut fuer Informations- und Daten-verarbeitung, 1984, 375-385.

[7.14] Stone, A. Smith, S. Lucas, J. "Sensor For Automated Frontface Weldbead Area Control, Measurement Science & Technology, **5** (2), 1994, 93-99.

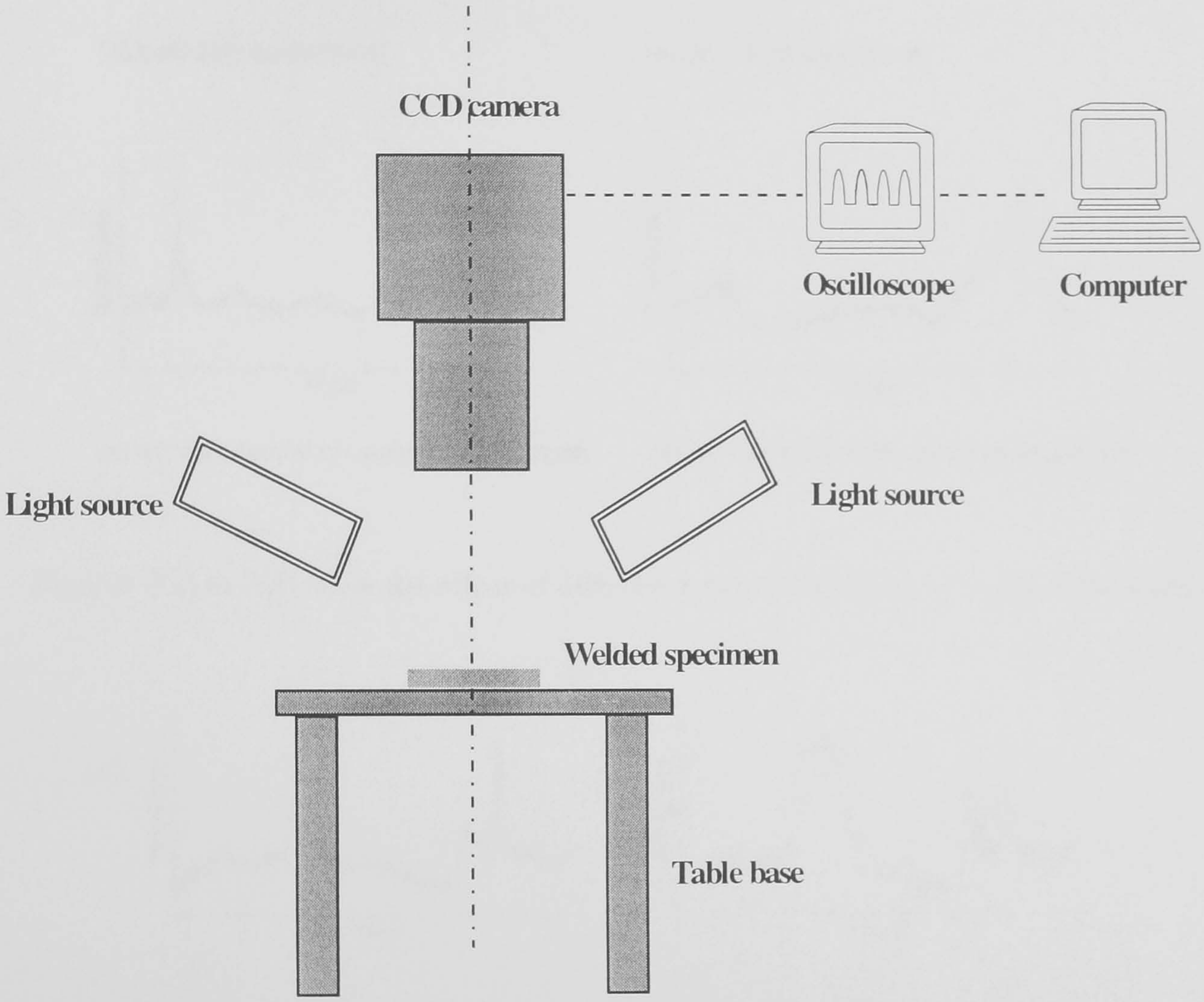

Figure 7.1. A schematic diagram of optical monitoring system

(a) both light sources on

(b) both light sources off

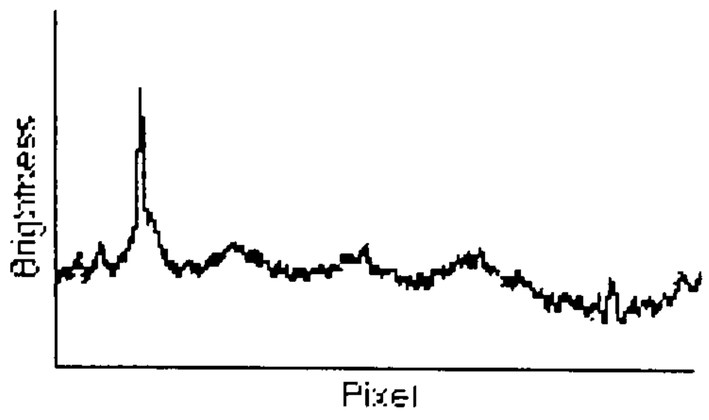

(c) left light source on, right light source off

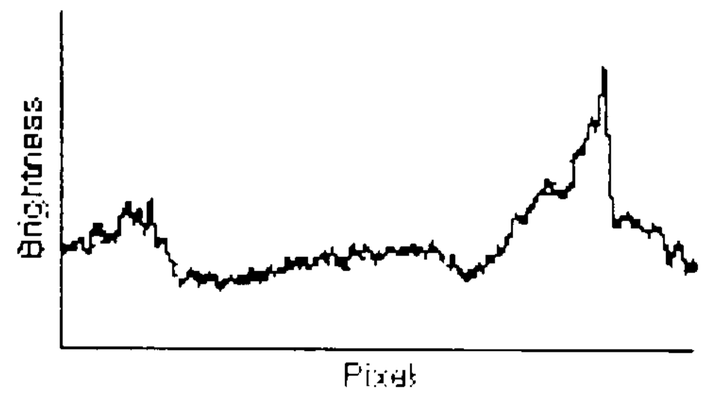

(d) left light source off, right light source on

Figures 7(a) to 7(d) show the effect of different type of illumination on the weld seam

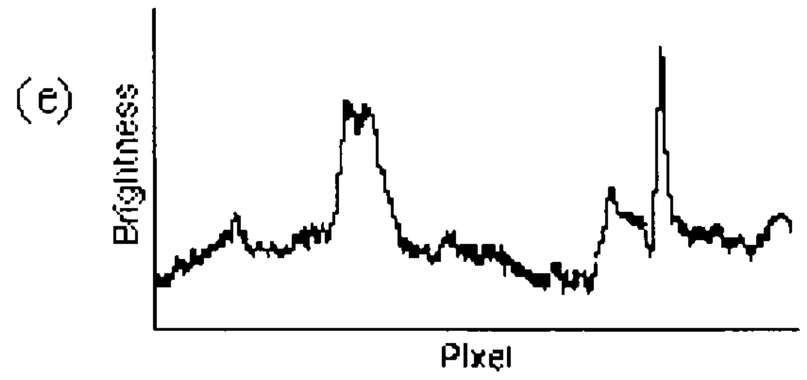

$\alpha = 88°$

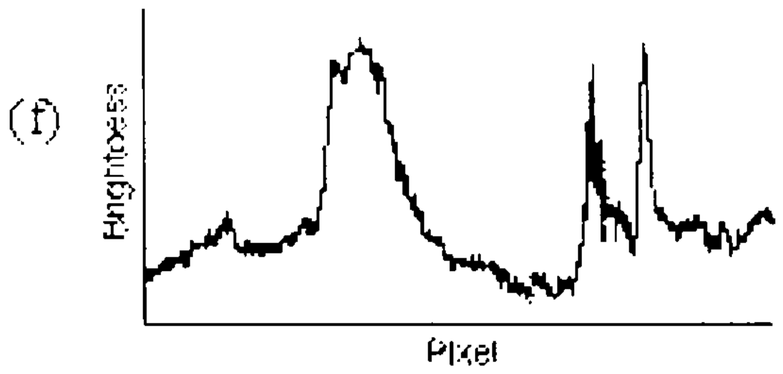

$\alpha = 85°$

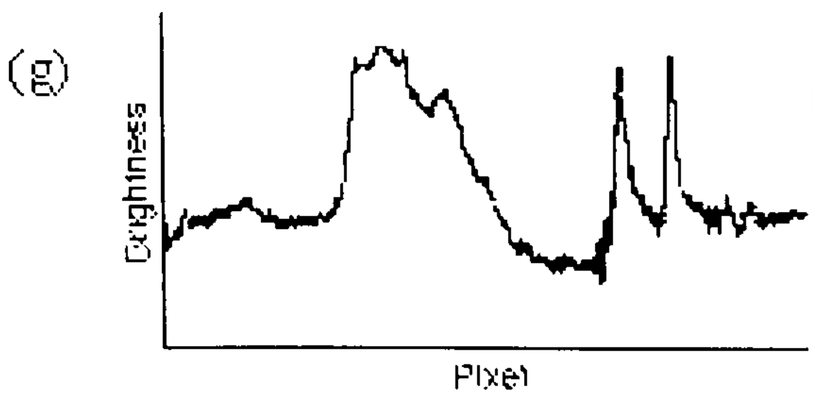

$\alpha = 80°$

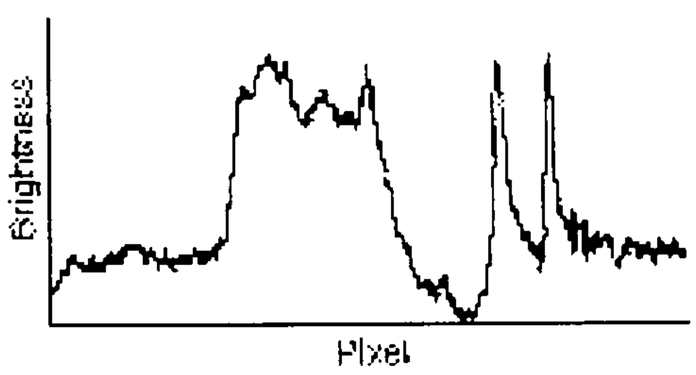

$\alpha = 75°$

Figures 7(e) to 7(f) show the effect of different angles of incident light source.

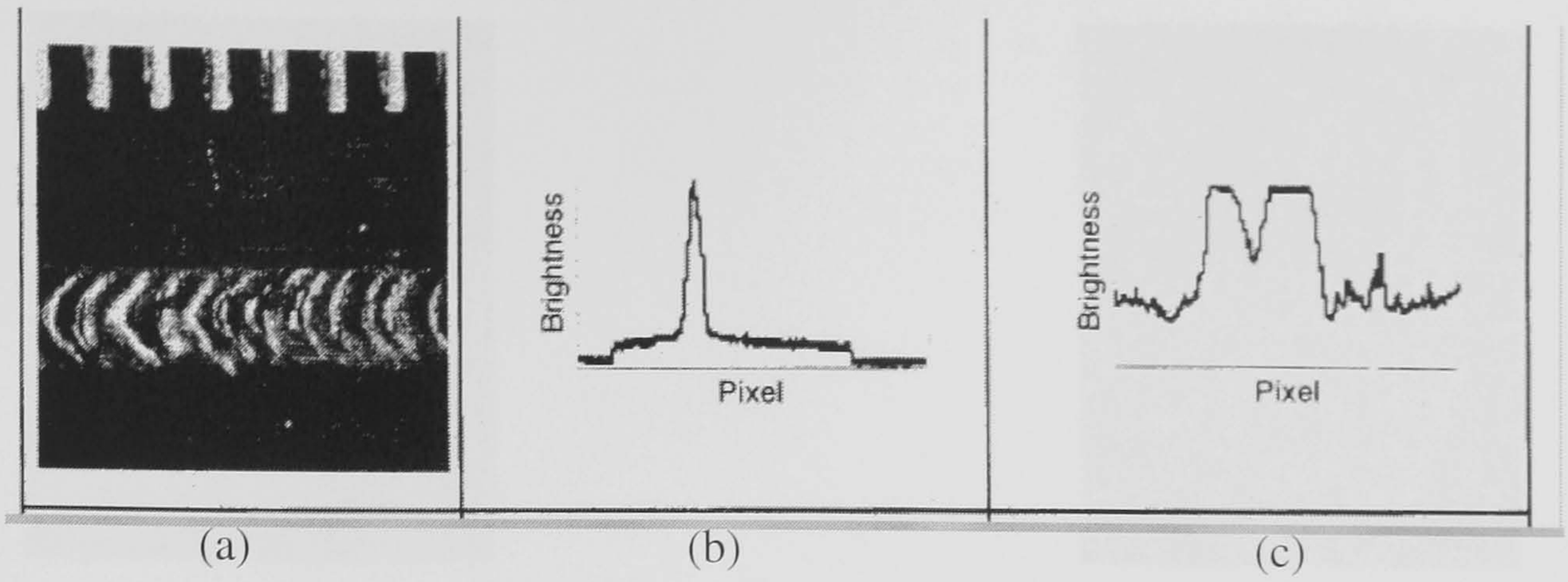

(a) (b) (c)

Figure 7.2 shows typical results of Nd:YAG pulsed laser welds; (a) the weld appearance of Nd:YAG pulsed laser weld, (b) the trace captured by the single line detector and (c) the trace captured by the CCD camera.

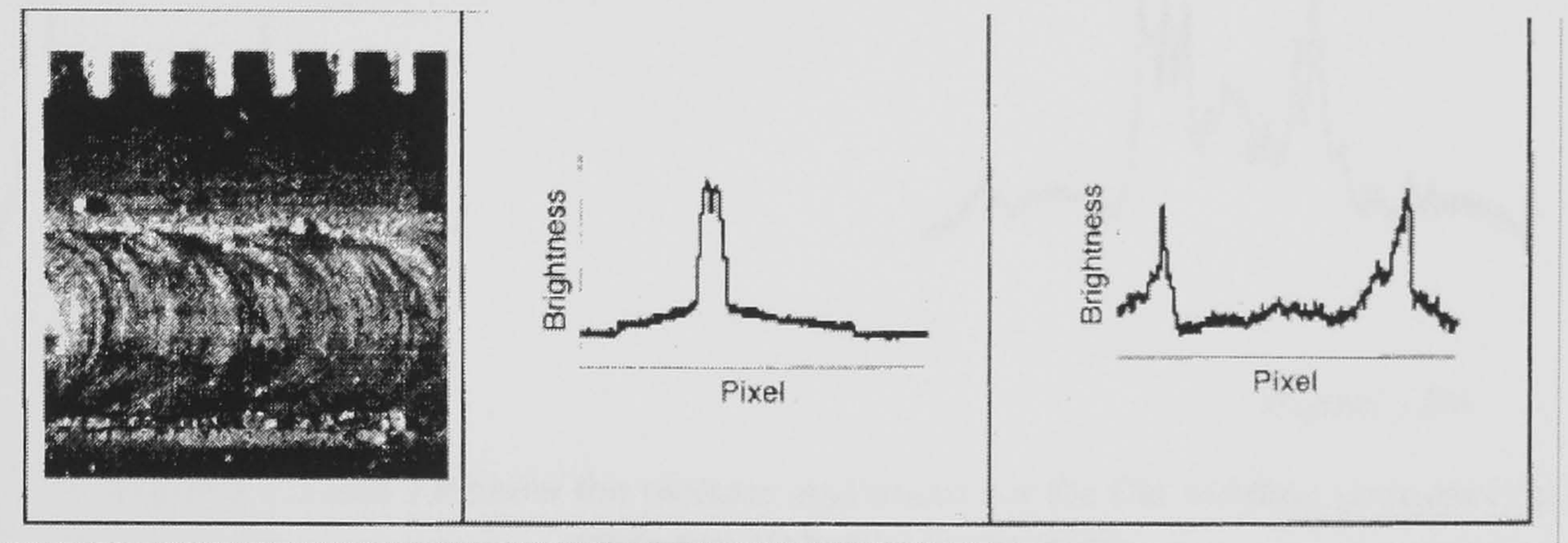

(a) (b) (c)

Figure 7.3 shows typical results of CO_2 laser welds; (a) the weld appearance of CO_2 laser weld, (b) the trace captured by the single line detector and (c) the trace captured by the CCD camera.

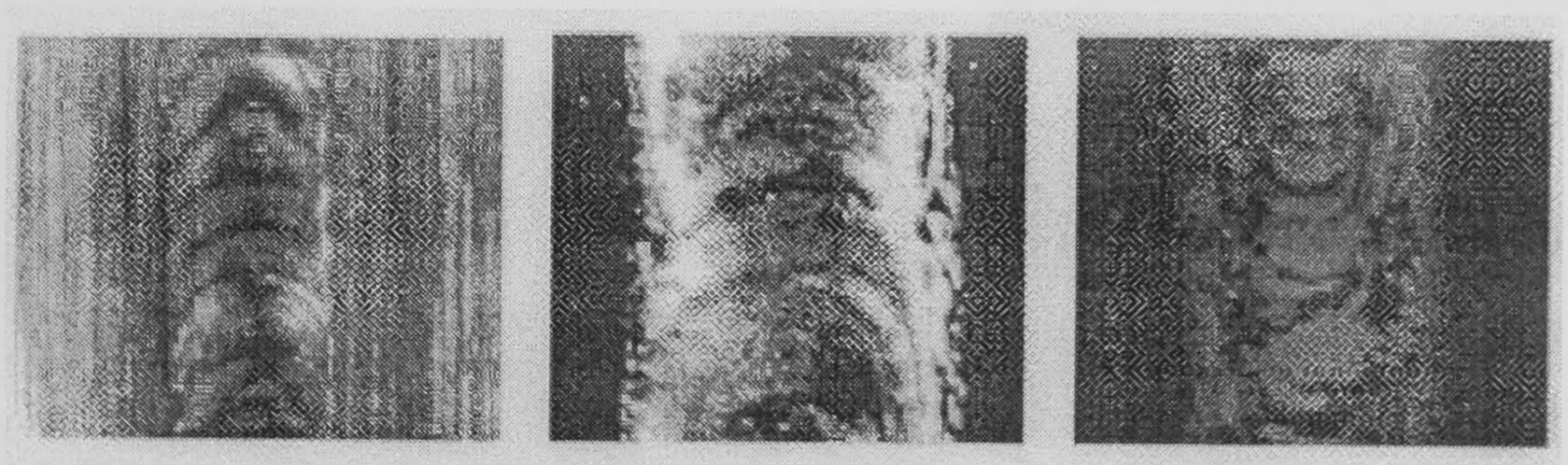

(a) (b) (c)

Figure 7.4 shows typical results of; (a) Nd:YAG pulsed laser weld, (b) high quality CW, CO_2 laser weld and (c) poor quality CW, CO_2 laser weld.

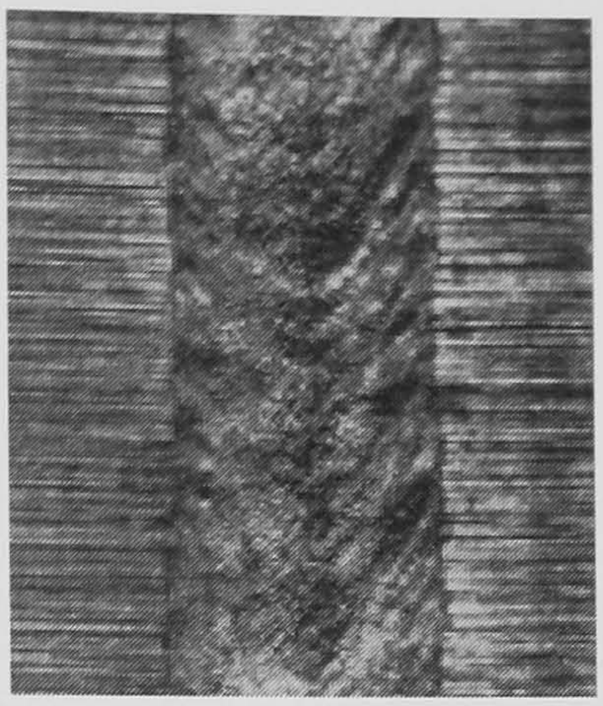

Figure 7.5a

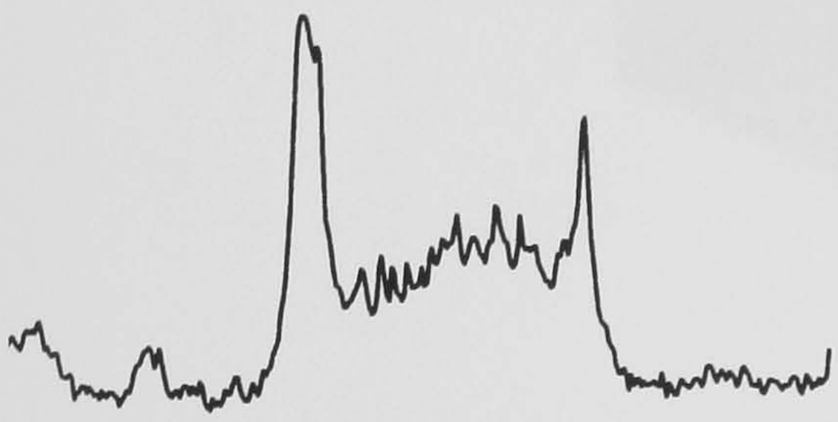

Figure 7.5b

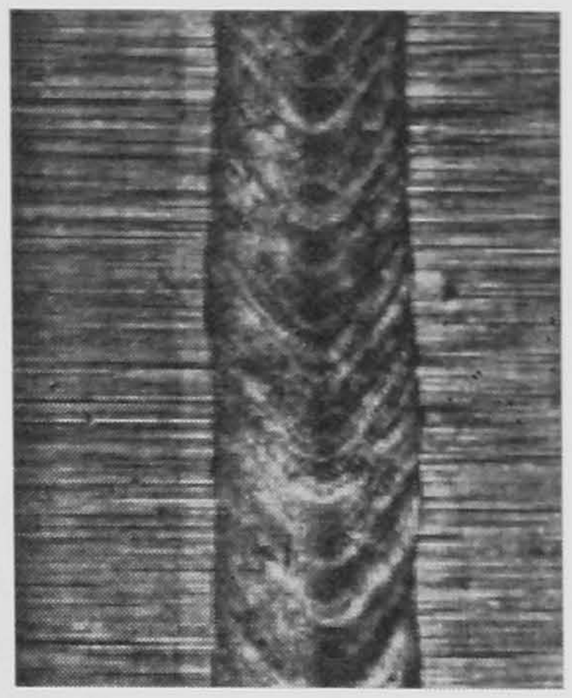

Figure 7.6a

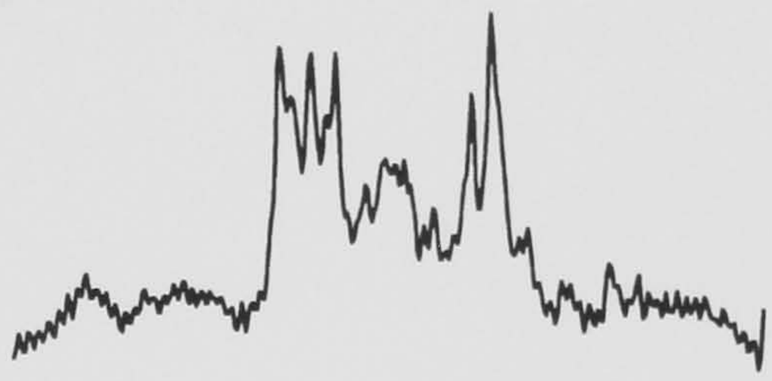

Figure 7.6b

Figures 7.5 and 7.6 show the pictures and traces for the flat welding geometry, at 8 mm/s and 10 mm/s, respectively.

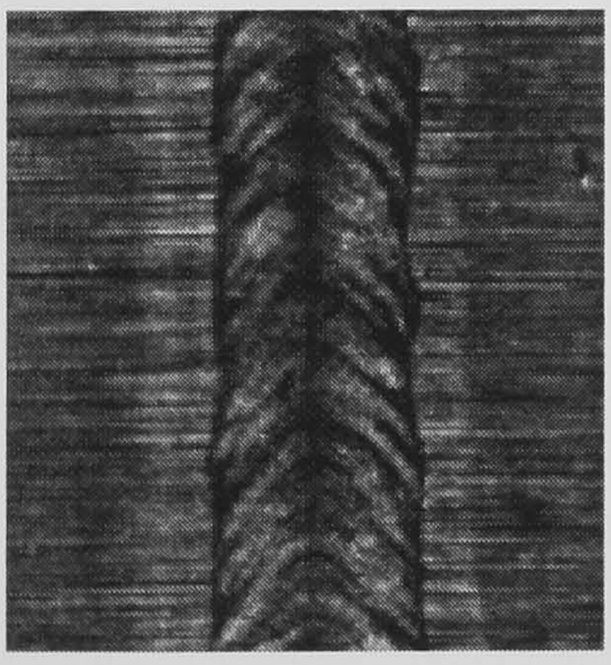

Figure 7.7a

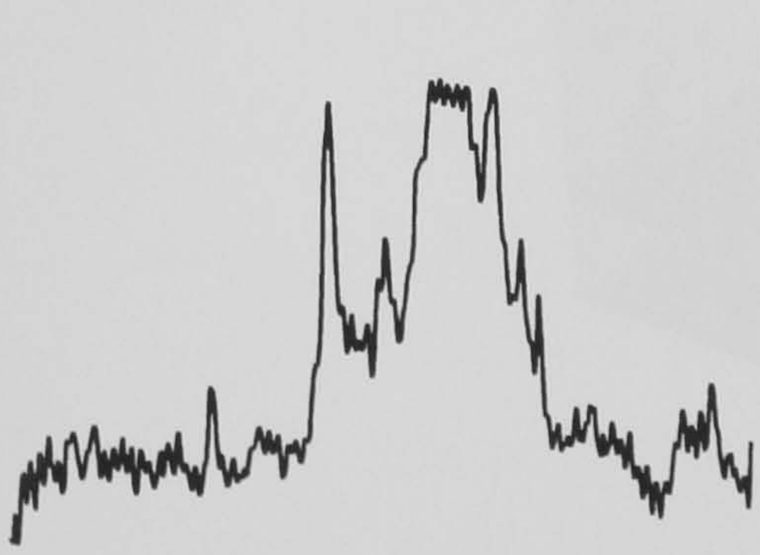

Figure 7.7b

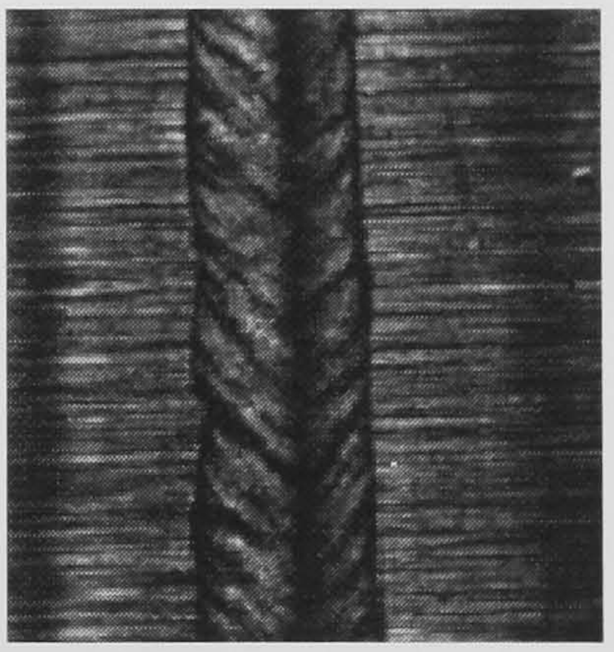

Figure 7.8a

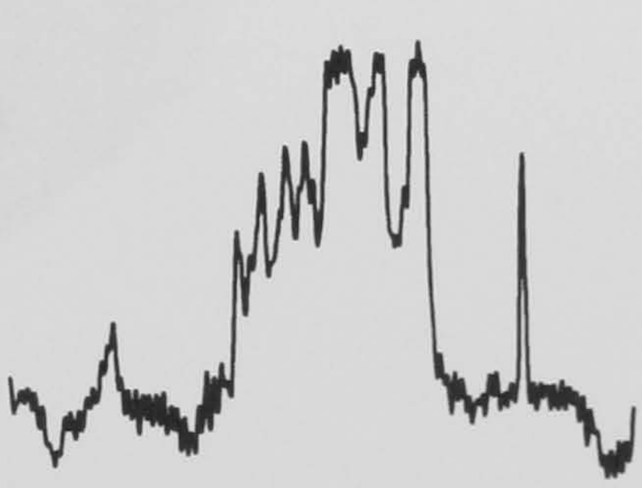

Figure 7.8b

Figures 7. 7and 7.8 show the pictures and traces for the 30° welding geometry, at 8 mm/s and 10 mm/s.

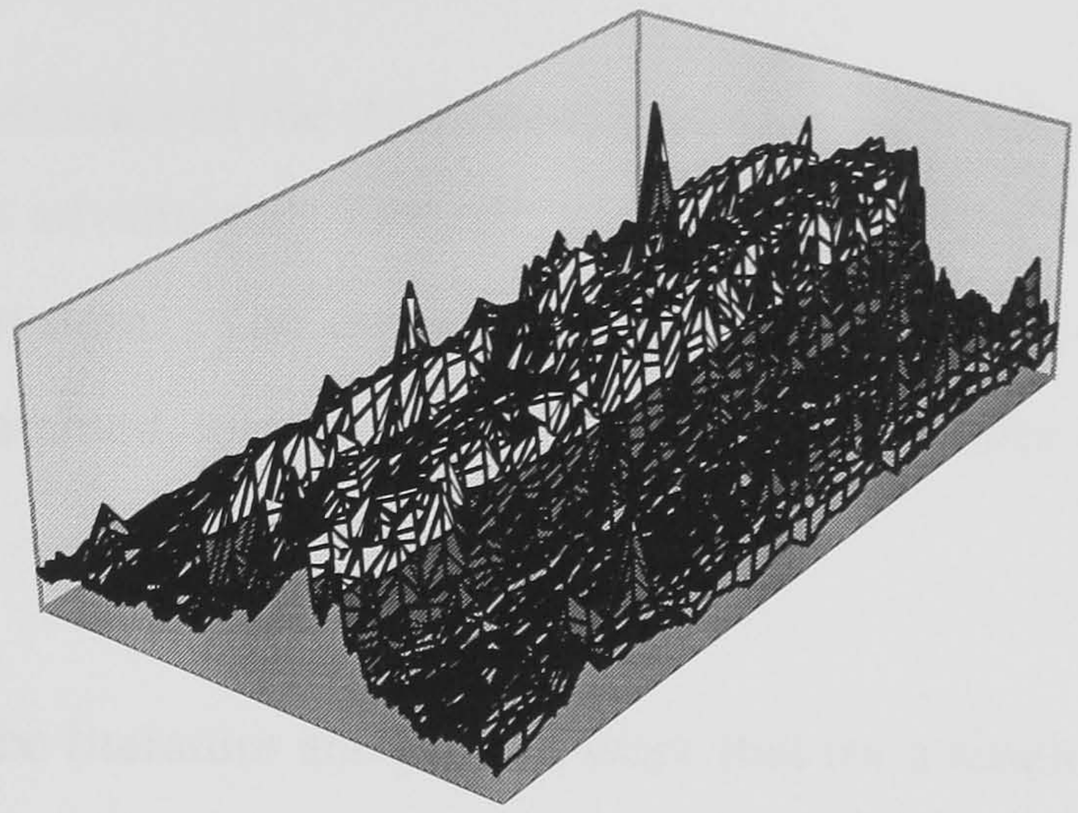

Figure 9(a) shows the 3-D scan of the weld bead formation for 30° welding geometry

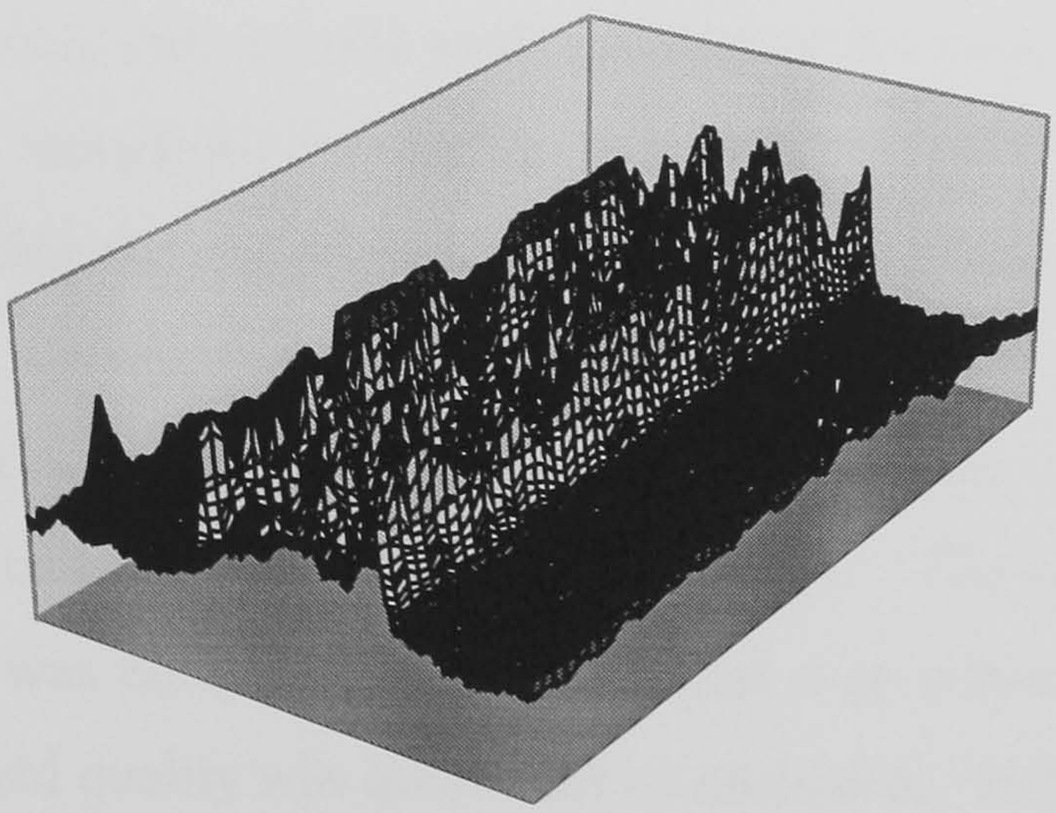

Figure 9(b) shows the 3-D scan of the weld bead formation for flat welding geometry

CHAPTER EIGHT

CONCLUSIONS AND FUTURE WORK

8.1 Conclusions

The unique capabilities of the dual beam system, as noted in preceding chapters, has led to numerous advantages. Overall, the results compare favourably with a single beam delivery system. The rate of heating and cooling for a dual beam delivery system were examined, and a model was developed, briefly discussed in **Appendix A**.

It is clear from the literature and present work that for a single beam delivery system, the welding performance of high carbon steel (HCS) with a Nd:YAG pulsed laser was strongly influenced by the welding velocity, pulse width and pulse repetition frequency (PRF). It was shown that by increasing the pulse width and PRF a deeper weld penetration and a wider weld bead width were achieved, moreover, the weld region become tougher. It was found that the strength of the welded joint greatly increased with pulse width and PRF. For a higher PRF and pulse width, and a slower welding velocity, the structure was completely modified at the fusion zone. The grain structure that appeared in the fusion zone was typically a more refine and granular grain. It is evident that the hardness profile was dependent on the thermal distribution around the fusion zone. Moreover, in the present case, the hardness profiles were greatly reduced due to the overlap of the beam on the workpiece at the slower welding velocities, for higher pulse widths and PRF. This resulted in effectively reducing the rate of cooling which lead to less brittle welds.

In the present case, a dual beam delivery system was used to implement heat treatment, simultaneously with the welding process. The weld quality for the dual beam geometry was compared to that achieved with normal welding (single beam system). The weld quality was quantified by measuring the hardness profiles, tensile strength, aspect ratio, weld width and examining the microstructure behaviour for a range of selected weld parameters, including pulse width and PRF. However, a propitious selection of preheating and post-heating techniques was used to reduce

the quenching rate to achieve a tempering process. But it was found that the pre-heating of the sample was more effective in reducing the hardness profiles compared to post-heated weld. Thus, the post-heated weld was a more effective technique to reduce the rate of cooling, but the pre-heating technique was more effective in reducing the temperature gradient in the transverse direction. It was noticed that pre-heating the sample allowed a greater energy absorption onto the welded sample, achieving a wider weld bead width. In all cases, full penetration welds were achieved with the pre-heating technique. Due to the wider weld width, this resulted in a lower aspect ratio and greater weld volume formation rate compared to the post-heated weld. For the post-heated weld, the tensile strength of welded joint was superior to that of the pre-heated weld. It was observed that it also raised the tensile strength as compared to the pre-heated weld, which produced a softer region in the heat affected zone which was generally narrow. This softer region produced by the post-heated weld was restrained on both sides by harder material, which opposed its deformation. For the post-heated weld, the spatter loss resulted in reducing the strength at a higher PRF. The strength of the welded joint increased with the PRF and pulse width, for the pre-heated weld geometry.

A multi-factorial experiment was devised so as to reduce the cost and time involved in analysing the effect of individual laser parameters in an attempt to find the most significant parameters that influence the welds quality. The number of experiments required to investigate the effect of each parameter were significantly reduced with the multi-factorial designed experiment. This enabled assessment of the effect of a number laser variables in normal, post-heated and pre-heated welds. These results only show the trend and lead to a final assumption through a methodology of measuring the weld quality; for instance: measuring the aspect ratio, tensile strength and weld volume formation rate at a selected range of welding speed, pulse widths and PRF. It was found that the trends showed the aspect ratio decreased with increasing PRF and pulse width, at a lower welding velocity. For the post-heated weld, these observation suggested that an interaction between the welding speed and pulse width were highly significant on the aspect ratio of the weld. Consequently, the tensile strength increased with the PRF selected, but the trend showed that the greatest weld strength was achieved with a higher pulse width for the normal, post-

heated and pre-heated welds. For the pre-heated weld geometry, the interaction between the welding velocity and pulse width showed some significant effect on the weld strength. Measurement of the aspect ratio and weld strength clearly indicated the pulse width was highly significant on the weld quality, where a higher pulse width was desirable. However, the results from general linear model, agreed with the conclusions drawn in Chapter 3. Because of wider weld bead achieved at a higher pulse width, this resulted in a greater weld volume formation rate. For the pre-heated geometry, there was significant interaction for the welding speed, pulse width and PRF for the weld volume formation rate.

It was noticed that high cooling rates lead to deterioration of the weld quality due to hardness discontinuities between the fusion and heat affected zones. An attempt was made to reduce the hardness profile by using a dual beam delivery system to implement a heat-treatment process; these experiments improved the weld quality. Moreover, a 30° clamping geometry was fabricated to improve the weld quality and hardness characteristics, by improving the beam geometry-material interaction; this ameliorated the poor characteristics associated with rapid cooling. Two different angles of incidence (0°,30°) for welding were compared as were effects of the pulse width and pulse repetition frequency (PRF). These effects were quantified by measuring the hardness transverse to the weld direction, tensile strength, aspect ratio, weld volume formation rate and examining the phase transformation. For both geometries, the hardness profiles decreased with increasing pulse width and PRF, however, the hardness gradients were lower for the 30° welding configuration. The hardness profile was dependent on the thermal distribution around the fusion and heat affected zones. Because of the rapidity of cooling for the normal weld geometry, a fine grain was found in the main weld region which consisted of a martensitics structure, dispersed carbides, and retained austenite. For the 30° welding configuration, a slower cooling rate was achieved, leading to a less brittle weld. The grain structure was typically fine and granular, and the structure was completely modified at the fusion zone. For flat welding, at a higher PRF, spatter loss was a serve problem; however, these experiments showed the preventive methods for reducing the spatter loss such as using a defocussed beam. Compared to the flat welding geometry, full penetration and wider wedl widths were achieved

with welding at 30°, thus, the drop out in the fusion zone could be eliminated with a higher welding speed, for 30° geometry. It was observed that using the 30° clamped geometry, bubbles became trapped from the bottom and tip of the keyhole, due to the angle of the weld sample. Additionally, a lower aspect ratio was obtained; this was due to the wider weld width produced with this geometry.

Benefits of welding at 30° include: improved microstructure and reduced peak hardness profiles, higher tensile strength and greater weld volume formation rate. Ultimately, for 30° welding configuration, a higher welding speed was achieved to eliminate the drop out occurred in the fusion zone.

The performance and the weld quality of a dual beam Nd:YAG system was examined and compared to those from single beam system. It yielded substantial improvement over a single beam system. An analysis of the performance of 30° welding, single and dual beam geometries, were compared and it was indicated that both the pre-heating and post-heating techniques resulted in reduced hardness discontinuities, additionally the likelihood of cracking, when subjected to cyclic loading, was greatly reduced. It was concluded that for the dual beam system, the tensile strength of the welded joint was lower compared to the single beam system. This was due to the serve drop out problem that occurred in the fusion zone for the 30° welding configuration, as discussed in Section 5.1.3.5. Consequently, the pre-heated geometry produced a wider weld bead compared to the normal and post-heated weld, which resulted in a lower aspect ratio and the greatest weld volume formation rate. The grain structure was completely modified at the fusion zone, this was explained by observing that the rate of cooling was slower for the dual beam system.

It would be interesting to model in greater detail the rate of heating and cooling of the single and dual beam system in order to understand the critical thermal transfer factors that resulted in different grain sizes and transformations. An attempt was made to model and provide fundamental understanding of the rate of heating and

cooling of a welded sample by delaying the time for pre-heating or post-heating the sample.

The welding performance of CO_2 lasers was strongly affected by the clamping geometry and welding speed. Two weld geometries, namely clamped and unclamped, were considered. An experimental investigation into the weld quality was performed to quantify the effect of clamping and translation velocity. The spatial hardness discontinuities were dependent on the temperature distribution during the welding process. Moreover, different welding geometries (clamped and unclamped) lead to different thermal heat transfer characteristics. The unclamped geometry had a greater surface area in contact with the worktable; this resulted in a faster cooling rate and a higher hardenability in the fusion and heat affected zones as compared to that achieved with the clamped geometry. For both welding configurations, the weld penetration depth and weld bead decreased with increasing translation speed. However, the unclamped geometry produced a deeper and wider weld bead, which lead to the greatest rate of formation of the weld volume, as compared to the clamped geometry. By increasing the translation velocity and using the clamping geometry, a denser and coarser grain structure was observed in the fusion zone.

It was apparent that the different welding geometries and beam delivery systems (Chapters 3 and 5) can be used to improve laser weld quality for Nd:YAG pulsed lasers. In all cases, these experimental results were further improved with a multiple beam delivery system. Here, the workpiece spatial and temporal temperature distribution were controlled to generate desired mechanical properties without losing the benefits of this low distortion joining process. The preliminary experiments were devised to investigate a beam scanning technique for pre-heating or post-heating the samples to control the phase transitions and to deliver specific weld characteristics. Whilst not precluding it, this obviated the need of multiple beam delivery systems and is an ideal approach for industrial users with small batch job requirements. It was observed that post-heating of the workpiece was more effective in improving weld characteristics than pre-heating. As expected a lower translation velocity tended to produce a wider weld bead and greater penetration depth than a

higher translation velocity. A pre-heated weld gave the greatest penetration than the normal and post-heated welds, whereas, the post-heated geometry produced a wider weld bead. For the scanning technique. a complex transformation structure was found for the pre-heated and post-heated weld geometries, comprising a heat affected zone with sharply defined narrow bands.

An analysis of the performance of scanning technique was used to develop a dual beam system to improve the weld quality. A dual beam delivery system was designed and fabricated to achieve in-line process heat treatment to ameliorate poor weld characteristics. Apart from the benefit of using the dual beam system, several problems were identified which lead to the failure of the dual beam CO_2 laser system. It was difficult to cool the ZnSe beam splitter, however, this system faced a serve problem of thermal distortion, which may be responsible for the changes in the output power of the beam or interference. Moreover, another possibility was the CO_2 laser power fluctuated due to the reflection of light from the workpiece going back into the cavity, hence modulating the output of the system. This was not examined further.

A double pass technique was developed to investigated the effect of delay on the pre-heating and post-heating of the weld. This experiment successfully demonstrated how to quickly assess and optimise the effect of a dual beam delivery system. It was found that the rapid cooling rate can be effectively suppressed by using the post-heating technique, and this produced the lowest hardness profiles compared to the normal and pre-heated welds.

It was observed that the high power diode laser beam processing yields many different characteristics than see with the CO_2 laser. Generally, the beam from the high power diode lasers was poor but the beam quality was sufficient for welding. Compared to the diode laser weld, lower hardness profiles were achieved with the CO_2 laser; this resulted in a wider weld bead and a microstructure that corresponded to a slower cooling rate than achieved with the diode laser. Because of the rapid quenching rate of laser welding, at the higher welding velocity for the HPDL, centre-line cracks were found in the fusion zone. Interestingly, the rate of weld volume

formation and weld bead decreased with increasing welding velocity. The irradiance for the HPDL and CO_2 lasers were 1.3 x 10^7 W/cm^2 and 2 x 10^4 W/cm^2.

For the pulsed Nd:YAG laser system, a 30° clamped geometry was fabricated and used for welding, these results indicated substantial improvement of weld quality compared to the flat welding process. However, this was found to be different case for CO_2 welding at 30°, and it was found that there was no appropriate improvement in the weld strength. The hardness gradient was less for 30° welding configuration. Because of the wider weld bead and greater rate of weld volume formation, the flat welding provided a greater strength than 30° welding configuration for the CO_2 laser welds.

An image processing system was developed and tested successfully, to accurately record the weld characteristics; this system offered real time capability to determine the weld quality via measuring the width of the weld bead and surface roughness. An inexpensive data acquisition system was developed to capture the data associated with the weld seam and to analyze the bad and good quality welds. The variation in the trace between the extreme peaks correlated with the surface roughness profile across the weld. The system was used to differentiate the weld characteristics produced by the two different angles of incidence (0°,30°) for welding.

8.2 Future work

From the technical standpoint, it has been demonstrated that good quality laser welds can be formed in high carbon steels from 0.8 mm to 2 mm in thickness. Although comparable success has been attained in gauge plates, results generated indicate that the dual beam and 30° welding processes show the expanded possibilities for influencing the welding results for the CO_2 and Nd:YAG lasers - without loss of laser-specific advantages, which manifest themselves in narrow, clean, almost distortion free welds. The disadvantages from having a high energy density, for instance: rapid cooling rate, increases in hardness and crack formation, can be eliminated easily.

It is readily apparent that the introduction of dual beam CO_2 laser system provide higher welding efficiencies. Further improvements are expected with the implementation of the dual beam delivery system that has been fabricated. This system has not been fully tested. This will further promote industrial laser welding applications. Some problems were experienced with this system that need solving. The laser beam must not reflect back to the laser cavity from the workpiece. This can be achieved simply by directing the beams at an angle to the workpiece, away from normal incidence. The cooling system for the beam splitter and optics need redesigning.

It is recommended that the performance of 30° welding, should be further studied to eliminate the drop-out problem that occurred in the fusion zone. For example, investigating the effect of welding at a higher speed, using an assist gas to blow against the drop-out, and a filler material could be used. The indication of this work is that the drop out problem may easily be eliminated by welding at a higher translation velocity.

It would be interesting to model in detail the different phase transformations of a single and dual beam system inorder to understand the heat transfer and cooling process of the workpiece. This would provide important information regarding the temporal temperature distribution during welding, and allow prediction of the grain sizes and microstructures that appear in the fusion and heat affected zones. It is recommended that equations should be to determine the weld characteristics with input of the chemical composition of the material, laser process parameters and clamp geometry.

Measurements can be applied during the welding process to monitor and control the quality of the laser welds. In an industrial application, measuring the weld bead and penetration depth could be calculated in real time, with the results used in a feedback loop to control the welding speed in a real time, continuously optimising the weld quality.

Experiments should be performed to measure the temperature distribution on the bottom surface of the workpiece, using an infrared sensor for example to examine

the performance of the dual beam system. The spatial distance between the welding and post-heating or pre-heating beams which influences the mechanical properties of the weld should be studied and optimized. This system can be easily integrated and automated. This dual beam delivery system is clearly a more precise and cost favourable method of pre-heating or post-heating than a conventional heat treatment in a continuous furnace or with induction heating.

Joining of dissimilar materials is a long term problem in manufacturing. Therefore, experiments should be performed, using different welding geometries, and single and dual beam system to study and understand the physical mechanisms and problems occurring.

The success of the initial diode laser welding will undoubtedly contribute to rapid expansion of the industrial use of diode laser welding. To lower the capital costs of industrial welding application, the dual beam diode laser system should be designed, and the experimental results compared to the conventional CO_2 and Nd:YAG laser weld quality.

Future work should address the potential of HPDL for welding with emphasis on minimising the beam size to increase the irradiances. This would allow a more favourable comparison between HPDL and other laser devices. Ultimately, these machine may yield cost benefits and performance far in excess of CO_2 and Nd:YAG lasers on a cost per Watt basis. The preliminary studies, however, demonstrated that a 1.4 kW diode laser was outperformed by a 1kW CO_2 laser. This, however, is probably due to the differences in the irradiance of the two lasers that from the diode laser being lower because of the poor beam quality and larger beam size.

APPENDIX A

A A simple modelling of laser heating - one dimensional heat flow

A.1 Introduction

The purpose of the present work is to develop a simple model that can be used to estimate the temporal temperature distribution of the laser beam irradiated the weld sample's associated with different beam delivery systems; for instance: single and dual beam used for welding. This appendix will describe the effect of heating a workpiece surface with a single or dual beam delivery system. Moreover, the effect between single and dual beam systems that directly affect the temperature can be easily identified. The main advantage of using pre-heating or post-heating technique is to slow down the rate of cooling process, and the amount of heating can be chosen accurately to suit the needs of the welding process. Such information may be very helpful to establish laser operating parameters that used to optimise the welding process to achieve desired microstructure and mechanical properties.

A.2 Heat transfer single laser beam

The heating model developed herein was designed to predict the rate of cooling process and investigate the behavior of temporal temperature distribution within the welded region, for the single and dual beam delivery system. The absorption of laser radiation in a solid is equivalent to a source of heat existing in that solid. The effect of the heat source and temperature distribution can be modelled as the three dimensional heat transfer equation:

$$\mathrm{p\,C}\,\frac{\mathrm{d\,T}}{\mathrm{d\,t}} = K\left(\frac{d^2T}{d^2x} + \frac{d^2T}{d\ y} + \frac{d^2T}{d^2z}\right) + A(x,y,z) \qquad (1)$$

with:

ρ:	Materials Density	[kg / m^3]
C:	Specific Heat Capacity	[J / (kg K)]
K:	Thermal Conductivity	[W / (m K)]

T: Temperature [K]

t: Time [s]

A: Source distribution function

Thermal diffusivity is a measure of how quickly thermal equilibrium is established after the application of a source:

$$\kappa = \frac{K}{\rho C} \quad [m^2 / s] \tag{2}$$

The distance z that heat has penetrated into the sample is given by:

$$z = (\kappa t)^{1/2} [m] \tag{3}$$

To estimate the temperature rise of the workpiece surface ($z = 0$) belonging to a carbon steel sheet caused by a pulsed Nd:YAG laser following values are supposed, see **Table 1**:

Material	Thermal conductivity (K) ($W\ m^{-1}\ K^{-1}$)	Thermal diffusivity (κ) ($m^2\ s^{-1}$) (10^{-6})	Specific heat capacity (C) ($J\ kg^{-1}\ K^{-1}$)	Density (ρ) ($kg\ m^{-3}$)	Melting point (T_m) (K)	Boiling point (T_b) (K)	Latent heat of vaporization (L_v) ($J\ kg^{-1}$) (10^6)
Aluminium	238	97.30	903	2710	932	2720	10.90
Copper	400	116.30	385	8960	1356	2855	4.75
Iron	82	23.20	449	7870	1810	3160	6.80
Mild steel	45	13.60	420	7860	1700		
Carbon steel	60.5	17.70	434	7854	1700		
Nickel	90	22.80	444	8900	1726	3110	6.47
Silver	418	169.00	235	10500	1234	2466	2.31
Alumina (ceramic)	29	9.54	800	3800	2300		
Perspex	0.2	0.11	1500	1190	350		
Silicon	170	103.00	707	2330	1680	2628	10.60

Table 1: Thermo-physical properties of selected material

- intensity profile = Gaussian of radius d = 1 mm
- material = Carbon steel
- Emissivity [3] $\varepsilon = 0.8$
- material thickness L = 1.5 mm

- $K = 60.5\ W\ m^{-1}\ K^{-1}$
- $\kappa = 17.7 \cdot 10^{-6}\ m^2\ s^{-1}$
- beam radius d = 1 mm or 0.001 m
- $P_{o\ average} = 200\ W$

Specific experimental values used for Nd:YAG pulsed laser is explained in Chapter 3 are:

- mean output power $P_o = 200\ W$
- pulse repetition rate R = 10 Hz
- pulse energy E = 20 J
- pulse duration D = 10 ms

The following figure 1 shows the intensity profile of a Gaussian laser beam:

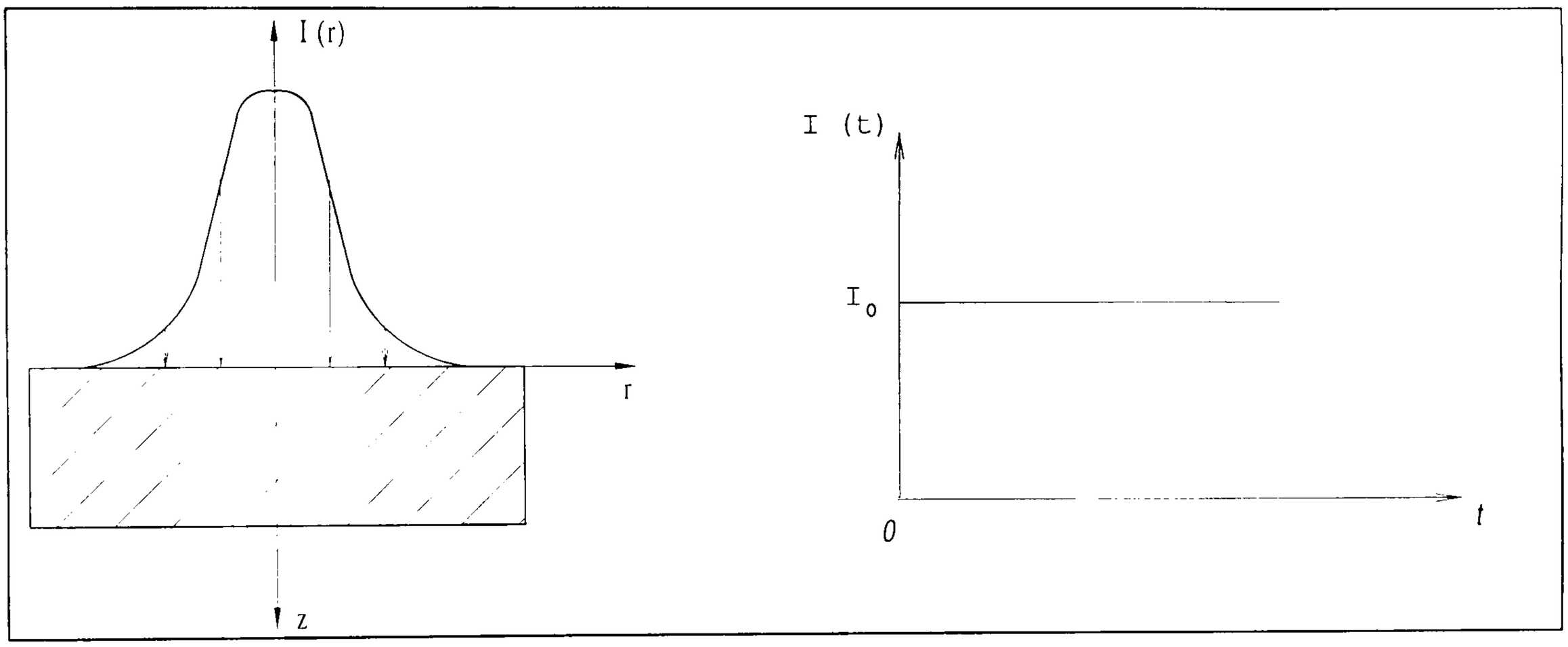

Figure 1: Intensity profile of a Gaussian beam. Infinite half - space.

The solution for Gaussian distribution of type $T(z=0,r=0,t>0)$ of the heat transfer equation mentioned above is given by:

$$T(0,0,t) = \frac{\varepsilon I_o d}{K \pi^{1/2}} \tan^{-1}\left(\frac{4 \kappa t}{d^2}\right)^{1/2} \qquad (4)$$

This solution defines the change of temperature at the workpiece surface $(z=0)$ at the focus point $(r=0)$ versus time and is equal to equation:

$$T(0,t) = \frac{2\varepsilon I_o}{K}\left(\frac{\kappa t}{\pi}\right)^{1/2} \qquad (5)$$

if $\tan^{-1}\left(\frac{4 \kappa t}{d^2}\right)^{1/2} \approx \left(\frac{4 \kappa t}{d^2}\right)^{1/2}$ and if *beam radius* $d >> (\kappa t)^{1/2}$ is fulfilled.

Equation (5) originally is the solution of the heat transfer equation for following intensity profile, see **Figure 1**.

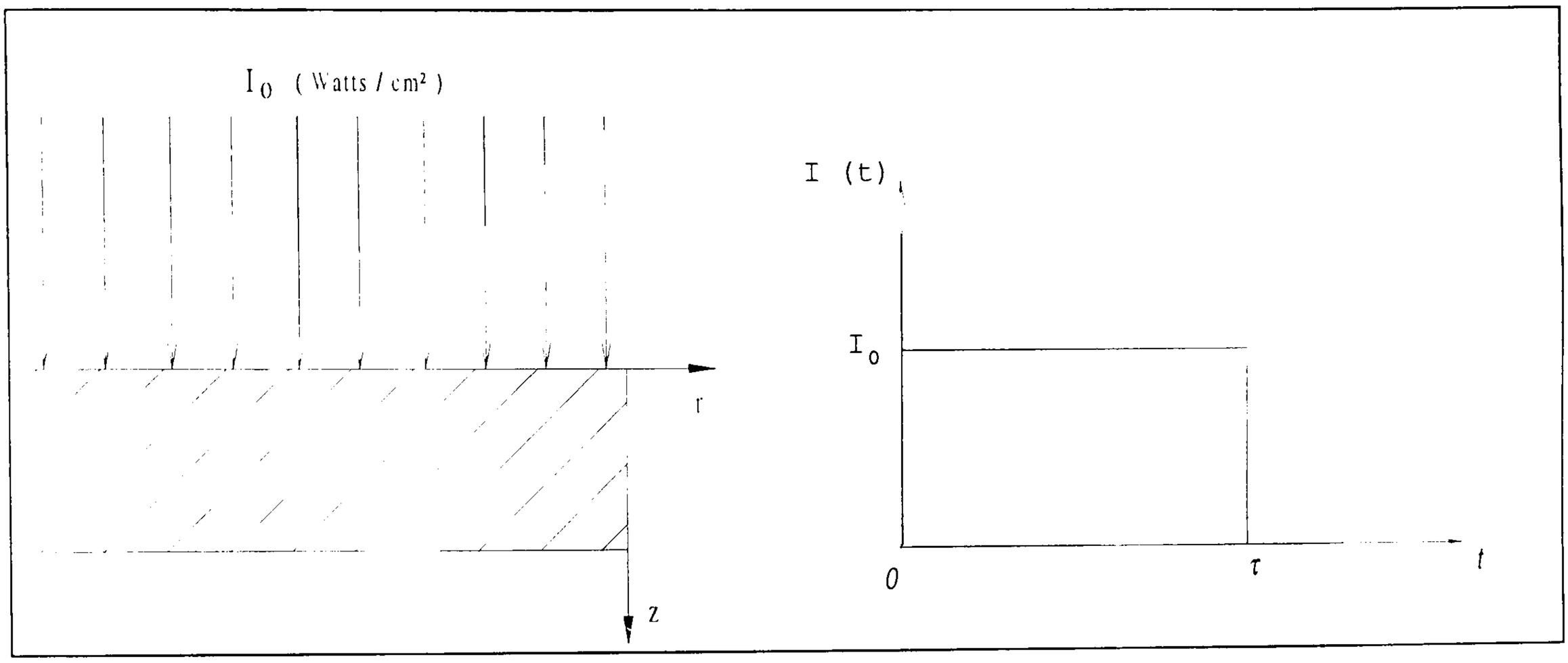

Figure 2: Assumed intensity profile. Infinite half - space

Thus, the investigation of temperature rise caused by laser beam interactions onto the workpiece surface (z = 0) is not falsified if the intensity profile of **Figure.2** is assumed. Thus, the laser power intensity I_O will be calculated:

Equation (5): $$I_O = \frac{P_P}{A}$$

By (Table.1): $peak\ power \quad P_P = 200\ W$

Area $$A = \frac{\pi \cdot (d)^2}{4} = 0.784 \cdot 10^{-6}$$

Thus:

$$I_O = 2.54 \cdot 10^{8}$$

$$T(0,t) = \frac{2e\ I\ o}{K}\left(\frac{k\ t}{\pi}\right)^{1/2} \quad (6)$$

The initial whole temperature within the welded region was assumed to be uniform and equal to the temperature of the ambient air. This assumption leads to the following initial condition:

$$T = 0 \qquad at\ \ t = 0$$

At all boundaries of the heating as a results of conduction, convection and radiation, however, only conduction is significant, and the heat transfer characteristics between the phase transformation is not taken into considerations.

Hence, Eqn. (5) can be solved with the boundary condition controlled by Eqn. (6), and **Figure 3** shows the change of temperature as function of time during laser heating the workpiece with a pulsed Nd:YAG laser used.

However, the cooling time between two pulses is not taken into consideration. Therefore, if t > pulse width τ and $z = 0$, thus, the following term represents the cooling effect:

$$T(0,t) = \frac{2\ Io\ e\ k^{1/2}}{K}\left[\left(\frac{t}{\pi}\right)^{1/2} - \left(\frac{(t\ -\ \tau)}{\pi}\right)^{1/2}\right]^{0}C \quad (7)$$

where τ is the pulse width or heating time (ms); Io is the power density of the incident beam at the surface (W/m^2); ε is the absorptivity of the material; κ is the thermal diffusivity (m^2/s); K is the thermal conductivity of the material (W/m k); t is time (s).

Although the actual heat flow is three dimensional, the one dimensional analysis is used in this model to predict the rate of cooling behavior is fairly good enough assuming that the heat divergence is very small.

Based on **Table 1** and Eqn. (5);

$$T(0,t) = \frac{2 \cdot 2.54 \cdot 10^{8} \cdot 17.7 \cdot 10^{-6}}{60.5} \cdot \left[\left(\frac{t}{\pi} \right)^{1/2} - \left(\frac{(t - 0.01)}{\pi} \right)^{1/2} \right] \qquad (8)$$

Eqn. (8) for $t > \tau$ leads to **Figure 4.**

This figure illustrates the effect of rate of heating and cooling effect, where laser beam with $I_O = 2.54 \cdot 10^{8}$ W / m ^{2}. The dual laser beam system used for pre-heating or post-heating the sample will result in different laser power intensities (Io), because the heating beam is branched off from the main welding beam and will arrive on the workpiece surface before or after welding. Thus, the experimental results are further explained in Chapter 3 - see Section 3.2 and 3.3. Thus, the irradiated area of this defocused heating beam will be larger than the main focused welding beam. Therefore, the laser power intensity will decrease, according to equation (5).

A.3 Heat transfer of dual laser beam

Here the laser power was divided so that 70 % was coupled to the weld beam and 30 % was directed into post-heating or pre-heating.

Investigations on the welding beam :

Using Eqn (5): $$I_O = \frac{70}{100} \cdot \frac{Po}{A} \quad \Rightarrow \quad Io = 1.78 \cdot 10^{8} \frac{W}{m^2}$$

During heating use Eqn. (6), where $t < \tau$:

$$T(0, t < \tau) = \frac{2\varepsilon I_o}{K} \left(\frac{\kappa t}{\pi} \right)^{1/2}$$

(6)

During cooling use Eqn. (9.7), where $t > \tau$:

$$T(0,t > \tau) = \frac{2 \cdot \varepsilon \cdot\cdot Io \cdot \kappa^{\frac{1}{2}}}{K} \bullet \left[\left(\frac{t}{\pi} \right)^{1/2} - \left(\frac{(t - 0.01)}{\pi} \right)^{1/2} \right] {}^{o}C \qquad (7)$$

Thus, **Figure 5** describes equation (6) and (7), this showed the results of heating and cooling of the welded samples where the absorption is taken as 70 %, and the power density being calculated to be 70 % of the normal welding.

The pre-heating or post-heating defocused beam:

Thus, 30 % of the output power Po (200 W) can be used for pre-heating or post-heating the samples:

Using Eqn. (5): $$I_O = \frac{30}{100} \cdot \frac{Po}{A} \quad \Rightarrow \quad Io = 0.76 \cdot 10^{8} \frac{W}{m^2}$$

During heating use Eqn. (6), where $t < \tau$:

$$T(0,t < \tau) = \frac{2\varepsilon I_o}{K} \left(\frac{\kappa t}{\pi} \right)^{1/2} \qquad (6)$$

During cooling use Eqn. (7), where $t > \tau$:

$$T(0,t > \tau) = \frac{2 \cdot \varepsilon \cdot\cdot Io \cdot \kappa^{\frac{1}{2}}}{K} \bullet \left[\left(\frac{t}{\pi} \right)^{1/2} - \left(\frac{(t - 0.01)}{\pi} \right)^{1/2} \right] {}^{o}C \qquad (7)$$

Therefore, **Figure 6** describes the rate of heating and cooling of the pre-heating or post-heating beam.

Dual beam system:

Now, **Figures 7 and 8** show, the rate of heating and cooling of the welded samples, for the pre-heated and post-heated welds. Here, the time υ (ms) indicates the arriving of pre-heating or post-heating beam onto the workpiece.

Investigations of the temporal temperature distribution at different depths:

The temperature rise at a depth z and $0 < t < \tau$ is given by:

"heating equation":
$$T(z,t) = \frac{2\varepsilon I_o}{K} (\kappa t)^{1/2} \; ierfc\left[\frac{z}{2(\kappa t)^{1/2}}\right] \tag{8}$$

with
$$x = \frac{z}{2(\kappa t)^{1/2}}$$

The inverse error function (*ierfc*) is defined as:

$$ierfc(x) = \frac{1}{\sqrt{\pi}} [\, exp(-x^2) - x(1 - erf(x)) \,] \tag{9}$$

with error function (*erf*):
$$erf(x) = \frac{2}{\sqrt{\pi}} \int_o^x e^{-\xi^2} d\xi$$

(10)

Figure 9 shows, the error function (*erf*) with respect to time.

Hence, the term uses for the "cooling equation" for different z-values and $t > \tau$ is given by:

$$T(z,t) = \frac{2e\, I\, o \cdot (k \cdot t)^{1/2}}{K} [\, t^{1/2}\, ierfc\left[\frac{z}{2(k\,t)^{1/2}}\right] - (t-\tau)^{1/2} ierfc\left[\frac{z}{2\left(k(t-\tau)^{1/2}\right)}\right]] \tag{11}$$

The following data is used to calculate the temporal temperature distribution of the sample over the range of depth (z)

- intensity profile = Gaussian of radius d = 1 mm
- material = Carbon steel
- $K = 0.0605$ W mm^{-1} K^{-1}
- $\kappa = 17.7$ mm^2 s^{-1}
- Emissivity $\varepsilon = 0.8$
- material thickness L = 1.5 mm
- beam radius d = 1 mm or 0.001 m
- $P_{o\ average} = 200$ W

So, the temperature distribution over the range of depth investigated is shown in **Figure 10**, where τ is the pulse width or heating time (ms); Io is the power density of the incident beam at the surface (W/mm^2); ε is the absorptivity of the material: κ is the thermal diffusivity (nm^2/s): K is the thermal conductivity of the material (W/nm k): t is time (s).

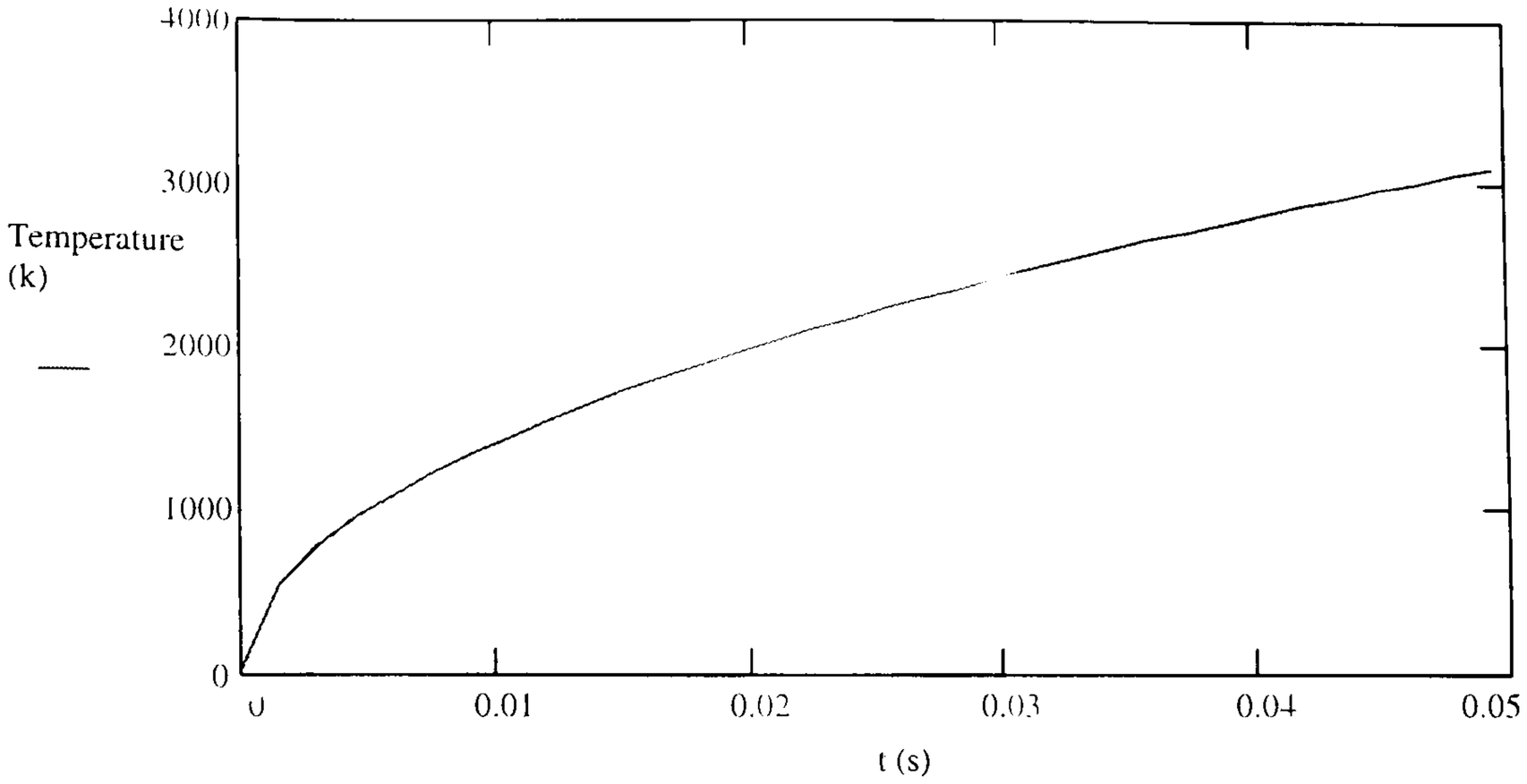

Figure 3 The temperature rise of heating the sample as a function of time.

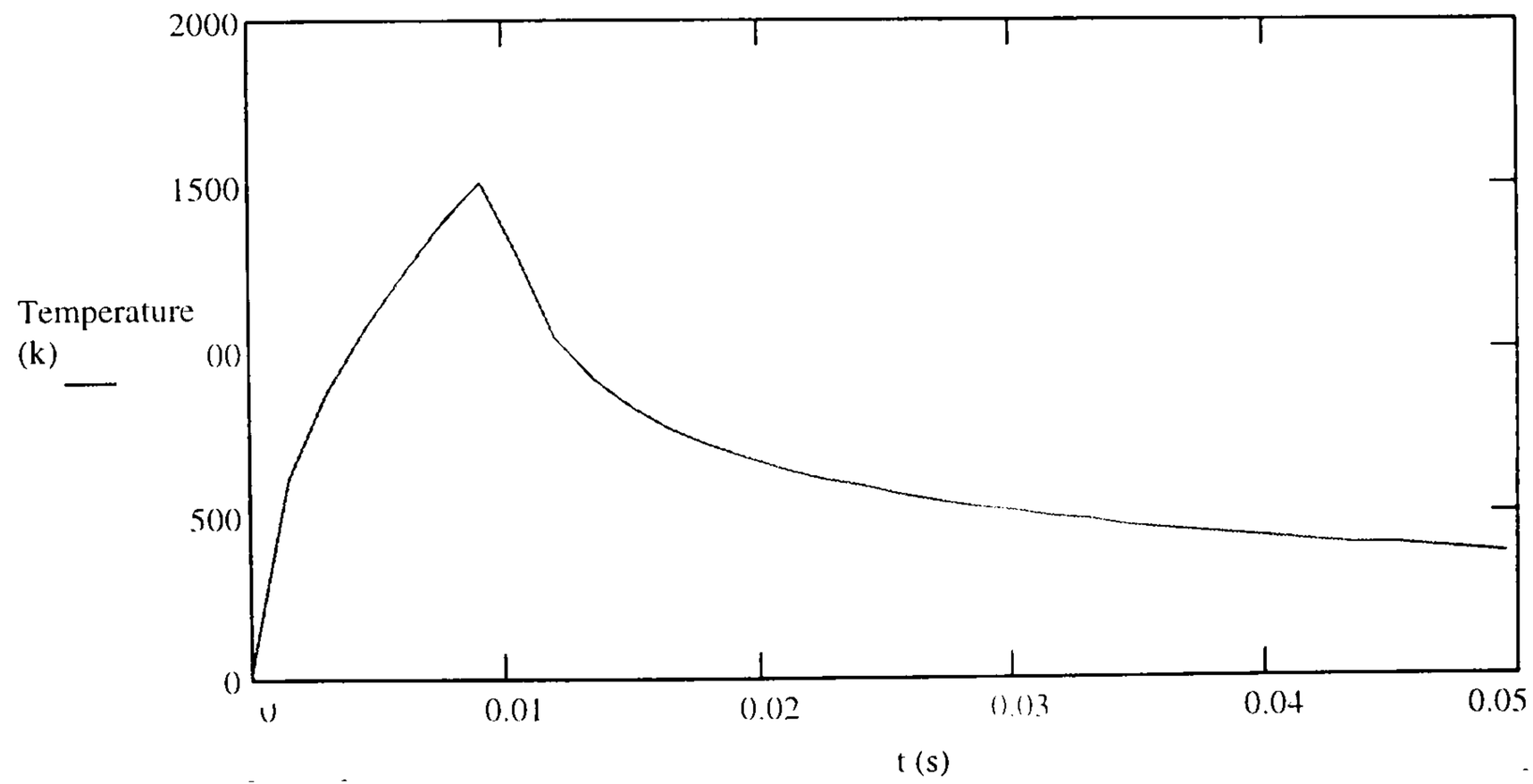

Figure 4 The temperature rise of heating the sample with cooling period as a function of time.

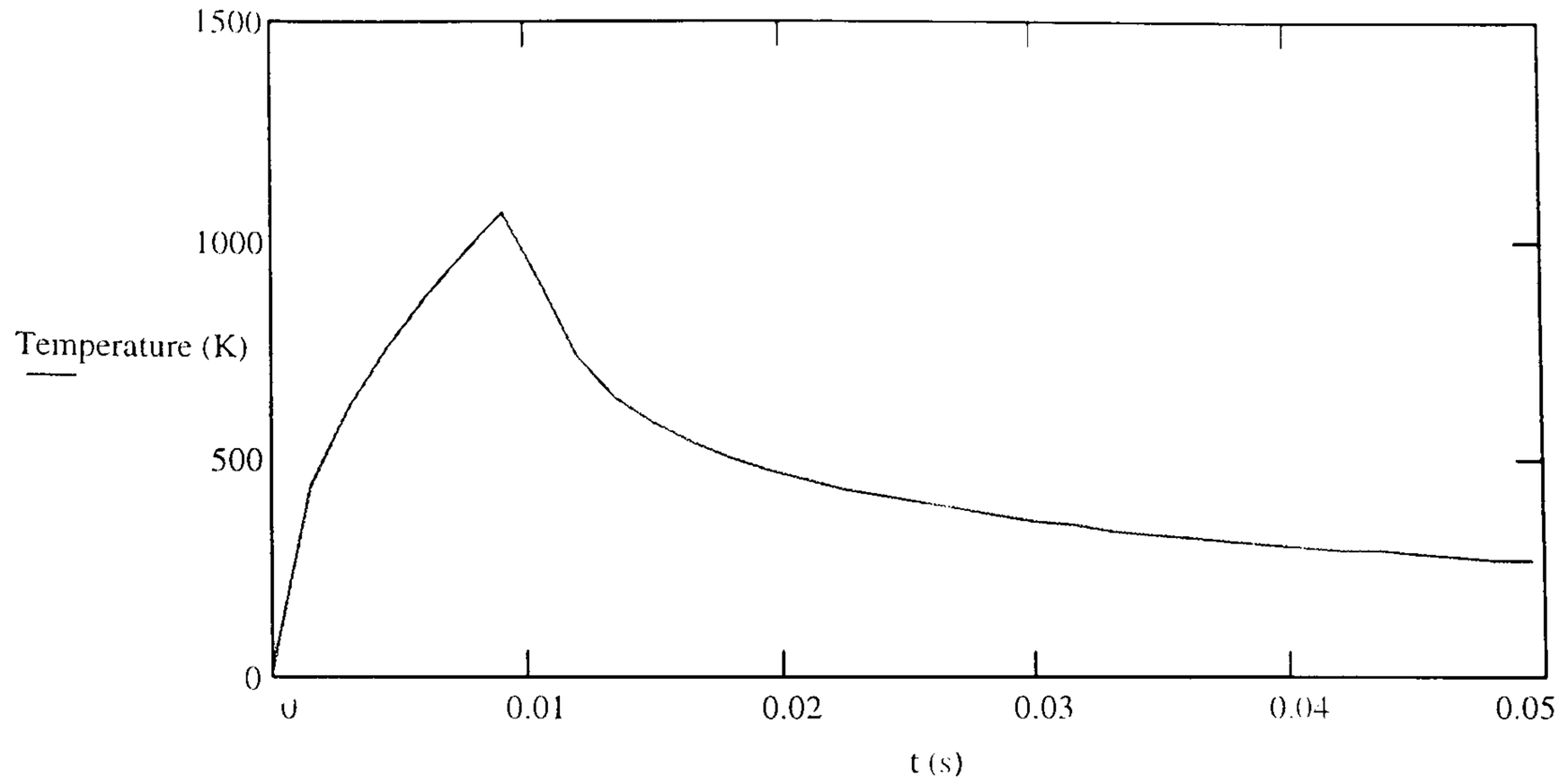

Figure 5 The temperature rise for welding at z = 0 for dual beam system

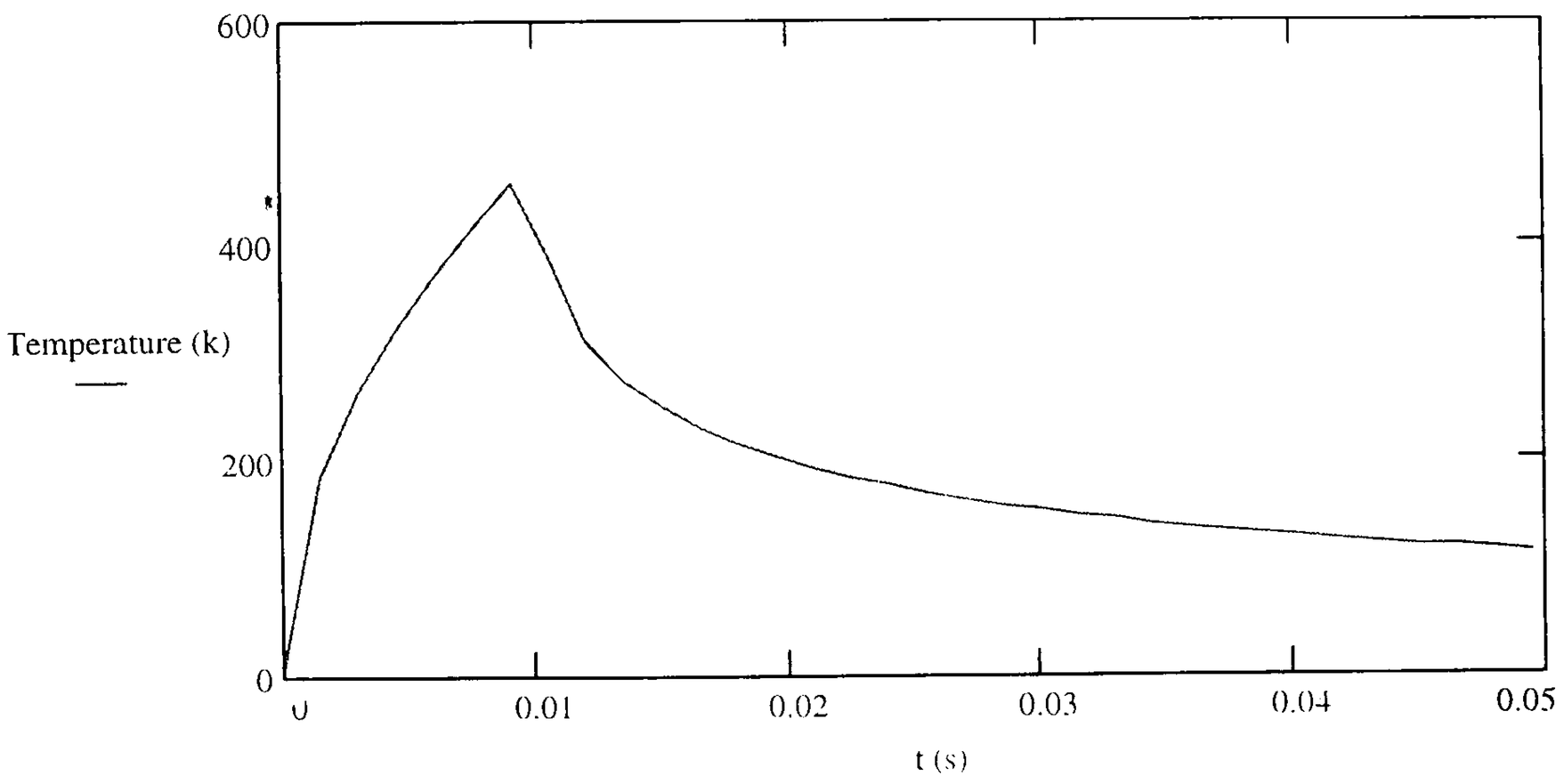

Figure 6 The temperature rise for pre-heating or post-heating the sample at z = 0 for dual beam system

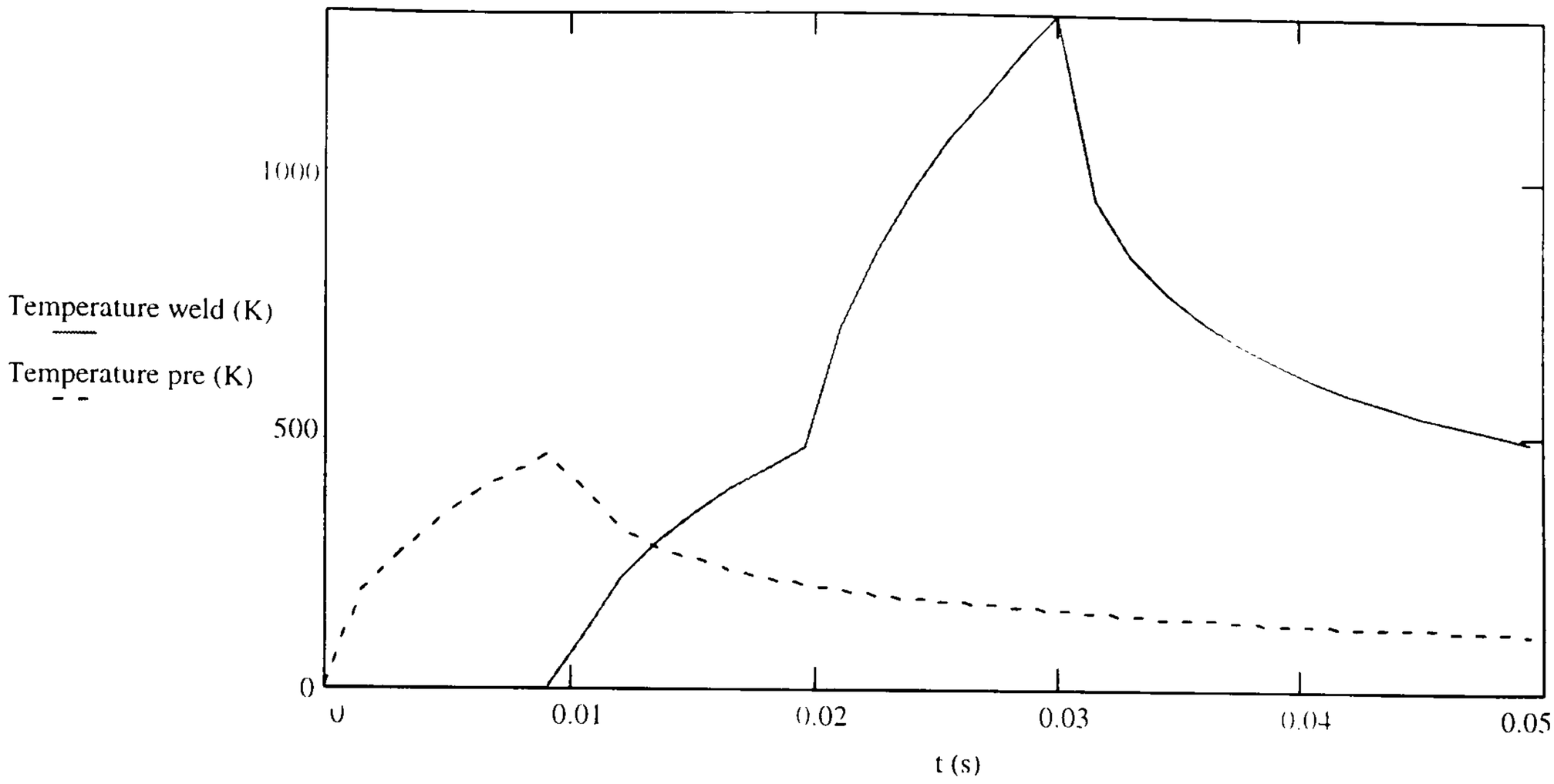

Figure 7 The temperature distribution of welding (—–) and temperature distribution of pre-heating the sample(-----) at z = 0 for the dual beam system.

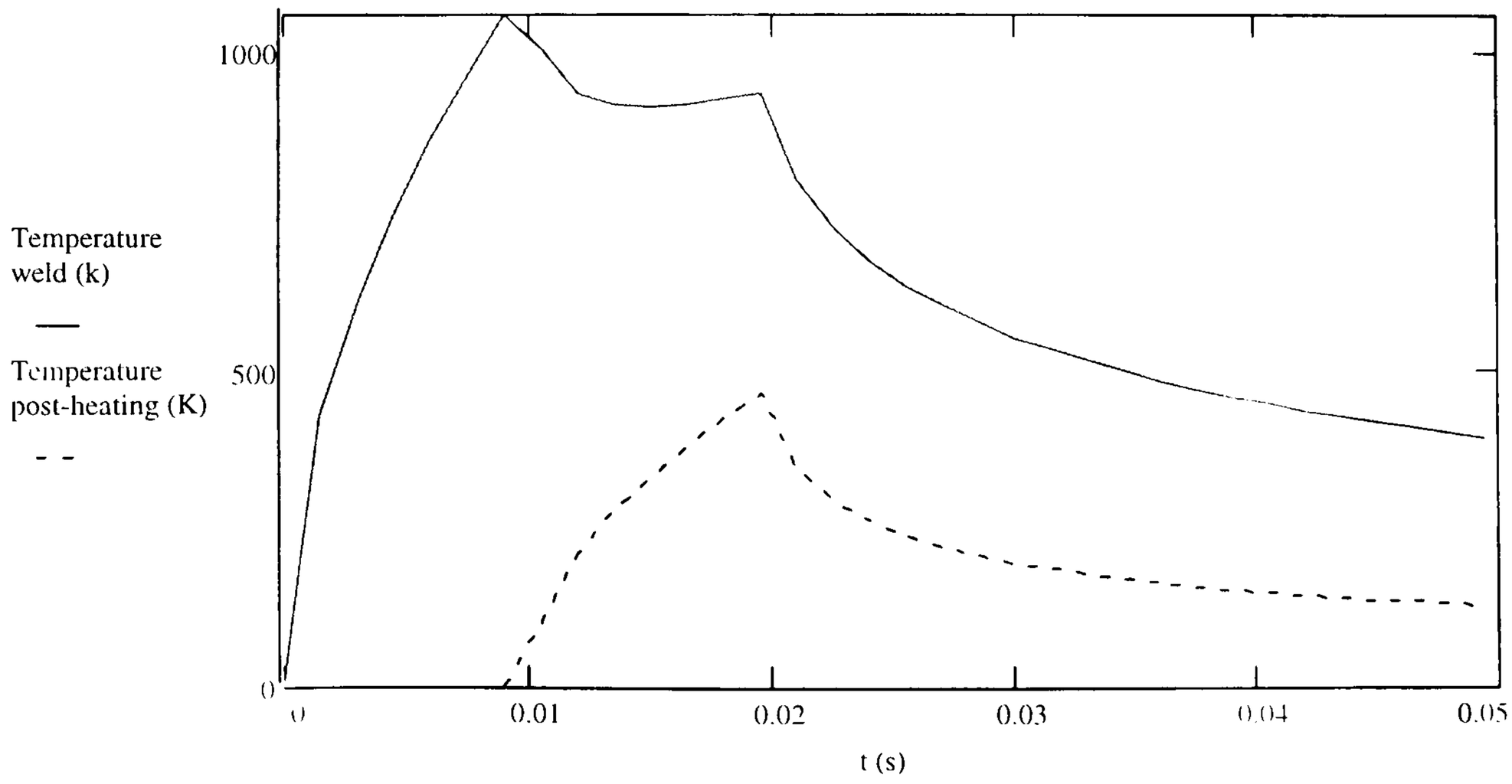

Figure 8 The temperature distribution of welding (——) and temperature distribution of pre-heating the sample(-----) at z = 0 for the dual beam system.

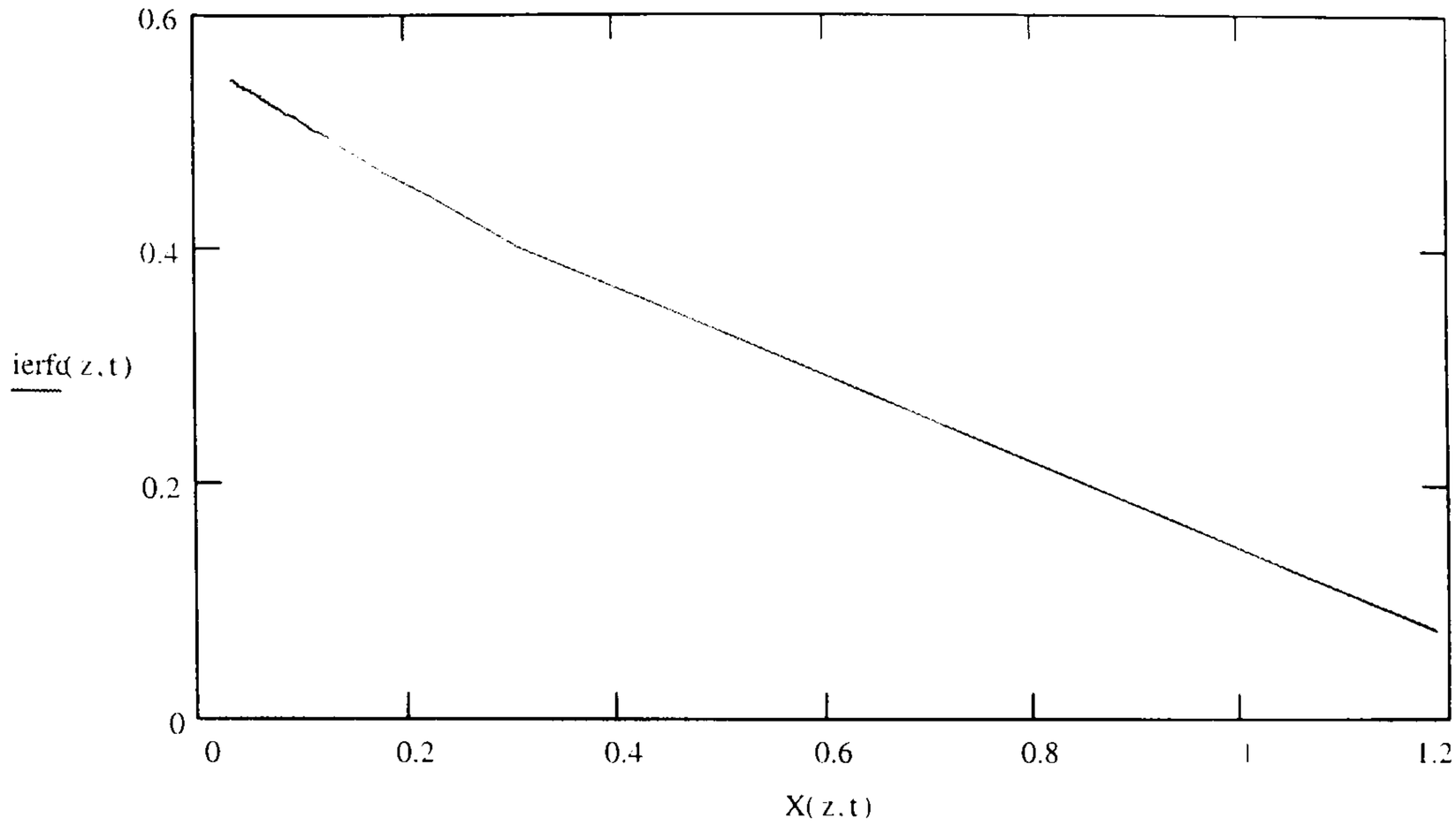

Figure 9 The effect of error function with respect to the time for single beam system

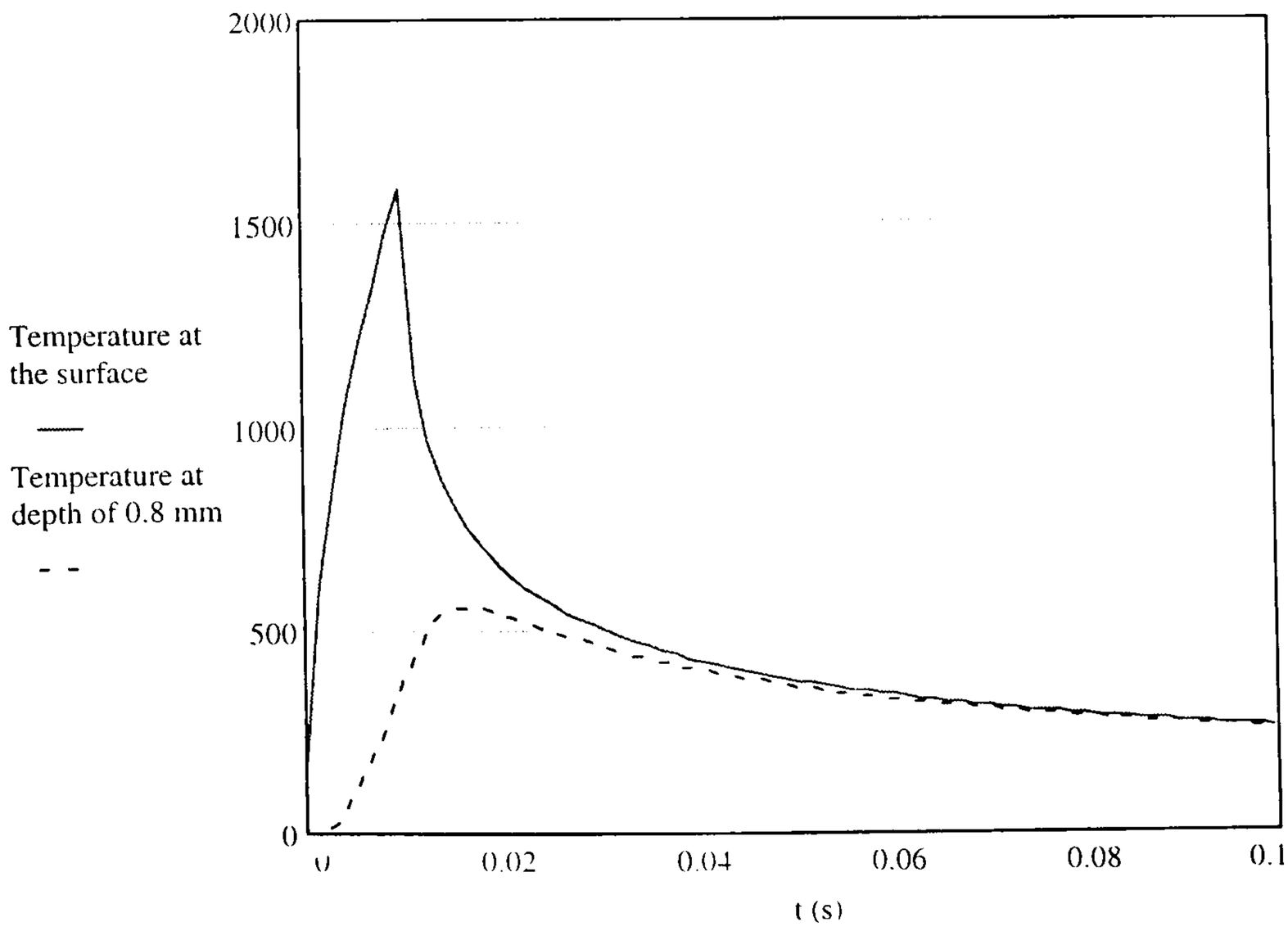

Figure 10 The temperature change of welding at different depth of workpiece for normal welding at z = 0 (——) and at z = 0.8mm (- - - - -)